FERMILAB-DESIGN-1996-01

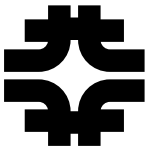

Fermi National Accelerator Laboratory

FERMILAB-Pub-96/390-E
CDF

The CDF II Detector Technical Design Report

The CDF II Collaboration

Fermi National Accelerator Laboratory
P.O. Box 500, Batavia, Illinois 60510

November 1996

Operated by Universities Research Association Inc. under Contract No. DE-AC02-76CH03000 with the United States Department of Energy

Disclaimer

Distribution

FERMILAB-DESIGN-1996-01

The CDF II Detector

Technical Design Report

Chapter 1

Overview

1.1 Introduction

For the next decade, the Fermilab Tevatron Collider remains the high energy frontier of particle physics. The luminosity enhancement provided by the Main Injector dramatically increases the discovery reach and, in conjunction with the upgrade of the collider detectors, moves the experimental program into a regime of *precision* hadron collider physics. Precision capability at the energy frontier will allow simultaneous attack on the open questions of high energy physics from many complementary directions, including:

- characterization of the properties of the top quark
- a global precision electroweak program
- direct search for new phenomena
- tests of perturbative QCD at Next-to-Leading-Order and large Q^2
- constraint of the CKM matrix with high statistics B decays

Each of these topics has the potential for revealing new physics; taken together they offer the most comprehensive discovery potential anywhere in particle physics for at least another decade.

The high luminosity Tevatron of Run II requires extensive changes to the experimental apparatus. We have applied 10 years of experience with CDF and Tevatron physics in the design of an upgraded CDF detector with many powerful new features. This report is a description of the design and expected performance of this upgrade, which we call CDF II.

We devote the rest of Chapter 1 to some history, a tabulation of our design goals, and a brief overview of the upgrade detector and project plan.

In Chapter 2 we motivate the detector design with a quick review of the physics program, extrapolating from our understanding of Run I to the prospects for Run II.

Chapters 3 through 7 describe the motivation and implementation of the CDF II integrated tracking system, and its expected performance for tracking and b-tagging out to $|\eta| = 2$ and in the presence of multiple interactions.

Chapter 8 describes the reuse of the central calorimeter, and Chapter 9 describes the new scintillating tile calorimeter in the plug region.

Chapter 10 describes the improvements to the central muon systems and the addition of muon coverage beyond $|\eta| = 1.0$.

Chapter 11 describes the new pipelined data acquisition system with bandwidth increased by a factor of ten over the old design.

Chapter 12 describes the new deadtimeless trigger system, with tracking at Level-1 and impact parameter discrimination at Level-2.

Chapter 13 describes the off-line computing challenge and Chapter 14 describes the needed facilities support, including the continued use of the superconducting solenoid.

We are confident that this design and a data set increased by a factor of 20 or more will put CDF II and the Tevatron in the exciting position to discover physics beyond the Standard Model.

1.2 History

The Collider Detector at Fermilab (CDF) is a general purpose experiment for the study of $p\bar{p}$ collisions at $\sqrt{s} = 1.8$ TeV at the Fermilab Tevatron Collider. First collisions were produced and detected in October of 1985, and the Tevatron and CDF performance have evolved together to yield data sets of ever in-

creasing sensitivity:

- $\sim$ 25 nb^{-1} in 1987
- $\sim$ 4.5 pb^{-1} in 1988-1989 (Run 0)
- $\sim$ 19 pb^{-1} in 1992-1993 (Run Ia)
- $\sim$ 90 pb^{-1} in 1994-1996 (Run Ib)

During the 1988 run the Tevatron met and surpassed its design luminosity of 1×10^{30}cm^{-2}s^{-1}. The 1994 accumulation utilized instantaneous Tevatron luminosities in excess of 2×10^{31}cm^{-2}s^{-1}.

The particle physics returns on this steadily evolving sensitivity include the discovery of the top quark and an accurate measurement of its mass $m_t = 176.8 \pm 6.5$, precision measurement of $m_W = 80.41 \pm 0.180$ GeV/c^2, measurement of the inclusive jet cross section out to transverse energies of 400 GeV, precision measurement of many b hadron lifetimes, and many of the most stringent limits on non-standard processes. The complete CDF physics archive (see Chapter 15), as of 1 September 1996, is a collection of over 100 published papers ranging over the full state of the art in hadron collider physics.

1.3 Design Parameters

We describe here the relevant conditions of the Tevatron Run II environment, and the physics driven detector performance requirements which we demand there.

1.3.1 Accelerator Configuration

The stated goal of Tevatron Run II is the accumulation of 2 fb^{-1} at $\sqrt{s} = 2.0$ TeV, using luminosities up to 2×10^{32}cm^{-2}s^{-1}. This modest increase in the Tevatron energy has a major impact on physics, (for instance increasing the $t\bar{t}$ yield by 40%) but little impact on the detector performance. Detector issues are driven instead by the luminosity, the number of bunches, and the time between crossings.

The crossing time defines an overall time constant for signal integration, data acquisition and triggering. Two crossing times are discussed for Run II: 396 ns for 36 bunches and 132 ns for 108 bunches. With either of these short times, detectors with long collection times experience pile-up, and trigger and readout latency requires pipelines. Much of the CDF upgrade is necessitated by the new time structure.

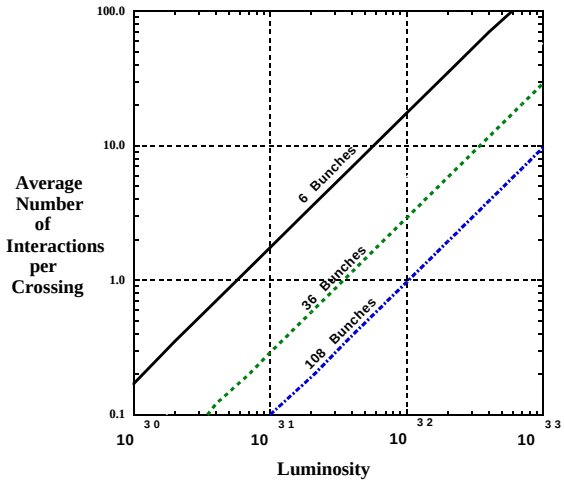

Figure 1.1: $\bar{N}$ for various conditions at CDF. 36 bunches $\equiv$ 396 ns crossings, 108 bunches $\equiv$ 132 ns crossings

The number of bunches and the luminosity together determine another key design input, $\bar{N}$, the average number of overlapping interactions in a given beam crossing. $\bar{N}$ is displayed as a function of luminosity and crossing rate in Fig 1.1.

This detector design targets two sets of operating conditions for Run II:

- $\mathcal{L} = 1 \times 10^{32}$cm^{-2}s^{-1}, 396 nsec bunch, $\bar{N} \sim 3$,
- $\mathcal{L} = 2 \times 10^{32}$cm^{-2}s^{-1}, 132 nsec bunch, $\bar{N} \sim 2$

$\bar{N}$ is Poisson-distributed, and a prudent design should be robust on the tails as well as the mean. To fix our upper limit, we recognize the possibility of the hypothetical, but not unreasonable situation

- $\mathcal{L} = 2 \times 10^{32}$cm^{-2}s^{-1}, 396 nsec bunch, $\bar{N} \sim 6$.

When occupancy or pile-up from multiple interactions are important, we will use the conditions N = 0, 3, and 6 extra overlapping minimum bias events to evaluate detector performance and margins.

1.3.2 Physics Performance Requirements

A comprehensive summary of the Tevatron Run II physics objectives is presented in Chapter 2. The complexity of the hadronic environment, coupled with the richness and frequent subtlety of the physics signatures, dictates a "general purpose" detection strategy:

- The detector should be able to trigger on and measure as many individual elements of each event as possible.

The ability to compare many independent measurements, across different samples, or even across the same event, leads to a powerful analysis framework where the data itself provides the ultimate precision in the calibration of the hardware and the control of systematic effects. With large data sets at the Tevatron Collider this precision can be applied in a surprising number of different regimes. For example:

- Classic "precision" measurements, such as $\delta m_W \leq 40$ MeV/c^2 and $\delta m_t \leq 3$ GeV/c^2.
- The baseline survey of the top sector, utilizing secondary vertex based flavor discrimination and precision kinematic reconstruction.
- The search for quark compositeness via the jet E_T spectrum, requiring detailed understanding of calorimeter response.

Many other examples from the physics program outlined in Chapter 2 lead to the following physics performance goals for the CDF II Detector. There are some new capabilities here but all of these goals are reasonable extrapolations based on performance achieved and understood in Run I. We emphasize that these are *goals*.

In either of the two main Run II Tevatron scenarios, CDF II should:

- Reconstruct charged particle tracks with efficiency greater than 95%, over the full range $|\eta| \leq 2.0$.
- Measure charged particle momenta with precision of $\delta p_T/p_T^2 = 0.1\%$ over the range $|\eta| \leq 1.0$, and with precision adequate for lepton identification, $\delta p_T/p_T^2 \sim 0.4\%$, over the range $1.0 \leq |\eta| \leq 2.0$.
- Trigger on, identify, and reconstruct the kinematics and charge of e and μ leptons with high efficiency over the full range $|\eta| \leq 2.0$.
- Tag secondary vertices with the greatest possible efficiency over the full range $|\eta| \leq 2.0$ and over the full interaction region, and trigger on displaced impact parameters over the widest practical range out to $|\eta| = 2.0$.
- Trigger on, identify, and reconstruct the kinematics of photons over the range $|\eta| \leq 2.0$.
- Trigger on and reconstruct jets over the range $|\eta| \leq 3.0$, measure jet energies with resolution of $\sigma_{E_T} = 10\% \cdot E_T + 1$ GeV and with absolute energy scale precision better than 2.5%.
- Measure particle types using dE/dx and time-of-flight in the region $|\eta| \leq 1.0$.

Most (but not all) of these goals will be met in the baseline proposal. See Sec. 1.5 for further detail on this point.

1.4 The CDF II Detector

CDF II is a general purpose solenoidal detector which combines precision charged particle tracking with fast projective calorimetry and fine grained muon detection.

The detector is shown in a solid cutaway view on the cover of this report, and in an elevation view in Fig. 1.2. Tracking systems are contained in a superconducting solenoid, 1.5 m in radius and 4.8 m in length, which generates a 1.4 T magnetic field parallel to the beam axis. The status of the solenoid is discussed in Chapter 14. Calorimetry and muon systems are all outside the solenoid. The main features of the detector systems are summarized below and described in greater detail in Chapters 3 to 12. We use a coordinate system where the polar angle θ is measured from the proton direction, the azimuthal angle ϕ is measured from the Tevatron plane, and the pseudo-rapidity is defined as $\eta = -\ln(\tan(\theta/2))$.

1.4.1 Tracking Systems

Efficient, precision charged particle tracking is at the heart of the CDF analysis technique. An incomplete catalog of some of the applications of charged particle tracking at the Tevatron Collider includes:

- Efficient, precision reconstruction of track momentum for measurements at both high (m_W) and low ($B \to J/\psi K$) p_T.
- The ability to combine tracks with information from EM calorimetry or muon chambers to provide efficient electron and muon identification with excellent purity at both the trigger and offline level.

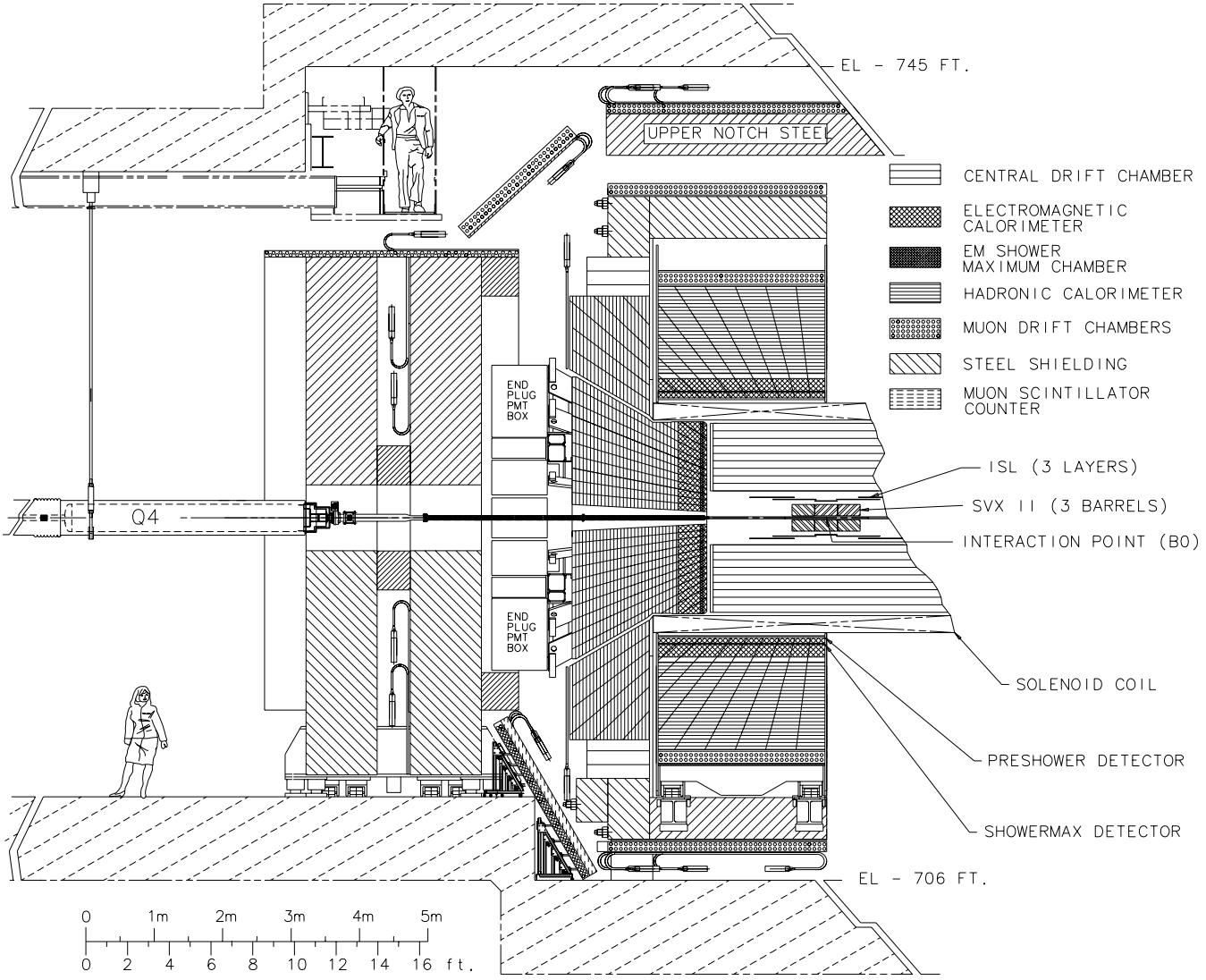

Figure 1.2: Elevation view of one half of the CDF II detector

- Precision reconstruction of track impact parameter and efficient reconstruction of tracks in dense jets, to provide b-tagging which is essential for top physics and searches for new phenomena.
- The ability to rule out tracks in combination with information from EM calorimetry in order to provide efficient photon identification at both the trigger and off-line level.
- The ability to collect low bias triggers on tracks alone.
- The measurement of isolated track momenta as the primary tool and starting point for the calibration of calorimeter response in both the EM and hadronic systems.
- Precision reconstruction of the interaction vertex z coordinate to allow counting and calibration of multiple interactions.
- The ability to map and quantify material in the tracking volume using the distribution of photon conversions.

To meet our physics goals we must maintain or improve the efficiency for these capabilities at high luminosity, and add these capabilities for tracks in the region $1.0 \leq |\eta| \leq 2.0$. At the same time, we wish to remedy the weaknesses of the Run I system, notably the mismatch between the acceptance and capabilities of the central drift chamber and the silicon vertex detector.

For Run II, we propose an optimized "integrated tracking system" shown schematically in Fig. 1.3. At large radii, a new open cell drift chamber, the COT, recovers the functionality of the CTC at high luminosity over the region $|\eta| \leq 1.0$. Inside the COT, a silicon "inner tracker" is built from two components. A micro-vertex detector at very small radii establishes the ultimate impact parameter resolution. Two additional silicon layers at intermediate radii provide p_T resolution and b-tagging in the forward region $1.0 \leq |\eta| \leq 2.0$, and *stand-alone* silicon tracking over the full region $|\eta| \leq 2.0$.

As discussed in Chapter 7, stand-alone silicon segments allow integrated tracking algorithms which maximize tracking performance over the whole region $|\eta| \leq 2.0$. We show there that a good signal to noise ratio for the silicon segments requires at least five measurements. Good efficiency then requires the addition of a sixth layer everywhere. This will be placed at 20 cm in the region $|\eta| \leq 1.0$ and at 22 cm in the region $1.0 \leq |\eta| \leq 2.0$. In the central region, the stand-alone silicon segment can be linked to the full COT track to give excellent p_T and impact parameter resolution. Beyond $|\eta| = 1.0$, where the COT acceptance and efficiency falls precipitously, a seventh silicon layer at 28 cm is required in order to recover acceptable p_T and impact parameter resolution for a stand-alone silicon track (not segment!) in that region.

The main parameters of the integrated tracking system are summarized in Table 1.1, and the system components are described briefly below, and in greater detail in Chapters 4, 5, and 6. The motivation of the system is described in greater detail in Chapter 3, and its performance is benchmarked in Chapter 7.

1.4.1.1 Central Outer Tracker: COT

Tracking in the region $|\eta| \leq 1.0$ will be done with an open cell drift chamber, the COT, covering radii between 44 and 132 cm. This device replaces the venerable CTC of Run 0 and Run I, which would suffer from severe occupancy problems at $\mathcal{L} \geq 1 \times 10^{32} cm^{-2} s^{-1}$.

The design goal of the COT is to reproduce the functionality of the CTC, but using small drift cells and a fast gas to limit drift times to less than 100 ns. The basic drift cell will have a line of 12 sense wires alternating with shaper wires every 3.8 mm, running down the middle of two gold-on-mylar cathode planes which are separated by $\sim$ 2 cm. Four axial and four stereo superlayers will provide 96 measurements between 44 and 132 cm, requiring a total of 2,520 drift cells and 30,240 readout channels. The wires and cathode planes are strung between two precision milled endplates, and the complete chamber is roughly 1.3% of a radiation length at normal incidence.

The COT is read out using a pipelined TDC which is standard for CDF II wire chamber systems, and the tracking information will be available for the Level-1 trigger.

The COT construction, operation, and off-line reconstruction draw heavily on the experience with the CTC, leading to a profound economy in time, expense, and code development. Scaling from the known CTC performance we expect comparable mo-

COT	
Radial coverage	44 to 132 cm
Number of superlayers	8
Measurements per superlayer	12
Readout coordinates of SLs	$+3^\circ$ 0 -3° 0 $+3^\circ$ 0 -3 0°
Maximum drift distance	0.88 cm
Resolution per measurement	180 μm
Rapidity coverage	$\|\eta\| \leq 1.0$
Number of channels	30,240
Material thickness	1.3% X_0
SVX II	
Radial coverage	2.4 to 10.7 cm, staggered quadrants
Number of layers	5
Readout coordinates	r-ϕ on one side of all layers
Stereo side	r-z, r-z, r-uv, r-z, r-uv (uv $\equiv 1.2^\circ$ stereo)
Readout pitch	60-65 μm r-ϕ; 60-150 μm stereo
Resolution per measurement	12 μm (axial)
Total length	96.0 cm
Rapidity coverage	$\|\eta\| \leq 2.0$
Number of channels	405,504
Material thickness	3.5% X_0
Power dissipated	1.8 KW
ISL	
Radial coverage	20 to 28 cm
Number of layers	one for $\|\eta\| < 1$; two for $1 < \|\eta\| < 2$
Readout coordinates	r-ϕ and r-uv (1.2° stereo) (all layers)
Readout pitch	110 μm (axial); 146 μm (stereo)
Resolution per measurement	16 μm (axial)
Total length	174 cm
Rapidity coverage	$\|\eta\| \leq 1.9$
Number of channels	268,800
Material thickness	2% X_0

Table 1.1: Design parameters of the baseline tracking systems

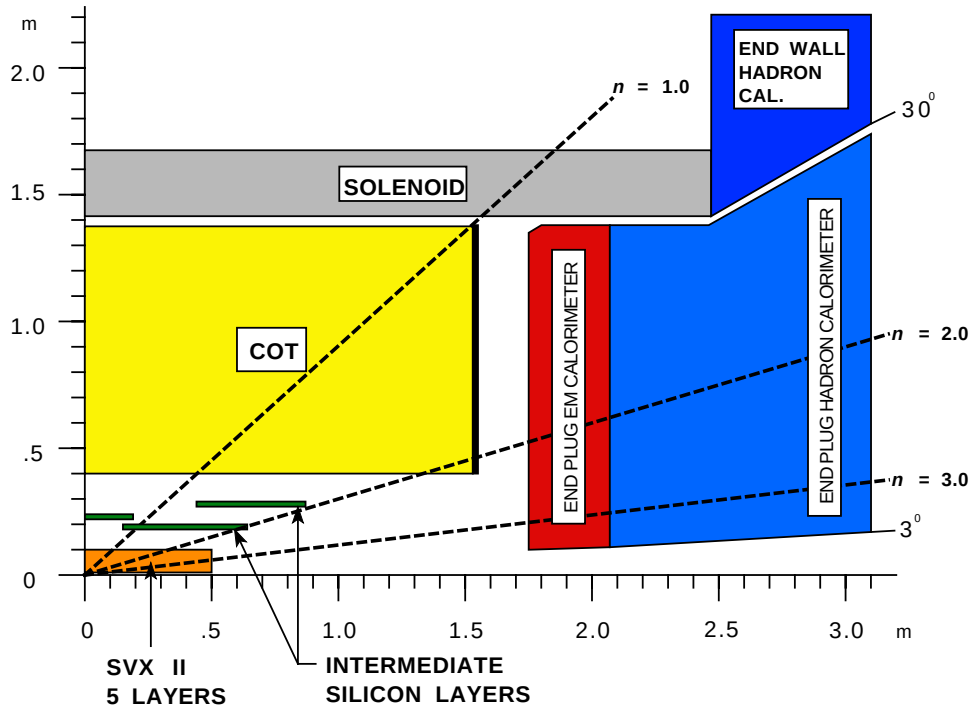

Figure 1.3: Longitudinal View of the CDF II Tracking System

mentum resolution (with SVX II or beam constraint), improved track pair separation, and much improved stereo pattern recognition up to luminosities of $2 \times 10^{32} cm^{-2} s^{-1}$ @ 132 ns. A detailed description of the COT is given in Chapter 4.

1.4.1.2 Inner Tracker: SVX II + ISL

CDF has established the viability and utility of silicon tracking at hadron colliders. For Run II, we propose a silicon "inner tracker" comprising a five-layer detector at small radii for micro-vertex detection and additional silicon layers at intermediate radii to provide stand-alone segment finding in the combined system. As discussed in Chapter 7, stand-alone silicon segments allow integrated tracking strategies which maximize tracking performance over the whole region $|\eta| \leq 2.0$.

SVX II: Silicon Vertex Detector

The silicon vertex detector will be built in three cylindrical barrels with a total length of 96 cm, covering $\sim 2.5\sigma$ of the luminous region, and leading to contained b-tagging in almost all events. Each barrel supports five layers of double sided silicon microstrip detectors between radii of 2.4 and 10.7 cm. Three of the layers combine an $r-\phi$ measurement on one side with 90° stereo measurement on the other, and the remaining two layers combine $r-\phi$ with small angle stereo at 1.2°.

The silicon crystals are supported by low mass substrates in assemblies called "ladders". Twelve ladders of the appropriate width make a layer, and the 60 ladders in each barrel are mounted between two precision-machined beryllium bulkheads which also carry the water cooling channels for the readout electronics.

The total of 405,504 channels in the system are connected to radiation-hardened readout chips mounted on electrical hybrids on the surface of the silicon detectors. Each readout chip set (SVX3) has 128 channels, each with a charge-sensitive amplifier, 42-cell dual-ported pipeline with four additional cells for buffers, and an ADC. A highly parallel fiber-based data acquisition system reads out the entire detector in approximately 10 μs.

The high speed and dual porting of the readout allows the SVX II information to be used for impact parameter discrimination in the SVT processor of the Level-2 trigger. The ability to *trigger on b's* adds to the power and generality of the CDF II events, ex-

tends the sensitivity to new phenomena, broadens the catalog of heavy flavor measurements, and provides important control samples for top measurements.

The radiation level at the inner layer is expected to be $\sim$ 0.5 MRad per fb^{-1}. The silicon sensors are expected to operate through inversion, up to a total dose of 1.0-1.5 MRad. A precision locking pin on the bulkheads allows the inner two layers to be removed and replaced with 3 μm accuracy.

ISL: Intermediate Silicon Layers

In the central region, a single ISL layer is placed at a radius of 22 cm. In the plug region, $1.0 \leq |\eta| \leq 2.0$, two layers of silicon are placed at radii of 20 cm and 28 cm. The mechanical problems associated with mounting silicon detectors at these radii are different (and less severe) than in the case of the micro-vertex detector, and in this sense it is logical to treat the ISL as a separate device. We emphasize however, that SVX II and ISL together are a single functional system which provides stand-alone silicon tracking and b-tagging over the full region $|\eta| \leq 2.0$.

Double sided silicon is used with 55 μm strip pitch on the axial side and 73 μm pitch on the stereo side with a 1.2° stereo angle. Every other strip is read out to reduce the total channel count to 268,800. Due to charge sharing through the intermediate strips, the single hit resolution perpendicular to the strip direction will be $\leq$ 16 μm on the axial side and $\leq$ 23 μm on the stereo side.

The silicon crystals are mounted in "ladder" assemblies similar to SVX II. The low radiation levels encountered at larger radii allow the use of longer strips to reduce the channel count. Three crystals are used in each ladder compared to two in SVX II. The ladders are mounted between carbon fiber disks

The ISL readout electronics are identical to the SVX II. The readout segmentation is in 30° wedges which exactly match the SVX II segmentation. This preserves the possibility of adding information from the ISL into the SVT trigger in the future.

1.4.2 Calorimeter Systems

Outside the solenoid, scintillator-based calorimetry covers the region $|\eta| \leq 3.0$ with separate electromagnetic and hadronic measurements. The CDF calorimeters have obviously played a key role in the physics program by measuring electron and photon energies, jet energies, and net transverse energy flow.

$\|\eta\|$ Range	$\Delta\phi$	$\Delta\eta$
0. - 1.1 (1.2 h)	15°	$\sim$ 0.1
1.1 (1.2 h) - 1.8	7.5°	$\sim$ 0.1
1.8 - 2.1	7.5°	$\sim$ 0.16
2.1 - 3.64	15°	0.2 - 0.6

Table 1.2: CDF II Calorimeter Segmentation

	Central	Plug
EM:		
Thickness	$19X_0, 1\lambda$	$21X_0, 1\lambda$
Sample (Pb)	$0.6X_0$	$0.8X_0$
Sample (scint.)	5 mm	4.5 mm
WLS	sheet	fiber
Light yield	160 pe/GeV	300 pe/GeV
Sampling res.	$11.6\%/\sqrt{E_T}$	$14\%/\sqrt{E}$
Stoch. res.	$14\%/\sqrt{E_T}$	$16\%/\sqrt{E}$
SM size (cm)	$1.4\phi\times$(1.6-2.0)Z	0.5×0.5 UV
Pre-shower size	$1.4\phi \times$ 65Z cm	by tower
Hadron:		
Thickness	4.5λ	7λ
Sample (Fe)	1 in. C, 2 in. W	2 in.
Sample (scint.)	10 mm	6 mm
WLS	finger	fiber
Light yield	$\sim$ 40 pe/GeV	39 pe/GeV

Table 1.3: Central and Plug Upgraded Calorimeter Comparison

As outlined in Sec 1.4.1, the ability to match tracks with projective towers and EM shower position in the central region has lead to a powerful analysis and calibration framework, including an understanding of the absolute jet energy scale to 2.5%.

For Run II, the existing scintillator-based central calorimeters will continue to perform well. However, the gas calorimeters in the region $\eta \geq 1.0$ are incompatible with the crossing rates for Run II, and will be replaced with a new scintillating tile plug calorimeter. As seen in Fig 1.4, the new calorimeter consists of an electromagnetic (EM) section followed by a hadronic section. In both sections the active elements are scintillator tiles read out by wavelength shifting (WLS) fibers embedded in the scintillator. The WLS fibers are spliced to clear fibers, which carry the light out to photomultiplier tubes (PMT) located on the back

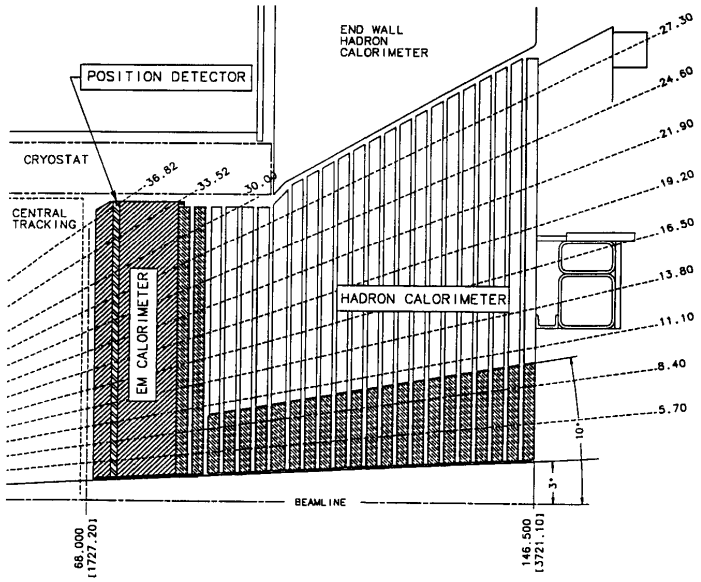

Figure 1.4: Cross section of upper part of new end plug calorimeter.

plane of each endplug.

The EM calorimeter is a lead/scintillator sampling device with a unit layer composed of 4.5 mm lead and 4 mm scintillator. There are 23 layers in depth for a total thickness of about 21 X_0 (radiation lengths) at normal incidence. The detecting elements are arranged in a tower geometry pointing back towards the interaction region. The energy resolution of the EM section is approximately $16\%/\sqrt{E}$ with a 1% constant term. The scintillator tiles of the first layer of the EM section are made out of 10 mm thick scintillator and are read out by multi-anode photomultipliers (MAPMTs). They will act as a pre-shower detector. A position detector is located at the depth of the EM shower maximum (approximately $6X_0$). This shower maximum detector is made of scintillator strips read out by WLS fibers; clear fibers carry the light to MAPMTs.

The hadron calorimeter is a 23 layer iron and scintillator sampling device with a unit layer composed of 2 inch iron and 6 mm scintillator. The existing iron of the CDF endplugs is used in the new hadron calorimeter: stainless steel disks are attached to the inner 10° cone to extend the coverage to 3°. Two additional stainless steel disks are added behind the electromagnetic section to increase the thickness of the hadron calorimeter. In this way the magnetic field in the tracking volume and the magnetic forces on the end plugs are unchanged. The hadron section has the same tower segmentation as the EM section.

With the completion of the upgrade, the CDF II calorimeters will have a uniform pattern of matched projective towers of EM and hadron calorimeters. The overall segmentation is given in Table 1.2. The common segmentation pattern continues to allow straightforward calorimetry trigger implementation. Both EM calorimeters have stereo shower maximum detectors as well as pre-shower capability. The EM sections are all lead scintillator sampling and the hadronic sections are iron scintillator sampling.

The central and plug upgrade calorimeters both have fast enough energy measurement response times to take full advantage of the 132 ns bunch spacing. Shower maximum and pre-shower functions in the plug upgrade are also fast enough, while the wire chamber pre-shower and shower maximum in the central system will need to integrate several bunches. A general comparison of the central and plug upgrade calorimeters is given in Table 1.3.

1.4.3 Muon Systems

CDF II will use four systems of scintillators and proportional chambers in the detection of muons over the region $|\eta| \leq 2.0$. The absorbers for these systems are the calorimeter steel, the magnet return yoke, additional steel walls, and the steel from the Run I forward muon toroids. The geometric and engineer-

	CMU	CMP/CSP	CMX/CSX	IMU
Pseudo-rapidity coverage	$\lvert\eta\rvert \leq\sim 0.6$	$\lvert\eta\rvert \leq\sim 0.6$	$\sim 0.6 \leq \lvert\eta\rvert \leq\sim 1.0$	$\sim 1.0 \leq \lvert\eta\rvert \leq\sim 1.5$
Drift tube cross-section	2.68 x 6.35 cm	2.5 x 15 cm	2.5 x 15 cm	2.5 x 8.4 cm
Drift tube length	226 cm	640 cm	180 cm	363 cm
Max drift time	800 ns	1.4 μs	1.4 μs	800 ns
Total drift tubes (present)	2304	864	1536	none
Total drift tubes (Run II)	2304	1076	2208	1728
Scintillation counter thickness		2.5 cm	1.5 cm	2.5 cm
Scintillation counter width		30 cm	30-40 cm	17 cm
Scintillation counter length		320 cm	180 cm	180 cm
Total counters (present)		128	256	none
Total counters (Run II)		269	324	864
Pion interaction lengths	5.5	7.8	6.2	6.2-20
Minimum detectable muon p_T	1.4 GeV/c	2.2 GeV/c	1.4 GeV/c	1.4-2.0 GeV/c
Multiple scattering resolution	12 cm/p (GeV/p)	15 cm/p	13 cm/p	13-25 cm/p

Table 1.4: Design Parameters of the CDF II Muon Detectors. Pion interaction lengths and multiple scattering are computed at a reference angle of $\theta = 90°$ in CMU and CMP/CSP, at an angle of $\theta = 55°$ in CMX/CSX, and show the range of values for the IMU.

ing problems of covering the full η region using these absorbers leads to the four logical systems, but as seen in Table 1.4, they are all functionally similar.

The central muon systems functioned well in Run I, and changes for Run II represent incremental improvements. New chambers will be added to the CMP and CMX systems to close gaps in the azimuthal coverage. Each of these additions presents interesting mechanical problems discussed in detail in Chapter 10. In the CMU system, the cell ganging scheme will be changed from alternate cells to adjacent cells, improving the granularity at the trigger level from a 5° azimuthal arc to 2.5°. In addition, because of the high rates in Run II, the CMU chambers will be run in proportional, rather than limited streamer mode, and this requires that gain be recovered by installing new pre-amplifiers on the chambers. In the CMP system, new pre-amps will eliminate intermittent problems with oscillations. In all of these systems, the long drift times relative to the beam crossing time necessitate a pipelined TDC, which is described in detail in Secs. 11.3 and 11.4.

Detailed studies of occupancy and aging for these systems have been performed using the the Run I data set. Extrapolating these results to Run II conditions, including the absence of the Main Ring, and beam pipe shielding, we expect that these systems will show *improved* performance in Run II. Further detail can be found in Chapter 10.

The CDF II tracking system, particular the ISL, provides a new capability for muon detection, the ability to reconstruct trajectories with $|\eta| > 1.0$ in the solenoid, where the resolution is not dominated by multiple scattering. The region contiguous with the present coverage, $1.0 \leq |\eta|$ and extending out to $|\eta| \sim 2.0$ is most important for improved acceptance for the decays of heavy centrally produced objects. The Run I forward muon system, even if pushed up, would cover only $|\eta| \geq 1.5$, and worse, has low granularity which translates into high occupancy and uncertain efficiency at the high luminosities of Run II.

These considerations motivate the replacement of the forward muon system with a new Intermediate Muon System (IMU), covering from $1.0 \leq |\eta| \leq 1.5$ with fine granularity, and providing coverage sufficient to identify isolated high p_T tracks as muons or hadrons between $\eta = 1.5$ and $\eta = 2.0$. The IMU consists of a barrel of drift chambers and scintillation counters around the present FMU toroid steel, with additional counters between the toroids and on the endwall to provide additional projectivity at the trigger level. The IMU chambers and counters are virtually identical to the existing central muon detectors and use the same readout electronics. The toroids will not be energized; the p_T measurement will be provided by the tracking systems. The IMU system

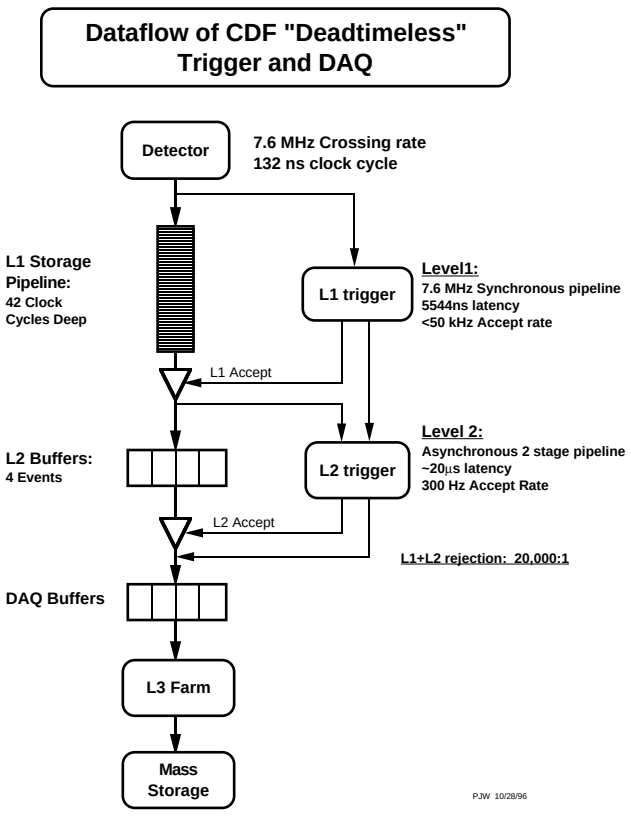

Figure 1.5: Functional block diagram of the CDF II data flow

covers more solid angle and in the more crucial region of lower η than the FMU, will have improved momentum resolution and corresponding trigger improvements, and will operate at luminosities substantially greater than expected during Run II. Further detail on this system can be found in Sec. 10.6.

1.4.4 Electronics and Triggering

The CDF electronics systems must be substantially altered to handle Run II accelerator conditions. The increased instantaneous luminosity requires a similar increase in data transfer rates. However it is the reduced separation between accelerator bunches that has the greatest impact, necessitating a new architecture for the readout system.

Figure 1.5 shows the functional block diagram of the readout electronics. To accommodate a 132 ns bunch-crossing time and a 4 μs decision time for the first trigger level, all front-end electronics are fully pipelined, with on-board buffering for 42 beam crossings. Data from the calorimeters, the central tracking chamber, and the muon detectors are sent to the Level-1 trigger system, which determines whether a $\bar{p}p$ collision is sufficiently interesting to hold the data for the Level-2 trigger hardware. The Level-1 trigger is a synchronous system with a decision reaching each front-end card at the end of the 42-crossing pipeline. Upon a Level-1 trigger accept, the data on each front-end card are transferred to one of four local Level-2 buffers. The second trigger level is an asynchronous system with an average decision time of 20 μs.

A Level-2 trigger accept flags an event for readout. Data are collected in DAQ buffers and then transferred via a network switch to a Level-3 CPU node, where the complete event is assembled, analyzed, and, if accepted, written out to permanent storage. These events can also be viewed by online monitoring programs running on other workstations.

1.4.4.1 Front-End Electronics

The installation of new scintillator-based calorimeters in the plug region allows a common design to be used for much of the front-end electronics for the central and plug calorimeters and their associated preradiators and shower-maximum detectors. The calorimeter ADC readout is based on the QIE (Charge Integrating and Encoding) chip, a custom multi-ranging circuit developed for the KTEV experiment. A VME based front-end board carries the QIE, a commercial ADC, and programmable circuits to perform pipelining, buffering, and the creation of traverse-energy sums for the trigger. A simplified version of the QIE design is used for all shower maximum and pre-shower detectors.

Dynode signals from the phototubes for the central, wall, and plug hadron calorimeters will be discriminated and timed using the custom pipelined TDC chip described below.

Analog drift time signals from the COT are first processed using a custom chip, ASD, optimized for the straw systems in the SDC and ATLAS detectors. The eight channel chip has a fast, low noise preamplifier, ion tail cancellation, and a discriminator. The ASD's are mounted on printed circuit boards on the chamber endplate. The discriminated signals are read out with a custom multi-hit TDC, JMC96, which encodes leading and trailing edge information, and has the 5.3 microsecond Level-1 buffer and four Level-2 buffers on-chip. The design includes a full custom integrated circuit, 96 channel VME

boards, and a calibration system.

As described above in Sec. 1.4.3, we are building new preamps and ASD's for the central muon system, CMU, and changing the mother-board system (but not the pre-amplifier) for the CMP muon system. Drift time information from all muon systems will be recorded using the JMC96 TDC.

1.4.4.2 Data Acquisition

A block diagram of the data acquisition system is shown in Fig. 1.6. The basic architecture is very similar to that used successfully in Run Ib. Front-end and trigger electronics are housed in VME crates replacing the FASTBUS and RABBIT crates used in the original detector. Timing signals associated with the beam crossing are distributed to each crate by the Master-Clock subsystem. Trigger decision information is distributed by the Trigger-System-Interface subsystem. Commercial processors read data from modules in their local crate and deliver it to the VME Readout Boards (VRBs) and the Event-Building subsystem. This system concentrates the data and delivers it to the Level-3 trigger subsystem through a commercial network switch. The Level-3 trigger is a "farm" of parallel processors, each fully analyzing a single event. The Data-Logging subsystem delivers events to mass storage and also to online monitoring processes to verify that the detector, trigger, and data acquisition system are functioning correctly. While the architecture is similar to the Run Ib system, many individual components will be upgraded or replaced. This is necessary to deal with the new VME-based front-end electronics, and to provide increased throughput required for the higher luminosity now expected in Run II. Also, in some cases commercial products in the Run Ib system are no longer supported by the manufacturer and must be replaced.

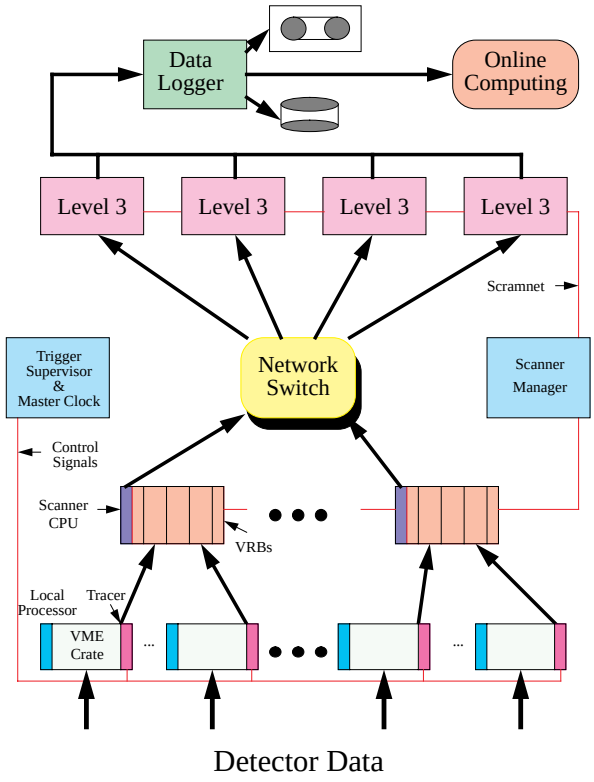

Figure 1.6: A schematic of the CDF II Data Acquisition system, showing data flow from the front-end and trigger VME crates to the Online Computing system.

1.4.4.3 Trigger

In Run Ib, the trigger had to reduce the raw collision rate by a factor of 10^5 to reach < 10 Hz, an event rate that could be written to magnetic tape. With an order of magnitude increase in luminosity for Run II, the trigger must have a larger rejection factor while maintaining high efficiency for the broad range of physics topics we study.

We will use a tiered "deadtimeless" trigger architecture. The event is considered sequentially at three levels of approximation, with each level providing sufficient rate reduction for the next level to have minimal deadtime. Level-1 and Level-2 use custom hardware on a limited subset of the data and Level-3 uses a processor farm running on the full event readout. The trigger, like the DAQ, is fully pipelined, and has improved background rejection over Run I from additional detector information to be supplied to the Level-1 and Level-2 systems.

The block diagram for the CDF II trigger system is presented in Fig. 1.7. The most significant change for Level-1 is the addition of track finding, which was previously available only at Level-2. This allows a track to be matched to an electromagnetic-calorimeter energy cluster for improved electron identification, or to a stub in the muon system for better muon identification and momentum resolution. Also, tracks may be used alone for triggers such as $B^0 \to \pi^+\pi^-$. A Level-1 accept can also be generated based on calorimeter energy, $\not\!\!E_T$, or the kinematic properties of observed track pairs.

Events accepted by the Level-1 system are pro-

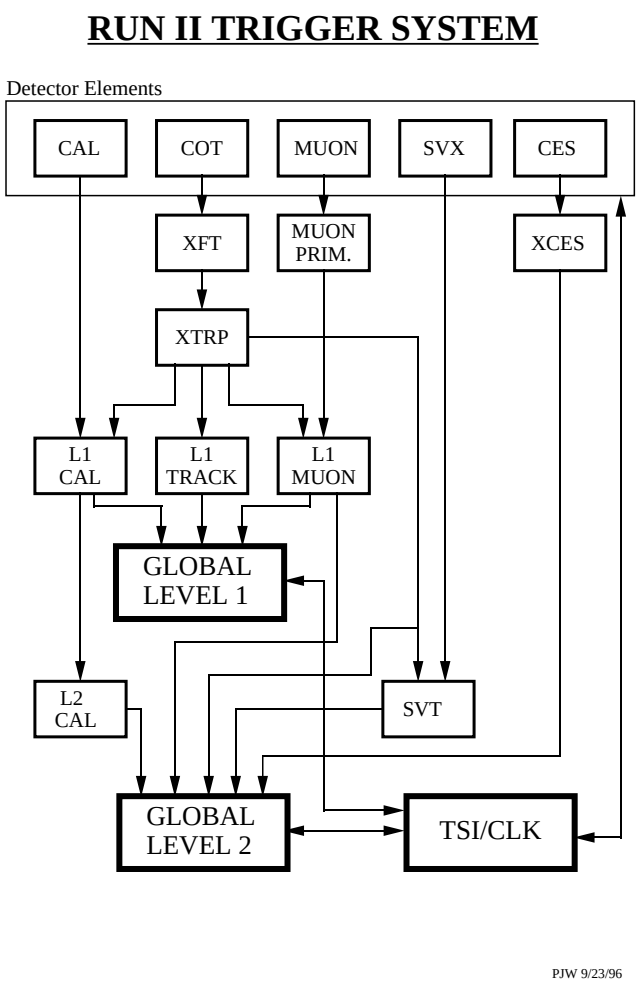

Figure 1.7: Block diagram of the CDF II trigger system.

cessed by the Level-2 hardware, which will also have more and improved input data. The Silicon Vertex Tracker (SVT) will provide, for the first time in a hadron-collider experiment, the ability to trigger on tracks with large impact parameters. This will make accessible a large number of important processes involving hadronic decay of b-quarks, such as $Z \to b\bar{b}$, $B^0 \to \pi^+\pi^-$, and exotic processes like SUSY and Technicolor that copiously produce b quarks. The Level-2 system will have improved momentum resolution for tracks, finer angular matching between muon stubs and central tracks, and data from the central shower-max detector (CES) for improved identification of electrons and photons. Jet reconstruction is provided by the Level-2 cluster finder, which, although rebuilt for the new architecture, retains the same algorithm used successfully in previous running.

The trigger system is very flexible and will be able to accommodate over 100 separate trigger selections. With a 40 kHz accept rate at Level-1 and a 300 Hz rate out of Level-2, we expect to limit deadtime to $< 10\%$ at full luminosity, while writing events to mass storage at 30-50 Hz. Rates for the more challenging signatures are discussed at the end of Chapter 12.

1.5 The CDF II Upgrade Plan

Our goal is to rebuild CDF into CDF II as quickly as possible, and resume data taking at the Tevatron in a timely way after the completion of the Main Injector.

Because of the realities of budget and schedule, our proposal for CDF II accepts some compromises to the goals outlined in Sec. 1.3.2. In particular, we will defer further discussion of the time-of-flight system and full trigger capability at $|\eta| \geq 1.0$ until the baseline detector described in this document is convincingly in hand.

This document is the TECHNICAL DESCRIPTION of the baseline CDF II detector. Additional documents describe the managerial, cost, and schedule aspects of the project:

- CDF Project Management Plan
- Memoranda of Understanding (MOU) and Work Plans for each subproject
- Cost and Schedule Plan
  - Task-based resource-loaded schedule, including labor estimates
  - Cost Estimate and Work Breakdown Structure (WBS), including contingency analysis
  - WBS Dictionary
  - Financial Plan for U.S. and non-U.S. funding

1.5.1 Outlook

The baseline scope of the detector proposed here meets every goal for a rejuvenated detector capable of operations with the Tevatron + Main Injector at $\mathcal{L} = 2 \times 10^{32}\text{cm}^{-2}\text{s}^{-1}$ and 132 ns bunch spacings.

- The tracking system will be a fully optimized combination of drift chamber and silicon with powerful redundancy that insures excellent pattern recognition, momentum resolution, and b-tagging out to $|\eta| = 2$, even in the presence of multiple interactions.

- The calorimetry will be exclusively scintillator based, fast, and have resolution equal to or better than the existing detector.
- The muon system will have almost full azimuthal coverage in the central region, and expanded coverage out to $|\eta| = 2.0$.
- The electronics will be fully compliant with the 132 ns bunch crossing in every channel, and the data acquisition system and Level-3 trigger will be capable of 300 Hz operation.
- The trigger will be deadtimeless, ready for every crossing, with tracking information at Level-1 and impact parameter discrimination at Level-2.

This design reflects the accumulated experience of a decade of physics with CDF at the Tevatron. With CDF II and anticipated data sets in excess of 2 fb^{-1} in Run II, we look forward to major discoveries at Fermilab in the decade to come.

Chapter 2

Physics Goals

2.1 Overview

In this chapter we will outline the physics prospects of CDF II at the Tevatron + Main Injector, and the connection between the physics and the detector design. Our physics plan encompasses five complementary lines of attack on the open questions of the Standard Model:

- characterization of the properties of the top quark
- a global precision electroweak program
- direct search for new phenomena
- tests of perturbative QCD at Next-to-Leading-Order and large Q^2
- constraint of the CKM matrix with high statistics B decays

This physics program is comprehensive in its methods and its scope. It has classic precision measurements, such as m_W and α_s, taken to a new level of accuracy; it has a survey of newly discovered territory, in the first complete study of the top quark; and it extends our reach for new phenomena into a regime where current theoretical speculation suggests new structure. We believe that power of the CDF II detector combined with the sensitivity of the Run II data sets will result in a significant advance in our understanding of the behavior of matter at high energy, if not outright discovery of new physics beyond the Standard Model.

In this chapter we will justify this claim. We begin with a summary of our conclusions and then turn to each of the five topics in detail. Since CDF II re-uses or extends many of the same detector technologies and strategies as its predecessor, the physics analyses of Run II will employ many of the techniques refined during Run I. The physics projections and detector specifications will therefore frequently appeal to a brief review of the current status. We note in this vein that our conclusions have the power of direct extrapolations from a well tuned device in a well measured environment.

2.1.1 Summary of CDF II Physics

Table 2.1 shows the expected yields for some benchmark processes with 2 fb^{-1}of Tevatron collisions recorded by the CDF II detector. These are the numbers of identified events available for offline analysis. The statistical precision of Run II, combined with capability of the CDF II detector, will provide rich programs of measurement in each of the five sub-fields, summarized below.

2.1.1.1 Properties of the Top Quark

A sample of almost 1,000 b-tagged, identified events will allow a detailed survey of the properties of the top quark. A review of this program is given in Section 2.2.

The top mass will be measured with a precision conservatively estimated to be 3.5 GeV/c^2. The total cross section will be measured to 9%, and non-standard production mechanisms will be resolvable down to total cross sections of $\sim$ 90 fb. The branching fraction to b quarks will be measured to 3%, decays to non-W states may be explored at the level of 9%, and branching ratios to the various W helicity states will be measured with uncertainties of order 5%. The magnitude of any FCNC decay will be probed down to branching fractions of 1% or less. We will isolate the electroweak production of single top, allowing determination of , ($t \to Wb$) to 26%, and inference of $|V_{tb}|$ with a precision of 13%.

Mode	Yield (2 fb^{-1})
TOP	
dilepton	150
$W + 3j * b$	900
$W + 4j * b$	725
$W + 4j * bb$	180
VECTOR BOSONS	
$W \to l\nu$ (e,μ)	4.3M
$Z \to l^+l^-$(e,μ)	600K
$W\gamma, W \to e\nu$	4.0K
$Z\gamma, Z \to e^+e^-$	1.8K
$W^+W^- \to l\nu l\nu$	200
$W^+Z^- \to l\nu ll$	50
QCD	
j + X, $|\eta| \leq 1.0, E_T \geq$300 GeV	6.4K
jj + X, $M_{jj} \geq$ 600 GeV	30K
γ + X, $p_T(\gamma) \geq$ 25 GeV	6.0M
$\gamma\gamma$ + X, $p_T(\gamma_1, \gamma_2) \geq$ 12 GeV	14 K
$W+ \geq 1j$, $E_T(W) \geq$ 100 GeV	10K
$Z+ \geq 1j$, $E_T(Z) \geq$100 GeV	1.0K
B	
$B^0 \to J/\psi K_S$	15K
$B^0 \to \pi^+\pi^-$	10K
$B_s \to J/\psi\phi$	9K

Table 2.1: Representative yields for known processes, after selection. We use the CDF Run I selections modified for increased coverage of the CDF II detector (see text) and we assume 2.0 TeV collisions. $j \equiv$ jet, and $j*b \equiv$ b-tagged jet.

The final top physics program will undoubtedly be richer than this list, which should be interpreted as a catalog of probable sensitivities for the baseline top survey and whatever surprises the top may have in store.

2.1.1.2 A Precision Electroweak Program

The study of the weak vector bosons at the Tevatron is anchored in the leptonic decay modes. The new plug, intermediate muon system and integrated tracking will give triggerable electron coverage out to $|\eta| = 2.0$, triggerable muon coverage out to $|\eta|$ of at least 1.2 and taggable muon coverage out to $|\eta| = 2.0$. This will double the number of $W \to e\nu$ events and *triple* the acceptance for Z's and dibosons in the electron and muon channels. A data set of 2 fb^{-1}in combination with the acceptance and precision of the CDF II detector results in the comprehensive program in electroweak physics discussed in detail in Section 2.3.

One of our main goals is the measurement of m_W with a precision of $\pm$40 MeV/c^2. The combined precision on m_W and m_{top} will allow inference of the Standard Model Higgs mass m_H with precision of $\sim 2m_H$.

The W decay width, , $_W$ will be measured to 30 MeV, a factor of six improvement on the LEP-II expectation. The precision on A_{FB} at the Z^0 pole will be adequate to measure $sin^2\theta_W^{eff}$ to comparable precision to LEPI and SLD, and measurement off the pole will be sensitive to new phenomena at high mass scales. Limits on anomalous WWV and ZZγ couplings, bolstered by the forward tracking and lepton identification, will be comparable and complementary to those of LEP-II. The W charge asymmetry measurement, also augmented by unambiguous lepton ID in the plug region, will provide much improved constraints on parton distribution functions.

2.1.1.3 Search for New Phenomena

At the Tevatron+Main Injector, CDF II will search for new objects at and above the electroweak scale. There is at present a great deal of theoretical activity focussed on new phenomena in this regime, with predictions from models invoking supersymmetry, technicolor, and new U(1) symmetries. The magnitude of the top quark mass and speculation about an excess in the top cross-section have led to other theoretical predictions about phenomena well within our reach in Run II, such as topcolor. Search strategies for these and other models are discussed in Section 2.4.

We will be sensitive to charginos up to 130 GeV/c^2, to gluinos up to 270 GeV/c^2, and to stop squarks up to 150 GeV/c^2. Second generation lepto-quarks can be observed up to masses of 300 GeV/c^2, new vector bosons can be probed up to masses of 900 GeV/c^2, and excited quarks up to 800 GeV/c^2. Quark compositeness can be observed up to a scale of approximately 5 TeV. These are all model dependent limits, and, as in the case of the top survey above, we believe that our catalog of prospects here is best interpreted as a list of probable sensitivities for the real surprises waiting at the electroweak scale.

2.1.1.4 Precision QCD at Large Q^2

The QCD sector of the Standard Model will be stringently tested using the production and fragmentation properties of jets, and the production properties of W/Z bosons, Drell-Yan lepton pairs, and direct photons. We will evaluate the precision of QCD calculations beyond leading order (higher order perturbative calculations and soft gluon resummation corrections), and determine the fundamental input ingredients, namely parton distribution functions and the running coupling constant α_s.

The precision of QCD measurements at CDF II with 2 fb^{-1} will provide sensitivity to many sources of new physics. For example, the strong coupling constant α_s will be measured over the entire range $(10\text{'s}\ GeV)^2 < Q^2 < (500\ GeV)^2$, and deviations from the Standard Model running could signal loop contributions from new particles. A direct search for the substructure of quarks at the level of 10^{-19}m will be possible with high E_T jets and the production angular distribution of di-jets. Finally a broad range of searches will be carried out for the decays of massive particles to various combinations of jets, W/Z bosons, photons and neutrinos via missing E_T. A survey of the sensitivity of these QCD studies to new physics is presented in Section 2.5 of this report.

2.1.1.5 Constraining the CKM Matrix

CDF II plans to take advantage of the copious production of the various species of b hadrons at the Tevatron to make measurements which will test the consistency of the Standard (CKM) Model of weak quark mixing and CP violation. By extending the capabilities developed in Run I into Run II, CDF II expects to be able to measure CP asymmetries in $B^0 \to J/\psi K_S$ and $B^0 \to \pi^+\pi^-$ decays with a precision comparable to the e^+e^- colliders. Complementary information will come from a sensitive search for CP violation in $B_s \to J/\psi\phi$ decays. The effects of mixing in the $B_s^0 - \bar{B}_s^0$ system will be measured, allowing a determination of the ratio of CKM elements $|V_{td}/V_{ts}|$ over the full range allowed by the Standard Model.

In addition CDF II will continue to improve the precision on measurements of b hadron decay properties (*e.g.* B^0 vs. B^+ lifetimes) and pursue the observation and study of rare decays (*e.g.* $B^0 \to K^{*0}\mu^+\mu^-$). The physics of heavier b hadrons, for instance B_c, will be the exclusive domain of the Tevatron collider for at least the next decade. An overview of CDF II expectations for B physics in Run II is given in Section 2.6.

2.1.2 Physics and Detector

Exploitation of the statistical precision available in Run II will depend heavily on a thorough understanding of the detector. Two aspects are critical: the identification of objects that make up each signature, and the understanding of the calibration and resolution of the detector.

The objects for which we have already a good understanding of the efficiencies and fake-rates are those for which tracking is essential: electrons, muons, tau's, b's, and photons (*i.e.*, a high confidence of the absence of a track), all in the central region. Much of our discussion below concerns our ability to maintain, improve, and extend tracking capabilities pertinent to each of the physics objects.

Similarly, the energy scale and resolutions of the calorimeters, critical to the reconstruction of masses, are well understood in the central region, where the precision tracking information can be used to calibrate the calorimeters. This calibration procedure relies on an interlocking set of samples and capabilities, and exemplifies the power of the "general purpose" strategy (see Sec. 1.3.2). Further description of the calorimeter calibration can be found in Sec. 3.1.

In CDF II, the integrated tracking, the new plug calorimeter, and the intermediate muon system will extend the 'good' region where tracking is robust for e, μ, τ, γ and b identification, and will provide the precision calorimeter calibration out to $|\eta| = 2$.

2.1.3 Detailed Discussion

The scientific prospects for CDF II are discussed in more detail in the following sections of this chapter.

The physics opportunities detailed here provide much of the rationale for the CDF II Upgrade design choices, and the discovery prospects detailed here underscore our excitement about completing this upgrade and returning to high luminosity data taking at the Fermilab Tevatron Collider as quickly as possible.

2.2 Properties of the Top Quark

The top quark, with mass ~ 175 GeV/c^2, is strongly coupled to the electroweak symmetry breaking mechanism, and decays to a real W and a b-quark before hadronizing. A program to characterize the properties of this unconventional fermion is an obvious scientific priority. The accessibility of the top quark at the Fermilab Tevatron, in conjunction with the planned luminosity and detector upgrades for Run II, creates a new arena for experimental particle physics at an existing facility, and we should fully exploit this unique opportunity over the next decade.

Tevatron Run I brought the discovery of the top quark, the first direct measurements of its mass and cross section [2, 3, 4], and valuable first experience in top quark physics. We established techniques to identify b-quark jets using secondary vertices and soft leptons from the decays $B \to \ell\nu X$, and the essential utility of b-tagging in the isolation of the top signal and the reconstruction of the final state. We established techniques for the accurate measurement of the mass and decay kinematics of a heavy object in final states with jets, and the essential utility of *in situ* jet calibration techniques. We have begun to explore a variety of other measurements, all of them presently limited by statistics.

Armed with this experience, we have considered the program of Top Quark Physics accessible at CDF II with 2 fb^{-1} at the Tevatron [1]. Our study differs from the usual "future program" proposal by being grounded in a well understood detector in a well studied environment. We will show that the CDF II detector will be capable of a complete characterization of the main properties of the top quark, and we will establish the probable precisions that can be achieved using 2 fb^{-1} of Tevatron collider data.

We begin here by reviewing the top analysis results of Run I. Next, we discuss the impact of the detector upgrade components on the top physics of Run II. Finally we describe the Run II top physics program, including yields, the mass measurement, production properties, branching ratios, and decays.

2.2.1 Review of Run I Analysis

Using 19.3 pb^{-1} from Run Ia, CDF presented initial evidence for the top quark in the spring of 1994 [2]. A year later, with an additional 48 pb^{-1} from Run Ib, CDF confirmed its original evidence for the top quark[3]. We describe below the isolation of the signal in several different decay modes and the measurements made with these first small samples.

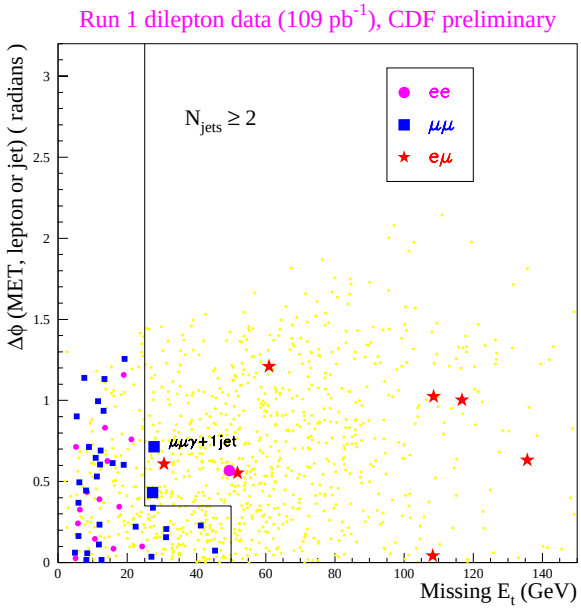

Figure 2.1: $\Delta\phi$ vs. $\not\!\!E_T$ in the dilepton sample. The small grey dots are the result of a $t\bar{t}$ Monte Carlo simulation with $m_{top} = 175$ GeV/c^2.

2.2.1.1 Dilepton Mode

In the standard model, the t and $\bar{t}$-quarks both decay almost exclusively to a W-boson and a b-quark. In the "dilepton" channel, both W's decay leptonically ($W \to \ell\nu$), and we search for leptonic W decays to an electron or a muon. The nominal signature in this channel is two high-P_T leptons, missing transverse energy (from the two ν's), and two jets from the b-quarks. Acceptance for this channel is small, mostly due to the product branching ratio of both W's decaying leptonically (only about 5%). In the 110 pb^{-1} from Run I, CDF observed 7 $e\mu$ events, 2 $\mu\mu$ events, and 1 ee event. Figure 2.1 shows the 10 candidate events in the parameter space $\Delta\phi$ (the angle between the $\not\!\!E_T$ and the nearest lepton or jet) vs $\not\!\!E_T$ (the missing transverse energy) as well as where one would expect top to lie. The background estimate for the dilepton channel is 2.1 ± 0.4 events[3]. Although not *a priori* part of the search, we examine the jets in dilepton events for indications that they originated from b-quarks. In the 10 dilepton events, we find 6 jets in 4 events (1 $\mu\mu$ and 3 $e\mu$) which

are identified ("tagged") as b-jets. This provides evidence for b-quarks produced in association with two W's, as expected from the decay of a $t\bar{t}$ pair.

CDF has also investigated top decays involving the τ-lepton. We have searched for dilepton events with one high-p_T electron or muon and one hadronically decaying τ-lepton which is identified using tracking and calorimeter quantities[7]. As in the $e\mu, ee$, or $\mu\mu$ channel two jets from b-quarks and significant missing transverse energy are required. Due to the additional undetectable τ-neutrino, the τ hadronic branching ratio and the lower efficiency for τ identification, the acceptance in this channel is considerably smaller than in the case of $e\mu, ee$, or $\mu\mu$. In 110 pb^{-1} we expect about 1 event from $t\bar{t}$ and 2 events from background. We observe 4 candidate events (2 $e\tau$ and 2 $\mu\tau$). There are 4 jets in 3 candidate events that are identified as b-jets ("tagged"). More data with excellent tracking will enable us to conclusively establish this "all 3^{rd} generation" decay mode of the top quark, which is important for charged Higgs searches and tests of weak universality.

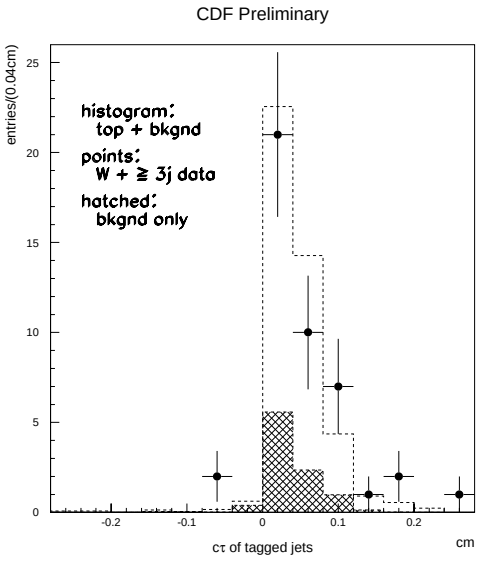

Figure 2.2: The proper time distribution for the b-tagged jets in the signal region (W+$\geq$ 3 jets). The open histogram shows the expected distribution of b's from 175 GeV/c^2 $t\bar{t}$ Monte Carlo simulation. The shaded histogram indicates the background in W+jet events.

2.2.1.2 Lepton + Jets Mode

In this channel, one of the W's decays leptonically to either an electron or muon (plus neutrino) and the other W decays hadronically to a pair of quarks. The nominal signature is a lepton, missing transverse energy (the neutrino from the leptonic W decay), and four jets; two from the b-quarks and two from the decay of the W. Approximately 30% of the $t\bar{t}$ events have this decay signature. Our lepton+jets selection requires that a leptonic W decay be accompanied by at least three central ($|\eta| < 2.0$) jets for an event to be considered part of the sample.

The background from W+multijet production is large. However, $t\bar{t}$ events contain two b-quark jets, and these can be distinguished from gluon and light quark jets in the background using two b-quark tagging techniques. The first technique locates a displaced vertex using the silicon-vertex detector (SVX Tag). The second locates a low-P_T electron or muon primarily from the semileptonic decay of a b-quark or sequential c-quark (SLT Tag). The efficiency for tagging a $t\bar{t}$ event is $(40 \pm 4)\%$ and $(20 \pm 3)\%$ for the SVX and SLT algorithms, respectively. In 110 pb^{-1}, 42 SVX tags are observed in 34 events. The background, in the 34 SVX tagged events, is estimated from a combination of data and Monte Carlo simulation to be 9.4 ± 1.4 events. Using the SLT tagging algorithm, 44 tags are found in 40 events. The background here is estimated to be 25.2 ± 3.8 events. The two samples have 11 events in common[3]. Figure 2.3 (upper left) shows the jet multiplicity spectrum for the SVX b-tags and the background.

In the 1 and 2-jet bins, we expect little contribution from $t\bar{t}$ events. The predicted background and the observed number of events agree well in the 1-jet bin, and agree at the 1.5 sigma level in the 2-jet bin as well. In the 3 and $\geq$4-jet bins, a clear excess of tagged events is observed. Fig. 2.2 shows the proper time distribution expected for b-tagged jets in the signal region ($\geq$ 3 jets), compared with that for the SVX b-tagged jets in the data: the tagged jets are consistent with b decays.

2.2.1.3 All Hadronic Mode

We have found a clear signal in the all-hadronic decay channel for $t\bar{t}$ events. In this decay mode there are six final state jets, four of which come from the hadronic decays of the two W's and two from the b-quarks. Approximately 44% of $t\bar{t}$ events have this decay signature. Achieving a reasonable signal-to-background ratio is the challenge in this data set

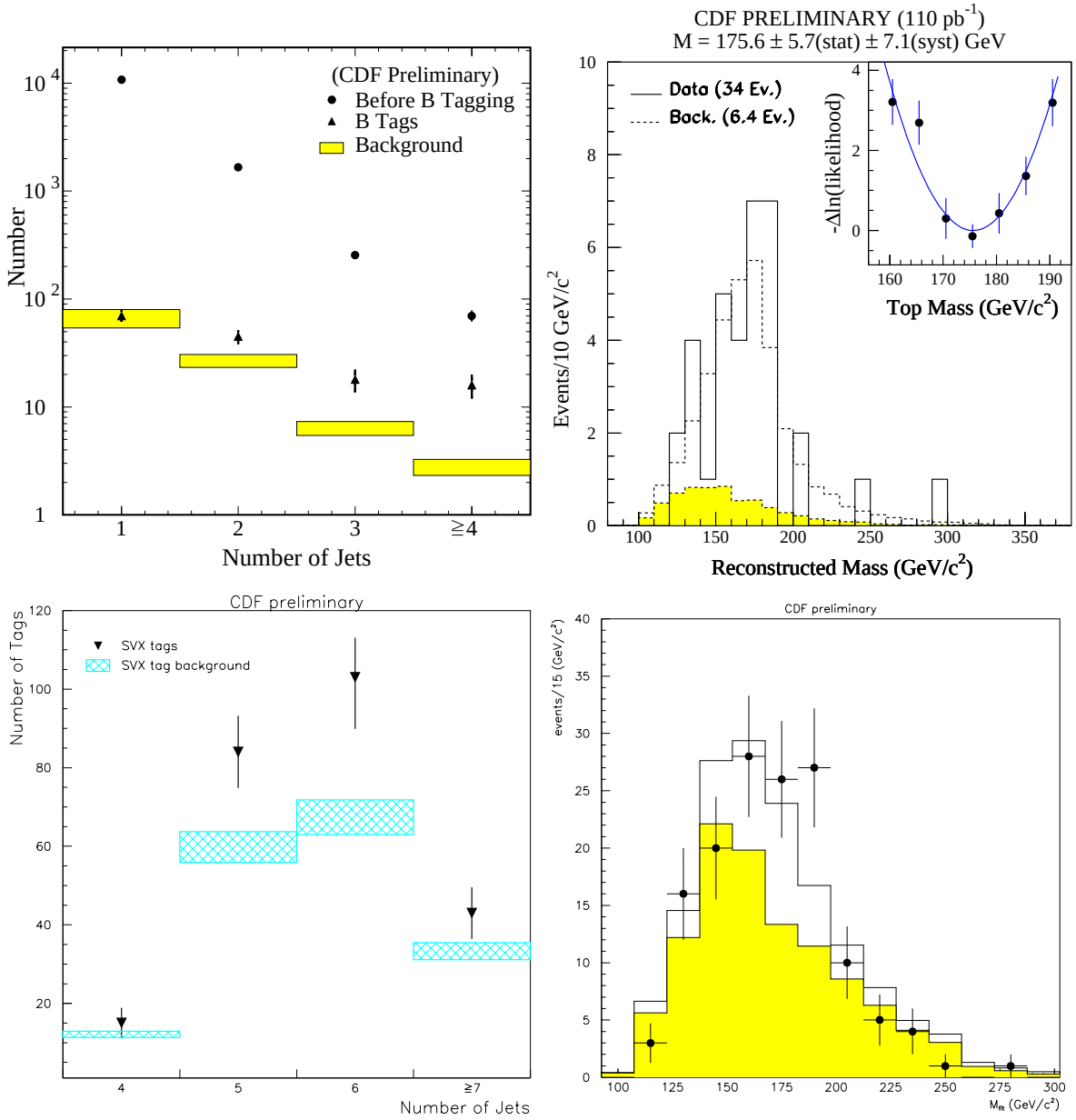

Figure 2.3: **Top Left:** The jet multiplicity distribution in SVX tagged W+jet events. Closed circles are number of events before b-tagging, dark triangles are number of b-tagged events in each bin and hatched areas are the background prediction for the number of tagged events and its uncertainty. **Top Right:** Mass spectrum for b-tagged lepton+jet events in 110 pb^{-1} of data. The shaded area is the expectation from background. The dashed curve is from background plus top production. The likelihood fit is shown as an inset. **Bottom Left:** The jet multiplicity distribution for the all-hadronic mode. The dark triangles represent the observed number of b-tags in each jet multiplicity bin and the hatched areas represent the background prediction as well as its estimated uncertainty. **Bottom Right:** Mass spectrum for all-hadronic b-tagged events in 110 pb^{-1} of data. The shaded area is the expectation from background. The histogram is from background plus top production.

which is dominated by QCD multijet production. In order to isolate a signal and maintain efficiency, we require at least five well-separated jets, one of which must be SVX b-tagged. After additional topological cuts, we find 230 tags in 192 events with an estimated background of 148 $\pm$ 10 events. Figure 2.3 (lower left) shows the jet multiplicity spectrum for the all-hadronic channel. In the 4-jet bin where we expect little contribution from $t\bar{t}$ events, the background and observed tags are in good agreement. Where we expect to see a signal for $t\bar{t}$, in the 5, 6, and $\geq$7-jet bins, an excess of tags is observed over the background predictions. [8]

2.2.1.4 Kinematic Discrimination

In addition to the search techniques based on the dileptons and b-quark tagging, CDF has isolated $t\bar{t}$ events based on the kinematical properties predicted from Monte Carlo simulations. These methods use the lepton+jets event sample but do not rely on b-tagging to reduce the background. One technique examines the jet E_T spectra of the second and third highest E_T jets [5]. The second technique uses the total transverse energy of the event [6]. In both cases, there is a clear $t\bar{t}$ component in our data.

2.2.1.5 $t\bar{t}$ Production Cross Section

The counting experiments which lead to a confirmed signal can be turned directly into measurements of the $t\bar{t}$ production rate. Figure 2.4 shows the $t\bar{t}$ production cross section measured in several channels in comparison to recent theoretical predictions. The best measurement to date is obtained from the weighted average of the counting experiments performed in the dilepton channel and the two lepton+jets channels, SVX b-tagging and SLT b-tagging. With 110 pb^{-1} of data, we measure a production cross section of $7.5^{+1.9}_{-1.6}$ pb[9, 10]. An independent measurement in the all-hadronic channel results in a cross section of 10.7 $^{+7.6}_{-4.0}$ pb [12]. A theoretical cross section calculation by Laenen *et al.* predicts 4.8 pb[17] at 176 GeV/c^2, and other recent theoretical cross sections are within approximately 15% of this value.[18, 19]

2.2.1.6 Top Quark Mass

The top quark mass has been measured in three different channels. The primary method is based on fully reconstructing the $t\bar{t}$ system with lepton+jets events. These events must contain a lepton and at least four jets such that each final state parton can be assigned to an observed jet or lepton. The reconstruction is performed using a constrained fitting technique which selects the best assignment of observed jets to final state partons based on the lowest χ^2. Without any b-tagging information there are 24 combinations which must be considered (12 parton assignments $\times$ 2 possible longitudinal momentum components for the neutrino). When one or two jets are tagged as b-quarks, the number of combinations is reduced to 12 and 4, respectively. The events containing at least one b-tagged jet provide the most precise mass measurement to date. Figure 2.3 (upper right) shows the reconstructed mass distribution for 34 events with at least one b-tag. The background estimate for this sample is $6.4^{+2.0}_{-1.5}$ events. Using a maximum likelihood technique, we determine a top quark mass of 175 ± 5.7 (stat.) $\pm$ 7.1 (syst.) GeV/c^2[3]. The systematic uncertainty is dominated by the uncertainty in final state gluon radiation, the b-tagging bias, and the detector energy scale.

The same constrained fitting technique was also used to reconstruct the top mass in the all-hadronic

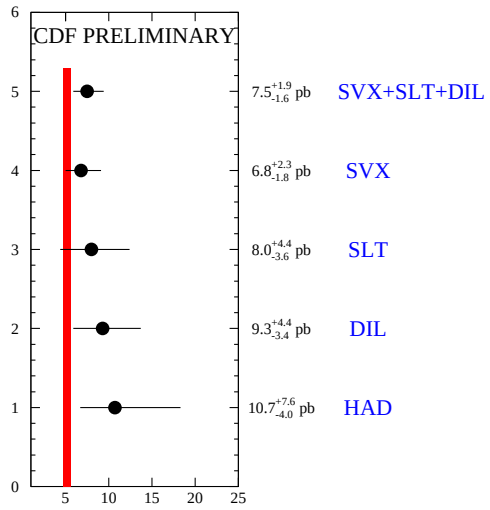

Figure 2.4: The measured cross section for $t\bar{t}$ production for each of the separate production channels measured at CDF as well as the combined lepton+jets and dilepton measurements. The vertical line represents the spread of the central values of the three most current theoretical calculations evaluated at a top mass of 175 GeV/c^2.

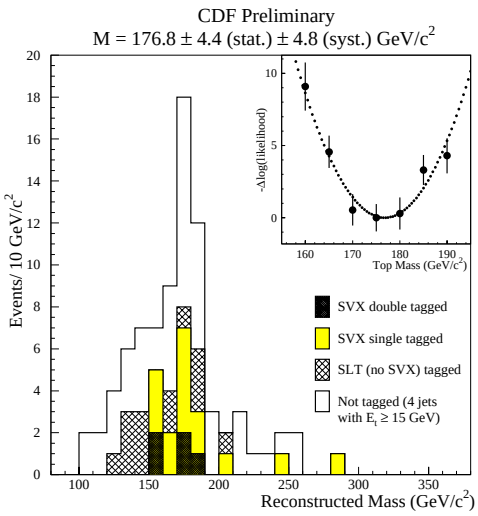

Figure 2.5: The optimized lepton+jets top quark mass plot for each of the four data samples. The insert shows the -Δlog(likelihood) for the data in comparison to mass spectra derived from Monte Carlo samples of various m_{top}. This technique results in a measured top quark mass of 176.8 ± 4.4 (stat.) ± 4.8 (syst.) GeV/c^2 – a 30% improvement over the old analysis.

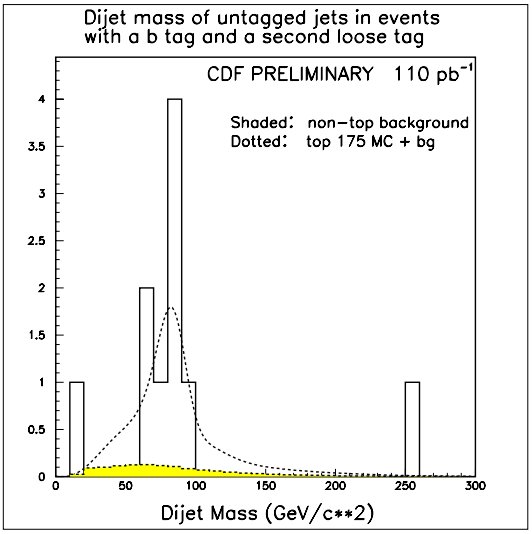

Figure 2.6: The M_{jj}^W distribution is shown for data (solid), expected top+background (dashed), and background (shaded), for W+4 jet events which contain two b-tagged jets. The value of M_{jj}^W is 79.8 $\pm$ 6.2 GeV/c^2. The top mass from this subsample has been determined to be 174.8 ± 9.7 GeV/c^2.

channel where at least one b-tag was required; the result is seen in Figure 2.3 (lower right). Applying a maximum likelihood technique to the data in this channel results in a top mass of 187 ± 8 (stat.) ± 12 (syst.) GeV/c^2.

A new optimization technique has recently been developed for determining the top quark mass in the lepton+jets mode [13]. The "original" method described above neglects information that is contained in the untagged sample, that is those events which satisfy all of our kinematic selection criteria but contain no b-tags. Moreover, the previous analysis combines the SLT and SVX data sets together, and information is lost because the signal-to-background ratio in those two channels is very different. The new optimized mass technique calculates the mass in four orthogonal data samples: the SVX single-tagged events, the SVX double-tagged events, the SLT tagged events which contain no SVX tags, and the not-tagged sample. The backgrounds are determined separately for each subset. The mass is then determined separately in each of these channels as described above and then combined by multiplying the individual mass likelihoods together. From this, one gets a top quark mass of 176.8 ± 4.4 (stat.) ± 4.8 (syst.) GeV/c^2 (see Figure 2.5). This optimization process reduces the total uncertainty on the top quark mass in the lepton + jets channel by 30%.

Reconstructing a top mass in the dilepton channel is difficult because this system is underconstrained. Instead, we measure the energy of the two b-jets and use a likelihood fit to compare the energy distribution in the data to Monte Carlo templates. This technique gives a top mass from dileptons of 156 ± 23 (stat.) ± 17 (syst.) GeV/c^2.

In the subsample of lepton+$\geq$ 4-jet events where two b-tags are required, we have looked for evidence of the decay of the hadronic W-boson. Fig. 2.6 shows the reconstructed mass of the unconstrained jet-jet system. A fit yields a jet-jet mass of 79.8 $\pm$ 6.2 GeV/c^2 [15]. This will be an important *in situ* technique for jet energy scale calibration in Run II. The top mass from this double b-tagged subsample has been determined to be 174.8 ± 8 (stat.) ± 6 (syst.) GeV/c^2.[14]

2.2.2 Lessons from Run I

- The detector should have the greatest possible acceptance for high-p_T electrons and muons from the chain $t \to W \to l\nu$.
- The detector should have the greatest possible acceptance and efficiency for tagging b-jets. This is a question of geometrical coverage, efficiency, and signal-to-noise ratio, most importantly for secondary vertex finding but also for soft lepton identification.
- Precision measurement of the top mass requires that the detector have *in situ* capability for understanding the systematics of jet energy calibration, including the ability to accumulate large samples triggered on low-p_T charged tracks, inclusive photons, and inclusive $W \to l\nu$ and $Z \to ll$.
- Understanding of b-tagging systematics has relied on the ability to accumulate a large, reasonably pure control sample of inclusive b-jets using low-p_T inclusive lepton triggers. We anticipate doing this again, with some demand on DAQ bandwidth. However, we have learned that jets containing $b \to cl\nu_l X$ are a biased control sample, and we believe that a large sample of b-jets collected with a secondary vertex trigger will be extremely useful.

2.2.3 Impact of Upgrades on Top Physics

The impact of the CDF II upgrades is to significantly increase the overall top acceptance and to maintain acceptance and precision at high luminosity.

- **Silicon Vertex Detector (SVX II)**: The tagging of b-quarks from top quark decay will be greatly improved in the long, 5-layer, double-sided device. Increasing the length of the silicon from 52 cm to 96 cm will extend the region of "contained b-jets" to cover the entire interaction region. With ten measurements in two views for any given track, it will be possible to make stringent track quality requirements, reducing the level of mistags, while still improving the overall track finding efficiency.

  A three-dimensional vertexing device will improve the b-tagging efficiency by making it possible to find b's whose displacement is predominantly in the Z direction. In addition, unlike a 2D vertex, a 3D vertex is unique with even 2 tracks, again raising the possibility of reducing backgrounds while increasing efficiency relative to the present analysis.

  Taking all of these factors into account, we anticipate that the SVX II will increase the efficiency for tagging at least one b-jet in a $t\bar{t}$ event to better than 65% (a 62% increase over the Run 1 efficiency), and will raise the double b-tag efficiency to 20% (a 200% increase from current performance) [23].

  Finally we point out that the 3D capability of the SVX II will allow a precision measurement of primary vertex in the event, improving a variety of measurements including the E_t/P_t of the primary leptons, the E_t of the jets, and the missing transverse energy.

- **Intermediate Silicon Layers (ISL)**: The ability to find unambiguous tracks pointing at the new plug calorimeter will provide clean identification of electrons from $W \to e\nu$ in the region $1.0 \leq |\eta| \leq 2.0$, improving the top yield in the electron channel by 33%. With the expected standalone tracking capability of the SVXII-ISL combination, b-tagging of top events will be possible out to $|\eta| = 2$, significantly improving the double-tagged top yield. The improved electron ID may also extend b-tagging with soft leptons into the plug region.

- **Central Outer Tracker (COT)**: The top analysis of Run I depended crucially on the large central tracking chamber. The new COT device will function better at the Run II luminosities than the current CTC did during Run I. It has more robust stereo tracking, lower mass, and better momentum resolution at the trigger level. As discussed in Chapter 7, the *integrated* system of COT-SVXII-ISL will bring much new power to bear on tracking at CDF II, and we are confident that we will exceed any performance estimate which is based on scaling from the Run I capabilities.

- **Plug Calorimeter Upgrade**: The new scintillating-tile fiber calorimeter with its shower max detector will provide improved jet resolution and electron identification in the forward region. The effect of improved electron identification is discussed above. The use of plug jets

Channel	Acc. A_{IB} (Run Ib)	Acc.,A_{II} (Run II)	Run I Results	Run II Yield (w/ A_{II})
Produced $t\bar{t}$	-	-	525	13.6k
Dileptons (ee,$\mu\mu$,$e\mu$)	0.78%	1.1%	10	155
Tau dileptons ($e\tau$, $\mu\tau$)	0.12%	0.14%	4	19
lepton+$\geq$3j	9.2%	11.2%	324	1520
lepton+$\geq$3j w/ $\geq$1 b tag	3.7%	7.3%	34	990
mass sample w/ $\geq$1 b SVX tag	3.0%	5.8%	20	790
mass sample w/ $\geq$2 b SVX tags	0.52%	1.8%	5	240

Table 2.2:
Acceptance and yield of $t\bar{t}$ events for a Run II upgraded detector. The yield is determined using the theoretical cross section (6.8 pb) at m_{top} = 175 GeV/c^2 and $\sqrt{s}$ = 2 TeV. For comparison, the acceptances for Run Ib are shown as well as the number of events seen in Run 1 prior to background subtraction. The acceptances include branching ratios and leptonic and kinematic selection (*e.g.* jet counting).

in a precision mass measurement will require ISL tracking in order that the *in situ* jet energy calibrations established for the central calorimeter can be extended to the plug region.

- **Muon Detection System**: The more complete ϕ and η coverage will assist in the identification of primary muons from W decay and low-P_T muons from semileptonic b-quark decay. The closure of the gaps in the muon system will increase the total muon acceptance for top by 12%. Equally important but difficult to quantify at this point in time is the impact these changes will have on the muon trigger rates. The additions to the CMP increase its total physical coverage by 30% [23], but since the CMP is a confirmation layer behind the CMU, the effect will be on rates rather than acceptance. We expect a much simplified set of muon triggers and trigger systematics, with implications for measurement of the $t\bar{t}$ cross section, and we also expect a much purer sample of b-jets where $b \rightarrow \mu\nu X$ jets for the study of b-tagging systematics.

2.2.4 Event Yield

To estimate the yield of top events, we extrapolate from our current measured acceptance using the theoretical cross section (6.8 pb) at m_{top} = 175 GeV/c^2 and $\sqrt{s}$ = 2 TeV [22, 11].

At $\sqrt{s}$ =2 TeV, the $t\bar{t}$ cross section is approximately 40% higher than at $\sqrt{s}$=1.8 TeV. We assume that the additional lepton and b-tagging acceptance outlined in Sec. 2.2.3 above can be incorporated while maintaining a signal-to-background ratio comparable to the Run I analysis.

Table 2.2 summarizes the acceptance and yields for various decay channels in the Run II configuration. The Run Ib acceptances are shown for comparison. A sample of 2 fb^{-1} at the Tevatron will provide over 1000 identified b-tagged $t\bar{t}$ events.

2.2.5 Measurement of the Top Quark Mass

The top quark mass will be one of the most important electroweak measurements made at the Tevatron. In combination with the W mass, m_t gives information about the mass of the standard model Higgs boson. The precision electroweak program and the W mass measurement are discussed in the electro-weak section of Chapter 2. Figure 2.13 shows how the predicted top and W mass measurements constrain the Higgs mass. In that figure, the uncertainty on the top mass is taken as 4 GeV/c^2.

Currently, the statistical and systematic uncertainties on CDF's top mass measurement are both about 5 GeV. The statistical uncertainty should scale as $1/\sqrt{N}$. Using the yields in Table 2.2, we anticipate that the statistical uncertainty on the top mass in the optimized lepton+$\geq$ 4-jet sample with at least one b-tagged jet will be $\approx$ 1 GeV/c^2. We see that in Run II the uncertainty will be dominated by systematics.

Note that with the new integrated tracking, the acceptance for double-tagged lepton+$\geq$ 4-jet events increases by about a factor of 2.5. In these double-tagged events, the number of unique combinations for the constrained mass fitter to test is 4 instead of 12, improving the mass resolution by 20%. Thus, using only double-tagged events, CDF II can still achieve a statistical uncertainty which approaches 1 GeV/c^2. Because both b-quarks are identified in double-tagged events, the systematics ultimately may be better understood for this class of events.

Almost all of the systematic uncertainties in the top mass measurement are coupled to the reliability of the Monte Carlo models for the spectrum of fit masses in signal and background. Assuming the theory model is accurate, most of the uncertainty is related to resolution effects. Instrumental contributions include calorimeter nonlinearity, losses in cracks, dead zones, and absolute energy scale. A larger and more difficult part of the energy resolution concerns the reliability of the extrapolation to parton energies. Ultimately, it may be our understanding of QCD and not the detector which limits the mass resolution.

Many of these issues can be addressed by *in situ* calibration procedures. For example, Z+jet events are used to understand the systematic uncertainty due to energy scale and gluon radiation, two of the dominant uncertainties. In 2 fb^{-1}, we expect to have 27K (70) Z's with 1 (4) or more jets. The effect of gluon radiation will also be studied in large statistics samples of W+jets, γ+jets, and $b\bar{b}$ events. In addition, the mass peak from $W \rightarrow qq'$ (see Figure 2.6) in the lepton + jets top sample allows an energy scale calibration *in exactly the same events and environment* as the mass measurement. A complete model study of the extrapolation of the systematic uncertainty on the top mass can be found in Ref. [1].

In any case, if all systematic effects can be measured or otherwise connected with mean quantities in large statistics control samples, the systematic uncertainties should also scale as $1/\sqrt{\mathcal{L}}$. We can conservatively assume in this case that we can reduce our systematic error to $\approx$ 2 GeV/c^2. This is probably our lower limit. We use 3 GeV/c^2 as our goal for the total uncertainty on the top quark mass.

2.2.6 Production Cross Section, $\sigma_{t\bar{t}}$

An accurate measurement of the $t\bar{t}$ production cross section is a precision test of QCD. A cross section which is significantly higher than the theoretical expectation would be a sign of non-standard model production mechanisms, for example the decay of a heavy resonant state into $t\bar{t}$ pairs or anomalous couplings in QCD. As in the case of the top mass, large statistics in the lepton+jets mode imply that systematic uncertainties will be the limiting factor in the cross section measurement.

For the acceptance, the reliability of jet counting and b-tagging are at issue. Initial state radiation can be examined using a sample of Z+jets, while the jet energy threshold uncertainty can be addressed as in the top mass discussion. With 2 fb^{-1} of data it will be possible to measure the b-tagging efficiency *in top events*, using dilepton events selected without a b-tag and the ratio of single to double tags in lepton+jets events. We assume that these studies will give uncertainties that scale with $\sqrt{N}$.

With large samples, one can measure the bottom and charm content as a function of jet multiplicity in W + jet events using the cτ distribution of the tagged jets and use this to tune the Monte Carlo models for W+$\geq$ 3-jet backgrounds. Finally, in Run II and beyond, the luminosity will be measured either through the $W \rightarrow l\nu$ rate, or the mean number of interactions per crossing, and we will assume 5% for the future precision of the luminosity normalization.

Accounting for all effects we find that the total $t\bar{t}$ cross section can be measured with a precision of 9% for 2 fb^{-1}. This will challenge QCD, and provide a sensitive test for non-standard production and decay mechanisms.

2.2.6.1 Measurement of a t $\rightarrow$ W Branching Fraction

The ratio of the $t\bar{t}$ cross section measured using dilepton events to that measured using lepton+jets events is a test for non-standard model decay modes of the top quark. Since the cross section in each case assumes that each top decays into W-bosons, a ratio different from 1.0 would signal decays *without* a W-boson, such as charged Higgs (t $\rightarrow$ H$^+$ b) or light supersymmetric top (stop). The reach for a particular non-standard decay is model dependent, but we can say that with 2 fb^{-1} of data, we will be able to measure the basic dilepton to lepton+jets ratio to 12%,

and the top branching fraction to W in association with b with a precision of 9%.

2.2.7 Measurement of a t → b Branching Fraction and a Lower Limit on V_{tb}

In the standard model with 3 generations, existing experimental constraints and the unitarity of the CKM matrix require $V_{tb} \simeq 1$, predicting that the weak decay of the top will proceed almost exclusively through W + b. In events containing a W, the top branching fraction to b's is related to the CKM element according to:

$$\begin{aligned} B_b &= B(t \to W(b)) \\ &= \frac{\sigma(t \to Wb)}{\sigma(t \to Wq)} \\ &= \frac{|V_{tb}|^2}{|V_{td}|^2 + |V_{ts}|^2 + |V_{tb}|^2} \end{aligned}$$

The notation above is meant to indicate that a W has been required in the final state, and this is not the decay fraction to W+b, but the fraction of decays with W's which *also* contain b's. Since the standard analysis identifies $t\bar{t}$ events by requiring at least 1 W and 1 b, $B(t \to W(b))$ is measured from the number and distribution of tagged b-jets in top events. Four different techniques can be used to measure this distribution: [20, 21]

- The ratio of double b-tagged to single b-tagged events in the b-tagged lepton+jets sample: requiring one b-jet to be tagged leaves the second jet unbiased, and from a known tagging efficiency, one can extract the branching ratio from the ratio of tagged to untagged "second jets". [20]
- The ratio of single b-tagged to no b-tagged events in a lepton+jets sample in which kinematic criteria have been applied: since there is no a-priori tag requirement, we can extract the branching ratio from the ratio of single tagged events to not-tagged events. An ideal sample for this is the W+4 jet mass sample prior to applying the χ^2 cut. [21]
- The number of b-tagged jets in the dilepton sample: Since b-tagging is not required to identify tops decaying to dileptons, the whole b-tag multiplicity distribution in these events contains information on $B(t \to W(b))$. Despite the smaller branching fraction to dileptons, the statistical powers of the dilepton and lepton+jets samples are comparable.
- The distribution of double tags: If there are two tagging algorithms (soft leptons and secondary vertex), one can compare the number of times that events tagged by both algorithms have both tags in the same jet vs. the number of times the tags are in different jets. Small values of $B(t \to Wb)/B(t \to Wq)$ result in large values of the same to different jet ratio.

These techniques are not exclusive, and can be combined. We have used a maximum likelihood estimator to do this combination in Run I data. With 100 pb^{-1}, CDF has a ±25% statistical uncertainty on the branching fraction, but only an ±11% systematic uncertainty. The systematic uncertainty is dominated by the uncertainty on the tagging efficiency, which is measured in the data using b-rich inclusive lepton samples. This uncertainty should fall as $1/\sqrt{N}$. The small non-$t\bar{t}$ backgrounds will be measured to high accuracy by Run II. For Run II, we expect to measure $B(t \to W(b))$ to 3.0% and place a 95% CL lower limit of 0.25 on $|V_{tb}|$.

2.2.7.1 Anomalous Couplings and Weak Universality

Since the top quark is so heavy, it is possible that the physics of the underlying theory may manifest itself via new non-universal top interactions. The top quark is unique in that it decays prior to hadronization and therefore the decay products carry helicity information related to the fundamental couplings. In the standard model, the top quark decays only to longitudinal or left-handed W's, where the ratio is given by

$$\frac{W_{long}}{W_{left}} = \frac{1}{2}\left(\frac{m_{top}}{m_W}\right)^2$$

For $m_{top} = 170$ GeV/c^2, the branching fraction to longitudinal W's is 69.2%. In many cases non-universal top couplings will appear as a departure of B($t \to bW_{\rm long}$) from the standard value and we use this quantity as our precision benchmark for probes of anomalous weak couplings.

Experimentally, we have access to the polarization state of the decay W through the charged lepton helicity angle, $cos\theta^*_e$ which can be measured in the lab

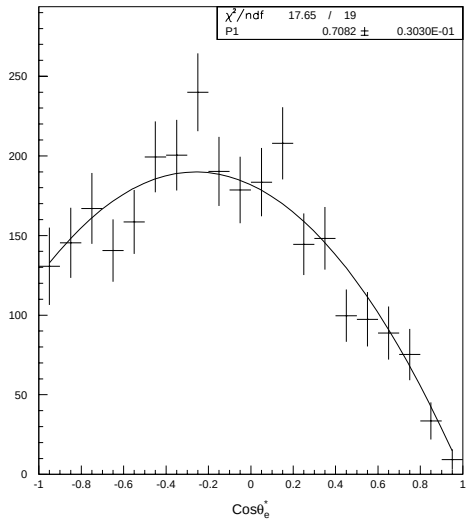

Figure 2.7: The $\cos\theta_e^*$ distribution for 1000 events and fit to the standard model hypothesis $\sim 30\%$ $W_{\rm left} + 70\%$ $W_{\rm long}$

frame as

$$\cos\theta_e^* \approx \frac{2M_{eb}^2}{m_{e\bar{b}\nu}^2 - M_W^2} - 1 \qquad (2.1)$$

The resulting distribution can then be fit to a superposition of W helicity amplitudes in order to measure any possible contribution of non-universal weak couplings in the top decay.

Our model study uses a four-vector level Monte Carlo [16] with selection bias and resolution smearing modeled on the CDF experience. We assume the constrained mass fit will allow us to know perfectly which b-jet belongs to the semi-leptonic top decay. This is clearly optimistic. We correct the $\cos\theta_e^*$ distribution for the bias imposed by the selection cuts. This acceptance corrected distribution for 1000 events is shown as the data points in Fig. 2.7. We fit the distribution to the standard model hypothesis for the admixture of $W_{\rm long}$ and $W_{\rm left}$ and get a good fit with $\mathrm{B}(t \to bW_{\rm long}) = 0.708 \pm 0.030$, as shown.

We have estimated the systematic uncertainty from W-b combinatorics, energy scale uncertainties, and backgrounds. We find that with 2 fb^{-1}the top quark decay branching fraction to longitudinal W-bosons can be measured with a total precision approaching 5%. We have also studied the effect of a V+A term in top decay and find similar sensitivity.

2.2.7.2 Single Top Quark Production

In addition to $t\bar{t}$ pair production via the strong interactions, top quarks can also be produced singly via the electroweak interaction. This process depends on the t-W-b vertex, and the production rate is a measure of the top decay width to W+b and the CKM matrix element $|V_{tb}|^2$.

The two dominant single top processes at the Tevatron are the s-channel mechanism $qq \to t\bar{b}$, referred to here as W^* production, and the t-channel interaction $qb \to qt$, referred to as W-gluon fusion. Other processes become important at higher energies, but are negligible here. The W-gluon fusion process is thought to dominate the production with an estimated cross section of 1.44 pb; the uncertainties on this calculation are large – on the order of 30%. The W^* production mode has an estimated cross section of 0.74 pb with an uncertainty of 6%. The combined rate for single top production by these two processes is ≈ 2.2 pb, only a factor of 3.5 down from the $t\bar{t}$ rate at this energy.

The TeV-2000 group studied single top production using the ONETOP Monte Carlo with $m_t = 170$ GeV/c^2 [16]. The detector performance for b-tagging was based on the CDF Run Ib result, as was the size of the b-tagging backgrounds. The jet energies were smeared according to the resolution model $(82\%/\sqrt{E} + 18\%)$, which is very conservative compared to the CDF II goal of $\sigma_{E_T} = 0.1 \cdot E_T + 1$ GeV.

The data selection criteria that were used to isolate the signal over background include:

- Exactly two jets with $E_T > 20$ GeV, $|\eta|_{\rm jets} < 2.5$
- $\Delta R = \sqrt{(\Delta\phi)^2 + (\Delta\eta)^2} > 0.5$ between all jet pairs and jet-electron pairs
- $\not\!\!E_T > 20$ GeV
- $E_T(\text{electron}) > 20$ GeV
- $|\eta|_{\rm electron} < 2.5$
- No second isolated electron present with $E_T > 20$ GeV
- At least one jet tagged as a b-jet.

The signal for single top production is a peak in the Wb invariant mass plot. The shape of the signal-plus-background curve is easily distinguished from the background shape alone using the conservative

resolution. The size of signal (S) and background (B) are counted using the number of events in a mass peak window of 50 GeV/c^2 around the generated top quark mass: there is a signal yield of approximately 100 events per fb^{-1}, above a background about twice as large, mainly from W + $b\bar{b}$. Assuming that the background normalization is understood (through the large statistics top cross section measurement), the statistical precision on the single top cross section using 2 fb^{-1} will be about 12%.

Many of the sources of systematic uncertainty in the single top cross section are common to the $t\bar{t}$ cross section discussed earlier. We assume that systematic uncertainties related to selection efficiencies and backgrounds will shrink as $\sqrt{N}$. For the case of 2 fb^{-1} we find that the measurement of the single top cross section will have a total uncertainty of approximately 24%.

The single top cross section is directly proportional to the partial width , ($t \to Wb$) and assuming there are no anomalous couplings, this is a direct measure of $|V_{tb}|^2$. There are theoretical uncertainties in converting the cross section to the width, notably for the gluon fusion process. Taking these into account, we anticipate that a measurement of the total single top rate with 2 fb^{-1} will translate in a precision of 26% on , ($t \to Wb$) and 13% on $|V_{tb}|$.

The theoretical determination of W* is more reliable than that of W-gluon fusion since initial state effects can be measured in the similar Drell-Yan process, and if the data set is large enough this may afford the best precision on the width. The two processes can be separated by requiring two b-tags since the double tag rate for W* production is close to a factor of 5 more than that of W-gluon fusion.

2.2.8 Search for Anomalously Large Rare Decays

- $t \to Zc, \gamma c$
- $t \to WZb$
- $t \to W^+W^-c$
- $t \to Hc$

The standard model predicts that the branching fractions of FCNC top decays are around 10^{-10} [29], out of reach for even the LHC. Any observation of such decays will signal new physics. As illustration, we consider the signal for a flavor changing neutral current decay $t \to c\gamma$ in a $t\bar{t}$ event. If the other top in the event decays in the leptonic channel, the acceptance is almost the same as the standard model lepton+jets mode, and it then becomes a simple matter to scale from present results. The background from $W + \gamma$ + two jets is about 1 fb. Although it is unlikely that this background will be kinematically consistent with $t\bar{t}$ (for example, that $m(\gamma + j) = m(t)$), we take the very conservative assumption that this background is irreducible. We find that 2 fb^{-1} will probe branching fractions for this decay down to 3.0×10^{-3}

Sensitivity to other rare decays can be scaled from this estimate. For the case $t \to Z + c$, where the Z decays to leptons, after adjusting for branching ratios and different backgrounds, we find sensitivity down to 1.5%.

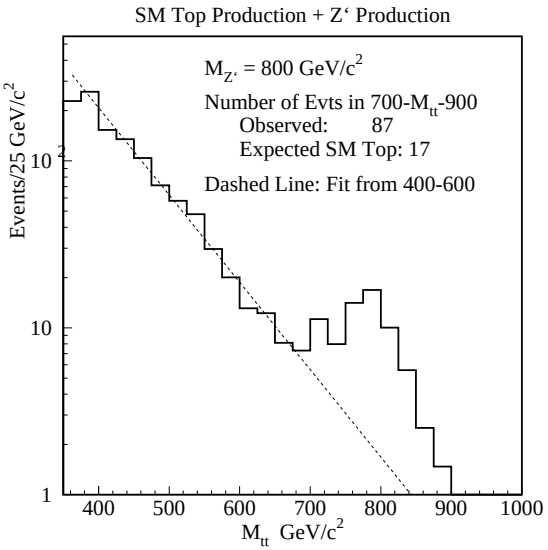

Figure 2.8: A hypothetical $m_{t\bar{t}}$ spectrum with an 800 GeV/c^2 Z$'$ topcolor boson. The rate is based on the theoretical predicted cross section for $t\bar{t}$ production and Z$'$ production [31] with 2 fb^{-1}.

2.2.8.1 Dynamical Symmetry Breaking

Because of its large mass, the top quark is an excellent probe for physics beyond the standard model. Theories which implicate top in the electroweak symmetry breaking mechanism, such as a color-octet vector meson associated with a top condensate[33] or multiscale technicolor[34], predict enhancements or changes in the shape of the $t\bar{t}$ invariant mass spectrum ($m_{t\bar{t}}$) and the top quark transverse momentum

Measurement	2 fb^{-1}	Comment
Yields		
N_{3jet*b}	990	*identified* events
$N_{4jet*2b}$	240	clean m_t sample
δm_t	3	total precision GeV/c^2
Production		
$\delta\sigma_{t\bar{t}}$	9%	test top QCD couplings
$\delta\sigma_{ll}/\sigma_{l+j}$	12%	test non W decay
$\delta\sigma_{t\bar{b}X+b\bar{t}X}$	24%	isolate "single top"
$\delta\sigma \cdot B(Z' \to t\bar{t})$	90 fb	"topcolor" $M_{Z'}$ = 1 TeV/c^2
Decay		
$\delta B(t \to W(b))$	2.8%	from N(bb)/N(bX)
$\delta B(t \to b(W))$	9%	from N(ll)/N(lX)
$\delta B(W_{V+A})$	2.7%	$W \to l\nu$ helicity
$\delta B(W_{long})$	5.5%	$\frac{W_{long}}{W_{left}} = \frac{1}{2}(\frac{m_{top}}{m_W})^2$
δ, $(t \to Wb)$	26%	using single top
δV_{tb}	13%	from above
Rare Decays		
B(c γ)	$\leq 2.8 \times 10^{-3}$	(95% CL)
B(cZ)	$\leq 1.3 \times 10^{-2}$	(95% CL)
B(Hb)	$\leq$ 12%	from σ_{ll}/σ_{l+j}

Table 2.3: Summary of expected measurement accuracies for an integrated luminosity of 2 fb^{-1}

distribution (P_T^{top}).

CDF is currently searching for resonances, $X \to t\bar{t}$, in the $M_{t\bar{t}}$ spectrum by reconstructing $M_{t\bar{t}}$ on an event-by-event basis using the same event sample and constrained fitting techniques used in the top mass measurement, with an additional constraint that the t and $\bar{t}$ decay products have a mass equal to the measured m_{top}. By the end of Run I, we should have sensitivity to new objects with masses as large as 500-600 GeV/c^2. In the absence of a signal, limits in Run II will be as high as 1000 GeV/c^2. New resonances with masses below the limit could be observed. For example, Figure 2.8 shows the $M_{t\bar{t}}$ spectrum for 2 fb^{-1} with standard model $t\bar{t}$ production plus the addition of a topcolor Z′ at 800 GeV/c^2 [31], where the Z′ decays to a $t\bar{t}$ pair. In this theory, the branching fraction of Z′ to $t\bar{t}$ pairs is potentially large (50-80%) but depends on the Z′ width. In the case shown in Figure 2.8, we would expect 17 events from standard model $t\bar{t}$ production in the range $700 < M_{t\bar{t}} < 900$ GeV/c^2 and 70 events from $Z' \to t\bar{t}$ in this range. The $M_{t\bar{t}}$ spectrum along with other $t\bar{t}$ production distributions provide an excellent means for searching for new phenomena.

2.2.9 Summary of Top Physics

For the next decade, the Tevatron will be the only accelerator capable of producing the top quark, and an upgraded CDF II detector will be well-suited for the study of top physics. The increased coverage of the SVX II detector and muon systems will allow us to tag at least one b-quark in $\approx$ 65% of $t\bar{t}$ events and both b-quarks in 20% of the events. With 2 fb^{-1} of integrated luminosity, we expect 1000 single SVX-tagged $t\bar{t}$ events in the lepton+jets channel.

The top physics program possible with this sample is summarized in Table 2.3. We expect to measure the top mass, a fundamental electroweak parameter, with a precision of approximately 3 GeV/c^2. Measurements of branching ratios, angular distributions, and top production mechanisms with the sensitivities listed in Table 2.3 will provide the first complete

characterization of this new fermion. Our catalog of possible measurements is hardly complete. But in the event that the top quark yields surprises, these sensitivities benchmark the capability to explore new physics at the Fermilab Tevatron.

Bibliography

[1] *Future ElectroWeak Physics at the Fermilab Tevatron: Report of the TeV_2000 Study Group*, Editors D. Amidei and R. Brock Fermilab–Pub–96/082

[2] F. Abe *et al.* (CDF Collaboration), Phys. Rev. D **50**, 2966 (1994); F. Abe *et. al.* (CDF Collaboration), Phys. Rev. Lett. **73**, 225 (1994).

[3] F. Abe *et al.* (CDF Collaboration), Phys. Rev. Lett. **74**, 2626 (1995).

[4] S. Abachi *et al.* (D0 Collaboration), Phys. Rev. Lett. **74**, 2632 (1995).

[5] F. Abe *et al.* (CDF Collaboration), Phys. Rev. D **52**, R2605 (1995).

[6] F. Abe *et al.* (CDF collaboration), Phys. Rev. Lett. **75**, 3997 (1995).

[7] M. Hohlmann, *Observation of Top quarks in the dilepton decay channel* $t\bar{t} \rightarrow e(\mu)\nu_{e(\mu)}\ \tau\nu_\tau\ b\bar{b}$ *Using Hadronic Tau Decays At CDF*, Proc., Lake Louise Winter Institute (1996)

[8] P. Azzi *et al.*, *Hadronic Top Production at CDF*, CDF Note 3679.

[9] R. Hughes, B. Winer, T. Liss, *Combining the SVX, SLT, and Dilepton* $t\bar{t}$ *Cross Sections*, CDF Note 3111.

[10] T. Liss, R. Roser, $t\bar{t}$ *Production Cross Section for 110* pb^{-1}, CDF Note 3481.

[11] A. Beretvas, Int. J. Mod. Phys. A11, 2045 (1996)

[12] P. Azzi *et al.*, $t\bar{t}$ *Production Cross Section in the All-hadronic Channel*, CDF Note 3464.

[13] K. Tollefson *et al.*, *Optimizing the Top Quark Mass Measurement*, CDF Note 3606.

[14] S. Aota *et al.*, *Update to Top Mass on Double b-tagged Events Using Loose Jet Probability Tagging*, CDF Note 3604.

[15] R. Wilkinson *et al.*, *Update to Hadronic W Decays in Double b tagged Top Candidates*, CDF Note 3543.

[16] E. Malkawi, C.-P. Yuan, *A Global Analysis of the Top Quark Couplings to Gauge Bosons*, Phys. Rev. D **50**, R4462 (1994).

[17] E. Laenen, J. Smith, W.L. van Neerven, Phys. Lett. **321B**, 254 (1994).

[18] Catani, Mangano, Nason and Trentadue, CERN Preprint, CERN-TH/96-21 hep-ph/9602208.

[19] E. Berger, Argonne Nat. Lab. Preprint ANL-HEP-PR-95-31

[20] T. LeCompte, R. Roser, *Measurement of* $BF(t \rightarrow Wb)$ *and the CKM Matrix Element* $|V_{tb}|$ *in Top Decays*, CDF Note 3056.

[21] F. Bedeschi, G. Chiarelli, F. Tartarelli, *Measurement of* $BF(t \rightarrow Wb)$ *in Top Decays*, CDF Note 3853.

[22] E. Laenen, private communication.

[23] R. Hughes, R. Roser, from a series of talks at the CDF upgrade meetings

[24] D. Atwood, A. Kagan, T.G. Rizzo, *Constraining Anomalous Top Quark Couplings at the Tevatron*, SLAC-PUB-6580, July 1994.

[25] G. Kane, C.-P. Yuan, and D. Ladinsky, Phys. Rev. D **45**, 124, (1992); D. Atwood, A. Aeppli, and A. Soni, Phys. Rev. Lett. **69**, 2754, (1992); R.S. Chivukula, S.B. Selipsky, E.H. Simmons, Phys. Rev. Lett. **69**, 575, (1992); M.Peskin, talk presented at the *Second International Workshop on Physics and Experiments at a Linear e+e- Collider*, Waikoloa, HI, April 1993; M.Peskin and P. Zerwas, talks presented at the *First International Workshop on Physics and Experiments at a Linear e+e- Collider*, Saariselka, Finland, September 1991.

[26] S. Dawson, Nucl. Phys. **B249**, 42 (1985); S.S.D. Willenbrock and D.A. Dicus, Phys. Rev. D **34**, 155 (1986); S. Dawson and S.S.D. Willenbrock, Nucl. Phys. **B284**, 449 (1987); C.-P. Yuan, Phys. Rev. D **41**, 42 (1990); S. Cortese and R. Petronzio, Phys. Lett. **B253**, 494 (1991); G.V. Jikia and S.R. Slabospitsky, Phys. Lett **B295**, 136 (1992), R.K. Ellis and S. Parke, Phys. Rev. D **46**, 3785 (1992); G. Bordes and B. van Eijk, Z. Phys. **C57**, 81 (1993); G. Bordes and B. van Eijk, Nucl. Phys. **B435**, 23 (1995): T. Stelzer and S. Willenbrock, Phys. Lett. **B357**, 125-130 (1995).

[27] D. Winn, D. Amidei, *Study of the $t \to Wb$ Vertex at CDF*, CDF Note 2914.

[28] D.O.Carlson, C.-P. Yuan, Phys. Lett. **306B**, 386 (1993).

[29] S. Parke, *Summary of Top Quark Physics*, FERMILAB -Conf-94/322-T. Presented at DPF'94, University of New Mexico, Albuquerque, NM, August 2-6, 1994.

[30] T. Stelzer, S. Willenbrock, *Single-Top-Quark Production via $q\bar{q} \to t\bar{b}$*, DTP/95/40, ILL-(TH)-95-30 (1995).

[31] C. Hill, *Topcolor Assisted Technicolor*, Fermilab-Pub-94/395-T

[32] K. Lane, *Top Quarks and Flavor Physics*, BUHEP–95–2.

[33] C. T. Hill, Physics Lett. **266B**, 419 (1991).

[34] K. Lane, E. Eichten, Phys. Lett. **222B**, 274 (1989); K. Lane and M.V. Ramana, Phys. Rev. D **44**, 2678, (1991).

2.3 Precision Electroweak Program

2.3.1 Introduction

The comparison of diverse precision experimental measurements to expectations from the Standard Model [1] allows precise tests sensitive to new physics at scales above the electroweak scale, as well as a determination of the Higgs mass within the framework of the model [2]. Global electroweak fits until now have been largely dominated by LEP data, with contributions from the SLAC polarization measurement, W mass measurements in $\bar{p}p$ interactions, neutrino neutral current data, and most recently the measurement of the top mass [3] at the Tevatron.

Precision measurement of the top mass and the W mass are primary goals of CDF II. In addition, in the electroweak sector, the W width and leptonic branching ratio, the tri-linear couplings of the W, Z and γ, and the forward-backward charge asymmetry of dileptons at the Z pole and above are important Standard Model parameters. These measurements together will take the global electroweak fit to a new level of precision, and do so completely in the context of a single experiment.

In this section we discuss measurements directly involving the gauge bosons. We begin with the expected event yields of W, Z, and diboson production for Run II with 2 fb^{-1}. We then discuss the CDF Electroweak measurements for Run I and CDF II prospects for Run II.

Studies of the Run II sensitivities for Electroweak physics at CDF II, and their competitiveness with LEP-II, LHC and NLC experiments are also detailed in the DPF Summary Report of the Working Subgroup on Anomalous Gauge Boson Interactions [4] and more recently in the Intermediate Vector Boson Physics chapter of the TeV-2000 Report [5].

2.3.2 Event Yields

The Electroweak physics potential can best be illustrated by the expected event yields for W, Z, and diboson production. We first list the event yields with 2 fb^{-1} with the Run Ib configuration, and compare the lepton identification and acceptances for Run Ib with those for Run II. There is a significant improvement in the event yields of W, Z, and diboson production when the lepton and photon acceptances are extended to high η, and the high η leptons and photons also enable some previously inaccessible physics.

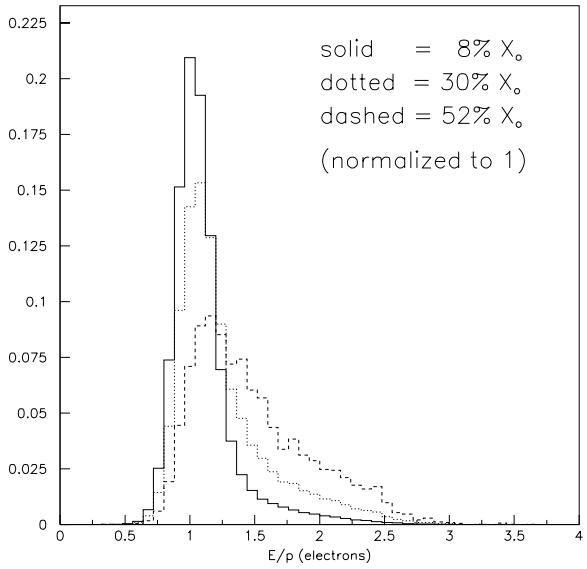

Figure 2.9: E/p distribution of electrons from W decays. The solid (dotted, dashed) histogram uses 8% X$_o$ (17% X$_o$, 30% X$_o$) of the detector material up to the middle of the CTC.

2.3.2.1 Improvement from the integrated luminosity and $\sqrt{s}$

The expected event yields for W, Z, and diboson production, when the Run Ib configuration is assumed, are listed in Table 2.4. The results are based on the acceptances and efficiencies measured from Run I analyses. For Run II, $\sqrt{s}$ will be 2.0 TeV instead of 1.8 TeV, which will increase W and Z cross sections by $\sim$12% and diboson cross sections by 13% $\sim$ 22%.

2.3.2.2 Lepton Identification and Acceptances

We compare the lepton identification and acceptances for Run I with those for Run II.

- **Electrons**

  The identification of electrons relies heavily on the correlation of tracking information with calorimetric measurement of shower energy and position.

  For Run II, the identification and treatment of central electrons will be very reminiscent of Run

channel		number of events $\sqrt{s}$ = 1.8 TeV, $(A,\epsilon)^{\text{RunIb}}$	$\sigma_{2.0\text{TeV}}/\sigma_{1.8\text{TeV}}$
$W \to e\nu$	(e^c)	1,000,000	1.12
$W \to e\nu$	(e^p)	400,000	1.12
$W \to \mu\nu$	(μ^c)	600,000	1.12
$W \to \mu\nu$	(μ^f)	44,000	1.12
$Z \to ee$	$(e^c,\ e^{c,p,f})$	130,000	1.12
$Z \to \mu\mu$	$(\mu^c,\ \mu^c)$	50,000	1.12
$W\gamma$, $E_T^\gamma > 10$ GeV	$(\gamma^{c,p})$	1,500	1.13
$Z\gamma$, $E_T^\gamma > 10$ GeV	$(\gamma^{c,p})$	450	1.13
$WW \to \ell\nu\ell\nu$		77	1.17
$WZ \to \ell\nu\ell\ell$		9.6	1.22
$ZZ \to \ell\ell\ell\ell$		1.2	1.19

Table 2.4: Expected W, Z, and diboson event yields with 2 fb^{-1} when the Run Ib configuration is assumed, and the increase in cross sections with $\sqrt{s}$ = 2.0 TeV. c, p, and f for electrons represent Run I CEM, PEM, and FEM, and c and f for muons represent Run I CMU/P and FMU.

channel	lepton (e) rapidity			
	1.0	1.5	2.0	2.5
$W \to \ell\nu$	(1.00)	1.42	1.98	2.26
$Z \to \ell\ell$	(1.00)	2.13	3.30	3.61
$W\gamma$, $E_T^\gamma > 10$ GeV, $\eta^\gamma < 1.0$	(1.00)	1.26	1.48	1.53
$W\gamma$, $E_T^\gamma > 10$ GeV, $\eta^\gamma < 1.5$	1.28	1.64	1.95	2.03
$W\gamma$, $E_T^\gamma > 10$ GeV, $\eta^\gamma < 2.0$	1.54	2.01	2.42	2.53
$W\gamma$, $E_T^\gamma > 10$ GeV, $\eta^\gamma < 2.5$	1.63	2.14	2.59	2.72
$Z\gamma$, $E_T^\gamma > 10$ GeV, $\eta^\gamma < 1.0$	(1.00)	1.68	2.26	2.36
$Z\gamma$, $E_T^\gamma > 10$ GeV, $\eta^\gamma < 1.5$	1.27	2.17	2.96	3.11
$Z\gamma$, $E_T^\gamma > 10$ GeV, $\eta^\gamma < 2.0$	1.51	2.63	3.65	3.85
$Z\gamma$, $E_T^\gamma > 10$ GeV, $\eta^\gamma < 2.5$	1.59	2.79	3.92	4.15
$WW \to \ell\nu\ell\nu$	(1.00)	1.70	2.14	2.33
$WZ \to \ell\nu\ell\ell$	(1.00)	2.68	4.37	5.33
$ZZ \to \ell\ell\ell\ell$	(1.00)	2.62	4.10	4.81

Table 2.5: Improvement in acceptances of W, Z, and diboson production for various lepton and photon η cuts, normalized to those with η of leptons and photons less than 1 (listed in parentheses), by using Monte Carlo events simulated on the basis of the Run I detector and triggers. The entries below are for the electron channel only, and the muon channel results will be very similar to the electron ones. Electrons are required to have $E_T > 25$ GeV.

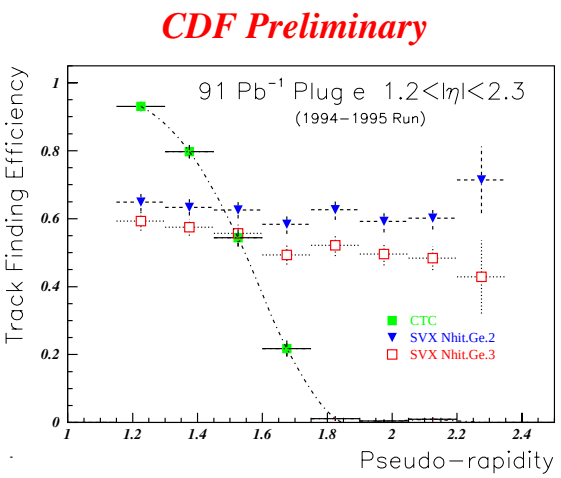

Figure 2.10: The $|\eta_{\rm det}|$ distributions of plug W electrons. Events in CTC sample are concentrated in the low $|\eta_{\rm det}|$ because the CTC track finding efficiency quickly falls. The SVX sample events are populated more uniformly in $|\eta_{\rm det}|$.

I: the EM calorimeter is identical, and the tracking performance and amount of material traversed will be very similar.

The interesting new feature for Run II will be the identification of electrons in the plug region $1.0 \leq |\eta| \leq 2.0$. For Run I, the purity of the plug electrons was relatively poor mainly because the tracking information in this region was poor or completely absent. The CTC track-finding efficiency fell very rapidly in the range of detector η ($\eta_{\rm det}$) covered by the plug calorimeter. As shown in Figure 2.10, it is about 60% at $|\eta_{\rm det}| \sim 1.5$ and almost 0 at $|\eta_{\rm det}| \sim 1.8$.

Recently a new technique for the charge determination was developed where the SVX track is used in conjunction with the plug electromagnetic cluster (see Section 2.3.7). With this technique, the electron charge can be determined up to $|\eta_{\rm det}| \sim 2.3$. The efficiency of this technique at present is only $50-60$ % due to the short length of the SVX′.

With SVX II+ISL+COT integrated tracking for Run II, the momentum information will be better, more efficient, and available over a wider range in η. The total material before electrons hit the plug upgrade detector will be roughly 50-60wide E/p distribution as shown in Figure 2.9, but overall we will improve the electron efficiency quite a bit, reduce QCD background, and make the QCD background estimate easier. Plug electrons will significantly improve the yields for W and Z bosons, and allow us to examine some previously inaccessible electroweak physics topics at high η.

As listed in Table 2.5, the acceptances of W and Z production are almost doubled by changing the η cut from $|\eta| < 1$ to $|\eta| < 2$. The acceptances of the diboson productions are almost tripled (see Table 2.5 and Figures 2.11 and 2.12. More importantly, the high η leptons and photons provide opportunities for previously inaccessible physics. The high η leptons are very sensitive to physics in the small x region (the W charge asymmetry and Drell-Yan cross sections; see Section 2.3.7), and the high η leptons and photons are essential to observe the radiation zero in the $W\gamma$ production (see Section 2.3.5).

Therefore it is important to trigger on plug electrons. The expected Level-1 and Level-3 trigger rates for the plug electrons are much smaller than the available bandwidth, but Level-2 is an issue. Extrapolating from Run Ib Level-2 plug electron trigger rates, the Run II plug electron rate in the region $1.1 < |\eta_{\rm det}| < 2.4$ using the simple requirement $E_T^{\rm PEM} > 20GeV$ is estimated to be about 40 Hz at $\mathcal{L} = 2 \times 10^{32}$ and the 132 ns bunch spacing. This trigger was not efficient enough for W events for Run I. The more efficient trigger was $E_T^{\rm PEM} > 15GeV$ and $\not\!\!E_T > 15GeV$. At $\mathcal{L} = 2 \times 10^{32}$ and the 132 ns bunch spacing, the rate of this trigger is estimated to be about 70 Hz. For the trigger system designed to handle 300 Hz at Level 2, this is uncomfortably high. Therefore it is essential to improve the background rejection by providing additional detector information to the Level-2 system. For example, the Plug shower maximum detector information, the isolation requirement, or the high η track requirement can improve the rejection.

- **Central muons**

  The central muon quality won't change much from Run I to Run II. The Run II tracking de-

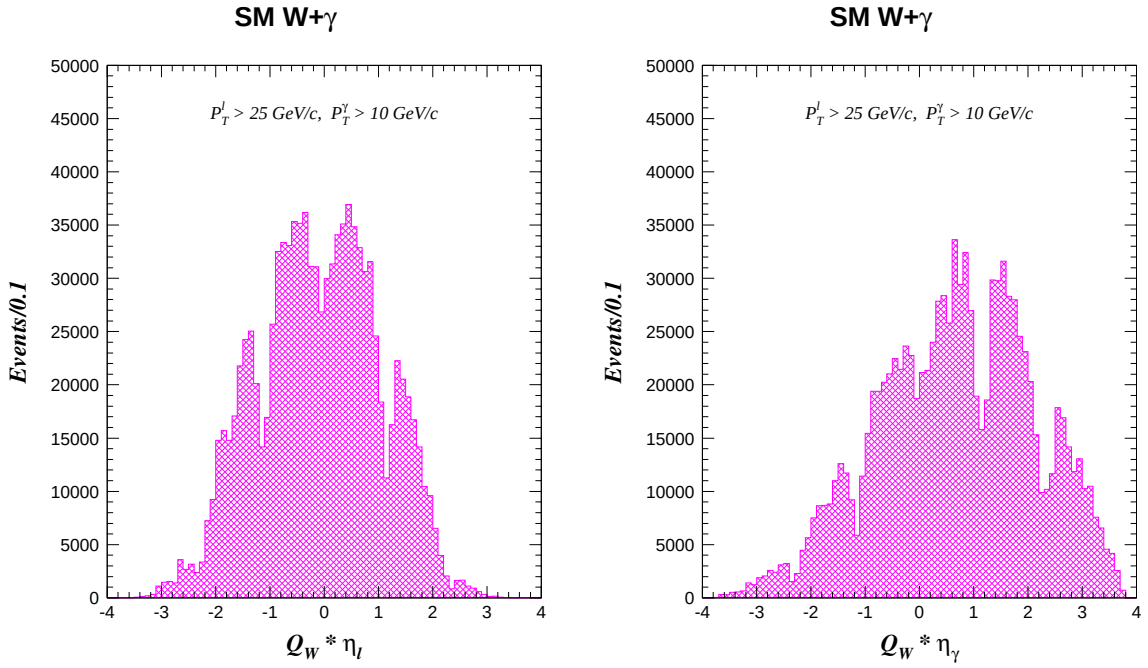

Figure 2.11: The lepton charge signed pseudo-rapidity distribution of the lepton and the photon in the $W\gamma$ production.

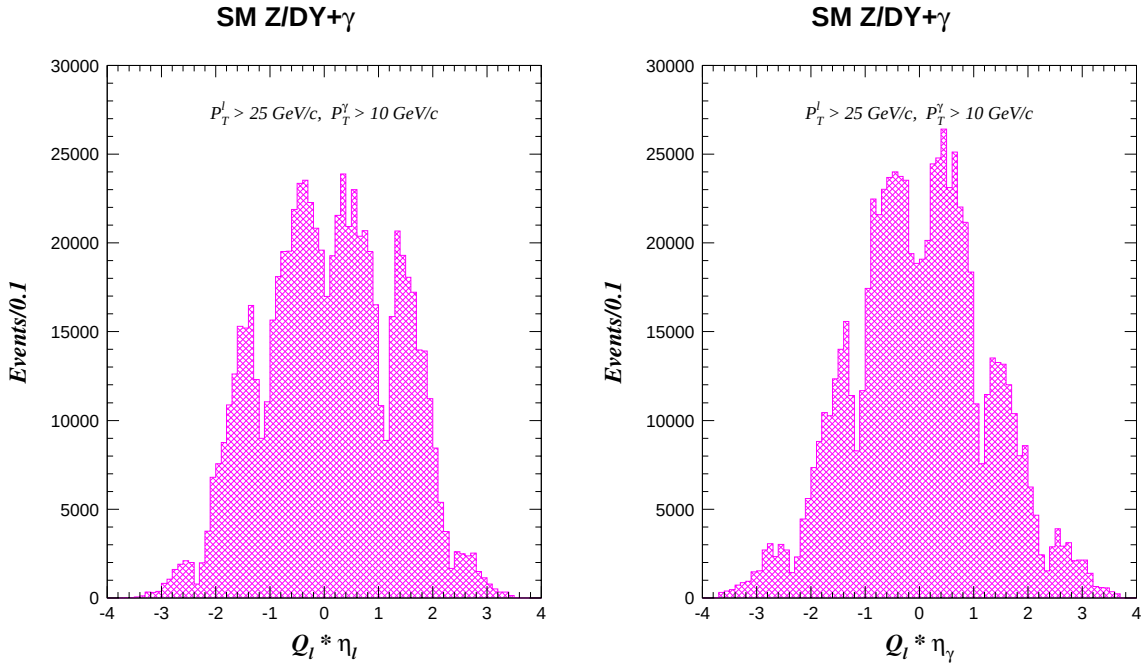

Figure 2.12: The lepton charge signed pseudo-rapidity distribution of the lepton and the photon in $Z\gamma$ production.

tectors will be able to maintain the good resolution and efficiency despite the higher luminosity. There will be additional muon acceptance for Run II, and the samples of $W \rightarrow \mu\nu$ and $Z \rightarrow \mu\mu$ will both be increased by 30%.

- **Intermediate muons** As described in Sec 10.6, muon detection will be added in the region $1.0 \leq |\eta| \leq 2.0$. The arguments for intermediate muons are similar to those for plug electrons: they will be quite helpful for multilepton signatures such as WW, WZ, ZZ decaying to leptons, and for the W charge asymmetry measurement. These will also provide a good handle to reduce the $Z \rightarrow \mu\mu$ background in the $W \rightarrow \mu\nu$ sample.

2.3.3 W Mass

The mass of the W boson is a fundamental parameter of the Standard Model. A direct measurement of M_W can be compared with the prediction from LEP and SLC results as a test of the SM. In the context of other precise electroweak measurements, direct and precise measurements of M_W and $M_{\rm top}$ provide an indirect constraint on the Higgs boson mass, M_H, via electroweak radiative corrections. The ultimate test of the SM may lie in the comparison of this indirect determination of M_H with its direct observation.

At the Tevatron, the W mass is extracted from a fit to the W transverse mass, M_T^W, distribution which sharply peaks in the vicinity of M_W. The 4 pb^{-1} of the 1988-89 Tevatron Collider run enabled CDF to measure the W mass to be

$$M_W = 79.91 \pm 0.39 \text{ GeV/c}^2 \text{ [7]},$$

and with 19 pb^{-1} from Run Ia CDF measured

$$M_W = 80.41 \pm 0.18 \text{ GeV/c}^2 \text{ [8]}.$$

This measurement is an important component of the world average of $M_W = 80.35 \pm 0.13$ GeV. The uncertainties for the Run Ia measurement are shown in Table 2.6. Figure 2.13 (a) shows the sensitivity in the M_W-$M_{\rm top}$ plane of this result when combined with the value $M_{\rm top} = 176.8 \pm 6.5$ GeV/c^2, compared to theoretical predictions based on electroweak radiative corrections [9].

In the following section we will argue that a data set of 2 fb^{-1} will allow CDF II to measure the W mass to ± 40 MeV/c^2, which is comparable to the overall LEP2 expectation (~ 40 MeV). Figure 2.13 (b) shows the sensitivity in the M_W-$M_{\rm top}$ plane of this estimate when combined with the expected precision $\delta M_{\rm top}$ for the same dataset. The precision measurement of the W boson and top quark mass with CDF II will allow inference of the Standard Model Higgs boson mass with an uncertainty of less than $\delta M_H \sim 2 M_H$ [2].

The uncertainties in the current Run Ib measurement scale rather well with statistics from the previous measurement; while the difficulty of the measurement has increased, no systematic limitation is yet evident. The statistical improvement using $\sim$90 pb^{-1} of data from Run Ib is illustrated in Figure 2.14. For Run II, statistical uncertainty and most of systematic uncertainties are expected to be reduced significantly. The individual uncertainties are briefly discussed.

- **Statistical uncertainty**

  For Run Ib the typical instantaneous luminosity at the beginning of runs was about 2×10^{31} cm^{-2} sec^{-1} and we had about 2.5 extra minimum bias events overlying W and Z events on average. This results in about a 10% loss in statistical precision due to the degraded resolution in the recoil measurement in Run Ib as opposed to Run Ia. For 132 ns operation in Run II the increased number of bunches will more than compensate for the higher luminosity and the number of extra minimum bias events will be to the Run Ia level. This will give us a situation which is better than Run Ib.

- **Track momentum scale and resolution**

  Scale: Knowledge of material in the tracking volume is of importance in determining the momentum and energy scale. The associated systematics are the uncertainties in the muon energy loss (dE/dx) for the momentum scale and in the radiative shift of the electron E/p peak for the energy scale. Although the amount of material in the tracking volume will be changed we have shown that photon conversions allow us to measure the amount of material in radiation length quite accurately, as illustrated in Figure 2.15 and can reduce the uncertainties on the W mass measurement. However, the dE/dx muon energy loss requires information of the material type in addition to the radiation length. For example, unknown type of 1% X_o material leads to about 10 MeV uncertainty in the W

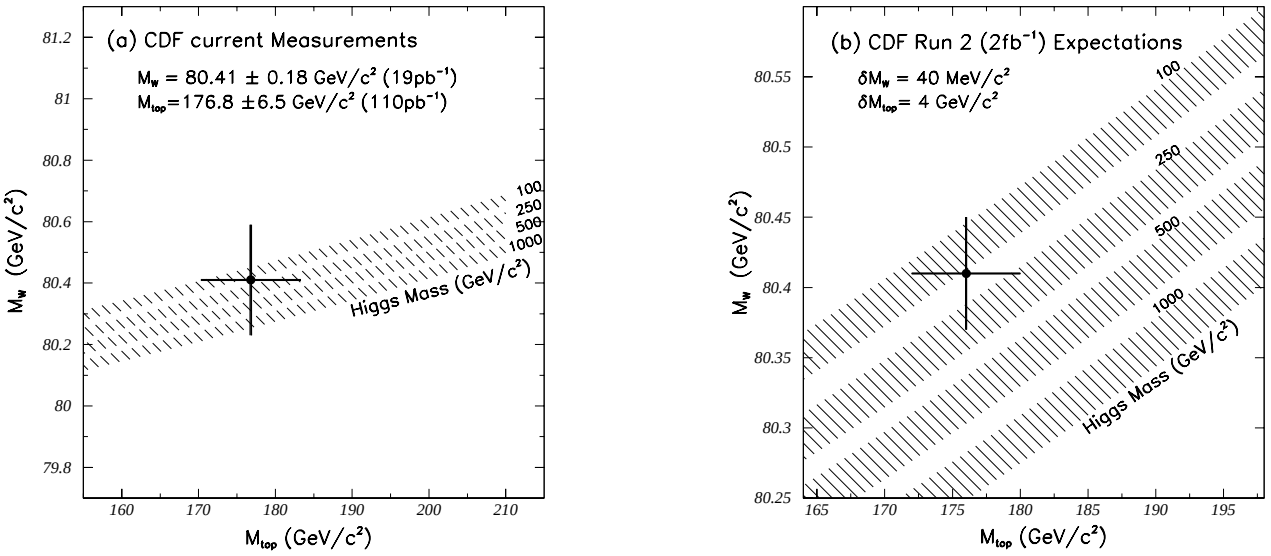

Figure 2.13: The data point in the left figure represents the CDF measurements of M_W and $M_{\rm top}$, and the point in the right figure represents the CDF II estimate for 2 fb^{-1}. The curves are from a calculation [9] of the dependence of M_W on $M_{\rm top}$ in the minimal standard model using several Higgs masses. The bands are the uncertainties obtained by folding in quadrature uncertainties on $\alpha(M_Z^2)$, M_Z, and $\alpha_s(M_Z^2)$.

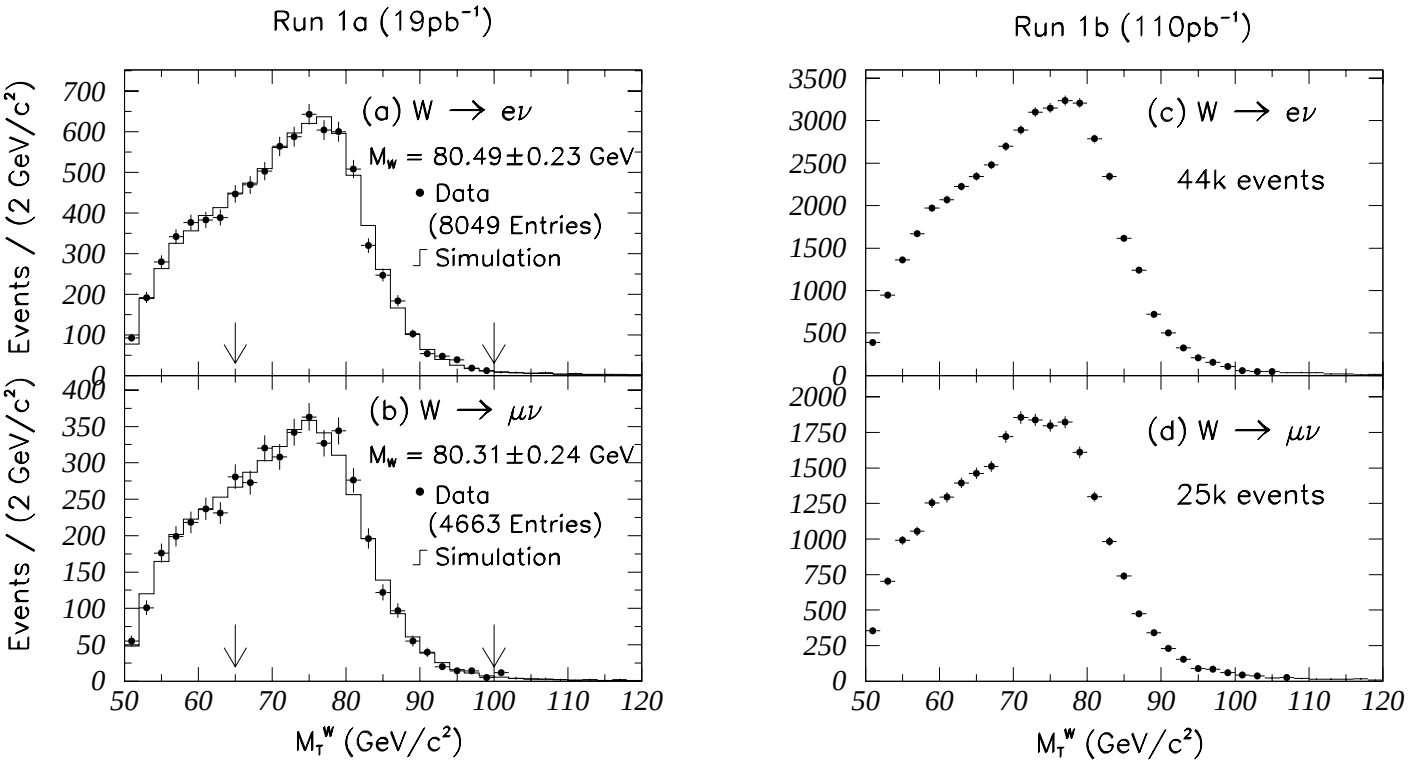

Figure 2.14: Transverse mass distributions for $W \to e\nu$ and $W \to \mu\nu$ from Run Ia (a and b) which gave a $\pm$180 MeV/c^2 measurement of the W mass, and the equivalent preliminary distributions from the first 67 pb^{-1} of Run Ib (c and d).

Source of Uncertainty	Uncertainty (MeV/c^2)		
	$W \to e\nu$	$W \to \mu\nu$	Common
Statistical	145	205	–
Lepton Energy/Momentum Scale	120	50	50
Lepton Energy/Momentum Resolution	80	60	–
Recoil modeling	60	60	60
Trigger, Event Selection	25	25	–
Backgrounds	10	25	–
W Production Model	75	75	65
(P_T^W, PDF, QCD higher order corr., QED rad. corr.)			
Fitting	10	10	–
Total Uncertainty	230	240	100
e and μ Combined Uncertainty		180	

Table 2.6: Summary of uncertainties in the Run Ia W mass measurement.

Source of Uncertainty	Uncertainty (MeV/c^2)		
	$W \to e\nu$	$W \to \mu\nu$	Common
Statistical	14	20	–
Lepton Energy/Momentum Scale	20	15	15
Lepton Energy/Momentum Resolution	8	6	–
Recoil modeling	6	6	6
Trigger, Event Selection	10	10	–
Backgrounds	5	10	–
W Production Model	30	30	30
(P_T^W, PDF, QCD higher order corr., QED rad. corr.)			
Fitting	5	5	–
Total Uncertainty	42	40	34
e and μ Combined Uncertainty		38	

Table 2.7: Estimate of uncertainties in the W mass measurement for 2 fb^{-1}.

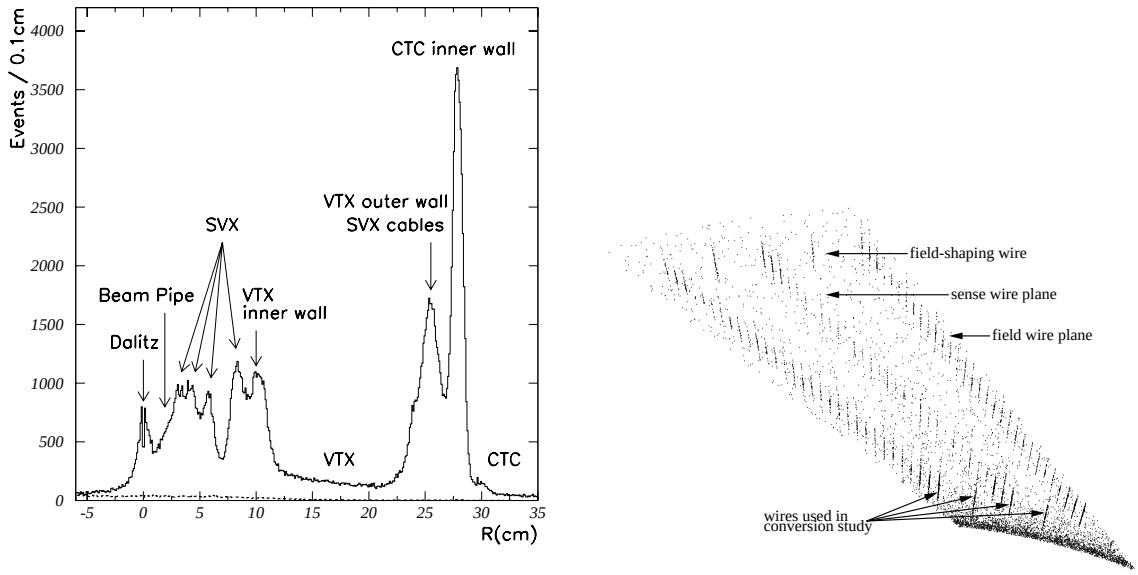

Figure 2.15: Left: The radial distributions for conversions (solid line) and background (dashed line). Right: Reconstructed photon conversion vertex density in the r-ϕ plane for the innermost super-layer in the CTC, folded into 1/30 of the circumference (this layer has 30-fold symmetry).

mass measurement.

Resolution: It is important to assess the impact of high luminosity running on the track momentum resolution. In Run Ib, the CTC track resolution degraded with luminosity, but could be recovered when SVX hits or the SVX beam position were added to the tracking. For instance, if we compare early Run Ib ($\mathcal{L} \sim 0.2 \times 10^{31}$) to later Run Ib ($\mathcal{L} \sim 1 \times 10^{31}$), the CTC track resolution observed in the width of the J/ψ peak worsens by 35%, but the SVX + CTC track resolution worsens by only 10%. The new tracking system incorporates this linking naturally across all detectors (for $|\eta| \leq 1.0$), and as a consequence, the momentum resolution at N = 6 ($\mathcal{L} = 2 \times 10^{32}\mathrm{cm}^{-2}\mathrm{s}^{-1}$) is almost identical to the resolution at N = 1. This is discussed in detail in Chapter 7, see especially Sec. 7.6.3 and Fig. 7.14.

The M_W uncertainty due to the momentum resolution uncertainty will scale with statistics since the resolution is determined using $Z \rightarrow \mu\mu$ events.

- **Calorimeter energy scale and resolution**

The dominant uncertainty in the electron energy scale for Run Ia was from the uncertainty in amount of material in radiation length, and statistics. As described above, the amount of material is expected to be well measured by photon conversion events for Run II, but with complications due to the increase in the amount of material: the statistics of the conversion sample will be reduced by $\sim$ 13% (because of the broadening of the electron E/p), and higher order QED corrections might be necessary.

The M_W uncertainty due to the energy resolution uncertainty will scale with statstics since the resolution is determined using $Z \rightarrow ee$ events.

- **Recoiling energy modeling**

The detector response to the recoil energy against W is directly calibrated using $Z \rightarrow ee$. Therefore the uncertainty will scale with statistics. For Run II with the muon coverage at high η, $Z \rightarrow \mu\mu$ can also be used.

- ***W* Production model**

P_T^W : For the P_T^W spectrum, the P_T^Z distribution from $ee, \mu\mu$ and a new theoretical calculation which includes soft gluon resummation effects

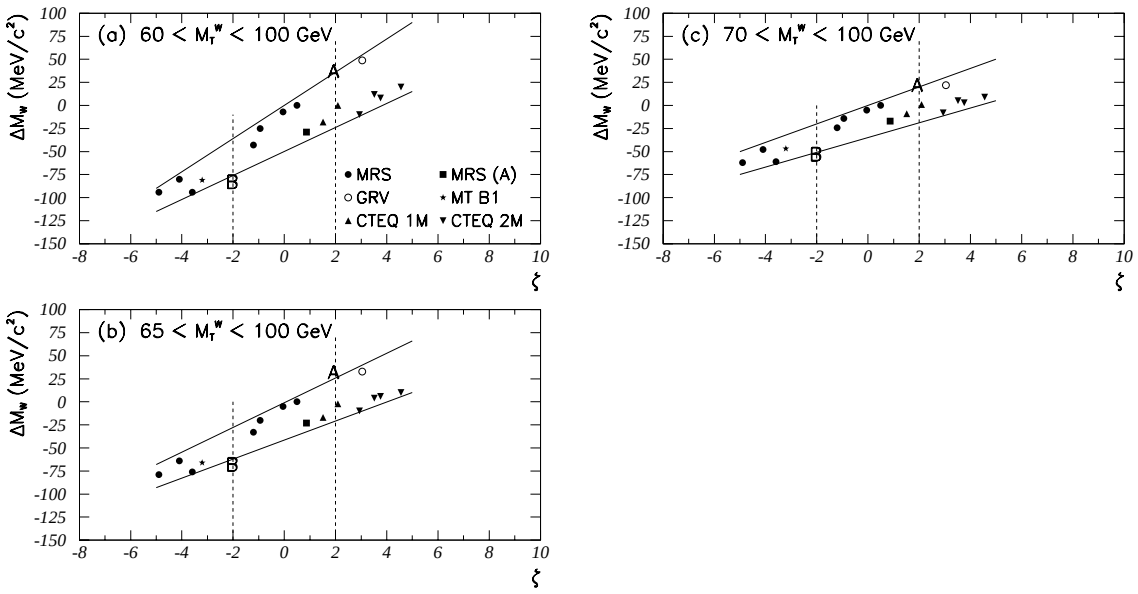

Figure 2.16: Change in derived $W \to e\nu$ mass (ΔM_W^e) versus the signed deviation in units of standard deviations from the average Run Ia W asymmetry measurement (ζ) for various PDFs. The lower edge of the fitting region is (a) 60, (b) 65, and (c) 70 GeV. Note that raising the lower edge of the fitting region makes the result less sensitive to PDFs, particularly for variation not correlated to the asymmetry.

and W, Z decays are expected to provide appropriate checks and improved theoretical guidance, and will make it possible to reduce the current uncertainty of 45 MeV in M_W substantially.

Parton Distribution Functions: The Run Ia uncertainty in PDF's (50 MeV) was constrained by the CDF W asymmetry measurement (see Figure 2.16; the dotted lines indicate ± 2 standard deviations from the Run Ia W asymmetry measurement.) This particular advantage in constraining the PDF systematic uncertainty in the W mass may soon be saturated, and with the same technique the uncertainty of 25 MeV in M_W is estimated for Run II. (With more statistics, the dotted lines in Figure 2.16 will get closer to zero, but ΔM_W won't.) This will then be the dominant uncertainty in M_W for Run II.

The fact that the PDF uncertainty in M_W does not scale with the W asymmetry uncertainty indicates that parameters in PDFs sensitive to the W charge asymmetry are not the only ones sensitive to the M_T^W distribution. Monte Carlo studies show that the W charge asymmetry is sensitive to $< u >$ and $< d >$, and the M_T^W distribution has a weak but not small dependence on $\sigma_u^{\rm RMS}$ and $\sigma_d^{\rm RMS}$ in addition to a strong dependence on $< u >$ and $< d >$. The y distributions of Z (y_Z) from dileptons have some sensitivity to constrain PDFs in $\sigma_u^{\rm RMS}$ and $\sigma_d^{\rm RMS}$, and this may help reducing the PDF uncertainty in M_W. However, to do this a precise measurement (better than 1%) of Z efficiency as a function y_Z in a wide rapidity region is required.

An alternative solution to reduce the PDF uncertainty will be raising the minimum M_T^W for fitting. This is illustrated in Figure 2.16 (a), (b) and (c). However, this will imply a larger statistical uncertainty.

QCD higher order corrections : The effects of higher-order QCD corrections on the W polarization and on a correlation between P_T^W and y_W were investigated for Run Ia and were estimated to be 20 MeV in M_W. There have been an improved theoretical calculation of W and Z production, which may allow to reduce this uncertainty further.

QED Radiative corrections : Radiative corrections in M_W are rather large: the shifts in M_W due to the final state radiation are 65 MeV in the $W \to e\nu$ channel and 168 MeV in the $W \to \mu\nu$ channel. For Run Ia, the uncertainty in these shifts due to missing diagrams was estimated to be 20 MeV. Recently, a more thorough calculation [10] of radiative W and Z boson production and decay, including initial and final state radiation, finite lepton masses, and finite W, Z width effects. This will make it possible to reduce the error associated with radiative corrections substantially in the future.

- **Backgrounds**

  The uncertainty which does not scale with statistics will be from the $Z \to \mu\mu$ background (one muon in the central muon chambers and the other muon in high η region) in the $W \to \mu\nu$ sample. The uncertainty due to the choice of PDF's for this background led to 10 MeV uncertainty in M_W for Run Ia. For Run II, the tracking upgrade (well measured IFT+SVX II tracks in the region $1 < |\eta| < 2$) and the forward muon upgrade (muons in the region $1.5 < |\eta| < 3$) together with the muon signature in the plug upgrade calorimeter will remove most of this background and will reduce the uncertainty.

- **Trigger Bias**

  For Run Ia, there was 25 MeV uncertainty due to a possible momentum dependence of the muon triggers in the $W \to \mu\nu$ channel. For Run Ib, E_T threshold for Level-2 electrons was raised and the track resolution was degraded with luminosity. This may have caused trigger biases in both e and μ samples, which can be included in the simulation. Even though these biases are in the simulation, the uncertainty does not necessarily scale with statistics. For Run II, it is important to have unbiased triggers. That is, the momentum thresholds are low enough not to introduce a P_T or E_T dependence above 25 GeV. Also it is essential to keep triggers without any isolation requirement.

We make a conservative estimate that 2 fb^{-1} will allow CDF II to measure the W mass to ± 40 MeV/c^2, which is comparable to the overall LEP2 expectation ($\sim$ 40 MeV). The list of uncertainties is shown in Table 2.7. In making this estimate, we have not included important beneficial effects of the muon upgrades, such as the increase in the central muon acceptance and the improved forward muon acceptance to reduce the uncertainty in the $Z \to \mu\mu$ background.

2.3.4 W Width

The leptonic branching ratio of the W may be inferred from the ratio $R = \sigma \cdot Br(W \to l\nu)/\sigma \cdot Br(Z \to ll)$, using LEP measurements for the Z couplings and a theoretical prediction of the production cross section ratio. Before the top quark was discovered, this measurement was used to exclude hidden top scenarios. Now it is a standard model consistency check. For Run Ia [11] CDF measured $Br(W \to e\nu) = 0.109 \pm 0.005$. If one further assumes standard couplings for $W \to e\nu$, one can derive a value for the total width of the W, , $_W = 2.064 \pm 0.085$ GeV. The theoretical uncertainty in the cross section ratio is expected to limit precision to about $\pm 1\%$. However, the upgraded momentum measurement in the region $1 < |\eta| < 2$ should give improved acceptance systematics, lessening the dependence on the parton distribution functions.

For Run Ia, CDF measured $\sigma \cdot Br(W \to e\nu) = 2.51 \pm 0.12$ nb and $\sigma \cdot Br(Z \to ee) = 0.231 \pm 0.012$ nb [13]. These measurements are approaching the $\pm 3.6\%$ level of the luminosity normalization [14].

The W width can be measured directly from the shape of the transverse mass distribution (see Figure 2.17). For $M_T^W > 110$ GeV/c^2 resolution effects are under control and using Run Ia in the mode $W \to e\nu$, CDF measured , $_W = 2.11 \pm 0.32$ GeV [15]. The uncertainties will likely scale with statistics allowing a ± 30 MeV measurement for 2 fb^{-1}, much better than the LEP2 expectation of ± 200 MeV. Figure 2.18 summarizes indirect and direct measurements of , $_W$ so far and the predicted uncertainty for 2 fb^{-1} from the direct measurement.

2.3.5 Gauge Boson Couplings

The Standard Model makes specific predictions for the trilinear couplings of the gauge bosons, W, Z, and γ. The nature of these couplings can be investigated via studies of $W\gamma$ and $Z\gamma$ production [16] and WW, WZ and ZZ pair production [17]. The major goals of these studies will be testing the Standard Model prediction(s) and searching for new physics. The numbers of candidates and backgrounds, and

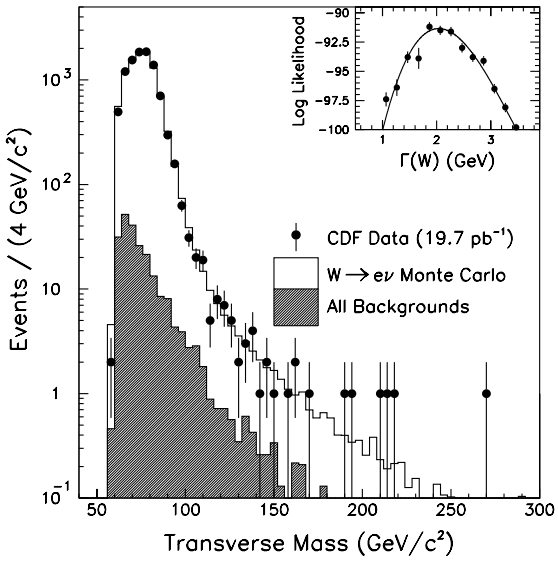

Figure 2.17: Transverse mass distribution (M_T^W) for $W \rightarrow e\nu$ candidates along with background and signal expectation. The inset is the fit to $M_T^W > 110$ GeV/c^2.

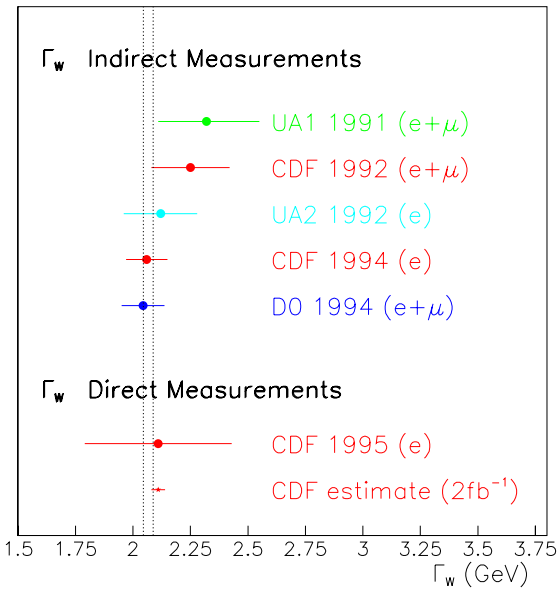

Figure 2.18: Indirect and direct measurements of , $_W$ and the predicted uncertainty from the direct measurement for 2 fb^{-1} of data. The dotted band represents the standard model prediction.

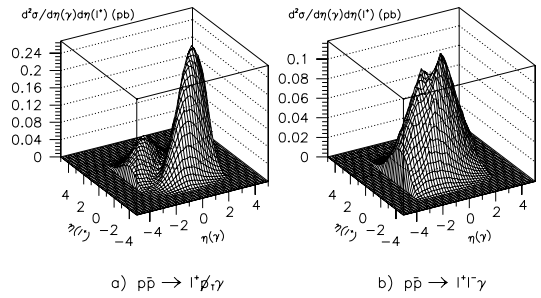

Figure 3

Figure 2.19: The double differential distribution $d^2/dy(\gamma)dy(\ell)$ for $p\bar{p} \rightarrow W^+\gamma \rightarrow \ell\nu\gamma$ (Left) and $Z\gamma \rightarrow \ell\ell\gamma$ (Right).

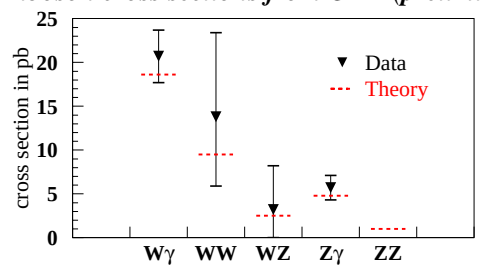

Figure 2.20: The measured cross sections of diboson productions and the theoretical predictions

the measured cross section for each production mode are summarized and the cross section is compared with the theoretical expectation in Table 2.8 and Figure 2.8.

From the absence of an excess of events at large E_T^γ in $W\gamma$ and $Z\gamma$ production, with 67 pb^{-1} combined $e + \mu$ Run Ia+Ib data we have extracted 95% CL limits on $WW\gamma$ and $ZZ\gamma$ anomalous couplings, such as $-1.8 < \Delta\kappa_\gamma < 2.0$ and $-0.7 < \lambda < 0.6$.

$W\gamma$ production in $p\bar{p}$ collisions is of special interest due to the SM prediction of a radiation amplitude zero in the charge-signed $Q_W \cdot \cos\theta_\gamma^*$ distribution at ~ -0.3. The radiation zero is also predicted to manifest itself as a "channel" in the charge-signed $Q_W\eta_\ell$ *vs.* $Q_W\eta_\gamma$ 2-dimensional distribution [18] shown in Figure 2.19, and as a strong "dip" in the charge-signed photon-W decay lepton rapidity difference distribution, $Q_W \cdot (\eta_\gamma - \eta_\ell)$ at ~ -0.3. For Run II data

Mode ($\ell = e, \mu$)	L (pb^{-1})	Data (events)	Backgrounds (events)	$\sigma_{exp}^{\mathrm{diboson}}$ (pb)	$\sigma_{theory}^{\mathrm{diboson}}$ (pb)
$W\gamma \to \ell\nu, \gamma$	67	109	26.4 ± 3.6	20.7 ± 3.0	18.6
$WW \to \ell\nu, \ell\nu$	1 10	5	1.21 ± 0.30	$10.2^{+6.5}_{-5.3}$	9.5
$WZ \to \ell\nu, \ell\ell$	110	1	$0.3^{+0.8}_{-0.3}$	$3.2^{+5.0}_{-3.2}$	2.5
$Z\gamma \to \ell\ell, \gamma$	67	31	1.4 ± 0.4	5.7 ± 1.4	4.8
$ZZ \to \ell\ell, \ell\ell$	120	1	?	?	1.0

Table 2.8: The numbers of candidates and backgrounds, and the integrated luminosity for each production mode. Also the measured cross sections and the theoretical expectations are listed.

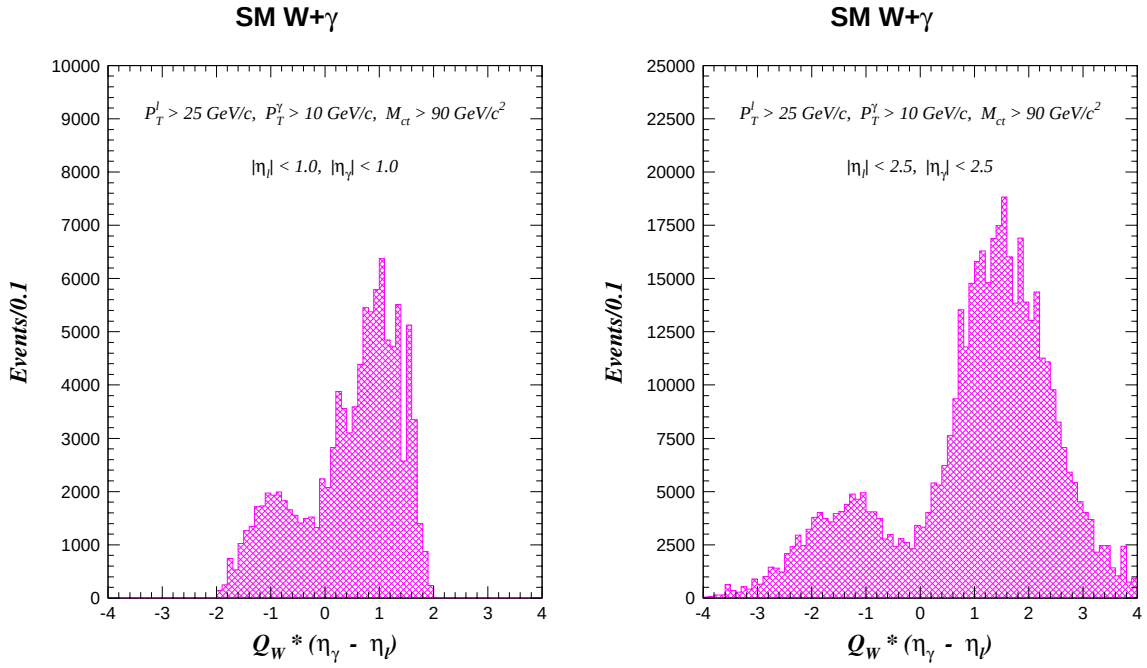

Figure 2.21: The lepton charge signed pseudo-rapidity difference distribution in the $W\gamma$ production for $|\eta_\ell| < 1.0$ and $|\eta_\gamma| < 1.0$ (Left), and $|\eta_\ell| < 2.5$ and $|\eta_\gamma| < 2.5$ (Right).

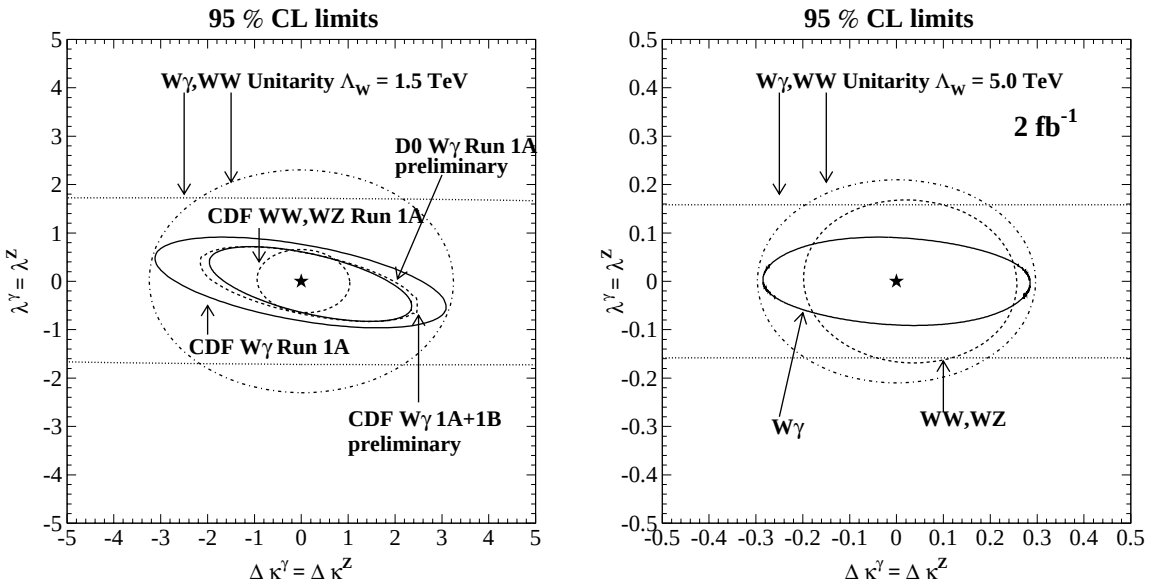

Figure 2.22: 95% CL limits on anomalous couplings. Present limits (Left) and expected limits with 2 fb^{-1} (Right) on WWV $(V = W, \gamma)$ anomalous couplings.

sets the rapidity difference distribution is a more useful variable. A sufficient rapidity coverage is essential to observe the radiation zero, which is demonstrated in Figure 2.21. If both central and plug ($|\eta| < 2.5$) electrons and photons can be used, the simulations indicate that with integrated luminosities of 1 fb^{-1} it will be possible to conclusively establish the dip in the photon lepton rapidity difference distribution. On the other hand, for central electrons and photons only, the dip is not statistically significant.

Currently, we are in the process of analyzing our Run Ib data, and have succeeded in extending our photon selection into the plug region. We are also in the process of re-analyzing our Run Ia data with the new plug photon selection. From 110 pb^{-1} combined Run Ia+Ib $e + \mu$ data, including plug photons, we have increased our $W\gamma$, $Z\gamma$ data sample sizes by more than a factor of 10 over the original Run Ia $W\gamma$, $Z\gamma$ analysis. We hope to have preliminary results on (significantly) improved limits on $WW\gamma$ and $ZZ\gamma$ anomalous couplings, the $W\gamma$ radiation zero and other interesting results from analysis of the full Run Ia+Ib $e + \mu$ combined $W\gamma$, $Z\gamma$ data in the very near future.

For Run II, we anticipate that the current results from CDF will undergo further significant improve-

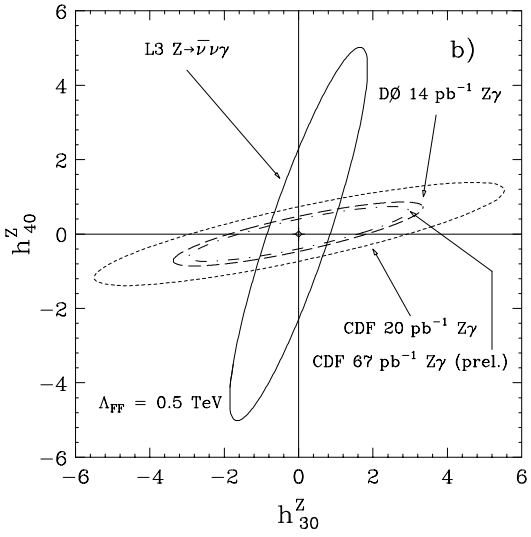

Figure 2.23: Present limits on $ZZ\gamma$ anomalous couplings.

ment(s) with 2 fb^{-1} integrated luminosity, in conjunction with the Run II upgrades of the overall tracking, calorimeter, muon and DAQ systems. Run II SM $W\gamma$ and $Z\gamma$ event yields are expected to be $\sim$ 1500 and 450, respectively, using the current event selection criteria.

Limits on $WW\gamma$ and WWZ anomalous couplings are also obtained from the absence of an excess of high-P_T WW and WZ boson pairs [17]. In this analysis, one vector boson is observed to decay leptonically and the other hadronically, as a jet pair of appropriate mass. The boson P_T is required to be high enough to avoid W + jets background. Analysis of the Run Ia+Ib $WW, WZ \to \ell\nu +$ 2 jets data result in the limits $-0.7 < \Delta\kappa_V < 0.9$ and $-0.5 < \lambda_V < 0.5$ at 95% CL. The absence of an excess of high-P_T WW pair events in our data also simultaneously excludes a zero-strength WWZ coupling at greater than 99% CL, thus beautifully confirming the *existence* of the delicate γWW-ZWW gauge cancellation predicted by the Standard Model, which is required if the theory is to be renormalizable!

Figure 2.22 (Left) summarizes current limits on WWV ($V = \gamma, Z$) anomalous couplings. Figure 2.23 summarizes current limits on $ZZ\gamma$ anomalous couplings. The limits on $Z\gamma\gamma$ anomalous couplings are comparable to those of $ZZ\gamma$ couplings. The sensitivity for CDF II WWV and $ZZ\gamma$ anomalous coupling measurements with 2 fb^{-1} are anticipated to be comparable, and complementary, to those anticipated from LEP-II experiments. For example, with 2 fb^{-1} of data, limits on $|\Delta\kappa_V|$ should get to about 0.3 and limits on $|\lambda_V|$ to about 0.1 (see Figure 2.22, right).

WW boson pair production, where both W's decay leptonically can be readily distinguished from $t\bar{t}$ production and decay to dilepton final states. Using $\sim$110 pb^{-1} from Run Ia+Ib data, CDF sees 5 candidates with an expected background of 1.3 events and an expected signal of 2.6 events. These events are quite central and the additional acceptance provided by the upgrades of about 30-40% comes primarily from central muon upgrades. For 2 fb^{-1} integrated luminosity, $\sim$ 100 WW dilepton pairs are expected, for the Standard Model prediction.

2.3.6 Forward-Backward Z Asymmetry

The presence of both vector and axial-vector couplings of electroweak bosons to fermions in the process $q\bar{q} \to Z^0/\gamma \to e^+e^-$ gives rise to an angular asymmetry, "Forward-Backward Asymmetry", in the emission angle of the electron in the rest frame of the electron-positron pair. This asymmetry, A_{FB}, is a direct probe of the relative strengths of the vector and axial-vector couplings over the range of Q^2 being considered. In addition, A_{FB} constrains the properties of any hypothetical heavy neutral gauge bosons not included in the Standard Model. For values of Q^2 significantly larger than M_Z^2, A_{FB} is predicted to be large and positive (approximately 0.5), so a statistically significant measurement can be made with a small number of events.

From $\sim$110 pb^{-1} of the Run I dielectron data, CDF has measured A_{FB} to be 0.074 ± 0.017 using a sample of 5473 events in the Z pole region defined by $75 < M_{ee} < 105$ GeV, and 0.45 ± 0.11 using a sample of 172 events in the high mass region defined by $M_{ee} > 105$ GeV. These measurements can be compared with the Standard Model predictions of 0.052 ± 0.002 and 0.528 ± 0.009. Table 2.9 summarizes our measured values for A_{FB} and its uncertainties in both invariant mass regions.

With 2 fb^{-1} of data from Run II, we anticipate the detection of over 100,000 electron pairs resulting from Drell-Yan processes, all with invariant masses in excess of 75 GeV/c^2. Such a large number of events will allow for precision measurements of the angular distributions of the electron pairs both at and above the Z^0 pole.

In the vicinity of the Z^0 pole, for electron pairs with invariant mass between 75 GeV/c^2 and 105 GeV/c^2, it will be possible to extract a precision measurement of $\sin^2\theta_W^{eff}$ from A_{FB}. The Run I measurement of A_{FB} at the Z^0 pole [19] has a total uncertainty dominated by statistical uncertainty, with the other sources of uncertainty (from background level determination and electron pair mass resolution) expected to scale with statistics as well. For instance, the Run II upgraded plug detector and tracking system expanded to higher eta region will reduce the background. The uncertainty in $\sin^2\theta_W^{eff}$ should also scale with statistics since A_{FB} is proportional to $(\sin^2\theta_W^{eff} - 0.25)$. Under the assumption that all uncertainties scale with statistics, we expect an uncertainty in A_{FB} of 0.003 and an uncertainty in $\sin^2\theta_W^{eff}$ of 0.001. The Run II measurement of A_{FB} at the Z^0 pole is not expected to discriminate between different choices of parton distribution functions, as the current theoretical uncertainty in A_{FB} due to struc-

	$75\ \mathrm{GeV/c^2} < \mathrm{M}_{ee} < 105\ \mathrm{GeV/c^2}$		$\mathrm{M}_{ee} > 105\ \mathrm{GeV/c^2}$	
	CC	CP	CC	CP
Raw event sample	2611	2862	91	81
Background	6 ± 2	139 ± 26	1^{+2}_{-1}	27 ± 15
Predicted Asymmetry	0.048		0.52	
Measured Asymmetry	0.074		0.45	
Uncertainty in A_{FB}				
Statistical	0.016		0.10	
Background subtraction	0.003		0.05	
Mass Deconvolution	0.003		0.04	
Total uncertainty	0.017		0.11	

Table 2.9: Run I ($110\ \mathrm{pb}^{-1}$) measurements of A_{FB}.

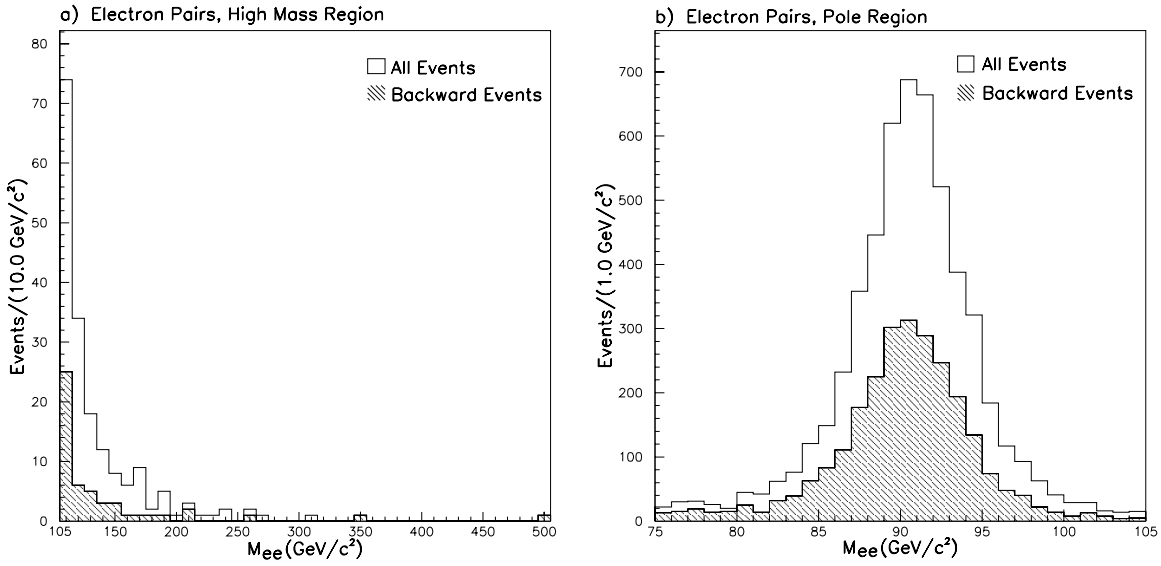

Figure 2.24: The invariant mass distribution of events in the high mass sample.(Left) and the pole region sample (Right).

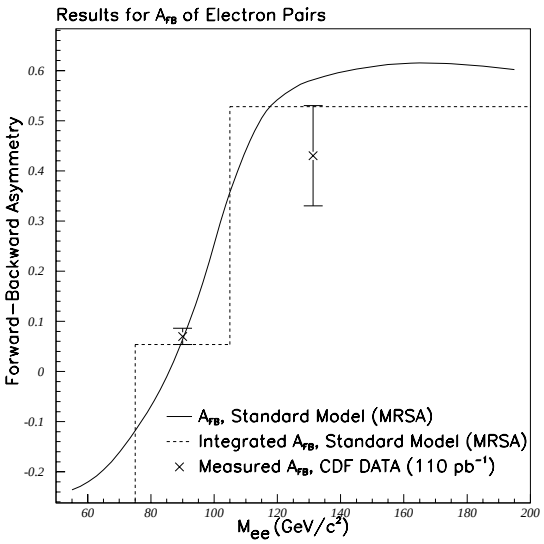

Figure 2.25: Results of our measurement of A_{FB}, compared with a Standard Model calculation. The solid line is a bin-by-bin calculation of A_{FB} (MRSA), and the dashed line is the same calculation integrated over the two mass regions.

ture function uncertainty is approximately 0.001 [20]. With the increased statistics it may also be possible to observe the rapid variation of A_{FB} as the electron pair mass varies between 75 GeV/c^2 and 105 GeV/c^2.

It should be noted that if $\sin^2\theta_W^{eff}$ is measured to within 0.001 as expected, then the CDF II result will be competitive with the LEP I and SLD results which measure $\sin^2\theta_W^{eff}$ from jet charge asymmetries in hadronic Z^0 decays. For example, the ALEPH collaboration reports a measurement of $\sin^2\theta_W^{eff}$ from light quark jets of 0.23222 ± 0.00081(stat.) $\pm$ 0.00070(syst.) $\pm$ 0.00080(theor.), where the last two sources of uncertainty arise chiefly from mismeasurement of jet charge and theoretical assumptions about jet fragmentation, respectively [21]. By virtue of measuring the inverse process, where electrons are in the final state and quarks are in the initial state, the CDF II measurement will not be sensitive to these systematic effects, and may therefore have a comparable total uncertainty with very different systematic uncertainties.

Well above the Z^0 pole, for electron pairs with invariant mass in excess of 105 GeV/c^2, A_{FB} is dominated by Z^0/γ interference, and a large positive value is predicted for A_{FB} with a very flat dependence in electron pair invariant mass. There can be strong variations in A_{FB} with invariant mass due to a variety of exotic physics at higher invariant mass scales, including most Z′ or composite Z models [22], and also lepton compositeness models. Moreover, if a Z′ is discovered at CDF II, A_{FB} measurements will provide discrimination between various Z′ models [22].

As with the measurements of A_{FB} at the Z^0 pole, we expect the uncertainty in the measurements above the Z^0 pole to scale with statistics compared to the Run I measurement [19]. For electron pairs with invariant mass between 105 GeV/c^2 and 195 GeV/c^2, we expect to collect approximately 2500-3000 events. Using this entire sample we expect to measure A_{FB} to within 0.02, and it will be possible to explore the variation of A_{FB} with invariant mass in some detail. For electron pairs with invariant mass above 195 GeV/c^2 (above the LEP 200 maximum $\sqrt{s}$), we expect to collect approximately 200-300 events, which should allow a measurement of A_{FB} to within 0.07. We note that these measurements neither discriminate between nor depend significantly upon the choice of proton structure function, since the theoretical uncertainty of A_{FB} in this invariant mass range due to choice of structure function is approximately 0.009 [20].

2.3.7 PDF Measurements and Issues

2.3.7.1 W Charge Asymmetry

The Run Ia CDF measurement of the W asymmetry shown in Figure 2.26 (Left) [23] is an important constraint on parton distribution functions for collider experiments, and has been used as input by both the MRS and CTEQ groups. Note that the sensitivity to the PDF's increases with lepton eta. The Ia measurement ends at $|\eta| \sim 1.8$ because the CTC track finding efficiency (see Figure 2.10) falls rapidly beyond $|\eta| \sim 1.2$ and becomes almost 0 at $|\eta| \sim 1.8$.

A new technique for extending the asymmetry measurement using electrons at higher $|\eta|$ has recently been developed by CDF for the Run Ib measurements. Here, the plug calorimeter is used to determine the energy and the shower centroid location of the electron, and the SVX is used to determine the track. No central tracking is required. A comparison of the extrapolated SVX track with the shower centroid in the calorimeter is used to determine the charge of the electron. With this technique the electron η coverage is extended up to 2.3. Due to the

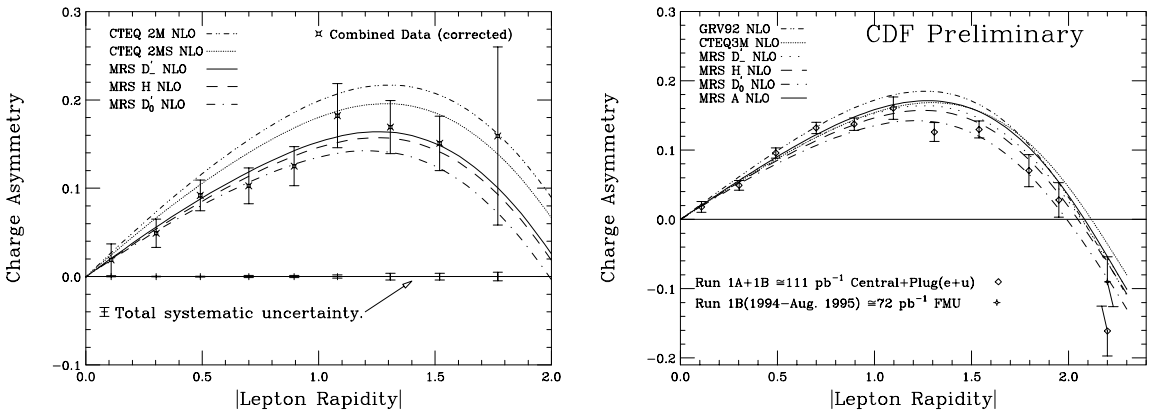

Figure 2.26: Left: Combined Run Ia W charge asymmetry measurement using muons and central and plug electrons. These data have been used as input in determining recent PDF sets. Right: Combined W charge asymmetry using Run Ia and Ib data including the forward muons.

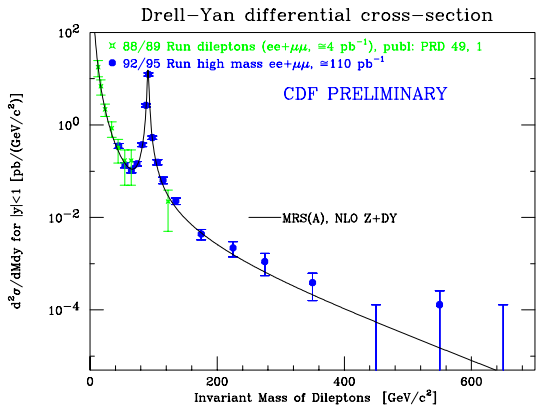

Figure 2.27: Drell-Yan dilepton $(e^+e^-, \mu^+\mu^-)$ production cross section from Run Ia and Ib as a function of the dilepton invariant mass.

short length of the SVX′, the SVX tracking finding efficiency is only $50-60\%$ as shown in see Figure 2.10. For Run Ib, we have also measured the W charge asymmetry in $2 < |\eta^\mu| < 2.5$ using the current forward muon detector. All of these measurements from central electrons, plug electrons, central muons, and forward muons are combined and are shown in Figure 2.26 (Right).

The data in the central region probes the d and u distributions in the x region between 0.02 and 0.15. The forward data probes the region between 0.006 (a new region of x) and 0.35. These forward data indicate that further tuning of the d and u distributions in the current PDF's might be needed.

The new Run II plug electromagnetic calorimeter and shower max detectors offer greater improvement over the present plug. In addition, the tracking with SVX II and IFT will be much better. These new detectors can be used to further extend the W asymmetry electron data in the forward directions. The tracking upgrade and the muon toroid move will allow the extension of the asymmetry measurement using muons to higher $|\eta|$ as well. The measurements should remain statistically dominated through 2 fb^{-1}.

2.3.7.2 Drell-Yan production

Cross section measurements of Drell-Yan production [24] (especially the low mass region) can be used to get further constraints on PDFs. The Run Ia+Ib Drell-Yan cross section measurements using central electrons are shown in Figure 2.27. The low mass Drell-Yan data and forward data are currently under analysis. The main difficulties in these area are estimating QCD backgrounds. The new technique described in previous paragraphs now provides the ability to determine the charge of an electron in the forward direction, and allows a direct measurement of the QCD background by a comparison of like-sign to opposite-sign events. Therefore, the Drell-Yan measurement can now be extended to the forward direction (for both electron and muon pairs), and the low mass region. The low mass data is sensitive to the very low x region which has never been explored be-

fore at the Tevatron. Run II upgrades to the DAQ bandwidth will be important for this program in order to preserve our ability to trigger on low p_T lepton pairs.

The y distributions of Drell-Yan dilepton pairs can be measured as a function of the dilepton invariant mass. These distributions will also contain the information of PDF's.

The high mass Drell Yan data from Run IA and IB, on the other hand, can now be used to place limits on compositeness around the 3 TeV range. These limits can be greatly improved in Run II.

Bibliography

[1] S. L. Glashow, Nucl. Phys. **22**, 579 (1961); S. Weinberg, Phys. Rev. Lett. **19**, 1264 (1967); A. Salam, in *Elementary Particle Theory: Relativistic Groups and Analyticity*, ed. N. Svartholm (Almqvist and Wiksell, Stockholm, 1968), p. 367.

[2] F. S. Merritt, H. Montgomery, A. Sirlin and M. Swartz, DPF report on Precision Tests of Electroweak Physics, CDF Note 3154.

[3] F. Abe *et al.* (CDF Collaboration), Phys. Rev. Lett. **74**, 2626 (1995), S. Abachi *et al.* (D0 Collaboration), Phys. Rev. Lett. **74**, 2632 (1995).

[4] H. Aihara, *et al.*, "Anomalous Gauge Boson Interactions", Summary of the Subgroup on Anomalous Gauge Boson Interactions of the DPF Long-Range Planning Study, in "Electroweak Symmetry Breaking and Beyond the Standard Model, edited by T. Barklow, S. Dawson, H. Haber and J. Siegrist, World Scientific, Singapore (1995).

[5] H. Aihara, *et al.*, "Intermediate Vector Boson Physics", Summary of the TeV-2000 Working Subgroup on Electroweak Physics, edited by R. Brock and D. Amidei, Fermilab, (1996).

[6] D. Schaile, presented at 10th International Workshop on $p\bar{p}$ Interactions, Fermilab 1995.

[7] F. Abe *et al.*(CDF), Phys. Rev. **D43**, 2070 (1991).

[8] F. Abe *et al.*(CDF), Accepted for publication in Phys. Rev., FERMILAB-PUB-95/033-E.

[9] The curves are calculated using a FORTRAN program from F. Halzen and B.A. Kniehl (private communication), described in Nucl. Phys. **B353**, 567 (1990). See Ref. 4 for details.

[10] U. Baur and D. Zeppenfeld, Phys. Rev. Lett. **75**, 1002 (1995).

[11] F. Abe *et al.*(CDF), Phys. Rev. Lett. **73**, 220 (1994).

[12] Particle Data Group, Phys. Rev. **D50**, p 1173 (1994).

[13] W. Badgett (CDF), proc. DPF Abaquerque (1994), FERMILAB-CONF-95/258-E.

[14] F. Abe *et al.*(CDF), Phys. Rev. **D50**, 5550 (1994).

[15] F. Abe *et al.*(CDF), Phys. Rev. Lett. **74**, 341 (1995).

[16] F. Abe, *et al.*, The CDF Collaboration, "Measurement of $W-$Photon Couplings in p-$\bar{p}$ Collisions at $\sqrt{s} = 1.8$ TeV", Phys. Rev. Lett. **74**, 1936 (1995); F. Abe, *et al.*, The CDF Collaboration, "Limits on $Z-$Photon Couplings from p-$\bar{p}$ Interactions at $\sqrt{s} = 1.8$ TeV", Phys. Rev. Lett. **74**, 1941 (1995).

[17] F. Abe, *et al.*, The CDF Collaboration, "Limits on WWZ and $WW\gamma$ Couplings from WW and WZ Production in p-$\bar{p}$ Interactions at $\sqrt{s} = 1.8$ TeV", Phys. Rev. Lett. **75**, 1017 (1995).

[18] U. Baur, S. Errede and G. Landsberg, "Rapidity Correlations in $W\gamma$ Production at Hadron Colliders", Phys. Rev. D**50**, 1917 (1994).

[19] F. Abe *et al.*, Fermilab Report No. FERMILAB-PUB-96/071-E.

[20] U. Baur (private communication).

[21] ALEPH Collaboration, D. Buskulic *et al.*, CERN-PPE/96-09.

[22] J. L. Rosner, Fermilab Report No. FERMILAB-PUB-95/394-T.

[23] F. Abe *et al.*(CDF), Phys. Rev. Lett. **74**, 850 (1995).

[24] F. Abe *et al.*(CDF), Phys. Rev. **D49**, R1 (1994).

2.4 Search for New Phenomena

2.4.1 Introduction

We know that the Standard Model is incomplete– it has a non-physical high-energy behavior, and also lacks the deep explanatory power that we seek in a fundamental theory of space-time, forces, and particles. There is currently a great deal of theoretical activity focussed on new physics that would solve the problems with the Standard Model and which would also be detectable in the energy scale accessible to CDF II at the Main Injector. Predictions from models invoking new phenomena at the 100-200 GeV/c^2 mass scale, the scale we will be exploring, have been made for Supersymmetry [1, 2, 3, 4, 5, 6], Technicolor [7], new U(1) symmetries [8], and Topcolor [9, 10, 11], for example.

The cross-sections for new states with masses in the 100-200 GeV/c^2 range (*i.e.*, systems with total invariant mass in the 200-400 GeV/c^2 range) are typically predicted to be in the range 10-1000 fb [2, 3, 4, 5, 6, 7, 8], so that with 2 fb^{-1} detailed measurements are possible. The broad-band nature of the production process in $\bar{p}p$ collisions is an advantage for searching as there is coupling to many different production processes: for example, in addition to Drell-Yan production, pairs of new particles such as charginos can be produced through gluons or through top decay.

2.4.1.1 Impact of the Upgrade

Discovery relies heavily on a thorough understanding of the detector. Establishing a new and perhaps unexpected phenomena does not allow the luxury of systematic uncertainty; instead, there arise the most stringent requirements on confidence in all the parts of the measurement and the device. Two aspects are critical: the identification of objects that make up each signature, and the understanding of the calibration and resolution of the detector.

The objects for which we have already a good understanding of the efficiencies and fake-rates are those for which tracking is essential: electrons, muons, tau's, b's, and photons (*i.e.*, a high confidence of the absence of a track), all in the central region. At Run II luminosities, the presence of multiple vertices will confuse the algorithms, with complications for object identification. The addition of the stereo capability to SVX and the strengthened COT stereo capabilities will help enormously. An improved tracking system and improved calorimeter, along with its calibration, resolution, efficiency and coverage should also help to better understand $\not\!\!E_T$ measurements.

Similarly, the energy scale and resolutions of the calorimeters, critical to the reconstruction of masses, are well understood in the central region, where the tracking information is used to calibrate the calorimeters. The integrated tracking and new plug calorimeter of the upgrade will extend the 'good' region where tracking is robust for e, μ, τ, γ and b identification, and will provide the calorimeter energy scale calibration, out to $|\eta| = 2$.

There are a number of other limitations in present searches that the upgrade will ameliorate. For instance, at present many channels with b decays are triggered on objects other than the b. Many signatures for new physics are tied to the heavy third generation, and thresholds can be lowered substantially by requiring a b at the trigger level. The $\gamma bc\not\!\!E_T$ combination proposed by Kane [3] as a top squark (supersymmetric partner of a top quark) signature is a good example: at present the photon trigger threshold is set at 23 GeV, and in the absence of the SVT would have to be raised substantially in Run II, as we have no ability to trigger at present on the b. Other postulated states [2, 3, 7, 8] in the same mass region will have signatures of $b\bar{b}$ or $b\bar{c}$, and will be triggerable.

In summary, the new plug calorimeter, new integrated tracking, and extended b-detection and triggering capability will provide a much larger and more uniform kinematic region in η and p_T for measurements of leptons, b-quarks, photons, jets, and $\not\!\!E_T$, while also providing the redundancy and cross checking that are crucial for precision calibration and the understanding of systematic effects.

2.4.1.2 Current Situation and Plan

To date, many of the highest limits in direct searches for physics beyond the Standard Model come from CDF. Table 2.10 summarizes the current CDF limits on various new particles. In the sections below we describe our ongoing new phenomena searches and current results together with extrapolating the present performance to the upgrade. The following topics are covered: Supersymmetry, New Gauge Bosons Z' and W', New Particles decaying to Dijets, Topcolor and the b-tagged Dijet Search, Leptoquarks, Compositeness, Massive Stable Particles, Technicolor, and

CDF Exotic Particle Searches: Results and Run II Prospects

Searches	current CDF limit (Gev) Excluded region @ 95% C.L.		data set	run II (GeV) with 2 fb^{-1}
W'→ ev(SM)	< 652		1a (20 pb-1)	< 990
W'→ WZ	<560 (ref. model excluded)	*	1a+1b (110 pb-1)	
Z'→ *ll* (SM)	< 690	*	1a+1b (110 pb-1)	< 900
$Z\psi, Z\eta, Z\chi, Z_I$	< 580,610,585,555	*	1a+1b (110 pb-1)	< 800
Z_{LR}, Z_{ALRM}	< 620,590	*	1a+1b (110 pb-1)	< 800
Axigluon→ qq	200<M<930	*	1a+1b (103 pb-1)	< 1160
Techniro→ dijet	250<M<500	*	1a+1b (103 pb-1)	200<M<770
E_6 Diquark →qq	280<M<350	*	1a+1b (103 pb-1)	200<M<570
topgluon Γ=.1M	200<M<550	*	1a (20 pb-1)	
topgluon Γ=.3M	210<M<450	*	1a (20 pb-1)	
topgluon Γ=.5M	200<M<370	*	1a (20 pb-1)	
Leptoquark (μq,τq)	< 180, 94 (scalar, β=1)	*	1a+1b (70 pb-1)	< 300
Pati-Salam LQ (Bs - eμ)	< 12900	*	1b (88 pb-1)	
Pati-Salam LQ (Bd - eμ)	< 18300	*	1b (88 pb-1)	
Composit. Scale (qq*ll*)	3800(-), 2600(+) (ee)	*	1a+1b (110pb-1)	< 5000
q* (W+jet, γ+jet)	< 540	*	1a (20 pb-1)	< 820
q*→ dijet	200<M<750	*	1a+1b (103 pb-1)	<820
massive stable ptl.	< 190 (col. tri. q)	*	1b (48 pb-1)	<300
gluino	< 180 (any $m\tilde{q}$), < 230 ($m\tilde{g}=m\tilde{q}$)	#	1b (80 pb-1)	<200/<250
gaugino	$\chi_1^{\pm}$ < 68, χ_2^0 < 68	#	1a+1b (100 pb-1)	<130
$H^{\pm}$	< 130 (tanβ>100)	*	1b (88 pb-1)	

* Current world best limit in direct search mode for the model.

\# Same as *, but D0 (also LEP1.5) has comparable limits.

update May 1st, 1996

Table 2.10: A summary of CDF's searches for physics beyond the standard model along with the prospects for Run II.

Charged Higgs Searches. All quoted limits are at 95% confidence level (C.L.), unless explicitly stated otherwise. For simplicity we define 'mass reach' as the largest excluded mass at 95% C.L. [12, 13].

2.4.2 Supersymmetry

Supersymmetry (SUSY) [14] is a symmetry between bosons and fermions, and is the only known symmetry to provide the solution to a problem of the quadratic divergence of scalar mass parameters in the Standard Model. The experimental signatures of supersymmetry are complex, as all known fermions of the Standard Model have bosons as supersymmetric partners while all bosons acquire fermions as superpartners, and in addition the symmetry is obviously broken, with possible additional large numbers of new fields. Due to the large number of free parameters, it is necessary to make further assumptions in the context of specific SUSY models. Two possibilities are that the breaking of SUSY is transmitted to the observable sector by gravitational interactions (supergravity models) [15, 16], or by gauge interactions [17]. Within these frameworks there are many variations, depending on specific assumptions of parameters. However general arguments can be made that the masses of the superpartners may lie in the region accessible by the Tevatron in Run II or Run III [1]. The Tevatron can explore a significant portion of the

parameter space using a number of possible signatures. The searches described below have been done using the framework of the MSSM, but are appreciably more general. Other searches, specific to certain models, are also now in progress.

One canonical signature is trilepton events, which would come from chargino-neutralino (*e.g.*, $\tilde{\chi}_1^{\pm}\tilde{\chi}_2^0$) pair production with subsequent leptonic decays (*e.g.*, $\tilde{\chi}_1^{\pm} \to l\nu\tilde{\chi}_1^0$ and $\tilde{\chi}_2^0 \to l\bar{l}\tilde{\chi}_1^0$) [18]. Here $\tilde{\chi}_1^0$ is assumed to be the lightest supersymmetric particle (LSP) and expected to escape from the detector ($\not\!\!E_T$). Another signature is squark and gluino ($\tilde{q}$ and $\tilde{g}$) production followed by decays into the LSP and jets. Yet another is based on the Majorana nature of the gluino, which allows the gluino to decay into a chargino of either sign. One consequently searches for like-sign (LS) dilepton pairs from cases where a pair of gluinos have decayed into charginos of the same sign [19]. Searches for these three signatures, as well as a number of searches for the top squark (stop), predicted to be the lightest of the squarks, are underway with the Run I data.

More recently, there has been a flurry of activity on models in which radiative decays of neutralinos, either $\tilde{\chi}_1^0$ [2, 3, 4, 5, 6] or $\tilde{\chi}_2^0$ [3] are expected. These speculations are based on a single CDF $ee\gamma\gamma\not\!\!E_T$ candidate event. Searches for sleptons, for charginos and neutralinos, the gravitino, and for the light stop are also underway in these scenarios.

2.4.2.1 The Trilepton Search

For this search pair-produced $\tilde{\chi}_1^{\pm}\tilde{\chi}_2^0$ are assumed to decay as $\tilde{\chi}_1^{\pm} \to l^{\pm}\nu\tilde{\chi}^0$ and $\tilde{\chi}_2^0 \to l^+l^-\tilde{\chi}^0$. Here $\tilde{\chi}^0$ is assumed to be the lightest supersymmetric particle (LSP). The striking signature of these events is thus three isolated leptons plus $\not\!\!E_T$ [18]. The CDF search is based on 100 pb^{-1} data. Most of the events are from inclusive e and μ triggers at $p_T \sim 10$ GeV/c. The trilepton requirements are $p_T(l_1) > 11$ GeV/c and $p_T(l_{2,3}) > 5$ (4) GeV/c for e (μ), which is the same as in the previous analysis (based on 19 pb^{-1}) [20]. Eight events survive the selection, consistent with the SM background. A further cut of $\not\!\!E_T > 15$ GeV is imposed to reduce the background. No trilepton event candidates are found, which is consistent with an expected background of 0.4 ± 0.1 for four trilepton (eee, $ee\mu$, $e\mu\mu$, $\mu\mu\mu$) modes. Figure 2.28 shows the 95% C.L. upper limit on $\sigma \cdot BR(\tilde{\chi}_1^{\pm}\tilde{\chi}_2^0 \to 3l + X)$ as a function of $M_{\tilde{\chi}_1^{\pm}}$, where "3 l" is any 3-way combination of

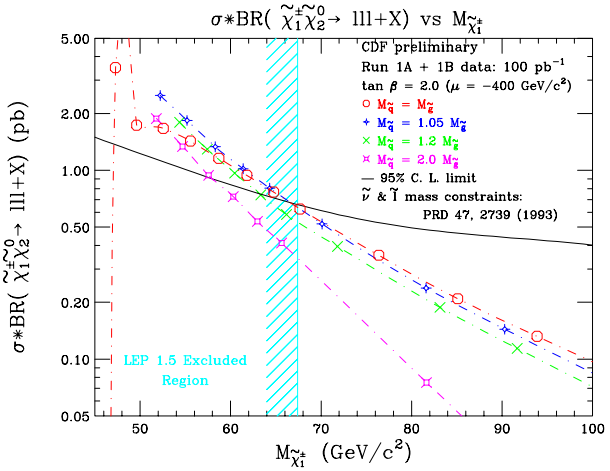

Figure 2.28: $\sigma \cdot BR$ versus $\tilde{\chi}_1^{\pm}$ mass for a representative point in MSSM parameter space ($\tan\beta = 2$, $\mu = -400$ GeV/c^2. BR is the sum of the branching ratios for the four trilepton modes. The solid line is the 95% C.L. limit based on an observation of zero events. All points above the line are excluded.

e and μ as above. To obtain limits, CDF imposes a constraint inspired by supergravity models [21]. The CDF analysis [20] calculates slepton ($\tilde{l}$) and sneutrino ($\tilde{\nu}$) masses from $\tan\beta$, $M_{\tilde{g}}$, and $M_{\tilde{q}}$ using the renormalization group equations [22]. In these models, the chargino and neutralino have three-body decays. The CDF analysis excludes $M_{\tilde{\chi}_1^{\pm}} < 68$ GeV/c^2 (95% C.L.) at $\tan\beta = 2$, $M_{\tilde{q}} = M_{\tilde{g}}$ and $\mu = -600$ GeV (the region of maximum experimental sensitivity). The CDF limit on $\tilde{\chi}_1^{\pm}$ (68 GeV/c^2) is comparable to the LEP1.5 result [23], assuming a heavy sneutrino. A limit on $\sigma \cdot BR(\tilde{\chi}_1^{\pm}\tilde{\chi}_2^0 \to 3l + X)$ is also obtained: 0.6 pb (CDF) for a 70-GeV/c^2 chargino. CDF also examines one particular supergravity model, a flipped SU(5) model [24]. In this model, $M_{\tilde{l}_R} < M_{\tilde{\chi}_2^0} < M_{\tilde{l}_L}$, so that the trilepton signal is nearly maximized via $BR(\tilde{\chi}_2^0 \to \tilde{l}_R^{\pm}l^{\mp}) \sim 66\%$ (e and μ) and $BR(\tilde{l}_R^{\pm} \to l_R^{\pm}\tilde{\chi}_1^0) = 100\%$. However, the mass difference of $\tilde{l}_R$ and $\tilde{\chi}_1^0$ decreases as $M_{\tilde{\chi}_1^{\pm}}$ increases, so that the total trilepton acceptance as a function of $M_{\tilde{\chi}_1^{\pm}}$ becomes flat at about 5% at 60 GeV/c^2 and falls off for $M_{\tilde{\chi}_1^{\pm}} \gtrsim 75$ GeV/c^2. The limit on $M(\tilde{\chi}_1^{\pm})$ is 73 GeV/c^2.

Extrapolations of the chargino/neutralino search using the trilepton channel to higher integrated luminosities have been made by three groups [25, 26, 27]. Both Refs. [26, 27] assumed a large acceptance ($|\eta| < 2.5$) for the leptons (e and μ), while coverage similar

to the current CDF detector is assumed in Ref. [25]. It should be noted that the selection cuts in Ref. [27] are optimized for the higher $\tilde{\chi}_1^{\pm}$ mass region using high luminosity (*e.g.*, TeV33).

We take an extrapolation in Ref. [25] as a conservative estimate, because the tracking coverage is consistent with that by the SVX-II (5 layers) and COT system. We have revised the analysis in Ref. [25] by requiring $\not\!\!E_T > 20$ GeV. The background cross section for DY/Z + X is expected to be 0.1 fb, while about 80% of 120-GeV/c^2 $\tilde{\chi}_1^{\pm}$ events are accepted. The total background (DY/Z, $t\bar{t}$, dibosons) becomes 0.5 fb which is the same level as in Ref. [26]. Taking into account the difference in the geometric coverage and details of the selection cuts, there are no obvious disagreements for the estimate of the total background. If we take the specific model used in the Run Ia and Ib analyses [20], the current mass limit can be extended to about 130 GeV/c^2 with 2 fb^{-1} of data in Run II.

Refs. [13, 26] studied the maximum mass reach in more generic MSSM models. In those studies, the coverage for leptons was assumed to be $|\eta| < 2.5$. The maximum chargino mass we can probe at 2 fb^{-1} was found to be 210 GeV/c^2 for a 5σ significance above background. This is far above the maximum limit of 90 GeV/c^2 from LEP-II ($\sqrt{s}$ = 190 GeV and $\int \mathcal{L}dt$ = 500 pb^{-1}) and is competitive to the limit of 248 GeV/c^2 from NLC ($\sqrt{s}$ = 500 GeV and $\int \mathcal{L}dt$ = 20 fb^{-1}) [13].

2.4.2.2 Classic Multi-jet Plus $\not\!\!E_T$ Search

Pairs of squarks and gluinos, $\tilde{q}\tilde{q}$, $\tilde{g}\tilde{g}$, and $\tilde{q}\tilde{g}$, would be produced via the strong interaction. Depending on the relative masses of squarks and gluinos, production of $\tilde{q}\tilde{q}$, $\tilde{q}\tilde{g}$, or $\tilde{g}\tilde{g}$ may predominate. Direct decays of each $\tilde{q}$ and $\tilde{g}$ to quark + $\tilde{\chi}^0$ (assumed to be the LSP) result in one and two quark jets respectively, while cascade decays through charginos and neutralinos may result in two or more additional jets. Events therefore always contain two jets, and most should contain three or more jets, in addition to missing energy. Two strategies are being followed: A high $\not\!\!E_T$ plus three or more jet requirement to cover regions in supersymmetric parameter space in which squark production is dominant, and a more moderate $\not\!\!E_T$ requirement in combination with a higher jet multiplicity for regions where gluino pair production has the highest cross-section.

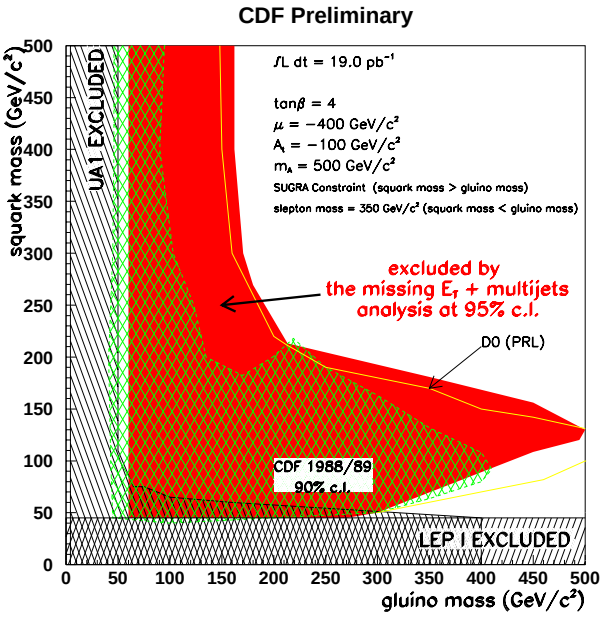

Figure 2.29: The 95% C.L. mass limit as a function of the squark and gluino mass values in jets plus $\not\!\!E_T$ channels.

The Run Ia CDF search for multijet plus $\not\!\!E_T$ events from SUSY requires 3 or more jets (E_T > 15 GeV) and $\not\!\!E_T$ > 60 GeV. Additional cuts are imposed to reduce backgrounds from cosmic rays, mismeasured QCD multijet events, W/Z plus jet events, and other sources, to a reasonable level. The removal of W/Z plus jets backgrounds requires rejection of events with electrons or muons. In the final data sample there are 23 events with 3 or more jets over an estimated background of $35.1^{+11.6}_{-9.1}$(stat) $^{+15.3}_{-5.5}$ (sys) and 6 events with 4 or more jets over an estimated background of $8.5^{+4.2}_{-3.0}$ (stat) $^{+2.6}_{-1.9}$ (sys). The background estimate contains W and Z leptonic, and top semileptonic decays. The W and Z hadronic decay backgrounds (lepton not observed) are normalized directly to the data, using multijet events in which a lepton is observed. We conclude that no significant excess is observed, and set a conservative upper limit on potential SUSY contributions by assuming a zero background contribution from QCD mismeasurement. The region of the $M_{\tilde{q}} - M_{\tilde{g}}$ plane which is excluded by this analysis is shown in Figure 2.29. For arbitrary $M_{\tilde{q}}$ the data require $M_{\tilde{g}} > 160$ GeV/c^2 and for $M_{\tilde{g}} \approx M_{\tilde{q}}$ we deduce $M_{\tilde{g}} > 220$ GeV/c^2.

The larger data samples of Run Ib and Run II will allow proportionally better determination of the backgrounds. However, since the analysis is back-

ground dominated, better limits will be obtained by tightening analysis cuts and perhaps fitting the shape of the $\not\!\!E_T$ spectrum.

For 0.1 fb^{-1}, we need to reduce the background substantially. CDF used cuts of $\not\!\!E_T > 60$ GeV and $N_{jet}(E_T > 15 \text{ GeV}) \geq 3$ in the Run Ia analysis. We have revised this analysis with cuts of $\not\!\!E_T > 80$ GeV and $N_{jet}(E_T > 20 \text{ GeV}) \geq 4$. The other cuts on lepton veto fake $\not\!\!E_T$ due to mismeasured jet *etc.* remain the same. With the new cuts, our expectation of the background cross section is 0.16 pb. The 1.64σ significance above background for 0.1 fb^{-1} is 0.07 pb (or 7 events). Therefore, we find the 95% C.L. limit on the gluino mass of 270 GeV/c^2 if $M_{\tilde{q}} \simeq M_{\tilde{g}}$ for a specific choice of SUSY model [13].

The dominant background sources are $t\bar{t}$, W and Z events. Further reduction of background can be reduced by requiring $E_{T\,j_1} + E_{T\,j_1} + \not\!\!E_T > 300$ GeV [26]. The total background is then estimated to be 40 fb. With more generic SUSY models, the maximum possible reach (95% C.L. upper limit is $\sigma = 7.3$ fb) can be over 400 GeV/c^2 [26].

Some help from theorists may be forthcoming when recent NLO calculations of squark pair production, which show cross-sections approximately double those of the leading order calculations, are extended to squark/gluino and gluino/gluino production.

2.4.2.3 Search for Gluino Cascade Decays in the Dilepton Channel

Light gluinos ($M_{\tilde{g}} \lesssim 70$ GeV/c^2) decay preferentially into a quark-antiquark pair and an LSP. However, the decays into a chargino will dominate as soon as they are kinematically allowed [28]. Since the gluino is a Majorana particle, the charge of the chargino can be either $+1$ or -1 in a gluino decay. For example, $\tilde{g} \to \tilde{u}^*\bar{u} \to (d\tilde{\chi}_1^+)\bar{u}$ and $\tilde{g} \to u\bar{\tilde{u}}^* \to u + (\bar{d}\tilde{\chi}_1^-)$ will equally be seen, if $M_{\tilde{q}} > M_{\tilde{g}} > M_{\tilde{\chi}_1^\pm}$. A subsequent chargino decay can yield a lepton, a neutrino and an LSP (*e.g.*, $\tilde{\chi}_1^\pm \to l^\pm \nu \tilde{\chi}_1^0$). Thus, a dilepton pair (OS or LS) + multijets + $\not\!\!E_T$ is a signature of gluino pair production. Moreover, LS dileptons are a distinctive signature with small SM backgrounds[19]. The dilepton analysis complements the classic $\not\!\!E_T$ plus multijet analyses: while the $\not\!\!E_T$ plus multijet analysis is degraded by cascade decays [1], the dilepton analysis is based upon them.

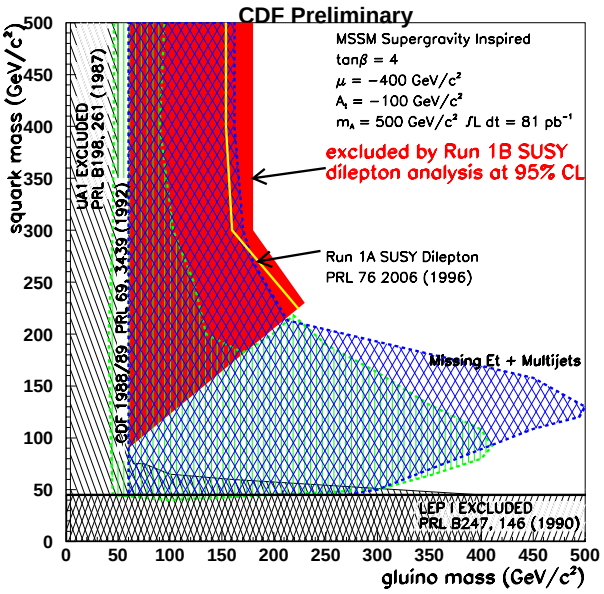

Figure 2.30: The 95% C.L. mass limit as a function of squark and gluino mass values from the LS dilepton + jets + $\not\!\!E_T$ channel.

In Run Ia (19 pb^{-1}), we did not apply the LS requirement [29]. The dilepton requirements are $p_T(l_1) > 12$ GeV/c ($|\eta_e| < 1.1$ or $|\eta_\mu < 0.6$) and $p_T(l_2) > 11$ GeV/c ($|\eta_e| < 2.4$ or $|\eta_\mu < 1.0$). Electron or muon pairs with opposite charge with 70 GeV/c^2 $< M_{ll} <$ 105 GeV/c^2 are removed. In addition, we require: (a) 2 or more jets ($E_T > 15$ GeV) in $|\eta| < 2.4$ with at least one of them in the central region ($|\eta| < 1.1$); (b) $\not\!\!E_T > 25$ GeV; (c) $I(l_1) + I(l_2) <$ 8 GeV, where I is a measure of the amount of energy surrouding each lepton using a combination of calorimeter and tracking information; (d) $\Delta\phi_{ll} < 60°$ or $60° < \Delta\phi_{ll} < 120°$ if $p_T(ll) < 40$ GeV/c or $\Delta\phi_{ll} < 120°$ if $p_T(ll) < 20$ GeV/c. Only one candidate event (a $\mu^+\mu^-$ event) is observed. In comparison, the expected number of background events from SM processes is $2.39 \pm 0.63(\text{stat})^{+0.77}_{-0.42}(\text{sys})$. We have set limits on gluino and squark production in the MSSM. For squark mass equal to the gluino mass, we exclude gluinos up to 224 GeV/c^2. For heavy squarks, $M_{\tilde{q}} = 400$ GeV/c^2, we exclude gluinos up to 154 GeV/c^2 ($\tan\beta = 4.0$ and $\mu = -400$ GeV/c^2) [29].

For the Run Ib data (81 pb^{-1}), we have repeated the Run Ia dilepton analysis without the $\Delta\phi_{ll}$ and $p_T(ll)$ cuts, but with the LS requirement and lower

[1] Cascade decays reduce the amount of $\not\!\!E_T$ produced in a gluino or squark decay (compared to the direct decay into LSP) and thus the detection efficiency in the $\not\!\!E_T$ based searches.

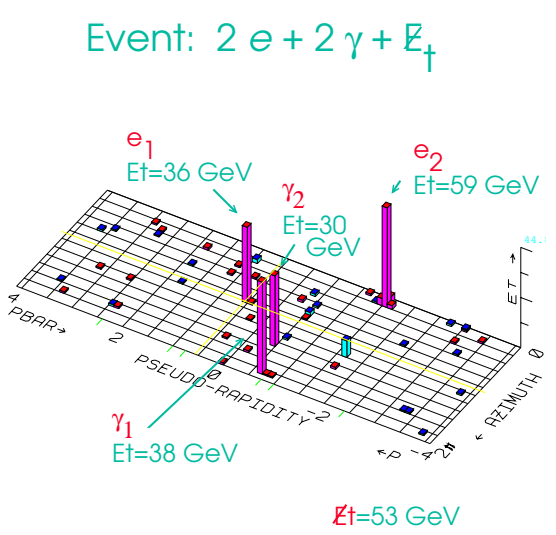

Figure 2.31: The Lego plot of the $ee\gamma\gamma\not\!\!E_T$ candidate event.

lepton p_T cuts ($p_T(l_1) > 11$ GeV/c and $p_T(l_2) > 5$ GeV/c). It should be noted that the LS requirement reduces the signal events by a factor of four. Lowering the lepton p_T cuts was necessary to recover the loss of acceptance. In a preliminary analysis, we observed two events, where the expected number of background events was $1.29 \pm 0.62(\text{stat}) \pm 0.35(\text{sys})$: dominant sources are 0.58 events from $t\bar{t}$, 0.46 events from DY, and 0.22 events from W plus a misidentified additional lepton. The 95% C.L. upper limits on gluino and squark masses were determined in the same manner as in the Run Ia analysis [29]. The resultant limits as a function of the squark and gluino mass values are shown in Figure 2.30. For squark mass equal to the gluino mass, we exclude gluinos up to 230 GeV/c^2. For heavy squarks, $M_{\tilde{q}} = 400$ GeV/c^2, we exclude gluinos up to 180 GeV/c^2 ($\tan\beta = 4.0$ and $\mu = -400$ GeV/c^2). We are investigating additional cuts to improve the signal-to-background ratio.

The LS dilepton analysis is complementary to the classic $\not\!\!E_T$ + jets analysis and has very little background. The striking signature of LS dilepton + jets + $\not\!\!E_T$ makes this analysis ideal for Run II (and Run III). We also note that two analyses can be combined to improve the mass limits. This is underway for Run Ib data.

2.4.2.4 Radiative Decays of Neutralinos

One can interpret the signature $ee\gamma\gamma\not\!\!E_T$ of one event in our data, shown in Figure 2.31, as a possible supersymmetry candidate. A search is underway for similar events in the diphoton channel; this is the dominant channel in scenarios in which the gravitino is the LSP [5] as well in the slepton or chargino production scenarios [2, 3, 4, 6]. A search for the the light stop in the signature $\gamma + b + jet + \not\!\!E_T$ is also underway in these scenarios, as are other searches involving photons plus missing Et and/or leptons. In all of these scenarios the ability to identify a b quark is a powerful tool (for example, most stop signatures involve b quarks); in Run II the SVT will allow us the ability to trigger on the b allowing lower photon or lepton thresholds, and the extended coverage and improved pattern recognition of the integrated tracking system will substantially increase the tagging efficiency.

2.4.2.5 The Light Stop Quark

One of two top squarks (stops) may have a mass significantly lower than other squarks. Here, $\tilde{t}_1$ is the lighter stop. The cross section for stop pair production is expected to be an order of magnitude smaller than the production of 'ordinary' top quark pairs for equal masses. For example, a stop with mass around 110 GeV/c^2 is expected to have about the same production rate as the 175 GeV/c^2 top quark. Two decay modes for the light stop which could be detectable at the Tevatron [13]: ($M_{\tilde{t}} < M_{top}$): (a) $\tilde{t}_1 \to \tilde{\chi}_1^+ b$; (b) $\tilde{t}_1 \to \tilde{\chi}_1^0 c$. Several searches are underway for the stop using Run I data.

A Monte Carlo study for the mass reach of the stop in Run II, has been made and described in Ref. [13]. The 5σ mass limit was found to be 150 GeV/c^2 for 2 fb^{-1}.

2.4.3 New Gauge Bosons Z' and W'

Heavy neutral gauge bosons in addition to the Z^0, generically denoted as Z', occur in any extension of the Standard Model that contains an extra U(1) after symmetry breaking. For example, in one model with E_6 as the grand unified gauge group [30] there exists a Z_ψ from the symmetry breaking $E_6 \to SO(10) \times U(1)_\psi$ and a Z_χ from the symmetry breaking $SO(10) \to SU(5) \times U(1)_\chi$. Finally the SU(5) symmetry breaks to recover the Standard Model:

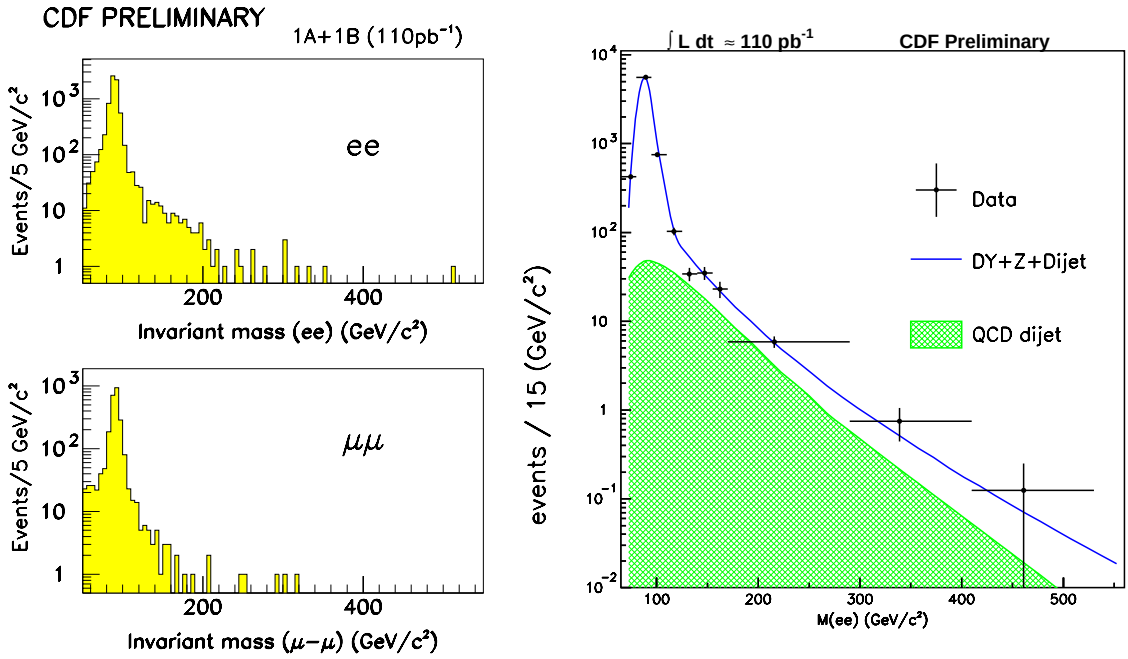

Figure 2.32: Left: The dielectron and dimuon invariant mass distributions for the Z' search data sample. Right:The dielectron invariant mass distributions compared to background predictions.

$SU(5) \rightarrow SU(3)_C \times SU(2)_L \times U(1)_Y$. In superstring inspired E_6 models there exists a Z_η which is the linear combination $Z_\eta = \sqrt{3/8}Z_\chi + \sqrt{5/8}Z_\psi$.

In each running period (88/89, Run Ia, and Run Ib), we have searched for $Z' \rightarrow ll$ and set the world's best mass limit. Most recently, we have analysed 110 pb^{-1} of Run Ia and Ib data in both dimuon and dielectron decay modes. Figure 2.32 shows the invariant mass distributions of dimuons and dielectrons in the Z' search data sample and the comparison of data with background predictions. From this analysis, we set the current best limit of $M_{Z'} > 690$ GeV/c^2 for Standard Model couplings.

This experimental limit can be compared with specific models. For example, we set the lower mass limits for Z_ψ, Z_η, Z_χ, Z_I, Z_{LR} and Z_{ALRM} to be 580, 610, 585, 555, 620, and 590 GeV/c^2, respectively. Extrapolating to Run II we predict that the mass reach can be extended to 900 GeV/c^2, assuming Standard Model couplings, and to about 800 GeV/c^2 for the specific cases mentioned above, assuming $\sqrt{s} = 1.8$ TeV. (Extrapolated mass limits are higher by approximately 100 GeV/c^2 if we assume $\sqrt{s} = 2.0$ TeV.) See Figure 2.33.

Heavy W bosons, W', occur in some extended gauge models, for example, the left-right symmetric model [31] of electroweak interactions $SU(2)_R \times SU(2)_L \times U(1)_Y$. CDF has searched for $W' \rightarrow l\nu$ in the electron and muon channels [32, 33]. The analysis of Run Ia electron data yielded a limit of $M_{W'} > 652$ GeV/c^2, assuming Standard Model couplings and that the decay $W' \rightarrow WZ$ is not allowed. The analysis of $W' \rightarrow e\nu$ and $\mu\nu$ Run Ib data is in progress. Extrapolating to a Run II luminosity of 2 fb^{-1} we predict that the mass reach can be extended to 990 GeV/c^2 in the $W' \rightarrow e\nu$ mode. See Figure 2.33.

We have also performed a new search for W' decaying to WZ [34] and have excluded a range region of mass vs. mixing angle (ξ) space. This region is shown on the left in Figure 2.33. Searches for $W' \rightarrow tb$ and $W' \rightarrow WH$ are in progress.

We have also searched for $Z' \rightarrow q\bar{q}$ and $W' \rightarrow q\bar{q}$ in the dijet channel using the entire run Ia and Ib dataset. We set upper limits on the cross section which are currently larger than the theoretical prediction of Z' and W' production cross sections which assumes Standard Model couplings, in all dijet mass regions. Extrapolating the cross section limits to 2 fb^{-1} we expect to have a mass reach of approximately 720 GeV/c^2 for both Z' and W' from the dijet decay mode.

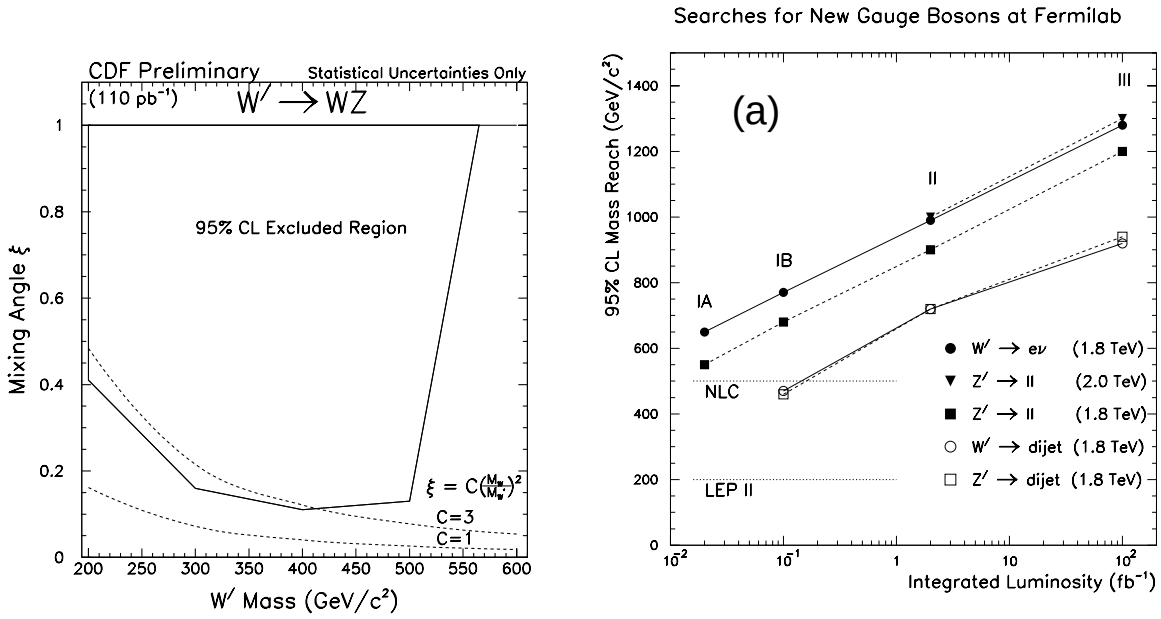

Figure 2.33: Left: Limits are shown for $W' \to WZ$. Right: The expected mass reach, defined as the 95% C.L. lower limit on the mass vs. integrated luminosity at the Tevatron for searches for new gauge bosons.

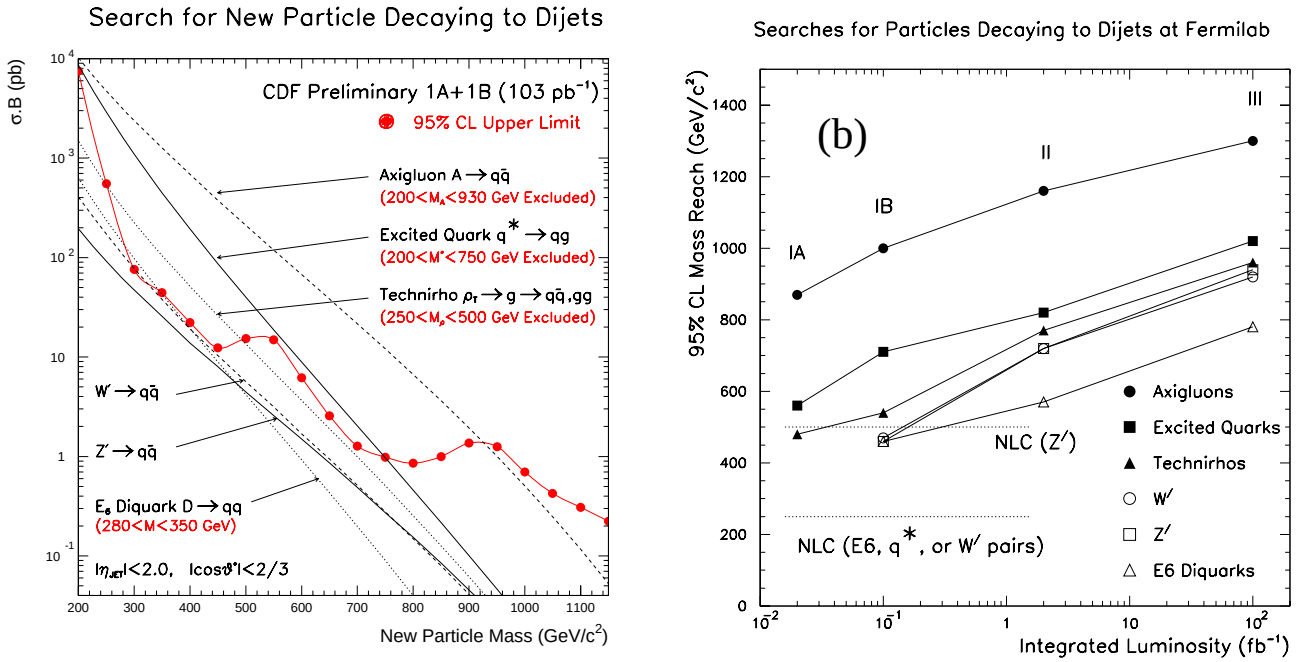

Figure 2.34: Left: The cross section times branching ratio limits as a function of dijet mass, as well as the resulting limits for various specific models. Right: The expected mass reach, defined as the 95% C.L. lower limit on the mass, vs. integrated luminosity at the Tevatron for searches for new particles decaying to dijets.

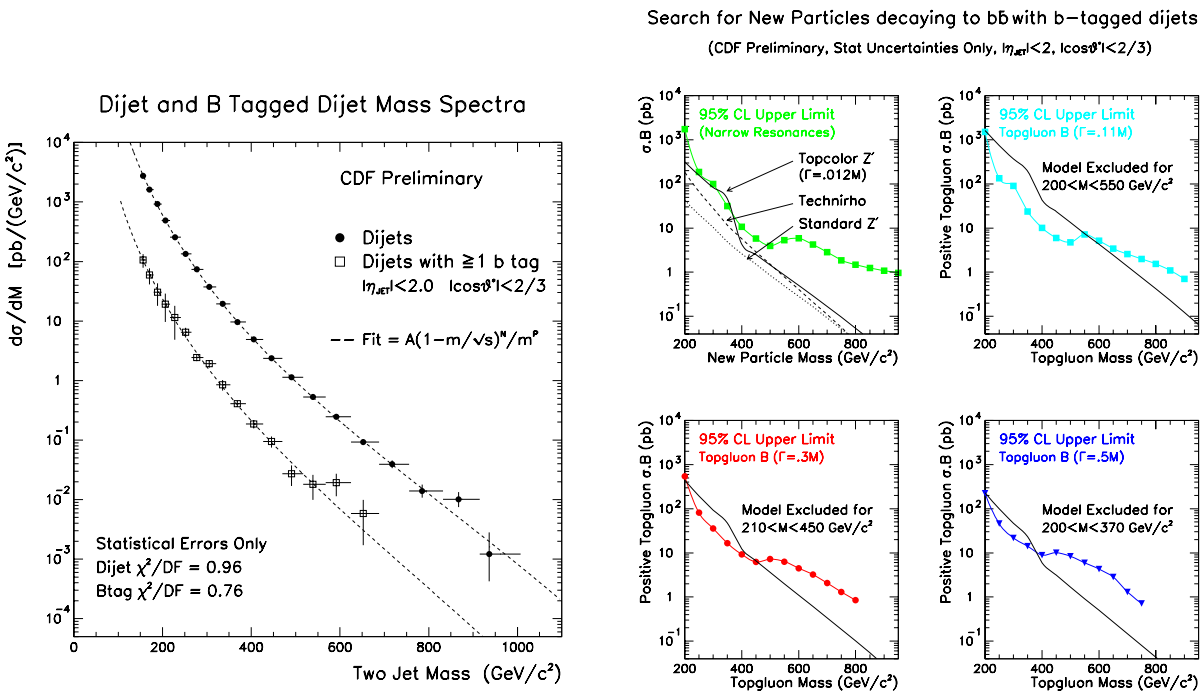

Figure 2.35: Left: The invariant mass distribution of b-tagged dijets. Right: The limits on Z'_{TopC} and topgluons of various widths.

2.4.4 New Particles decaying to Dijets

Many theories predict particles which decay to dijets. These would appear as bumps in the dijet mass spectrum. The existence of a larger chiral color group, $SU(3)_L \times SU(3)_R$, would lead to massive color-octet axial vector gluons, axigluons, which would be produced and decay strongly giving a very large cross section times branching ratio to dijets [35, 36]. A recent technicolor model [37, 38] predicts a color octet technirho (ρ_T) which couples to $q\bar{q}$ and gg via a gluon. If quarks are composite particles, then excited states of composite quarks are expected and couple to qg as discussed in section 2.4.7. New gauge bosons, W' and Z', in addition to coupling to leptons as discussed in section 2.4.3, would produce dijet mass bumps. Superstring-inspired E_6 models predict the existence of many new particles [40] including a color triplet scalar diquark $D(D^c)$ with charge $-(+)\frac{1}{3}$ which couples to $\bar{u}\bar{d}(ud)$. Continuing our Run Ia search [41], in Run Ib we have searched for resonances and set limits on these theories. At high mass, the data are consistently higher than the QCD Monte Carlo prediction. This issue is discussed in more detail in the QCD section of this document. To search for high mass resonances, we compare the data with a curve obtained from a fit to the data. The cross section times branching ratio limits which we derive are shown as a function of dijet mass in Figure 2.34, as well as the resulting limits for various specific models. The predictions for Run II are shown on the right in Figure 2.34 and listed in Table 2.10.

2.4.5 Topcolor Theory and the b-tagged Dijet Search

The large mass of the top quark suggests that the third generation may be special. This has motivated the Topcolor model [9, 10, 11] which assumes that the top mass is large mainly because of a dynamical $t\bar{t}$ condensate generated by a new strong dynamics coupling to the third generation. It predicts massive color-octet bosons, topgluons (B), and a new gauge boson, Z'_{TopC}, from an additional $U(1)$ symmetry. Both of these new particles couple largely to $b\bar{b}$ and $t\bar{t}$. Using CDF's b-tagging capabilities we have searched for topgluons B and Z'_{TopC} in the $b\bar{b}$ channel. Figure 2.35 shows the invariant mass distri-

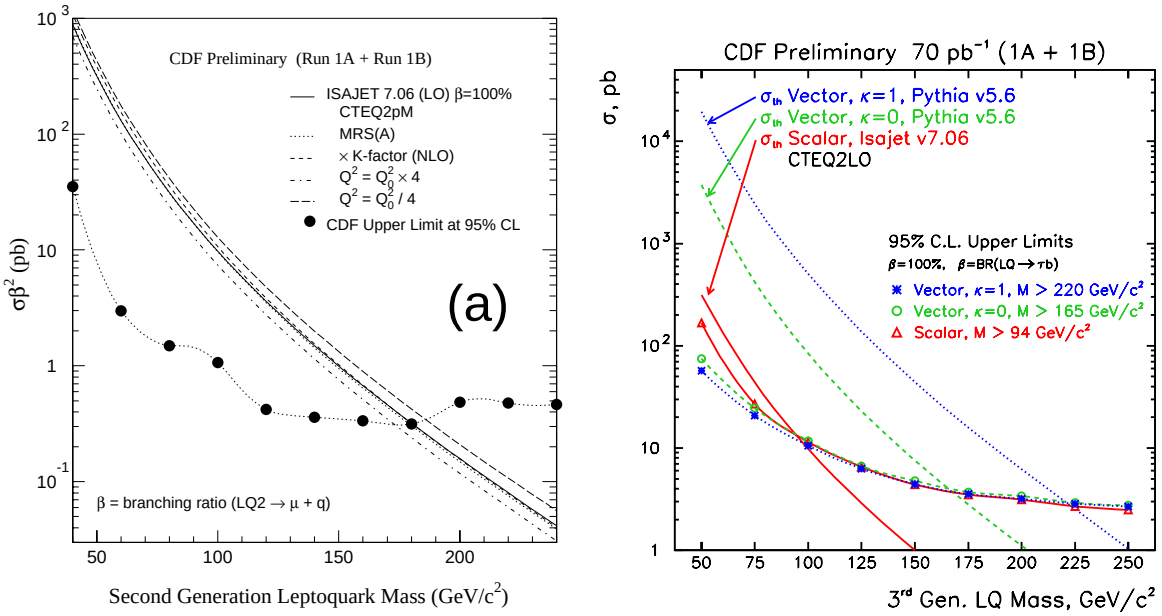

Figure 2.36: Left: The limit on $\sigma \cdot \beta^2$ is shown as a function of LQ2 mass. Right: The limit on $\sigma \cdot \beta^2$ is shown as a function of LQ3 mass.

bution of b-tagged dijets and the limits on Z'_{TopC} and topgluons of various widths. A search is also underway in the $t\bar{t}$ mass distribution, as described in the top section. We estimate that a Z'_{TopC} decaying into $t\bar{t}$ can be discovered (5 sigma) in run II if its mass is less than 900 GeV.

2.4.6 Leptoquarks

Leptoquarks belong to a class of particles carrying both color and lepton quantum numbers which mediate transitions between quarks and leptons. Leptoquarks do not exist within the Standard Model but appear in many SM extensions which predict a symmetry between quarks and leptons at a fundamental level [42, 43, 44]. At CDF we have performed two qualitatively different searches for leptoquarks which will be described in the following two subsections.

2.4.6.1 Direct search for pair produced leptoquarks

Leptoquark masses and coupling strengths are severely constrained by experimental bounds on rare processes, so one has to make the following assumptions about the properties of leptoquarks and their couplings to allow masses which are directly observable in collider experiments:

1. to evade mass bounds from proton decay, lepton and baryon number have to be conserved;

2. to prevent leptoquark-induced FCNC, leptoquarks are generally assumed to link, through an unknown coupling strength, quark and lepton multiplets of the same generation, and

3. to avoid LQ contributions to the helicity suppressed $\pi \to e\nu$ decay, the couplings have to be chiral.

We have searched for pair production of scalar leptoquarks in the dilepton plus dijet channels. In the 88/89 run, we set a first generation leptoquark (LQ1) mass limit of $M_{LQ1} > 113$ GeV/c^2 for $\beta = 100\%$ and $M_{LQ1} > 80$ GeV/c^2 for $\beta = 50\%$, where β is the branching ratio for a leptoquark decaying to a charged lepton and quark. Since then, HERA has improved the first generation limits. But their limits depend on the (unknown) coupling strength λ, unlike at hadron colliders where because the leptoquarks are produced strongly there is only a weak dependence between the production cross section and λ. In Run

Ia we set the world's best limit on second generation scalar leptoquarks (LQ2) and have subsequently improved it with Run Ib data. The current best limit is $M_{LQ2} > 180$ GeV/c^2 for $\beta = 100\%$ and $M_{LQ2} > 140$ GeV/c^2 for $\beta = 50\%$. Figure 2.36 shows the limit on $\sigma \cdot \beta^2$ as a function of LQ2 mass. Extrapolating to Run II, we expect to extend the second generation mass reach to 300 GeV/c^2.

Just recently we have completed a search for third generation leptoquarks (LQ3) into the $\tau\tau$ plus dijet final state where one τ decays leptonically and the other hadronically. For scalar leptoquarks we set a limit at $M_{LQ3} > 94\ GeV/c^2$. We also considered vector leptoquarks with "anomalous chromomagnetic moments" parametrized by κ. For this type of leptoquark assuming $\beta = 1$, the limits are $M_{LQ3} > 165$ GeV/c^2 and $M_{LQ3} > 222$ GeV/c^2 for κ=0 and $\kappa = 1$ respectively. See the right plot in Figure 2.36.

2.4.6.2 Search for the decays $B_s^0 \to e\mu$ and $B_d^0 \to e\mu$

Within the Pati-Salam model [42], which is based on the group SU(4)$_c$, lepton number is regarded as the fourth "color". At some high-energy scale, the group SU(4)$_c$ is spontaneously broken to SU(3)$_c$, liberating the leptons from the influence of the strong interaction and breaking the symmetry between quarks and leptons. This model predicts a heavy spin-one gauge boson with non-chiral couplings called the Pati-Salam boson. The lepton and quark components in this kind of leptoquark are not necessarily from the same generation as pointed out in [45]. This would make decays like $B_s^0 \to e\mu$ and $B_d^0 \to e\mu$ possible. Setting limits on the branching ratio of these rare processes can probe masses in the multi-TeV range, *i.e.*, masses not accessible directly. We have searched for the decays $B_s^0 \to e\mu$ and $B_d^0 \to e\mu$ using ≈ 90 pb^{-1} of Run Ib data. We find no B_d^0 candidates in a mass window of 5.174-5.384 GeV/c^2 and one B_s^0 candidate in a mass window of 5.270-5.480 GeV/c^2. We set limits at $\mathrm{Br}(B_s^0 \to e\mu) < 1.8(2.3) \times 10^{-5}$ and $\mathrm{Br}(B_d^0 \to e\mu) < 3.3(4.4) \times 10^{-6}$ at 90(95) % C.L. after systematic uncertainties have been included. From this we derive a limit on the mass of a certain Pati-Salam leptoquark of 12.8 (12.1) TeV/c^2 at 90(95)% C.L. for the B_s and 19.6 (18.3) TeV/c^2 at 90(95)% C.L. for the B_d.

The Run II prospects for this analysis are promising. The new Silicon Vertex detector SVX-II, which is crucial for this kind of analysis, will have twice the acceptance of the current SVX′. In addition the ability to trigger on displaced vertices from b decays with the SVT will have a big impact, allowing us access B-mesons with lower momentum. For the current analysis the μ p_T and electron E_T trigger thresholds are 3 GeV/c and 5 GeV respectively, resulting in a mean B- meson p_t of $\approx$ 13 GeV/c. Since the B-meson cross section is falling rapidly with p_T one gains by lowering the momentum threshold (by lowering the threshold from 12 to 6 GeV/c one gains a factor of ≈ 10).

2.4.7 Compositeness

The Standard Model has a large number of parameters and particles. One way to simplify is to consider a possibility that these parameters and particles are composed of a smaller and simpler set. If quarks and leptons are composite particles we expect four-fermion contact interactions [46] to modify the quark and lepton production cross sections at high transverse momentum. Excited states [47] would also be expected and can be searched for in the invariant mass spectrum.

We have searched for an excess of events in the inclusive jet cross section which could result from the four-quark contact interaction. An excess of events has been observed in the Run Ia data [48]. The Run Ib data are now being analysed: preliminary results show good agreement with the Run Ia results. However, we should note that inclusion of our data in a global fit with those from other experiments may yield a consistent set of PDFs that accommodate the high-E_T excess within the scope of QCD [49, 50, 51].

If quarks and leptons are both composite and share constituents, then effective contact interactions arise between them at low energies [46]. We have searched for the quark-lepton contact interaction in the dielectron and dimuon channels by looking for an excess of high mass dileptons compared to the Drell-Yan prediction. From the 1988-89 data we had set limits on the lepton-quark compositeness scale of $\Lambda^- > 2.2$ TeV and $\Lambda^+ > 1.7$ TeV for electrons [52], where $-(+)$ corresponds to the constructive (destructive) interference with the dominant up-quark contribution to the cross section. In the muon channel, the limits are $\Lambda^- > 1.6$ TeV and $\Lambda^+ > 1.4$ TeV [53]. Preliminary results using the Run Ib data in the dielectron channel extend the limits on the compositeness scale

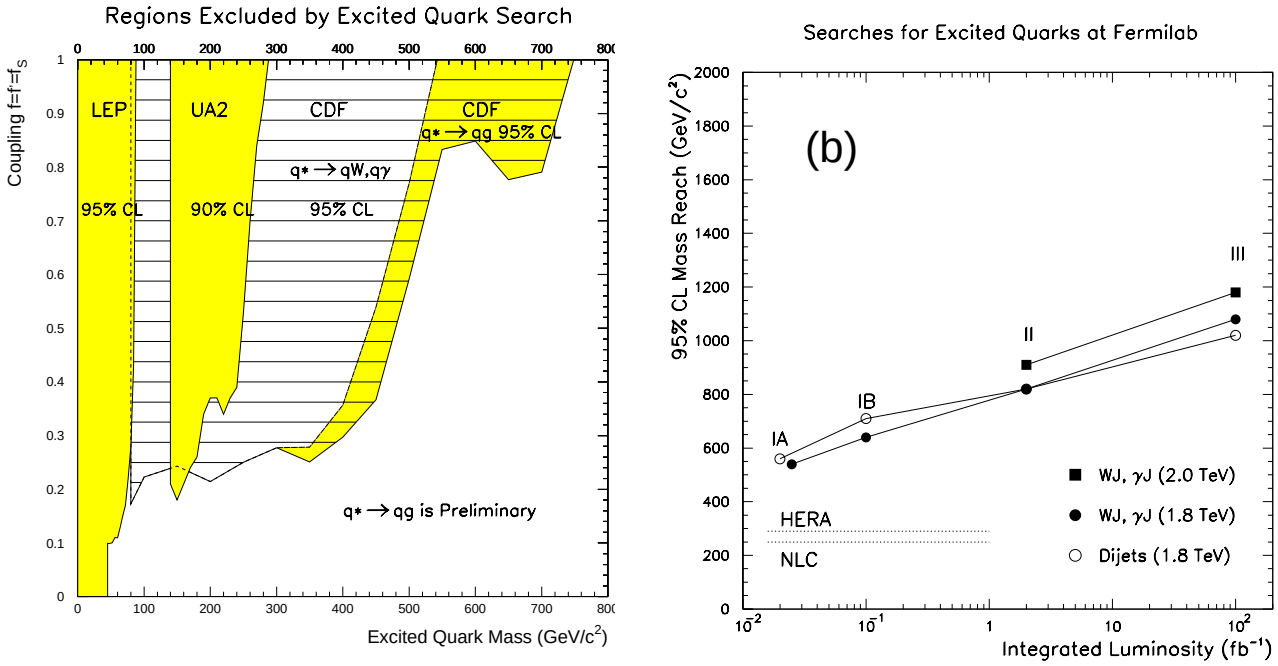

Figure 2.37: Left:The mass regions currently excluded by the dijet q^* search. Right: The expected q^* mass reach, defined as the 95% C.L. lower limit on the mass, plotted vs. integrated luminosity.

to $\Lambda^- > 3.8$ TeV and $\Lambda^+ > 2.6$ TeV. In Run II we expect to be able to explore up to limits of approximately 5 TeV.

Excited states of composite quarks, denoted q^*, have been searched for at UA2 [54] and CDF [55]. They would be produced singly by quark gluon fusion and could decay to a common quark and any gauge boson (g, γ, W or Z) [47]. Using the photon + jet and W + jet channels in the Run Ia data, we have excluded the mass region below 540 GeV/c^2 for the simplest model of q^*[55]. We have also searched for q^* decaying into a dijet mode ($q^* \rightarrow qg$) with 70 pb^{-1} of Run Ia and Ib data, and we have excluded the mass range between 200 and 600 GeV/c^2 for the simplest model of q^* (Figure 2.34). Extrapolating to a Run II luminosity of 2 fb^{-1} we predict that the q^* mass reach can be extended to 820 GeV/c^2 in each of these decay modes. See Figure 2.37 and Table 2.10.

Currently the best limit for excited states of composite leptons, l^*, is set by a LEP experiment. The lower limit is 45 GeV/c^2 for pair production and 90 GeV/c^2 for single production. Recently, we have started an analysis searching for l^* in the $e\gamma$ final state. We expect that we will explore up to a mass limit of several hundred GeV with the current data, and as for the q^* search, the mass reach will be substantially extended in Run II.

2.4.8 Massive Stable Particles

Massive stable particles are possible features of several theories for physics beyond the standard model including supersymmetry, mirror fermions, technicolor, and compositeness. We have searched in the 88/89 data for heavy stable charged particles [56, 57] based upon their expected high transverse momenta, relatively low velocities (via time-of-flight), and muon-like penetration of matter. We obtained upper limits on the cross-section for the production of heavy stable particles as a function of their mass. This can be translated into a mass limit from the cross-section for any particular theory and varies from about 140 GeV/c^2 for color triplets to 255 GeV/c^2 for color decuplets as shown in Figure 2.38b. This analysis is currently being extended using Run I data. Rather than using time-of-flight, the analysis takes advantage of the large ionization depositions, $\frac{dE}{dx}$, expected for massive particles, with measurements in both the SVX and in the outer tracker (CTC for Run I). For example, see Figure 2.38a. Using half of the Run Ib data, we have obtained a preliminary limit of 190 GeV/c^2 for color triplets. The extrapolations to Run II are shown in Figure 2.38b.

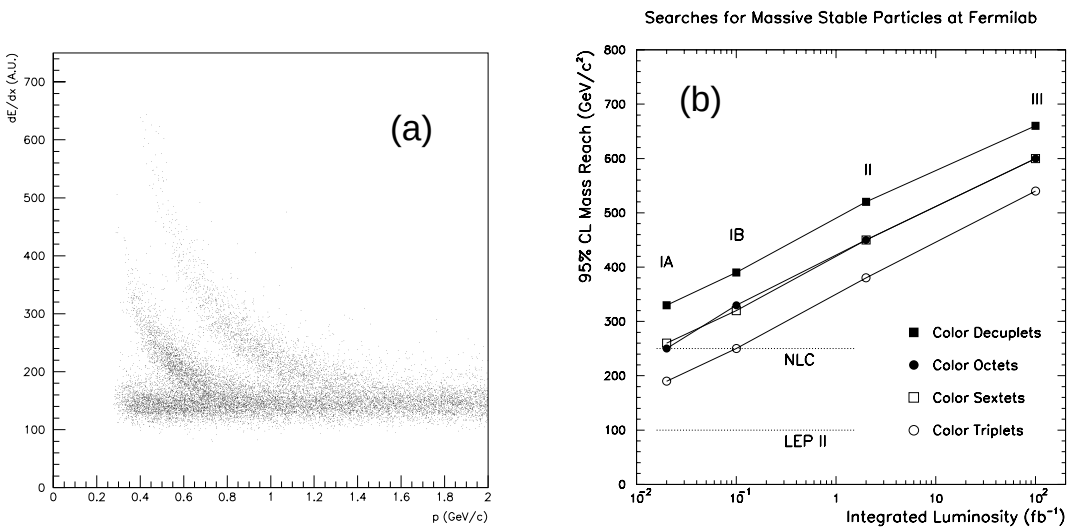

Figure 2.38: (a) A scatter plot of the $\frac{dE}{dx}$ vs momentum is shown for the Run Ib silicon detector after a cut has been applied on the $\frac{dE}{dx}$ from the main tracking chamber. Known particles (kaons and protons) can be clearly distinguished for $p/m < 1.2$, *i.e.*, $\beta < 0.6$. New massive particles would look similar but at higher momentum. (b) The expected mass reach is plotted vs. integrated luminosity at the Tevatron. The maximum mass reach of other accelerators is shown for comparison.

2.4.9 Technicolor

Technicolor assumes that pairs of fundamental techniquarks are bound into a composite scalar, a technipion, which generates a dynamical symmetry breaking. In recent technicolor models[37, 38] there exists a color octet technirho (ρ_T) which couples to $q\bar{q}$ and gg via a virtual intermediate gluon ($\rho_T \rightarrow g \rightarrow q\bar{q}$, gg) and would show up in the detector as dijets in all cases except when it decays into $t\bar{t}$. In the limit that the ρ_T branching ratio to dijets is 100% our present searches exclude the region 250 GeV/c^2 $< M_{\rho_T} <$ 500 GeV/c^2. We expect to have sensitivity to the mass region $200 < M_{\rho_T} < 770$ with 2 fb^{-1}. A color singlet technirho, on the other hand, can couple to the W, Z and technipions (Π_T)[39]. It is currently thought that Π_T decays via $\Pi_T^0 \rightarrow b\bar{b}$ and $\Pi_T \rightarrow b\bar{c}$, both of which would show up as (tagged) dijets. The branching ratios into the various decay modes depend heavily on the masses of the ρ_T and Π_T. In many of the other cases ($WW, WZ, W\Pi$) cases there is also a W+2 Jet signal, for which searches are underway.

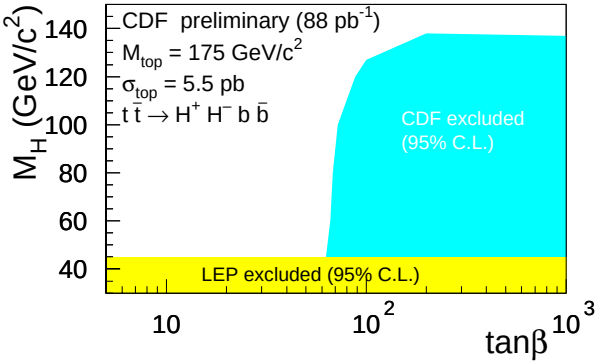

Figure 2.39: The charged Higgs exclusion region in charged Higgs mass vs. tanβ plane.

2.4.10 Charged Higgs Search

An expanded Higgs sector containing charged Higgs bosons is a persistent feature of candidate theories to replace the Standard Model. The minimal supersymmetric extention of the Standard Model, for example, predicts that the dominant decay mode of the top quark is $t \rightarrow H^+ b \rightarrow \tau^+ \nu b$ for large values of tanβ. CDF has excluded charged Higgs production with $M_{H^\pm} < 140$ GeV/c^2 for large values of tanβ using the hadronic decays of the tau lepton in this channel using Run Ib data.(see Fig 2.39). Currently, background from jets which mimic a tau lepton limit this analysis. However, the larger data samples of

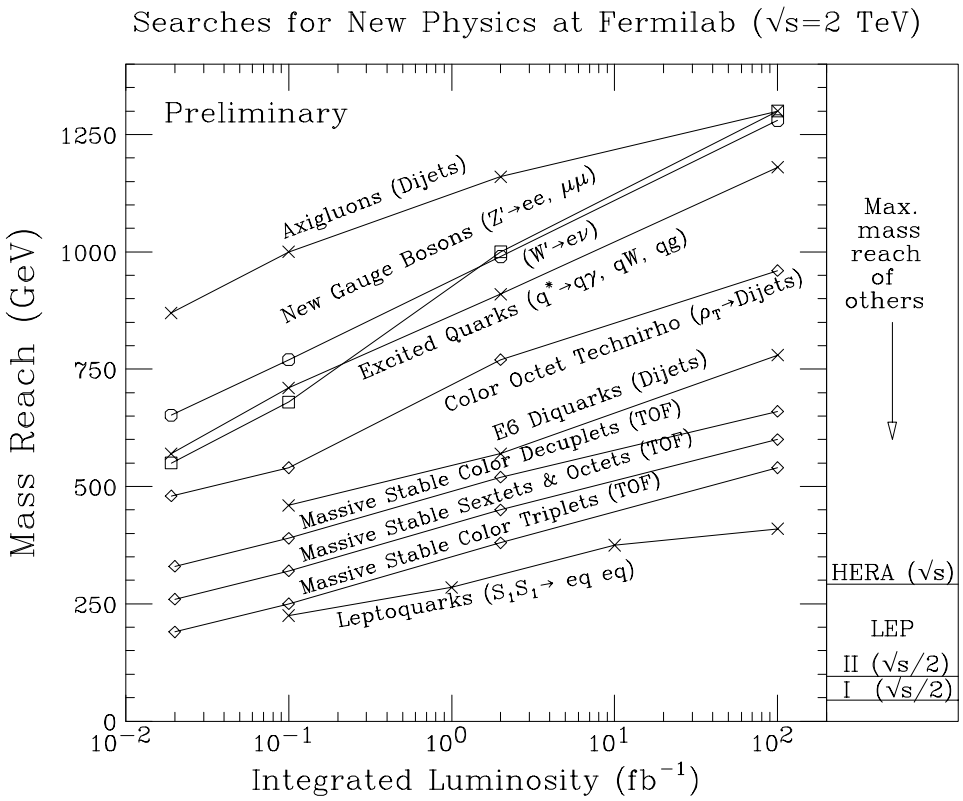

Figure 2.40: The mass reach of CDF II, defined as the 95% C.L. lower limit on the mass, is plotted for several new physics models as a function of integrated luminosity at the Tevatron. The maximum mass reach of other accelerators is shown for selected processes.

Run II will allow better determination of all of the backgrounds and will offer the opportunity to look for charged Higgs pair production to extend the limit to lower $\tan\beta$.

2.4.11 Summary

CDF has produced most of the current highest limits in direct searches for physics beyond the Standard Model. This experience allows us to make realistic predictions of how the additional luminosity obtained in Run II will substantially extend our reach for new physics, as summarized in Figure 2.40 and Table 2.10. The prospects of exploring the regions opened to us in Run II with integrated tracking with better pattern recognition, improved calorimeter, tracking, muon, and b-tagging coverage, and the ability to trigger on b jets are immensely exciting.

Bibliography

[1] G.W. Anderson and D.J. Castaño, hep-ph/9509212, Phys. Rev. **D53**, 2403 (1996).

[2] S. Dimopoulos, M. Dine, S. Raby, and S. Thomas, hep-ph/9601367, Phys. Rev. Lett. **76**, 3494 (1996); S. Dimopoulos, S. Thomas, J.D. Wells, hep-ph/9604452 and preprint SLAC-PUB-7148 (1996).

[3] S. Ambrosanio, G. Kane, G. Kribs, S. Martin, and S. Mrenna, hep-ph/9602239, Phys. Rev. Lett. **76**, 3498 (1996).

[4] S. Ambrosanio, G. Kane, G. Kribs, S. Martin, and S. Mrenna, hep-ph/9605398 (1996).

[5] K.S. Babu, C. Kolda, and F. Wilczek, hep-ph/9605408 (1996).

[6] J.L. Lopez and D.V. Nanopoulos, hep-ph/9607220 and preprint CTP-TAMU-23/96 (1996).

[7] K. Lane, and E. Eichten, BUHEP-95-11, Mar 1995; hep-ph/9503433; Phys. Lett. **B352**, 382, (1995).

[8] V. Barger, K. Cheung, and P. Langacker, preprint MADPH-96-936, April 1996.

[9] C. Hill and S. Parke, Phys. Rev. **D49**, 4454 (1994).

[10] C. Hill and X. Zang, Fermilab-PUB-94/231-T (1994).

[11] C. Hill, Phys. Lett. **B345**, 483 (1995); hep-ph/9411426

[12] In all of the new particle searches discussed here, except for the dijet and b-tagged dijet searches, there are almost no events in the mass region where the limits are set. To obtain a number for the Run II extrapolation, we assume this will remain the case so that the cross section limit will roughly scale inversely with luminosity. In the dijet and b tagged dijet mass searches, there are significant backgrounds in the search region so the cross section limit will scale inversely with the square root of the luminosity.

[13] The TeV-2000 Group Report, Fermilab-PUB-96/082. See Section 6 (Supersymmetric Physics) and Section 7 (Prospects for Exotic Physics at the Tevatron).

[14] D.V. Volkov and V.P. Akulov, Phys. Lett. **46B**, 109 (1973); J. Wess and B. Zumino, Nucl. Phys. **B70**, 39 (1974).

[15] For reviews, see H.P. Nilles, Phys. Rep. **110**, 1 (1984); H.E. Haber and G.L. Kane, Phys. Rep. **117**, 75 (1985).

[16] For a recent review, see J.L. Lopez, "Supersymmetry: From the Fermi Scale to the Planck Scale," hep-ph/9601208, to appear in Report on Progress in Physics.

[17] M. Dine, W. Fischler, and M Srdnicki, Nucl. Phys. **B189**, 575 (1981); S. Dimopoulos and S. Raby, Nucl. Phys. B192, **353** (1981). For a more recent view, see M. Dine, A.E. Nelson, and Y. Shirman, Phys. Rev. **D51**, 1362, (1995).

[18] P. Nath and R. Arnowitt, Mod. Phys. Lett. **A2**, 331 (1987); R. Barbieri, F. Caravaglios, M. Frigeni and M. Mangano, Nucl. Phys. **B367**, 28 (1991); H. Baer and X. Tata, Phys. Rev. **D47**, 2739 (1993); J.L. Lopez, D.V. Nanopoulos, X. Wang and A. Zichichi, Phys. Rev. **D48**, 2062 (1993); H. Baer, C. Kao, and X. Tata, Phys. Rev. **D48**, 5175 (1993).

[19] H. Baer, X. Tata, and J. Woodside, Phys. Rev. **D45**, 142 (1992).

[20] F. Abe *et. al.* (CDF Collaboration), Phys. Rev. Lett. **76**, 4307 (1996).

[21] For a recent review, see R. Arnowitt and P. Nath, "Supersymmetry and Supergravity: Phenomenology and Grand Unification," Proceedings of VIIth J.A. Swieca Summer School, Campos de Jordao, Brazil, 1993 (World Scientific, Singapore, 1994).

[22] L.E. Ibañez, C. Lopez, and C. Muoñz, Nucl. Phys. **B256**, 218 (1985). G.G. Ross and R.G. Roberts, Nucl. Phys. **B377**, 571 (1992); R. Arnowitt and P. Nath, Phys. Rev. Lett. **69**, 725 (1992); S. Kelley, J.L. Lopez, D.V. Nanopoulos, H. Pois, and K. Yuan, Nucl. Phys. **B398**, 31 (1993); G.L. Kane, C. Kolda, L. Roszkowski, and J.D. Wells, Phys. Rev. **D49**, 6173 (1994). We used an approximate formula ($\tilde{l}$ and $\tilde{\nu}$ masses to $\tilde{q}$ and $\tilde{g}$ masses) in H.Baer *et al.*, Phys. Rev. **D47**, 2739 (1993).

[23] ALEPH Collaboration, CERN-PPE/96-10, submitted to Phys. Lett. B (1996); OPAL Collaboration, CERN-PPE/96-20, submitted to Phys. Lett. B (1996).

[24] J.L. Lopez, D.V. Nanopoulos, and A. Zichichi, Phys. Rev. **D52**, 4178 (1995). Input parameters for ISAJET are provided by J.L. Lopez.

[25] T. Kamon, J.L. Lopez, P. McIntyre, and J.T. White, Phys. Rev. D **50**, 5676 (1994).

[26] S. Mrenna, G.L. Kane, G.D. Kribs, and J.D. Wells, "Possible Signals of Constrained Minimal Supersymmetry at a High Luminosity Fermilab Tevatron Collider," hep-ph/9505245, CIT 68-1986, UM-TH-95-14 (1995).

[27] H. Baer, C.-H. Chen, C. Kao, and X. Tata, "Supersymmetry Reach of an Upgraded Tevatron Collider," hep-ph/9504234, FSU-HEP-950301, UR-1411, UH-511-826-95 (1995).

[28] H. Baer *et el.*, Phys. Rev. **D36**, 96 (1987).

[29] F. Abe *et. al.* (CDF Collaboration), Phys. Rev. Lett. **76**, 2006 (1996).

[30] See F. del Aguila, M. Quiros, and F. Zwirner, Nucl. Phys. **B287**, 457 (1987) and references therein.

[31] For a review and original references see R. N. Mohapatra, "Unification and Supersymmetry," (Springer, New York, 1986).

[32] F. Abe *et. al.* (CDF Collaboration), Phys. Rev. Lett. **67**, 2609 (1991).

[33] F. Abe *et. al.* (CDF Collaboration), Fermilab-PUB-94/268-E, submitted to Phys. Rev. Lett.

[34] G. Altarelli, B. Mele and M. Ruiz-Altaba, Z. Phys. **C45**, 109 (1989).

[35] P. Frampton and S. Glashow, Phys. Lett. **B190**, 157 (1987).

[36] C. Albajar *et al.* (UA1 Collaboration), Phys. Lett. **B209**, 127 (1988).

[37] K. Lane and M. V. Ramana, Phys. Rev. **D44**, 2678 (1991).

[38] E. Eichten and K. Lane, Phys. Lett. **B327**, 129 (1994).

[39] K. Lane and E. Eichten, Phys. Lett. **B222**, 274 (1989).

[40] J. Hewett and T. Rizzo, Phys. Rep. **C183**, 193 (1989).

[41] F. Abe *et. al.* (CDF Collaboration), Phys. Rev. Lett. **74**, 3538 (1995).

[42] J. Pati and A. Salam, Phys. Rev. **D10**, 275 (1974).

[43] J. Hewett and S. Pakvasa, Phys. Rev. **D37**, 3165 (1988).

[44] W. Buckmüller and D. Wyler, Phys. Lett. **B177**, 377 (1986).

[45] G. Valencia and S. Willenbrock, Phys. Rev. **D50**, 6843 (1994).

[46] E. Eichten, K. Lane, and M. Peskin, Phys. Rev. Lett. **50**, 811 (1983).

[47] U. Baur, I. Hinchliffe, and D. Zeppenfeld, Int. J. Mod. Phys. **A2**, 1285 (1987); U. Baur, M. Spira and P. Zerwas, Phys. Rev. **D37**, 1188 (1988).

[48] F. Abe *et al.* (CDF Collaboration), FERMILAB -PUB-96/020-E; Submitted to Phys. Rev. Lett. January 1996.

[49] J. Huston *et al.*, MSU-HEP-50812, FSU-HEP-951031, CTEQ-512 (1995).

[50] E.W.N. Glover, A.D. Martin, R.G. Roberts, K.J. Stevenson and W.J. Stirling, DTP-96-22 (1996).

[51] H.L. Lai, W.K. Tung, hep-ph/9605269 (1996).

[52] F. Abe *et al.* (CDF Collaboration), Phys. Rev. Lett. **67**, 2418 (1991).

[53] F. Abe *et al.* (CDF Collaboration), Phys. Rev. Lett. **68**, 1463 (1992).

[54] J. Alitti *et al.* (UA2 Collaboration), Nucl. Phys. **B400**, 3 (1993).

[55] F. Abe *et al.* (CDF Collaboration), Phys. Rev. Lett. **72**, 3004 (1994).

[56] F. Abe *et al.* (CDF Collaboration), Phys. Rev. Lett. **63**, 1447 (1989).

[57] F. Abe *et al.* (CDF Collaboration), Phys. Rev. **D46**, 1889 (1992).

2.5 Precision QCD at Large Q^2

QCD, the theory of the strong interaction, is the least precisely tested component of the Standard Model. High statistics data samples at the Tevatron Collider combined with increasingly sophisticated higher order perturbative QCD calculations not only provide stringent tests of perturbative QCD, but do so at distance scales which extend down to 0.1 milli fermi. This is an order of magnitude smaller than the weak scale, and the smallest distance currently probed in experimental particle physics. It is therefore quite plausible that new physics beyond the Standard Model associated with a new interaction at very small distance scales would first manifest itself as a deviation from QCD predictions at the Tevatron Collider.

The present focus of QCD analyses in CDF goes beyond the traditional comparison of observed distributions to leading-order (LO) or next-to-leading-order (NLO) QCD predictions. CDF measurements of the Drell-Yan cross-section and of the asymmetry in W production and decay have already been used to constrain parameterizations of parton densities. It is expected that Run II data samples will enable the explicit extraction of the fundamental parameters of the theory (α_S and the parton distributions) in several different processes. The agreement or disagreement between these measured parameters and the corresponding measurements from other experiments at lower Q^2 provides a rigorous test of QCD in the same way that different measurements of $\sin^2\theta_W$ tests the electroweak sector of the standard model.

The luminosity upgrades to the Tevatron for Run II will extend the sensitivity of studies of QCD into a substantially higher energy regime where new high-Q^2 phenomena may be found. In addition, new calculations, higher statistics, and improvements in the understanding of detector performance will increase the precision and scope of the present tests of QCD. To illustrate the extended region that will be probed by the upgrade, the following topics will be discussed along with the discovery potential in each channel: a) jet cross section, b) direct photons, c) W and Z boson production, d) multijet events, and e) the extraction of α_S and the parton densities. These analyses in Run II will rely upon the plug upgrade to extend high quality jet measurements to $|\eta| < 3.0$, the SVX II to provide high efficiency b-tagging, and the high rate DAQ system to collect very high statistics data samples.

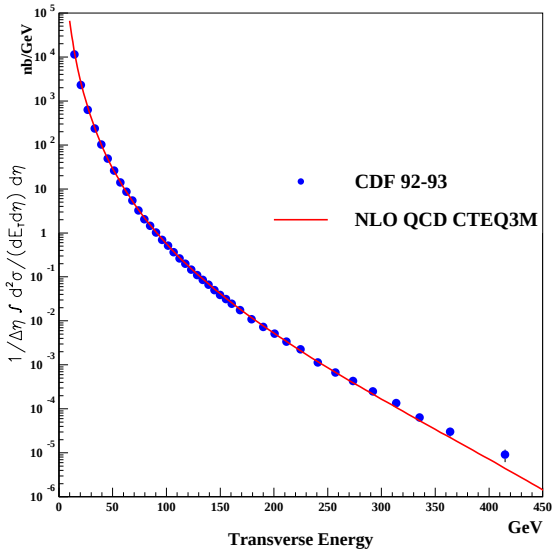

Figure 2.41: The inclusive jet cross section measured by the CDF detector compared to the NLO QCD prediction.

2.5.1 Jet Cross Section

Recently the inclusive jet cross section ($p\overline{p} \rightarrow$ jet + X) has been calculated[1] to order α_s^3. This calculation greatly reduces the theoretical uncertainty associated with choice of renormalization scale. Figure 2.41 shows, as a function of jet E_t, the jet cross section measured by CDF, based on an integrated luminosity of 21 pb^{-1}. The cross-section has been measured over a range ≈ 9 orders of magnitude. The solid line in Figure 2.41 is the prediction of NLO QCD. This provides a remarkably good description of the data except for the highest E_t jets. A more detailed comparison of the data to NLO QCD is shown in Figure 2.42 where (data - theory)/theory is plotted on a linear scale. The data from Run Ia (21 pb^{-1}) is plotted as the open circles and preliminary results from Run Ib (87 pb^{-1}) as the solid circles. The data sets are statistically consistent and show an excess of observed jets over theory for jet E_t above 250 GeV. The deviations could indicate (i) the need for corrections to the perturbative QCD calculations that go beyond NLO, (ii) modifications of the parton distribution functions, or (iii) something new beyond the standard model. Measurements using higher statistics data samples are clearly needed in the E_t range

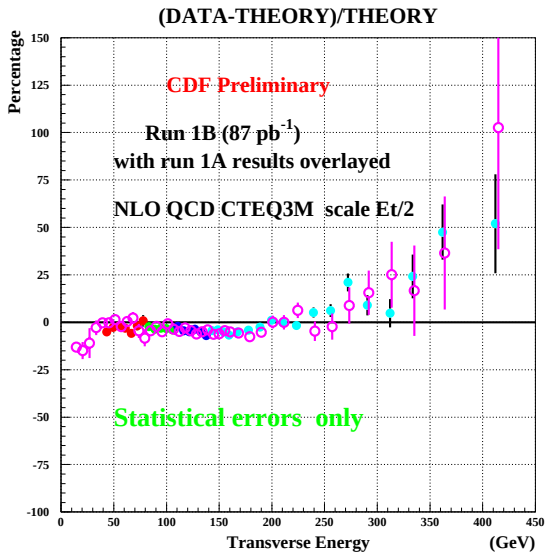

Figure 2.42: Comparison of the observed inclusive jet cross section measured by the CDF detector with the prediction of next to leading order QCD. The comparison shows (data - theory)/theory as a function of jet transverse energy. The open circles are Run Ia data, solid circles Run Ib.

above 300 GeV where there are only 308 jets from the Run I data set. Extrapolating to an expected 2 fb^{-1} for Run II, we would measure about 6000 jets with $E_t > 300$ GeV and extend the measurement shown in Figure 2.42 to a jet E_t of about 500 GeV.

Two other distributions which provide additional sensitive tests of perturbative QCD at small distance scales are the two-jet mass distribution (Fig. 2.43) and the distribution of total transverse energies (summed over all jets in the event) shown in Fig. 2.44. Preliminary measurements of both these distributions also show an excess of events at large di-jet mass and sum E_t. As for the inclusive jets, the region of deviation from the QCD prediction will be explored in much more detail with the factor of 20 statistical improvement expected in Run II.

High statistics data samples from Run II will improve the ability to test QCD at sufficiently small distances to search for new physics beyond the standard model. Quark substructure would give rise to an increase in jet production at large transverse energy. This property can be incorporated into the QCD Lagrangian by adding a short range contact term with an effective distance scale defined by the parameter Λ_C [2]. Figure 2.45 shows the theoretical prediction for the high energy end of the inclusive jet cross section. The solid curves are the ratios of the cross sections with a compositeness scale Λ_C to the cross section predicted by QCD with no compositeness. Also shown is the ratio of the measured inclusive jet cross section from 21 pb $^{-1}$ of data to the QCD prediction. Measuring this jet spectrum from 2 fb $^{-1}$ will decrease the statistical errors shown in Figure 2.45 by a factor of about 10. This would yield a sensitivity that corresponds to a Λ_C value in the range 1.8 to 2.0 TeV. In addition to providing a sensitive search for new small-distance interactions, the shape of the spectrum at transverse energies as large as 500 GeV will be sensitive to soft gluon resummation effects associated with the approaching kinematic limit at high E_t, and therefore provide an important test of resummation techniques [8]. The measured inclusive jet spectrum would also tie down the high x end of the parton distribution functions. The Tevatron measurement at high x will eventually be very valuable when compared to LHC measurements in order to understand if the excess is due to parton distribution functions or some new effective interaction.

The two-jet invariant mass spectrum is sensitive to heavy objects produced with a strong coupling. In chiral color models[3], a massive octet of gluons is predicted which would lead to a broad (axigluon) resonance in the two-jet invariant mass spectrum. This resonance, because of its strong coupling, would produce a sizable enhancement in the di-jet mass spectrum above the QCD background. The two-jet mass spectrum from approximately 106 pb^{-1} of data is consistent with a smooth (nonresonant) distribution. This excludes axigluons in the mass range $200 \leq M_a \leq 1000$ GeV. A data sample of 2 fb^{-1} should extend the search for axigluon contribution up to a mass limit of 1.2 TeV. Other models also predict resonant enhancements in the dijet mass spectrum. Current CDF limits on ability to distinguish between model are summarized in Fig. 2.46. The sensitivity achieved by analyses of the di-jet mass spectrum is clearly competitive with other searches based on the worlds data. A data sample of 2 fb^{-1} will extend the range of di-jet mass that can be examined by about 200 GeV.

Finally, the NLO calculations (order α_s^3) have the additional feature that the jet cross section depends on the effective radius in the η-ϕ metric used for clustering. Comparing these predictions to data will permit a more detailed investigation of the relationship

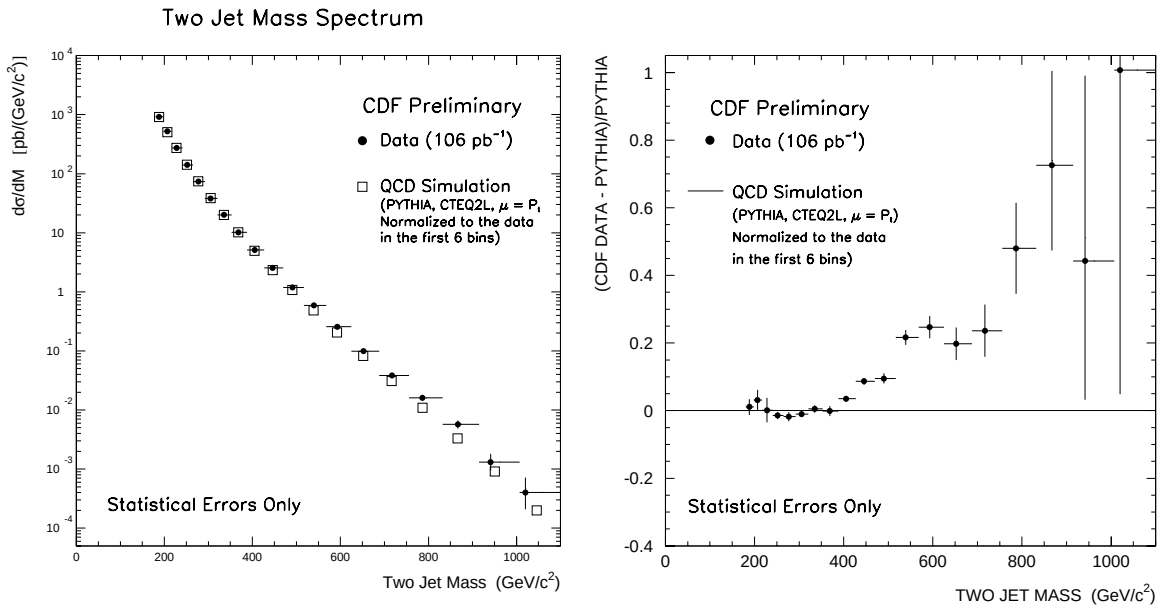

Figure 2.43: Left: Two-jet mass distribution compared to LO QCD simulation. Right: Two jet invariant mass spectrum compared to LO QCD predictions in terms of (data-theory)/theory.

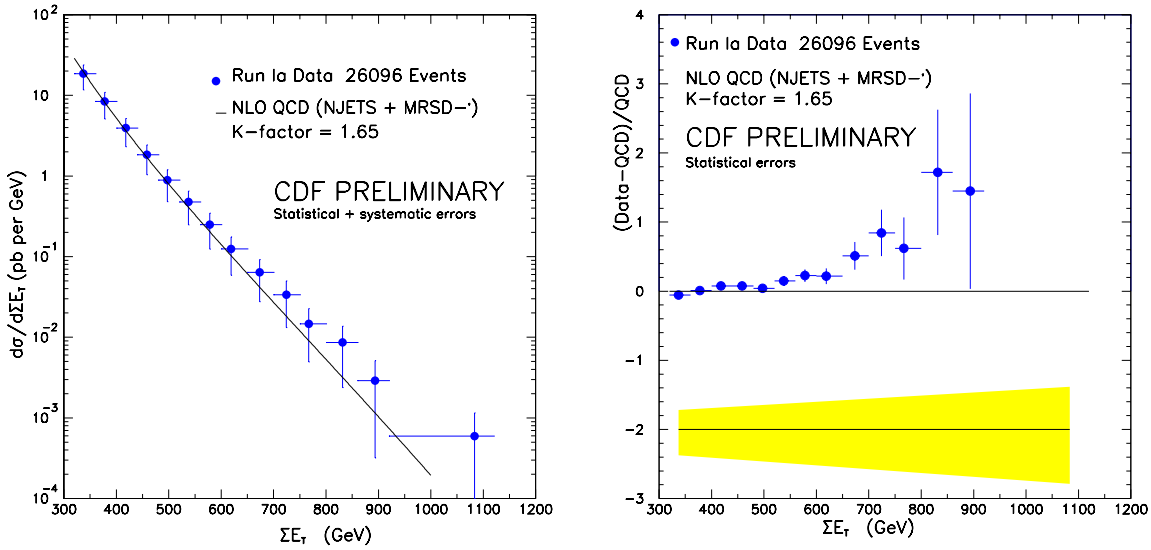

Figure 2.44: Left: Total transverse energy distribution compared to a NLO QCD prediction. Right: The same comparison in terms of (data - theory)/theory.

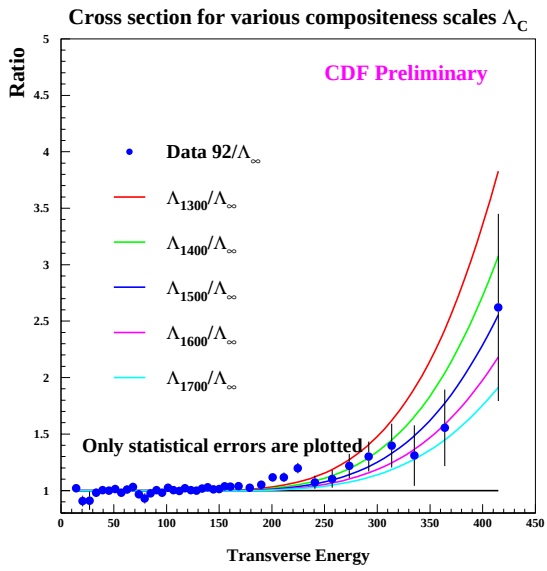

Figure 2.45: The ratios of inclusive jet cross sections with compositeness scales Λ_C to the QCD prediction with no compositeness. Also shown is the ratio of data/QCD prediction for 21 pb $^{-1}$ of data from Run Ia (solid points).

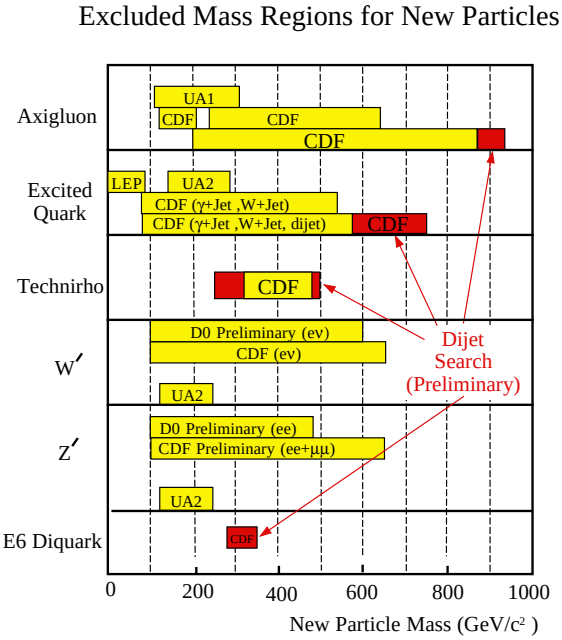

Figure 2.46: CDF limits resulting from the absence of a dijet resonance in the observed two-jet mass spectrum, compared with the worlds limits.

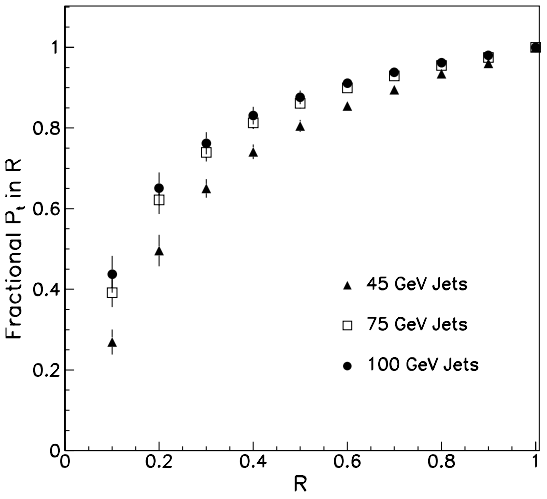

Figure 2.47: The variation in jet size with E_t as measured by the fractional P_t of tracks within a cone of radius R.

between hadronic jets and the underlying scattered partons, and in particular enable a detailed study of jet merging and sharing of energy between two nearby jets. As shown from Figure 2.47 the jet size narrows with increasing E_t as measured from the fractional P_t of tracks within a jet cone of radius R. Understanding these features of jets is necessary for precise measurements of the properties of particles decaying to jets, for example the top quark and a possible light Higgs bosons.

2.5.2 Multijet Events

The study of events with three or more jets in the final state provides a test of perturbative QCD that complements the inclusive jet and two-jet measurements. A comparison of recent CDF measurements of the mass dependent jet multiplicity distributions (Fig. 2.48) shows that LO QCD predictions give a reasonable description of the measurements. However, at the highest energies, both the statistical uncertainties on the measurements and the systematic uncertainties on the predictions are large. With a 2 fb^{-1} data sample the statistical uncertainties on the data points will shrink by more than a factor of 5. Improvements in computing resources will be needed to provide corresponding improvements in the statistical uncertainties on parton shower Monte Carlo predictions. Furthermore, the availability of a

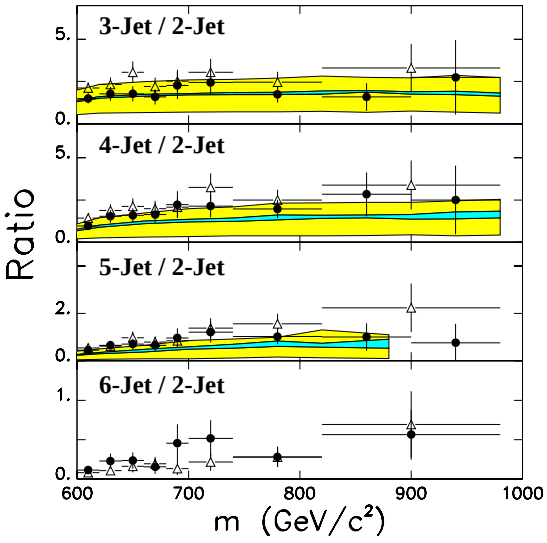

Figure 2.48: CDF measured ratios of N-jet to 2-jet events shown as a function of multijet mass (points) for jets with $E_t > 20$ GeV, compared to LO QCD predictions from a matrix element calculation (bands) and from the HERWIG parton shower Monte Carlo program (open triangles).

NLO three-jet calculation together with further understanding of the theoretical uncertainties based on analyses of current data samples may well result in substantial reductions in the estimates of these uncertainties. Hence it is likely that the precision of quantitative comparisons between predicted and observed multijet properties will improve by about a factor of 5.

2.5.3 Direct Photons

Studies of direct photon production in CDF complement jet studies, and have the advantage that photon energies are measured with greater precision than the energies of jets. So far direct photons have provided the best experimental and theoretical probe of low x parton distributions and QCD at the Tevatron. The current measurements indicate the presence of a source of photon transverse momentum in addition to that calculated from NLO QCD, as illustrated in figure 2.49. The normal QCD prediction falls below the data at low p_t, while the addition of the parton shower matches the data quite well. This has implications for any hadron collision measurement using NLO QCD. It is also clear from this plot that the increased luminosities will help this measurement statistically at high p_t.

Direct photon + jet angular distributions are interesting due to the quark propagator, as opposed to jet production with its gluon propagators. This is shown in the right part of figure 2.49, where the dijet, W+jet and photon+jet angular distributions are shown along with their NLO QCD predictions. One sees the dramatic differences between jets and photon/W production. Further studies of the photon+jet measurement as well as photon + 2 jets will probe the direct photon production mechanisms.

2.5.4 W and Z boson production

The data collected at the Tevatron Collider during Run I should provide 100,000 $p\overline{p} \rightarrow$ W + X and 10,000 $p\overline{p} \rightarrow$ Z + X events after all selection cuts (including both electron and muon W/Z decays). Figure 2.50 shows the $W(Z\ )$ cross sections as a function of the number of associated jets in the event using 107 pb^{-1} of electron decays from Run I. 20% of these events have associated QCD jets, with approximately 1% having 3 or more jets (jet E_t>15 GeV). An extrapolation to a 2 fb^{-1} data sample from Run II yields, for example, 1.9 million W bosons, including approximately 380,000 with associated jets. These data can be used for a variety of important tests of the Standard Model, for top quark studies and to search for new phenomena. A brief discussion of the potential for these measurements is given below, based upon the assumption of a 2 fb^{-1} data sample from Run II. It is important to note that the high rate DAQ system available for Run II will record all available W/Z triggers onto tape.

The hadronic production of W and Z bosons provides the opportunity to test the Standard Model in processes where the parton level scattering is identified by the presence of the bosons and which naturally occur at a high Q^2 scale. Measurements of α_s can be extracted from jet multiplicity spectra. The data shown in Fig. 2.50 would be increased by a factor of about 40 in Run II. This would allow measurements of the jet multiplicity associated with W bosons out to six jets. A complementary measurement of α_s can be obtained from W and Z P_t spectra of the type shown in Figure 2.51. Recently, calculations have been performed at order α_s^2 for the P_t spectra of the W/Z.[5] These calculations reduce the theoretical uncertainty in the cross section. With 2 fb^{-1} of data, the P_t reach for W's would allow a significant

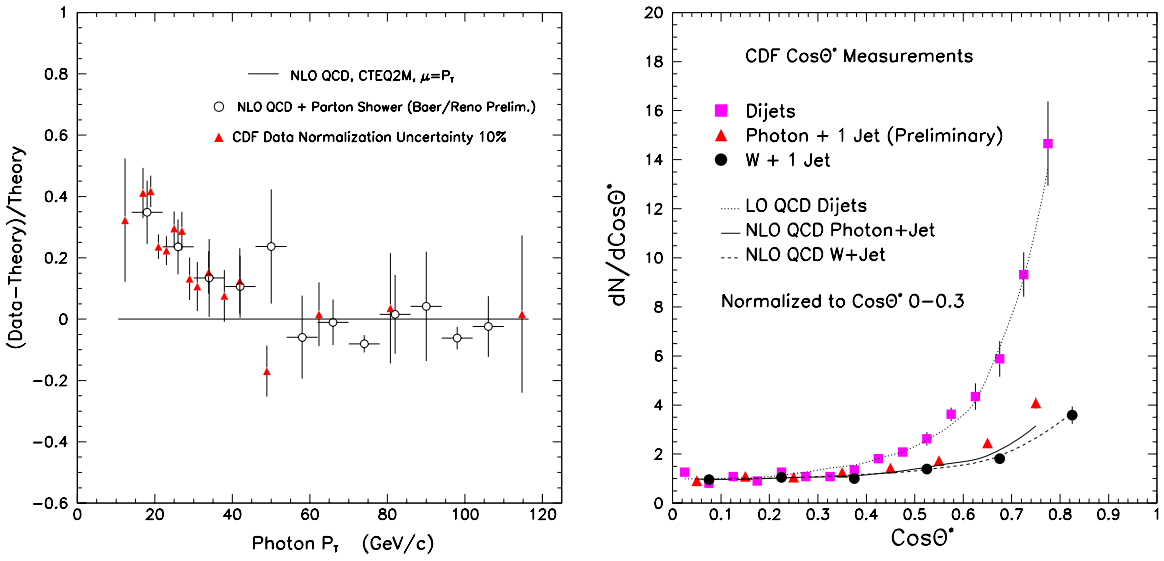

Figure 2.49: Left: Comparison of the direct photon differential cross-section with NLO QCD predictions. Right: Photon, W boson and di-jet angular distributions

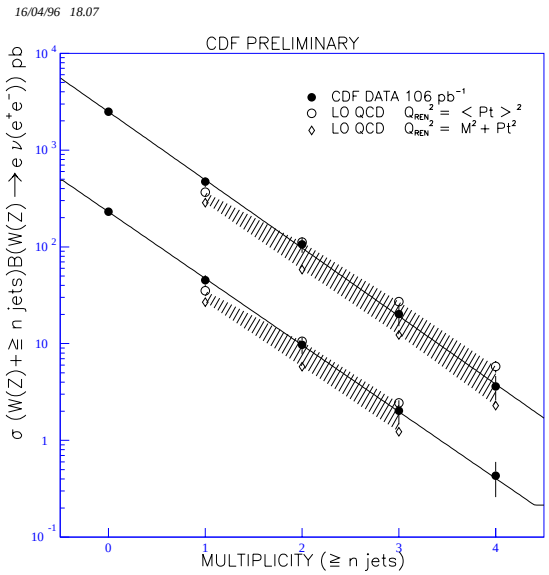

Figure 2.50: $W(Z\ ) + \geq n$ jets cross sections compared with the QCD LO predictions.

measurement out to 250 GeV. The Z P_t spectrum can be measured with very low background. The Run II data sample would be 40 times larger than that shown in Figure 2.51, providing about 200,000 Z bosons. The low P_t part of the W and Z spectra provide data useful for a measurement of gluon resummation effects. Non-standard processes, such as a techni-rho would appear as an enhancement in the P_t spectrum.[4]

A critical analysis of the direct production of W and Z bosons with QCD jets can be made from the 380,000 W+jet and 38,000 Z+jet events expected from 2 fb^{-1} of data. Figures 2.51 through 2.53 illustrate measurements made from a sample of data (73 pb^{-1}) from the current Tevatron run. The E_t distribution of the highest energy jet from W + 1 and 2 jet events is plotted in Fig. 2.52. The W-jet and Z-jet invariant mass distributions are shown in Figure 2.51. In all these Figures the data (points) are compared to LO QCD calculations (histogram). A 50 fold increase in the statistics (electron plus muon decay channels) shown in these plots (electron decays only) will allow a study of the QCD jet spectra out to E_t of about 250 GeV. Currently NLO predictions are available only for W/Z + 1 jet events, but calculations for higher multiplicities should be available for comparison to the Run II data.

A careful study of direct W and Z boson production with jets is important both for an accurate mea-

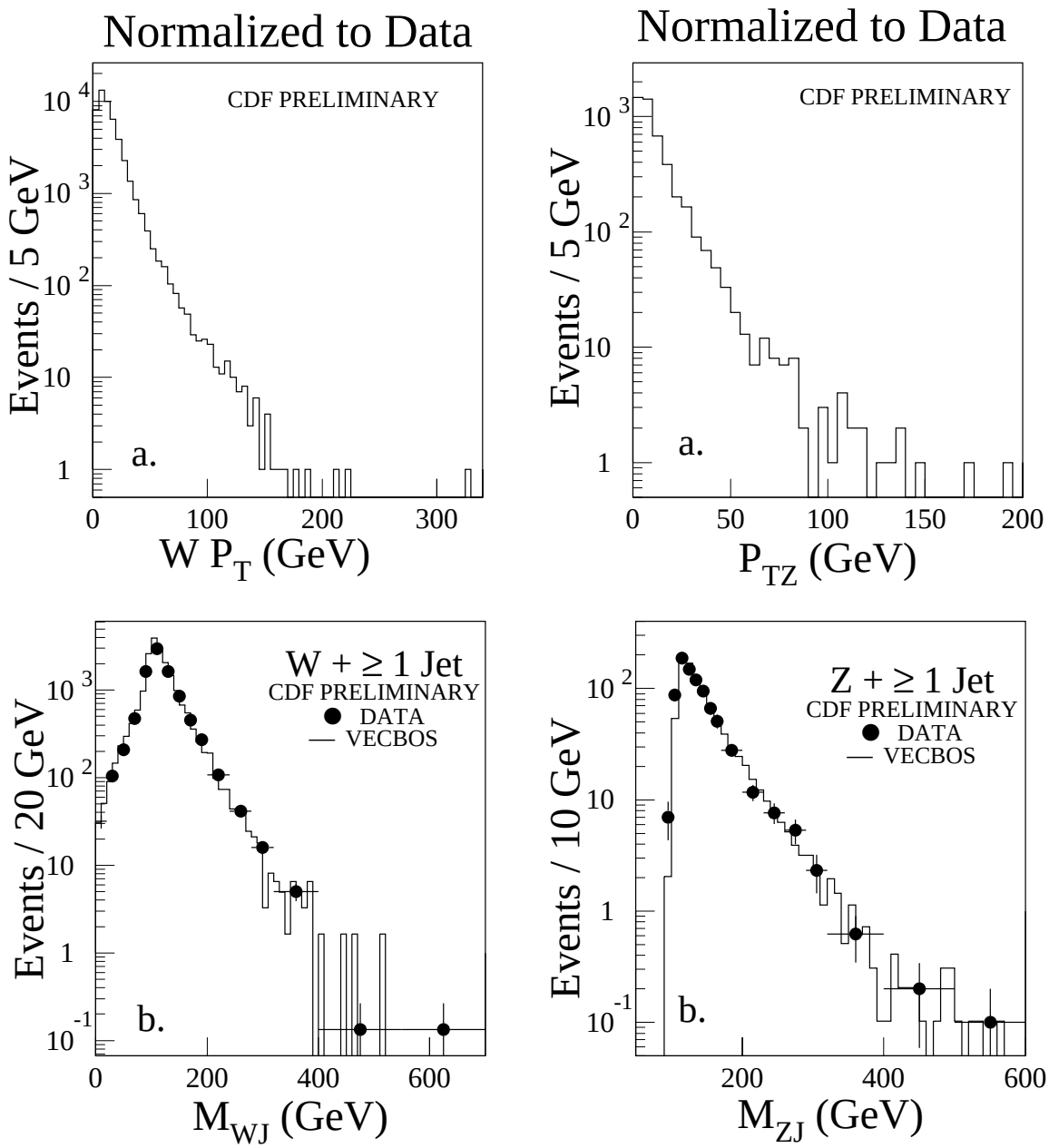

Figure 2.51: Top left: The W transverse momentum distribution from 73 pb^{-1} of Run I data. Bottom left: The invariant mass distribution of the W boson and the highest energy jet. Top right: The Z transverse momentum distribution from 73 pb^{-1} of Run I data. Bottom right: The invariant mass distribution of the Z boson and the highest energy jet

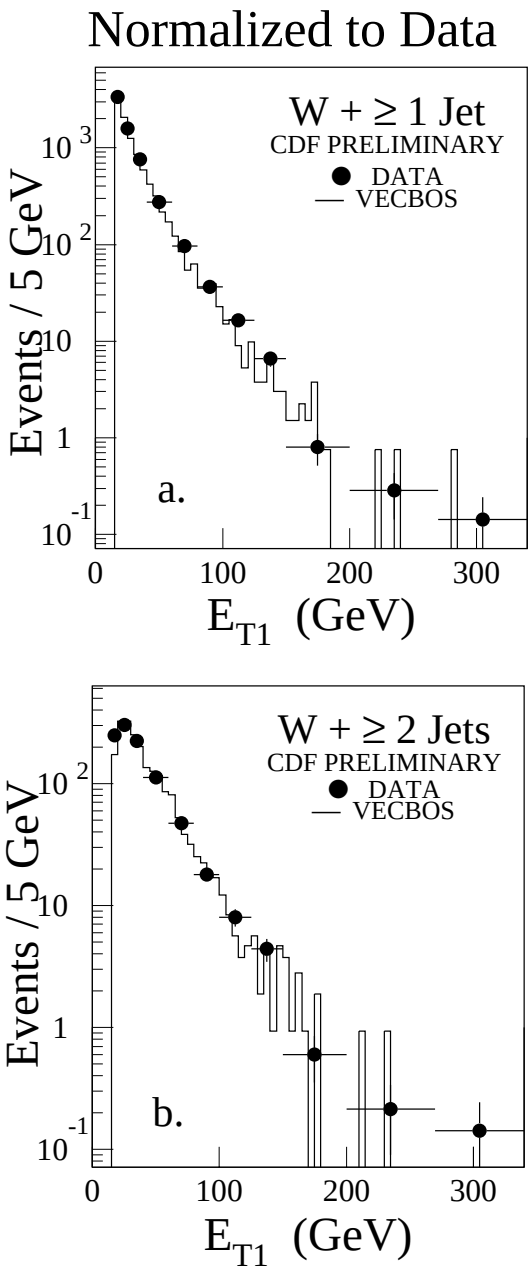

Figure 2.52: The jet E_{T1} spectra for events with a) $W+$ $\geq$1 jet, and b) $W+$ $\geq$2 jets.

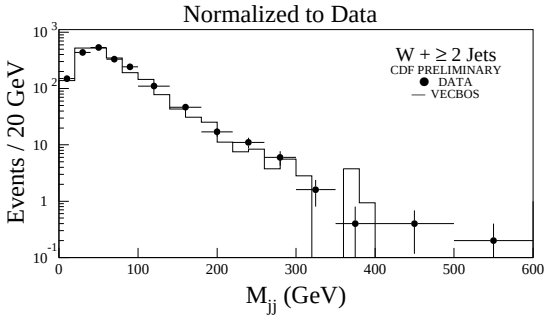

Figure 2.53: a) The invariant mass of the two highest-E_T jets.

surement of the top mass and in searches for new particles which decay to W/Z's or are produced in association with them. Processes involving technicolor-type models could produce heavy particles decaying into W pairs. The exact nature of such couplings are not certain, but do provide some impetus to examine the potential discovery limits. From different scenarios, and depending on the coupling, it may be possible to detect techni-rho's with masses up to 250 GeV. Backgrounds for Higgs bosons can be reduced by searching for production in channels with associated W/Z bosons. The jet-jet invariant mass spectrum from events with W bosons is shown in Fig. 2.53 for a sample of Run I data. The data (points) are well reproduced by a leading order QCD calculation out to jet-jet masses of 300 GeV. Scaling this up to a 2 fb^{-1} data sample predicts on the order of 600 W events with a di-jet in the invariant mass range from 260 to 300 GeV/c^2. This provides the background to any new particle with mass in this range decaying to dijets and produced in association with a W boson. The high statistics W/Z + jet sample available in Run II should permit a good understanding of the normal QCD production and allow a search for new particles out to masses of 300 GeV/c^2.

2.5.5 The extraction of α_S and the parton densities

An important goal of QCD analyses of CDF data in the near future is the extraction of α_S and/or the parton densities from all processes for which there are reasonable data samples and reliable predictions. Some examples are the inclusive jet differential cross-section, the two-jet mass and angular dis-

tributions, jet and photon rapidity distributions, the charge asymmetry in leptonic W decays, the direct photon differential cross-section, jet multiplicity distributions, and the W, Z, and Drell-Yan transverse momentum distributions. These measurements will provide new constraints on the parameters of the theory. The self consistency of the extracted parameters, together with their consistency with measurements from other experiments at lower energies and Q^2-scales, provides a rigorous test of perturbative QCD.

The published CDF inclusive jet differential cross-section has been used to extract α_S ([7]). Preliminary results are shown in Fig. 2.54. These are not only consistent and competitive with the worlds knowledge of α_S, but also demonstrate in a single measurement the running of the strong coupling "constant". The real strength of the measurements of α_S based on the CDF jet spectrum is that these measurements probe the behaviour of the QCD coupling at high Q^2, extending the Q^2 range of the worlds data by more than a factor of 4. With a data sample of 2 fb^{-1} the statistical errors will shrink by a factor of 10 with respect to those shown in the figure, and the measurement will extend out to a Q^2 of about $(500\ GeV)^2$. In addition a 2 fb^{-1} data sample would facilitate a precise simultaneous determination of α_S and the parton distributions, which will enable systematic uncertainties associated with global structure function fits to be minimized. This is important since the global fit systematic uncertainties are difficult to quantify.

Reliable QCD predictions require a precise knowledge of the parton distributions. CDF Drell-Yan and W lepton charge asymmetry measurements are already being used to constrain these distribution functions. For example the current W asymmetry measurements are shown in Fig. 2.55 for a data sample of about 70 pb^{-1}. Hence, for a 2 fb^{-1} data sample the statistical uncertainties will shrink by a factor of 5, and provide a very interesting constraint on the parton distributions.

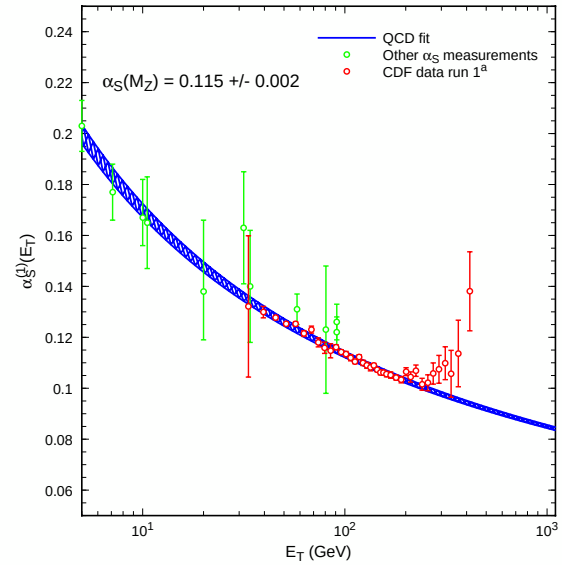

Figure 2.54: The value of $\alpha_S(E_T)$ extracted by Giele and Glover using published CDF data.

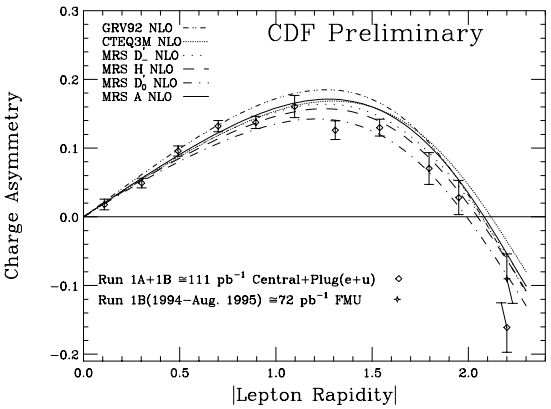

Figure 2.55: The lepton charge asymmetry measured in W decays.

2.5.6 Summary of the benefits of Tevatron Run II to QCD studies

The QCD studies described in this section will be greatly extended through the combination of the very large data samples expected in Run II and complementary improvements of the CDF II detector described in this TDR. The new plug calorimeter will permit high quality jet measurements out to

$|\eta| < 3.0$, thus extending measurements to a region of phase space where resummation effects could be tested. Tagging jets containing a b hadron decay with the SVX II permits a clean study of top quarks, a sensitive search for light Higgs bosons, and searches for other new particles. Clearly most of the QCD studies will profit from the potential of a factor of 20 increased statistics in Run II. To take advantage of this in terms of data recorded, the upgraded DAQ system is essential.

Table 2.11 shows the events expected in some selected channels from a Run II exposure of 2 fb^{-1}, based upon extrapolations from Run I data already analyzed.

Table 2.11: QCD events expected from a 2 fb^{-1} Run II data sample

Production Channel	Events
jet (j) + X, $\|\eta\| \leq 1.0$, $E_T \geq$300 GeV	6.4×10^3
jj + X, $M_{jj} \geq 600$ GeV	3.0×10^4
γ + X, $p_T(\gamma) \geq 25$ GeV	6.0×10^6
$\gamma\gamma$ + X, $p_T(\gamma_1, \gamma_2) \geq 12$ GeV	1.4×10^4
$Z+ \geq 1j$, $E_T(j) \geq$100 GeV	1.0×10^3
$W+ \geq 1j$, $E_T(j) \geq 100$ GeV	1.0×10^4

To take full advantage of these data the systematic errors associated with jet measurements will have to be reduced by making internal consistency checks on the data. For example the high statistics Z+jet and photon+jet data samples will permit balancing precisely measured electromagnetic calorimeter energy (a photon or Z boson) against jet calorimeter energy. With reduced systematic errors, these data have the potential for testing QCD down to length scales of about 0.1 milli fermi. The running of α_S can be measured in detail in a Q^2 range from about (30 GeV)^2 to (500 GeV)^2, and parton distribution functions measured with high precision. In total these data have the potential for making stringent tests of the QCD sector of the Standard Model and hopefully revealing a deeper understanding of elementary particle physics.

Bibliography

[1] S. Ellis, Z. Kunszt and D. Soper, Phys. Rev. **D40** 2188 (1989); U. of Oregon Preprint OITS 436 (1990).

[2] E. Eichten, K. Lane and M. Peskin, Phys. Rev. Lett. **50**, 811 (1983).

[3] J. Bagger, C. Schmidt, S. King, Phys. Rev. **D37** 1188 (1988).

[4] E. Eichten and K. Lane, Phys. Lett. **222** 274 (1989).

[5] P. Arnold and M.H. Reno, FERMILAB-Pub-88/168 (1988).

[6] Martins, Roberts and Stirling, Z. Phys. **C42**, 277 (1989).

[7] W.T. Giele and E.W.N. Glover, Moriond 95.

[8] S. Catani, M. Mangano, P. Nason and L. Trentadue, CERN-TH/96-86 hep-ph/9604351.

2.6 Constraining the CKM Matrix

2.6.1 Introduction

The study of particles containing the bottom quark has provided valuable insights into the weak interactions and QCD: *e.g.* the long lifetime of b hadrons, the large mixing observed in the B^0–$\bar{B}^0$ system, the discovery of heavy quark symmetries and the utility of heavy quark effective theories, the observation of "penguin" decays. This is not surprising given that the bottom quark is heavy and that its preferred charged current coupling to the top quark occurs only in virtual higher–order processes. The b hadrons provide a valuable laboratory in which to extract fundamental parameters of the Standard Model and test its consistency and search for rare processes which are sensitive to physics beyond the Standard Model.

Measurements with b hadrons can in principle be used to extract information on 5 of the 9 elements of the CKM matrix that relates the weak–interaction and mass eigenstates of quarks. The CKM matrix can be written as:

$$V = \begin{pmatrix} V_{ud} & V_{us} & V_{ub} \\ V_{cd} & V_{cs} & V_{cb} \\ V_{td} & V_{ts} & V_{tb} \end{pmatrix} \tag{2.2}$$

or in the Wolfenstein [1] parameterization:

$$\simeq \begin{pmatrix} 1-\lambda^2/2 & \lambda & A\lambda^3(\rho - i\eta) \\ -\lambda & 1-\lambda^2/2 & A\lambda^2 \\ A\lambda^3(1-\rho-i\eta) & -A\lambda^2 & 1 \end{pmatrix} \tag{2.3}$$

given here to $O(\lambda^4)$, where $\lambda = \sin(\theta_{\rm Cabibbo})$ and the other three parameters A, ρ, and η encode the remaining two weak mixing angles and the irreducible complex phase that introduces CP violation.

Unitarity of the CKM matrix requires the relationship

$$V_{tb}^* V_{td} + V_{cb}^* V_{cd} + V_{ub}^* V_{ud} = 0, \tag{2.4}$$

which can be displayed as a triangle in the complex plane, as shown in Figure 2.56. The base of this triangle has been rescaled by $A\lambda^3$ to be of unit length. Also shown are the angles α, β, and γ which lead to CP violating effects (provided the triangle does not collapse to a line) that can, in principle, be measured with b hadrons.

The b physics goals for CDF II include:

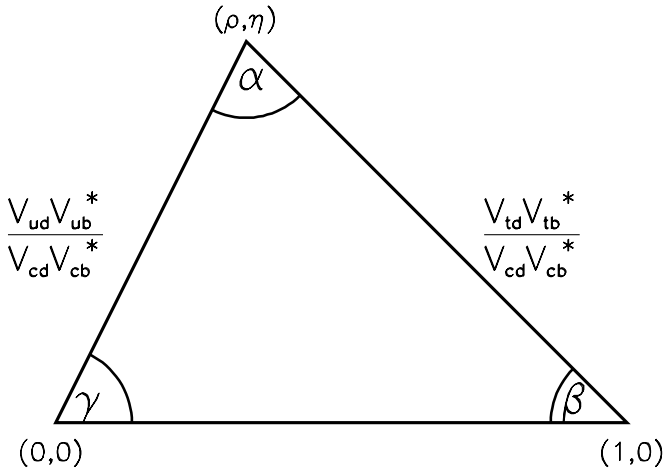

Figure 2.56: The unitarity triangle indicating the relationship between the CKM elements.

- An observation of CP violation in $B^0 \to J/\psi K_S^0$ and a measurement of $\sin(2\beta)$ with a precision comparable to e^+e^- machines
- An observation of CP violation in $B^0 \to \pi^+\pi^-$ and a measurement of $\sin(2\alpha)$ to ± 0.10
- Determination of $|V_{td}/V_{ts}|$ with a precision of 20% over the full range allowed by the Standard Model

The copious production of b hadrons of several species at the Tevatron offers the opportunity to provide measurements that will allow us to fully check the consistency of the CKM picture. To take advantage of the broad spectrum and high rate of production of b hadrons at the Tevatron, the challenges of triggering and event reconstruction in high energy $p\bar{p}$ collisions must be successfully met.

2.6.2 The current CDF b program

CDF has demonstrated the ability to mount a b physics program exploiting the unique aspects of hadron production. Approximately twenty papers have been published (or are submitted and under review) in PRL and PRD by CDF on the subject. Many of the CDF results are highly competitive with measurements from LEP or CLEO and some of them are the best measurements from a single experiment. These measurements include:

- Individual b hadron masses (B^+, B^0, B_s, Λ_b) [2, 3]
- Individual b hadron lifetimes (B^+, B^0, B_s, Λ_b) [4, 5, 6]
- Polarization in $B^0 \to J/\psi K^{*0}$ and $B_s \to J/\psi\phi$ [7]
- Search for $B_c \to J/\psi\pi$ [8]
- Searches for rare decays ($B^0, B_s \to \mu^+\mu^-$; $B^\pm \to \mu\mu K^\pm$; $B^0 \to \mu\mu K^{*0}$; $B^0, B_s \to \mu e$) [9]

There are other physics topics for which CDF has preliminary results based on Run Ia data ($\approx$ 20 pb^{-1}). These ongoing analyses will also be competitive with LEP and CESR with the full Run I data set ($\approx$ 110 pb^{-1}) and include: a measurement of the B_d mixing parameter x_d, limits on the B_s mixing parameter x_s, measurement of the ratio of branching ratios for color–suppressed B meson decays, and a search for $B_c \to J/\psi\ell\nu$.

CDF has also carried out several studies of B and quarkonium production and of $b\bar{b}$ production correlations [10, 11]. The QCD aspects of these results have generated much interest. In addition, they provide the understanding of B production necessary for studies of B decay.

The analyses carried out by CDF have shown that the mass resolution obtained with the CTC coupled with the vertex resolution obtained with the SVX allows us to (a) isolate fully–reconstructed B decays and (b) measure the lifetime of the decaying mesons. Point (a) is illustrated in Figure 2.57 where the observed signals for $B^\pm \to J/\psi K^\pm$ and $B^0 \to J/\psi K^{*0}$ are displayed. These data samples are currently the world's largest for these decay modes. Point (b) is illustrated in Figure 2.58 where the lifetime distribution for exclusive $B \to \psi K$ modes is used to extract the individual $B^\pm$ and B^0 meson lifetimes.

In addition, we have gained considerable experience in measuring the B decay vertex in partially reconstructed B semileptonic decays. For example, we have used the decays $B^- \to \ell^- D^0 \bar{\nu}$ and $B^0 \to \ell^- D^{*+} \bar{\nu}$ to measure the lifetimes of the charged and neutral B mesons. The D meson signals are displayed in Figure 2.59, and the corresponding B lifetime distributions are displayed in Figure 2.60. Note that these measurements do not rely on the presence of a J/ψ in the final state for triggering or reconstruction purposes. These results (and similar ones shown later for B_s decays) demonstrate the ability to measure B lifetimes in decays involving two secondary vertices (one due to the B decay and one due to the D decay).

By combining our Run I results using exclusive decays and semileptonic decays, we obtain a ratio of the B^+ to B^0 lifetimes of 1.09 ± 0.05. Figure 2.61 graphically compares CDF's results on b hadron lifetimes with the combined results of the LEP experiments (from the 1995 Lepton Photon Symposium).

Currently, CDF is unique in having a sample of $B \to J/\psi K_S$ events that can be tagged for a CP asymmetry analysis. We are working on several flavor tagging methods and expect to apply these methods to a first study of the CP asymmetry using the Run I data.

2.6.3 CDF II strategy for b physics

The current generation of B experiments, CDF, CLEO, LEP and SLD, are already making important measurements and placing constraints on the parameters of the CKM matrix. On the time scale of Run II, there will be competition among many new or upgraded experiments. CDF II will take advantage of the broad spectrum of b hadrons produced at the Tevatron which makes measurements with B_s, B_c and b baryons as well as with B^0 and B^+ possible. Key elements of CDF that made the Run I high–p_T physics program (*e.g.* top and W) so successful include excellent tracking resolution, lepton identification (including dE/dx), secondary–vertex reconstruction and a flexible and powerful trigger and data acquisition system. These same elements are also the foundation upon which a successful b physics program has been built.

The strategy for CDF II is to build on our experience in Run I, to optimize the quality of information in the central region while expanding coverage, and to exploit many additional b hadron decay channels. The tracking upgrades (SVXII/ISL/COT) are expected to improve the present mass resolution while the 3D silicon tracker (SVXII) is expected to improve the vertex finding ability. The lepton and tracking coverage will be increased (SVXII, ISL and CMX/IMU). The dE/dx information from the COT will be employed for particle identification. In CDF II we also plan to leave sufficient space at the outer diameter of the tracking volume (COT) for a Time–of–Flight system designed to provide for K/π separation

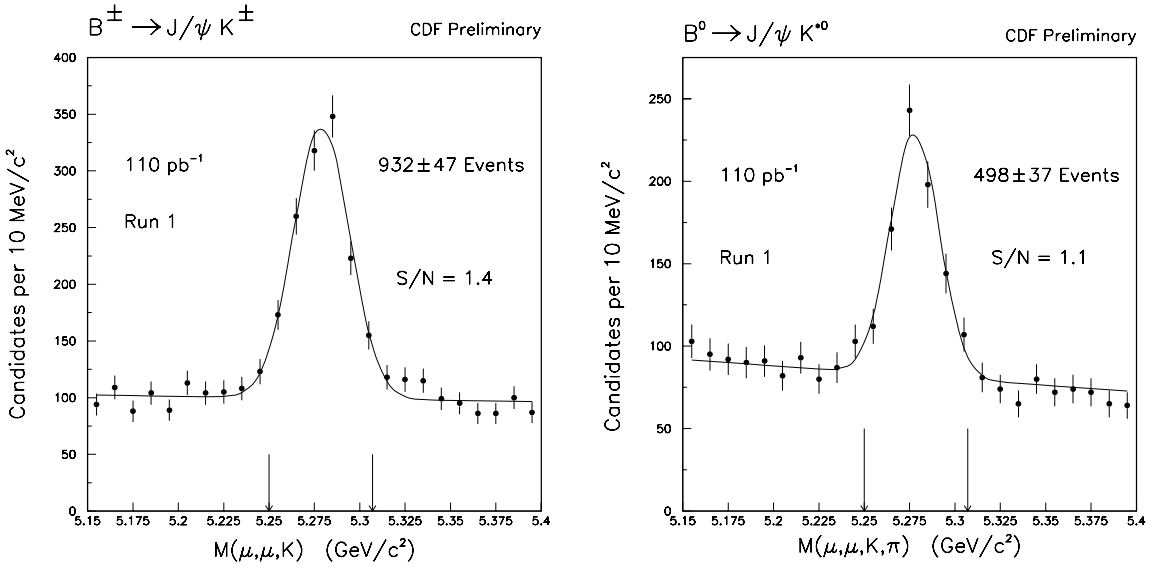

Figure 2.57: The invariant mass distributions for charged and neutral B mesons reconstructed via the decay modes $B^+ \to J/\psi K^+$ and $B^0 \to J/\psi K^{*0}$ as observed by CDF.

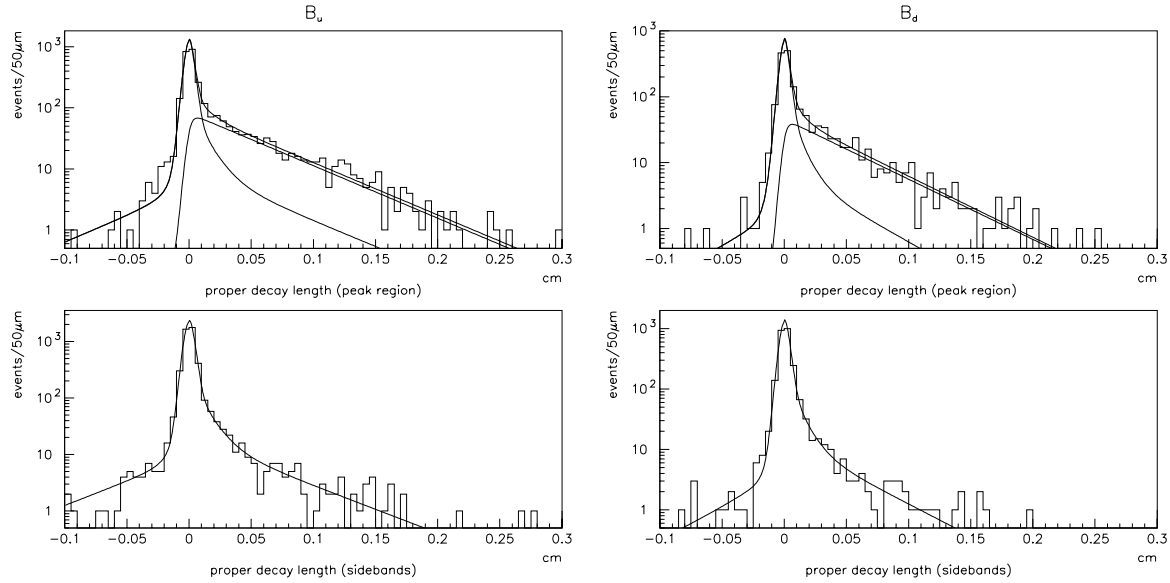

Figure 2.58: The proper lifetime distributions for charged and neutral B mesons reconstructed via the exclusive $B \to \psi K$ decay modes are shown in the upper plots. The lower plots display the background distributions for the B sidebands.

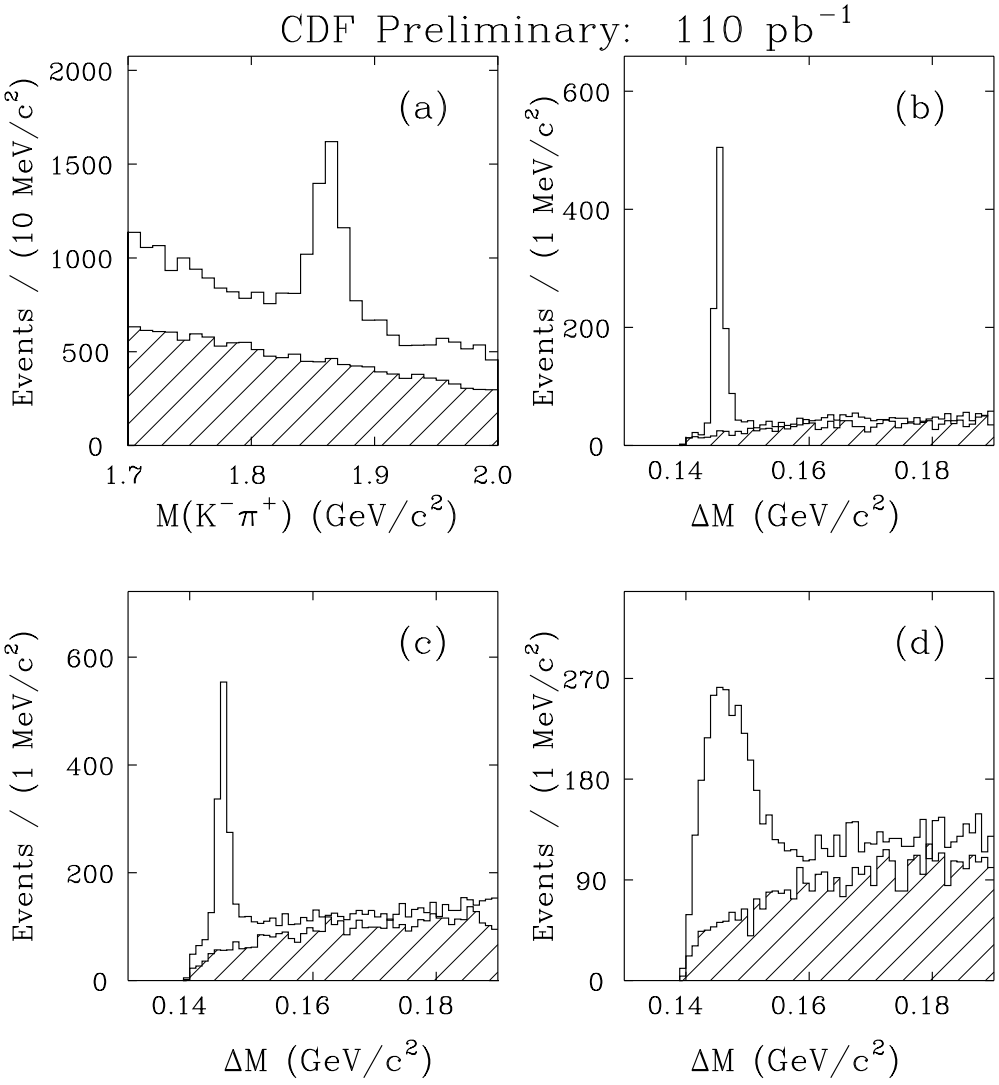

Figure 2.59: Charm signals reconstructed in association with a high-p_T lepton.
(a): Signal for $\bar{B} \to D^0 \ell^- \bar{\nu} X; D^0 \to K^- \pi^+$ (+ c.c.)
(b): Signal for $\bar{B} \to D^{*+} \ell^- \bar{\nu} X; D^{*+} \to D^0 \pi^+; D^0 \to K^- \pi^+$ (+ c.c.)
(c): Signal for $\bar{B} \to D^{*+} \ell^- \bar{\nu} X; D^{*+} \to D^0 \pi^+; D^0 \to K^- \pi^+ \pi^- \pi^+$ (+ c.c.)
(d): Signal for $\bar{B} \to D^{*+} \ell^- \bar{\nu} X; D^{*+} \to D^0 \pi^+; D^0 \to K^- \pi^+ X$ (+ c.c.)
Mode (a) is dominated by B^- decays and modes (b) – (d) by $\bar{B}^0$ decays (ΔM is the mass difference between the $D^0 \pi^+$ and the D^0). Shaded histograms show wrong-charge combinations (*e.g.*, $\ell^- K^+$); in (a) these are scaled by 0.5 for display purposes.

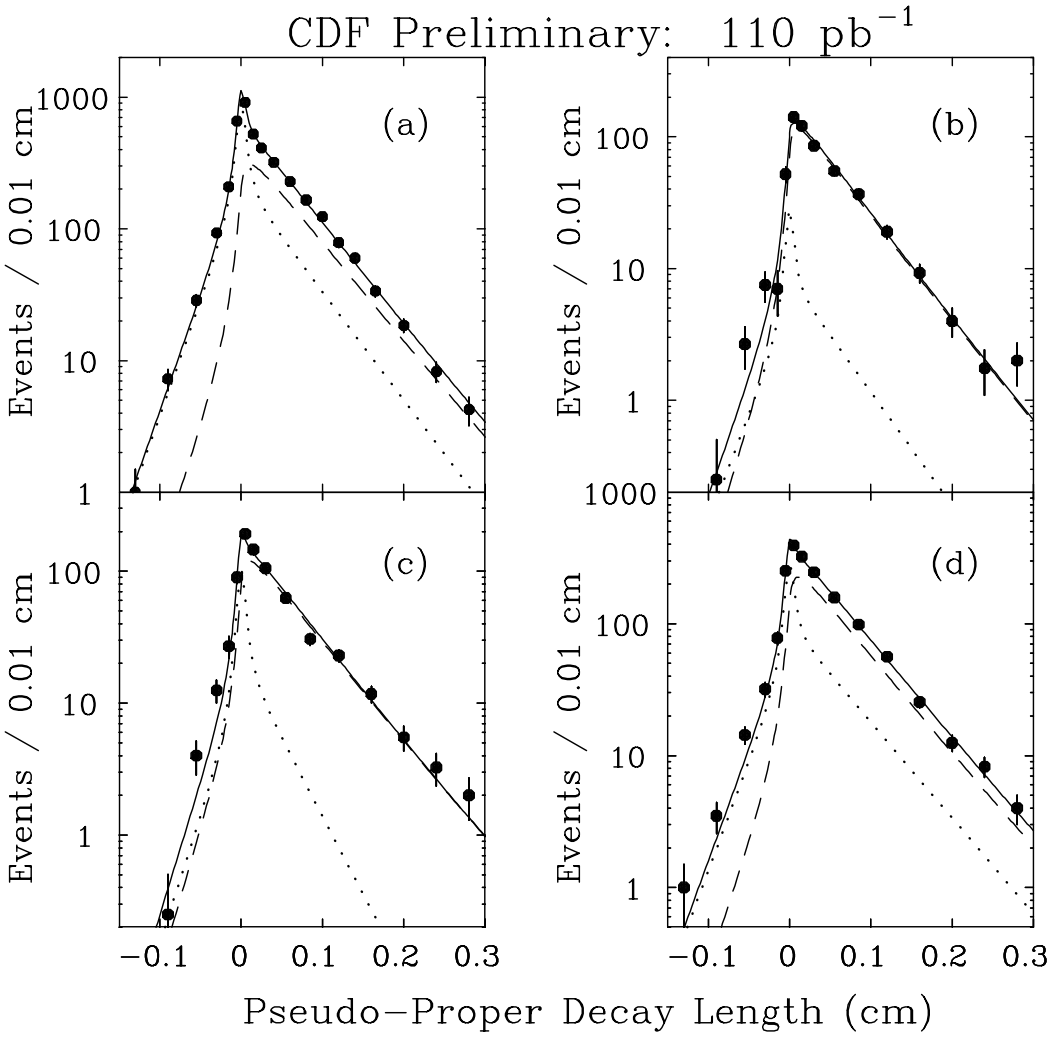

Figure 2.60: Distributions of pseudo-proper decay lengths for lepton + "D" signal samples (points). In all the plots the fits are shown for the signal (dashed line), background (dotted line) and sum (solid line). The four decay channels are represented in (a) – (d) as in the previous figure.

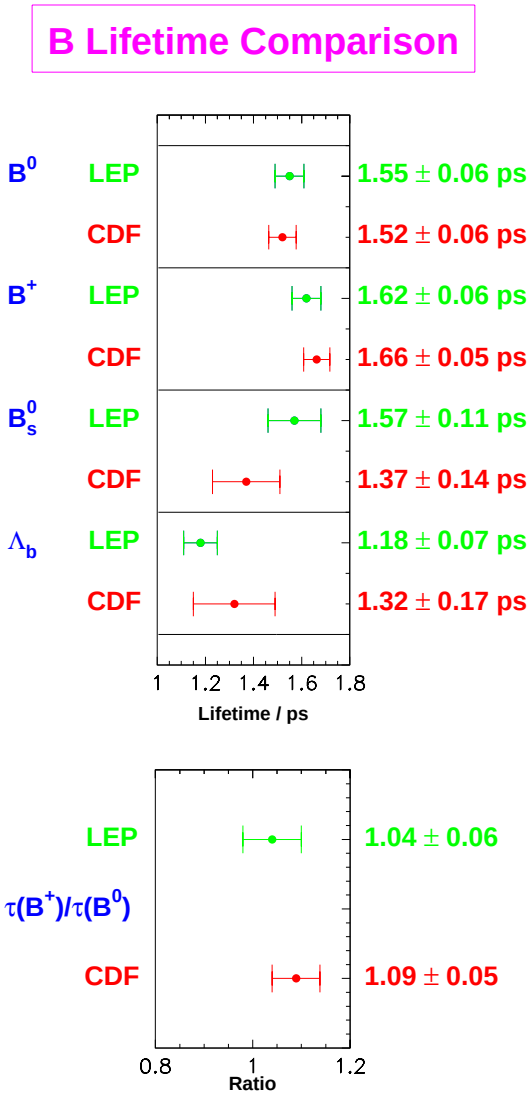

Figure 2.61: CDF and combined LEP (1995) results for b hadron lifetimes.

at low to moderate p_T.

In addition, the high–rate capability of the upgraded trigger/data acquisition system will enable us to handle the high luminosity of the Main Injector era while lowering thresholds and acquiring events in many more channels. Of particular importance will be the ability to form triggers based on track information alone at Level 1 (XFT) and detect the presence of tracks with displaced vertices at Level 2 (SVT).

Thus, the CDF II detector will provide for a competitive b physics program that has unique features and addresses a wide variety of topics of fundamental importance. Below we discuss several specific topics:

- Observation of CP violation in $B^0 \to J/\psi K_S$
- Observation of CP violation in $B^0 \to \pi^+\pi^-$
- Search for CP violation in $B_s \to J/\psi\phi$
- Reconstruction of channels useful for measuring the angle γ.
- Measurement of the ratio of CKM matrix elements $|V_{td}/V_{ts}|$
  - B_s mixing, Δ, $_s/$, $_s$
  - Radiative B decays
- Observation of the rare decays $B^0 \to \mu\mu K^{*0}$ and $B^\pm \to \mu\mu K^\pm$

These topics are of high priority on our physics menu and they highlight the needed capabilities of the CDF II detector. With these capabilities we also expect to be able to make significant progress on several other topics in b-quark physics, including the observation and study of B_c decays, and on measurements of CKM matrix elements V_{ub} and V_{cb} in exclusive semileptonic decays of B meson and baryons (*e.g.* $B \to \rho\ell\nu$).

2.6.4 CP Violation in the B system

2.6.4.1 CP Asymmetry in $B^0 \to J/\psi K_S$

By far the most important goal of the CDF II B physics program is the observation of CP violation in the B system. The decay mode most frequently discussed in the literature [12] is $B^0 \to J/\psi K_S$. CP violation would manifest itself as an asymmetry in the partial decay rates of B^0 and $\bar{B}^0$ to the same final

state, $J/\psi K_S$ (a CP eigenstate). This will result in an asymmetry:

$$A_{CP} = (N - \bar{N})/(N + \bar{N}) \qquad (2.5)$$

in the number of decays from B^0 (N) and $\bar{B}^0$ ($\bar{N}$) mesons. The asymmetry in the partial decay rates is directly related to the angle β of the CKM unitary triangle:

$$, (B^0, \bar{B}^0 \to J/\psi K_S) \propto e^{-\Gamma t}[1 \pm \sin(2\beta)\sin(x,\, t)] \qquad (2.6)$$

where $x = \Delta m/$, is the ratio of the mass difference of the heavy and light B meson states to the total decay rate, also known as the mixing parameter, and t is the decay time. The observed asymmetry A_{CP}^{obs} will be smaller than A_{CP} by a factor known as the "dilution" D; $A_{CP}^{obs} = DA_{CP}$. As discussed below the dilution receives contributions from the time evolution of the B meson under study and from the method used to tag the flavor of the B meson at the time of production.

CDF has already collected the world's largest sample of $B^0 \to J/\psi K_S$ decays: a preliminary analysis of the full data sample accumulated in Run I (110 pb^{-1}) results in 240 of these events, shown in Figure 2.62 with S/N better than 1 : 1. We obtained this sample with a dimuon trigger that required both muons to have transverse momentum (p_T) greater than 2.0 GeV/c. For this analysis, we have not required that the events be in the SVX fiducial region, although we used SVX information if available. Also shown in Figure 2.62 is the same data sample with the additional requirement that SVX track information be available for the J/ψ decay muons, demonstrating an improvement in S/N within the limited acceptance of the SVX. The improved capability and increased coverage obtained with the SVX II should result in a much improved signal to noise; in what follows we have conservatively assumed $S/N = 2 : 1$.

Our goal for Run II is to improve the trigger efficiency to the point that we reconstruct three to four times as many $B^0 \to J/\psi K_S$ events per pb^{-1}. We expect to achieve this by lowering the p_T threshold to 1.5 GeV/c (made possible in Run II by having a tracking trigger at Level 1), by using $J/\psi \to e^+e^-$ as well as $J/\psi \to \mu^+\mu^-$ decays, and by improving the coverage for lepton identification.

The decrease of the muon threshold alone is expected to double the current $\mu^+\mu^- K_S$ yield (events per pb^{-1}). Including the acceptance gained by the completion of the CMX detector, we then expect $\approx$ 10,000 events for 2 fb^{-1} from the dimuon triggers in the central region ($|\eta| < 1$, *i.e.* CMU and/or CMX).

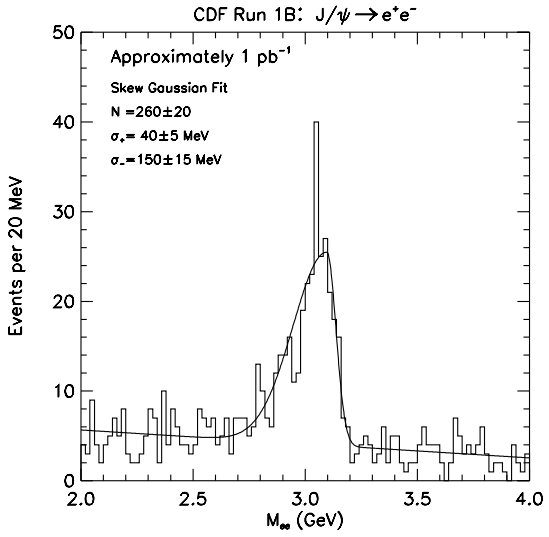

Figure 2.63: $J/\psi \to e^+e^-$ signal from a test trigger during Run I.

The inclusion of electrons was studied with some tests of di–electron triggers during Run I. Figure 2.63 shows a reconstructed $J/\psi \to e^+e^-$ signal obtained with a test trigger based on a 3 GeV/c electron p_T threshold. From these studies it is estimated that a Level 2 trigger rate of 20 Hz could be achieved assuming a 2 GeV/c threshold and the requisite improvements for the CES electronics to cope with the lower threshold and higher crossing frequency for Run II. If possible we wish to use a 1.5 GeV/c threshold; However, in the estimates of sensitivity which follow we assume a 2 GeV/c threshold for electrons, for an overall factor of three increase on the Run I $B^0 \to$ dilepton $+K_S$ yield.

There are also possibilities for further increasing the number of reconstructed $B^0 \to J/\psi K_S$ events, such as improving the coverage for lepton identification beyond the central region. Some of them are listed at the end of this section.

In what follows we will not take any such possible improvements into account, but we investigate only two scenarios, one in which we have only the dimuon channel available for J/ψ reconstruction (resulting in 10,000 $B^0 \to J/\psi K_S$ events) and one in which the

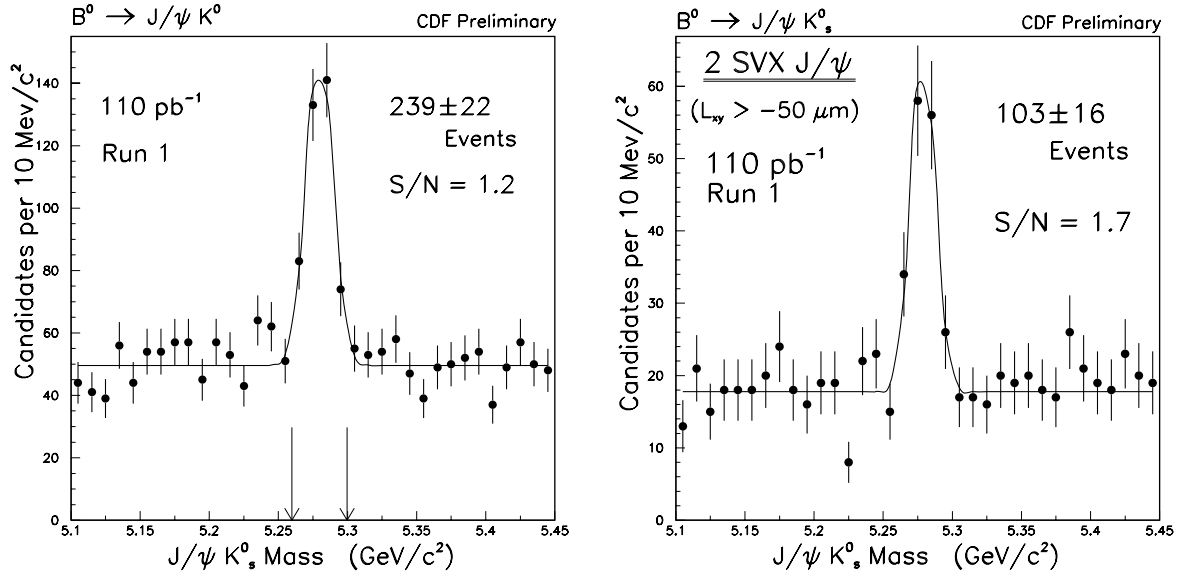

Figure 2.62: CDF's $B^0 \to J/\psi K_S$ signal from Run I. For the plot on the right, SVX track information has been required for muons from the J/ψ. It is noted that the S/N improves to 2.3 : 1 without additional loss of signal if the transverse decay length (L_{xy}) is required to be greater than zero.

di–electron channel is also available, resulting in the total of 15,000 events.

To obtain the CP asymmetry we must tag the flavor of the B meson at the time at which it was produced. The flavor tagging efficiency is more uncertain than the $B^0 \to J/\psi K_S$ yield. We are currently investigating several flavor tagging methods. Work is under way to use a combination of Run I data and Monte Carlo to establish the "effective tagging efficiency" for each possible method with the CDF II detector configuration. The "effective tagging efficiency" is is defined to be ϵD^2 for a flavor tagging method with efficiency ϵ and dilution D. The uncertainty on the CP asymmetry, δA_{CP}, is given by

$$(\delta A_{CP})^2 \approx \frac{1}{\epsilon D^2 N} \frac{S+B}{S} \qquad (2.7)$$

where N is the total number of events prior to flavor tagging and $N = S + B$ includes signal (S) and background (B) events (and we assume $S/B = 2:1$). The dilution is defined as $D = (N_R - N_W)/(N_R + N_W)$, where N_R and N_W are the number of events with right and wrong tags respectively.

We currently have results for three flavor tagging methods (the effectiveness of these methods has been demonstrated in our measurements of $B^0 - \bar{B}^0$ mixing as shown later):

1. Jet Charge [13], where the weighted sum of the charge of tracks recoiling against a B meson is used to determine the flavor of the second b hadron in the event

2. Lepton tagging [14], where a lepton from the second b hadron in the event is used to tag its flavor

3. Same-Side Tagging [15], where charge correlations between the B meson and charged tracks in its vicinity are used to identify the flavor of the B meson at the time of production [16].

The sum of the individual ϵD^2 for these three algorithms is $\approx 3.4\%$, although correlations among the flavor tagging methods are expected to reduce the combined effective tagging efficiency. The study of these correlations is in progress. A conservative estimate is that using the three algorithms together results in a combined ϵD^2 which is $\approx 80\%$ of the sum of the individual ϵD^2 for each algorithm.

Table 2.12 lists the tagging methods we expect to exploit, the effective tagging efficiency measured in

Run I, and the elements of the CDF II detector upgrade that impact these algorithms. The dilution effects due to mixing and mistags for the opposite–side tagging algorithms are included in the values given for ϵD^2.

For Run II, we expect improvements in the total ϵD^2 from the following sources:

- An improvement is expected for lepton tagging by extending the coverage beyond the central region, giving a total $\epsilon D^2 = 1.7\%$ from lepton tagging.
- The increased coverage of the SVX II, together with its three-dimensional track reconstruction capability, will result in a cleaner selection of fragmentation tracks around the B meson. We expect ϵD^2 for Same Side Tagging to increase to 2%.
- A significant improvement in ϵD^2 is possible for the Jet Charge algorithm. The extended coverage of the SVX II and ISL and their added pattern recognition capability will enhance substantially the purity of this algorithm. Monte Carlo studies indicate that $\epsilon D^2 \approx 3\%$ is possible.
- Further improvement in ϵD^2 is expected if a Time–of–Flight system is eventually installed. In the current baseline detector design a TOF system is not included; however, there are provisions (*i.e.* empty space) for the installation of such a system at some point in the future. The main motivation for such an addition is the added tagging efficiency ($\epsilon D^2 \approx 3\%$) from using the charge of kaons opposite to the $B^0 \to J/\psi K_S$ decay.

The uncertainty expected on the measurement of $\sin(2\beta)$ is given by

$$\delta \sin(2\beta) \approx \frac{1 + x_d^2}{x_d} \frac{1}{\sqrt{\epsilon D^2 N}} \sqrt{\frac{S+B}{S}} \qquad (2.8)$$

where $x_d/(1 + x_d^2) = 0.47$ accounts for the dilution due to the time evolution of the signal B^0 in a time–integrated asymmetry measurement (for the time being we ignore the improvement afforded by fitting the time development of the asymmetry). The Run II expectation based on the above yields and effective tagging efficiencies is listed in Table 2.13. The effective tagging efficiency includes the 80% derating for overlaps among the flavor tagging algorithms employed.

We consider the estimate of $\delta \sin(2\beta) = 0.13$ to be a very conservative scenario which is essentially established based on Run I data. In the optimistic scenario with the inclusion of dielectron triggers, improved Jet Charge flavor tagging and a TOF system, we could obtain a total $\epsilon D^2 = 7.8\%$ yielding $\delta \sin(2\beta) = 0.076$.

Finally, in addition to the above expectation of $15,000$ $B^0 \to J/\psi K_S$ events in 2 fb^{-1}, the $B^0 \to J/\psi K_S$ yield can be increased by employing (a) the increased tracking coverage and (b) new ways of triggering using the SVT upgrade:

(a) The additional coverage of the IMU for the dimuon trigger can increase the event yield by about 30%. The acceptance for K_S decays is also expected to increase by using tracks at higher pseudorapidity from the ISL.

(b) Simulations of the SVT indicate that it may be possible to trigger requiring one lepton and one additional track with large impact parameter [17]. In the offline analysis, the second lepton is found primarily using tracking information.

In summary, based on the results we have obtained so far, we expect that the dimuon channel, with the improved trigger and coverage, combined with the tagging methods established already, will yield $\delta \sin(2\beta) = 0.13$. Standard Model predictions for $\sin(2\beta)$ are $\sin(2\beta) > 0.17$ [18] and $\sin(2\beta) = 0.65 \pm 0.12$ [19]. Thus, even in the most conservative case, with $\delta \sin(2\beta) = 0.13$, we will have a very interesting measurement of $\sin(2\beta)$ that will probably result in the observation of CP violation.

It is likely that we will do better than the conservative case. The addition of the di–electron channel, improved detector performance for Jet Charge flavor tagging and a TOF system would increase the accuracy to $\delta \sin(2\beta) = 0.076$. This level of sensitivity is similar to that which might be achieved after two years of running at 10^{33} cm^{-2}sec^{-1} at the B factories by (appropriately) summing over several final states. As we gain experience, additional triggering and reconstruction techniques may allow an even more precise measurement that will tightly constrain the parameters of the Standard Model.

Tagging Method	ϵD^2 (%) (measured)	ϵD^2 (%) (expected)	Relevant CDF II Upgrade
Central Muon	0.6 ± 0.1	1.0	Complete CMX/Add IMU
Electron	0.3 ± 0.1	0.7	Plug calorimeter/ISL
Same-side pion	1.5 ± 0.4	2.0	SVX II/ISL
Jet Charge	1.0 ± 0.3	3.0	SVX II/ISL
Opposite-side Kaon		3.0	Time–of–Flight

Table 2.12: Flavor tagging methods currently under consideration, the effective tagging efficiency, ϵD^2, for algorithms established with Run I data, the expected ϵD^2 in Run II, and the list of detector upgrades that will improve ϵD^2.

Scenario	ϵD^2 (%)	$N(J/\psi K_S)$	$\delta \sin(2\beta)$
$\mu^+\mu^-$ triggers; "measured" tags only	2.7	10,000	0.16
Improved lepton and same–side π tags	3.8	10,000	0.13
Add $J/\psi \to e^+e^-$ triggers	3.8	15,000	0.11
Improved Jet Charge tag	5.4	15,000	0.09
Add Time–of–Flight	7.8	15,000	0.076

Table 2.13: The expected uncertainty on the measurement of $\sin(2\beta)$ under different assumptions on the total effective tagging efficiency and the number of $J/\psi K_S$ events.

2.6.4.2 *CP* Asymmetry in $B^0 \to \pi^+\pi^-$

A measurement of $\sin(2\alpha)$ in conjunction with $\sin(2\beta)$ provides powerful constraints on the unitarity triangle [20]. The greatest challenge in this measurement is the trigger requirement at a luminosity of $1 \times 10^{32}\text{cm}^{-2}\text{sec}^{-1}$. Our plan (described in detail in Reference [21]) consists of

Level 1: Requiring that two oppositely–charged tracks be found with the XFT track processor (capable of finding tracks in the COT with $p_T >$ 1.5 GeV/c with $\delta p_T/p_T^2 < 0.01$ [GeV/c]$^{-1}$). Imposing $\Delta\phi$ cuts on oppositely–charged 2 GeV/c track pairs yields an expected Level 1 accept rate of 16 kHz as measured using Run I data.

Level 2: Using the SVT processor (capable of extrapolating the XFT tracks in the SVX II detector and determining their impact parameter, d, with resolution $\sigma_d \approx 25\mu$m). Demanding $d > 100$ μm yields an expected Level 2 accept rate of less than 20 Hz.

Level 3: Here the full event information is available. We expect to be able to reduce the rate out of Level 3 to about 1 Hz.

With these trigger requirements we expect $\approx$ 5 $B^0 \to \pi^+\pi^-$ events per pb^{-1} for a yield of 10,000 events in 2 fb^{-1}. Since these events must pass the SVT requirement, they have a proper lifetime distribution starting at $\approx$ 1.5 lifetimes. After fitting the time development, the dilution of the *CP* asymmetry due to the time evolution of the signal B will be 0.82, rather than the time averaged value, 0.47, which we assumed for $\sin(2\beta)$.

To measure the *CP* asymmetry in $B^0 \to \pi^+\pi^-$ events one needs to extract the *physics* backgrounds from $B^0 \to K\pi$, $B_s \to K\pi$ and $B_s \to KK$ decays. Figure 2.64 displays the expected mass distribution for the combination of the above four signals, assuming [21] all charged kaons to be pions, equal partial rates for the four decay modes and a 3 : 1 production ratio for $B^0 : B_s$. The $B^0 \to \pi\pi$ and $B^0 \to K\pi$ peaks are separated by 40 MeV/c^2. An initial simulation of the upgraded detector indicates that the resolution at $p_T(B) \approx 6$ GeV/c will be about 20 MeV/c^2. Note that the $B_s \to KK$ peak lies directly under the $B^0 \to \pi\pi$ peak and is not resolved by improved mass resolution and thus particle ID will be required.

In order to extract the $\pi\pi$ signal it will be essential to make use of the dE/dx information provided by the COT. With the CTC we achieve a one standard

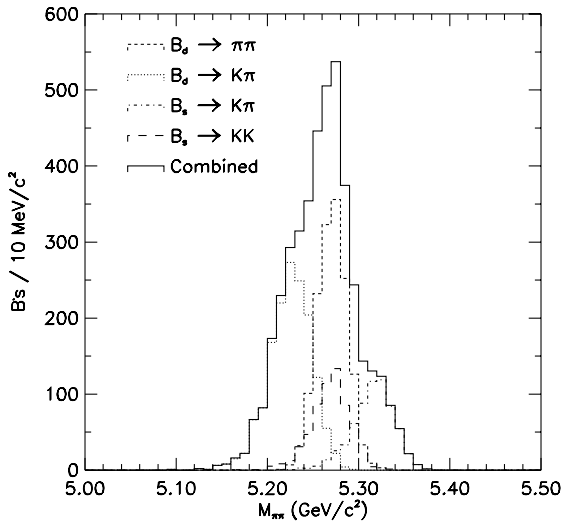

Figure 2.64: Mass distribution for the combination $B^0 \to \pi^+\pi^-$, $B^0 \to K\pi$, $B_s \to K\pi$ and $B_s \to KK$ assuming all charged kaons to be pions. The assumed mass resolution is $\sim$20 MeV/c^2. (Note that the vertical scale should be treated as arbitrary.)

deviation separation between the K and π signals for momenta > 2 GeV/c. We expect the COT dE/dx performance to be as good as that for the CTC and perhaps better due to the increased number of samples and efficiency for dE/dx hit usage. With dE/dx information and the mass distribution we can statistically extract the $B^0 \to \pi\pi$ component from the total invariant mass distribution. It is useful to point out that this evaluation will be carried out with the full sample, that is, before B flavor tagging.

Another issue for this analysis is the combinatorial background under the B peak. Although in the Run I data we expect only a fraction of a signal event, we can estimate the background level for the CDF II detector using inclusive electron data. Using standard cuts on the decay vertex and the isolation of the two-track combination, we obtain an observed background N comparable to the expected signal S for $p_T > 4$ GeV/c on each track: $S/N \approx 1:1$. Lowering the p_T threshold to 2 GeV/c will allow us to double our efficiency. We expect to do this with the CDF II detector while maintaining S/N better than $1:1$ by exploiting the 3D information from the SVX II and optimizing cuts.

The final issue related to the extraction of the angle α from the measured CP asymmetry in $B^0 \to \pi\pi$ is the extraction of possible penguin contributions in addition to the tree diagram which is expected to dominate this decay mode. We can estimate this penguin contamination, and thus extract α, from a combination of experimental measurements and theoretical inputs. A detailed analysis can be found in reference [22]. Assuming a flavor-tagging efficiency (ϵD^2) of 7.8% as in the $J/\psi K_S$ case, and a conservative $S/N = 1/4$, we expect an overall uncertainty on $\sin(2\alpha)$ of 0.10.

2.6.4.3 CP Asymmetry in $B_s \to J/\psi\phi$

While the CP asymmetry in $B^0 \to J/\psi K_S$ measures the weak phase of the CKM matrix element V_{td}, the CP asymmetry in $B_s \to J/\psi\phi$ measures the weak phase of the CKM matrix element V_{ts}. The latter asymmetry is expected to be very small in the Standard Model, but in the context of testing the Standard Model has the same fundamental importance as measuring the more familiar CP asymmetries. This measurement is most accessible, if not unique, to experiments at a hadron collider.

Our Run I B_s mass analysis indicates that our yield of reconstructed $B_s \to J/\psi\phi$ events is 60% that of $B^0 \to J/\psi K_S$ (see Figure 2.65). Since the modest trigger improvements for $B^0 \to J/\psi K_S$ ($\approx 15{,}000$ events) apply equally to $B_s \to J/\psi\phi$, we can expect ≈ 9000 events for this decay mode in Run II.

The flavor tagging techniques described for the B^0 case apply to the B_s with one exception: The fragmentation track correlated with the B_s meson is a kaon instead of a pion. A PYTHIA study indicates that a Time–of–Flight system, by identifying kaons, would allow us to increase the efficiency of the same-side kaon algorithm from 2% to 5% [23]. In this case we could assume a total flavor tagging efficiency (ϵD^2) for B_s mesons of $\approx 10\%$.

The magnitude of a CP asymmetry in $B_s \to J/\psi\phi$ decays will be modulated by the frequency of B_s oscillations. Thus, for a meaningful limit, we must be able to resolve B_s oscillations. If we neglect $(c\tau)$ resolution effects, we can expect a precision on the asymmetry of ± 0.09 from a time dependent measurement. However, resolution effects smear the oscillations and produce an additional dilution. For our Run I data, if we determine the primary vertex event-by-event, the proper lifetime resolution for fully reconstructed B decays is $\approx 30\mu$m [24]. We expect that the proper lifetime resolution for the SVX II will be $\approx 10\%$ bet-

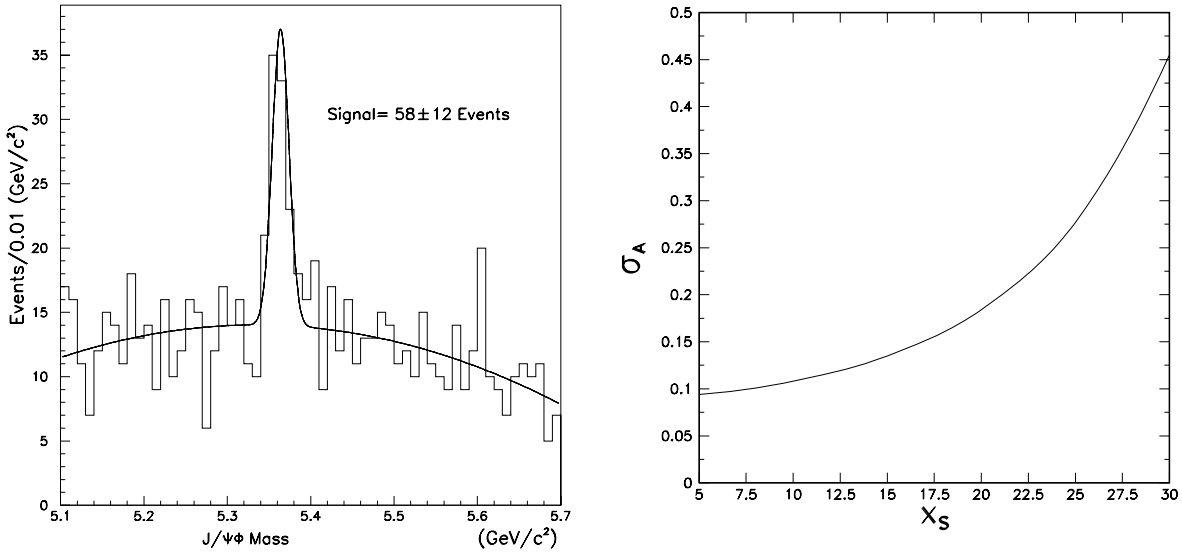

Figure 2.65: Left: The reconstructed mass distribution for $B_s \to J/\psi\phi$ decays. SVX track information has been required for the muons from the J/ψ. Right: The uncertainty on the CP asymmetry for $B_s \to J/\psi\phi$ as a function of the B_s mixing parameter x_s.

ter than that for the Run I detector [25]. Figure 2.65 shows our expected precision on the asymmetry as a function of x_s.

2.6.4.4 Feasibility of measuring γ

Measuring the third angle, γ, in the unitarity triangle completes the test of the unitarity of the CKM matrix. The angle γ can be probed via the decays [26]

1. $B_s^0 \to D_s^- K^+$ and $D_s^+ K^-$
2. $B^+ \to \bar{D}^0 K^+$, $B^+ \to D^0 K^+$, and $B^+ \to D^0_{CP+} K^+$

where D_{CP+} refers to the CP even state $(|D^0\rangle + |\bar{D}^0\rangle)/\sqrt{2}$.

These decay modes have been considered in Reference [27]. As with the $B^0 \to \pi^+\pi^-$ decay mode, these analyses depend on an all–hadronic decay mode trigger (*i.e.* charged tracks). Assuming a Level 1 trigger of two tracks with opposite charge and $p_T > 2$ GeV/c, and a Level 2 trigger cut of 100 μm on the impact parameter, we expect an overall efficiency times acceptance of $\approx 3 \times 10^{-4}$ for the B_s and $B^\pm$ decay modes above.

Unfortunately, the decay modes $B_s^0 \to D_s^- K^+$ and $D_s^+ K^-$ require a time-dependent analysis and therefore their utility depends on the B_s mixing parameter, x_s. Moreover, the results in Reference [27] indicate that a very small tagged signal is expected. However, if Δ, /, for the B_s is large enough and can be measured independently, γ can be extracted by measuring the relative fraction of the two lifetime components in the untagged $D_s K$ sample. [28] Also, it has been recently noted [29] that a determination of the CKM angle γ may be obtained through measurements of the time evolution of angular distributions for B_s decays into final states which are CP admixtures.

The charged B modes are very interesting since the observation of an asymmetry between B^+ and B^- would indicate the presence of direct CP violation. Experimentally, measurement of the asymmetry involves only time–integrated quantities; these decays are self–tagging. The uncertainty on the observed CP asymmetry is now a function of (a) the angle γ and (b) the strong phase difference, δ. In the most favorable case, $\gamma = \pi/2$ and $\delta = \pi/2$. Then the CP asymmetry, A_{CP}, and the uncertainty on it, δA_{CP}, are $A_{CP} = 0.2$ and $\delta A_{CP} = 0.05$ respectively. The detailed discussion of the uncertainty on A_{CP} is contained in [27].

2.6.5 Determination of $|V_{td}/V_{ts}|$

Within the CKM model, $|V_{td}/V_{ts}|$ is constrained at 95% confidence level to lie in the range [18]:

$$0.11 \leq \left|\frac{V_{td}}{V_{ts}}\right| \leq 0.36 \qquad (2.9)$$

Experiments operating on the $\Upsilon(4S)$ can determine $|V_{td}/V_{ts}|$ by measuring the ratio of decay rates of radiative B decays $B(B \to \rho\gamma)/B(B \to K^*\gamma)$ [30]. However, recent studies [31] have shown that such decays have potentially large long-distance contributions, making extraction of $|\frac{V_{td}}{V_{ts}}|$ difficult.

In contrast, experiments at hadron colliders can also use B_s mesons, which are amply produced, and determine $|V_{td}/V_{ts}|$ using several independent techniques, including some with quite small theoretical uncertainties as discussed below. Combining these techniques, CDF II should, with 2 fb^{-1} of data, not only be able to constrain $|V_{td}/V_{ts}|$, but also *measure* its value over the full range permitted by the Standard Model.

2.6.5.1 B_s Mixing

Mixing in the B system has been discussed extensively in the literature [18]. In the Standard Model, $B\overline{B}$ oscillations occur dominantly through top quark contributions to the electroweak box diagram. The size of the mixing is expressed in terms of the parameter $x \equiv \Delta m/$, where Δm is the difference in mass between the heavy and light B meson states and , $= \hbar/\tau$ where τ is the average lifetime of the states. The value of x depends on the top quark mass, the B decay constant, the QCD bag parameter and corrections due to the breaking of SU(3) flavor symmetry. Theoretical uncertainties in the determination of the CKM parameters can be greatly reduced by considering the ratio of x_s to x_d:

$$\frac{x_s}{x_d} = \frac{(m_{B_s}\eta_{B_s}B_{B_s}f^2_{B_s})}{(m_{B_d}\eta_{B_d}B_{B_d}f^2_{B_d})}\left|\frac{V_{ts}}{V_{td}}\right|^2 \qquad (2.10)$$

where η_{B_i} are QCD corrections of order 1 ($i = d, s$), B_{B_i} are B meson bag parameters, and f_{B_i} are B meson weak decay constants.

In the limit of SU(3) symmetry, the factors in front of the ratio of CKM elements would be unity. Lattice Gauge theory determines the value of these factors to be 1.3 ± 0.2 [32]. Since x_d/x_s depends on $|\frac{V_{td}}{V_{ts}}|^2$, the theoretical uncertainty on $|V_{td}/V_{ts}|$ is $\sim 10\%$.

Because x_s is large, it must be determined by fitting the time-dependent oscillation

$$\text{Prob}(B_s \to \overline{B}_s) = \frac{1}{2}e^{-t/\tau}\left(1 - \cos(x_s t/\tau)\right). \qquad (2.11)$$

The quality of the measurement depends upon the experimental proper decay time resolution and the ability to tag the flavor of the B at production time. CDF has already performed measurements of x_d (see Figures 2.66 and 2.67) [33]. Because B_s oscillations are rapid, an x_s measurement will place stringent demands on the experiment's ability to determine the proper time of the decay.

Vertex finding requirements for the x_s measurement are discussed in detail in Reference [34]. In general, the proper time resolution can be parameterized in terms of two constants

$$\sigma_t = \sqrt{a^2 + b^2 t^2} \qquad (2.12)$$

Here a is determined from the resolution on the primary and secondary vertex positions and b depends on the accuracy with which the momentum of the B_s is known. The decay time t and its uncertainty σ_t are measured in units of proper time, relative to the B_s lifetime. The values of a and b depend upon the decay mode under consideration. In general, the resolution is significantly worse for semileptonic decays ($B_s \to D_s\ell\nu$) than for fully–reconstructed events ($B_s \to D_s + \text{n}\pi$). The number of semileptonic decays is, however, significantly larger. The x_s reach of both decay modes has been studied [35].

CDF already has experience analysing semileptonic B_s decays. In the Run I data [36], 254 ± 21 $B_s \to D_s\ell\nu$ events were reconstructed and a B_s lifetime measurement of $1.37 \pm 0.13 \pm 0.04$ ps was obtained (see Figure 2.68). For Run II, triggering and reconstruction of this channel with very high statistics is straightforward. Our x_s reach will be limited by our proper lifetime resolution. Simulation studies of the SVX II detector [25] have determined that for semileptonic decays $a = 0.11$ and $b = 0.15$. This resolution limits the measurement to values of x_s less than about 15.

For fully–reconstructed decays $a = 0.06$ and $b = 0.03$ [37]. This value of a is based on our Run I proper lifetime resolution using fully reconstructed B events for which we determine the primary vertex event by event. Figure 2.69 shows that with sufficient statistics (the figure contains 2000 fully reconstructed events with perfect tagging) oscillations can

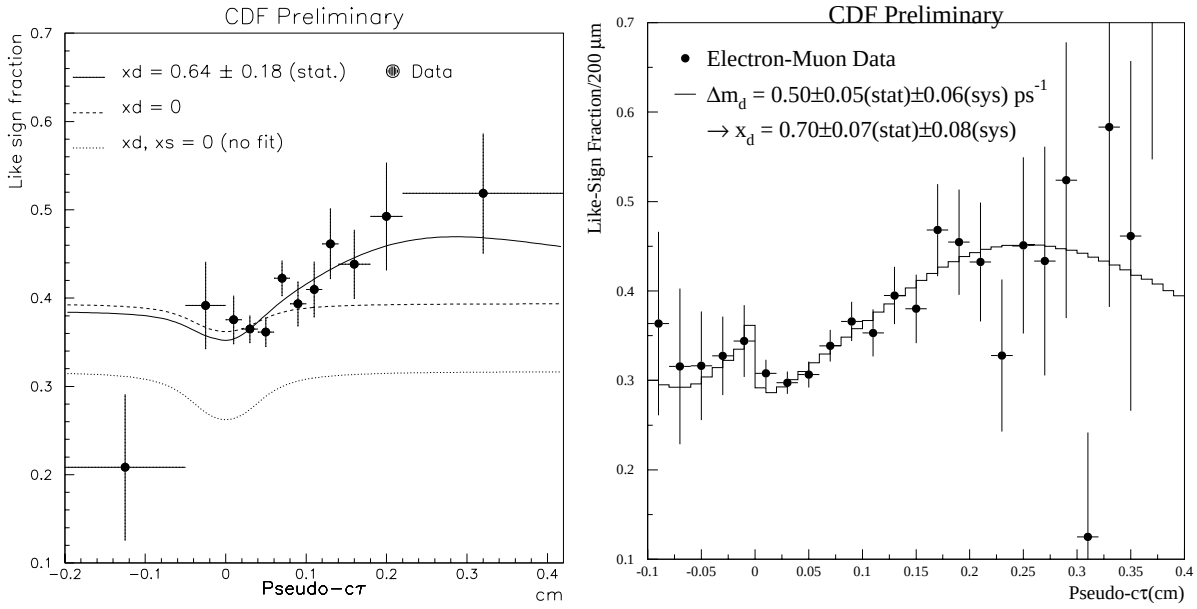

Figure 2.66: Two studies of $B^0 - \bar{B}^0$ mixing performed by CDF using different dilepton triggers. Results of a fit to the like-sign fraction vs proper lifetime are shown on the left for a Run Ia sample (20 pb^{-1}) collected using a dimuon trigger and on the right for a combined Run Ia and Run Ib sample (110 pb^{-1}) collected with an electron-muon trigger. In both cases, one lepton was associated with a secondary vertex and the other lepton served as a flavor tag. For these fits, maximal B_s mixing is assumed.

still be clearly resolved in the SVX II for $x_s = 20$. In practice, the ultimate x_s reach for fully reconstructed decays will depend on the number of decays available in the channel rather than on the proper lifetime resolution. The challenge for CDF II is to trigger on, and isolate from background, signals of this type.

One trigger strategy is to trigger on a single lepton (e or μ), which will serve as the flavor tag, and then reconstruct B_s decays in this sample [34]. For a 6 GeV lepton threshold in Run II, and using selection criteria similar to those commonly used in Run I analyses, the expected yield is low, $\sim$ 250 events. However, it is likely that the lepton trigger threshold could be lower with some of the decay products of the B_s included in the trigger requirement as well. We note that the presence of a Time–of–Flight system in CDF II could significantly improve the reconstruction purity by allowing efficient selection of kaons and rejection of pions at low P_T, where the backgrounds are largest.

A promising strategy is to use a fully hadronic trigger, in which case all tagging techniques may be applied. In fact, the Level 1 and Level 2 triggers designed for $B \to \pi^+\pi^-$ will also provide good acceptance for the decay products of the B_s. Using the same assumptions as for $B_d \to \pi^+\pi^-$, we expect a yield of more than 1600 fully reconstructed and tagged B_s decays. We show in Figure 2.69 the resulting precision on x_s as a function of x_s.

2.6.5.2 $\Delta\Gamma_{B_s}/\Gamma_{B_s}$

The calculation of x_s depends upon the evaluation of the real part of the mass matrix element. The imaginary part of the same matrix describes the decay widths of the two mass eigenstates B_s^H and B_s^L. Within the Standard Model it is possible to calculate the ratio $\Delta\Gamma_{B_s}/\Delta m_{B_s}$ [38]:

$$\Delta\Gamma_{B_s}/\Delta m_{B_s} = -\frac{3}{2}\pi\frac{m_b^2}{m_t^2}\frac{\eta_{QCD}^{\Delta\Gamma_{B_s}}}{\eta_{QCD}^{\Delta m_{B_s}}} \qquad (2.13)$$

where the ratio of the QCD correction factors (η) in the numerator and denominator is expected to be of order unity [39]. This ratio does not depend on CKM parameters. Thus, a measurement of $\Delta\Gamma_{B_s}$ determines Δm_{B_s} up to QCD uncertainties. Moreover, the larger Δm_{B_s} becomes the larger $\Delta\Gamma_{B_s}$ is. Thus,

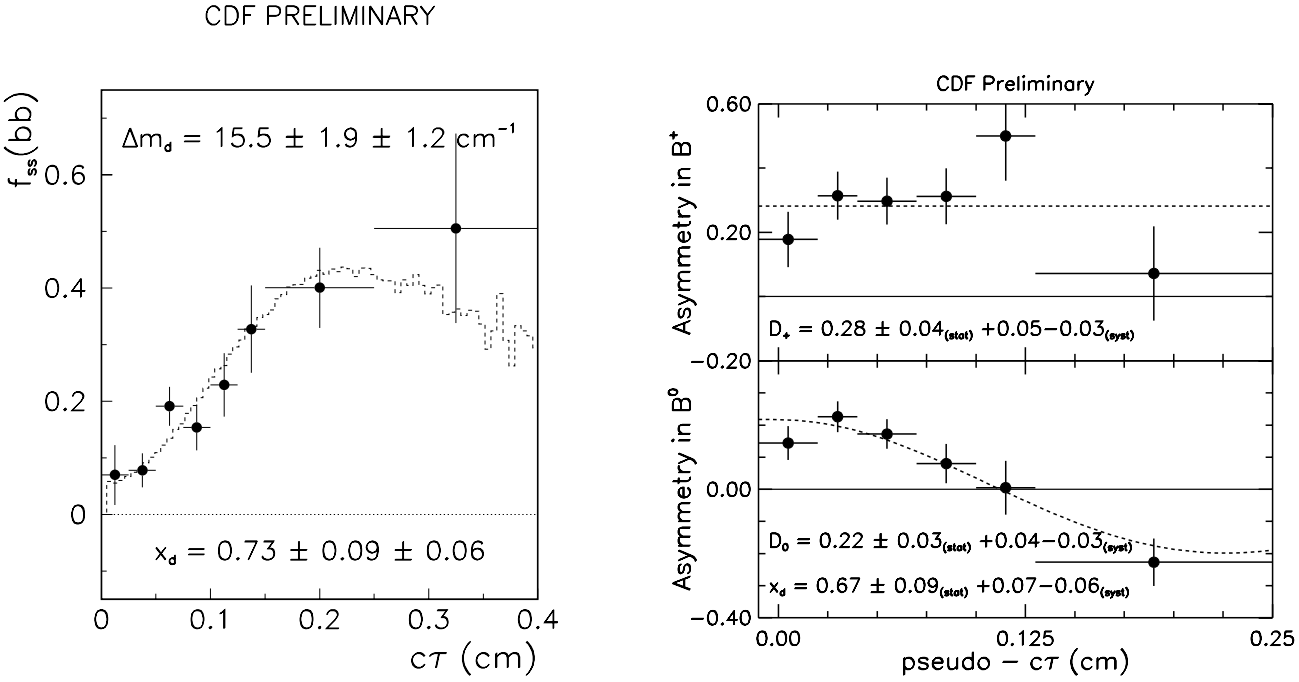

Figure 2.67: Two studies of $B^0 - \bar{B}^0$ mixing performed by CDF using lepton triggers and different tagging strategies. Left: The $b\bar{b}$ same sign fraction as a function of proper time for events from the Run Ib inclusive electron and muon triggers. The trigger lepton is associated with a secondary vertex which gives the proper time. An additional soft lepton or the jet charge of an opposite side jet is used for a flavor tag. The dashed histogram represents the result of an unbinned likelihood fit for Δm_d. Right: Measurement of the asymmetry $(N_R - N_W)/(N_R + N_W)$ as a function of proper time for charged B (upper plot) and neutral B (lower plot) mesons reconstructed from a single lepton trigger sample and flavor tagged using a same-side pion tag. Here, the charge of the B meson is determined by reconstructing the D^0 or D^{*+} meson from the semileptonic decay. A clear mixing signal is present for the neutral B while no mixing is observed for charged B mesons.

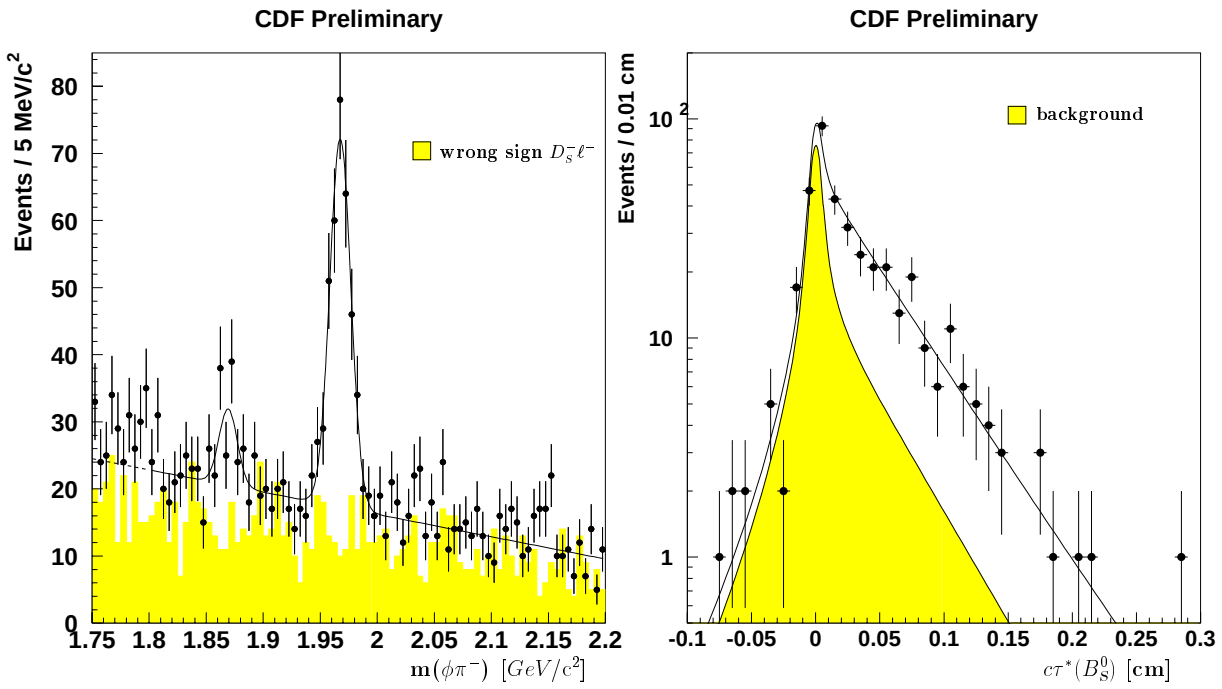

Figure 2.68: Left: invariant mass distribution for D_s mesons produced in right-sign $(D_s^+\ell^-)$ events with $D_s^+ \to \phi\pi^+$ and $\phi \to K^+K^-$; the wrong-sign combinations are shown as a shaded histogram. There is also evidence of the Cabibbo suppressed decay $D^+ \to \phi\pi^+$. Right: pseudo–ctau distributions for the B_s signal and background (shaded).

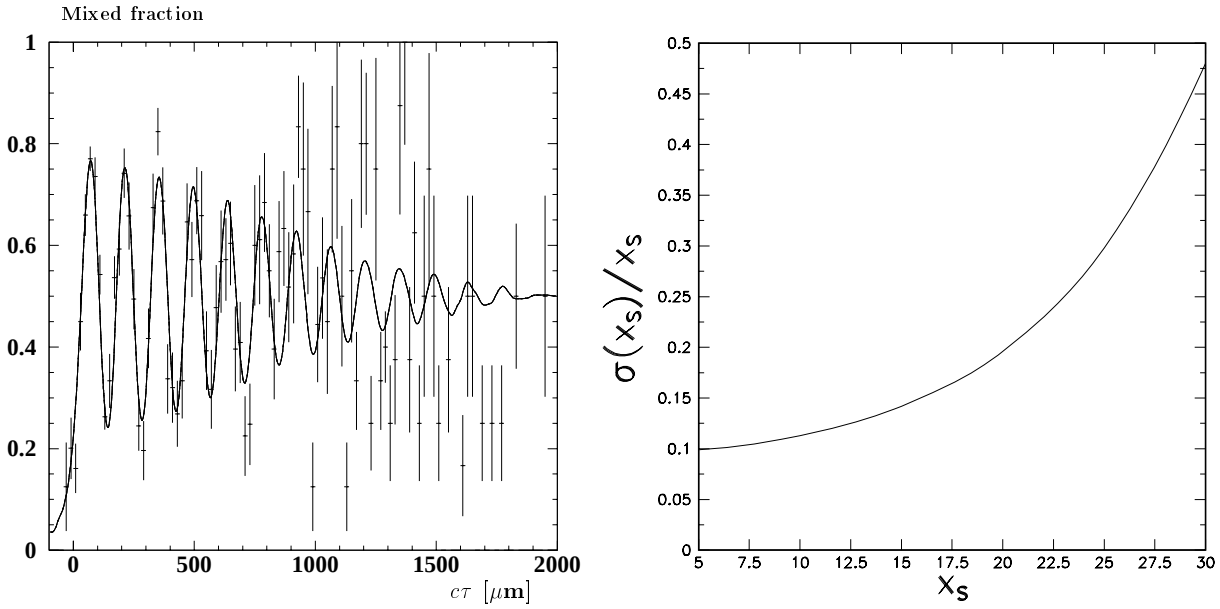

Figure 2.69: Left: A Monte Carlo simulation of the reconstructed B_s mixing signal for a Run II sample with the CDF II detector. Right: Relative uncertainty on x_s for fully reconstructed B_s decays.

as it becomes more difficult to measure x_s, Δ, becomes more accessible. Using the above expression, Browder *et al.* [39] show that if $x_s = 15$, a 7% difference in lifetime is expected.[2] They estimate that the uncertainties in calculating Δ, $/\Delta m$ contribute an uncertainty of $\sim 30\%$ on $|V_{td}/V_{ts}|^2$ (*i.e.* a 15% uncertainty on $|V_{td}/V_{ts}|$). This contribution to the theoretical uncertainty should be added in quadrature to the 10% uncertainty discussed in the previous section, for a total uncertainty of $\approx 20\%$.

Several techniques can be used to determine Δ, $_{B_s}$ [40]. First, the proper time distribution of a flavor-specific B_s mode (*e.g.* $B_s \to D_s \ell \nu$) can be fit to the sum of two exponentials. Second, the average lifetime of such a flavor specific mode can be compared to the lifetime of a mode that is dominated by a single *CP* state (it is expected that $B_s \to J/\psi\phi$ will be such a mode) [41]. Finally, a decay such as $B_s \to J/\psi\phi$ can be decomposed into its two *CP* components (via a transversity analysis [42]) and fit for a separate lifetime for each component. It is noted that CDF has measured the helicity structure of the decays $B \to J/\psi K^*$ and $B_s \to J/\psi\phi$ using Run Ia data [7]. The results obtained are $, _L/, = 0.65 \pm 0.10 \pm 0.04$ for $B \to J/\psi K^*$ and $, _L/, = 0.56 \pm 0.21 \pm 0.03$ for $B_s \to J/\psi\phi$.

The statistical uncertainty on the B_s lifetime from semileptonic B decays in Run II will be below 1%. The Run II expectation, including only the modest set of trigger improvements described in section 2.6.4.1, is for ≈ 9000 $B_s \to J/\psi\phi$ events. The $B_s \to J/\psi\phi$ helicity structure should then be known to about 1% [3]. Using the current CDF number for the $B_s \to J/\psi\phi$ helicity structure, with 2 fb^{-1}, the lifetime difference could be determined to $2-3\%$. Including current theoretical uncertainties of 20%, this determination of Δ, $_{B_s}$ would either measure $|V_{td}/V_{ts}|$ or set an *upper* bound on $x_s \leq 15$. Thus, using the direct x_s measurement and Δ, $_s/$, $_s$, CDF II should be able to measure $|V_{td}/V_{ts}|$ over the full range permitted by the Standard Model in Run II.

It is important to note that the discussion of B_s mixing (and *CP* violation) has been in the context of the three generation Standard Model. New physics

[2] This large $\Delta\Gamma_{B_s}$ is possible because there are large branching fraction common decay modes available to the B_s and $\overline{B_s}$ (*e.g.* $D_s^{(*)+} D_s^{(*)-}$).

[3] The systematic uncertainties in the polarization measurements are dominated by the estimate of the size and helicity of the background under the B mass peak. These systematic uncertainties should scale with the square root of the number of events in the sample.

associated with large mass scales can also reveal itself through a study of the mass and width differences for the neutral B mesons [43].

2.6.5.3 Radiative B Decays

In the absence of long distance effects, radiative B decays provide an alternative approach for measuring $|V_{td}/V_{ts}|$.

$$\frac{B(B^- \to \rho^-\gamma)}{B(B^- \to K^{*-}\gamma)} = \frac{B(B^0 \to \rho^0\gamma) + B(B^0 \to \omega\gamma)}{B(B^0 \to K^{*0}\gamma)} = \left|\frac{V_{td}}{V_{ts}}\right|^2 \xi\Omega$$

where Ω is a phase space correction and ξ is a model dependent factor in the range 0.58 - 0.81 [30]. The relative rates for $\rho^0\gamma$ and $\omega\gamma$ decays are equal in the quark model. Based upon a 2 fb^{-1} sample containing 13 $K^*\gamma$ candidates (with an estimated background of 1.9) and 2 $\rho\gamma + \omega\gamma$ candidates (with an estimated background of 4.1), CLEO has used this technique to set a bound on $|V_{td}/V_{ts}|$ in the range 0.64 - 0.76, depending upon theoretical model [44].

CDF has already installed a trigger to collect radiative penguin decays (see Reference [45] for details). The limited bandwidth available of the Run I trigger and data acquisition system required the trigger to have quite high thresholds (10 GeV photon plus two 2 GeV tracks). The expected yield with this trigger is $\approx$ 20 γK^* events per 100 pb^{-1}. In Run II, we expect to lower the photon E_t threshold to 5 GeV and the track P_t threshold to 1.5 GeV, with a resulting yield of $\sim$ 135 events per 100 pb^{-1} or $\sim$ 2700 for 2 fb^{-1}.

The mass resolution of the reconstructed B is dominated by the resolution on the photon energy and is $\sim$ 140 MeV. We have studied our ability to reject combinatorial background using Run Ia photon data and have studied with Monte Carlo the discrimination against $B \to K^*\pi^0$ and $\rho\pi^0$ and higher multiplicity penguin decays [45]. These backgrounds are manageable. However, the offline cuts to remove background are expected to reduce the signal by about a factor of 2. The mass resolution is not adequate to separate $\gamma\rho$ from γK^* on an event-by-event basis; however, a statistical separation is possible. In addition, the COT dE/dx system should provide 1σ K-π separation in the momentum range of interest.

These radiative B decays can also be observed using converted photons. The probability for a photon to convert ($\sim$ 5%) will be offset by a lower photon E_t threshold. Also, the mass resolution is $\sim$ 5 times better than for the signals with unconverted photons and the γ/π^0 separation is $\approx$20 times better, allowing a cleaner separation between $B \to \gamma K^*$ and $B \to \gamma\rho$.

At the Tevatron it is possible to study B_s penguin decays as well. Information on $|V_{td}/V_{ts}|$ can be obtained in the same manner as above from studying the ratio of $B(B_s \to \gamma K^*)/B(B_s \to \gamma\phi)$. The size of the B_s penguin sample is expected to be 1/2 to 1/3 the size of the B_d sample. Comparison of the two results would help constrain the size of the long distance contributions to the decays.

2.6.6 B_c and Cabibbo suppressed decays

CDF II will continue to search for and study additional b hadron states. Figure 2.70 shows the CDF limit on B_c production and decay to $J/\psi\pi$. The study of this $q\bar{q}$ system would be particularly interesting because of the unequal heavy quark masses [46].

We also note that the decay $B^+ \to J/\psi\pi^+$ is a Cabibbo and color suppressed decay which may exhibit a *direct CP* violating effect at the few percent level [47]. The mode is self–tagging and no time dependence is required. Any non–vanishing effect would immediately exclude the superweak model of *CP* violation. In Run II, extrapolating from the $\approx$ 30 events observed, we expect about a 3% error on the asymmetry.

2.6.7 Rare B decays

Rare B decays provide a stringent test of the Standard Model for possible new physics effects, such as an anomalous magnetic moment of the W and the presence of a charged Higgs. Experimentally, these rare decays are accessible via the dimuon trigger. Using these triggers, CDF has performed a search for the decay modes $B^\pm \to \mu^+\mu^- K^\pm, B^0 \to \mu^+\mu^- K^{*0}$ and $B_{d,s} \to \mu^+\mu^-$. The Standard Model predictions [48] for the branching ratio for these decay modes, together with the expected sensitivity for CDF II, are listed in Table 2.14. The projections for $B^\pm \to \mu^+\mu^- K^\pm$ and $B^0 \to \mu^+\mu^- K^{*0}$ conservatively assume the same signal-to-noise ($\sim 1:10$) as obtained for the Run Ia searches. We expect that a CDF II analysis will benefit from a much improved signal-to-noise.

Assuming Standard Model branching ratios for $B^+ \to \mu^+\mu^- K^+$ and $B^0 \to \mu^+\mu^- K^{*0}$, we will have

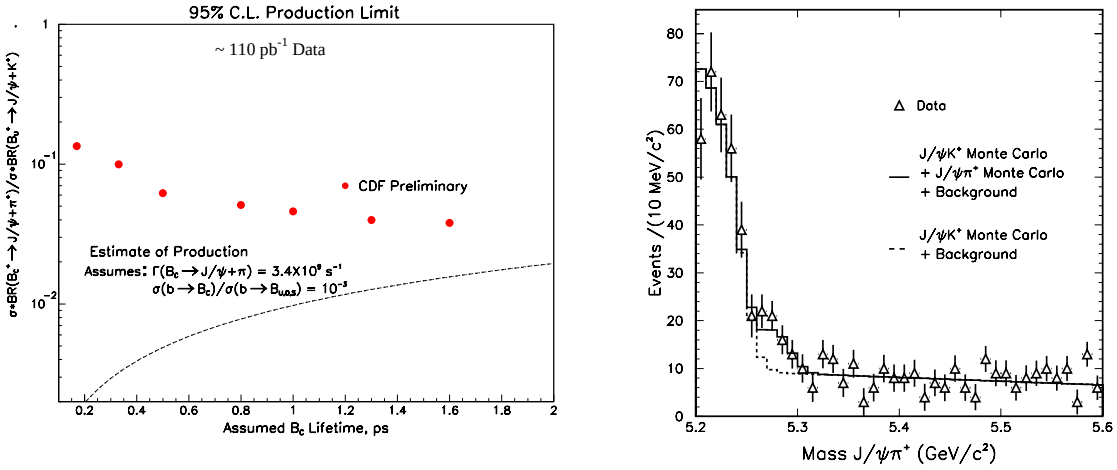

Figure 2.70: On the left: Limit from Run I on the ratio of production and decay of $B_c \to J/\psi\pi$ vs. $B^+ \to J/\psi\pi^+$ as a function of lifetime. On the right: the signal for $B^+ \to J/\psi\pi^+$ is seen as an enhancement in the $J/\psi\pi$ distribution at the upper edge of the $J/\psi K$ contribution which dominates the lower edge of the plot.

B Decay Mode	Standard Model	CDF Run I	CDF II
$\mu^+\mu^- K^+$	$(2-5)\times10^{-7}$	$1.0 \times 10^{-5}(20\ \text{pb}^{-1})$	2×10^{-7}
$\mu^+\mu^- K^{*0}$	$(2-5)\times10^{-6}$	$2.5 \times 10^{-5}(20\ \text{pb}^{-1})$	4×10^{-7}
$B_d \to \mu^+\mu^-$	$(0.6-1.9)\times10^{-10}$	$2.6 \times 10^{-7}\ (110\ \text{pb}^{-1})$	1×10^{-8}
$B_s \to \mu^+\mu^-$	$(1.5-4.5)\times10^{-9}$	$7.7 \times 10^{-7}\ (110\ \text{pb}^{-1})$	4×10^{-8}

Table 2.14: Rare B decay modes, Standard Model predictions for their branching ratios, 90% limits set with Run I CDF data and the expected sensitivity (90% CL) for CDF II.

visible signals for these decays. In particular, we expect $\approx$ 100 to 300 $B^+ \to \mu^+\mu^- K^+$ and $\approx$ 400 to 1100 $B^0 \to \mu^+\mu^- K^{*0}$ events. This will enable us to study both (a) the invariant mass distribution of the dimuon pair and (b) the forward-backward charge asymmetry in the decay. Both of these distributions are sensitive to physics beyond the Standard Model, *e.g.* the presence of a charged Higgs or charginos [49], [50],[51].

2.6.8 Concluding remarks

From the previous discussion it should be clear that CDF II plans to fully exploit the copious production of b hadrons in all of the species produced at the Tevatron. We believe we will have a complete and competitive program, with unique strengths for example in rare decays and B_s physics.

With the experience gained so far in the analyses of Run I data and the planned capabilities of the CDF II detector we are able to confidently project our expectations for Run II which include:

- Observation of CP violation in $B^0 \to J/\psi K^0_S$ and measurement of $\sin(2\beta)$ to better than ± 0.13.
- Observation of CP violation in $B^0 \to \pi^+\pi^-$ and measurement of $\sin(2\alpha)$ to better than ± 0.14.
- Determination of $|V_{td}/V_{ts}|$ with a precision of 20% over the full range allowed by the Standard Model
- Observation of the rare decays $B^0 \to \mu\mu K^{*0}$ and $B^\pm \to \mu\mu K^\pm$

With these and other measurements that we will pursue with b hadrons with CDF II, we expect to impose severe constraints on the Standard Model of weak quark mixing and CP violation and be very sensitive to new physics.

Bibliography

[1] L. Wolfenstein, Phys. Rev. Lett. **51**, 1945 (1984).

[2] "Measurement of the Mass of the B_s^0 Meson." F. Abe *et al.*, Phys. Rev. **D53** 3496 (1996); "Observation of the Decay $B_s^0 \to J/\psi\phi$ in $p\overline{p}$ Collisions at $\sqrt{s}$ = 1.8 TeV." F. Abe *et al.*, Phys. Rev. Lett. **71** 1685 (1993).

[3] "Observation of $\Lambda_b \to J/\psi\Lambda^0$ at the Fermilab Proton–Antiproton Collider." F. Abe *et al.*, FERMILAB-PUB-96/270-E, August 1996. Submitted to Phys. Rev. D.

[4] "Measurement of the Average Lifetime of B Hadrons Produced in $p\overline{p}$ Collisions at $\sqrt{s}$ = 1.8 TeV." F. Abe *et al.*, Phys. Rev. Lett. **71** 3421 (1993); "Measurement of the B^+ and B^0 Meson Lifetimes." F. Abe *et al.*, Phys. Rev. Lett. **72** 3456 (1994).; "Measurement of the B and $\bar{B}$ Meson Lifetimes Using Semileptonic Decays." F. Abe *et al.*, Phys. Rev. Lett. **76** 4462 (1996).

[5] "Measurement of the B_s^0 Meson Lifetime." F. Abe *et al.*, Phys. Rev. Lett. **74** 4988 (1995); "Measurement of the Lifetime of the B_s^0 Meson Using the Exclusive Decay Mode $B_s^0 \to J/\psi\phi$." F. Abe *et al.*, Phys. Rev. Lett. **77** 1945 (1996).

[6] "Measurement of Λ_b^0 Lifetime Using $\Lambda_b^0 \to \Lambda_c^+\ell^-\bar{\nu}_\ell$." F. Abe *et al.*, Phys. Rev. Lett. **77** 1439 (1996).

[7] "Measurement of the Polarization in the Decays $B_d^0 \to J/\psi K^{*0}(892)$ and $B_s^0 \to J/\psi\phi$." F. Abe *et al.*, Phys. Rev. Lett. **75** 3068 (1995).

[8] "Measurement of the Branching Fraction for $B^+ \to J/\psi\pi^+$ and Search for $B_c^+ \to J/\psi\pi^+$. F. Abe *et al.*, FERMILAB-PUB-96/300-E, September 1996. Submitted to Phys. Rev. Lett.

[9] "Search for Flavor Changing Neutral Current in B Meson Decays in $p\overline{p}$ Collisions at $\sqrt{s}$ = 1.8 TeV." F. Abe *et al.*, Phys. Rev. Lett. **76** 4675 (1996).

[10] "A Measurement of the B Meson and b Quark Cross-Sections at $\sqrt{s}$ =1.8 TeV Using the Exclusive Decay $B^\pm \to J/\psi K^\pm$." F. Abe *et al.*, Phys. Rev. Lett. **68** 3403 (1992); "Measurement of the Bottom Quark Production Cross-Section Using Semileptonic Decay Electrons in $p-\overline{p}$ Collisions at $\sqrt{s}$ = 1.8 TeV". F. Abe *et al.*, Phys. Rev. Lett. **71** 500 1993); "Measurement of Bottom Quark Production in 1.8-TeV $p\overline{p}$ Collisions Using Semileptonic Decay Muons." F. Abe *et al.*, Phys. Rev. Lett. **71** 2396 (1993); "Measurement of the B Meson and b Quark Cross-Sections at $\sqrt{s}$ =1.8-TeV using the Exclusive Decay $B_d^0 \to J/\psi K^{*0}(892)$." F. Abe *et al.*, Phys. Rev. **D50** 4252 (1994). "Measurement of the B Meson Differential Cross-Section, $\frac{d\sigma}{dP_t}$, in $p-\overline{p}$ Collisions at $\sqrt{s}$ = 1.8 TeV." F. Abe *et al.*, Phys. Rev. Lett. **75** 1451 (1995).

[11] "Measurement of Correlated $\mu-\bar{b}$ Jet Cross Sections in $p\overline{p}$ Collisions at $\sqrt{s}$ =1.8 TeV." F. Abe *et al.*, Phys. Rev. **D53** 1051 (1996). "Measurements of $b\bar{b}$ Production Correlations, $B\bar{B}$ Mixing and a Limit on ϵ_B." F. Abe *et al.*, FERMILAB-PUB-96/216-E, August 1996. Submitted to Phys. Rev. D.

[12] H. Quinn, *B^0–$\bar{B}^0$ Mixing and CP Violation in B Decay*, in Review of Particle Properties, Phys. Rev. **D50**, 1632 (1994) and references therein.

[13] O. Long and J. Kroll, *A Jet Charge B-Tagging Method*, CDF note 3069. See also CDF note 3810.

[14] M. D. Peters *et al.*, *A Study of B-Flavor Tagging Using Soft Muons*, CDF note 3098. See also CDF notes 3808 and 3809.

[15] *Observation of $\pi-B$ Charge–Flavor Correlations and Measurement of Time–Dependent $B\bar{B}$ Mixing in $p\bar{p}$ Collisions*, The CDF Collaboration. Contributed paper to the XXVIII Inter-

national Conference on High Energy Physics, Warsaw, 1996, FERMILAB-CONF-96/175-E. K. Kelley and P. Sphicas, *Same-Side Tagging in Exclusive B decays*, CDF note 3638.
F. DeJongh, P. Maksimovic and P. Sphicas, *An Investigation of Time–Dependent B^0 Mixing in Tagged Lepton+Charm Events*, CDF note 3644. See also CDF note 3701.

[16] M. Gronau and J.L. Rosner, Phys. Rev. **D49**, 254 (1994).

[17] S. Belforte *et al.*, *Silicon Vertex Tracker (SVT) Technical Design Report*, CDF note 3108.

[18] A. Ali and D. London, Z. Phys. **C65**, 431 (1995).

[19] M. Ciuchini *et. al.*, Z. Phys. **C68**, 239 (1995).

[20] M.E. Lautenbacher, Proceedings of the 27th Int. Conf. on High Energy Physics, Glasgow, Scotland, 20-27 Jul 1994.

[21] S. Donati and G. Punzi $B^0 \to \pi^+\pi^-$ *Trigger Studies with Run Ia Data*, CDF note 3167; J. Mueller and P. Wilson, *A 2 Track $B \to \pi\pi$ Trigger for Run II*, CDF note 2665; see also J.D. Lewis, J. Muller, J. Spalding and P. Wilson in "Proceedings of the Workshop on B physics at Hadron Accelerators", Snowmass, Colorado, June 21-July 2, 1993, eds. P. McBride and C.S. Mishra, p. 217.

[22] F. DeJongh and P. Sphicas, Phys. Rev. **D53**, 4930 (1996).

[23] The CDF Collaboration, *A Time–of–Flight System for CDF* Proposal submitted to the FNAL PAC, 28 March 1995.

[24] A. Spies and O. Schneider, *A Measurement of the B^+ and B^0 Lifetimes using Exclusive Decay Channels*, CDF note 2345.

[25] The CDF Collaboration, *SVXII Simulation Study and Upgrade Proposal*, CDF Note 1922, (see in particular Table 13).

[26] R. Aleksan, B. Kayser and P. Sphicas, in "Proceedings of the Workshop on B physics at Hadron Accelerators", Snowmass, Colorado, June 21-July 2, 1993, eds. P. McBride and C.S. Mishra, p. 291.

[27] E. Blucher, J. Cunningham, J. Kroll, F. Snider and P. Sphicas in "Proceedings of the Workshop on B physics at Hadron Accelerators", Snowmass, Colorado, June 21-July 2, 1993, eds. P. McBride and C.S. Mishra, p.309.

[28] I. Dunietz in Phys. Rev. **D52**, 3064 (1995).

[29] R. Fleischer and I. Dunietz, Fermilab-PUB-96/079-T, HEP-PH/9605220.

[30] A. Ali, V.M. Braun and H. Simma, Z. Phys. **C63**, 437 (1994); J.M. Soares, Phys. Rev. **D49**, 283 (1994); S. Narison, Phys. Lett. **B327** 354 (1994).

[31] E. Golowich and S. Pakvasa, UH-511-800-94; H. Y. Cheng, Phys. Rev. **D51**, 6228 (1995); D. Atwood, B. Blok and A. Soni, SLAC-PUB-6635.

[32] For a recent review, see J. Shigemitsu, *Lattice Gauge Theory: Status Report 1994* Proceedings of the XXVII International Conference on High Energy Physics, Glasgow, Scotland (1994).

[33] The industrious reader is advised to NOT attempt to form an average of these results as they are NOT all strictly independent. For the individual results see F. Bedeshci *et al., Measurement of the Mixing Parameter x_d via Time Evolution*, CDF note 2971; C. Gay *et al., A Measurement of the Time–Dependence of $B^0\bar{B}^0$ Oscillations using Low–p_T Electron–Muon Data*, CDF note 3791; O. Long *et al., Time Dependent B^0 Mixing in Inclusive Lepton Data using Jet Charge and Soft Lepton Flavor Tags*, CDF note 3810; F. DeJongh, P. Maksimovic and P. Sphicas, *An Investigation of Time–Dependent B^0 Mixing in Tagged Lepton+Charm Events*, CDF note 3644 (see also CDF note 3701.)

[34] D.J. Ritchie, J.E. Skarha and A. Zieminski, *Report of the Mixing Sub-Group of the δ Working Group*, Proceedings of the Workshop on B Physics at Hadron Accelerators, Snowmass, Colorado (1993); J. Skarha and A.B. Wicklund *Prospects for Measuring B_s Mixing at CDF*, Proceedings of the Workshop on B Physics at Hadron Accelerators, Snowmass, Colorado (1993).

[35] M. Paulini and M. Shapiro, *Study of x_s Reach for TDR*, CDF note 3693.

Chapter 3

Overview of Tracking

We now begin discussion of the tracking systems for the CDF Upgrade. In this chapter we describe the general context of tracking measurements in CDF, and our plan for the Upgrade. The individual detector components are described in detail in Chapters 4, 5, 6. The projected performance of the proposed system is described in Chapter 7.

3.1 History and Capability

Charged particle tracking has played a major role in almost every physics analysis done with the CDF detector.

The CDF Run I tracking system consisted of a Central Tracking Chamber (CTC), used to measure charged particle momenta, a vertex drift chamber (VTX) used to measure event z vertices, and a silicon vertex detector (SVX) used to detect secondary vertices. The CTC, designed for $\mathcal{L} = 10^{30}\text{cm}^{-2}\text{s}^{-1}$ and in use since 1987, has performed well up to luminosities of $2\times10^{31}\text{cm}^{-2}\text{s}^{-1}$. This detector provides 84 measurement points over the radial range of 31 to 132 cm, covering the $|\eta|$ range ≤ 1.0. The VTX, installed in 1992, makes time projection r-z measurements at radii inside of 31 cm to find the vertex z position, which is important for stereo pattern finding in the CTC.

Track reconstruction in the CTC is highly efficient for the detection of charged particles down to momenta of 300 MeV/c, with a momentum resolution of $\delta p_T/p_T^2 \leq 0.002(GeV/c)^{-1}$. When combined with beam constraint or inner silicon tracker information, this improves to $\delta p_T/p_T^2 \leq 0.001(GeV/c)^{-1}$ at high momentum.

The correlation of CTC tracks with EM calorimetry and muon chamber information is the basis of lepton identification. Correlation at the trigger level allows low p_T thresholds for efficient collection of top candidates, W boson decays, and high rate B physics triggers. At the offline level, more precise versions of this correlation, using shower position and E/p for electrons, and stub position and slope for muons give high purity, high efficiency lepton selection.

The CTC is also used for *in situ* calibration of the central calorimeter. A J/ψ peak, recorded with low p_T muon triggers is compared with the world average J/ψ mass to normalize the momentum scale of the tracking system. This calibration is transferred tower-by-tower to the EM calorimeter using the electron tracks in a large sample of inclusive electrons. The response of the hadron calorimeter is measured using a large sample of isolated tracks, and this is combined with test beam data to normalize the absolute scale. The scale of the hadron system is then checked against the EM calibration using events where a single jet recoils against a well-identified photon or a $Z \rightarrow e^+e^-$ decay.

In 1992, a silicon vertex detecor (SVX) was added to CDF. This device provided r-ϕ points with resolution of approximately 10 μm at four radii between 3 and 10 cm. For high momentum tracks the extrapolated impact parameter resolution is $\approx 15\mu$m. Midway through Run I, the SVX was replaced with a new device, SVX′, of similar geometry but using AC-coupled silicon detectors and a radiation-hard chip. In this report, "SVX" is sometimes used to refer to either of the Run I silicon devices.

Precise measurement of the track impact parameter and azimuth in the SVX is complementary to the precision measurement of p_T and dip angle in the CTC. The combination of these measurements allows the identification of secondary vertices in jets and the measurement of particle lifetimes and masses. This capability has been key to many of the Run I physics highlights at CDF:

- The ability to identify displaced vertices was

crucial in the first direct observation of Top in 1994. The top samples isolated using the SVX b-tagging are very pure, with a signal to noise ratio of almost 4 to 1, and ultimately lead to accurate measurements of the $t\bar{t}$ production cross section and the top mass.

- The combined CTC-SVX tracking system has been used to isolate a number of exclusive B decays, including the world's largest sample of B$\rightarrow J/\psi K_S$ events. This decay will be used for a CP asymmetry analysis in Run II.

- The combined CTC-SVX system has been used to measure the lifetime and masses of B hadrons. Exclusive measurements at CDF are competitive with the combined results of the four LEP experiments.

3.2 Run I Tracking Strategy, and Shortcomings of the System

In Run I, the tracking strategy was fully dependent upon the performance of the CTC. Tracks were found in the CTC by first looking for segments in the axial super-layers. These segments were then linked together and an r-ϕ or 2D track was formed. Since each stereo super-layer had only 6 wires (compared to 12 in an axial super-layer), segment finding in these layers, in a manner similar to the axial super-layers, was not practical. Instead, attaching stereo hits to the r-ϕ CTC track required the additional external input of the z_0 supplied by the VTX. Once 3D tracks were found in the CTC, the resulting helix parameters were then used to extrapolate tracks into the SVX. Hits were attached to the CTC track in each layer of the SVX, beginning with the outermost. At each layer where a hit was found, the helix parameters were recalculated, and the search continued into the next innermost layer. This procedure leads to a multiplication of efficiencies, with the primary loss being track reconstruction efficiency in the CTC. In addition, association of an incorrect SVX hit with a CTC track results in large errors in the measured track parameters.

This tracking strategy produced excellent physics, but as we have gained experience with this system, we have come to understand its intrinsic weakness. Looking ahead, in addition to the expected deterioration in tracking performance at high luminosity, we realize the limitations are inherent to the basic design of both the SVX and CTC.

- **Length of the SVX:**
  Both the SVX and SVX′ detectors were 50 cm long. Since the $p\bar{p}$ luminous region can be described by a Gaussian of width $\sim$ 30 cm, many events are not contained, and the overall geometrical acceptance is only 60%. This has a direct impact on analyses which depend critically on B identification (such as the top analysis), but also has a broader impact.

  If the SVX had covered the entire luminous region, then a CTC track which could not be linked to hits in the SVX would most likely be a conversion (from material outside the SVX) or a daughter of a long-lived particle such as a K_S. The presence or absence of hits can thus be an integral part of the pattern recognition. With a short SVX this is not possible.

- **Too few layers in the SVX:**
  Ideally, one would like to find track segments in the SVX, and link these with tracks found in the CTC, instead of the present scheme of a tree search in the SVX within a road defined by the CTC track. The efficiency and the accuracy with which one finds segments will depend on the number of points used in defining the segment. Both the SVX and SVX′ detectors had four single-sided layers. The average hit efficiency for each layer was $\sim$ 90%, dominated by the gap between barrels. Therefore the probability for a track within the acceptance of SVX to have four or three measurements was $\sim$ 60%, and $\sim$ 30% respectively. Since any three hits define a circle, only combinations of four hits are useful for identifying track segments, and 60% is an unacceptably small tracking efficiency. In addition, with only four hits, the fraction of fake SVX segments (those with at least one hit incorrectly assigned) is quite high. Finally, due to the short lever arm, the resulting momentum resolution of such tracks is poor.

- **No stereo in SVX:**
  The SVX was a two-dimensional device, providing measurements in the r-ϕ plane only. The addition of the SVX information to a CTC track improved the determination of the impact parameter and ϕ_0 dramatically. Lack of a stereo

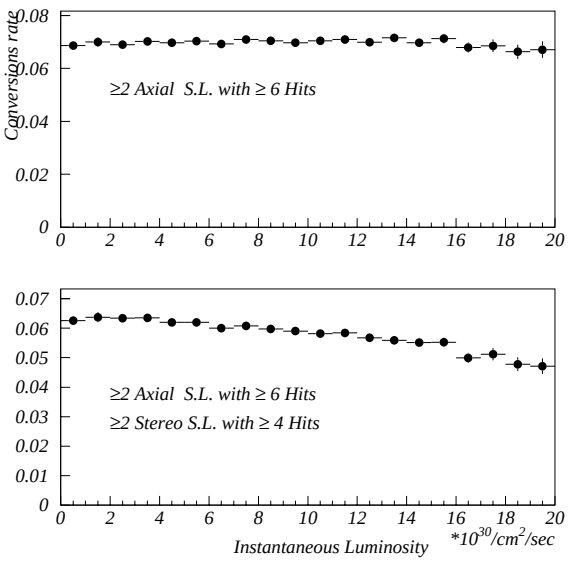

Figure 3.1: Conversion rate vs. luminosity in Run I.

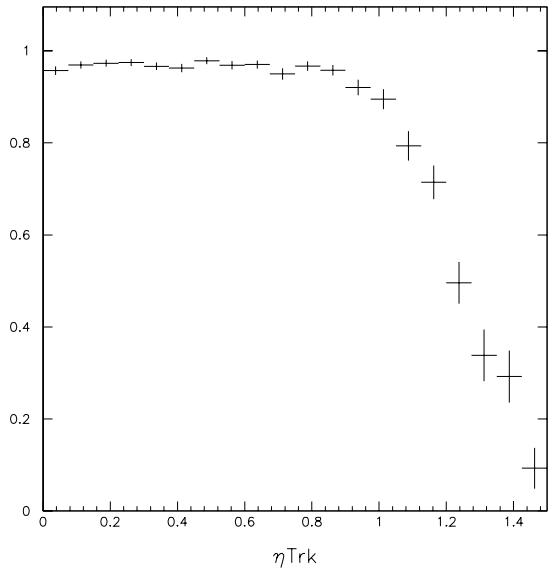

Figure 3.2: Tracking Efficiency vs. track η in CTC.

view in the SVX prevented similar improvement in the r-z parameters $\cot\theta$ and z_0.

- **Weak stereo in CTC:**
  The number of stereo measurements in the CTC is small, 24 out of the 84 total. These are arranged as four stereo super-layers of six wires each. In contrast, the CTC has five axial super-layers with 12 wires each. This choice lead to two effects. As mentioned above, the stereo view could not be completed without an externally supplied z_0. In addition, at high luminosity, the occupancy related efficiency loss on the inner stereo layers caused a significant decrease in 3D reconstruction efficiency. Figure 3.1 shows the rate of reconstructed conversion electrons as a function of instantaneous luminosity in Run I. In the upper plot we require at least two axial super-layers with six or more hits each. The rate is independent of luminosity up to 2×10^{31}. In the lower plot we apply the additional criterion of at least two stereo super-layers with four or more hits each. Now a decrease in efficiency with increasing luminosity is observed, demonstrating that the CTC performance is limited at high luminosity by the stereo reconstruction.

During Run I the only stand-alone tracker in CDF was the CTC. The SVX functioned only as a source of additional points to attach to tracks already found in the CTC, a particularly unfortunate arrangement in light of the fact that the SVX coverage extended to $\eta \geq 2.0$. In Fig. 3.2 we show the track finding efficiency vs η in the CTC. One can see a strong fall-off in efficiency at $\eta \geq 1.0$. Basically, at higher η tracks traverse fewer CTC layers, and the CTC pattern recognition has more difficulty reconstructing the track helix parameters. This affects many analyses. In the top analysis, approximately 40% of the acceptance in the lepton + jet channel is inaccessible due to inability to cleanly identify leptons with rapidity $\eta \geq 1.0$, and another 30% of the b-tagging in all events is lost because the b-jets are in this region.

A much more robust approach would be to have a tracking system with the ability to track not only from the outer tracker to the inner tracker, but also from the inner tracker to the outer. In what follows, we describe such a design.

3.3 Overview of the proposed system

CDF will upgrade the tracking system to accommodate the higher luminosities and shorter bunch crossing times planned for Run II and to correct the known limitations of our old system.

The proposed upgrades include a replacement of the CTC with a small cell, high luminosity variant - the COT, and a replacement of the SVX with a much more powerful silicon system. However, the baseline

tracking configuration that we propose is extremely similar to that which worked successfully in Run I. It is a two component system comprising a silicon vertex detector at the smallest radii, and a large open cell drift chamber covering the radial range from 48 to 131 cm. Both of these detector types are well-proven technologies with which CDF has a great deal of experience. However, this system will have truly integrated pattern recognition and will almost double the tracking coverage.

The main parameters of the tracking system are summarized in Table 1.1 and reviewed briefly below in the context of our observations on tracking strategy. The component designs are described in detail in Chapters 4, 5, and 6, and a detailed study of the system performance is describe in Chap. 7.

- **Central Outer Tracker** The anchor of the Run II CDF tracking system is a large open cell drift chamber for charged particle reconstruction in the central region $|\eta| \leq 1.0$.

  The design goal of the COT is to reproduce the functionality of the CTC with drift times less than 100 ns by using smaller drift cells and a fast gas. The COT will use many of the construction techniques developed for the CTC, and occupies about the same volume. The basic drift cell will make 12 measurements along a radial track, but will have a maximum drift distance of $\sim$ 0.9 cm. The CTC stereo deficiency will be removed by increasing the number of stereo measurements from 24 to 48. In the COT four axial and four stereo super-layers with 12 wires each will provide 96 measurements between 48 and 131 cm, using a total of 30,240 readout channels for the entire detector.

  The complete chamber is roughly 1.3% of a radiation length at normal incidence. The similarity of the device to the CTC is used extensively in our performance studies below, and also has a very practical impact in the economies of construction time, expense, and code development.

- **SVX II+ISL** For Tevatron Run II, we propose a "second-generation" silicon detector which is optimized for the CDF/Tevatron environment. SVX II is composed of three cylindrical barrels with a total length of 96 cm. It covers $\sim 2.5\sigma$ of the luminous region, raising the geometrical acceptance for b-tagging from the present 60% to almost 100%. Each barrel supports five layers of double-sided silicon microstrip detectors between radii of 2.4 and 10.7 cm. One side of all layers is r-ϕ; on the other sides three layers are r-z and two are small angle stereo.

  The Intermediate Silicon Layers (ISL) use similar technology to that of SVX II, from the silicon itself, through the readout electronics. In the central region, a layer of double-sided silicon is placed at a radius of 22 cm. In the region $1.0 \leq |\eta| \leq 2.0$, two layers of double-silicon are placed at radii of 20 cm and 28 cm. All layers make an r-ϕ and a small angle stereo measurement.

This system of COT+SVX II+ISL addresses all of the shortcomings of the Run I configuration mentioned in the previous section:

- The inner detectors, SVX II+ISL, cover the entire luminous region.
- The inner tracker now has stand-alone capability, with 6 layers in the central region, and 7 in the forward region. With at least 6 possible measurements there is very good efficiency for $\geq$ 5, where the signal to noise ratio for stand-alone segments is very good.
- All of the silicon layers have stereo capability.
- The stereo capability of the outer tracker, the COT, is doubled in comparison to the CTC.

With this system, we can envision two primary tracking scenarios:

- COT+ISL+SVX II:
  In this case, we can get a good estimate of the tracking performance based on our current experience. However the SVX II+ISL will form an additional "anchor" for track finding, hence boosting tracking efficiency, as well as track resolution.
- ISL+SVX:
  This is a new feature. It allows tracking at high rapidity, and addresses the fact that many analyses suffer from the fall-off in tracking efficiency at $|\eta| \geq 1$. All of the capability described in Section 3.1 previously possible only in the central region, can now be extended to the plug region.

Comparisons of this system proposed for Run II with the system we actually used for Run I demonstrate that the Run II tracking system, if used with Run I algorithms, will perform at least as well as our Run I system. However, the new system is much more powerful. In Run I, we could find tracks in the COT and extrapolate inwards, but for Run II we will be able to link to *segments* not just individual hits in the SVX II + ISL system. In addition, we can envision finding track segments in the six (or seven) layer SVX II + ISL, and then extrapolating these outward to link with segments found in the COT. In the forward region, where there is no COT, seven silicon points give a good stand-alone momentum measurement. The rapidity coverage of the COT + ISL + SVX II system should almost double compared to that of Run I, with efficient and precise tracking out to $|\eta| \leq 2$.

Instead of a tracking strategy which is critically dependent on the performance of the outer tracker, CDF II will use a truly integrated tracking system, described in the next four chapters.

Chapter 4

Central Outer Tracker (COT)

4.1 Overview

As in Run I, tracking at large radii in the region $|\eta| \leq 1.0$ is done with a large open cell drift chamber. The goal of the Central Outer Tracker (COT) is to reproduce in the high luminosity Run II environment the positive characteristics of the Run I Central Tracking Chamber (CTC), improve upon identified deficiencies in the CTC design, and fit into an integrated tracking plan. In this Chapter, we discuss the detailed design of the COT and some performance expectations based on a straightforward scaling of CTC data.

The simplest strategy for operating a wire chamber in Run II is to ensure that the maximum drift time is less than the 132 nsec bunch spacing. The COT is designed to operate with a maximum drift of 100 nsec (compared with 706 nsec for the CTC) by reducing the maximum drift distance and by using a gas mixture with a faster drift velocity. A gas mixture containing 50:35:15 Ar-Et-CF_4 has drift velocity of ~ 100 μm/ns which implies a maximum drift distance of ~ 1 cm, about 1/4th that of the CTC. The simplest COT geometry would then be reminiscent of the CTC, but with 4 times the number of cells.

The similarity of the COT and CTC geometries implies that the COT and CTC performance should be similar at equal occupancy. Since both chambers integrate just one crossing, equal occupancy occurs for equal luminosity per bunch, and to lowest order the COT is expected to perform as the CTC, but at luminosities higher by the ratio of the number of bunches. An additional factor for increased luminosity reach comes from faster electronics and an advantageous geometry for more uniform charge collection. In Run I, the CTC performed well in 6 bunch operation at luminosities exceeding 2×10^{31} cm^{-1}s^{-1}. In 36 bunch operation, the COT would be expected to have the same performance at luminosities approximately eight times greater. In 108 bunch operation, the COT will expected to provide similar performance at a luminosity of $\sim 4 \times 10^{32}$ cm^{-1}s^{-1} – well above the anticipation for Run II.

We emphasize that this extrapolation from CTC performance does not include the effects of changes and improvements in the COT design. An accurate performance measure requires a detailed simulation, and we present the results of such a study in Chapter 7. However, the simple data driven nature of the scaling argument gives us deep confidence in this design.

One improvement in the COT is to remedy the weak stereo in the CTC. CTC r-z (stereo) reconstruction has four superlayers each having only six stereo wires, and Sec.3.2 discussed its weakness relative to the axial layers. At higher Run II luminosities, the stereo reconstruction in such a design would be further degraded by the presence of overlapping hits from multiple interactions. To improve the robustness of the COT stereo capabilities, the four stereo COT superlayers each consist of 12 sense wires, just like the axial layers. This design commonality also allows all superlayers to use the same electronics, wire guides, etc.

Besides a larger number of cells and additional stereo wires, several other geometric features of the CTC are modified in the COT design. In the CTC, the electrostatics of a cell is shaped by field wires whose potential varies to account for the tapered shape of the cell. In the COT, the field wires are replaced by a cathode "field panel" which is gold on a 0.25 mil thick Mylar sheet. Figure 4.1 illustrates the cell geometry using SL2 as an example. To adjust the electrostatics for the cell taper, the COT adjusts the voltage on the sense and potential wires within the cell. With a solid sheet for the cathode, the drift

field and cathode surface field are the same, which allows for a much higher drift fields than is possible with the CTC. With the smaller drift length it is advantageous to use a smaller tilt. We therefore raise the electric field to $\sim$ 2.5 kV/cm (compared with 1.3 kV/cm in the CTC) for a 35° Lorentz angle (compared with 45° in the CTC).

The ends of each cell are closed, both mechanically and electrostatically, by Mylar strips with field-shaping wires attached. These are referred to as inner (smaller radius) and outer (larger radius) "shaper panels." This is the electrostatic equivalent of the CTC's "shaper wires." The field and shaper panel design has an additional advantage of being able to contain a broken wire within one cell, minimizing the loss. The cell design with field and shaper panels also allows for a smaller gap between superlayers so that eight superlayers each with 12 wires can fit between the radii of 40 and 137 cm.

Between the field panels, sense wires alternate with potential wires in a plane. Wires are held and positioned by epoxying and soldering to a G10 board. We use 1.6 mil gold-plated tungsten wire for both sense and potential wires. Limitations in the range of gains and drift fields imposed by this choice of wires is discussed in the electrostatics section.

Figure 4.2 shows the (East) endplate layout. The longer slots are for field sheets, the shorter ones with a notch are for shaper panels and sense wires.

Table 4.1 summarizes the differences between the CTC and COT. In short, the design of the COT is guided by our experience with the similar CTC. The technology of operating such a wire based tracking chamber in a hadron collider environment is proven. The design differences of the COT allow for overall improvements and include straight-forward modifications of proven principles while allowing for operation in a Run II environment. We now turn to detailed descriptions of the design specifics.

4.2 Mechanical

The mechanical construction of the COT uses a combination of similar techniques used in the CTC construction and improved techniques to achieve better intrinsic precision as well as provide needed support for the COT specific geometry. Aluminum endplates are precision-machined with slots which hold pre-made field panel sheets and sense/potential wire planes.

4.2.1 End Plates

The design of the COT calls for precision-machined endplates as shown in Fig. 4.2. Compared with the CTC beginning at a radius of 27 cm from the beam axis, the COT covers a radial span beginning at 40 cm and ending at 137 cm.

A detailed drawing of sense and field slots is shown in Fig. 4.3. The number of precision edges with tolerance at 1 mil is small – only one surface of the slot edge for both sense and field slots and one edge of the notch on the sense slot. These edges define precision surfaces onto which sense wire planes and field sheets can be positioned. This intrinsic precision aids the track trigger resolution and minimizes the size of offline-determined alignment corrections.

The two endplates will be machined as mirror images. A stereo angle is generated analogous to the CTC: stereo cells will be strung using an offset between slots on opposing endplates. The CTC used a two cell offset and the COT will use an eight cell offset. Since each COT cell is a quarter the size, the COT eight cell offset will provide the same nominal 3° stereo angle as with the CTC. The stereo angle varies slightly with superlayer due to the quantization of cells.

The total force on the end plates from a single cell is given in Tab. 4.3. Each plate is made from 1.625" 6061-T651 aluminum. Finite element analysis (FEA) shows this is sufficient to support the 40 ton load with 300 mil maximum deflection, which is substantially more compared with the CTC's estimated deflection of 55 mil. The endplate deflection has no effect on the axial layers but causes a small change for the stereo layers. The stereo angle for each superlayer will be calculated accounting for the deflection.

The large deflection and use of pre-made parts requires we accurate pre-tensioning of the endplates to have them in their final position before installing wires or sheets. The COT's tungsten wire and Mylar sheets have approximately the same stretch as the CTC wires, so we need comparable precision on the pre-tension. We will use the same technique as the CTC: spring-loaded "piano wire" through each sense wire slot, with tension set by hanging a 15 kg weight on the wire. The procedure is iterative with each iteration obtaining a higher precision on the pre-tension. The first pre-tension with a 1" spring gives at worst 250 mil/1" = 25% precision. The pretension process repeats until an accuracy of 1% (3-4 mil in deflection)

	CTC	COT	
Gas	Ar-Et (50:50)	Ar-Et-CF_4 (50:35:15)	[1]
Max. Drift Distance	3.6 cm	0.88 cm	[2]
Max. Drift Time	706 ns	100 ns	[2,3]
Lorentz Angle	45°	35°	
Drift Field	1.35 kV/cm	2.5 kV/cm	
Radiation Lengths	1.7%	1.6%	
Total layers	84	96	
Layers/SL	12-6-12-6-12-6-12-6-12	12-12-12-12-12-12-12-12	
Stereo angle	±3°	±3°	
Total sense wires	6156	30,240	
Total wires	36,504	63,000	
Endplate Load	25 ton	40 ton	

1. Can also operate with Ar-Et-CF_4 at 2.34 kV/cm or Ar-Et at 1.9 kV/cm
2. Typical at center of superlayer.
3. Assuming Ar-Et-CF_4; 200 ns with Ar-Et.

Table 4.1: Comparison of CTC and COT.

Number of Layers	96
Number of Superlayers	8
Stereo Angle	+3 0 -3 0 +3 0 -3 0°
Cells/Layer	168 192 240 288 336 384 432 480
Sense wires/Cell	12 12 12 12 12 12 12 12
Radius at Center of SL	46 58 70 82 94 106 119 131cm
Sense wire Spacing	0.3″ (7.62 mm) in plane of wires
Wire Diameter	1.6 mil gold plated Tungsten
Wire tension	135 g
Tilt Angle	35°
Length of Active Region	310 cm
Total number of Wires	63000
Endplate Load	∼ 40 metric tons
Drift Field	2.5–3kV/cm (depending on gas)

Table 4.2: COT Mechanical Summary.

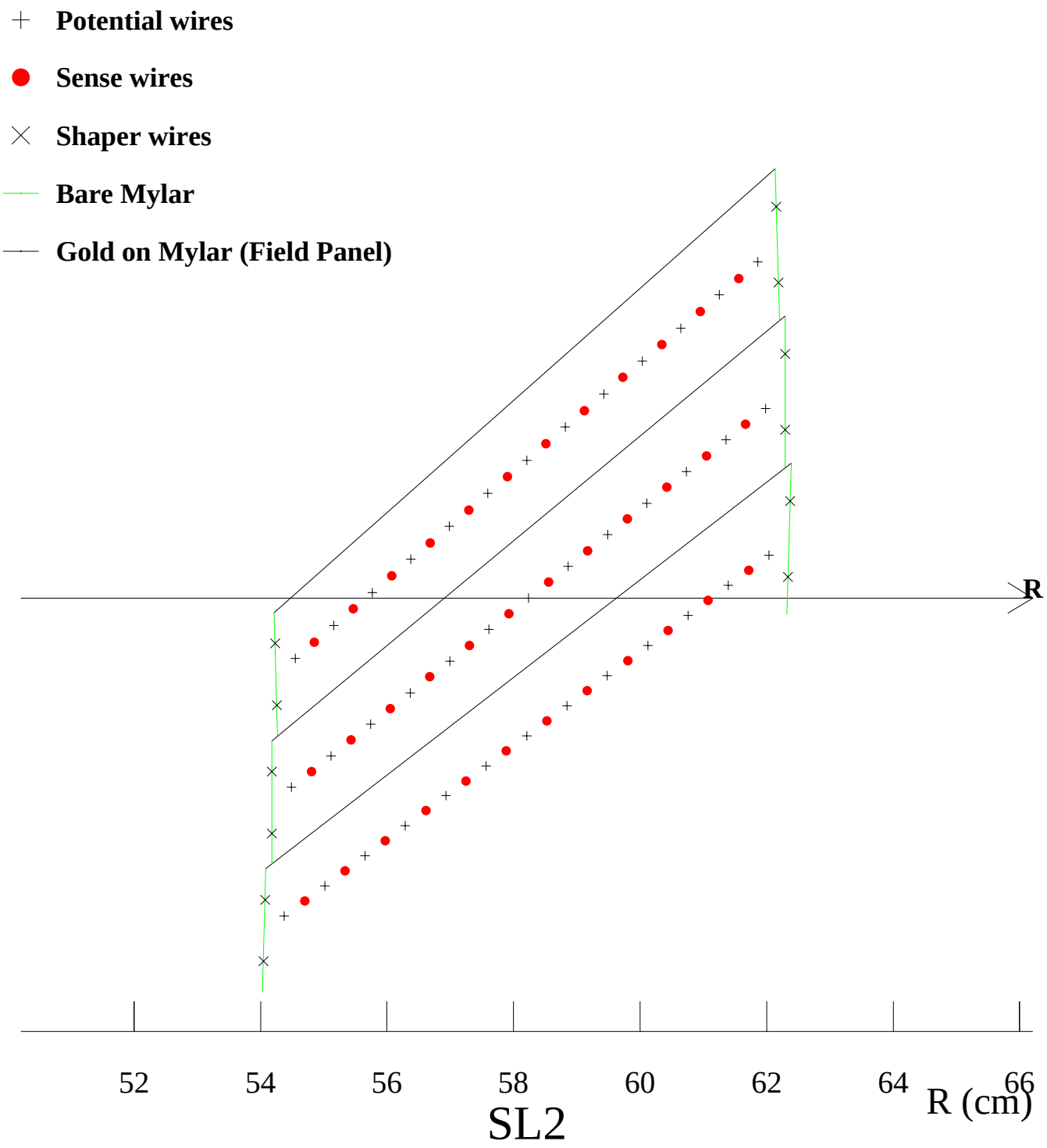

Figure 4.1: Nominal cell layout for SL2. Other superlayers — including stereo — are similar except for the taper.

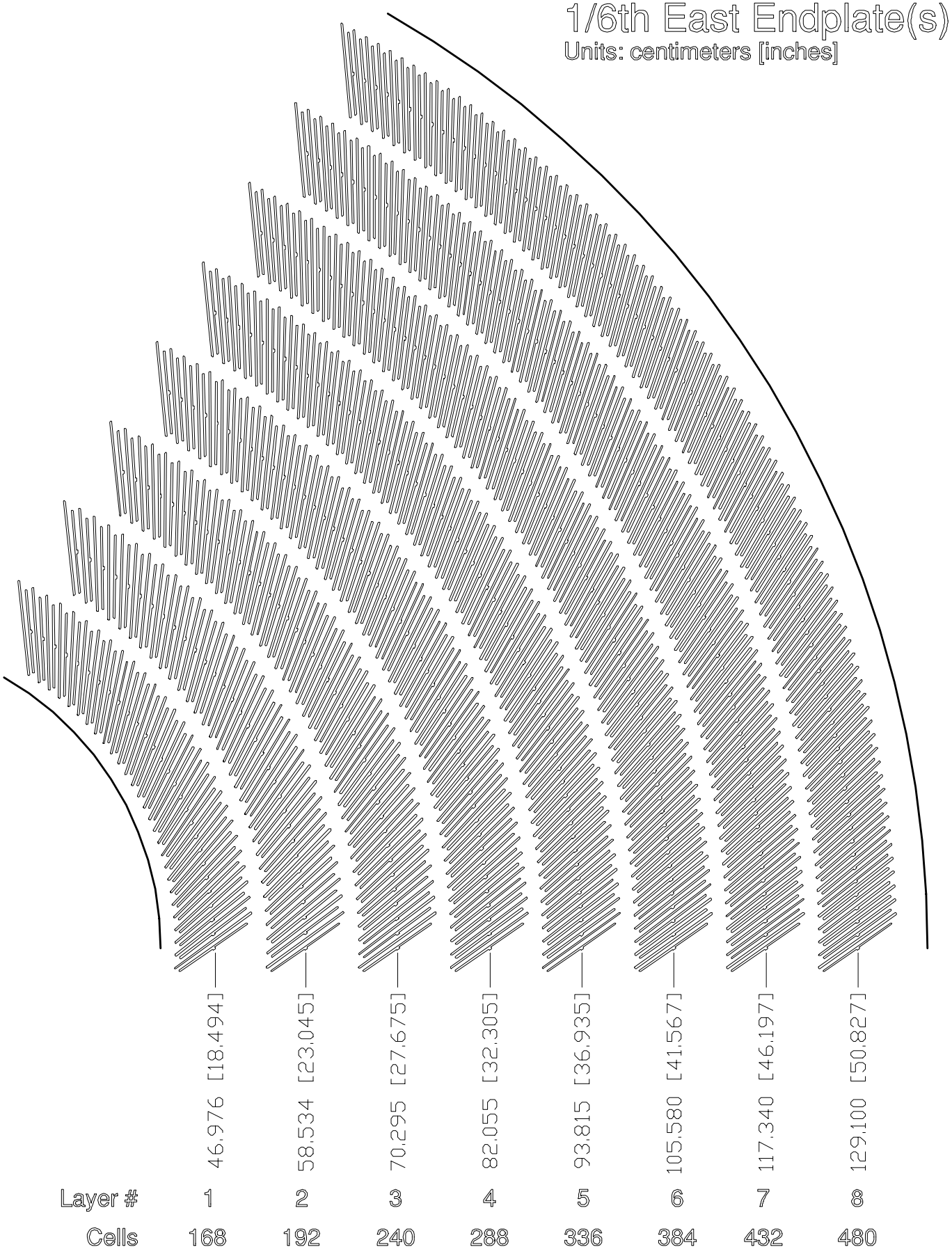

Figure 4.2: East endplate slots Sense and field planes are at the clock-wise edge of each slot.

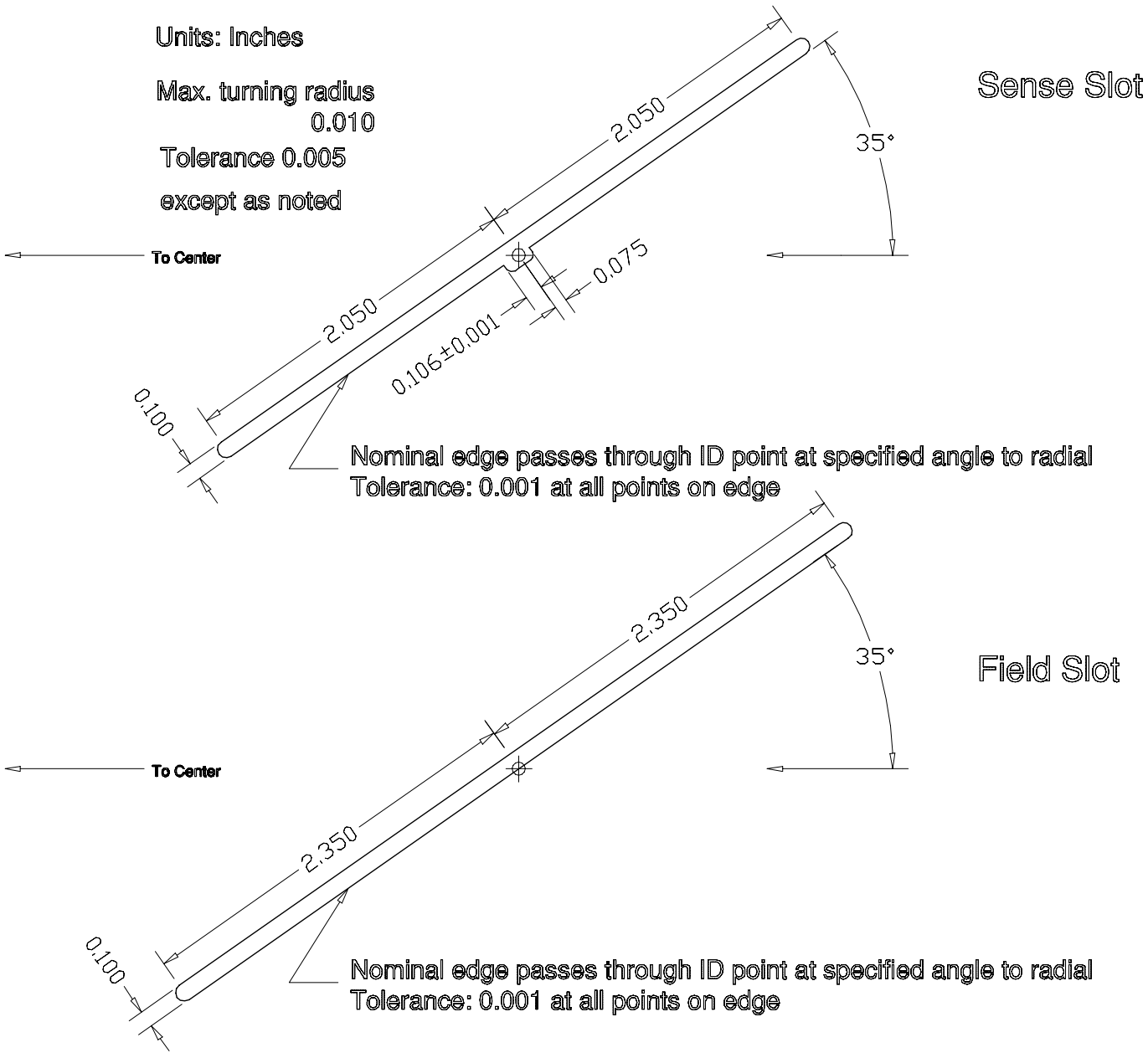

Figure 4.3: Slot details

			Cell Area (cm^2)	Density (g/cm^3)	Cell Density (g/cm)	Sag (cm)	Cell Tension (kg)	Modulus (Mpsi)	Stretch (inch)	Stress (kpsi)	X_0 (g/cm^2)	$<L>/X_0$
Field Sheet					**0.023069**	**0.0278**	**9.98**		**0.40**			**0.61%**
0.25	*mil*	Mylar	0.006452	1.39	0.008968			0.67		2.12	39.95	0.10%
4.50E-06	*cm*	Gold	0.000091	19.32	0.001767						6.44	0.12%
12	*mil*	SS wire	0.001459	7.75	0.011310			28.00		88.65	13.84	0.37%
		Epoxy			0.001025						40.00	0.01%
Wire Plane					**0.006572**	**0.0234**	**3.38**					**0.44%**
1.6	*mil*	Tungsten	0.000324	19.30	0.006259					148.0	6.76	0.42%
5%		Gold			0.000313						6.44	0.02%
Shaper Panel					**0.005224**	**0.0445**	**1.40**		**0.38**			**0.11%**
0.25	*mil*	Mylar	0.002250	1.39	0.003127			0.67		2.03	39.95	0.04%
4.50E-06	*cm*	Gold	0.000016	19.32	0.000308						6.44	0.02%
		Rohacell+Epoxy			0.000375						40.00	0.00%
3	*mil*	SS wire	0.000182	7.75	0.001414			28.00		84.93	13.84	0.05%
Total (2520 cells)							**37,187**					**1.15%**
			Fraction	**Length (cm)**							**X_0 (cm)**	**$<L>/X_0$**
Gas												**0.54%**
		Argon	50%	92.49							10,983	0.42%
		Ethane	35%	92.49							34,035	0.10%
		CF_4	15%	92.49							64,000	0.02%
Total												**1.69%**

Table 4.3: Material in COT active volume

is achieved.

4.2.2 Field Panels

The field panels consist of 0.25 mil Mylar with 450 Å gold completely covering both sides. The edges have 12 mil stainless steel (SS) wires epoxied to the Mylar in a parabola (very small curvature), as shown in Fig. 4.4. The parabolic shape of these edge wires converts wire tension to a uniform lateral tension on the Mylar. Mass, tension, and radiation lengths are given in Tab. 4.3. Note $> 90\%$ of the load is carried by the stainless steel wire.

For prototyping the field panel and its manufacturing process, we have used ~ 500Å aluminum on 0.25 mil Mylar, as well as with gold-on-Mylar sheets. With these prototypes we have investigated a number of areas of potential concern and have found that the gold on Mylar field panel design should work well with the COT.

A mechanical concern associated with the field panels is whether a constructed panel is stable after installation so that a drift cell experiences uniform and understood electrostatic properties. The elongation of the sheet is 0.35 cm, or 0.11%. We have checked published creep properties of Mylar and find the creep of Mylar is small, and most of it occurs within a few days. We have checked the flatness of field panels as a function of time over a period of several weeks and find no measurable variation.

The measured sag in the longitudinal direction is 300 μm with an additional 100 μm sag along the lateral direction, in agreement with the expected properties of the sheet. The lateral variation cannot be matched by the wires, resulting in $\sim 1\%$ variation in drift field. Note this uniform shift does *not* affect wire gain since the sheets on both sides sag the same amount, and the (small) effect on drift parameters can be mapped out.

Ripples of ~ 100 μm amplitude (~ 200 μm peak-to-peak) are also observed on some sheets. We have simulated the effect of such ripples on drift trajectories and wire gain using an electrostatics program which varies the amplitude while keeping the spacing fixed. Based on this, we find up to ~ 300 μm ripples cause $< 10\%$ variation in sense wire gain and no measurable effect on resolution.

The electrostatics program also shows that ~ 100 μm variation in sag (where two sheets adjacent to a wire plane move in opposite directions) gives $\sim 10\%$ variation in gain. This effect, rather than ripples, is expected to dominate potential gain variation. Unfortunately, it is difficult to distinguish sag from ripple in a simple test fixture. Therefore, for mass production, we define a ± 100 μm envelope around the nominal sheet position using a large grid of test

probes, and require all sheets lie within this window.

We have also done qualitative checks for the effect of local damage to the sheet by creating small tears in it. We found no visible impact on the surface quality beyond the tear itself. Visual inspection (using the mirrored surface) allows us to check for ripples at the 20 μm level.

We are also investigating the use of slightly conductive epoxies in order to prevent a possible charge-up problem on the Mylar. Adhesion to the epoxy to the material has been shown to be more than adequate in several tests at full tension.

4.2.3 Shaper Panel

The shaper panel consists of 0.25 mil Mylar coated on one side with 450 Å gold, plus two 3 mil stainless steel wires. The metalized Mylar is kept at ground, while the wires are connected to their nearest potential wires. Electrostatically, this gives adequate closure of the cells' end-effects.

By varying the assumed position in an electrostatics program, we have determined that 1000 μm uncertainty in the position of the side panel has less effect on the drift trajectories and sense wire gain than the 100 μm uncertainty in the field plane.

Because the shaper panel is narrow, and its position is not critical, it is held by simple tension on the Mylar and wires (no curve like that of the field panels). Electrostatic attraction between the wires (at $\sim$ 2 kV) and metalized Mylar (at ground) is counteracted by three evenly spaced Rohacell spacers. The mass of the Mylar-epoxy spacers is a negligible 6 mg per spacer (including epoxy).

4.2.4 Wires

The sense and potential wire planes are designed for precision placement and for having uniform electrostatic properties over the length of the chamber. Sense and potential wires are gold-plated tungsten (450 Å gold on 1.6 mil diameter tungsten) strung at 135 g tension.

The smaller drift length in the COT requires a correspondingly smaller "differential sag" than allowed in the CTC (600 μm sag on field wires, 230 μm on sense wires, 370 μm differential sag). We design for 300 μm nominal sag on sense wires and field wires which is equal to the sag expected for the field panels, i.e. zero differential sag. We allow no more than 100 μm variation in distance between the wires and the field panel.

To improve electrostatic stability at drift fields up to 2.5 kV/cm, the wire plane includes a wire support at the center. The wire support mechanically ties the wires to each other, removing "stepping" arising from wire-to-wire repulsion.

The 135 g tension per wire is required to assure stability against the coherent motion (i.e., all wires together) of the wire plane toward the field sheets. The wire sag at this tension is slightly less than the field sheets (Tab. 4.3); we deliberately increase the mass of the wire support until the wire sag matches the field sheet sag.

Wire planes are manufactured by winding $\sim$ 40 cells worth at one time on a large winding machine, analogous to the procedure used for MWPC construction. The winding machine has attached precision fixtures to define the location of the wires relative to a reference pin (for position along the wire plane) and a support rib (for position perpendicular to the plane) on the wire plane end-boards. These precision fixtures duplicate the geometry of the endplate and will allow wire planes to be inserted into the precision machined endplate with $\sim$1 mil accuracy. There will be some adjustment on the wire plane winding fixtures to allow for slightly different lengths due to the 300 mil expected endplate deflection.

Two additional advantages of the wire plane manufacturing procedure are that the wire planes can be built in advance of the chamber and that the completed wire planes can be tested prior to installation. We plan to expose each wire plane to a β-source to emulate high-rate operation. We expect this will substantially reduce the burn-in time and failures during data taking.

4.3 Material Count and Radiation Lengths

The contribution of each material is given in Tab. 4.3. We use:

$$L/X_0 = \underbrace{\frac{L}{A}}_{1/\text{width}} \times \frac{\varrho}{X_{0,\text{g/cm}^2}}$$

where ϱ is the linear density in g/cm. The "width" of a cell is simply the circumference of the superlayer divided by the number of cells; this is $\sim$ 1.76 cm

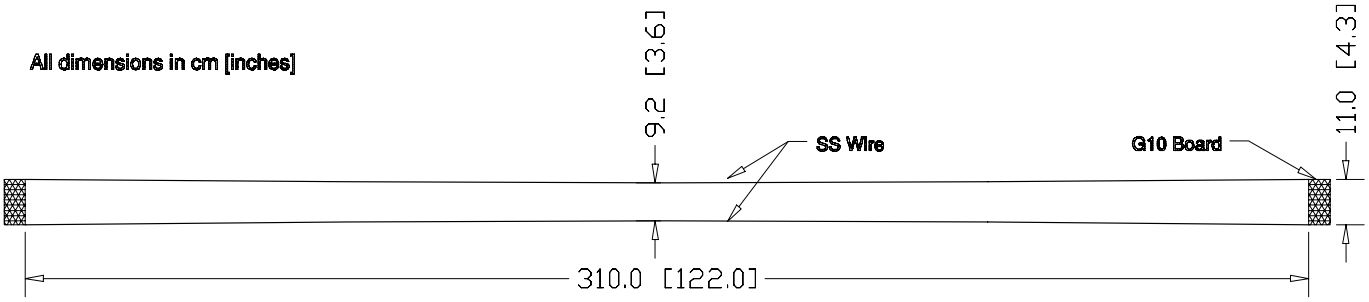

Figure 4.4: Field panel construction Curved string introduces a lateral force.

(twice the drift distance).

The various materials are combined by summing L/X_0 contributions and we find a total L/X_0 of 1.69%.

4.4 Electrostatics and High Voltage

In setting actual voltages, a full electrostatics calculation and fitting program is used. However, the following simple relations are useful in designing the HV system.

Treating the wires as lines of charge and ignoring edge effects, the drift field (E far from the line charges) is related to the wire surface field by

$$E_d = \frac{\pi}{s}(E_s r_s + E_p r_p)$$

where: s is the spacing between sense wires; E_s (E_p) are the surface fields of the sense (potential) wires; and r_s (r_p) are the radii of the sense (potential) wires. For uniform gain, E_s must be the same for all wires. The above relation assumes E_p are also the same, but by treating this as operative over a subset of the wires, we see that uniform E_p (given uniform E_s) is a requirement for a uniform E_d.

For uniform E_s (E_p), the field in the vicinity of each sense (potential) wire is the same; by design, far from the wires, $\vec{E}_d$ is also everywhere the same. Then the voltage of a wire is

$$V = V_0 + dE_d$$

where: d is the distance along $\vec{E}_d$, i.e. perpendicular to the field panels; and V_0 is a constant for all sense or potential wires.

We can immediately get the variation of voltage across the sense or potential wires as being

$$\Delta V = \frac{\Delta R}{R} E_d d_0$$

where: R is the radius at the center of the superlayer (varies); $\Delta R \sim 4.3$ cm is the radial extent of the superlayer; and $d_0 \sim 0.75$ cm is the distance between the wires and the field panel at the center of the superlayer. SL1 (smallest R) and $E_d = 3$ kV/cm (a reasonable safety margin over the anticipated operating point of 2.5 kV/cm) has a ΔV of 210 V.

4.4.1 Currents (Voltage sags and space charge distortions)

The field panel design has been examined for potential electrostatic problems. We consider the expected current on the field panels. The resistance of 450 Å gold is $\sim 0.36\ \Omega$/cm for our $\sim$10cm wide sheet. We can estimate the expected current on the field panels by extrapolating from the sense wire current observed with the CTC. The sense wire current in SL1 of the CTC at $\mathcal{L} \sim 10^{31}\mathrm{cm}^{-2}\mathrm{s}^{-1}$ is $\sim 0.5\mu$A/wire. Extrapolating to $\mathcal{L} = 10^{33}\mathrm{cm}^{-2}\mathrm{s}^{-1}$ to be conservative, with one quarter the drift length, the maximum expected current per sense wire is 12.5μA. Most of the ions end up at the field panel for a total current of 75μA at each surface. Based on the VTX experience, we expect this current is spread uniformly in z along each wire. Then the voltage drop from the end plates to $z = 0$ is

$$\Delta V = \tfrac{1}{4} \times 75\ \mu\mathrm{A} \times 0.36\ \Omega/\mathrm{cm} \times 160\ \mathrm{cm} = 1.1\ \mathrm{mV}$$

which is certainly not a problem.

At most, half the ions from the inner and outer most sense wires will go to the wires on the shaper panels. Therefore the voltage sag here will be at most half that along the sense wire.

Due to the higher drift field (about 2.5 kV/cm versus 1.3 kV/cm) and much shorter maximum drift length (0.88 cm versus 3.5 cm) of the COT compared with the CTC, space charge distortions in the COT should be less than a few percent of those in the CTC

for the same sense wire current. Since the COT sense wire current is a factor of four less than the CTC's at the same luminosity, space charge distortions will be very small in the COT during Run II.

4.4.2 High Voltage System

The high voltage system is similar to the system used for the CTC. Supplies and crowbars are located in the first floor counting room; filtering and fanout is done in the collision hall off of the chamber face and voltage is delivered to the chamber by superlayer and by quadrant. The precision required and high current draw (12.5 μA maximum) for the sense wires rules out a resistor divider chain. Current draw on the potential wires is low, but for simplicity and flexibility we will distribute these voltages in the same way as sense wires.

4.4.2.1 First Floor

High voltage will be supplied by VME-based pods. 200 HV channels are required, 25 per superlayer (12 sense wires and 13 potential wires). Each pod delivers up to 3 mA at 3.5 kV. The system is controlled by a PC.

Short RG-58 cables bring the voltage from the power supplies to the crowbar system. The crowbar system discharges the cables in the event of a trip in order to minimize the amount of energy dumped into the chamber. The crowbar relays are in-hand from the existing system, but a new crowbar driver board will need to be built.

After the crowbar system, the 200 channels fanout 1-to-4 for distribution by quadrant. 800 RG-58 cables carry the HV from the fanout to the collision hall.

4.4.2.2 Collision Hall

The 800 RG-58 cables connect to eight different filter boxes within the collision hall, one filter box per quadrant. The filter boxes electrically isolate the chamber ground from the first floor, as well as perform the transition from RG-58 to ribbon cable.

Although the sense wires are run at $\sim$ 3 kV, and potential wires are run at $\sim$ 2 kV, the voltage difference from wire-to-wire for all sense, or all potential, is $<$ 300 V; difference between neighboring wires is $<$ 25 V. Therefore, a 300 V rated ribbon cable is used for all sense wires, a second ribbon cable for all potential wires. The cables are isolated from ground by kapton wrap and plug in to mass-terminated connectors on both ends. The cables are also covered by copper cloth to eliminate shock hazard. There is one sense wire ribbon cable and one potential wire ribbon cable per superlayer per quadrant. The voltage for the wires on each the shaper panel is the same as for its neighboring potential wire; they will be tied to the corresponding potential wires.

An interlock ensures that the ΔV across any cable does not exceed the cable rating. This is done by putting a 1.5 kW, 200 V "transient suppression" diode per line, which absorbs a large energy dump in a short time period and causes a high voltage supply trip.

4.4.2.3 Chamber End Plate

High voltage is distributed to the chamber on the end opposite the readout. The ribbon cables plug into a $4'' \times 2''$ two-layer printed circuit board. This board brings the HV into the chamber and has 25 capacitors, 25 HV feed resistors, 12 termination resistors (sense wires only), two headers for the ribbon cables, and pin receptacles to mate to the gas seal board.

4.4.2.4 Failure Modes

In the case of a "bad" (*e.g.* glowing) wire, without access to the chamber face, it is possible to drop the gain of one layer of the quadrant by a factor of 2–4 by reducing the sense wire voltage by 100–200 V. Also, it is possible to drop the gain of any two layers of the quadrant by a factor of ~ 8 by raising the voltage of the intermediate potential wire. For a broken wire without access to the chamber face, the entire quadrant must be turned off.

With access to the chamber face, any one wire can be disconnected by clipping the HV feed resistor. It is also possible to disconnect an entire cell by pulling the connector from the termination board. This kills one cell and degrades the two neighboring cells because of the electrostatic pull on the field sheets.

4.4.3 Electrostatics

Figure 4.5 shows equi-potential and equi-$|E|$-field surfaces for the preferred drift field (2.5 kV/cm), wire size (1.6 mil) and gain setting (180 kV/cm surface field). The field along the drift trajectories is found to be very uniform. In this case, the electrostatics program used only 4 free parameters: the voltages at

SL	1	2	3	4	5	6	7	8
%/fb^{-1}	64	54	36	28	23	18	15	12

Table 4.4: Ageing rate vs SL. Assumes same gain loss per unit charge at sense wire as CTC toward end of Run-1B and chamber gain equal to CTC outer layer. We consider this an overly conservative projection, as explained in the text.

the inner and outer most sense and potential wires. Shaper panel voltages were set the same as the neighboring potential wire, and intervening wires were set by uniform steps. More uniform gain is possible by fine-tuning the individual wires.

The 2.5 kV/cm drift, 180 kV/cm surface field solution gives a potential wire surface field of 118 kV/cm (positive charge). So, it will have negligible gain. The sense wire gain changes a factor of two for every 6 kV/cm change in surface field, and the simple model given earlier tells us the potential wire charge has to change an equal amount in the opposite direction to keep the drift field fixed. Since the gain on the potential wires does not change by much, a wide range of drift fields and sense wire gains are accessible.

4.5 Gas System and Wire Ageing

4.5.1 CTC Wire ageing CTC in Ar-Et

The CTC drift gas was Argon/Ethane (50/50) bubbled through ethanol during the entire operation. We have made measurements of ageing effects in the CTC and in "Magic Chambers," drift tubes located at the gas input and output. We consider measurements beginning in March 1995 (after the gas system was cleaned). Table 4.4 scales the ageing effects to COT operation using charge collection rates of the CTC superlayers, scaled down a factor of four for the reduced drift length. We further scale the rate of the SL1 and SL2 by a factor of two (the chamber gain of the CTC is a factor of two lower in these layers). The effect of ageing is to reduce the sense wire gain.

The estimates shown in Tab. 4.4 are pessimistic for several reasons. First, they assume that the chamber gain is kept at the value used in the CTC outer layers, whereas the inner CTC layers were at approximately half that gain. Second, there is reason to believe the ageing in standard Ar-Et alcohol mixtures can be substantially improved by further cleaning of the CDF gas system and more effort to reduce alcohol mist entering the CTC. For example, the ageing of SL3 was twice as high before the gas system cleanup began. Also, a Magic Chamber at the CTC gas input showed a factor of two reduction in ageing in the last few weeks of Run IB, after the cleanup was complete.

Further improvements were observed in the input Magic Chamber (another two orders of magnitude) after the system was modified so that only a small fraction of the gas was run through the alcohol bubbler and heated copper filters were added. Both changes were intended to reduce alcohol mist arriving at the Magic Chambers and CTC. Unfortunately, there is insufficient integrated luminosity to get a direct measurement of the effect on the CTC. However, chemical analysis of CTC and Magic Chamber sense wires show they have similar contaminants after ageing so that we hope that the CTC ageing rate was also significantly reduced by the changes to the alcohol delivery system.

Additional cleaning of the CDF gas system will be done. However, since there is not a conclusive demonstration of a substantially lower ageing rate in the CTC with Ar-Et alone, the ageing rates for the COT would be worrisome in Run II if Ar-Et alone were to be used (without CF_4).

4.5.2 COT Wire Ageing in Ar-Et-CF_4.

Adding as little as 5% CF_4 has been found to reduce or eliminate wire ageing in Ar-Et [2]. Therefore, for operation with 396 ns bunch spacing, we have measured the drift velocity and Lorentz angle at 14.1 kG for the gas mixture of Ar-Et-CF_4 (50:45:5) bubbled through isopropyl alcohol. The expected COT operating point in this mixture is 2.3 kV/cm drift field and 64 μm/ns drift velocity.

For 132 ns bunch spacing, we require a much faster drift velocity in order to resolve crossings and minimize the occupancy. The gas mixture Ar-Et-CF_4 (50:35:15) bubbled through isopropyl alcohol was also measured at 14.1 kG. It has an operating point of 88 μm/ns at 2.5 kV/cm, giving a 100 ns maximum drift time in the COT. We have measured the ageing properties of this gas mixture using a realistic prototype COT cell, including field panels constructed from vapor deposited gold on 0.25 mil Mylar. Sense wires in the chamber were irradiated using a range of beta source intensities corresponding to instan-

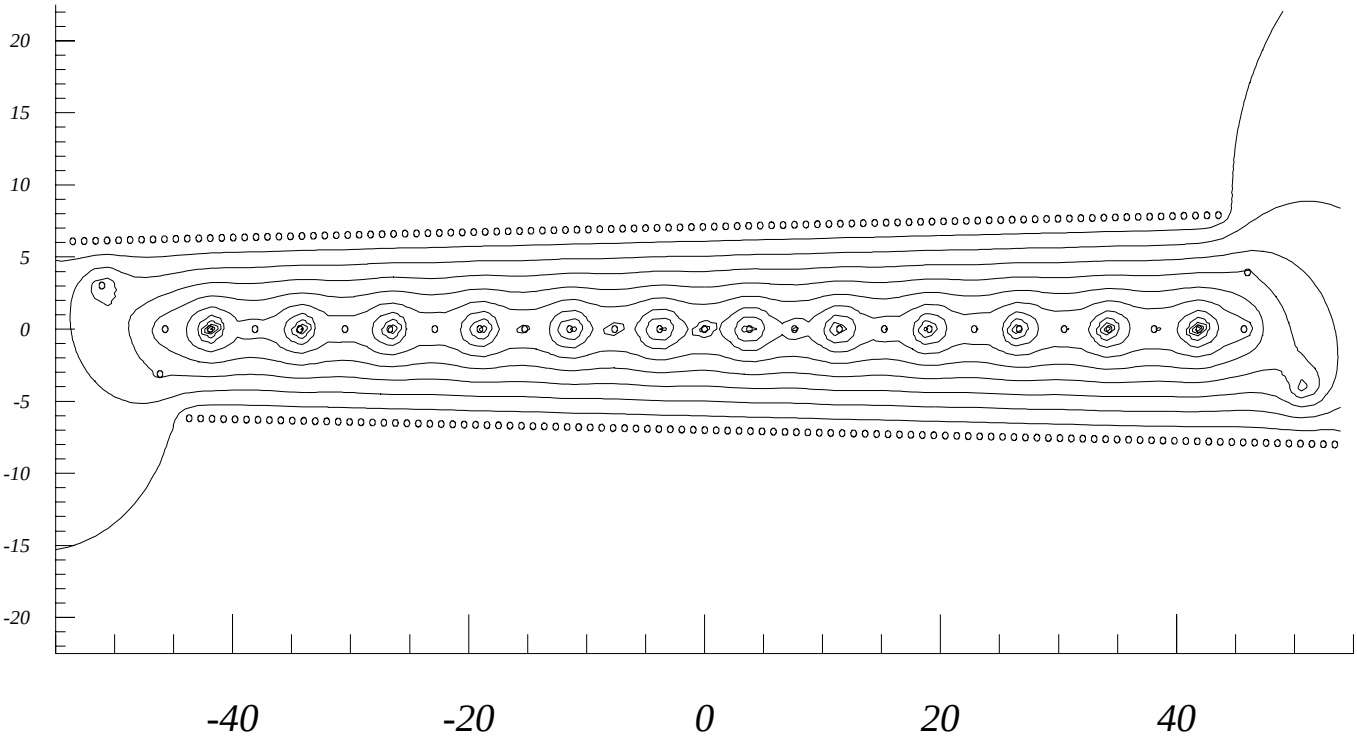

Figure 4.5: Equi-potential lines in SL1 (the superlayer with the largest taper).

taneous luminosities of approximately 10^{32} $cm^{-2}s^{-1}$ to 10^{33} $cm^{-2}s^{-1}$ resulting in charge accumulations of 0.05 Coul/(cm of sense wire) to 0.5 Coul/(cm of sense wire), respectively. Note that the COT inner layers will accumulate roughly 0.1 Coul/(cm of sense wire) at an integrated luminosity of 2 fb^{-1}. No where in the chamber did we observe Malter-effect currents, visible cathode etching, visible cathode or anode growths, or significant gain loss. In particular, the resistance of the cathode changed by less than 10% (the uniformity of the unirradiated material), the gain loss averaged over all sense wires was (0.7 +/- 0.8)%/Coul/(cm of sense wire), and the measured rate of gain loss for wires irradiated at Run II intensities implies a gain loss of less than 10% for the COT inner layers at 2 fb^{-1}. The ageing tests will continue with this gas mixture, the mixture with 5% CF_4, and other candidates.

The major drawback to CF_4 is cost. To keep this at a tolerable level, it may be necessary to re-cycle the gas. Of course, besides the impact on the chamber design, re-cycling requires a pumping and cleaning system. The Fermilab Physics Department will assist CDF in the design of the re-cycling system.

4.6 Readout Electronics and Trigger

The COT has 30,240 channels: 16,128 axial and 14,112 stereo. The breakdown by superlayer is shown in Table 4.5. The electronics and trigger systems of the COT are largely based upon the designs utilized for the CTC. Data acquisition is based upon standardized modules used elsewhere in the Run II CDF design.

The overall layout of the COT readout electronics chain is shown in Figure 4.6. Pulse amplification, shaping and discrimination is carried out on the chamber face using an Amplifier/Shaper/Discriminator (ASD) chip developed at the University of Pennsylvania. The differential discriminated signal is carried off the chamber face to TDC boards mounted in VME crates on the endwalls by a two-piece cable consisting of 4 meters of 0.023″ coaxial cable followed by 6 meters of a standard 50 mil spacing ribbon cable. Time-to-digital conversion is performed with TDCs designed at the University of Michigan for the Run II upgraded muon system. The TDC boards contain Level 1 and Level 2 trigger event buffering. TDC auxiliary cards latch hits for the eXtremely Fast Tracker (XFT) track trig-

Layer	Number of Cells	Sense Wires	ASD Boards
1	168	2016	84
2	192	2304	96
3	240	2880	120
4	288	3456	144
5	336	4032	168
6	384	4608	192
7	432	5184	216
8	480	5760	240
axial total (2,4,6,8)		16,128	672
stereo total (1,3,5,7)		14,112	588
total		30,240	1260

Table 4.5: Numbers of cells and sense wires per superlayer. Twelve sense wires per cell.

ger processor. (See Section 12.3 for details of the XFT.) Latched hit data are multiplexed and sent up to the first floor counting room via Ansley cables (we plan to reuse existing Ansley cables). Trigger segment finding and linking is done in 6 VME crates in the first floor counting room. Digitized timing information for the COT is readout via serial link to first floor VME readout buffers (VRBs) in a fashion similar to the readout of the SVX II.

This design offers the advantage of having all of the electronics except the ASDs off the face of the chamber and therefore accessible. The elements on the chamber face operate continually: no timing signals need to be sent to the chamber.

The following sections will describe the major elements of the COT electronics: front end, ASD, TDC, DAQ, and chamber cooling.

4.6.1 Front End

This section describes the front end board, the ASD chip, signal cables and low voltage power distribution.

4.6.1.1 Boards and connections

A two-layer printed circuit board holds pin receptacles which attach to the pins on the wire board. This motherboard plugs into two cells, holds high voltage decoupling capacitors (1 nF,3 kV for potential wires and 470 pF, 4 kV for sense wires) and provides a portion of the gas seal. Signals are brought out on a single-inline, 36-pin, 0.1″ spacing connector.

A second multi-layer PC board plugs into the motherboard and houses three Penn ASD chips (see Section 4.6.2). The ASD board also holds a calibration receiver, HV protection, crosstalk cancellation resistors, and low voltage bypass capacitors. The board receives ±3VDC for the ASD power.

4.6.1.2 Signal Cables

The ASD provides a programmable differential current output, typically 2 mA into a characteristic cable impedance of 40 Ω to ground. The differential signals are carried off of the chamber face through the gap between the endplug and endwall calorimeters by 0.023″ coaxial cable. Limited cable space through this gap is the motivation for the thin coaxial cable. Outside the endplug-endwall gap, a transition is made to standard 50 mil spacing ribbon cable which carry the signals the remaining $\sim$ 6 meters to the TDC. The larger cable is less expensive and has better transmission properties. The total cable run is approximately 10 meters from the chamber face to the TDC cards on the endwall.

For each ASD board, there is one 50 conductor cable which carries differential signals from 24 channels ($\times$2 per channel for differential output) plus two calibration lines.

The signal cables are terminated by hand into printed circuit boards which plug into the ASD boards and the mass-terminated ribbon cable. Measurements with sample cables indicate that

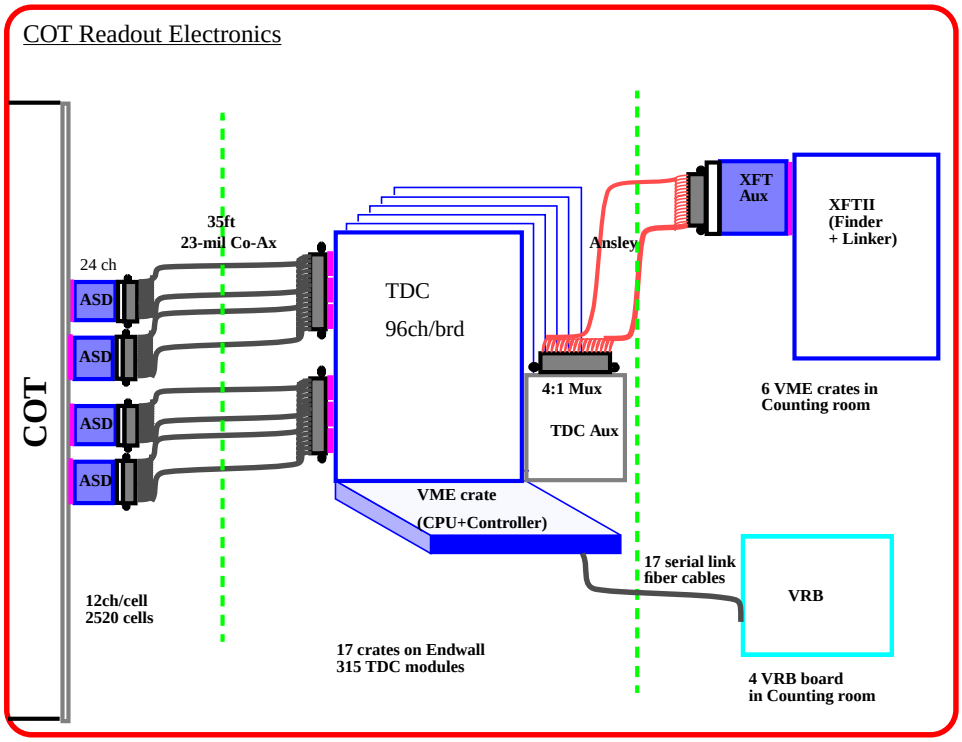

Figure 4.6: An overview of COT readout electronics.

impedance matching between the two cable types, as well as cable compensation, can be done in a straightforward manner. We are in the process of defining the optimal cable compensation circuit.

4.6.1.3 Low Voltage distribution

Two supplies per side per quadrant provide low voltage power (± 3 VDC) to the ASD cards mounted on the chamber end plate. Six cables distribute the voltage from each supply to the chamber. The number of cables is determined by current-per-cable safety requirements.

4.6.2 ASD

An Amplifier/Shaper/Discriminator (ASD) chip was developed for the SDC detector by the University of Pennsylvania group. The Penn ASD chip was optimized for straw systems in the SDC and ATLAS detectors [4]. Given that the charge collection and signal profile for hits in the COT will not be markedly different than for straws, the basic ASD design is applicable to both systems. The ASD provides all of the analog signal processing between the chamber and the TDC. The chip is fabricated by the inherently radiation hard bipolar process. Each channel of the eight-channel chip has a fast, low noise preamplifier, ion tail cancellation stage and discriminator. The shaping and discriminator stages are fully differential, the preamplifier is pseudo-differential.

In the proposed version of the ASD, a baseline restorer stage will be included before the discriminator to prevent changes in the effective threshold at high hit rates. A measurement of the charge will be encoded into the width of the discriminator output pulse in a manner similar to that employed by the CTC outer superlayers. This dE/dx measurement will cover about 16 bins of 1 ns resolution. The 24-channel ASD board, located on the chamber end plate, handles two 12-wire drift cells with three 8-channel ASDs per board.

4.6.2.1 Baseline Restoration

The multihit nature of the COT requires that the ASD not only shape the signal for optimal two-track resolution but also that high rates and/or large hits do not cause large baseline variations. Changes in baseline can distort the pulse shape and degrade the time resolution performance of a second hit. A version of the ASD with baseline restoration has been developed for the ATLAS Transition Radiation Tracker [5]. Optimization of the shaping and base-

line restoration for the COT will be done using data from the CTC and COT prototype chamber, as well as from SPICE model simulations of chamber and circuit performance.

4.6.2.2 dE/dx

The ASD will also be designed to encode the magnitude of the charge deposited in the chamber cell in the trailing edge of the discriminator output pulse. In this scheme, the leading edge of the discriminator output indicates the time of arrival of the primary ionization and the trailing edge (*e.g.* the pulse width) is logarithmically related to the total charge deposited on the sense wire.

For the CTC, superlayers 3–8 (54 layers) are instrumented with dE/dx circuitry. The resolution for the CTC is dominated by the sampling statistics and is measured to be approximately 10%. The dE/dx resolution and hence, particle identification capability of the COT will be better because all 96 layers will be instrumented with charge measurement capabilities. Also, due to the more uniform drift field of the COT near the cathode planes, a larger fraction of hits will be used to determine the dE/dx for each track.

In a fashion similar to the CTC, a tradeoff between two-hit resolution and dE/dx resolution is achieved by implementing a logarithmic relationship between the measured charge and the time over threshold ($\Delta t \sim \log(Q)$). This keeps the time for the trailing edge encoding short (approximately 10–15 ns beyond the width of the shaped pulse) while maintaining good resolution at the lower end of the dE/dx spectrum.

4.6.3 TDC

The signals from the ASD boards are sent differentially to TDC modules via a combination of coaxial cables (two per channel) and ribbon cable (section 4.6.1. A total of 315 TDC modules are located in the 17 VME crates on the endwall of the detector.

The DT96TDC[6] is a 96-channel VME module, being designed for the Run II CDF muon system by University of Michigan group. The TDC is designed to replace the existing Fastbus LeCroy 1879's and includes the necessary event buffering capability, sufficient pipeline length, and the necessary timing resolution[7].

The DT96TDC uses a custom chip, JMC96[8], which has been specifically developed for this TDC module. The JMC96 chip has 1 ns timing, multihit capabilities, and L1/L2 storage buffers. The TDC module contains a standard VME interface, receivers for 96 signals, a Xilinx based register file and a digital signal processor to perform the zero suppression of empty channels. The design of the module is flexible to allow for different readout options using a 32 bit word to encode board/channel ID, the time of the leading edge and the width. The output of the zero suppression is loaded into an on-board FIFO for the transmission via the VME Readout Controller to the 1st floor memories, the VME Readout Buffer modules.

Each TDC crate contains 18 or 19 TDC modules, a CPU crate controller and a TRACER[9]. The Motorola MVME162 is currently being considered for the CPU crate controller to download programs, diagnostics and global control from the DAQ network. The TRACER is a system interface module to provide an interface to the Trigger System Interface and the Master Clock. It also provides a path for sending the event data to the VME Readout Buffer.

4.6.4 DAQ

Data from the TDCs are read by a local processor in the crate and sent to the VME Readout Buffer (VRB)[10] through a TRACER type module. The VRB is a VME based slave module designed to be used in the calorimetry and SVX DAQ system. The VRB receives data via transition module data links, which are typically serial optical connections. The VRB can accept input data at a combined rate of up to 600 MBytes/sec on multiple channels.

The VRB crate is located in the counting room and is controlled by SRCs[11] to the trigger system. Each VRB has 10 channels input up to 50 Mbytes/sec. The output is driven at >40 Mbytes/sec using VME64 protocol.On board SARAM buffers (30 kB/channel) are programmable in terms of number of buffers and sizes. The J3 backplane is used for commands and status.

4.6.5 Trigger

The TDC signals for the axial superlayers are also tapped off of the modules and sent to the track processor (XFT) located in the 1st floor counting room.

The TDC Auxiliary card will take the 96 TDC signals, latch TDC hits in time bins, and send 3-to-1 multiplexed signals to the XFT Auxiliary card via 336 Ansley cables, two cables per TDC Auxiliary card.

The XFT Auxiliary cards reside in the first floor counting room. They demultiplex the latched TDC hits and pass them along to the XFT cards, which house segment finder and linker chips. See Section 12.3 for details of the XFT.

4.6.6 Calibration

Circuit operation can be verified and the system time and charge behavior can be calibrated by injecting charge into the front end of the ASD chip. The current design of the TRACER module will be slightly modified to include calibration capability. In calibration mode, the modified TRACER sends pulses along the VME backplane to each TDC board in the VME crate. The TDC in turn transmits the pulse down to the ASD cards through a single channel which is a part of the 50-conductor signal cable. The signal is received on the ASD board and injected into the chips via a pulse forming network.

4.6.7 Cooling

In the Run I tracking system, the total heat dissipated from the VTX is 150 W and from the CTC is 310 W, for a total of 460 W. The maximum heat load is on the axial side with 75 W (VTX) + 225 W (CTC) = 300 W. The CTC and VTX are cooled by the solenoid cryostat and chilled water lines connected to the CTC endplate at the inner diameter and outer diameter. Under the present cooling conditions, temperature probes near the CTC preamps read 2–7°C below ambient ("ambient" being the temperature when both power and cooling are turned off).

Assuming that the COT ASD dissipates 30 mW/channel, the total heat load due to the preamps is 907 W. At $4 \times 10^{32}\mathrm{cm}^{-2}\mathrm{s}^{-1}$ we expect a positive ion current in the drift gas of approximately 0.011 Amps per superlayer for a total of 0.089 Amps. For a voltage drop of 3 kV, the heat dissipated in the chamber gas is 266 W. The total heat load becomes 1.2 kW.

To handle this heat load, cooling lines are placed on both ends of the COT at the inner and outer diameters, as well as between each superlayer. Better estimates of cooling requirements will be done in the near future, but we do not anticipate a significant engineering effort.

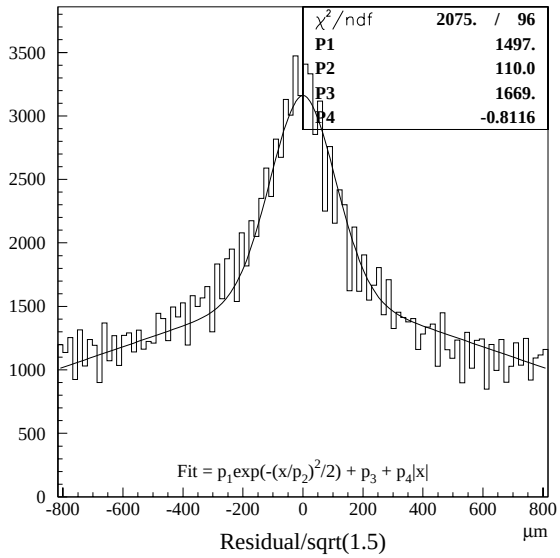

Figure 4.7: COT un-biased resolution using no pattern recognition. Scale factor on x axis corrects for combined error of three points, see text. Fit is Gaussian plus line.

4.7 Chamber Performance

The expected performance of the COT can be derived from measured performance of the CTC accounting for the COT-specific geometry and Run II operating conditions. We leave a detailed discussion of expected track reconstruction performance until Chap.7. In this section, we describe the detector-level performance issues in terms of the intrinsic position resolution and the resolution for separating two tracks. We measure the first quantity from an actual COT prototype cell and extract the second quantity from arguments based on the COT geometry and expected electronics performance. From these discussions, we can describe the expected COT performance in Run II conditions at a given luminosity based upon our measured CTC performance in Run I conditions.

4.7.1 Position Resolution

The single hit position resolution has been measured in a full-length COT prototype cell by fitting the

width of the residual distribution for hits on a track. To avoid biases due to the specifics in the pattern recognition algorithm, we use the following procedure. For each set of hits on three consecutive wires, we use the inner and outer hits to predict the location of the middle hit. We take the difference between the measured and predicted hit location. For three consecutive wires hit, there are eight combinations of possible hits since each wire in the prototype has two possible drift signs. The result is shown in Figure 4.7. All drift signs are considered: each "triplet" makes $2^3 = 8$ entries, only one of which is correct. So the size and shape of the entries contributing under the peak is as expected.

We find a hit resolution of the prototype cell of 110 μm. CTC prototypes without a magnetic field gave a resolution of ~ 120 μm, while the the CTC for $p\overline{p}$ data at 14 kG gives 180 μm. Based on this, we expect the resolution of the full COT chamber (including calibration uncertainties, wire position errors, etc.) to be 180 μm, the same as that measured by actual data in the CTC.

4.7.2 Two-track Resolution

The ability of the CTC and COT to distinguish between two closely overlapping hits is determined by the pulse shape at the discriminator input. The width of the pulse multiplied by the drift velocity gives the spatial extent of a single hit. For the purposes of this discussion (since prototype front-end electronics is currently under development), we assume that the electronic pulse shaping for the COT has a performance equal to that achieved in SL0-SL2 in the CTC (the outer CTC layers used slower electronics).

The pulse shape can be treated as the convolution of two terms.

- The response to a δ-function of charge arriving at the sense wire. The finite width comes from the avalanche response and electronic shaping.

  The contribution to the pulse width is the same for the CTC and COT ignoring improvements of the COT electronics. In terms of distance, the spatial resolution for two hits to be separated scales with drift velocity, *i.e.* the higher drift velocity of the COT would give an expected worse 2-track resolution.

- Variation in charge collection time. This is a function of track angle and electrostatics of the chamber.

  The COT is intended to operate above the v vs. E saturation point. The CTC operated just below this point which caused an additional spread in the pulse shape especially in the weak field regions between sense and potential wires. For a worst case estimate, we ignore the expected improvement in the COT, then the relative variation of the charge collection time depends on the track angle and path through a cell. In terms of 2-track spatial resolution, we find that this is better for the COT due to shorter drift length and a narrower charge collection region.

The discriminated pulse width has been measured for the CTC and can be characterized by the time over threshold. We use the pulse width for high-p_t tracks (muons in $W \rightarrow \mu\nu$ data) for the COT's response to radial tracks. To this, we add a "geometric width" set by the COT cell size and track angle as given by the angular distribution in minimum bias Monte Carlo (tuned to match CTC data). The simulation is further tuned so that the occupancy reproduces that observed in the CTC. Figure 4.8 shows the "dead space" (pulse width times drift velocity) given by the radial width, T_r, and geometric width, T_g, for typical tracks at low, medium, and high-p_t.

Figure 4.9 shows the resulting average spatial 2-track resolution for the CTC and COT as a function of superlayer. We see that, despite a $\sim 70\%$ increase in drift velocity for the COT for 132 ns operation, the overall dead space per track or 2-track resolution is lower by a factor of 0.87. For 396 ns operation, an improvement in resolution of 0.79 is predicted. The anticipated faster gas planned for 132 ns operation accounts for the difference between the two COT scenarios. The improvement relative to the CTC primarily comes from two sources:

1. We assume fast electronics (like the CTC has on SL0 – SL2) used throughout the COT. This gives a factor of 1.5 reduction in pulse width for radial tracks, partially compensating for the increase in drift velocity.

2. The cell boundaries help "hide" the radial response term (Fig. 4.8) resulting in less variation of charge collection time.

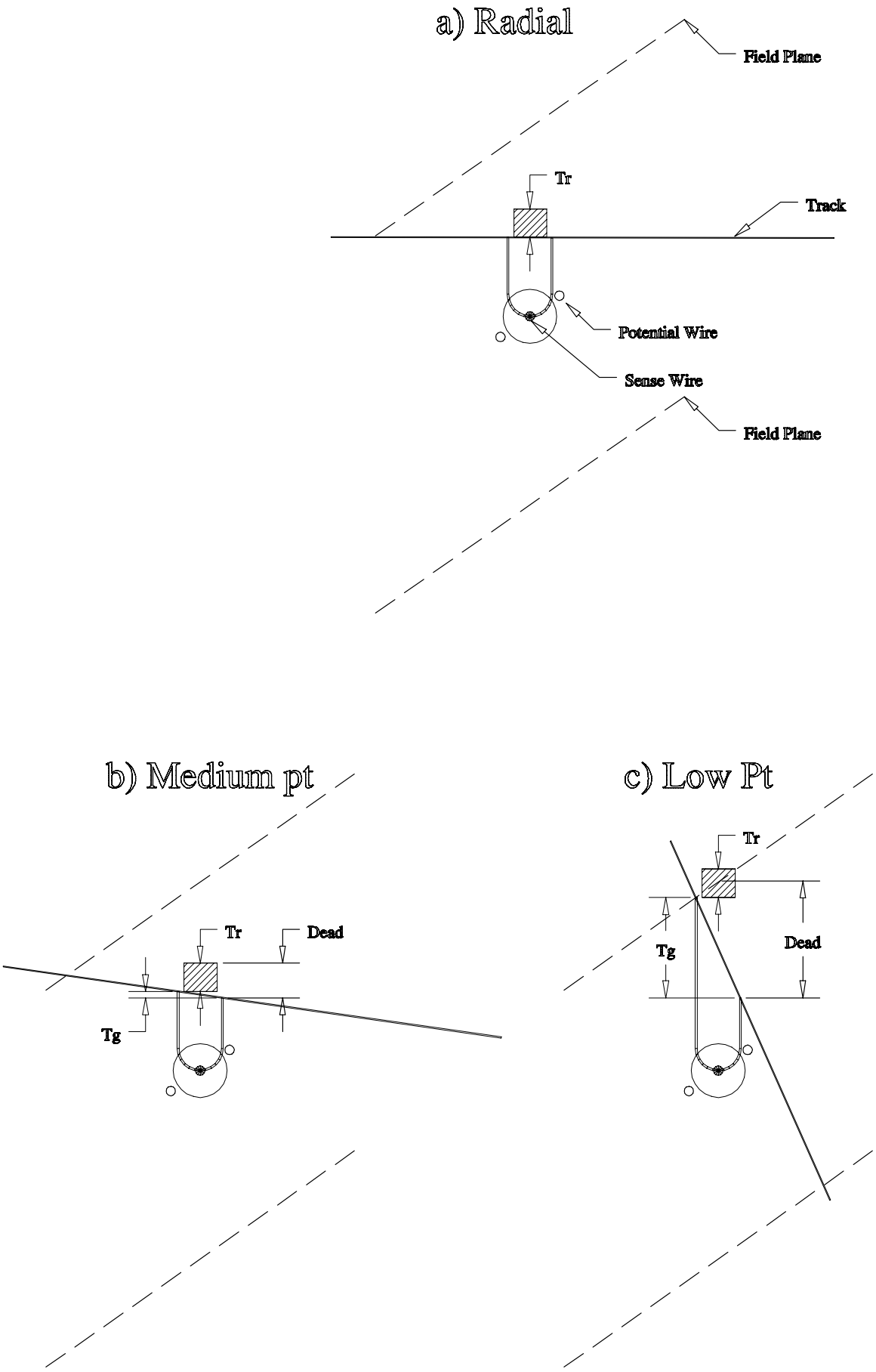

Figure 4.8: Contributions to "dead space" in COT. On the left is a track far from the cell boundaries. The case shown to the right has the effective dead space clipped by the cell boundary.

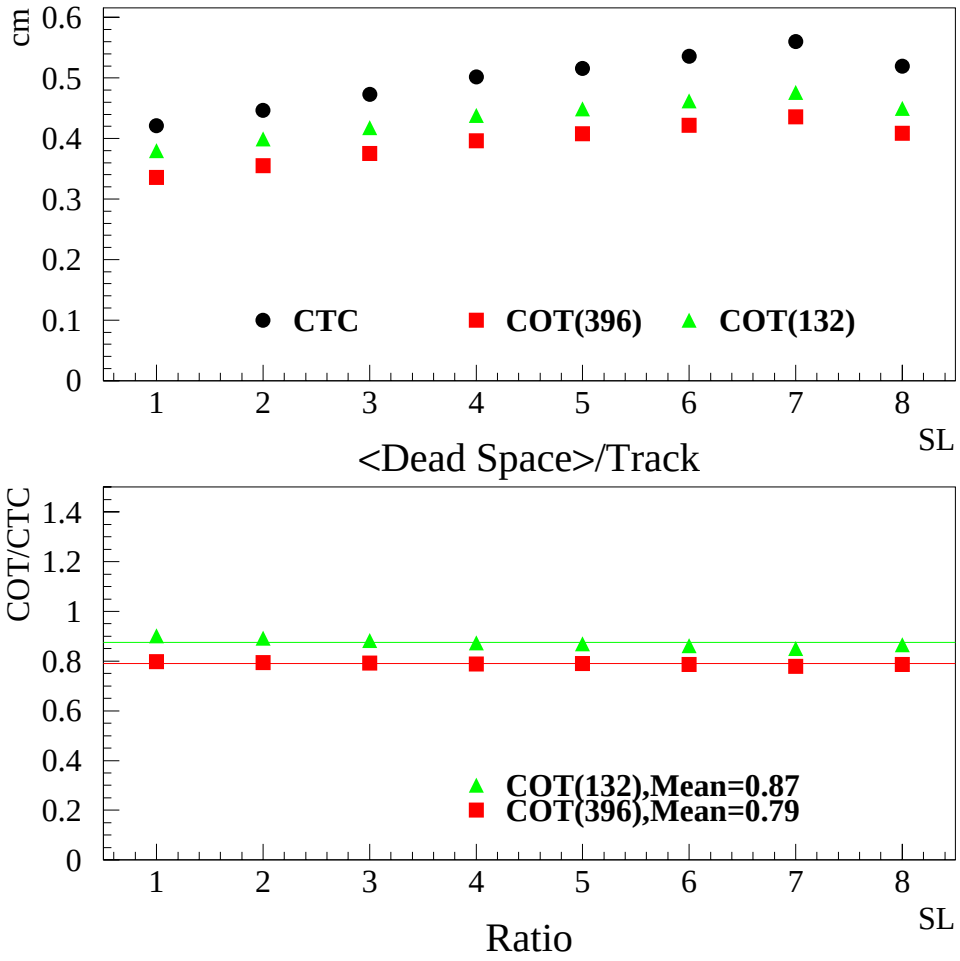

Figure 4.9: Mean pulse width in CTC and COT. Assumes no improvement in pulse shaping. Error on ratio is systematic, based on varying the radial response term 50% (CTC and COT in the same direction).

4.7.3 Luminosity Scaling

In the overview to this chapter we described a scaling rule for anticipating the performance of the COT at Run II luminosities by comparing to the CTC performance at certain Run I luminosities. In the simplest version of the argument, the luminosity scale factor is the ratio of the number of bunches. We now include an additional factor related to the relative 2-track resolution as determined in the previous section and then take a quantitative look at the prediction.

The 2-track resolution of the CTC, as measured by the average dead space per track in minimum bias simulation is approximately 0.45 cm averaged over superlayer. For the COT, we expect a 2-track resolution improvement by a factor of 0.79 for 396 ns operation and 0.87 for 132 ns operation.

The corrected scale factors between the CTC in Run I (6-bunch) and the COT in Run II are then given by the following:

- $\frac{36/6}{0.79} = 7.6$ @396 ns
- $\frac{108/6}{0.87} = 20$ @132 ns

i.e. The COT performance at $7.6 \times 10^{31}\text{cm}^{-2}\text{s}^{-1}$ in 396 ns operation and $2 \times 10^{32}\text{cm}^{-2}\text{s}^{-1}$ in 132 ns operation is expected to be comparable to the CTC performance at $1 \times 10^{31}\text{cm}^{-2}\text{s}^{-1}$ in Run I.

We note that luminosity scale factor still does not account for COT improvements in stereo reconstruction and possible improvements in the front-end electronics. Nevertheless, it gives us a data driven technique for anticipating in a rough way some details of expected COT behavior.

One very interesting benchmark is hit finding efficiency as a function of radius and luminosity. We have used conversion electrons as a control sample to study this in the CTC in Run I. Figure 4.10 shows hit usage as a function of superlayer for conversion electrons measured by the CTC; the abscissa also shows

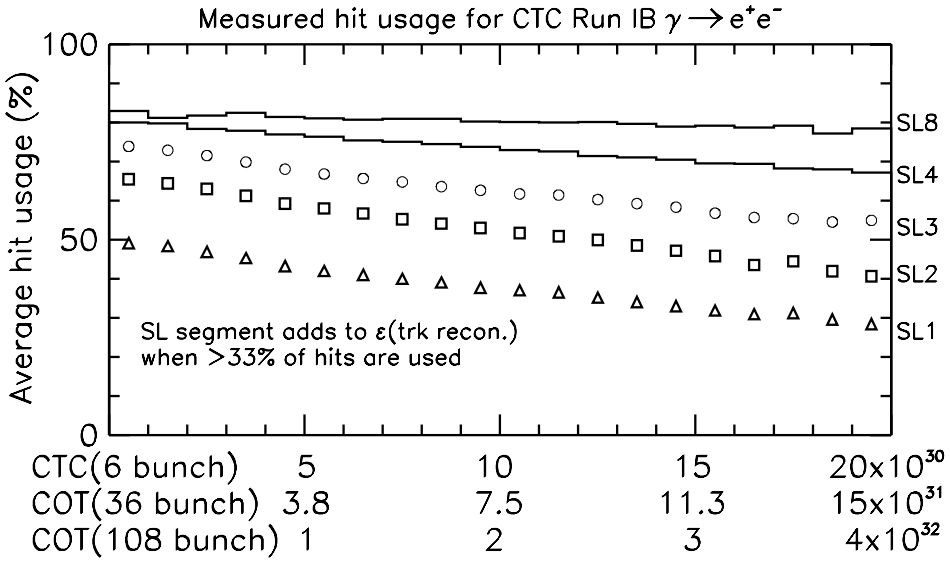

Figure 4.10: CTC conversion electron hit usage vs CTC and expected COT luminosities. The average hit usage for SL4–SL8 fall within the indicated band.

the equivalent luminosity for the COT performance. The exact shape of these curves depends on the data sample being analyzed and the nature of the track-finding and track quality requirements. In the figure, a maximum hit usage of approximately 80% is a consequence of optimizing track reconstruction by including only the best measured hits in a fit. The fraction of hits which are used on average at higher luminosities is smaller because hits are more likely obscured by those from other tracks. The density of overlapping tracks is higher at the smaller radii of the inner superlayers. Note that mid-point of Superlayer 1 for both the CTC and COT are at about the same 47 cm in radius.

A standard offline requirement for accepting a track as being "well-measured" is that the track uses at least 33% of the hits on a minimum of two superlayers. This requirement convoluted with the distribution shown in the figure shows that tracking efficiency for the COT is expected to remain high at the luminosities expected for Run II. However, we see that at luminosities in excess of $1 \times 10^{32}\mathrm{cm}^{-2}\mathrm{s}^{-1}$ the inner superlayers of the COT will be most efficient with 108 bunch operation, and the ability to link to a real silicon segment will be essential.

A detailed simulation study of the COT and complete integrated tracking performance is given in Chapter 7.

Bibliography

[1] F. Bedeshi *et al.,* "Design and Construction of the CDF Central Tracking Chamber" NIM A268 (1988) 50–74.

[2] SDC Collaboration, "SDC Technical Design Report", SDC-92-201 (1992)

[3] *Review of Particle Properties*, Phys. Rev. D45, (1992).

[4] F.M. Newcomer *et al.*, "A Fast, Low Power, Amplifier-Shaper-Discriminator for High Rate Straw Tracking Systems", IEEE Trans. on Nucl. Sci., 40 (1993).

[5] B. Bevensee *et al.*, "An Amplifier-Shaper-Discriminator with Baseline Restoration for the ATLAS Transition Radiation Tracker".

[6] M. Campbell *et al.*,"Deadtime-less 96 Channel Multihit TDC"

[7] J. Elias *et al.*, "Time to Digital Converter Module for Run II of the Fermilab TeVatron Collider - System and Performance Requirements", CDF/DOC/TRACKING/PUBLIC/2881, Nov 1994

[8] M. Campbell *et al.*, "JMC96 CDF TDC ASIC Description and Prototype Test Results", Jan 1995

[9] T. Shaw, " Specification for Trigger And Clock & Event Readout Module (TRACER)", Jan 1996

[10] M. Bowden *et al.*, "VME Readout Buffer", Mar 1996

[11] C. Gay *et al.*, " Silicon Readout Controller (SRC)", Jan 1996

[12] J. Hylen *et al.,* "Proposal for Run-II Tracking System Upgrades for CDF", CDF/DOC/TRACKING/PUBLIC/3079, Mar 1995

[36] K. Burkett and M. Paulini *Measurement of the Lifetime of the B_s^0 Meson from $D_s^+\ell^-$ Correlations*, CDF note 3519. See also, "Measurement of the B_s^0 Meson Lifetime." F. Abe *et al.*, Phys. Rev. Lett. **74** 4988 (1995).

[37] CDF SVX-II Upgrade Proposal, CDF Note No. 1922 (1993).

[38] J. Hagelin, Nucl. Phys. **B193**, 123 (1981); M.B. Voloshin *et. al* Sov. J. Nucl. Phys. **46**, 112 (1987).

[39] T.E. Browder and S. Pakvasa, UH 511-814-95. See also the recent discussion by M. Beneke, G. Buchalla and I. Dunietz, SLAC-PUB-7165, HEP-PH/9605259.

[40] I. Dunietz, Phys. Rev. **D51**, 2471 (1995).

[41] I. Bigi *et al.*, in "B Physics", 2nd edition, S. Stone editor.

[42] A.S. Dighe, I. Dunietz, H.J. Lipkin and J.L. Rosner, Phys. Lett. **B369**, 144 (1996).

[43] See Y. Grossman, WIS-96/13/Mar-PH, HEP-PH/9603244; M. Gronau and D. London, Technion-PH-96-37, HEP-PH/9608430, and Y. Nir, WIS-96/31/Jul-PH, HEP-PH/9607415 for recent discussions.

[44] The CLEO Collaboration, CLEO CONF 94-2.

[45] F. DeJongh and M. Shapiro, *A Proposal for Observing Radiative B Decays at CDF*, CDF Note 2570; K. Kordas *et al.*, *The CDF Penguin Trigger*, CDF Note 3771.

[46] E. Eichten and C. Quigg, Phys. Rev. **D49**, 5845 (1994).

[47] I. Dunietz, Phys. Lett. **B316**, 561 (1993).

[48] A. Ali, C. Greub, T. Mannel, *Proceedings of the ECFA Workshop on the Physics of the European B Meson Factory* (1993), 155. A. Ali and T. Mannel, Phys. Lett. **B264**, 447 (1991). Erratum, Phys. Lett. **B274**, 526 (1992).

[49] A. Ali, T. Mannel and T. Morozumi, Phys. Lett. **B273**, 473 (1991); B. Grinstein, M.J. Savage and M.B. Wise, Nucl. Phys. **B319**, 271 (1989); W. Jaus and D. Wyler, Phys. Rev. **D41**, 3405 (1991).

[50] A. Ali, G. Giudice and T. Mannel, *Towards a Model Independent Analysis of Rare B Decays*, Proceedings of the XXVII International Conference on High Energy Physics, Glasgow, Scotland (1994).

[51] M. Gronau and D. London, Technion-PH-96-37, HEP-PH/9608430.

Chapter 5

Silicon Vertex Detector (SVX II)

5.1 Introduction

In 1992, a silicon vertex detector (SVX) was added to CDF to detect secondary vertices from heavy flavor weak decays and has proved to be an excellent tool for b-tagging in top searches and for b-physics. To control radiation damage, the original SVX was replaced with the SVX′ detector of similar geometry but using AC-coupled silicon detectors and a radiation hard readout chip.

The planned increase in the number of p and $\overline{p}$ bunches in the accelerator for Run II, and the resulting shorter bunch spacing (132 ns or 396 ns) requires a replacement for the SVX′ detector. We call the Run II silicon vertex detector SVX II [1]. The overall specifications of the SVX II detector are as follows:

- SVX II will be longer to provide more complete geometric coverage of the luminous region and to provide track information to $|\eta| < 2$ as shown in Fig. 5.1.
- The detectors will be double-sided to provide r-z readout for improved pattern recognition and 3-D vertex reconstruction with an impact parameter resolution $\sigma_\phi < 30$ μm and $\sigma_z < 60$ μm for central high momentum tracks.
- The detector should be sufficiently radiation hard for operation after a delivered luminosity of up to 3 fb^{-1}. The expected radiation dose for the Layer 0 sensors is approximately 0.5 Mrad/fb^{-1}.
- A 42 cell analog pipeline will store the data during the formation of the Level 1 trigger for either 396 ns or 132 ns between bunch crossings.
- The pipeline will be buffered and dual-ported to support simultaneous digitization and readout of data while additional analog data is entering the pipeline ("SVX3" chip). This permits a high Level 1 trigger accept rate of order 50 kHz with minimal deadtime.
- Digitization and readout of the SVX II analog data for Level 2 processing will take approximately 6-7 μs following a Level 1 trigger. The high speed of the readout is required in order to use the SVX II data in a Level 2 vertex trigger processor. A new Silicon Vertex Tracker (SVT) will find tracks with large impact parameters to be used in the trigger.

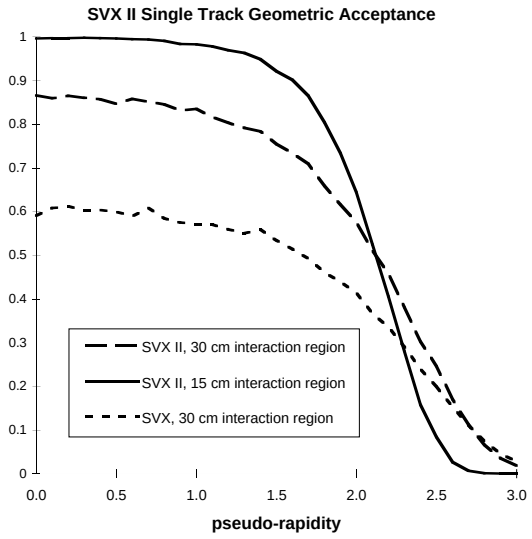

Figure 5.1: SVX II single track acceptance.

Table 5.1 compares SVX II design parameters with those of the current SVX′. The new detector will consist of three barrels, each 29 cm long. There are 12 wedges in ϕ, each with five layers of silicon. Of the five layers, three have 0°-90° stereo while two

Detector Parameter	SVX′	SVX II
Readout coordinates	r-ϕ	r-ϕ; r-z
Number of barrels	2	3
Number of layers per barrel	4	5
Number of wedges per barrel	12	12
Ladder length	25.5 cm	29.0 cm
Combined barrel length	51.0 cm	87.0 cm
Layer geometry	3° tilt	staggered radii
Radius innermost layer	3.0 cm	2.44 cm
Radius outermost layer	7.8 cm	10.6 cm
r-ϕ readout pitch	60;60;60;55 μm	60;62;60;60;65 μm
r-z readout pitch	absent	141;125.5;60;141;65 μm
Length of readout channel (r-ϕ)	25.5 cm	14.5 cm
r-ϕ readout chips per ladder	2;3;4;6	4;6;10;12;14
r-z readout chips per ladder	absent	4;6;10;8;14
r-ϕ readout channels	46,080	211,968
r-z readout channels	absent	193,536
Total number of channels	46,080	405,504
Total number of readout chips	360	3168
Total number of detectors	288	720
Total number of ladders	96	180

Table 5.1: Comparison of SVX′ and 5-layer SVX II.

have 1.2° small-angle stereo. This is designed to permit good resolution in locating the z-position of secondary vertices and to enhance the 3-D pattern recognition capability of the silicon tracker. For each barrel, the silicon ladders are mounted between two precision-machined beryllium bulkheads which also carry the water cooling channels for the readout electronics. Figure 5.2 shows a drawing of the SVX II bulkhead. The radial locations of the numbered labels shown in the figure are given in Table 5.2.

A sketch of the SVX II data acquisition system is shown in Fig. 5.3. The readout chips are mounted on an electrical hybrid on the surface of the silicon detectors. Including both sides of the detectors (r-ϕ and r-z or r-ϕ') there are 44 chips in a wedge with 12 wedges per barrel end and six barrel ends in total. Each readout chip set (SVX3) has 128 channels, each with a charge-sensitive amplifier, a 42-cell dual-ported pipeline with four additional cells for buffers, and an ADC. The chips from each wedge are read out over five high density interconnects (HDI), one per layer. The HDI's from each wedge are connected to a port card (PC) located around the periphery of the barrel ends. The PC decodes the control signals from the fiber interface board (FIB). Also at the PC, the analog data, already in digital form, are converted from electrical to optical signals by dense optical interface modules (DOIM's). Each DOIM drives a ribbon of optical fibers (eight data and one clock) at 53 MHz approximately 10 m to VME crates located on the sides of the CDF detector. This highly parallel readout permits the entire detector ($\approx$ 406,000 channels) to be read out in approximately 10 μs. The r-ϕ information is delivered to the SVT before the r-z/ϕ' information is read out.

Three VME crates on the west side of the CDF detector together house the FIB's and FIB fanout modules. Each PC is controlled by its respective FIB through a set of copper control lines with one FIB controlling 2 PC's. The FIB board generates control signals for the PC based on commands sent from the silicon readout controller (SRC) located in the CDF counting room. The command signals from the SRC are transmitted serially over a single high speed optical link (G-link) running at 1.5 GHz. They are processed at the FIB crate by a fanout module which distributes them to the FIB boards over the J3 backplane. In addition to its command function, each

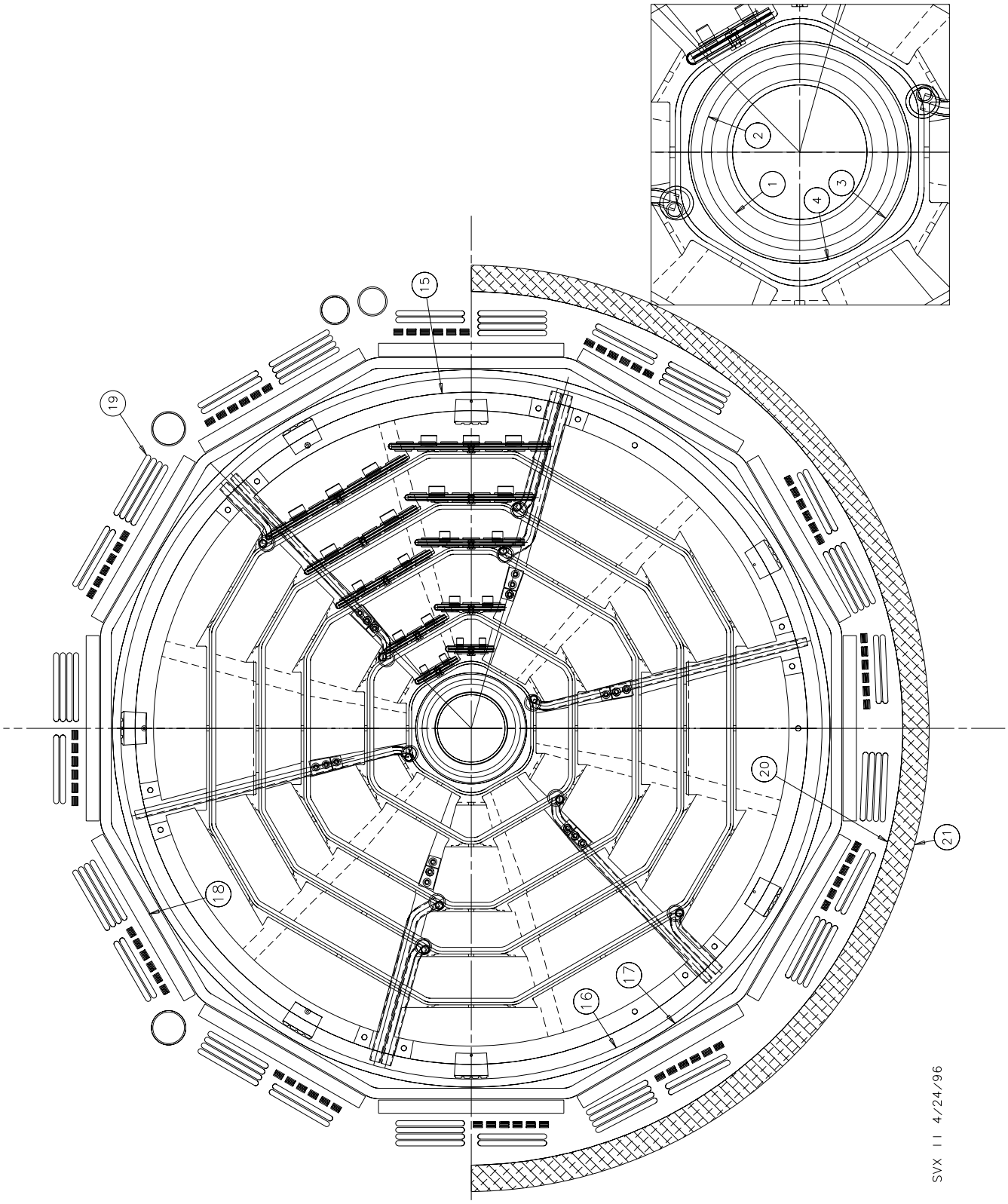

Figure 5.2: The SVX II bulkhead design

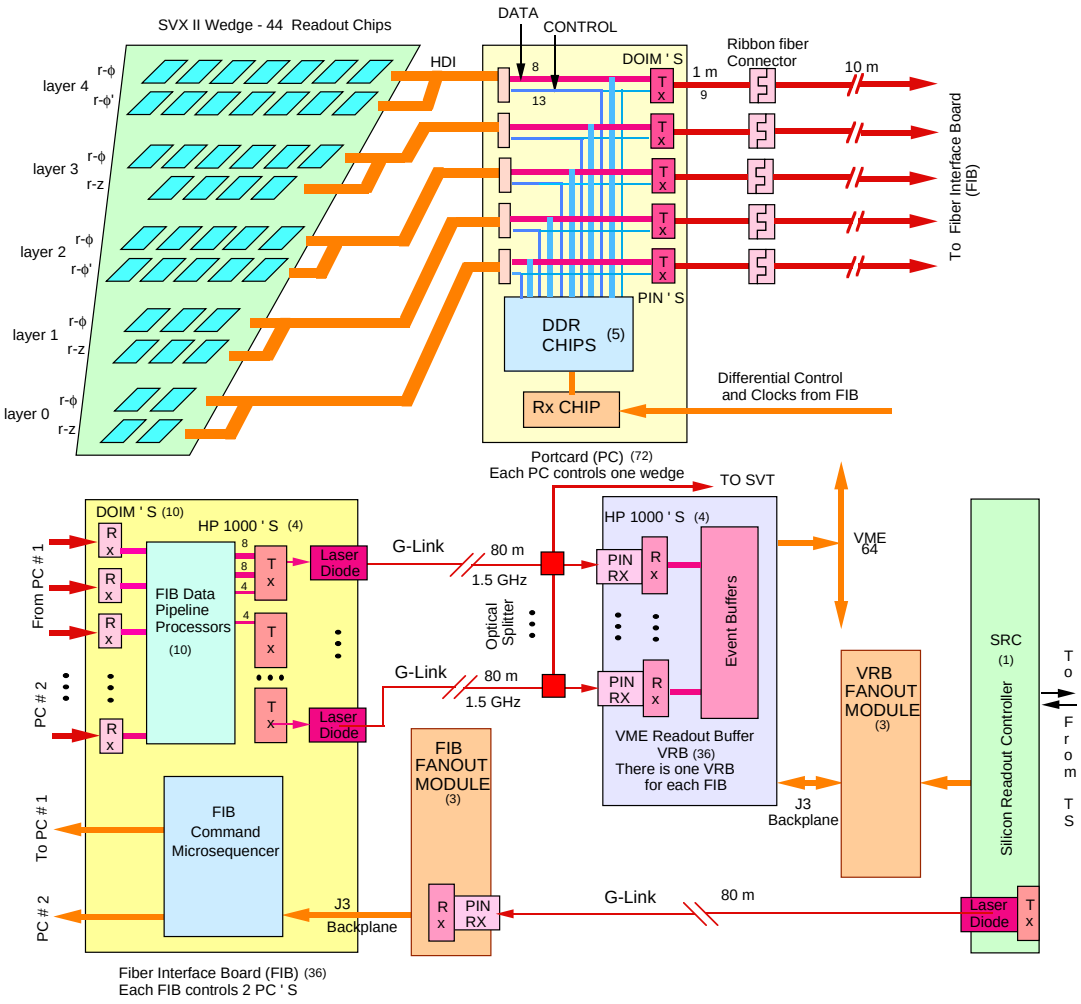

Figure 5.3: Schematic of the SVX II data acquisition system.

FIB serializes the data from 10 DOIM's onto high-speed optical G-links. For each FIB the data from 90 low-speed fibers are sent by only four high-speed fibers. These high-speed optical fibers carry the data approximately 70 m to the counting room where the data are stored in event buffers located on the VME readout buffer cards (VRB's) where it waits for a Level 2 trigger decision and subsequent readout into Level 3.

In the counting room there are three VRB VME crates, one for each barrel of the detector, and each containing 12 VRB's. Each crate is controlled by the SRC through the VRB fanout board located in each crate. The SRC in turn communicates by a serial optical fiber with the CDF Trigger System Interface. Control of the VRB boards by the VRB fanout module is accomplished over the J3 backplane. A set of optical splitters located just in front of the VRB modules sends a completely parallel stream of data to the SVT trigger processor so that the silicon data can be used in the Level 2 trigger decision.

	Description	R (cm)
1	Beam pipe outer radius	1.6700
2	Beam pipe flange outer radius	1.8542
3	Inner screen inner radius	2.0500
4	Bulkhead inner radius	2.1000
5	Layer 0a *	2.5450
6	Layer 0b	2.9950
7	Layer 1a	4.1200
8	Layer 1b	4.5700
9	Layer 2a	6.5200
10	Layer 2b	7.0200
11	Layer 3a	8.2200
12	Layer 3b	8.7200
13	Layer 4a	10.0950
14	Layer 4b	10.6450
15	Bulkhead outer radius	12.9000
16	Outer screen inner radius	12.9000
17	Outer screen outer radius	13.2500
18	Port card inner radius	14.1000
19	Cables	16.1000
20	Half cylinder inner radius	16.3000
21	Half cylinder outer radius	17.3000

* All layer radii are relative to center of silicon.

Table 5.2: SVX II Bulkhead Information

5.2 Silicon Crystals

The primary physics goals of the CDF vertex detector are to allow good secondary vertex reconstruction and pattern recognition. Monte Carlo studies showed that these require five layers of double-sided silicon microstrip sensors. Optimization of both vertex resolution and pattern recognition considerations lead to the first, second and fourth layers (Layers 0, 1 and 3) having a "90° stereo" design while the third and fifth layers (Layers 2 and 4) have a "small angle stereo" design. Technically, the "90° technology" is more difficult to design and construct than the small angle technology, so it will be described in greater detail. Some mechanical and electrical properties are given in Tables 5.3 and 5.4.

5.2.1 Silicon Detector Layout

Many characteristics are common to all the detectors regardless of layer or stereo angle. The HV biasing uses polysilicon resistors with 2.5 $\pm$ 0.5 Mohm resistance, and the readout is AC coupled. The detector bulk silicon thickness is 300 $\pm$ 15 μm for the double metal layers and 275 $\pm$ 15 μm for the small angle layers. The thickness variation within one detector is $\pm$ 5 μm. Bowing should be less than 100 μm in a detector. There should be fewer than 3% dead chan-

Property	Layer 0	Layer 1	Layer 2	Layer 3	Layer 4
number of ϕ strips	256	384	640	768	896
number of Z strips	256	576	640	512	896
number of ϕ chips	2	3	5	6	7
number of Z chips	2	3	5	4	7
stereo angle	90^o	90^o	$+1.2^o$	90^o	-1.2^o
ϕ strip pitch (μm)	60	62	60	60	65
Z strip pitch (μm)	141	125.5	60	141	65
total width (mm)	17.140	25.594	40.300	47.860	60.170
total length (mm)	74.3	74.3	74.3	74.3	74.3
active width (mm)	15.300	23.746	38.340	46.020	58.175
active length (mm)	72.43	72.43	72.38	72.43	72.38
number of detectors	144	144	144	144	144

Table 5.3: Silicon detector mechanical dimensions

nels per side and 50% of the detectors should have fewer than 2% dead channels.

5.2.2 The 90° stereo sensors

The 90° stereo sensors have strips running lengthwise on the sensor's p-n junction side to measure the r-ϕ position of the particle, and strips running laterally on the ohmic contact side (n-side) to measure the r-z position. Both sets of strips are read out from the end of the sensors. For the r-z signals this requires an additional layer of strips running longitudinally and contacting the lateral r-z strips through a 5 μm insulating layer of SiO_2 by means of small "via's". This is referred to as a double metal layer technology.

Key parameters associated with the SVX II 90° stereo sensors have been chosen to minimize readout capacitance, in order to minimize the amplifier noise level and to maximize radiation hardness. The readout capacitance is larger for the 90°, ohmic-side strips than for the p-n junction side strips. This is caused by several factors. One factor is that, to maintain electrical isolation of the n-side readout strips under high radiation levels, extra p-implant strips are placed between the ohmic contact strips. This gives operational simplicity and radiation hardness [2]. A second factor increasing the ohmic side capacitance is the double metal layer readout. It introduces additional capacitance because the second metal (longitudinal) strips couple to the first metal (90°) strips through the insulation layer.

Several steps were taken to reduce the 90° capacitance. The coupling capacitance of the double layer readout was minimized by making the insulating silicon dioxide (SiO_2) between the two metal layers as thick as possible, while maintaining the via reliability. SiO_2 was chosen as the insulator because of fabrication reliability and good radiation resistance. A new idea for the isolation p-stop pattern was introduced, in which a combination of an individual p-stop and a common p-stop is used.

The critical item limiting the useful lifetime of the silicon sensors is the radiation hardness. For a peak luminosity of 10^{32} $cm^{-2}s^{-1}$ the fluence received by Layer 0 is expected to be about 1.7 x 10^{13} particles/cm^2/year, i.e. about a half Mrad/year. This is the same order of magnitude radiation level as expected on the LHC silicon trackers, which are placed further from the beamline. This radiation causes the silicon bulk to change from n-type to p-type during the operation of Run II. This is referred to as "type inversion" [3]. Because of type inversion and accumulation of defects caused by radiation damage, the bias voltage needed for full depletion of the bulk can become as high as 150V. The rate at which type inversion occurs depends strongly on the operation temperature [4], being slower at lower temperatures. High bias voltages need to be avoided if possible because they cause micro-discharge noise [5], which takes place before a junction breakdown. The design of surface structures for the SVX II incorporated many ideas [6] from our research in order to suppress the micro-discharge.

The coupling capacitors which are integrated onto

Electric Properties of Detectors	
initial $I_{leakage}$ at V_{bias}=80 V, T=20 °C:	
(bulk, surface and edge contribution)	< 100 nA/cm^2
initial full depletion voltage (V_{full}):	45 V<V_{full}<70 V
junction breakdown with open readout electrodes:	> 200 V
The breakdown is defined as:	I_{break} > 10 x I_{leak} with V_{bias} = 80V
onset voltage of micro discharge:	*p*-side, *n*-side balanced bias ($\pm V_{bias}/2$), both-side readout electrodes grounded
p-side	> 150 V (total bias potential)
n-side	> 150 V (total bias potential)
$V_{Breakdown}$ of coupling capacitor:	
n and *p*-side:	> 100 V
Interstrip resistance (DC):	>2 Gohm
Poly-silicon resistor value:	
mean value:	2.5 ± 0.5 Mohm
variation within one detector:	< 0.5 Mohm
resistivity of implant-strip:	<100 kohm/cm
resistivity of all metal layers: *n* & *p*-sides	<30 ohm/cm
capacitance of coupling capacitor:	
n and *p*-side:	>10 pF/cm
total capacitance (full length, at bias voltage of 1.2 x V_{full}):	
p-side (Layers 0, 1 and 3):	<10 pF
n-side (Layer 0):	<13 pF
n-side (Layer 1):	<14 pF
n-side (Layer 3):	<15 pF
p-side and *n*-side (Layer 2 and 4):	<10 pF
Specifications for Radiation Damage Tests for Pilot Detectors	
Ten days after irradiation of 500 krad Gamma-ray:	
leakage current at 20 °C:	<3 μAmp/cm^2
bias resistor change:	<20%
p-strip, *n*-strip $R_{interstrip}$:	>1 Gohm
junction breakdown voltage:	>200 V
onset voltage of the micro discharge:	>150 V
total capacitance (full length, at bias voltage of 1.2 x V_{full})	
p-side (Layers 0 and 1):	<11 pF
n-side (Layer 0):	<14 pF
n-side (Layer 1):	<15 pF
n-side (Layer 3):	<16 pF
p-side and *n*-side (Layer 2 and 4):	<11 pF

Table 5.4: Electrical Properties of Detectors

the sensor are another critical technological issue. They must be free of "pin holes" which allow breakdown. A double layer structure consisting of SiO_2 and silicon nitride (Si_3N_4) is employed to improve the capacitor production yield. But careful design and processing is required to avoid problems of electrical charge-up between the SiO_2 and Si_3N_4 layers.

5.2.3 Small Angle Stereo Detectors

The Layer 2 and Layer 4 sensors utilize "small angle stereo" for the strip layout instead of the 90° layout. The design requirements for radiation resistance, capacitance, etc. are very similar to those of the 90° sensors, so that discussion will not be repeated here. One difference is the wafer construction, which will be discussed.

Recent technological developments in the silicon detector manufacturing industry have increased the size of available wafers from 4 inch to 6 inch. The design of the detectors for Layers 2 and 4 takes advantage of the availability of 6 inch wafers. Such large wafers can host both a Layer 2 and a Layer 4 detector reducing dramatically the mask fabrication and processing costs. The 6" wafers are a new technology, but they have been proven to work on large area detectors. However, because our 90° sensors require challenging technology such as the double metal processing, they have intrinsically some extra degree of difficulty. For this reason it seemed appropriate to choose the 6" technology only for the small angle stereo design, shown in Fig. 5.4, where we do not require the double metal processing. If production problems happen to arise, the use of the standard 4" wafer approach is still possible for Layer 2 without any design modifications, but some modifications might be required for Layer 4.

The technical specifications we have required for Layer 2 and 4 are very similar to those of the other layers, though here the radiation hardness demand is less stringent. For example, the Layer 2 detectors are expected to receive only about 1/7 of the Layer 0 expected dose. One big difference is the fact that the 6" wafers available for manufacturing at the moment have a relatively low resistivity of about 3 kΩ-cm. Consequently we decided to reduce the thickness of the detectors to about 275 μm in order to keep the depletion voltage below 80 V. There are a minimum of 13 masks needed for the double side process. We added 2 more to allow for 1) the option of Si_3N_4 deposition to enhance the breakdown voltage of the coupling oxide and 2) a n^+ well implant extending to the junction side scribe line to avoid large currents being injected into the active area from the edges of the detector.

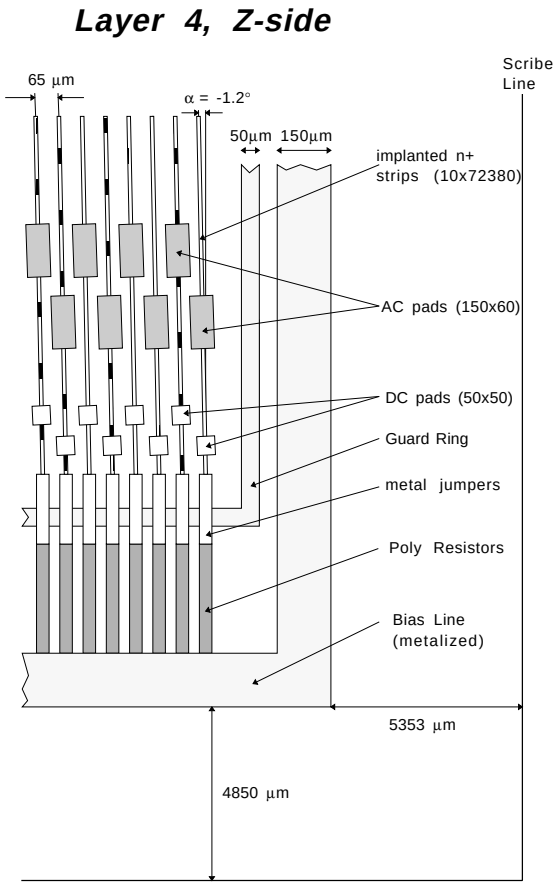

Figure 5.4: Silicon detector small angle stereo design.

5.2.4 Silicon Detector Tests

A substantial R&D program on silicon sensors has been carried out to achieve the full potential of the silicon tracker upgrade. This program has resulted in significant technical developments in the areas of capacitance and microdischarge minimization, geometrical layout optimization, large area detectors from 6 inch wafers, and determination of processing and operating conditions. The program has also investigated the sensors' signal-to-noise (S/N) ratio, efficiency, and position resolution before and after radiation damage similar to what is expected at Layer

0 during Run II. The program included full characterization of sensors utilizing many design options. These sensors were manufactured by three different vendors—Hamamatsu, SINTEF/SI and Micron Semiconductor. The characterization program involved the measurement of the electrical properties of the sensors on a probe station [7, 8, 9, 10, 11, 12], the study of the charge collection efficiency and determination of the optimal operating conditions with a pulsed laser system [13], and the operation of the detectors in conjunction with the SVXH [14] and SVX2 [15] chips in two beam tests [16, 17].

5.2.4.1 Capacitance Minimization

The detector capacitance plays a key role in determining the S/N ratio. The important components are the many parallel capacitances that load the amplifier front end, including C_{is}, the capacitance between implant strips, C_{back}, the backplane capacitance (between the implant strip and the opposite side of the detector), C_{ir}, the capacitance between the readout traces, and $C_{overlap}$, the capacitance between the second metal traces on the z-side and the AC-coupled first metal electrodes.

On the p-side (whose strips measure the r-ϕ coordinate), C_{is} and C_{back} have the largest effect. The capacitance with respect to the ground of the implant depends primarily on the ratio of the strip width to the pitch. To minimize this contribution to the total detector capacitance, the strip should be as narrow as possible.

The capacitance of the n-side strips (which measure the r-z coordinate) is the sum of C_{is}, C_{ir}, C_{back}, and $C_{overlap}$. We measured the n-side capacitance of prototype detectors [9, 11] and found agreement between the direct measurement of the capacitance with respect to ground and the sum of the various capacitive components. A fit of the measured total capacitance to a geometrical model [18] and a SPICE simulation [11] agree within 20%. For example, the measured n-side capacitance of the Layer 0 prototype detectors from Hamamatsu is 17 pF, in good agreement with two independent simulations which together predict a capacitance between 17 and 21 pF. The same two simulations applied to the Layer 0 production detectors predict an n-side capacitance for them between 10 and 12 pF.

By comparing detectors with different geometries, we have designed a readout scheme to minimize the n-side capacitance by

1. maximizing the thickness and minimizing the dielectric constant, ϵ_r, of the insulator between the metal layers,
2. limiting the multiplexing,
3. minimizing the width and length of the second metal strips and
4. avoiding ganging and intermediate strips.

A summary of the predicted capacitance for a full electrical unit consisting of two double metal production detectors wirebonded together is in Table 5.5.

Layer	p-side Husson	p-side Spice	n-side Husson	n-side Spice
0	15	17	20-24	21-25
1	15	16.5	22-26	22-26
2	19	19	24	26
3	15	17	24-28	24-29
4	19	19	26	27

Table 5.5: Predicted capacitance in pF

The RMS noise of the SVX2 chip versus input capacitance has been measured [19] for integration times of 107 ns and 371 ns and is shown in Fig. 5.5. Using a linear extrapolation between the measured data points an input capacitance of 25 pF predicts noise values of $\approx 2100\ e^-$ and $\approx 1100\ e^-$ for integration times of 107 ns and 371 ns, respectively.

5.2.4.2 Optimal Geometry and Processing

Studies of prototypes having a variety of geometrical options allowed us to investigate several issues, including the effect of intermediate strips on the $p-$ and n-sides, the performance of double metal readout compared with readout by interconnects on glass or Kapton, and the optimal insulator to be used in the double metal structure and/or for passivation. One of the major results of these investigations was the elimination of the option for intermediate strips on the n-side. Laser studies [13] and results from our first KEK run [16] showed that double metal detectors with intermediate strips lose efficiency by more than 90% when the beam strikes directly on the intermediate strip.

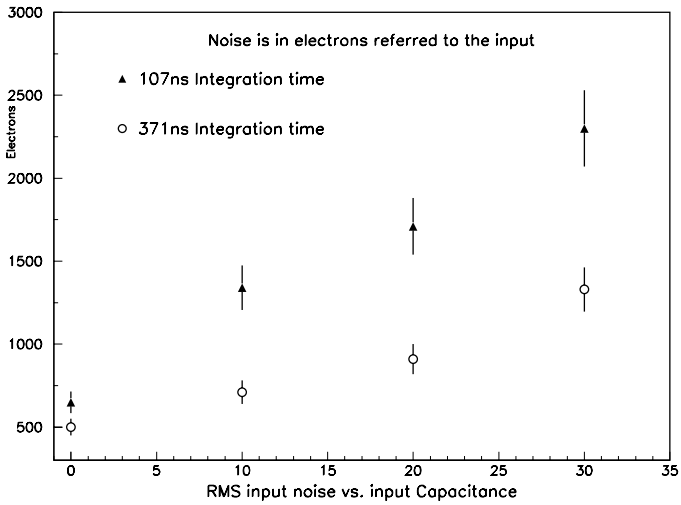

Figure 5.5: SVX2 measured noise as a function of input capacitance for integrations times of 107 ns (triangles) and 371 ns (circles).

5.2.5 Radiation Issues

The radiation levels experienced by silicon detectors have a multitude of effects. These have been investigated by irradiating detectors at TRIUMF and then checking them in the lab and in KEK test beams. Below we discuss the radiation levels we expect to encounter during Run II and the effects we have observed during our radiation tests.

5.2.5.1 Run II Expected Radiation Levels

The radiation levels in SVX II have been estimated for the Run II beam intensities and CDF geometry [20, 4]. The expected radiation dose is shown in Fig. 5.6 for SVX II Layers 0-4 as a function of time during Run II [4]. For the purpose of this study the CDF yearly integrated luminosity for Run II is assumed to be 1 fb^{-1} and 2 fb^{-1} for years 1 and 2, then 0 fb^{-1} for year 3, followed by 2 fb^{-1} and 3 fb^{-1} for years 4 and 5. We assume that SVX II Layer 0, and possibly Layer 1, will be replaced part way through Run II. This is shown happening during year 3 for SVX II Layer 0. The radiation dose is given as the equivalent fluence of 500 MeV protons [4]. This allows for a direct comparison with radiation damage results in the SVX II sensor prototypes at the TRIUMF radiation tests. As shown in the figure, the maximum fluence at TRIUMF ($\sim$ 0.9 Mrad) is comparable to the maximum fluence expected for SVX II sensors. Also shown in the figure is the approximate fluence when the silicon sensors will change from n-type bulk to p-type bulk, i.e., undergo type inversion. At inversion the n-p junction moves from the p-strip side of the sensor, which measures r-ϕ, to the n-strip side, which measures r-z.

5.2.5.2 Radiation effects

The expected radiation levels in SVX II require radiation hard electronics and sensors. The SVX3 chips will be fabricated using Honeywell's radiation hard CMOS processing. This is guaranteed radiation hard to 1.5 Mrad. A measurable but acceptable level of degradation is expected up to radiation levels of 5 Mrad [21]. Thus the SVX3 chip should perform satisfactorily at the expected radiation levels of 1-2 Mrad.

The effects of radiation on the SVX II sensors are more complex than on the SVX3 chip. The individual structures on the SVX II sensors, including bias resistors, n- and p-implants, p-block implants, metal readout strip geometry, AC coupling capacitors, etc., were chosen to be as radiation tolerant as possible [22, 23, 5]. The SVX II production sensors will have SiO_2 ($\epsilon_r = 3.8$) as an insulator between the double metal layers because of its demonstrated hardness to high radiation. Extensive pre- and post-irradiation testing of SVX II sensor prototypes from Hamamatsu, Micron and SINTEF/SI are continuing. Initial results [7, 24, 8, 25, 10, 26] are all consistent with a stability at the 10% level of these structures against radiation except for the interstrip resistance, where a substantial decrease with radiation was found [8]. Nonetheless, the value of the interstrip resistance remains large enough, $> 100 M\Omega$, that the sensor performance is not expected to be compromised.

Several other features of the silicon microstrip sensors show significant changes with radiation. These include the detector leakage current, the depletion voltage, and the interstrip capacitance. The changes in the leakage current and depletion voltage are a result of radiation damage in the bulk silicon and have been extensively studied [4]. Initial measurements of the radiation-induced bulk damage in the SVX II prototypes are in good agreement with expectations [25, 26]. The leakage current and depletion voltage changes affect the power dissipated in the detectors, which has implications for the SVX II cooling and power system designs. Furthermore, the increased leakage current decreases the S/N because of increased shot noise [27, 28].

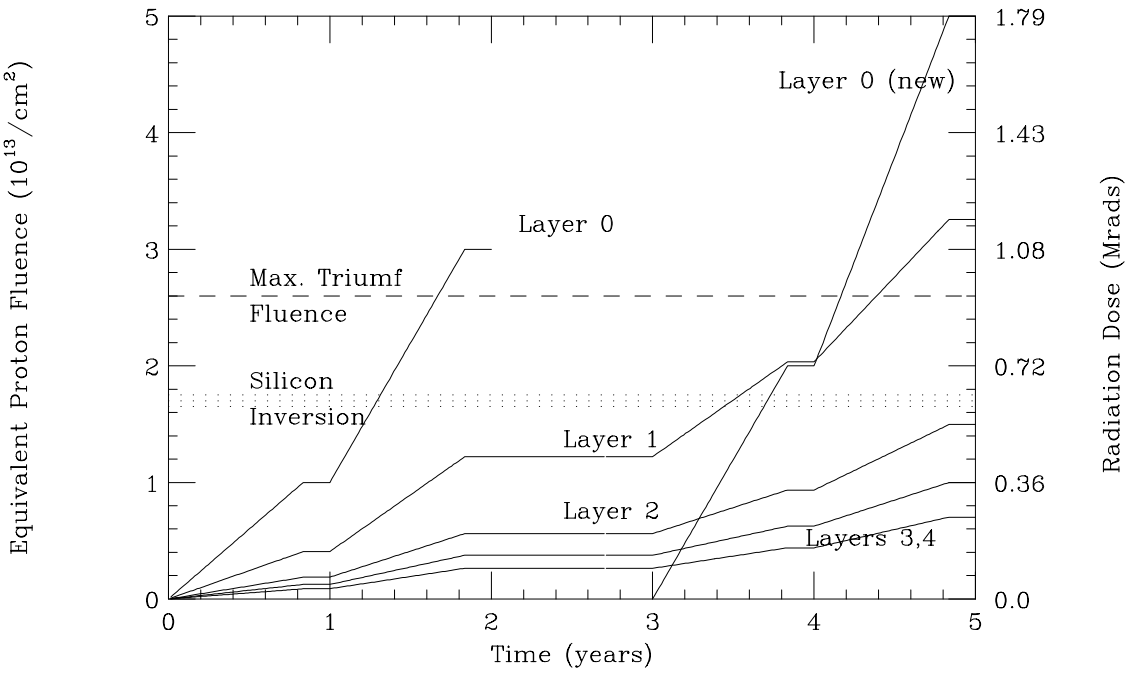

Figure 5.6: Estimated radiation levels for Layers 0-4 of SVX II in Tevatron Run II. The integrated luminosity is assumed to be 1 fb^{-1}, 2 fb^{-1}, 0 fb^{-1}, 2 fb^{-1}, 3 fb^{-1} for years 1, 2, 3, 4, and 5 respectively.

The change in the sensor interstrip capacitance is a result of surface damage caused by radiation at or near the silicon-SiO_2 interface. The observed trends at the sensor p-side are for the interstrip capacitance to increase by 20%-40% for the first few 100 Krads and then to become independent of radiation until type inversion occurs [29]. Following inversion the p-side interstrip capacitance becomes 1.4 to 2 times the unirradiated value [30]. Before inversion, the dependence on radiation of the interstrip capacitance of the sensor n-side with double metal readout should be much weaker than the p-side. Following inversion the n-side interstrip capacitance should decrease to a value less than that seen before irradiation [29].

Measurements of the interstrip and total input capacitance for unirradiated and irradiated SVX II prototype sensors are being made [11, 9]. The initial measurements are consistent with the above expectations [25, 26]. Because the sensor interstrip capacitance is a major component of the preamplifier input capacitance, increases in the sensor interstrip capacitance result in an increase in the noise [28].

Another issue is charge trapping due to radiation. Present evidence is that the radiation levels for Run II should not be enough to cause SVX II signal loss due to charge trapping [31].

5.2.5.3 KEK Test Beam Results

The principle difference between the two beam tests at KEK was the type of chip used to read out the sensors. In the first beam test the well-understood SVXH chip was used, while in the second test the prototype SVX2 chip was used [16, 17].

In the first KEK beam test, five (SINTEF/SI and Hamamatsu) double metal detectors were tested. The position resolution of these detectors as a function of angle is shown in Fig. 5.7. At normal incidence the strip pitch/$\sqrt{12}$ accounts for the resolution. For particles with oblique incident angles the resolution varies between 12 and 25 μm.

The S/N of irradiated and unirradiated SVX II prototype sensors was measured in the two beam tests at KEK. The unirradiated detectors have n-side S/N ratios of 17, 21 and 16, while detectors irradiated with between 0.25 and 1.0 MR have S/N ratios of 13 and 14. In the second KEK beam test, S/N ratios were measured for seven double metal detectors

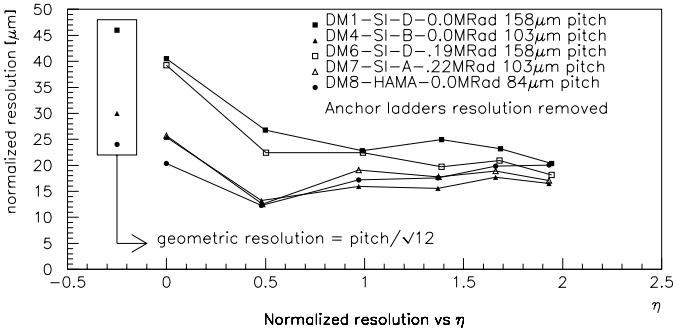

Figure 5.7: Silicon detector resolution versus particle angle of incidence.

supplied by SINTEF/SI, Hamamatsu, and Micron. Unirradiated detectors have ratios of 11, 14 and 10, while irradiated detectors, having doses between 0.1 and 0.7 MR, have ratios of 9, 10, 10 and 7.

The S/N measured during the second test beam is somewhat lower due to several effects. The dominant effect is from the increased noise of the SVX2 chip as operated for the KEK test, i.e. there was excess noise beyond what can be expected for optimized running conditions. Several $\approx$ 10% effects, including charge loss from the limited integration time window and the clustering algorithm, appear to account for the majority of the remaining difference. The gain of the SVX2 chip is a parameter in the calculation of the theoretical signal and noise, but it cancels in the calculation of the S/N ratio.

Prior to the beam test the leakage currents were measured in the sensors. The increases seen as a result of the radiation dosages were consistent with values found in the literature [27]. The noise as a function of average radiation dose is plotted for the p-side in Fig. 5.8 and for the n-side in Fig. 5.9. The p-side detectors had strips of two different lengths, 4.1 and 8.2 cm. The results for these are plotted separately. Whereas the n-side shows no evidence for an increase of noise with radiation dose, the p-side shows an increase. The n-side results are consistent with our expectation based on the first KEK test results, where the increase in noise could be accounted for by an increase in the shot noise. Since the SVX2 chip has an integration time an order of magnitude shorter than the SVXH chip, we expect almost no contribution to the noise due to shot noise. For the p-side, the solid lines in Fig. 5.8 indicate a range of expected noise as a function of dose. We have assumed the interstrip capacitance increases between 20% and 40%, representing the lower and upper lines. We have included the effect of the increased leakage current based on the radiation dose.

There are several potentially large uncertainties in these measurements. First, the temperature was not well controlled, an effect which could easily introduce a 10% variation in the noise. Second, the radiation dose used is an average value, whereas the dose profile is known from foil measurements to be non-uniform. Nonetheless, the observed increase in the noise on the p-side is consistent with our expectations.

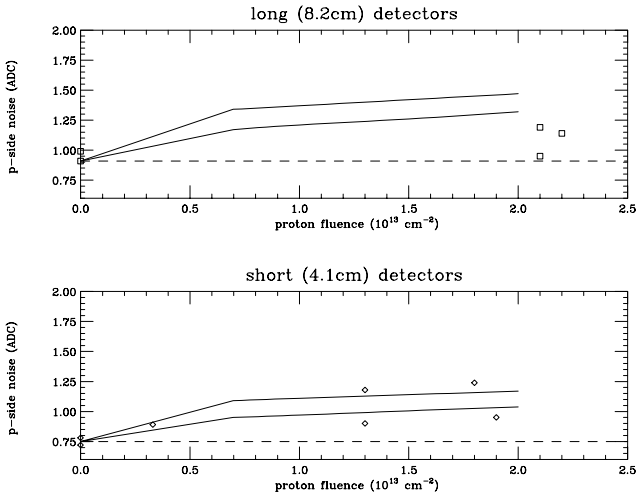

Figure 5.8: p-side noise versus average radiation dose for the 5 long and 7 short detectors. The solid lines in the figures indicate a range of expected noise as a function of dose. The dotted line indicates the average unirradiated noise value. None of the detectors were believed to have been inverted at the time of the measurements.

The signal, aside from clustering effects, is not expected to degrade with radiation dose. The data are consistent with this expectation. The S/N prior to irradiation was measured on average to be 10 on the p-side and 11.5 on the n-side. However, there was considerable variation in the p-side signal, so efforts are continuing to understand the p-side S/N.

5.2.5.4 Layer 0 and Layer 1 Replacement

It is anticipated that Layer 0 and possibly Layer 1 will need to be replaced after a delivered integrated luminosity of 2 or 3 fb^{-1}. This replacement could be silicon or a more radiation-hard device. Detectors based on chemical-vapor-deposition (CVD) diamond

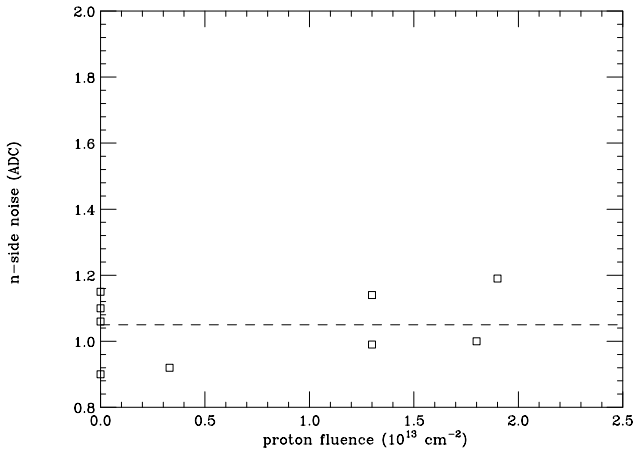

Figure 5.9: n-side noise versus radiation dose. The dotted line indicates the average unirradiated noise value. The irradiated n-side results are all of the short variety. None of the detectors were believed to have been inverted at the time of the measurements.

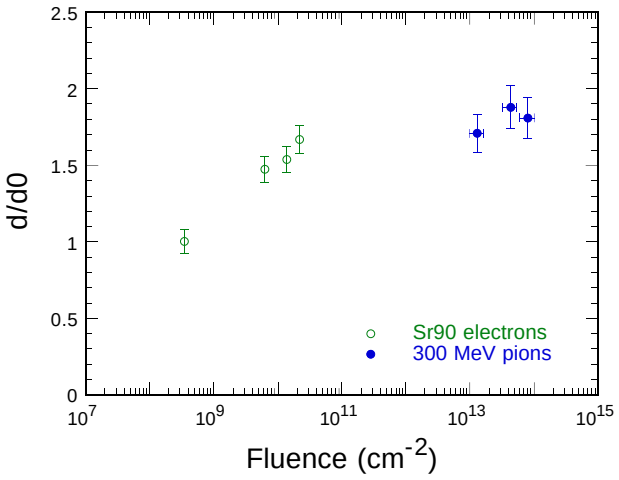

Figure 5.10: Charge collection in CVD diamond as a function of exposure to ^{90}Sr electrons and 300 MeV/c π^- relative to that of an unirradiated detector.

film rather than silicon offer a potential solution to this problem.

CVD diamond has numerous properties which make it attractive as a detection medium: it is highly electrically resistive, has high material strength, high thermal conductivity, low thermal expansion, and low density. The high electron and hole mobilities result in a very fast signal, on the order of 2 ns. Its stiff crystal lattice and low neutron transmutation cross section lead to extremely good radiation tolerance. Figure 5.10 shows, as an example, the relative signal size as a function of exposure to 300 MeV pions. No loss of signal appears after 10^{14} π^-/cm^2.

The main challenge in making CVD diamond-based detectors lies in the fact that electrons and holes travel only a certain distance in the crystal before being stopped by traps or lattice imperfections. This "collection distance" limits the size of the induced signal to a fraction of the deposited charge, which is 3600 e$^-$ per 100 μm thickness. The expected signal size is thus the ratio of the collection distance to 100 μm times 3600 e$^-$.

Collaboration with industry led to great improvements to CVD diamond quality, resulting in a CVD diamond calorimeter in 1993 [32]. Attention then turned to tracking detectors, and early in 1995 microstrip detectors made from CVD diamond wafers with collection distances in the range of 70-90 μm resulted on the pulse height and position resolution distributions shown in Fig. 5.11.

The goal in the near term is to obtain a 2 cm $\times$ 4 cm sample of the best possible quality, and test a microstrip detector made from it it in beam tests which commence late this fall. Construction of smaller prototypes with CDF SVX II electronics will begin in the mean time to gain experience.

5.2.5.5 Future Detector Testing at Fermilab

During the upcoming fixed target running period the SVX II detector groups will use the Fermilab Booster AP4 line for irradiating prototype detectors and the CDF test beam in Meson for detector studies. The Booster area has been used previously on at least a couple of occasions for irradiating single detector elements. The Booster cycles 8 GeV/c protons. One can achieve detector fluences well in excess of a Mrad in the course of a week by extracting a few percent of the normal 84 bunches. Most of the Booster protons are, of course, eventually delivered to fixed target areas.

The Meson Test line has historically been the site where CDF has conducted test beam studies during fixed target operations. The SVX II upgrade group intends to take full advantage of this facility, which is scheduled to commence operations starting in the fall of this year. A rotatable and translatable detector box is being prepared along with a set of "anchor plane" boxes, which will be fixed along the beamline. The primary focus of the silicon tests will be to study the detector ladders' response to negative pion beams (ranging from 100 to 200 GeV/c) as a function

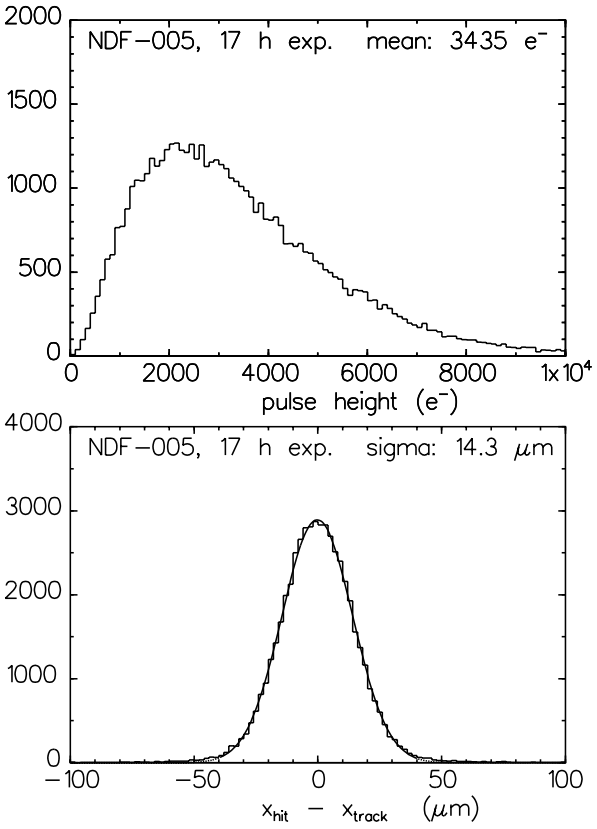

Figure 5.11: Pulse height in central three strips (above) and position resolution (below) for 50-micron-pitch CVD diamond microstrip detector.

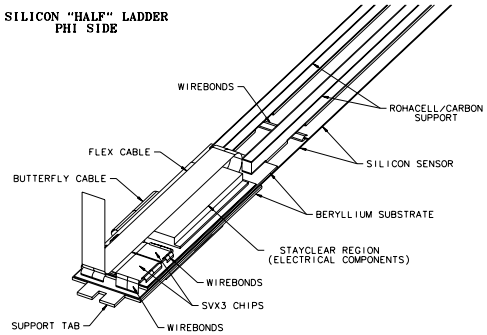

Figure 5.12: Perspective view of the ϕ-side of a Layer 0 ladder.

of the incident angle. The S/N, position resolution, cluster size, etc. will be of particular interest. The test beam activities will serve as an invaluable focus for the various sub-groups of the SVX II project, and results from test beam running will help refine detector design and construction techniques. It is also important to irradiate and beam test pilot versions of each detector type so that any future signal-to-noise degradation, due to long-term radiation damage, can at least be anticipated if not avoided.

5.3 Mechanical Design

5.3.1 Ladder Design

Shown in Figs. 5.12 and 5.13 are perspective views of a Layer 0 ladder. A notch on the ladder end is used during ladder construction and will precisely locate ladders relative to the support structure. The ϕ-side of the detector, i.e. the side with implant strips parallel to the beam line, is on the top of the ladder with the ϕ-side SVX3 chips directly opposite the cooling channel. This is the side shown in Fig. 5.12. The z-side SVX3 chips are on the underside of the ladder located inboard of the cooling channel. This this is the side shown in Fig. 5.13.

The SVX3 chips are mounted on hybrid integrated circuits. Two hybrid technologies are currently under consideration; copper on kapton thin film and BeO thick film (see Section 5.3.2). By the end of 1996 we expect to choose one of these two technologies. The hybrids are mounted directly on the surface of the

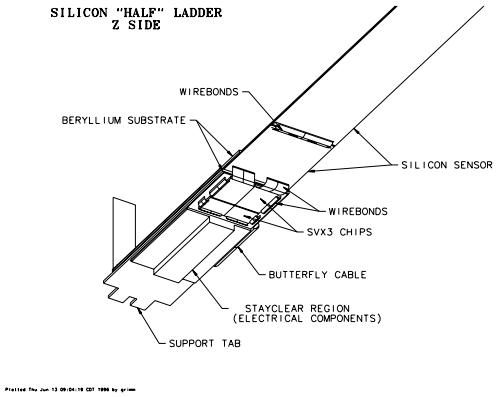

Figure 5.13: Perspective view of the z-side of a Layer 0 ladder.

silicon. The spacial requirements of the hybrid for passive components dictates the length of the hybrid, hence the location of the wirebonding pads on the z-side of the detector.

The thin film hybrids are mounted on beryllium substrates, chosen due to the structural integrity of beryllium, its thermal conductivity, and its favorable radiation length. The thickness of the substrate is chosen in order to adequately cool the z-side SVX3 chips. Cooling will be discussed in the next section.

The BeO hybrid can be designed in such a way that it requires less space for passive component placement than the thin film copper/kapton hybrid. For this reason, two rows of wirebond pads have been placed on the z-side of all detectors in order that the choice of technology may be delayed beyond the mask design of the silicon detectors.

The ladders will be constructed in halves, of length two crystals each. Once the ϕ-side hybrid is adhered to the surface, the second detector will be located precisely relative to the first and the two detectors will be wirebonded. After passing inspection the support rail will be adhered to the surface to make a single structure which can be flipped and the z-side completed.

The support rail itself is constructed of a mix of foam, epoxy, and fiber not unlike those used for SVX and SVX′. Fiber is adhered to Rohacell foam by applying an epoxy mix on the foam surface, and curing in a compression mold. The expansion coefficient of pure carbon fiber (as used in SVX and SVX′) is lower than that of silicon ($\approx$ 0 ppm/°C for carbon fiber vs. 2.6 ppm/°C for that of silicon) and could present structural bowing problems when the ladder is cooled to operating temperature. For this reason the rails will be constructed of a mix of carbon and boron fiber, which combined have an expansion coefficient equal to that of silicon [33]. The ladders will be joined in halves, once completed and tested, using an overlap joint in the ladder middle.

5.3.2 SVX II Readout Hybrid

The SVX II readout hybrid processes the detector signals into a format suitable for the port card. The hybrids are being developed in two technologies: (1) the high density flex circuit technology, and (2) the thick film (beryllia) technology. One of these will be chosen for the final detector depending upon the behavior of the prototypes. Associated with the readout hybrid is a cable that connects the power/signal functions from the hybrid to the port card. Hybrid prototypes which accommodate the SVX2 readout chip have already been fabricated using both technologies. The hybrids to read the SVX3 chip set have been designed and are being ordered. Their delivery time coincides with availability of the SVX3 chip.

5.3.2.1 Structure of the Flex Technology Hybrid and Cable

The hybrid and cable have both been fabricated using the multilayer flex technology. The hybrid has four layers of 10 μm Cu metal interconnect separated by three layers of 50 μm thick polyimide dielectric. This is covered with a top and bottom 'coverlay' dielectric. The coverlay provides 100% coverage of the ground planes on the back side of the hybrid. On the top side it has windows for the surface mounting of passive components and the wire bonding to SVX3 dies. The top layer metal includes Ni/Au layers to facilitate the surface mount soldering of passive components and the wire bonding to the readout dies. The signal line path and pitch are 100 μm and 200 μm, respectively. The layer to layer interconnect is provided by 150 μm diameter vias with 380 μm diameter connect pads. The minimum via pitch is 480 μm which gives a pad-pad gap of 100 μm. This is consistent with the signal line gap. The total thickness of the 4 layer hybrid is nominally $4*10+3*50+2*25 = 240$ μm, while the cable is nominally $2*10+1*50+2*25 = 120$ μm thick.

The hybrid and cable are designed to be separate parts which are surface soldered together during the assembly process. Identical arrays of via pads on both the cables and hybrids provide for interconnecting the cable and the hybrid. The SVX3 hybrid design, with differential paired readout signals, has 48 to 53 separate interconnections between the hybrid and the cable. The cable has fanout regions to the test connector field on one end and the hybrid/cable term field on the other end. The present cable design is $\approx$ 8000 μm wide between the fanouts.

The connection between the ϕ and z-side hybrids is a 'wrap' design. The ϕ and z-side hybrids are interconnected along their edges by a short 'wrap' cable, with the power cable connected to the end of the ϕ-side hybrid.

5.3.2.2 Beryllia Hybrid

Beryllia hybrid prototypes for the SVX2b chip and for the SVX3 chip set are being manufactured by two different vendors. They are constructed of thick film artwork printed on 95% beryllium oxide ceramic. This is a technology widely used for commercial chip-on-board assemblies. Both manufacturers use low temperature firing (800 °C) after the printing of each layer, but one vendor uses tape dielectric while the other vendor prints the dielectric as well as the metal layers. The minimum features on the artwork in both cases are 100 μm traces on 200 μm pitch, with 250 μm square vias for one vendor and 100 μm round via's for the other. These feature sizes are standard for these companies. Both hybrids consist of 6 interconnected gold ink layers, separated by dielectric, on top of the ceramic substrate. This is a standard ink for applications that require wire bonding. Additionally, there are palladium-gold ink pads on the top layer to permit soldering of surface mount components. Both vendors have manufactured parts with a larger number of layers. The total thickness of the printed material is less than 250 μm for the SVX2 hybrid. It will be 50% larger for the SVX3 prototypes, but can be special-ordered to be about 250 μm for production quantities.

Both hybrids are Layer 0 prototypes, which is to say that they contain 2 side-by-side chips. The width is determined by the ladder width, while the length is determined by the layout and component requirements. The length is 3.1 cm in the SVX2b case and 3.3 cm for SVX3. The SVX2 hybrid was not designed to minimize length, while the SVX3 was. Both hybrids have 2 rows of solder pads with 750 μm pitch on the end opposite the chips. This permits the soldering of a flexible circuit cable to connect the hybrid to the port card. Soldering of these test cables was found to be simple and reliable. Only one generic prototype SVX2 hybrid design was manufactured, with no special provision for interconnecting the ϕ and z-side hybrids on the ladder.

The SVX3 design is also a single layout, rather than separate ϕ and z- side designs. It includes a bonding pad field on one side to allow for the same hybrid to be used on the ϕ and z-sides of a ladder. The $\phi - z$ interconnection is accomplished via a custom thin film jumper which is glued to the side of the ladder. This jumper has not yet been prototyped, but a technology choice and prospective vendor have both been identified.

5.3.2.3 Test Results on Hybrids

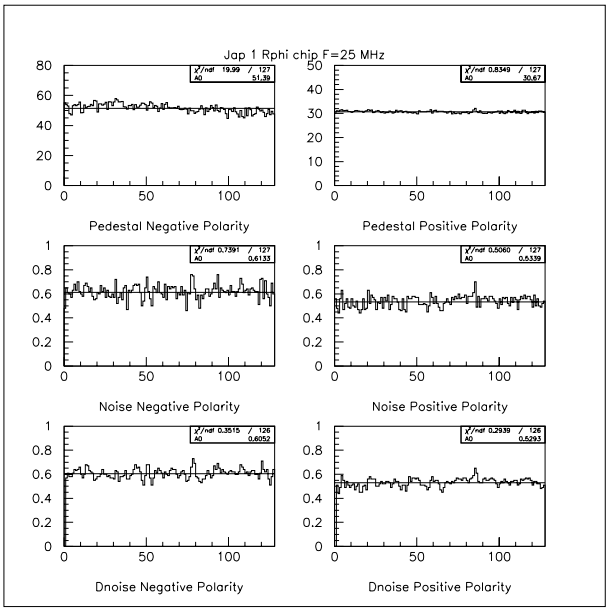

Figure 5.14: Hybrid Test Results: Pedestal and Noise Measurements.

Prototype hybrids equipped with SVX2 chips were tested using a prototype DAQ test stand. Noise, differential noise and chip gain were monitored for positive and negative input pulses. All of the measurements shown here were made with the SVX II DAQ system working at half speed (25 MHz). Future tests are planned at full speed (53 MHz). The test results show almost identical performance of both circuits.

ADC counts	J1	J2	US1	BeO
Ped. $r-\phi$	30.67	28.70	25.59	28.55
Ped. $r-z$	28.94	28.21	26.95	26.39
Noise $r-\phi$	0.53	0.57	0.58	0.53
Noise $r-z$	0.54	0.53	0.54	0.62
Dnoise $r-\phi$	0.53	0.56	0.59	0.48
Dnoise $r-z$	0.53	0.52	0.54	0.57

Table 5.6: Pedestal, Noise and Dnoise average values over 128 channels with chips configured in Positive Polarity

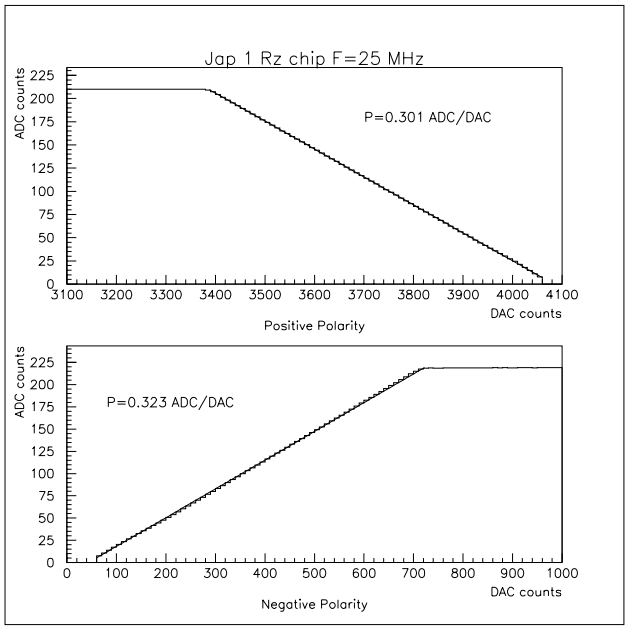

Figure 5.15: Hybrid Test Results: Linearity and Gain Check.

ADC counts	J1	J2	US1	BeO
Ped. $r-\phi$	51.39	55.10	50.40	56.02
Ped. $r-z$	54.20	57.97	53.97	57.18
Noise $r-\phi$	0.61	0.59	0.58	0.62
Noise $r-z$	0.58	0.59	0.59	0.63
Dnoise $r-\phi$	0.61	0.59	0.59	0.60
Dnoise $r-z$	0.58	0.59	0.57	0.62

Table 5.7: Pedestal, Noise and Dnoise average values over 128 channels with chips configured in Negative Polarity

	J1	J2	US1	BeO
Gain $(r-\phi)$ *+ Pol.*	4.49	4.57	4.54	4.48
Gain $(r-\phi)$ *- Pol.*	4.81	4.38	4.34	4.72
Gain $(r-z)$ *+ Pol.*	4.67	4.51	4.41	4.70
Gain $(r-z)$ *- Pol.*	4.61	4.58	4.47	4.57

Table 5.8: Hybrid gain measurements in ADC per fC for positive and negative polarity

The tests were done on four different hybrids: 3 flexible hybrids and 1 BeO. One of the flexible hybrids was made in the USA ("US1") and the other 2 were made in Japan ("J1" and "J2"). The noise, differential noise and the pedestal have been measured channel by channel. The gain for positive and negative polarity has been calculated for every chip on each test hybrid.

The noise for a given channel was defined as the RMS of the digital output for that channel. Because of the potential susceptibility of the system to external noise we also defined the "differential noise" for a given channel as $1/\sqrt{2}$ of the RMS of the difference between the output for that channel and the output of a neighboring channel. Typical results for the first chip of the J1 hybrid are shown in Fig. 5.14. Results for all of the hybrids are summarized in Table 5.6 and 5.7.

The internal calibration capacitor, which is implemented on the chip itself, is used to measure the gain. It is connected at the input of every single channel. A specific voltage is injected into this capacitance and the output is read out for those channels that have been pulsed. Figure 5.15 plots the channels' output after pedestal subtraction versus the input DAC counts (proportional to the injected calibration voltage). It shows that the output of the chip is lin-

ear with respect to the injected charge. The gain for individual channels has been measured and shows a variation of less than 2% within a chip. The results of the gain measurements for the 4 hybrids are summarized in Table 5.8.

5.3.3 Ladder Cabling

There are severe mechanical and electrical constraints for cables from the portcard to the ladder. The cables must have a negligible profile, both for assembly and for achieving a minimal barrel spacing. The cables must exit through the bulkhead, which constrains the width of the Layer 0 cable to less than 5 mm. The cables must make several very tight bends (radius $\sim$ 1.5 mm). Electrically, the principal issues are EMI and pulse shapes for the high speed clock and data lines. In addition, the cables carry a substantial amount of power. The total length for the longest (Layer 0) cable is about 25 cm.

The chosen technology is a conventional copper-kapton laminate flex cable. We have made a design of a prototype SVX3 cable, as shown in Fig. 5.16. This cable is made of two conducting layers of 0.5 oz copper (18 μm thick) and a 3 mil kapton dielectric layer. The signal traces are 100 μm on a 200 μm pitch. The power lines are made 700 μm wide to limit the IR drop to less than 100 mV. The width for this design is 8 mm, which is too wide for Layer 0. Our preferred solution to this Layer 0 problem is to split the cable into separate digital and analog cables. To limit the cable profile, the connector on the ladder will be a permanent (probably solder) connection; connections to the portcard will use a disconnectable technology.

The electrical issues related to cross talk, pulse shape, reflections, etc. were studied with prototypes and in simulation [34]. The cross talk was measured to be small for microstrips (signal lines over ground plane), and should be even smaller for broad-side coupled lines. Reflections were studied both in simulation and through prototype measurements. Acceptable digital pulse shapes were obtained. The remaining concerns were cross talk between neighboring cables and EMI picked up through detectors by the analog front end. For the SVXH3 chip we measured a 10 percent increase in noise from a nearby 53 MHz asynchronous clock driven differentially across two neighboring microstrip traces. While we expect the EMI from differentially driven, broad-side coupled lines to be reduced, this will be remeasured with SVX3 prototype cables.

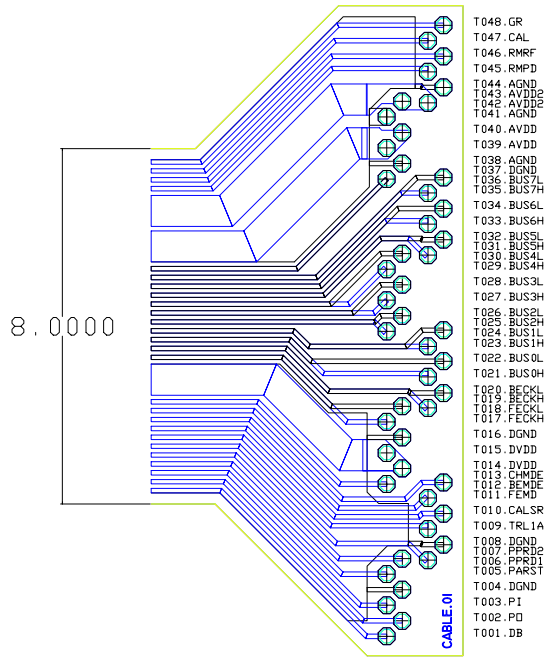

Figure 5.16: Prototype portcard-hybrid SVX3 flex cable. Total width of the cable is 8 mm. There are separate analog and digital ground planes. The data lines are broad-side coupled pairs of 100 μm (4 mil) traces on 200 μm pitch.

5.3.4 Bulkhead

The ladders are positioned between two intricately machined bulkheads. These bulkheads support the ladders at each end and serve as a heat sink for the electrical components mounted on the ends of the ladders. They establish the precision of the barrel assembly and, therefore, must be machined to very close tolerances. Beryllium is used because of its long radiation length and high stiffness. The bulkheads have integrated cooling channels through which the coolant is circulated at approximately -5 °C.

5.3.4.1 Baseline Bulkhead Design

The bulkhead geometry consists of 5 layers. Each layer is a 12 sided ring with flat faces corresponding to the 12 wedges of the detector. The layers are connected by 6 radial spokes that extend from the inner most layer to an outer ring. Ladders are mounted on

flat surfaces of each layer, called ledges. Ledges of adjacent wedges are at different radii determined by balancing the requirements for detector overlap and clearance for ladder installation. Ladders are positioned by pins which are installed through notches in each end of the ladder and matching notches in the bulkheads.

Cooling channels are machined directly into the bulkhead. Each layer has an independent cooling channel. The cooling channels are formed by gluing L-shaped covers to each layer of the bulkhead to form a 1 mm $\times$ 8 mm rectangular channel. The design provides close proximity of the ladder mounting surface to the cooling fluid. The fluid is distributed to each layer by aluminum tubes which run radially to each layer and are positioned in line with the bulkhead spokes so not to interfere with ladder installation.

In order to allow possible replacement of the inner two layers, the bulkhead assembly will be constructed of two parts, with the inner two layers separate from the outer three layers. This feature will allow for removal and replacement of the inner two layers of detectors part way through collider Run II without requiring complete disassembly of the entire barrel. The inner sections will be attached to the outer section with pins and splice plates that lie along the radial spokes.

During ladder installation into the barrel the bulkheads will be supported in a rotating fixture similar to that used for construction of SVX and SVX′. After ladder assembly is complete an outer screen will be slid over the barrel and attached to the outer ring of each bulkhead at 6 locations. Mounting blocks of the kinematic support system that will position the barrel in the spaceframe will also attach to the outer ring. The screen and support mounting blocks will be machined beryllium blocks that are glued with epoxy to the bulkhead outer ring.

5.3.4.2 Bulkhead Prototype Tests

One beryllium prototype bulkhead and two aluminum prototype bulkheads have been constructed for an earlier four layer design. Except for the fifth layer these prototypes are very similar to the baseline design. A number of tests have been conducted using these prototypes.

- The beryllium bulkhead was inspected on a coordinate measurement machine to compare the actual dimensions to the drawing specifications.
- A test was conducted on a prototype of the pin joint to be used to connect the inner bulkhead section to the outer section. The joint was reassembled several times and provided repeatable location of two parts within 3 μm.
- One aluminum prototype was used to measure pressure drops in the cooling channels. It was determined that the pressure drop will be acceptable for the flow rate required for a ΔT of 1.5°C of the cooling fluid from inlet to outlet. The measurements were made for pure water and for a 30% ethylene glycol/water mixture.
- Two candidate epoxies have been selected for gluing the covers to the cooling channels. Tests are under way to study the effects on the epoxies from long term exposure to the cooling fluids. Cyclic heating/cooling tests are also under way on cooling channel prototypes and the prototype beryllium bulkhead.

5.3.5 Spaceframe Specifications

The alignment of the SVX II barrels with respect to the beam axis is critical for the proper operation of the SVT. Studies indicate that the axis of the barrels must be aligned to within a slope of ± 100 μrad relative to the beam axis, corresponding to a placement of ± 25 μm from end-to-end along a barrel. To achieve such tight tolerances, the barrels will be mounted into a rigid spaceframe using high precision coordinate measurement machines to monitor and adjust the barrel position. The frame will then maintain the precise barrel alignment after the assembly is removed from the measurement platform.

The full mounting requirements for the barrels are:

1. slope within ± 100 μrad of nominal,
2. transverse position within ± 250 μm, and
3. longitudinal position within ± 1 mm.

These values include internal mis-alignments. The spaceframe and mounting specifications then follow.

1. The deflections under full load must be stable and repeatable to ± 10 μm before, during and after installation into the ISL.
2. The transverse barrel translation error must be less than ± 250 μm.

3. The longitudinal barrel translation error must be less than ± 1 mm.

4. The thermal stability must be better than ± 10 μm over a 25° C range.

5. The spaceframe should be of minimum mass.

6. The thermal resistance should be equal to 0.5 cm of foam, equivalent.

7. The torsional deflection due to variations in the strain from the cable, cooling pipe and other asymmetric loads should be less than 10 μm at the mounting points of the detector.

Because it is likely that the overall deflection of the spaceframe will be much larger than 10 μm, the frame will probably be pre-loaded during barrel installation. The barrel mounts will be adjustable at the level of 10 μm. Consequently, there must be accessibility to these adjustment points as well as to the cables and cooling pipes.

5.3.5.1 Baseline Mechanical Design of the Spaceframe

The main structural element of the spaceframe is a 1.4 m long, carbon fiber composite cylinder that contains the barrels. This geometry provides exceptional stiffness with a minimum of material. The cylinder consists of two, 300 μm thick carbon fiber skins separated by a 1 cm thick layer of polymethacrylimide foam. Each carbon fiber skin is made of three layers of epoxy-empregnated carbon fibers, with the fibers in each oriented for maximum strength. The tube is kinematically supported at the ends by the ISL (see Section 6.2.6). Carbon-fiber rings at the ends of the cylinder and other strategically located positions will prevent deformation of the cylindrical cross section under load.

Initially, the spaceframe is constructed as two, independent half-cylinders. The barrels and associated cables and cooling tubes will be mounted into the lower half-cylinder. This open geometry allows full access to the interior of the cylinder for the purpose of surveying and adjusting barrel positions. Once barrels are installed, the top half-cylinder will be bonded to the lower half-cylinder. In order to preserve the precise alignment of the barrels, this procedure may introduce no significant internal stresses. Experience with similar problems in constructing the SVX and SVX′ detectors suggests that this issue is easily solved using common construction techniques.

The barrels are kinematically mounted inside the spaceframe. Mounting blocks connected directly to the beryllium bulkheads transfer the barrel loads to a corresponding set of blocks located on the interior surface of the spaceframe. Carbon fiber ribs inside the spaceframe at these locations distribute this load over the surface of the frame. The initial positions of the blocks on the spaceframe will be set by fixturing to a precision better than 50 μm. The final position will be adjustable over a range of ± 0.5 mm.

The radius of the outermost layer of the bulkhead is expected to decrease by about 20 μm as the bulkhead cools from room temperature to its operating temperature. A judicious choice for the configuration of the mounting blocks can significantly reduce the effect of this contraction on the barrel alignment, and obviate the need to compensate the barrel alignment for thermal contraction of the bulkhead.

5.3.5.2 Barrel and Spaceframe Installation

Barrel installation will occur on a precision coordinate measurement machine. Fiducial markers on each barrel will allow the position of the internal barrel axis to be measured without direct reference to the silicon strips. Similar markers on the frame will characterize the position of the spaceframe. Once the barrels are mounted, the barrel references will be transferred to these frame markers so that the barrels can be aligned with external detectors.

The assembly of the barrels into the spaceframe takes several steps. Each barrel will be placed into the pre-loaded half-cylinder in an order dictated by the cable and cooling pipe layouts, etc., and then coarsely adjusted to some nominal position. After all of the barrels are installed, the cables and cooling pipes will be arranged into their final configurations. With the full load to the spaceframe now fixed, the final adjustment of the barrel positions proceeds. Once the final checks of the alignment are completed, the top half-cylinder is bonded to the lower half, and the end rings installed and glued in place.

After the cylinder is closed, the assembly will be mounted to a transfer fixture that will guide the frame through the ISL. The beam pipe is then threaded through the SVX II and attached to the spaceframe and transfer fixture. Once the detec-

tor is installed inside the ISL, the pipe will be rigidly attached to the ISL support cylinder at several places. By carefully over-constraining the pipe, we can greatly reduce the amplitude of oscillations at the middle of the pipe induced by jarring the pipe near its ends. The pipe mounts on the SVX II spaceframe will then serve only as deflection limiters.

5.3.5.3 Alignment with the Beam Axis

After the installation into the CDF central detector is complete, the position of SVX II will be adjusted by moving the combined SVX/ISL assembly. The initial position of the detectors will be determined and adjusted by referencing the fiducial markers on the ISL and SVX II with markers on the quadrupoles in B0. This alignment should place the detector within 1-2 mm of the correct position. Final adjustment of the detector's position is performed using CDF $p\overline{p}$ data to determine the position of the $p\overline{p}$ beams relative to the SVX II detector and then by moving the detector. It is possible that steering of the Tevatron beams can provide this final alignment instead of moving the SVX II. In either case, $p\overline{p}$ beam steering will certainly be used to maintain the position and alignment of the beams between and during stores so that adjustments in the SVX II detector's position should be needed only rarely. Beam steering is discussed in more detail in Sec. 5.9.2.

5.3.6 Cooling and Gas Systems

5.3.6.1 Ladder Cooling

Thin film copper on kapton hybrids mounted to a beryllium substrate are currently considered the baseline design, so the focus of the cooling analysis has been on this technology. A full thermal analysis of the CDF SVX II detector, assuming copper on kapton hybrids mounted on beryllium substrates, can be found in references [35, 36].

Two guidelines have been imposed which drive the design of the ladder from a cooling perspective:

- The silicon should be under 10 °C for nominal operating conditions.
- Thermal runaway does not occur in the innermost layer at the maximum expected chip power dissipation for 2 fb^{-1} of integrated luminosity.

A two dimensional finite difference cooling model has been constructed of a ladder. A one mm wide slice ladder is modeled with all proper scaling to represent the total 3 barrel, 5 layer detector. Nominal operating conditions are determined by the expected chip power dissipation under normal conditions; 300 mW per SVX3 front and back end chip pair. The maximum permissible chip power dissipation is 500 mW per SVX3 chip pair.

The ladder modeling has been broken up into two separate models in order to simplify the solution. First, the conduction region of the ladder is that region from the ladder end at the cooling channel, inboard to the end of the beryllium substrates. The silicon temperature profile is dictated in this region by SVX3 power dissipation, the coolant temperature, and the hybrid substrate thermal resistance (which is inversely proportional to the substrate thermal conductivity and the thickness).

The region inboard of the substrates to the ladder center is composed (in the thermal model) of only silicon, with a gap at the quarter points where there are only wirebonds. The temperature profile of the silicon in this region is dominated by convection. Conduction is inhibited in this region due to the low conduction area of the wirebonds at the ladder quarter points, and the thin silicon detector (300 μm) along the ladder length. It is this region which is heavily affected by external heat loads (such as high power dissipation in the signal cables or poor insulation between the detector region and the surrounding environment), high SVX3 chip temperatures, and internal power dissipation in the silicon due to high radiation damage.

Radiation damage in silicon detectors will result not only in a higher required bias voltage, but also a higher leakage current [4, 20]. The leakage current is temperature dependent, so potentially leads to the condition of thermal runaway in the ladders. Thermal runaway occurs when the internal (temperature dependent) heat generation within the silicon exceeds the heat removal rate by conduction and convection. The effect increases with radiation dose. Hence L0 is the most susceptible to thermal runaway. This effect has been observed experimentally [37] and the measurements have been successfully simulated in a test stand [37, 38]. Analytical approximations to thermal runaway have been provided in [39], some of which have been simulated using the finite difference technique [38].

The baseline temperature profile of the ladders, at the start of the run, is shown in Fig. 5.17. The tem-

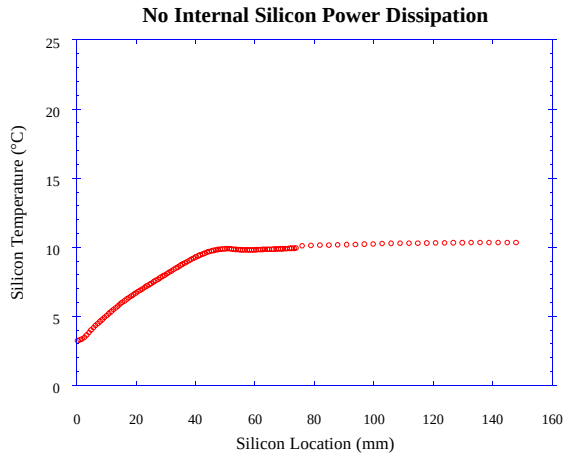

Figure 5.17: Baseline silicon temperature profile at the start of Run II.

perature increases along the conduction region from 3 °C near the cooling channel to 10 °C at the end of the conduction region. The temperature beyond the conduction region remains at 10 °C, due to the assumed insulation between the surrounding environment and the silicon region. These temperatures in the ladder are obtained by providing coolant to the bulkhead sufficient to keep the support ledge on which the ladders rest at 0 °C.

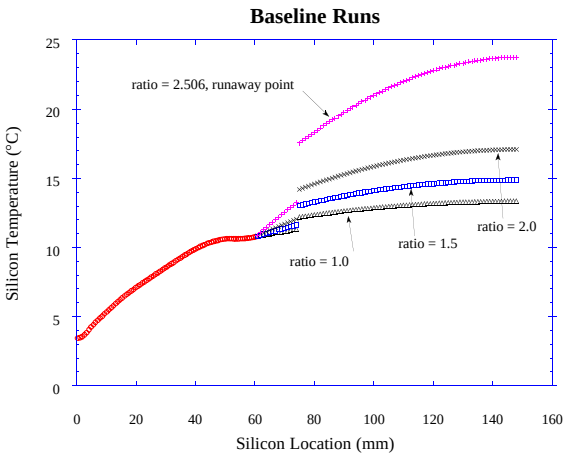

Figure 5.18: Silicon temperature profile after varying degrees of radiation damage assuming 300 mW SVX3 chip power dissipation.

When considering radiation damage, the temperature profile in the conduction region is determined to be essentially constant for variations in the power dissipation within the silicon. The convection region temperature profile varies widely as a function of the assumed level of radiation damage. Applying an upper limit for the bias voltage of 150 V at the end of the run with approximately 1 Mrad radiation damage [4], the leakage current at 0 °C is calculated using the method described in reference [20]. The temperature dependence of the leakage current is calculated on a per-node basis in the finite difference code. The expected temperature profile is shown in Fig. 5.18 at the value of "ratio" equal to 1.0. The power dissipated within the silicon is directly proportional to the integrated luminosity, the damage coefficient, and the applied bias voltage. For this reason other solutions of the temperature profile are determined by applying a multiplication factor to the leakage current at 0 °C, represented in Fig. 5.18 by other curves with differing values of ratio, which allows simple extrapolation to other conditions.

The temperature profile shown for ratio equal to 1.0 is the expected temperature profile at the end of Run II. Thermal runway occurs above the value of 2.506, which in some ways represents a safety factor against thermal runaway in the inner ladders of the SVX II.

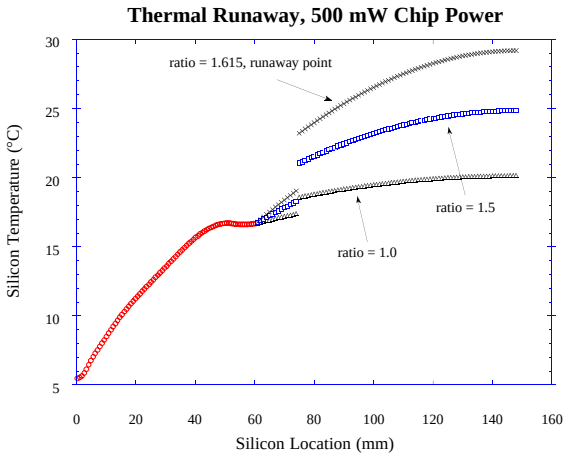

Figure 5.19: Silicon temperature profile with varying degrees of radiation damage assuming 500 mW SVX3 chip power dissipation.

In order to satisfy all design requirements, the temperature profile under higher SVX3 chip power is considered. Applying the same principles as for Fig. 5.18 above, the SVX3 chip power was increased to 500 mW (300 mW was used for Fig. 5.18). Figure 5.19

Ladders	Heat load/ ladder (W)	Ladders / barrel	Heat load/ barrel (W)
Layer 0	2.4	12	28.8
Layer 1	3.6	12	43.2
Layer 2	6.0	12	72.0
Layer 3	6.0	12	72.0
Layer 4	8.4	12	100.8
Total			316.8
Portcards	Heat load/ portcard (W)	Portcards/ barrel	Heat load/ barrel (W)
	12	24	288
Detector Total (W)			1814.4

Table 5.9: SVX II Detector Heat Load

shows the expected silicon temperature profile using the 0 °C support channel assumption as for Fig. 5.18. Although thermal runaway does not occur for the nominal operating conditions after 1 Mrad radiation damage (corresponds to ratio equal to 1.0), the level of safety against thermal runaway is somewhat diminished from the factor of 2.506 as stated above to 1.615 as shown in Fig. 5.19.

The heat load from the detector electronics is summarized in Table 5.9. The majority of the heat will be removed by a water mixture cooling system. A very small amount of heat will be removed by a nitrogen flow through the detector.

A flow rate of 287 g/s will be required to limit the rise in coolant temperature to 1.5 °C for the bulkhead cooling channels and 2.0 °C for the portcard cooling loops with a 30% ethylene glycol/water mixture. To prevent coolant from leaking into the detector, if a leak does occur, the system will be operated under a partial vacuum so that the system pressure in the cooling lines throughout the detector is less than 1 atmosphere.

The system will consists of a recirculating chiller, reservoir, deionizer, flow control and vacuum pump. The general design and operation of the system will be similar to the system for SVX and SVX′. Most components will be scaled in size or capacity for the higher cooling and flow requirements.

The present design provides for separate manifolds to distribute coolant for bulkhead and portcard cooling. Separate manifolds will allow the more critical flow to the bulkheads to be balanced more accurately. The insulated supply and return lines will pass through the 3 degree cone of the modified end plug. The supply and return lines will feed from one end of the spaceframe to simplify spaceframe installation into the ISL. The manifolds that distribute the coolant to the bulkheads and portcard loops will be located along the top half of the space frame to allow access to make connections during barrel installation into the spaceframe. Connections between the manifold and bulkheads will be made with flexible tubing to eliminate the possibility of transmitting loads that may affect barrel alignment.

The gas system for the detector will provide a constant gas flow of nitrogen at 20 SCFH to the barrels. The gas will be introduced to the detector at a temperature 10 °C cooler than the average gas temperature in the detector. The design of the gas cooling system has not begun but a similar system was designed for SVX and SVX′. The system will probably employ a small heat exchanger between the inlet gas and the outlet coolant lines of the portcard cooling. The gas supply will be monitored to prevent impurities from entering the system.

5.4 SVX II Frontend Electronics

The SVX II frontend electronics consists of a pair of radiation hardened CMOS custom integrated circuits which are mounted on the ladder hybrids. These chips are controlled over a high density copper cable through so-called "Port Cards". The hybrids have been discussed in Sec. 5.3.2, the readout chips and the Port Card are described below. The rest of the data acquisition electronics is discussed in Sec. 5.5.

5.4.1 The SVX3 Readout Chips

The silicon signals are readout by onboard, radiation hardened CMOS integrated circuits called SVX3FE and SVX3BE. Each chip set has 128 parallel input channels. The SVX3FE chip contains the input amplifier and integrator, the variable length pipeline and the logic necessary to handle pipeline and buffer control functions. Any four cells of the pipeline can be set to hold data awaiting readout. The SVX3BE chip

contains a Wilkinson ADC, a readout FIFO, and differential output current drivers [15, 5]. The chips are mounted in tandem on the hybrids.

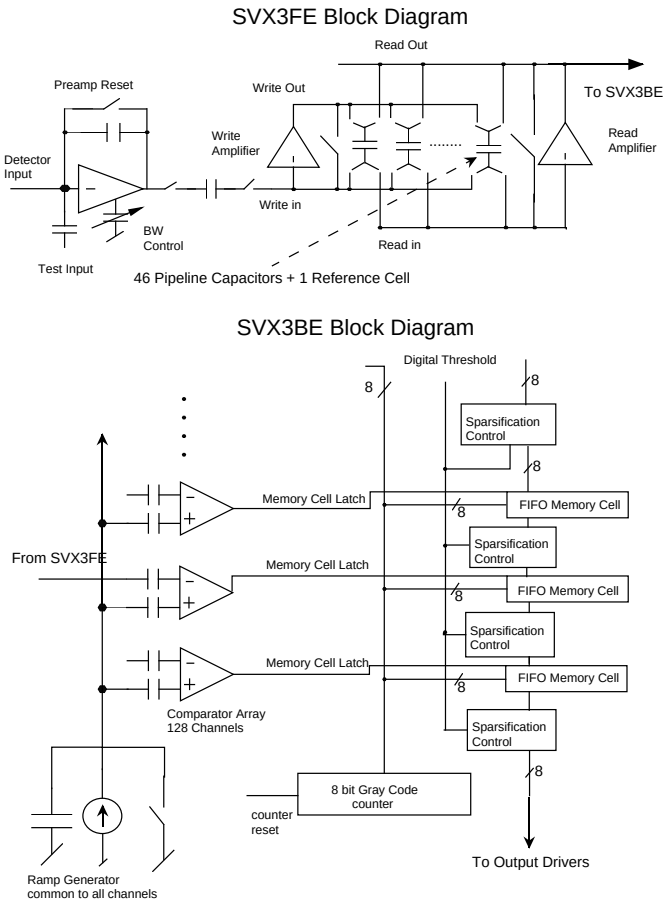

Figure 5.20: A block diagram of the SVX3 chip set.

Figure 5.20 is a block diagram showing the functionality of the SVX3 chip set. The analog SVX3FE chip contains the integrator and dual-ported pipeline while the digital SVX3BE chip houses the ADC (comparator, ramp, and counter), the sparsification logic, data FIFO, and the output drivers (not shown). This block diagram shows only one channel of the chip.

The SVX3FE has two gain stages. The first stage is a charge-to-voltage amplifier with a large dynamic range. The switch across the feedback capacitor resets the front end integrator. This is only done during abort gaps. Approximately 1.6 μs is required for both reset and settling time of this amplifier. The preamplifier gain is specified to be 5.0 mV/fC. The rise time is bandwidth dependent and adjustable (see below), but a 10-90% rise time of 60 ns with an input capacitance of 30 pF is achievable. The integrator's dynamic range is 450fC for unipolar operation.

During SVX3FE initialization, one has the option of switching extra capacitors into the node associated with the dominant pole of the amplifier. This provides control of the integrator's bandwidth and is used to optimize the chip set for the different input capacitances expected on the r-ϕ and r-z sides of the SVX II detector for a range of integration times down to 100 ns.

The second analog stage is another integrating amplifier with a 46 cell pipeline of capacitors in its feedback loop. This amplifier writes the data to the appropriate cell by selecting one and only one of the capacitors as a feedback element. Only the difference in integrated charge from before and after a beam crossing is placed in the pipeline. This allows the second analog stage to have a smaller dynamic range. The gain for the second stage is 3.0 V/V for a total gain of 15 mV/fC or approximately 60 mV/MIP.

The pipeline cell is reset just prior to a beam crossing. A reset time of 25 ns is required. The pipeline must hold the data long enough for a Level 1 trigger to arrive in order that the analog data can be flagged for eventual digitization and readout. The pipeline depth can be set to a maximum of 42 cells. At 132 ns between beam crossings this corresponds to a maximum delay of 5.5 μs. If a Level 1 trigger does not arrive in this time, the cell is overwritten.

If a Level 1 trigger does arrive, a pointer at the correct pipeline depth is set and that cell is bypassed by subsequent pipeline write operations until the analog information contained in the cell is digitized and read out. These bypassed cells are digitized and read out in the order in which Level 1 triggers are received by a unity gain read amplifier which feeds a comparator on the SVX3BE chip. By having four extra cells to hold data for later processing, and by being able to continue to write analog data into pipeline cells while bypassed cells are being digitized and readout, the SVX3 chip set is capable of operating with very little deadtime for Level 1 trigger rates up to 50 kHz.

Figure 5.21 shows a simplified block diagram of the SVX3FE pipeline controller. There are a total of 46 capacitors available in the pipeline for each of the 128 inputs. Up to 4 groups of cells can be queued for digitization and readout at one time.

A central element in the controller is the write pointer shift register. It consists of a ring of flip-flops which pass a token in response to a beam cross-

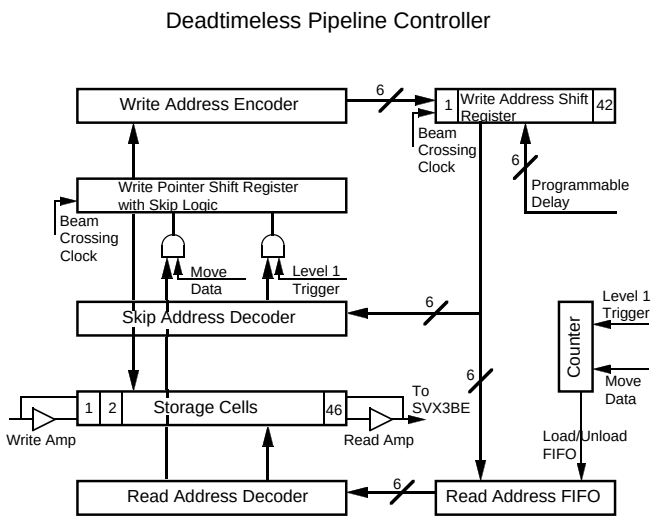

Figure 5.21: Simplified block diagram of the SVX3FE pipeline controller showing the buffering and skip logic architecture required for deadtimeless readout.

ing clock which is synchronized to the collider. Each flip-flop points to a set of 128 capacitor storage cells corresponding to the 128 independent input channels. The flip-flop which has the token causes the 128 pipeline write amplifiers to store the difference in integrated charge before and after the beam crossing in one particular set of the 46 groups of storage cells.

The 6-bit address of the set of cells corresponding to the token's position is passed by the write address encoder to a 6-bit 42 cell shift register and is shifted along from cell to cell once each beam crossing. At the time the chip is initialized a fixed delay from 1 to 42 beam crossings is set into its logic. This establish the Level 1 trigger latency. After the programmed number of crossings has occurred, the write address is shifted back out of the write address shift register and is passed to both the read address FIFO and the skip address decoder. If this occurs in coincidence with the arrival of a Level 1 trigger, then the write address is saved by the read address FIFO and is immediately acted on by the skip address decoder; otherwise, it is ignored. If it is ignored, then those pipeline storage cells referenced by the write address are available to be cleared and overwritten by analog data from subsequent beam crossings.

If a Level 1 trigger did occur, the skip address decoder immediately sets a bypass condition on the appropriate flip-flop in the write pointer shift register. This means that the token will be passed over this flip-flop and the corresponding pipeline storage cells cannot be overwritten by the write amplifiers. Hence, this analog data is saved for later transfer to the SVX3BE chip for digitization and readout.

The Level 1 trigger increments a counter which in turn causes the next available cell in the four cell read address FIFO to be loaded. The oldest address in the read address FIFO, if any, is always available to the read address decoder. When instructed by commands coming from the SVX3BE chip, the read address decoder causes the read amplifiers to pass the analog data from the appropriate group of capacitor storage cells to the comparators on the SVX3BE chip for digitization and readout.

Once the data has been digitized, the 128 pipeline cells associated with this event can be returned to the pipeline for further use. This is accomplished by a signal called "move data" coming from the SVX3BE chip. The signal is used in coincidence with the decoded address from the read address decoder to remove the bypass condition on the appropriate flip-flop in the write pointer shift register. Move data is also use to decrement the counter which effectively removes the oldest address in the read address FIFO.

The block diagram for the SVX3BE chip shown in Fig. 5.20 starts with the array of 128 comparators which are part of a Wilkinson ADC. This ADC simultaneously digitizes the analog voltages presented by the read amplifiers on the SVX3FE chip.

When digitization begins, the proper cell in the pipeline is compared to a voltage ramp generated by a capacitor connected to a current source. The size of the current is fixed by the value of a resistor external to the chip. The ramp voltage rises linearly as a Gray code counter counts cycles on both the rising and falling edges of a 53 MHz clock. The ramp voltage exceeds the read amplifier output voltage at some point and the comparator turns on, latching the counter's current value into the sparsification FIFO. This digital number is proportional to the charge collected for that event. The maximum count is 255, but CDF intends to use only 7 bits which requires 1.2 μs for the complete digitization cycle.

The SVX3BE chip can be configured to read out either all channels, only channels above a user defined threshold, or channels above threshold and their nearest neighbors. In normal operation the digital

SVX3BE chip sparsifies the data, keeping the data only from channels which are above a preset threshold and their nearest neighbors. After digitization at least 500ns is required for sparsification before readout can begin. During readout the data is presented on an 8-bit differential I/O bus. The data are read out on both the high and low levels of a 50% duty cycle 26.5 MHz clock.

Before the readout starts, the I/O bus is acting as an input to the chips and the chips are tri-stated. During readout, a "priority-in" (PI) pad on the first chip of a bus is set high, and it begins to download its data. When that chip finishes, it sends a "priority-out" (PO) pin high which is connected to the PI of the next chip. The last chip on a bus can be set to always readout channel 127. This provides a marker indicating the end of the readout of that bus. Because of sparsification, the actual readout time is highly dependent on the occupancy of the detector. Current estimates based on Monte Carlo studies indicate that the complete readout of a bus will take approximately 10 μs. The first 5-6 μs if for digitization and readout of the r-ϕ side of the detector, and the remaining time is for readout of the r-z side.

5.4.2 SVX 3 Port Card

The Port Card (PC) interfaces with the Fiber Interface Board (FIB) and with the hybrid containing several (4–14) SVX3 chip sets. Most of the communication of the PC is with the SVX3BE chip, while the SVX3FE connects directly to the silicon strip detectors. A schematic diagram of the PC is shown in Fig. 5.22. The basic features of the PC are as follows:

- Connects to five layers of SVX3 chips by means of the high density interconnects (HDI's).
- Initializes, controls and reads out the SVX3 chips through the HDI's.
- Provides regulated power supplies for the analog section of the SVX3 chips through the HDI's.
- Implements two digital-to-analog converters (DAC's) to generate the calibration voltages for the ϕ and z-sides of the silicon detector.
- Implements the PC Decoder, which interfaces with the FIB and decodes commands to the SVX3 chips.
- Forwards the Level 1 Accept (L1A) control signal to the SVX3 chips.
- Selects the appropriate HDI to download the initialization bit stream during SVX3 chip initialization.
- Transmits SVX3 event data (BUS[0:7]) with associated Odd Byte Data Valid strobe (OBDV) to the FIB.
- Buffers the front end clock (FECLK) and back end clock (BECLK) to the SVX3 chips.

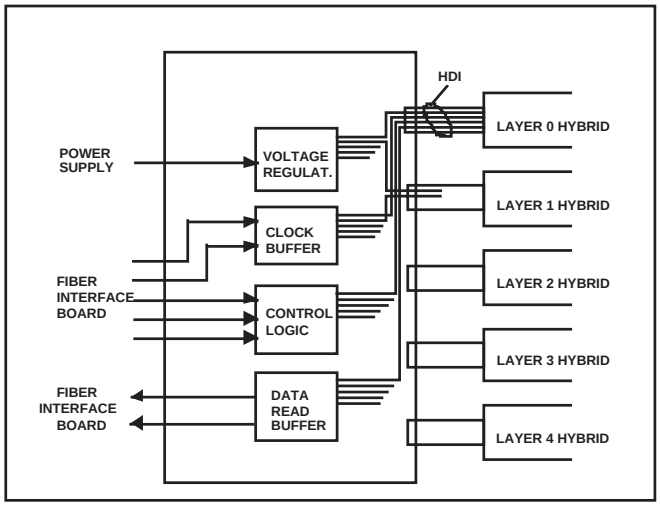

Figure 5.22: Schematic of SVX II Portcard.

5.4.2.1 Cabling

Data from the detector will travel over optical fibers while control signals, power and bias (high) voltage will travel over conventional copper lines. There are 11 differential control signals per PC, one of which is a 53 MHz clock while the other is a beam crossing clock. Each ladder will have an independent bias voltage and three power voltages. In addition, the PC requires 4 separate voltages. The complete cable scheme is not yet designed, but will tend to follow the SVX scheme whereby inside the detector conventional cables will connect at some point to a lower mass, copper-kapton flex cable.

We have estimated the amount of space required to cable SVX II. The low voltages will require 19 AWG 20 pairs per wedge, and the bias voltage will require 10 coax cables per wedge. These connections are in addition to 11 signal twisted pairs plus 5 optic fiber

ribbons, possibly bundled within a single protective coating. We expect 45-50 slots of the 125 available slots on one side will be needed.

5.4.2.2 Power Supply Regulators

Analog voltages (2) for the operation of the SVX3 chip are brought in from the power supplies and separated and controlled for each layer by series voltage regulators. The digital supply voltage is controlled by the external power supply.

5.4.2.3 Digital Control

The control lines from the Fiber Interface Board (FIB) that determine the operating mode (initialization, digitization or readout) are set and reset by individual commands via 5 control lines (C0 – C4), a direction signal (DIR), and a strobe clock; the maximum rate for the strobe is 26 MHz. All control signals are transmitted from the FIB to the PC as differential signals. Fanout of the command lines to the hybrids are single ended (TTL) for some and differential (PECL) for others. Enable logic in the control logic block allows individual control for each layer, i.e. commands can be fanned out to any one layer or several layers simultaneously.

5.4.2.4 Clock Buffering

The two clocks necessary for the proper operation of the SVX3 chips are the front end clock (FECLK) and the back end clock (BECLK). These clock signals come from the FIB in differential format, are buffered on board and repeated to each hybrid in differential format. The maximum frequency for the BE clock is 53 MHz. Except during initialization, the FE clock is the beam crossing clock. The single ended (TTL) asynchronous Level 1 Accept signal (L1A) is also buffered on the port card.

5.4.2.5 Data Readback

Data is read back on 8 differential data lines and a data valid signal (OBDV) from each hybrid. The signals are buffered and transmitted over a 9 bit wide fiber optic link (DOIM) to the FIB at a maximum rate of 53 Mbytes/s. During idle times this driver is disabled.

5.4.2.6 Calibration Voltage

A D/A converter in the control logic provides a calibration voltage in 2 ranges (0–0.5 V and 4.5–5.0 V) at a 5 bit resolution. Setting of this D/A is through the digital control by the FIB.

5.4.2.7 Port Card Construction

The PC circuitry will be packaged on a multilayer thick film board on beryllia substrate. Because even at the outer radius of the SVX II a fluence of nearly 300 kRad is anticipated during the lifetime of the detector, the PC components must be radiation hard. All logic functions will be performed in 5 identical multi-function ASIC's (one per layer). Additionally the receiver necessary to buffer the control signals reaching the PC must also be radiation hard ASIC's. Ten voltage regulators per PC will be implemented using control circuitry inside the the multi-function ASIC's together with Darlington pairs of commercial power transistors. These transistors have been shown to withstand the expected radiation dose.

5.5 SVX Data Acquisition

5.5.1 Dense Optical Interface Module

The dense optical interface module (DOIM) is the data link between PC and the FIB. It is a fiber optic transmission/receiver system that incorporates electrical and optical components integrated into densely packaged modules. The transmitter and receiver modules are connected with ribbon fiber that carry 8 data bits and a clock in parallel to the FIB. Below we will discuss the system requirements, characteristics and functioning of the DOIM.

5.5.1.1 System Requirements

Five DOIM transmitters are mounted on each PC. The total number of DOIM's for the 3 barrels is 360. The same number of receivers are located on the FIB's. Some of the system requirements are as follows:

1. Provide the path for 8 data bits and a clock.
2. The physical size should be as small as possible to fit into a very densely packed PC.
3. The power consumption should be small to reduce the burden on the cooling system.

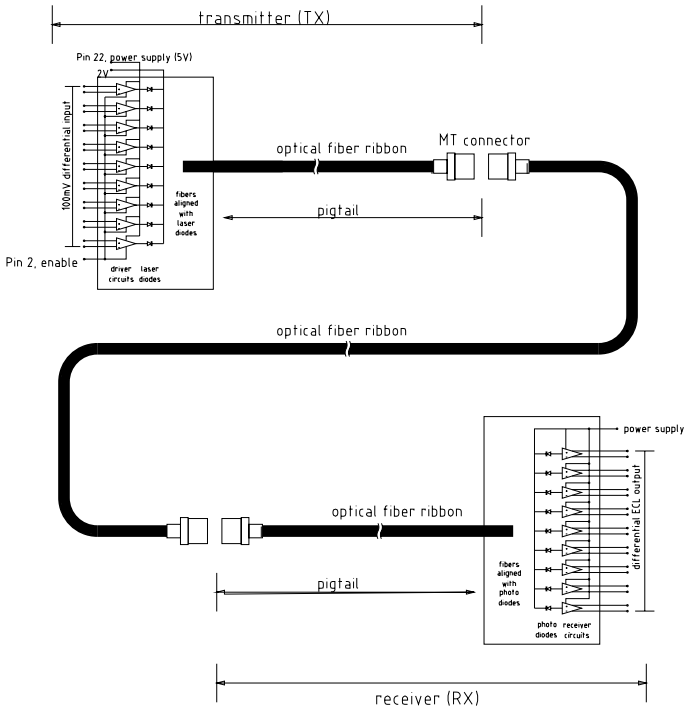

Figure 5.23: Block diagram of DOIM

4. Introduce as little material as possible to reduce the total radiation length.

5. Be radiation hard enough to run continuously and reliably.

5.5.1.2 Function and Operation

The DOIM provides a virtual circuit between the PC and the FIB. It accepts electric signals from the PC and delivers electric signals to the FIB. The electro-optical and opto-electric conversion are hidden from both the PC and the FIB. A block diagram is shown in Fig. 5.23 which demonstrates it's function and operation. The transmitter is a 9 channel laser array driven by a custom designed driver circuit. The driver accepts low current differential signals from the SVX3BE chip and provides the current necessary to turn on and off the laser according to the pattern of the data. The data in optical format is coupled to a ribbon fiber and transmitted to the FIB. On the receiver end, the optical signals are converted back to electric signals by a photodiode and an amplifier array which bring the signals to ECL levels.

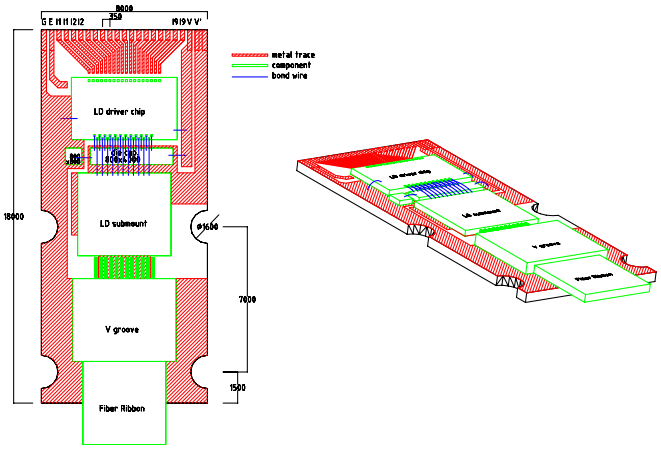

Figure 5.24: Layout of transmitter DOIM

5.5.1.3 Integration and Package

Figure 5.24 shows the layout of the transmitter module. The receiver module is the same in concept and very similar in design. The laser diode array is attached to its own individual submount. This submount, along with other components and the driver chip, are mounted on an aluminum nitride substrate. This material was chosen because of its good thermal conductivity. The components on the substrate are wire-bonded to provide the electric connections. The coupling of the optical fiber to the laser diode array is done with a silicon V-groove block. The V-grooves on the block guide the individual fibers in the ribbon so that they are face-to-face with one of the laser diodes of the array. The other end of the ribbon is terminated with a MT connector. The receiver chip is very similar except that the array of laser diodes is replaced with an array of PIN diodes and the driver chip becomes a set of amplifiers.

5.5.1.4 Characteristics

Both the laser and PIN diode arrays are being developed by the Telecommunication Laboratory in Taiwan. The transmitters are 1550 nm InGaAsP/InP edge emitting laser diodes. The receivers are InGaAs/InP planar PIN's. Their characteristics are listed in Tables 5.10 and 5.11.

Both the driver and receiver chips are also being developed in Taiwan. The input of the driver chip is a low current differential signal defined by a SVX3BE chip. The driver will deliver approximately 20 mA to

Laser Diode	
1550nm InGaAsP/InP edge emitting laser diode	
Wavelength	1550 nm nominal
Bias Current	20 mA
Threshold Current	10 mA
Optical Power	$\geq$ 200 mW coupled to fiber
Forward Voltage	1 V
Operating Temperature	0–40 (°C)

Table 5.10: Characteristics of laser diode

Photo Diode	
Description: InGaAs/InP planar PIN	
Sensitive Wavelength	1000–1605 nm
Responsivity (A/W)	0.9 @1550 nm
Dark Current (nA)	$\leq$ 1.5 @-5V 25°C
Capacitance (pf)	$\leq$ 4
Breakdown Voltage	15 V
Bandwidth (GHz)	1.9 @3dB
Operating Temperature	0–40 °C

Table 5.11: Characteristics of photodiode

Driver Chip	
Input	Differential with common mode voltage $2.5 \pm 0.5\ V$ and differential swing greater than 100 mV
Data rate	53 MHz
Switching time	$t_r, t_f \leq$ 1.5 ns
Channel skew	$< 1ns$
Supply Voltage	5 V
Control input	TTL signal to disable driver
Power dissipation	$<$ 2.3 mW

Table 5.12: Characteristics of driver circuit

Receiver Chip	
Output	ECL
Data rate (MHz)	53
Switching time (ns)	$t_r, t_f \leq 2.0$
Channel skew (ns)	< 1
Supply Voltage (V)	5
Power dissipation (mW)	< 2.0

Table 5.13: Characteristics of receiver circuit

the laser diode for a data high bit. The receiver has a transimpedance input stage followed by 2 or 3 amplification stages. The output is an ECL level. Some of the characteristics of driver and receiver are listed in Tables 5.12 and 5.13, respectively. Prototypes of both the driver and receiver chips are being implemented in CMOS, bipolar and GaAs technologies. The CMOS and bipolar versions have been submitted through Eurochip. The GaAs versions will be submitted to a local foundry in Taiwan.

5.5.2 Fiber Interface Board (FIB)

5.5.2.1 Functionality of the FIB

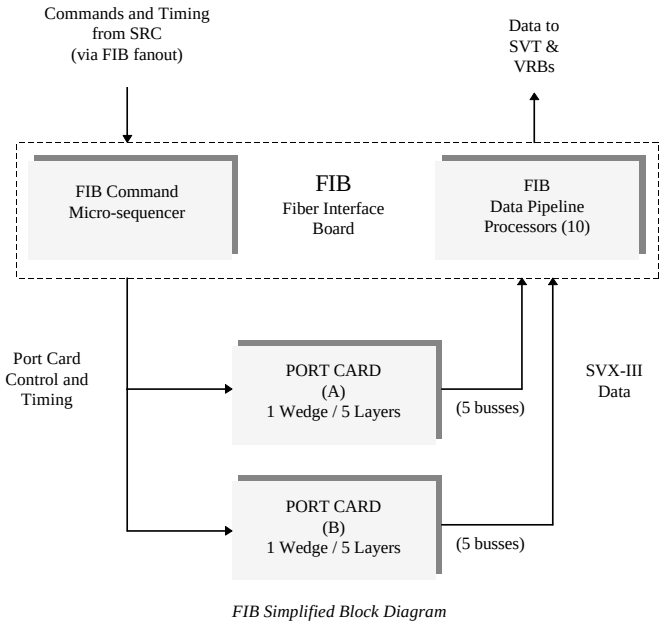

Figure 5.25: Schematic diagram of the FIB.

The FIB will be used to both control the SVX3 chips through the PC and to transfer collision event data from the SVX3 chips to the VRB's and to the SVT system [41]. A schematic diagram of the FIB is shown

in Fig. 5.25. During operation, the FIB receives commands and timing from the SRC via the FIB Fanout. The FIB interprets these in-coming commands and delivers encoded control and timing information to the two target PC's. The control information is decoded on the PC's which then generate the logic levels to control the SVX3 chips. Following a request for data (readout command from SRC), the PC's also transfer the SVX3 data back to the FIB where header information is added, gray-code conversion, pedestal subtraction, and gain corrections are completed, and end of record information is added. As the data stream is being processed it is also being transferred to the SVT and VRB's via fiber optic cable at a peak rate of 1.06 Gigabits per second.

The following is a list of the FIB requirements:

- 9U x 400 mm single width VME board.
- VME slave interface for status and control.
- Four G-Link transmitter daughter card interfaces for sending SVX3 data to the VRB's and SVT system.
- Interface to custom J3 backplane for receiving control and timing information from the SRC via the FIB Fanout.
- Interface to control two PC's.
- Ten data ports to receive data from two PC's at a data rate of 53 MBytes/sec in each.
- Append Bunch Crossing and HDI identification header frames to the data from the PC's.
- Gray Code convert all incoming data from the SVX3 chips.
- Perform pedestal subtraction and gain corrections on a channel by channel basis for all incoming SVX3 data.
- Append EOR frames at the end of the data from the SVX3 chips. Either End of Record Normal or End of Record Truncate (2x) followed by End of Record Fill (2x).
- Synchronize and shape the clocks for the SVX3 chips.
- Allow diagnostic testing of the SVX3 chips and PC.

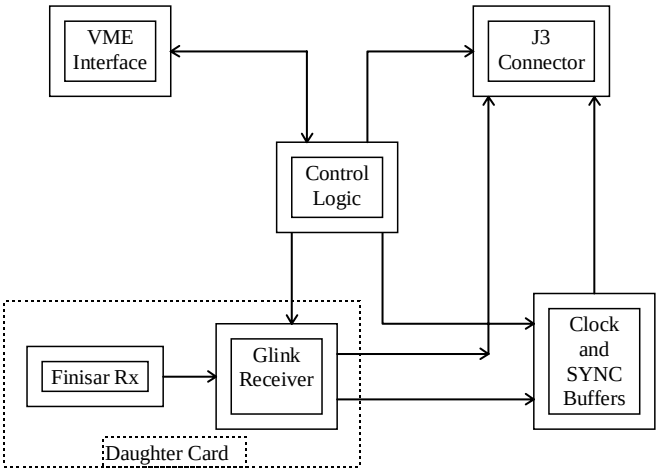

Figure 5.26: Schematic diagram of the FIB Fanout.

5.5.2.2 FIB Crate Fanout Board

The FIB Fanout is a 9Ux400 VME card which resides in a FIB crate. A schematic diagram of the FIB Fanout is shown in Fig. 5.26. The FIB Fanout provides the interface between the SRC module and the multiple FIB boards within the FIB VME crate. There is a single FIB Fanout board in slot 15 of each FIB crate. The FIB Fanout board receives commands and timing signals from the SRC module on a fiber optic G-Link and places them on the J3 backplane for use by the FIB's. The FIB Fanout is configured by the VME master in the FIB crate.

The following is a list of the FIB Fanout requirements:

- 9U x 400mm single width VME board.
- VME slave interface for status and control.
- G-Link receiver daughter card interface for receiving SRC control and timing. Interface to custom J3 backplane for sending control and timing information to FIB's.
- Generate a VME crate reset on command from the SRC.
- Provide MCLK and SYNC buffers for each FIB slot.

5.5.3 High Speed Fiber Link

The high speed Gigahertz fiber transmitter or G-Link TX is a daughter card that mounts on the FIB. Up

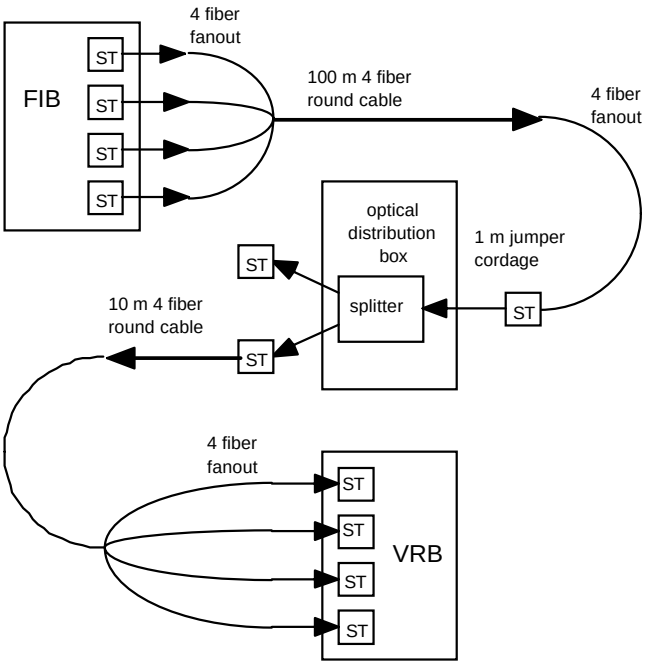

Figure 5.27: Schematic diagram of the G-link data path.

Device	Supply Voltage	Supply Current	Power
G-Link TX	+5.0 V	120 mA	0.63 W
	-5.2 V	400 mA	2.00 W
G-Link RX	+5.0 V	90 mA	0.48 W
	-5.2 V	520 mA	2.60 W

Table 5.14: Power requirements for G-link cards

to 20 bits of parallel data is serialized and transmitted over fiber at data rate speeds up to 1.25 Ghz. There will be four G-Link TX cards on a FIB. The Finisar optical devices on the G-Link card use a ST fiber connector and 50/125 μm or 62.5/125 μm multimode fiber. The four G-Link card fibers will have ST connectors on the front panel of the FIB. The data is transmitted over 4 individual fibers within a cable to an optical splitter. The data leaves the optical splitter on two fibers. One fiber goes to the G-Link receivers mounted on the VRB while the other fiber goes to the G-Link receivers at the SVT. A block diagram of the hardware that makes up the data path is shown in Fig. 5.27.

The G-Link TX is a 2 inch by 3.75 inch card containing a 60 pin AMP 104068-6 connector, a HP HDMP-1012 transmitter, a Finisar FTM-8510 transmitter, and a few discrete surface mount components. The G-Link cards are general purpose serial optical link cards that can be operated in several configurations. Control signals are available at the AMP connector to allow the motherboards to select the mode of operation. Table 5.14 provides an estimate on the power requirements for the G-Link TX and G-Link RX.

5.5.4 VRB and VRB Fanout Modules

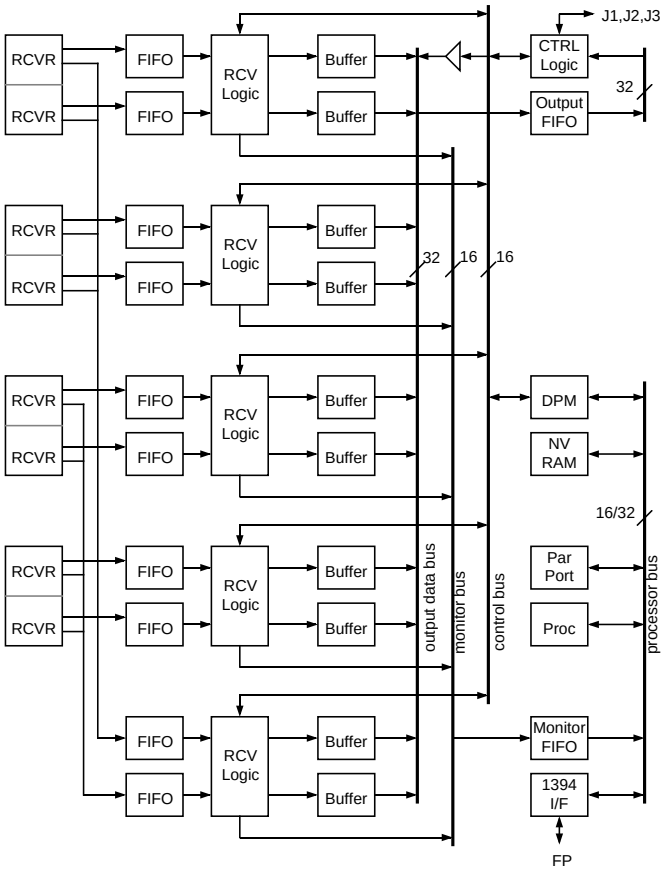

Figure 5.28: Schematic diagram of the VRB module.

The VRB (VME Readout Buffer) serves as an input buffer for the Level 3 trigger processors. It receives data from the FIB's following a Level 1 trigger accept and holds that data while the Level 2 trigger decision is made. To support very fast data readout, the VRB can accept input data at up to 60 Mbytes/s on each of ten channels. The output rate, following a Level 2 accept, is limited by VME bandwidth to approximately 50 Mbytes/s for each group of VRB modules. A schematic diagram of the VRB module is shown in Fig. 5.28.

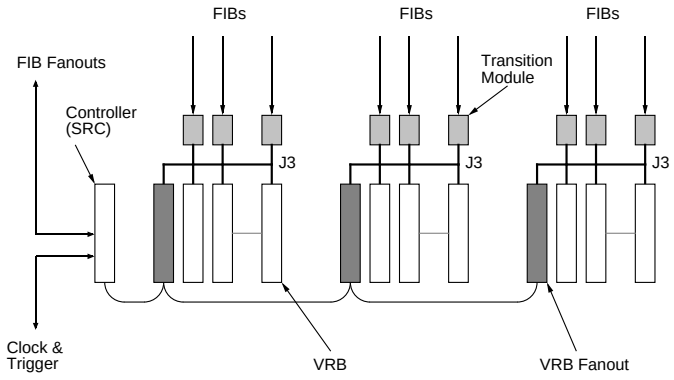

Figure 5.29: Schematic showing the use of the VRB Fanout module in a multicrate system.

The VRB supports a programmable number of internal dual-port buffers which are randomly accessible for simultaneous input and output. In the SVX application, the selection of input and output buffer number for each event is determined by the SRC module, which transmits this information to the VRB's through the VRB Fanout module and a special backplane in each VRB crate. Four buffers in the VRB are assigned to the corresponding four CDF trigger system buffers and the remainder are used to hold events awaiting transmission to the Level 3 system. The mapping of CDF trigger buffers to VRB internal buffers is also handled by the SRC. The VRB Fanout module serves as a repeater for SRC control messages. This allows use of a single SRC module which may be placed in or near one of the VRB crates. Figure 5.29 shows how the fanout module is used in a multicrate system.

When the VRB receives a write buffer message, it is accompanied by global SVX pipeline capacitor and bunch crossing numbers. This information is used by the VRB to check the integrity and synchronization of arriving data. On output, the read buffer message is accompanied by a Level 2 event number which is appended to the event for tracking by the Level 3 processors.

The VRB is a 9U X 400 mm, VME64 compatible module. The VME interface is designed to be very simple, with a 16 bit register providing the total byte count for all active channels and a single FIFO register for accessing the data in either 32 or 64 bit block transfer mode. The data is read out by a standard VME Processor module and transmitted to the Event Builder.

Functionality of the VRB is highly programmable, so that it can accommodate almost any input and output data format, with error checking and optional inline data processing. The buffer logic is implemented on mezzanine cards to allow upgrades in buffer size or processing features. The receivers for the high speed serial links are on a transition module which is common to that used in the SVT system. This transition module accepts data from ten logical channels multiplexed onto four physical data links. Each channel corresponds directly to one layer of an SVX wedge. The backplane which supplies SRC control messages and return status is identical to the FIB crate backplane.

A small on-board processor is used to initialize the programmable logic and to control an independent fast serial interface. The serial interface allows statistical sampling of the event stream without interrupting normal data flow. A non-volatile memory holds the processor code, programmable logic configuration data and the current module initialization information (active channels, number of buffers, buffer sizes, error detection features, etc). The VRB normally requires no external initialization at startup.

5.5.5 The SRC

The Silicon Readout Controller (SRC) operates as the interface of the SVX II DAQ subsystem with the Trigger Supervisor and the CDF Master Clock as well as the upper level controller over the state of the readout electronics. It therefore controls the mediation, interpretation, generation, execution and timing of all the commands that initiate, realize and complete the readout of the silicon detectors with the SVX3 chip set. The SRC is a D16 9U VME slave module, with most of the logic implemented via Xilinx FPGA's. Figure 5.30 shows the relation of the SRC to the rest of the DAQ system. The links of the SRC to the various components of the system are described below.

1. The unidirectional Master Clock link is implemented with 4 copper lines carrying the 53.104 MHz CDF Master Clock (synchronized to the Tevatron) , the SYNC signal which is 1/7 of the Master Clock rate and marks the time of possible proton-antiproton interaction, the Beam Crossing signal which tags the RF buckets with beam particles and the Bunch Zero signal that marks a

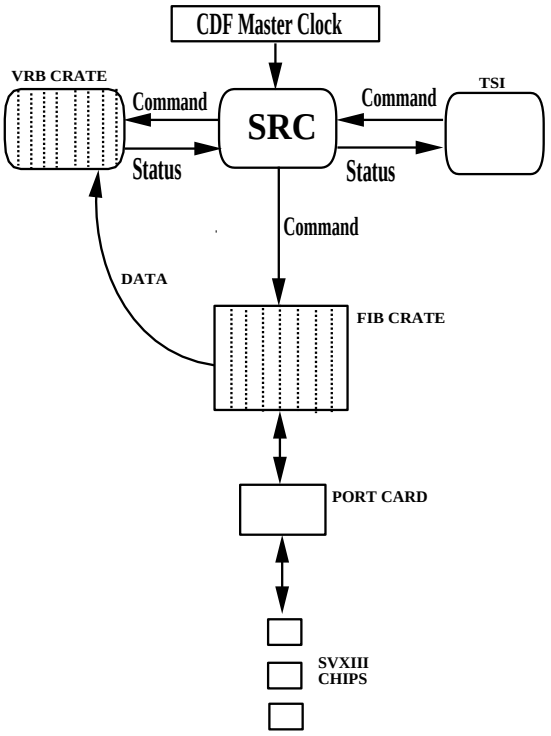

Figure 5.30: Schematic diagram of the SRC function.

reference bucket used for counting.The SRC provides a Phase-locked Loop to ensure the timing stability required by the G-Links used throughout the DAQ system.

2. The bidirectional Trigger Supervisor (TS) link is implemented with 9 lines of optical fiber carrying commands from the TS and 4 lines of copper returning status signals to the TS. The TS can broadcast up to 2 words every 132 ns: a Level 1 Accept (L1A) word and a Level 2 word (either L2-Accept (L2A) or L2-Reject (L2R)). The L1A word consists of the L1A code and a buffer number (0-3) in which to store the event while waiting for the L2 decision. It is the responsibility of the TS to ensure that the buffer allocated is free for use. The L2 word consists of the accept/reject code and the buffer number of the corresponding L1A.

   There are four signals returned from the SRC to the TSI, namely: L1_DONE, DONE, WAIT, ERROR. They serve as follows:

   The L1_DONE signal marks the return of a L1-Accepted cell to the chip pipeline. Upon receipt of a L1 Accept from the TS, the SRC sets the L1A line on the SVX3 chip high via the Fiber Interface Board (FIB), thus tagging a chip pipeline cell as the L1-Accepted cell and removing it from the pipeline. At a later time when the SRC is free, it initiates the digitization and readout cycle for the tagged event. Information about the event is sent to the VME Readout Board (VRB) as detailed in the following section. Once the digitization of the data has been completed and the beam structure allows it, the SRC issues a command to the SVX3 chip to untag the cell element and send it back to the pipeline. At this time L1_DONE is returned to the TS.

   Upon receipt of a L2A the SRC deasserts the DONE line to the TS. When the transfer of the data for the L2-Accepted buffer has been successfully completed to a VRB buffer location this buffer will then be marked as a Scan Buffer indicating that readout into L3 can take place. The SRC then reasserts DONE.

   If the VRB has no buffer location available to store another L2-Accepted event the SRC asserts WAIT. This results in the TS inhibiting further L2A's. When a buffer in the VRB is freed WAIT is deasserted.

   The ERROR signal is asserted only in the case of catastrophic error such as mismatch between the event being read by different wedges or loss of synchronization between the chips. This will cause the TS to initiate the HALT-RESET-RUN sequence. The errors which are considered catastrophic by the SRC are programmable at run time. A time history and statistics on each error type is stored for readout via VME.

3. The bidirectional VRB link is implemented via 23 copper lines of which 10 are status/error lines and 13 are command. The status/error lines from all the VRB's are OR'ed together.

   Upon receipt of a L1A the SRC sends to the VRB the buffer number in which the data is to be stored, the pipeline cell number and the bunch crossing number. The VRB indicates that it will be busy reading data from the chip by asserting the READOUT_BUSY line to the SRC. Once the transfer of the data from the chip to

this VRB location has been completed the VRB deasserts the READOUT_BUSY line. Upon receipt of L2A the SRC sends to the VRB the buffer number from which the data will be read into L3 as well as the event id, at which time the VRB asserts the SCAN_BUSY line to the SRC. When the data have been readout into L3, the VRB deasserts the SCAN_BUSY line.

It is the responsibility of the SRC to monitor and manage the data buffers in the VRB.

4. The unidirectional FIB link is implemented by means of 4 optical G-Links (one to each crate of FIB's). Twenty bits of information are transferred every 132 ns over each serial line implemented using the G-Links (each of which carries the same information to the 4 FIB crates). However, the signals on each can be delayed separately, allowing the synchronization of the system without having to match cable lengths. In addition to the command word, the SRC provides the Master Clock to the FIB (and hence to the SVX3 chips). Two of the 20 bits transmitted mark the status of the SVX3BE chip for any given L1A, marking whether it was quiescent, digitizing or reading out.

To aid in system integration tests, the SRC has the ability to emulate the CDF Master Clock and commands from the TS as well as to send arbitrary command sequences to the FIB.

5.5.6 Readout into Level 3

The output port of the VRB module is a VME connection supporting 64 bit block transfers. A commercial VME64 processor module (scan processor) in the VRB crate is used to access data from each VRB sequentially. The VRB contains an internal DMA controller which concatenates buffers to allow a single block transfer read of all data. The VRB output port is pipelined to permit VME transfers at up to 80 Mbytes/s with a high speed readout processor. The speed of available VME processors and output data links, plus normal VME overheads, will limit this rate to 30–40 Mbytes/s initially. A schematic diagram of the transfer of the data to Level 3 is shown in Fig. 5.31.

Depending on the VME transfer rate achieved, the VRB modules will be partitioned into three or six readout crates. Each crate drives a single data link

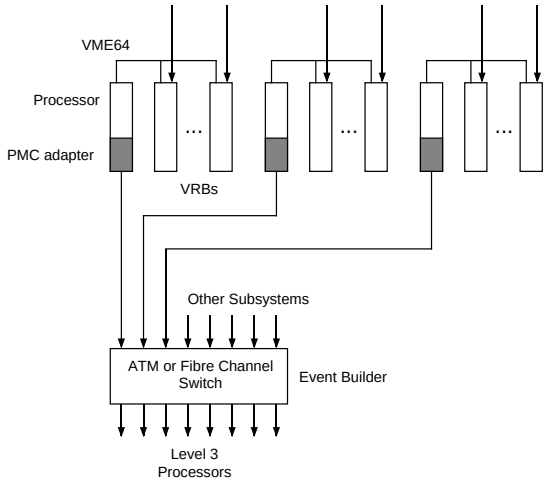

Figure 5.31: Schematic diagram of the transfer of SVX II data to Level 3.

to the Event Builder and Level 3 trigger system. The VRB crates are scanned in parallel, so doubling the number of VRB crates will, in principle, reduce the readout time to Level 3 by 50%. At an occupancy of 3 kbytes/event per VRB (data from ten layers), the scan time would be approximately 1 ms for a three VRB crate system, resulting in an average Level 2 accept rate of 1 kHz.

The readout processor in the VRB crate will likely include a PMC (PCI Mezzanine Card) port. This port is used for direct connection to the Event Builder through either a Fibre Channel or ATM adapter. Testing of a 500 Mbyte/s ATM switch for Event Builder applications is currently in progress, using the CDF Data Acquisition software. This switch supports input at rates of 15 Mbytes/s/port (up to 32 ports) or 60 Mbytes/s/port (up to 8 ports). The SVX II system would use three of the high speed ports or twelve of the low speed ports on this switch.

Readout of VRB data by the processors and transmission of this data to the Event Builder is an asynchronous process. The VRB's will signal the SRC when all data for an event has been copied to the scan processor so that the SRC can reuse the VRB scan buffer. If all VRB scan buffers are filled, the SRC will return a WAIT signal to the trigger system.

5.6 SVX II Power Supplies

The three basic requirements for the SVX II Power Supply system are: (1) to provide all the power for the silicon ladders, the SVX3 chip set, and the PC's, (2) to control and monitor all the relevant output voltages and currents, and (3) to provide failure mode protection for safe power supply and system operation.

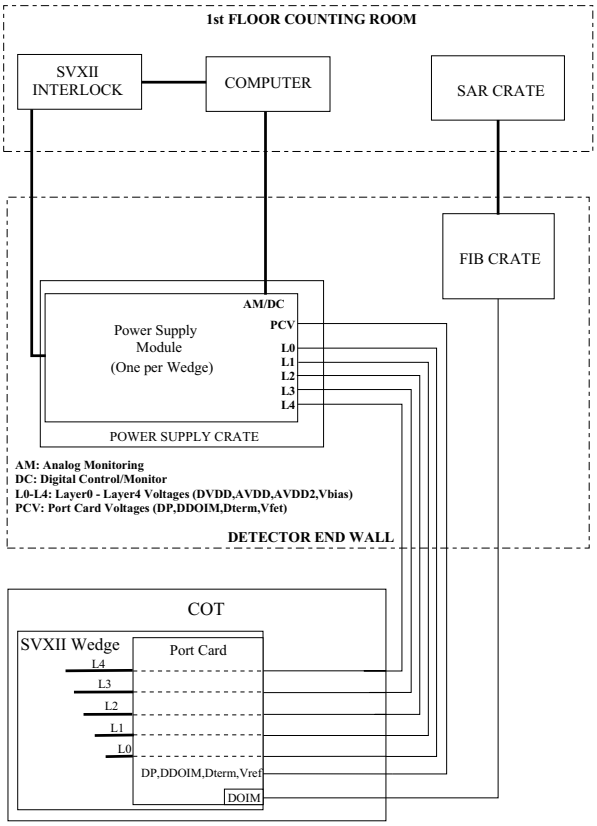

Figure 5.32: Silicon detector general power distribution layout.

The basic building block of the SVX II silicon vertex detector is the silicon ladder. The ladder consists of double-sided AC coupled silicon microstrip detectors, the analog and digital frontend electronics (SVX3 chip set), and a hybrid device with I/O drivers and receivers. DC high voltage (less than 200 V) power is needed to bias the silicon detectors, and DC low voltage (5 V) is needed to power the analog, digital, and I/O electronics. Thus, a Power Supply Module must deliver a number of voltages with different current, stability, and monitoring requirements. To compensate for radiation induced bulk damage to the silicon detectors, the cabling, power supply, monitoring and control systems allow for the setting of different detector bias voltages in different regions of the detector. Also required is a fail-safe system for monitoring and controlling all the output voltages and currents. Finally, the Power Supply System is integrated into the overall monitor, control, and interlock system for the CDF experiment.

While the preceding general requirements are based on the SVX′ Power Supply System, there are some major changes to the SVX′ system that directly impact specific requirements for the SVX II Power Supply System. The major changes include: 1) greater than a factor of 3 increase in components, caused by increasing the number of wedges from 24 to 72 and the number of layers from 4 to 5, 2) a significant increase in detector bias voltage (from 80 V to 200 V) and of power supplied to each wedge (from 6.5 W to 50 W), and 3) independent low voltage outputs to each of 5 layers on a wedge. Table (5.15) provides the specific power requirements for one SVX II wedge. Several comments apply to these specifications:

1. The DVDD outputs are not post-regulated on the PC. Thus, local current sensing at the Power Supply Module is used to compensate for the cable drop.

2. The AVDD and AVDD2 outputs are post-regulated on the PC.

3. All output voltages and currents are monitored to track the operating characteristics of the detector, electronics, and power supply.

4. All low voltage outputs have over-voltage and under-voltage trips, the V_{bias} outputs have over-voltage trips, and all output currents have over-current trips.

5. We will implement a split-bias voltage scheme to symmetrically bias the detectors.

6. The question of linear vs switching supplies to supply all outputs is being studied.

Figure (5.32) shows the general power distribution layout. Remote control of a Power Supply Crate is achieved through a computer located on the first floor counting room. A Power Supply Crate contains the

Layer 0 through Layer 4								
Output	V_o	V_{select}	Sense	I_o(L0)	I_o(L1)	I_o(L2)	I_o(L3)	I_o(L4)
DVDD	+5.0 V	Fixed	Current	0.20 A	0.30 A	0.45 A	0.45 A	0.60 A
AVDD	+6.0 V	Fixed	None	0.14 A	0.20 A	0.34 A	0.34 A	0.48 A
AVDD2	+4.5 V	Fixed	None	0.10 A	0.15 A	0.30 A	0.30 A	0.40 A
V_{bias}	0-200 V	Program	None	0.01 A	0.01 A	0.01 A	0.01 A	0.01 A
Port Card								
DP	+5.0 V	Fixed	Voltage	2.0 A				
DDOIM	+2.0 V	Fixed	Voltage	-1.5 A				
Dterm	+2.5 V	Fixed	None	0.1 A				
V_{FET}	+8.0 V	Fixed	None	0.1 A				

Table 5.15: SVX II Power Supply Requirements for One Wedge

Power Supply Modules and is located at the Detector End Wall. Each Power Supply Module supplies one wedge of the SVX II detector where one wedge includes 5 silicon ladder ends (Layer 0 through Layer 4) and a PC. Also, power to each of the 5 detector layers supplied by a single Power Supply Module is independent of the power supplied to any of the other layers. This is an important safety feature so that failures in one wedge do not affect the operation of any other wedge, and failures in a particular layer do not affect the other layers of the wedge. Each Power Supply Module contains on-board circuitry to implement the digital control and analog monitoring of the output voltages and currents. Power supply fault trip monitoring is designed into the Power Supply Module in terms of monitor and trip detection circuits that shut down power to a particular layer in the event that voltages or currents exceed predefined trip points. The second level is an interlock signal that turns off the Power Supply Modules in emergencies not related to the Power Supply System (eg. fire alarm, loss of cooling). This effectively integrates the Power Supply System monitoring and control into the overall monitor and control system for the SVX II detector.

5.7 SVX II Alarms and Limits System

The electrical power and cooling systems of the SVX II detector require monitoring in order to detect possible problems. This monitoring is implemented at two levels. At the first level, certain critical system parameters, such as the detector temperature and various low voltage levels, may reach values that require immediate intervention in order to prevent damage to the detector. These parameters will be continuously monitored by the controlling hardware, and these devices will intervene as necessary to maintain safe operating conditions. At the second level, parameters will be monitored by a passive "alarms and limits" system in order to observe the operating state of the system, track system performance, understand the cause of any protective actions taken by the first level and notify operators whenever anomalous conditions exist.

The alarms and limits system for SVX II will be modelled after that used by SVX and SVX′. As for the previous silicon detectors, the system will be based upon the accelerator control system, ACNET. The ACNET system provides a CAMAC-based front end and data acquisition system for measured parameters, a transparent communications protocol between the data acquisition hardware and workstations running ACNET software, a high-level software interface that allows access to each monitored channel and a graphical user interface. ACNET allows each monitored channel to have an upper and lower limit defined. Excursions of a parameter beyond either limit will set an alarm condition. Automatic data-logging systems are also available in ACNET and may be used to log information for later analysis.

The power supplies for SVX II will probably be controlled and monitored directly by a PC. In this configuration, the ACNET system will query the PC for power supply information, as was done for many

CDF sub-systems in Run I. This information will be integrated into the CDF detector-wide alarms and limits system. Temperatures and other cooling system parameters will be measured by CAMAC modules directly under control of the ACNET system.

5.8 SVX II Performance Issues

5.8.1 Hit Occupancies in the SVX II

Because both the tracking reconstruction resolution and the Level 2 trigger (through the SVT) depend critically on the SVX II, considerable effort has gone into understanding the expected hit occupancies in the SVX II detector [42]. Since much of the occupancy is the result of minimum bias interactions which accompany the triggered event, a careful effort was made to tune the Pythia event generator to the observed occupancy seen in the SVX′ detector during Run Ib [43]. Pythia was then used to generate minium bias events at the level of 2.7 interactions/crossing, the expected number at the beginning of Run II. In Table 5.16 we show the average and maximum occupancies for the various parts of the detector. The numbers are in percent and correspond to the case of 2.7 minimum bias events per crossing. Modules 0 and 5 are the outer most half ladders, 1 and 4 are the inner half ladders of the end barrels, and 2 and 3 are the two halves of the central barrel. We assumed nearest neighbor readout, a Gaussian shaped luminous regions with $\sigma_z = 24$ cm, signal/noise of 16, and a readout threshold of $3 \times \sigma_{noise}$. The columns labelled "most" mean that this is an average of the occupancy for this wedge when it had the highest occupancy of any wedge being readout. This is important in determing the time to read out the data because the wedge with the largest occupancy will always determine the readout time.

To estimate the readout time we assumed that a triggered event had an occupancy which was twice the maximal min bias occupancy. We added the average occupancy associated with 2.7 additional interactions. Finally we added an additional 2% occupancy for noise. In Table 5.17 is shown the actual number of hits for the various layers for the r-ϕ and r-z sides under these assumptions. The time to read out the data is also shown in Table 5.17.

5.9 Operating the SVX II

There are several challenges involved in successfully operating a system as complex as SVX II for an extended period of time. The biggest challenges are primarily calibrating the detector and monitoring it for problems. Fortunately, CDF has operated two silicon vertex detectors over the last four years, and that experience is a useful guide in planning for the operation of SVX II.

5.9.1 Calibration

CDF's previous silicon detectors were calibrated daily during quiet time by measuring the pedestal, noise, gain, and optimal threshold for each channel. As expected, these measurements exhibited no problematic short term variations, and all long term variations were common to all channels in a specific electrical segment (chip or ladder). The SVX II will have a larger channel count, but this should not be a problem since the segmentation of the readout is similar. Thus, we expect that the calibration approach for SVX II can be very similar to that for SVX and SVX′.

The primary operational challenges faced by the previous detectors were problems in the readout chain. The key to dealing with these problems was early detection through real time monitoring. This was accomplished with online monitoring programs which measured the occupancy of each chip and checked for readout problems. This approach identified most problems within minutes. Offline monitoring measured the occupancy of each channel and the tracking efficiency for each chip. It also provided redundancy for the online checks. A similar monitoring approach will be used for SVX II.

5.9.2 Beam Steering and Feedback Control

A program has begun to implement a beam steering and feedback control system to stabilize the position and angle of the beam with respect to the SVX II detector. Because the proposed SVT trigger hardware does not reconstruct a primary vertex, stability of the beam position is necessary for successful triggering. In addition, with SVT tracks only in the r-ϕ plane, it is essential that the detector axis and the beam axis be very close to parallel.

PYTHIA generator with pile up 2.7 events/crossing					
		Min bias occupancy		Min bias occupancy	
MODULE	LAYER	AVG R_ϕ	AVG Z	MOST R_ϕ	MOST Z
0 & 5	0	2.343	4.258	5.634	13.697
	1	1.362	1.661	3.306	5.359
	2	0.750	0.764	1.969	2.030
	3	0.605	0.885	1.607	2.779
	4	0.466	0.469	1.180	1.191
1 & 4	0	3.257	4.729	7.071	13.134
	1	1.836	1.889	4.202	5.457
	2	0.941	0.955	2.225	2.252
	3	0.743	1.001	1.830	2.787
	4	0.554	0.557	1.331	1.340
2 & 3	0	4.311	5.285	8.401	12.693
	1	2.278	2.070	4.726	5.276
	2	1.139	1.150	2.560	2.577
	3	0.887	1.147	2.052	2.904
	4	0.661	0.660	1.507	1.503

Table 5.16: Occupancies in % for average and maximal minimum bias events assuming 2.7 events/crossing and a luminous region with $\sigma_z = 24$ cm.

Expected hits in each layer and required time to readout the data					
		Hits in each layer		Time (μs) to readout data	
MODULE	LAYER	HITS R_ϕ	HITS Z	TIME R_ϕ	TIME Z
0 & 5	0	42	88	1.6	3.3
	1	41	58	1.6	2.2
	2	48	49	1.8	1.8
	3	51	47	1.9	1.8
	4	50	50	1.9	1.9
1 & 4	0	52	86	2.0	3.3
	1	50	60	1.9	2.3
	2	52	53	2.0	2.0
	3	55	48	2.1	1.8
	4	54	54	2.0	2.0
2 & 3	0	61	86	2.3	3.2
	1	56	59	2.1	2.2
	2	58	58	2.2	2.2
	3	60	50	2.3	1.9
	4	58	58	2.2	2.2

Table 5.17: Estimated hits by layer and side for triggered events. Also shown is the readout time for these events.

During Run Ia and Ib, changes in the beam position and beam angle were observed from store to store. The beam position even changed within the time period of a store, with time scales ranging from 10 minutes to hours. By using local bumps at the correction dipoles in the A4 and B1 sectors of the Tevatron, it is possible to correct for these changes in the beam position and angle at the B0 interaction region. However, a precise measurement of both the angle and position (in the horizontal and vertical planes) is required.

CDF will be able to make these measurements by using the information from the SVX II detector. During Run Ib, CDF used the information from the SVX′ detector to measure these 4 quantities and communicated them through the Accelerator Controls Network. The Accelerator Division Controls group implemented a program to use this information, along with desired positions and angles, to adjust the correction elements. Studies done during the Tevatron operation in January and February 1996 showed that the system works in principle. The AD/Controls group is creating a software based feedback algorithm for this interaction region beam steering.

Though we have demonstrated that the system will work in principle, there are additional questions that need to be answered before it works in practice. The most significant is possible limits in the range of motion. The correction dipoles used for the local bumps are also used in the establishment of a smooth closed orbit in the Tevatron, so it is possible that making local changes could disrupt the total Tevatron orbit. Consequently, we are continuing to work with the AD/Controls and AD/Main Accelerator groups on the design and implementation of a reliable and appropriate beam steering system.

Bibliography

[1] SVX II Upgrade Proposal and Simulation Study, CDF/DOC/SEC_VTX/CDFR/1922. Proposal submitted to the Fermilab Directorate on January 13, 1993 and approved in May, 1993.

[2] N. Tamura et al., NIM A342 (1994) 131.

[3] H. Ziock et al., NIM A342 (1994) 96.

[4] John A. J. Matthews, *et. al.,* Bulk Radiation Damage in Silicon Detectors and Implications for SVX II, November 1, 1995, CDF Note 3408.

[5] T. Ohsugi *et al.,* A Study of the Microdischarge Phenomenon at the Strip Edge of the Microstrip Sensors, I.E.E.E. Nucl. Sci. Sym., Norfolk, Virginia, November 1994, NIM A342 (1994) 22.

[6] T. Ohsugi et al., HUPD 9507, HUPD 9508, to be published in the proceedings of the 2nd International Symposium on Development and Application of Semiconductor Tracking Detectors at Hiroshima, Oct. 10 -13, 1995.

[7] D. Bortoletto, *et al.,* Evaluation of single metal SVX II prototypes manufactured by Micron Semiconductor, CDF/DOC/SEC_VTX/CDFR/3259.

[8] D. Bortoletto, *et al.,* Irradiated SVX II prototype probing results, CDF/DOC/SEC_VTX-/CDFR/3295.
A. Brandl, et al., Measurement of Proton-Induced Radiation Damage Effects in Double Sided Silicon Microstrip Detectors, CDF/DOC/SEC_VTX/PUBLIC/3512 (1996).

[9] D. Bortoletto, *et al.,* Capacitance measurement of double metal double sided silicon microstrip detector, Proc. Second International Symposium on Development and Application of Semiconductor Tracking Detectors, Hiroshima, 1995, to be published in Nucl. Inst. and Meth.

[10] A. Patton, *et al.,* Electrical Characterization of SINTEF/SI Prototype Double-sided Silicon Microstrip Detectors, CDF/DOC/SEC_VTX-/CDFR/2835.

[11] M. A. Frautschi, *et al.,* Capacitance Measurements of Double-sided Silicon Microstrip Detectors, FERMILAB-PUB-96/008-E, submitted to Nucl. Instr. and Meth.

[12] S. C. Seidel, *et al.,* Studies of Double-sided Silicon Microstrip Detectors, Proc. Second International Symposium on the Development and Application of Semiconductor Tracking Detectors, Hiroshima, 1995, FERMILAB-CONF-96/049-E, to be published in Nucl. Instr. and Meth.

[13] K. Hoffman, *et al.*, Laser Studies of Charge Collection Efficiency in SVX II Prototype Sensors, CDF/DOC/SEC_VTX/PUBLIC/3438.

[14] S. Kleinfelder,*et al.*, A flexible 128 channel silicon microstrip detector integrated circuit with sparse data readout, IEEE Trans. Nucl. Sci., Vol. 35, No.1, 171 (1988).

[15] R. Yarema, *et al.*, A Beginner's Guide to the SVX2, FERMILAB-TM-1892.

[16] N. Bacchetta, *et al.*, Resolution of Double-Sided Silicon Microstrip Sensors, CDF/DOC-/TRACKING/PUBLIC/3277.

[17] N. Bacchetta, *et al.*, Results of the KEK Beam Test of SVX II Prototype Detectors, CDF/DOC/TRACKING/PUBLIC/3547.

[18] D. Husson, IEEE Trans. Nucl. Sci. NS-36 (1994) 811.

[19] T. Huffman, private communication.

[20] M. A. Frautschi, Radiation Damage Issues for the SVX II Detector, January 27, 1994, CDF Note 2368.

[21] Alex Grillo, UCSC, private communication

[22] H-J. Ziock *et al.,* Tests of the Radiation Hardness of VLSI Integrated Circuits and Silicon Strip Detectors for the SSC Under n, p, and γ Irradiations, LANL Report LA-UR-90-4184 (1990).

[23] A.J. Weinstein, *et al.,* Silicon Tracking Conceptual Design Report, SCIPP 92/04 and SDC-91-133, March 1992.

[24] G. Bolla *et al.,* Double Metal SVX II Prototype Probing Results, CDF Note 3288 (1995).

[25] D. Bortoletto, private communication.

[26] S. Worm, private communication.

[27] P. Azzi *et al.,* Noise and Radiation Effects on SVX′ and other Silicon Sensors, CDF Note 3278 (1995).

[28] J. Matthews and T. Thomas, SVX II Signal to Noise Ratio, CDF Note 2397 (1994).

[29] E. Barberis *et al.,* Capacitance in Silicon Microstrip Detectors, Proceedings of the International Symposium on Development and Application of Semiconductor Tracking Detectors, May 22-24, 1993, Hiroshima, Japan, SCIPP 93/16 (1993); K. Yamamoto *et al.,* Interstrip Capacitance of the Double Sided Silicon Strip Detector, Proceedings of the SDC Collaboration Meeting at KEK, May 1991, SDC-91-33 (1991); R. Sonnenblick *et al.,* NIM **A310**, 189 (1991).

[30] RD20 Collaboration, A. Holmes-Siedle *et al.,* Radiation Tolerance of Single Sided Silicon Microstrips, CERN-PPE/93-137 (1993).

[31] Y. Unno *et al.,* Characterization of an Irradiated Double-sided Silicon Strip Detector with Fast Binary Readout Electronics in a Pion Beam, IEEE 1995 Nuclear Science Symposium, San Francisco, CA Oct 25, 1995, KEK Preprint 95-172 (1995).

[32] Nucl. Instrum. Meth. A349 (1994) 96-105.

[33] P. M. Ratzmann, Analysis of Ladder Support Fiber Options, December 2, 1993, CDF Note 2393.

[34] M. Albanese, M. Gold, M. R. Hoeferkamp, T. L. Thomas, S. Wells, Studies of a High Density Interconnect Cable for SVX II, CDF note 2785.

[35] P. M. Ratzmann, Ladder Thermal Analysis for CDF with SVX III Chips, June 5, 1995, CDF Note 3507.

[36] P. M. Ratzmann, SVX II Ladder Thermal Analysis, January 5, 1996, CDF Note 3508.

[37] Kohriki, *et. al.,* First Observation of Thermal Runaway in the Radiation Damaged Silicon Detector, submitted to the IEEE Trans. on Nucl. Sci., IEEE Nuclear Symposium, San Francisco, October, 1995 and KEK Preprint 95-157, November, 1995.

[38] P. M. Ratzmann, Thermal Analysis of the CDF SVX II Silicon Vertex Detector, FERMILAB-Pub-96/031-E, submitted for publication to Nuclear Instruments and Methods March, 1996.

[39] J. A. Hanlon, and H. J. Ziock, Design Equations for Silicon Detector Ladders with Heat Generated by Damage Induced Leakage Current LA-UR-95-893.

[40] The current SVX3 specifications are contained in "Device Specifications for the SVX3 Chip Set", Raimund Strohmer and Walter Knopf, http://www-ese.fnal.gov/eseproj/svx/svx3/svx3spec.htm.

[41] Hypertext references on the FIB and FIB Fanout can be found at: http://www-ese.fnal.gov/eseproj/svx/default.htm

[42] Hsaio Ying Chao and Jaroslav Antos, Occupancy Study for the SVX II, CDF note 2386, Nove. 21, 1994.

[43] R. Culbertson and G. Punzi, Occupancy in SVX II, December 14, 1995.

Chapter 6

Intermediate Silicon Layers (ISL)

6.1 Introduction

The SVX II silicon detector will provide coverage to $|\eta| \sim 2$. In the region $|\eta| < 1$ the combination of the SVX II and the Central Outer Tracker (COT) can provide full 3D tracking, but the reconstruction will need to be anchored on COT tracks, and suffer the multiplicative amplification of inefficiencies discussed in Chapter 3. For $|\eta| > 1$, SVX II can only perform 2D tracking and, in the absence of additional information, the impact parameter resolution for such tracks will be too poor to enable efficient b tagging.

Both of these problems are addressed by the Intermediate Silicon Layers (ISL): In the central region, a single layer of silicon is placed at a radius of 22 *cm*; six silicon based measurements in this region then provide a stand-alone segment for optimized tracking in conjunction with the COT. In the region $1.0 \leq |\eta| \leq 2.0$, where the COT coverage is incomplete or missing, two layers of silicon are placed at radii of 20 *cm* and 28 *cm*. Precision space point measurements at these radii will enable 3D track finding in the plug region and significantly improve the momentum resolution and, as a consequence, the impact parameter measurement. The ISL will thus extend tracking, lepton identification, and b-tagging capabilities over the full region $|\eta| \leq 2.0$.

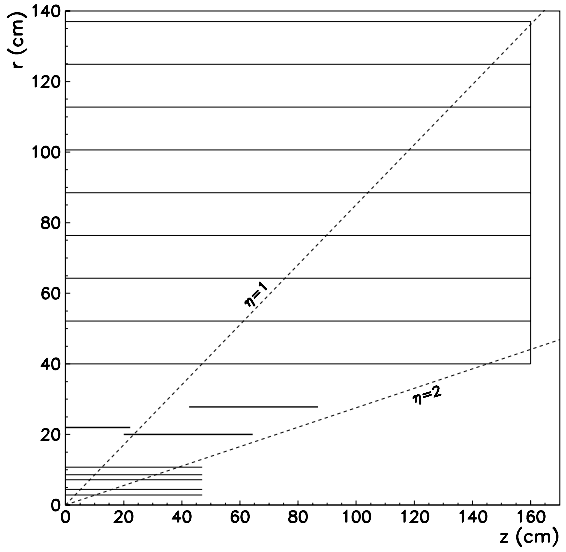

Figure 6.1: An r-z view of the ISL silicon layer placements. SVX II and COT are also shown.

6.2 Detector Design

6.2.1 Comparison to SVX II

The ISL incorporates many features of the SVX II design described in Chapter 5. For example, the two detectors are nearly identical with regard to:

- data acquisition
- power supplies
- cooling system.

This overlap in designs has the obvious advantage of recycling much of the R&D that has already been done for SVX II.

However, there are several ways in which the ISL design differs from SVX II. In particular, the large surface area of silicon needed by the ISL necessitates cost saving simplifications. These can be achieved because many of the difficult tasks associated with the construction of a silicon microvertex detector are eliminated at larger radii. For example, since the occupancy is lower and radiation damage occurs more slowly, it is possible to use longer strips and wider readout pitch to reduce the number of readout channels and subsequent cost of front-end electronics and data acquisition. In addition, the intermediate radius region of CDF is rather spacious. This added

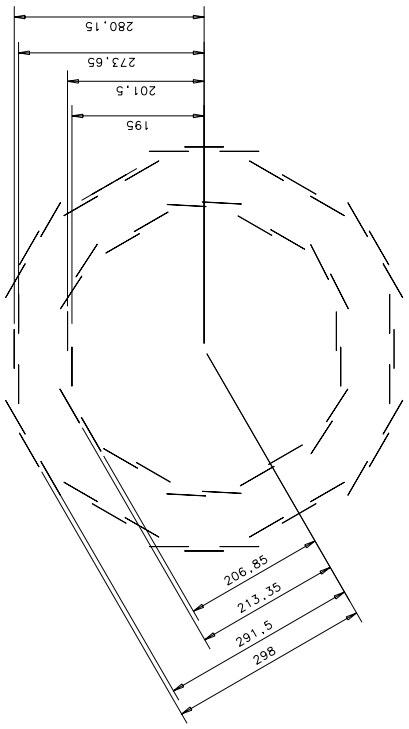

Figure 6.2: An r-ϕ view of the ISL silicon layer placements in the large η region.

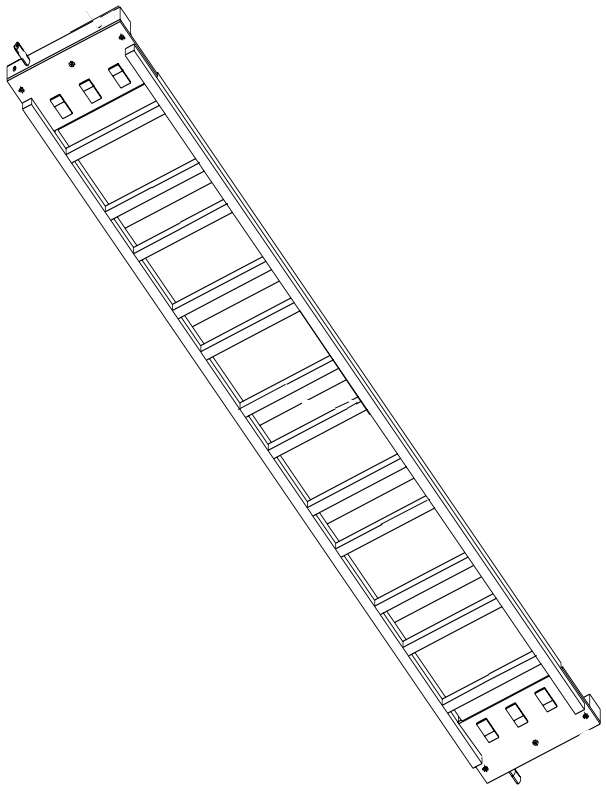

Figure 6.3: A view of the stereo side of a mechanical ladder which consists of two readout ladders.

real estate can be used to obtain a mechanical design for which the actual construction of the detector is more simple and robust while also less costly. Finally, since the layers are further from the interaction point, the construction tolerances are slightly more relaxed which again affords an opportunity to streamline the construction of the device.

6.2.2 Geometry

The positions of the silicon layers are shown in Figure 6.1. They lie within the radial range $20 < r < 30$ cm and extend to $|z| = 65$ cm for the inner layer and 87.5 cm for the outer layer ($|\eta| \sim 1.9$ in both cases). Figure 6.2 shows the end view of the two layers at large η.

6.2.3 Silicon Crystals

All silicon crystals used in ISL will be identical and measure 58 mm wide by 74 mm long; this is the largest size that still allows two crystals to be made on a single 6 inch Si wafer. As in layer 4 of SVX II, the crystals will be double-sided with axial strips on one side and small angle stereo strips on the other. The stereo angle is 1.2^o. The axial (p implant) side will have a strip pitch of 55 μm. The stereo (n implant) side will have a strip pitch of 73 μm. On both sides, the readout pitch will be twice the strip pitch to reduce the channel count. The intermediate strips will not be read out but will contribute to the resolution through charge sharing. The dimensions of the silicon crystals are summarized in Table 6.1. Several other experiments [1, 2] use silicon detectors with alternate strip readout. They are compared to the ISL design in Table 6.2.

6.2.4 Ladders

All ladders will be identical and will be made from 3 crystals laid end to end and microbonded to each other. The strips will be bonded to readout chips mounted on each side of a ceramic (alumina, AlN or BeO) readout hybrid. Four (three) SVX3 readout chips on the axial (stereo) side are matched to the detector strips by means of a pitch adapter. Figure 6.3 shows the stereo side of a mechanical ladder which is made up of two readout ladders containing 3 crystals each. Figure 6.4 shows close up views of the z and ϕ

	Atlas	Atlas	L3	L3	Delphi	Delphi	ISL	ISL
side	n	n	p	n	n	n	p	n
S/N	11	17	15	15	12	21	>12	12
RP (μm)	112	112	50	150	100	50	110	146
SP (μm)	56	56	25	50	100	50	55	73
SP/$\sqrt{12}$	16.0	16	7.2	14.4	28.0	14.4	16.0	21.0
σ (μm)	15.6	12.9	7.0	15.0	23.0	10.0	<16.0	<23.0

Table 6.2: Comparison to other silicon detectors with alternate strip readout.

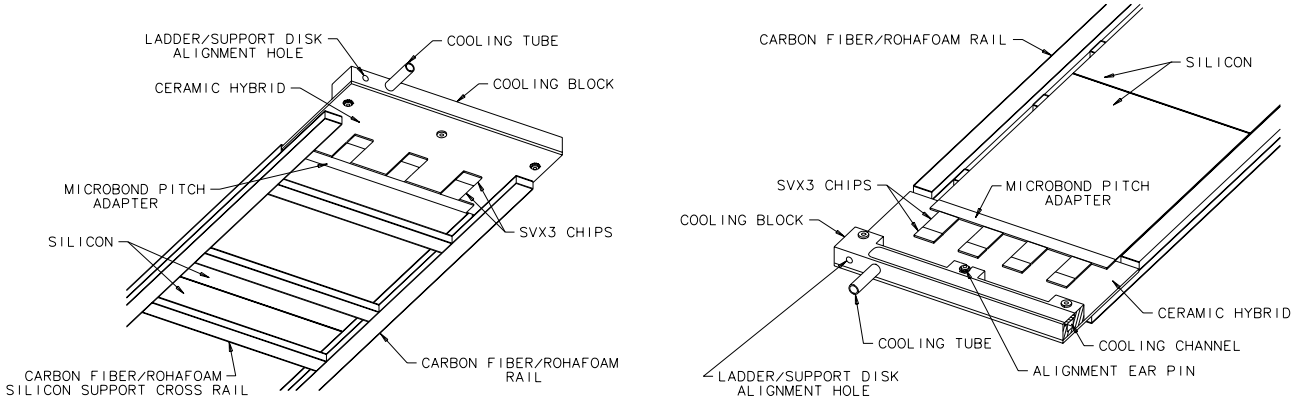

Figure 6.4: A close up view of the readout hybrid on the stereo side of a ladder (left) and the readout hybrid and cooling channel on the axial side of a ladder (right).

number of axial strips	1024
number of stereo strips	768
number of axial chips	4
number of stereo chips	3
stereo angle	1.2^o
axial strip pitch (μm)	55
stereo strip pitch (μm)	73
axial readout pitch (μm)	110
stereo readout pitch (μm)	146
total width (mm)	58
total length (mm)	74
active width (mm)	56.3
active length (mm)	72.4

Table 6.1: ISL Sensor mechanical dimensions

readout segments. The ϕ side shows the attachment of the ceramic to a Be block by means of 'ear-pins' like those used to attach ladders to the Be bulkheads in the CDF SVX and SVX$'$ detectors. The Be block contains a water cooling channel; the entrance pipe is shown near the end of the block and the cover for the channel is seen on the top of the block. The size of the cooling channel is $3.5 \times 3.5\text{mm}^2$ which was determined to be adequate by comparison with the SVX II design.

An important design feature of the ladder is the positioning of the carbon fiber and foam support rails. As seen in the figure, the main support rails running the length of the ladder do not overlap any part of the silicon crystals. The crystals are instead supported by 'rungs' which bridge the main rails. This 'outrigger' design differs from the SVX II ladder design and results in open access to all bonding pads on both sides of the Si crystals.

Another difference from the SVX II design is that the readout hybrids are not glued to the silicon, but

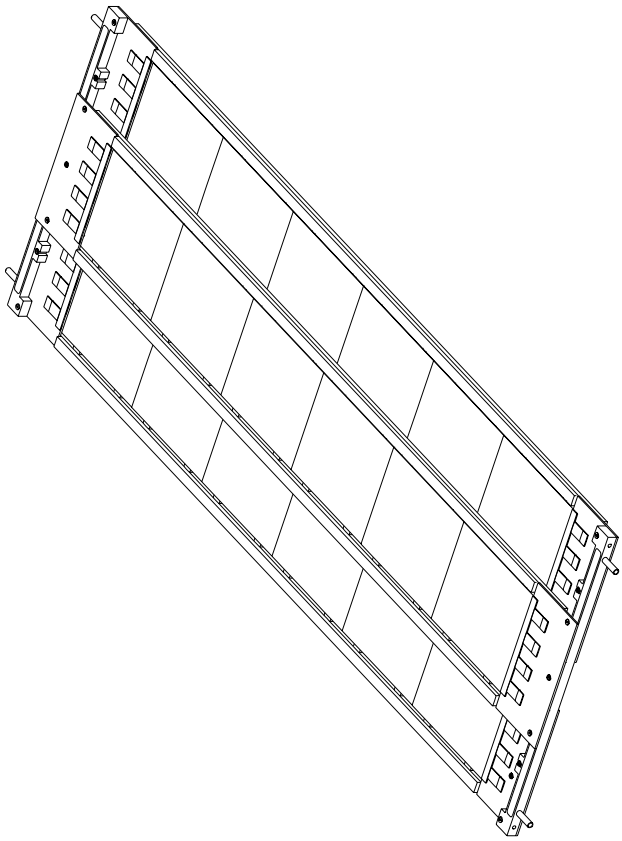

Figure 6.5: A view of a barrel 'slat' which consists of three ladders.

are placed at the ends as in the SVX and SVX′ designs. Since the hybrids do not lie directly on the Si wafers, the transfer of heat to the Si is determined mainly by the thermal pathways provided by the microbond wires. Heating of the Si itself is less of a problem than for SVX II. These two features can be achieved without introducing dead areas in the layers by taking advantage of the large amount of space available. The result is a simple and robust ladder design.

6.2.5 Bulkheads

The ladders will be supported by carbon fiber disks. Note that in the largest radius layer, three ladders are attached to a single cooling channel per 30^o wedge. A closeup is shown in Figure 6.6. The middle ladder is attached to one side of the block and the outer two are on the opposite side as shown in Fig. 6.5. This allows adjacent ladders to be overlapped. The overlap is $\sim$6 mm. For the inner radius layer two ladders are attached to the cooling block. This scheme results in a 30^o wedge structure as for SVX II.

Figure 6.7 shows the basic layout of the carbon fiber support disks. Oblong channels allow the passage of cables. Smaller holes are shown for cooling pipes and attachment and alignment pins. A cross sectional view (r-z plane) of the ISL with offset layers is shown in Figure 6.8.

6.2.6 ISL mechanical support

6.2.6.1 Support structure specification

In order to allow $r-\phi$ pattern recognition within the SVX II and ISL system, the ISL readout strips must

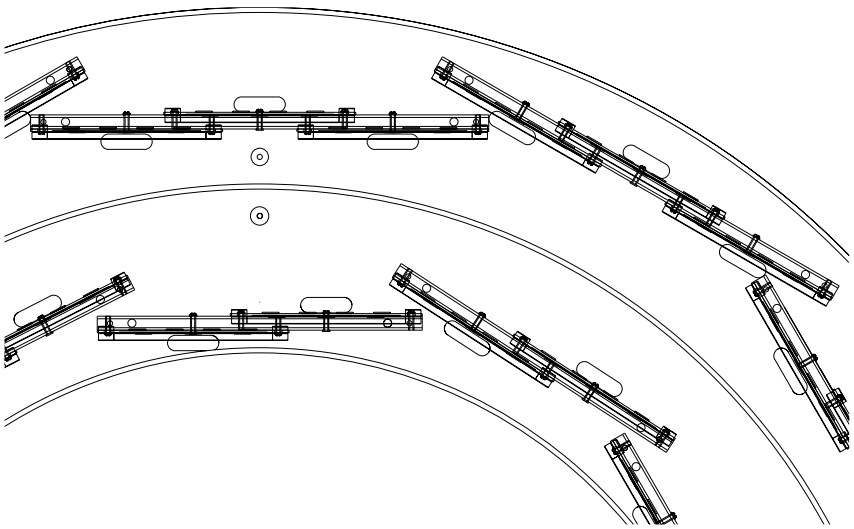

Figure 6.6: Closeup of one section of the end view of an endplug barrel.

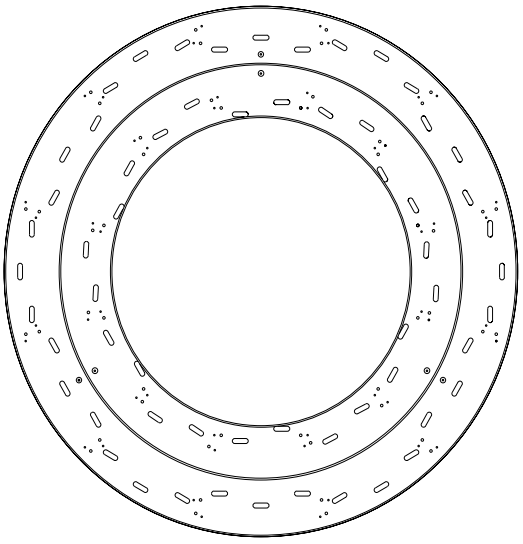

Figure 6.7: Carbon fiber support disks.

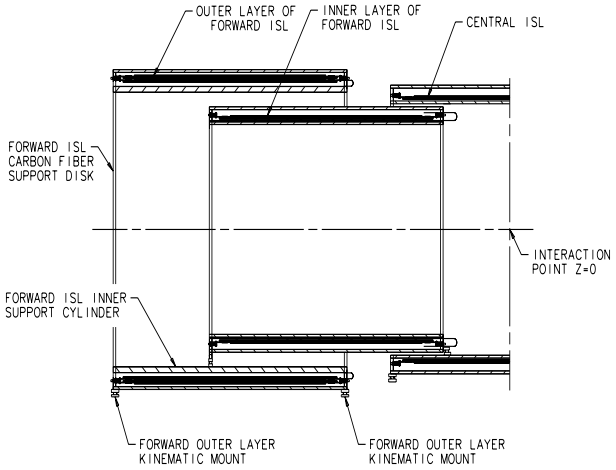

Figure 6.8: Schematic view of the ISL system.

be parallel to those of the SVX II within ± 200 μm over the length of the ISL ladder. Meeting this overall global specification requires that the axis of the ISL layers be aligned to within ± 180 μm of the SVX II axis over the length of an ISL layer. Such small alignment tolerances require that the layer positions be measured and adjusted on a precision coordinate measurement machine (CMM).

The ISL support structures provide a platform on which the layers can be mounted and surveyed using a CMM, and transfer the load of the layers to the COT endplates. In addition, the support system must carry the full mechanical load of the SVX II spaceframe assembly without compromising the precise alignment of the ISL. The system must also be stable against changes of temperature and humidity since the silicon detectors may require the circulation of cooled dry nitrogen to facilitate temperature regulation. Finally, the support system must introduce a minimum of material into the tracking volume in order to preserve the high precision of the tracking detectors.

6.2.6.2 ISL support system design

The main structural element of the ISL mechanical support system is a carbon fiber composite cylinder with an outer radius close to the inner radius of the COT. See Fig. 6.9. The large radius allows the construction of an extremely stiff tube with very little material. The cylinder consists of two carbon fiber skins separated by a honeycomb filler material. The Each carbon fiber layer is made of multiple plies of epoxy-impregnated carbon fibers, with the fibers in each oriented for maximum strength. The tube is kinematically supported at the ends by the COT endplates. Carbon fiber rings ("feedthrough flanges") at the ends of the tube will prevent deformation of the cylinder under the load of the SVX II and ISL detectors.

Initially, the tube is constructed as two, independent half-cylinders. During the detector mounting procedure, the lower half-cylinder, without feedthrough flanges, will be placed in a fixture to maintain its shape as load is added. This configuration allows full access to the interior of the tube for the purpose of surveying detector positions. The central and outer ISL layers will then be kinematically mounted inside the lower half-cylinder and adjusted into position. Carbon fiber rings inside the tube will distribute the point loads of the layers over the surface of the carbon fiber skins, thereby minimizing local deformations of the tube at the mount points. If the tube deflections under load are sufficiently small, then it should be possible to place the mounts with sufficient accuracy using a CMM to avoid the need for additional adjustments.

A third carbon fiber skin with a slightly smaller radius than the inner radius of the tube will be placed in the central part of the tube to provide a mounting platform for the central ISL.

After mounting the central and forward ISL layers, the inner layers will be kinematically mounted inside the outer layers. The load of the inner layers is first transferred to the inner surface of the outer layers, then to the ISL support cylinder through the outer layer support disks. Again, further adjustment of the layer positions may be unnecessary if the mounts can be placed with sufficient accuracy and the mounts do not move appreciably under load.

Cables and cooling pipes will be dressed along the sides of the lower half-cylinder. Additional nonstructural hoops mounted to the lower half-cylinder outboard of the forward layers can be used to strain relieve cables and cooling tubes from the upper portion of the layers.

After ISL installation and alignment, the SVX II spaceframe/beam pipe assembly is inserted via a transfer fixture and kinematically mounted in the ISL. (The SVX II barrels are assumed to be mounted and properly aligned prior to this step.) Two choices are possible for the mount points of the SVX II spaceframe. In the first option, the load of the SVX II can be placed on the inner support cylinder of the outer forward ISL (as in Fig. 6.9). This load is then transferred from the forward ISL to the ISL support cylinder through the support disks of the outer layers. The second option completely removes the load from the ISL inner cylinder by extending the SVX II spaceframe to the ends of the outer forward layers. The load of the SVX II can then be transferred directly through the ISL support disks to the ISL support cylinder. Lengthening the SVX II spaceframe without altering the basic design will increase the expected sag of the SVX II frame to 12 μm, compared to 7 μm for the shorter design. The larger value is well within the design specifications for the SVX II spaceframe. In either option, it should be possible to position the mounts for the SVX II spaceframe with sufficient precision that further adjustment of

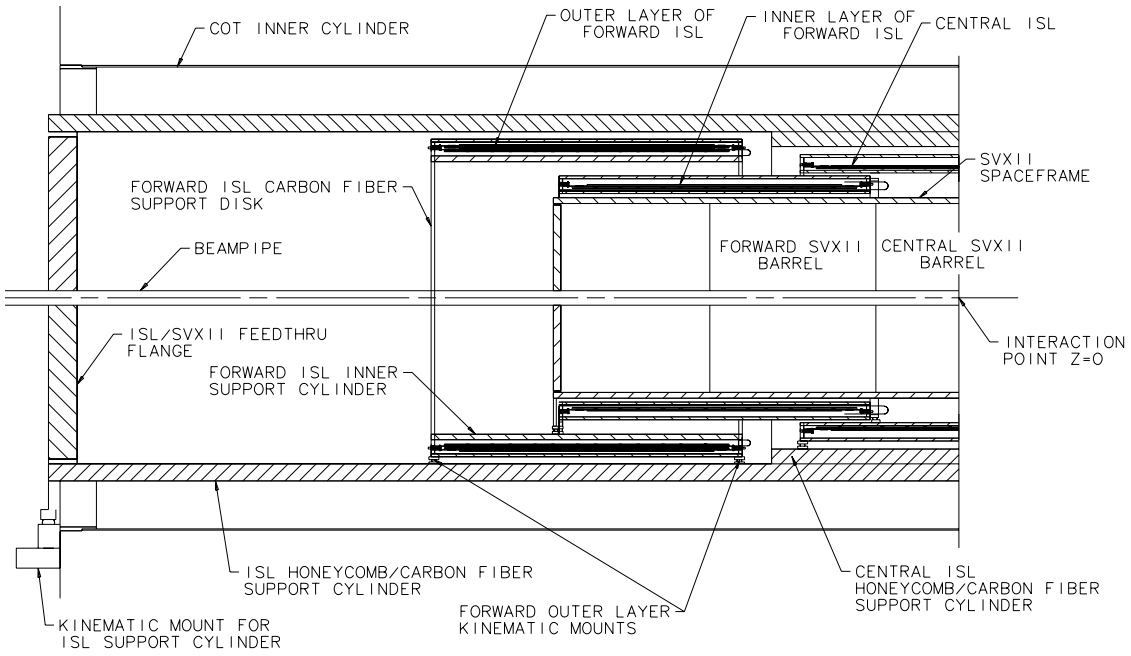

Figure 6.9: An r-z view of the ISL spaceframe support system.

the SVX II position is unnecessary.

The final steps in the assembly of the ISL support cylinder require mounting the top half-cylinder to the bottom half-cylinder and installing the feedthrough flanges to strengthen the ends of the completed tube. In order to preserve the alignment of the various detectors, this procedure may introduce no new internal stresses. A similar problem exists in SVX II for joining the bulkheads into a single barrel after all ladders have been installed, and has been successfully used during SVX and SVX′ construction. After joining the two half-cylinders, the beam pipe load will be transferred to the ISL support cylinder, and the feedthrough flanges installed and glued into place. Slots in the feedthrough flanges permit cables and cooling pipes to exit the tracking volume.

6.3 Readout and Data Acquisition

SVX3 readout chips are used so that the data acquisition (DAQ) system is identical to the SVX II system described in Chapter 5. However, the low occupancy of ISL allows a coarser DAQ segmentation to reduce the size and cost of the system. Two ladders will be attached to each portcard input so that a single portcard covers two 30° wedges. This assigns about 60% more channels to each portcard than is done in SVX II, but the readout time will be less than SVX II since less $\eta\phi$ space is covered by each portcard input. The component count for the ISL is compared to SVX II in Table 6.3. Notice that the ISL uses more silicon than SVX II, but it has about half as many channels and portcards.

	SVX II	ISL
Detectors	720	900
Half ladders	360	300
Chips	3168	2100
Channels	405,504	268,800
Hybrids	720	300
Port Cards	72	30

Table 6.3: Comparison of component counts in SVX II and ISL.

The cabling is also copied from the SVX II design. The space required to route cables from the port cards to the FIBs outside the detector volume is expected to be about 25 of the 250 available slots.

6.4 ISL Performance Issues

We address here a number of performance concerns which are close to the hardware: occupancy, signal-to-noise ratio, material, and hit resolution. We also show with a simple calculation that the ISL acceptance for tracks already in the SVX II is very high, which is crucial if the SVX II + ISL are to function as a single "inner tracker". A simulation study of the performance of the ISL in the CDF II "integrated tracking" environment is presented in Chapter 7.

6.4.1 Hit Occupancy

The large radius of the ISL leads to very low occupancies. Based on a measurement from SVX′ data in minimum bias triggers, the expected occupancy from a single minimum bias interaction is only 0.08%. For a $t\bar{t}$ event at $\mathcal{L} = 2\times10^{32}\mathrm{cm}^{-2}\mathrm{s}^{-1}$ @ 396 ns, the occupancy predicted from Monte Carlo is 0.7%. This low occupancy is a significant advantage for the pattern recognition.

6.4.2 Signal to Noise

Each ISL ladder contains three silicon crystals while SVX II ladders are made from two. The extra ladder length reduces the channel count, but it also increases the capacitance that loads the front end amplifier by about 50% to 30 pF for the axial side and 40 pF for the stereo side. The increased capacitance results in a larger RMS noise. From Fig. 5.5 in Chapter 5, the expected noise at 396 ns bunch crossing (371 ns integration time) is $1300e^-$ for the axial side and $1700e^-$ for the stereo side. For 132 ns bunch crossing (107 ns integration time), the noise increases to $2200e^-$ for the axial side and $3000e^-$ for the stereo side. In the worst case, the signal to noise is $\sim$ 8:1. Monte Carlo studies and experience with SVX′ have shown no significant deterioration in hit finding at signal to noise values as low as $\sim$ 4:1. The low radiation dose expected at the ISL radii reduces the need to begin with a higher signal to noise.

6.4.3 Material

The material contributed by each ISL ladder is similar to an SVX II ladder. In the central region, the single ISL layer amounts to $\sim$ 0.5% of a radiation length (at 90° incidence). The two layers in the plug region amount to $\sim$ 1%. The additional material from the hybrids, bulkheads, portcards, etc., amounts to an additional 1% when averaged over the length of the detector. The total material is then $\sim$ 2% of a radiation length.

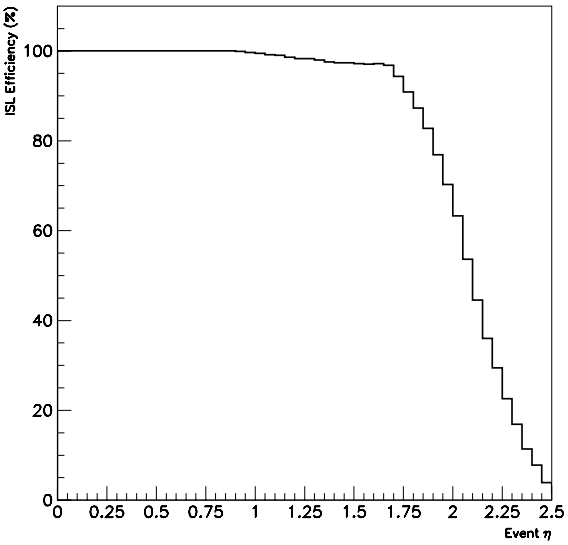

Figure 6.10: ISL acceptance for tracks which are contained within SVX II.

6.4.4 Hit resolution

The readout pitch is twice the strip pitch. By using charge sharing to interpolate the track impact position, the axial hit resolution is expected to be $\leq$ 16 μm. Similarly, the stereo hit resolution is expected to be $\leq$ 23 μm perpendicular to the strip direction. Of course, the alignment and construction tolerances are important to the final resolution as discussed below.

6.4.5 Acceptance

Since there is ample space in the intermediate region, the ladders are staggered in radius and in z to eliminate gaps. The overlap between adjacent ladders is $\sim$ 6 mm in $r-\phi$ to account for the insensitive regions on the stereo side. The acceptance is then dominated by the length of the detector, which extends to $|\eta| \sim 1.9$ (see Fig. 6.1). We have performed a simple simulation to calculate the ISL acceptance for particles already contained within SVX II, for the case of an extended luminous region with $\sigma_z = 30$ cm. The result, Fig. 6.10, shows that even with a long bunch, the ISL will record over 95% of the par-

ticles seen by the SVX II out to event $|\eta|$=1.7, and is still 50% efficient for tracks at $|\eta|$=2.0.

6.5 Construction Tolerances

The most crucial aspect of the construction of the detector is the ladder internal alignment. By this we mean the alignment of strips from wafer to wafer and the referencing of the strips to the ear-pin holes on the readout hybrid. Ideally one would like this alignment to be better than the intrinsic hit resolution of the sensors. Fortunately the construction of the ladder is carried out with a precision coordinate measuring machine (CMM) having typical resolution of 0.1-0.2 mil (2.5-5.0 μm) using positioning fixtures like those used in the SVX and SVX′ projects. In these projects, the ladder internal alignments that were achieved were consistent with the CMM resolution.

Ladder to ladder alignments in a given layer, from layer to layer, and relative to the SVX II ladders are important for the pattern recognition but do not necessarily limit the final resolution of the device. In particular, it is anticipated that the ladders will be aligned using tracks which traverse the COT and SVX II. Thus, given that the ladders are themselves very precisely constructed, it should be possible to locate them and determine alignment constants that describe how their positions deviate from nominal. This will insure that hit resolution is not degraded for those cases in which the z locations of the axial hits are known. The z position is necessary in order to remove $r-\phi$ displacements resulting from strips not being parallel to those in SVX II. We have chosen ± 75 μm as our specification for tolerable $r-\phi$ ladder-to-ladder misalignment (in a single layer) to insure the convergence of the alignment procedure. As discussed below, the actual misalignments are expected to be about half this amount.

If the pattern recognition relies on starting from axial-only reconstruction of tracks in Si layers, then the z location of axial hits will not yet be known and the actual relative misalignments of ladders will contribute an $r-\phi$ uncertainty which could be large. Ideally, you want the maximum $r-\phi$ deflection relative to SVX II ladders to be less than the two hit resolution ($\sigma = 220$ μm) and less than the $r-\phi$ pointing resolution from SVX II ($\sigma = 250$ μm). It can be shown that this means that the deflection angle $\delta\alpha$ which measures the degree to which the strips in an outer layer are not parallel to those in SVX II, should satisfy

$$\delta\alpha < \frac{2\sigma}{L(1.5 + \frac{3.0}{\sqrt{12}})} = 0.4 \text{ mrad}$$

Note that this corresponds to 8 mil across the $L \sim 50$ cm length of the barrel. As described above, it is our plan to build the intermediate radius Si layers and then assemble them together with the SVX II using a large CMM for alignment. This will allow the relative angle between the axis of SVX II and that of the ISL layers to be kept to $\delta\alpha < 0.2$ mrad. This is adequate to allow axial-only tracking provided the ladder to ladder alignment in the ISL is not itself worse than 8 mil.

The ladder to ladder $r-\phi$ alignment within the ISL is determined by several factors. First, the alignment of the hybrid connection holes to the pin holes on the cooling block which attach the ladder to the carbon fiber support disk will introduce an uncertainty of no more than 0.5 mil at each hybrid. The alignment of the Be block to the carbon fiber support disk is dominated by the reference hole positioning and clearance. This can be achieved with an uncertainty of less than 1.0 mil at each end. Taking the conservative estimate for the ladder internal alignment to be ± 10 μm, it then follows that the ladder to ladder alignment in a single layer will be

$$\sigma < \sqrt{2 \cdot (10^2 + 13^2 + 25^2)} \sim 40 \ \mu m$$

Layer to layer alignment will contribute an additional global uncertainty of 25-50 μm which however will not seriously impact tracking alignment or ultimate performance of the detector. We conclude that the design we have presented will allow construction within the tolerances necessary for the success of the

	Necessary	Achievable
Wafer-to-Wafer	± 5 μm	± 2.5 μm
Wafer-to-Hybrid	± 5 μm	± 2.5 μm
Hybrid-to-Block	± 25 μm	± 13 μm
Block-to-Disk	± 50 μm	± 25 μm
Ladder-to-Ladder	± 75 μm	± 40 μm
ISL-to-SVX II	± 200 μm	± 100 μm

Table 6.4: Summary of the necessary and achievable ISL construction tolerances.

axial-only stage of the pattern recognition and for the alignment and full resolving power of the detectors in 3D tracking. A summary of the necessary and achievable tolerances is contained in Table 6.4.

Bibliography

[1] P. Weilhammer "Double-sided Si strip sensors for LEP vertex detectors" Nucl.Instr. and Meth. A 342 (1994) 1

[2] P.P. Allport et al. "Performance of the ATLAS-A silicon detectors with analogue readout" ATLAS-INDET-NO-133 (1996)

Chapter 7

Simulated Performance of Integrated Tracking System

7.1 Introduction

In this section we describe the performance of the CDF integrated tracking system for Run II. This includes the new central tracker, COT, and the new silicon vertex detectors, SVX II+ISL.

In Section 7.2 we describe the simulation tools used for evaluating the performance of COT and SVX II. In Section 7.3 we define the data sample used to measure tracking performance of COT and SVX II. In Section 7.4, we describe how the performance of the COT in Run II can be gauged from the performance of the CTC in Run I, along with the simulation results. In Section 7.5, we demonstrate the performance of the combined SVX II and ISL system. In Section 7.6 we study the performance of the combined system: COT+ISL+SVX II. Section 7.6.1 outlines a method used to link tracks in the inner detector (i.e. SVX+ISL) to the COT, in the r-ϕ plane. We describe an algorithm developed for linking hits in the r-z plane in Section 7.6.2. Finally, in Section 7.6.3, we study the helix parameter resolution of the integrated tracker, as a function of luminosity.

7.2 Simulation of COT, ISL and SVX II

The COT simulation is a modification of the current full CTC simulation. It uses the correct COT geometry (e.g. the cell sizes, the different tilt of the cells, etc.) and incorporates the predicted pulse width and drift velocity. The single hit resolution is based on experience with the CTC and is a conservatively chosen to 200 μm.

For the SVX II we use a simulation which is an extension of our present full SVX′ simulation. It incorporates the fifth additional layer, the stereo layers, and the ambiguity in the 90° layers.

For the ISL, we use a simple simulation that generates hits by recording Monte Carlo track positions at the ISL radii. We then use a parameterization of the detectors' hit resolutions to study the helix fit resolutions of reconstructed tracks.

7.3 Data Sample

We have chosen tracking of b-daughters in $t\bar{t}$ events as the benchmark for the performance of the tracking system. This is one of the most important and challenging environments in which one needs to find tracks efficiently. The generator used is the HERWIG Monte Carlo. It is essential to understand the effects of multiple interactions (see Figure 1.1). Therefore, we have developed a procedure for mixing one $t\bar{t}$ event with any number of generated minimum bias events. The minimum bias Monte Carlo has been tuned to reproduce the observed multiplicities in CDF data. For these tracking studies, we use Monte Carlo data samples with $t\bar{t}$ events alone, one $t\bar{t}$ event with a mean of three underlying minimum bias events, or one $t\bar{t}$ event with a mean of six underlying minimum bias events. The actual number of underlying minimum bias events for each $t\bar{t}$ event is drawn from a Poisson distribution with the appropriate mean. The $t\bar{t}$-alone dataset corresponds to low luminosity, while the three overlayed minimum bias event sample corresponds to $\mathcal{L} = 1(3) \times 10^{32}\text{cm}^{-2}\text{s}^{-1}$ for 36 (108) Tevatron bunches, and the six overlayed minimum bias event samples corresponds to $\mathcal{L} = 2(6) \times 10^{32}\text{cm}^{-2}\text{s}^{-1}$ for 36 (108) Tevatron bunches, respectively.

7.4 COT performance

We begin by modeling the COT as a stand-alone tracker. Two approaches are used to understand its performance. First, we rely on the nine years of experience with the CTC and the fact that the COT is very similar in design. The pattern recognition algorithms and performance of the CTC in the Tevatron environment are well understood. From scaling arguments, we can compare the performance of the CTC at Run I luminosities with the performance of the COT at Run II luminosities. This gives us a data-driven prediction of the COT performance. However, this projected performance is a lower limit since the COT has twice as many stereo measurements and better two-track resolution than the CTC. The second technique uses a simplified pattern recognition procedure to evaluate the COT performance. This approach has the advantage that it can be used for stand-alone studies of the COT as well as integrated studies of the COT and SVX II+ISL.

7.4.1 Projected COT performance based on CTC data

We characterize tracking chamber performance with momentum resolution, impact parameter resolution and tracking efficiency for daughter tracks from B hadrons from top quark decays. At $\mathcal{L} = 1 \times 10^{31}\text{cm}^{-2}\text{s}^{-1}$ in Run I, we measured the CTC (stand-alone) momentum resolution as $\delta p_T/p_T^2$=0.2%, and the impact parameter resolution as $\approx$ 340 μm. We measured the efficiency for b-daughter tracks from top quark decays by superimposing a Monte Carlo track, with the expected p_T and ΔR(track-jet) given by HERWIG, onto a jet from the data and re-tracking the event. At $\mathcal{L} = 1 \times 10^{31}\text{cm}^{-2}\text{s}^{-1}$, the CTC efficiency was measured to be 94.6%.

As noted above (and described in detail in Section 4.7.3), the performance of the COT in Run II can be gauged from the performance of the CTC in Run I, by simple scaling arguments based on the chamber geometries, pulse shaping, drift velocities, and the number of Tevatron bunches. In many ways this is the *most* reliable predictor of minimum COT performance because it is based on real data, mature reconstruction code, and simple scaling principles. This scaling suggests that the performance of the axial layers of the CTC at $\mathcal{L} = 1 \times 10^{31}\text{cm}^{-2}\text{s}^{-1}$, is equivalent to the performance of the axial and stereo layers of the COT at $\mathcal{L} = 7.6 \times 10^{31}\text{cm}^{-2}\text{s}^{-1}$ (36 bunches) and $\mathcal{L} = 1.9 \times 10^{32}\text{cm}^{-2}\text{s}^{-1}$ (108 bunches). On the basis of these arguments alone we can predict high tracking efficiency and good momentum resolution for the COT in Run II.

7.4.2 Pattern Recognition in COT

Our experience with the CTC has taught us that tracking chambers of this design are extremely efficient for single wire hits, so, strictly speaking, track finding should not be a problem. The tracking inefficiency in the CTC was due to attaching wrong hits to tracks and hence pulling the fitted helix from the correct one. The information is there, but the tracks are "lost" to mismeasurement.

Since the COT and CTC have similar r-ϕ characteristics, we expect their pattern recognition problems to be similar. We have studied hit availability in the COT and "confusion" at high luminosity using tools developed with the CTC. For these studies a Monte Carlo track is simulated and hits are created on the chamber wires according to the track's helix parameters and the resolution of the COT. The challenge of finding the track, with the correct p_T, impact parameter, ϕ_0, etc., is the selection of the *correct* hits to use in the helix fitting procedure. To analyze our ability to do so in the COT under Run II conditions, we use the following procedure:

1. From the momentum of the generated particle in the Monte Carlo, we calculate the corresponding helix parameters. These helix parameters are then used to open a 1 mm wide road, in both r-ϕ and r-z .

2. All hits within the road are picked up and fed to the same helix fitting routine which we used in the Level 3 trigger of Run I. This is a sophisticated routine which adds and/or rejects hits based on the χ^2 of the fit.

3. The returned helix parameters are compared with the input track parameters to measure the p_T resolution (curvature), impact parameter resolution, z_0 resolution, and $\cot(\theta)$ resolution.

This procedure is performed on the $t\bar{t}$ plus minimum bias event samples to examine the performance of the COT under different Tevatron conditions. The results of these studies are summarized below.

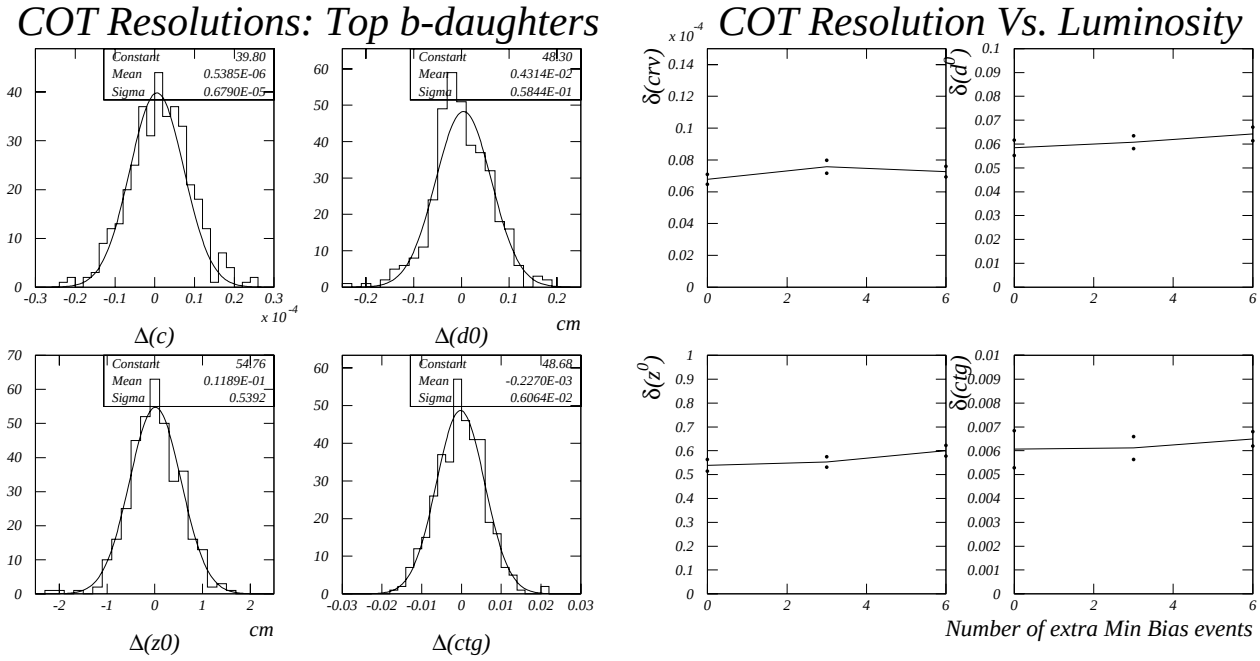

Figure 7.1: Left: Helix parameter resolutions at low luminosity. Right: Helix parameter resolutions versus the mean number of extra minimum bias events

7.4.3 COT Simulation Results

On the left in Figure 7.1 we show the resolution of the reconstructed curvature, impact parameter, z_0 and cotθ from COT tracking for low luminosity.

The resolution is defined as the difference between the reconstructed parameter and the helix parameters calculated from the trajectory of the generated particle. The resolution on the curvature is 0.68 $\times 10^{-4}$ cm^{-1} which corresponds to a momentum resolution of $\delta p_T/p_T^2 \simeq 0.3\%$ (GeV/c)$^{-1}$. The impact parameter resolution for the COT alone is about 600 μm while the z_0 resolution is about 5 mm and the cot θ resolution is 6 $\times 10^{-3}$.

These numbers agree with our expectations for COT performance given the larger inner radius of COT compared to CTC.

Although a single $t\bar{t}$ event represents a busy tracking environment, unless several minimum bias events are overlapped with this event, it still does not represent the operating conditions of Run II. Therefore, we have studied the effect of multiple interactions on the resolution of the tracking parameters. The right plot of Figure 7.1 shows the dependence of the resolution of the reconstructed curvature, impact parameter, z_0 and cotθ on the mean number of extra minimum bias events for means of 0, 3, and 6 extra minimum bias

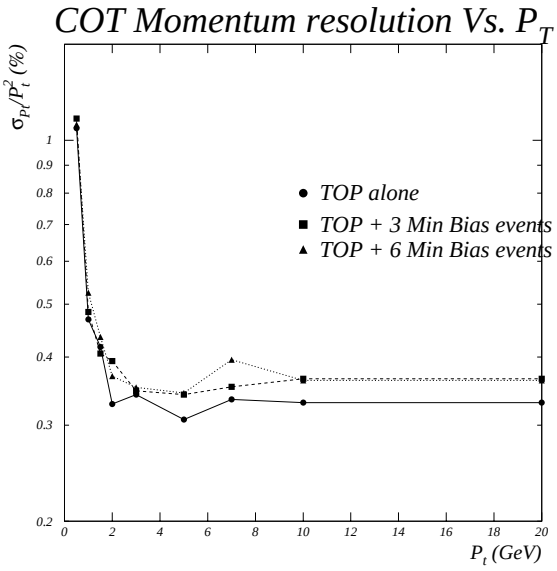

Figure 7.2: Momentum Resolution versus p_T for three luminosities.

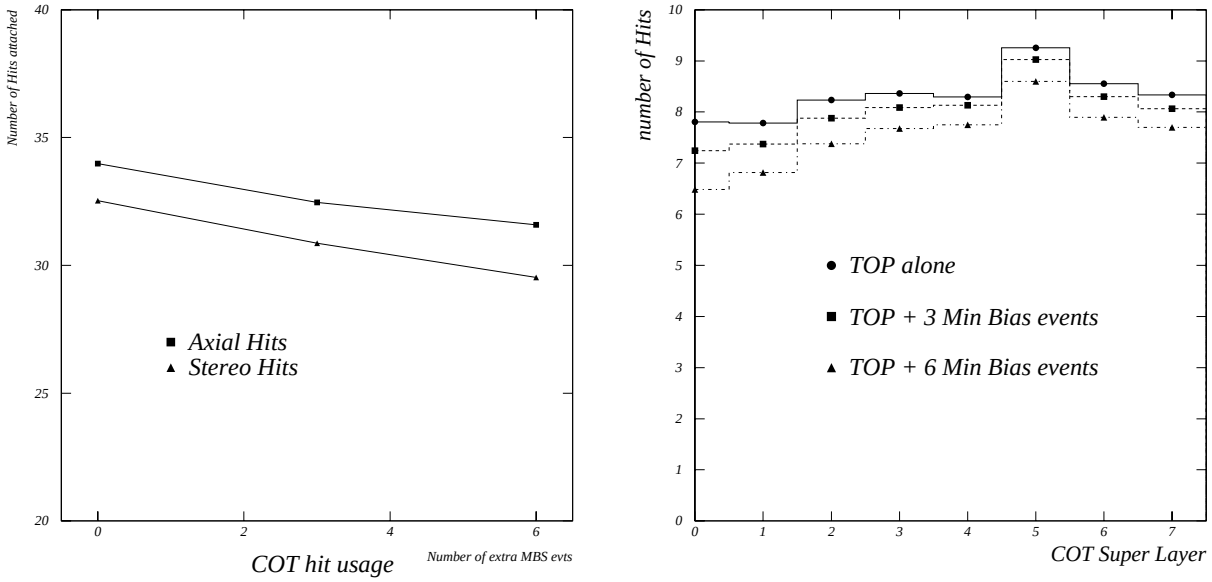

Figure 7.3: Left: Hit usage in COT versus mean number of overlapped minimum bias events. Right: Hit usage in COT versus super-layer for three different instantaneous luminosities.

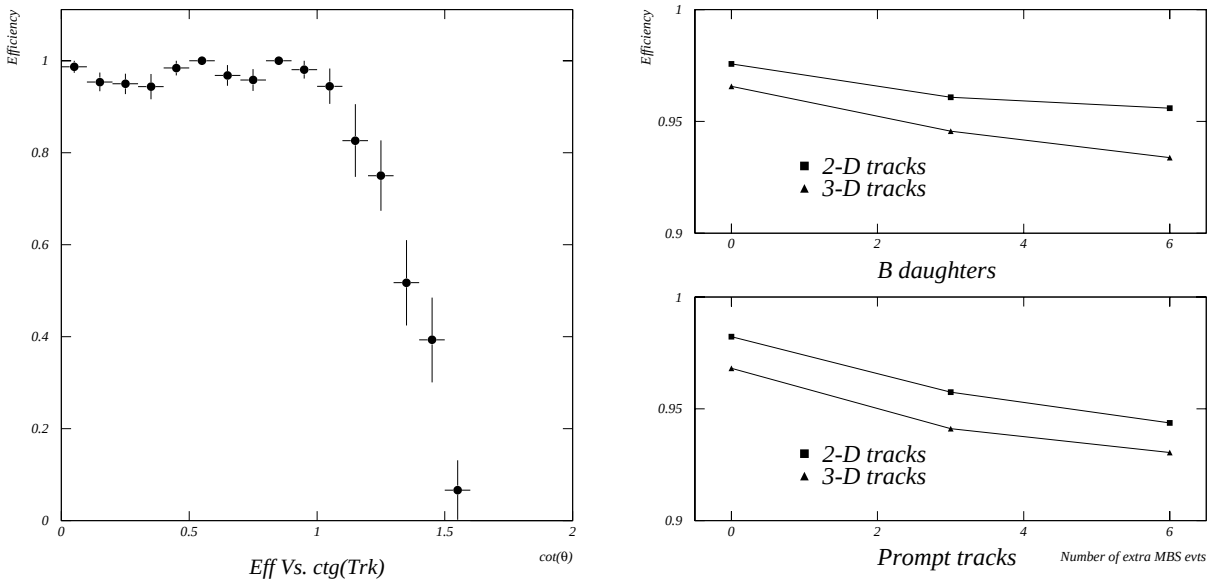

Figure 7.4: Left: Tracking efficiency versus $\cot\theta$ for prompt tracks at low luminosity in the COT. Right:COT track finding efficiency versus mean number of overlapped minimum bias event. The upper plot is for tracks from B meson daughters from $t\bar{t}$ decays, and the lower for prompt tracks.

events. The dots in Figure represent the 1σ uncertainty on the resolution measurement, note that some of the apparent performance variation with luminosity is nothing more than our Monte Carlo statistics! Recall that 6 extra minimum bias events corresponds to a luminosity of $6 \times 10^{32}\text{cm}^{-2}\text{s}^{-1}$ for 108 bunch operation. We see very little degradation of the COT performance with increasing luminosity.

We have also explicitly measured the p_T resolution versus track p_T (Figure 7.2) for the three different data samples and only a slight dependence on luminosity is observed.

High quality tracks typically use a large number of hits that have passed strict selection requirements. As the tracking environment becomes more confused, fewer hits may be used for track fitting. The left plot in Figure 7.3 shows the average number of axial and stereo hits attached to a track as a function of the number of underlying minimum bias events. Note that the maximum possible number of hits is 48 each for both axial and stereo measurements but the strict hit selection in the fitting procedure reduces the number of hits actually used. The reduction in hit usage from low luminosity to the equivalent of $6 \times 10^{32}\text{cm}^{-2}\text{s}^{-1}$ with 108 bunches, is modest; as seen in the right hand plot, the loss occurs mainly in the inner COT layers. Reduced performance caused by lost hits in the inner super-layers will be regained partially through the integrated use of the ISL and SVX II in the pattern recognition.

Besides excellent resolution on found tracks, it is essential that we have high efficiency for identifying tracks. We define the tracking efficiency as the fraction of tracks found with all of the helix parameters within five standard deviations of the correct value as defined by the Monte Carlo track. The standard deviation of a parameter is fixed to its value at low luminosity, shown in Figure 7.1. We measure the track finding efficiency both for prompt tracks and for tracks of B meson daughters from top quark decays. The tracking efficiency as a function of $\cot\theta$ for prompt tracks is shown in Figure 7.4. It is flat out to $\cot\theta$=1 after which the track no longer goes through all super-layers.

In Figure 7.4 we also show the efficiency as a function of the mean number of underlying minimum bias events. Earlier, we used scaling arguments to predict a COT efficiency for B meson daughters of 94.6% at a luminosity $7.6 \times 10^{31}\text{cm}^{-2}\text{s}^{-1}$ with 36 bunches. This corresponds to 2.4 underlying minimum bias events, where we measure now about 95% for 3-D tracks. Once again the performance of the COT with increasing luminosity does not degrade significantly and the slight degradation will be recovered by integrating the ISL and SVX II into the pattern recognition.

7.5 SVX II+ISL performance

In this section we describe the stand-alone performance of the "inner tracking" system of SVX II + ISL. This is of primary importance for tracking in the plug region, $1.0 < |\eta| < 2.0$, where there is little or no COT coverage, and it is also essential for integrated SVX II+ISL+COT tracking in the central region, $|\eta| < 1.0$.

7.5.1 r-ϕ Tracking

Ultimately, we will find track segments in the full seven layers of SVX II+ISL and link these to track segments found in the COT super-layers. However, for these studies we combined a full SVX II hit level simulation and pattern recognition with a simple ISL simulation and studied the power of the SVX II+ISL combination by projecting the SVX II tracks to the ISL radii and looking at hit matching.

7.5.1.1 SVX II r-ϕ Tracking

We first reconstruct tracks in the five layers of SVX II. The pattern recognition requires at least four hits to define a track.

The probability of a particle depositing four or more hits in the SVX II is 95% due to hits lost in interbarrel gaps. In order to remove effects due to SVX II length, this study considered only events with a primary vertex at $|Z| \leq 45$ cm.

Fake tracks are combinations of hits from several different tracks, so these hits are "shared" by two or more tracks. We use a pruning algorithm which discriminates against shared hits and increases the purity to S:N $\sim$ 4.5:1 while maintaining an efficiency of $\sim$ 93%.

The tracking efficiency is shown as a function of p_T and $|\eta|$ in Fig. 7.5. It is flat in p_T and flat in $|\eta|$ up to $\sim$ 2.

The helix parameter resolutions of the 2D tracks found in SVX II are shown in Fig. 7.5. The distributions are not well fit by a single gaussian because they are a mix of 4 and 5 hit tracks. The transverse

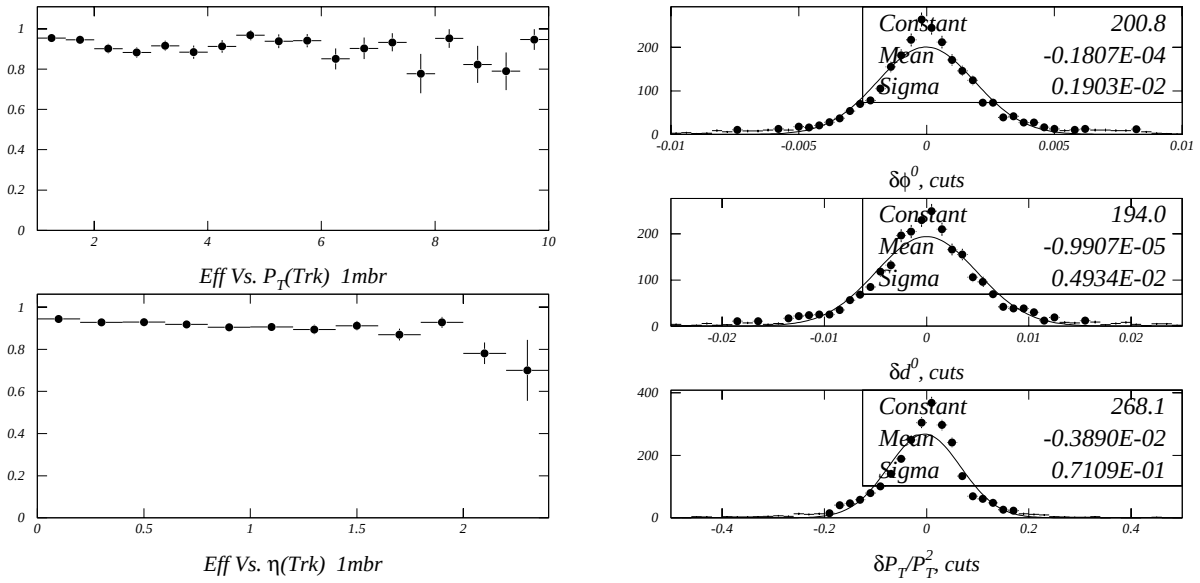

Figure 7.5: Left: The efficiency of finding r-ϕ tracks with the SVX II stand-alone pattern recognition and pruning is shown as a function of p_T and $|\eta|$ for b daughters in top + 1 minimum bias events. Right: The 2D helix parameter resolutions obtained with SVX II stand-alone tracks.

momentum resolution is $\delta p_T/p_T^2 \sim 7\%$. The impact parameter resolution is $\sim$ 50 μm and is dominated by the projection uncertainty that arises from the p_T resolution.

While the five layer SVX II can find 2D tracks with high efficiency it has the following shortcomings:

- low track purity (see below)
- poor resolution (p_T and impact parameter).

These limit the ability to link to COT, perform b-tagging, and identify leptons using track matching to a muon/electron tower. Additional information from ISL layers at larger radii is essential to:

- reject ghost tracks
- improve the p_T and hence the impact parameter resolution.

7.5.1.2 ISL hit matching

To evaluate the rejection power of a single ISL layer, we compute the distance between the extrapolated SVX II track and the nearest hit in the ISL layer at 20 cm. This is shown on the left in Figure 7.6 (open histogram). The bulk of nearest hits are correct hits, with an extrapolation accuracy of 50 μm. The fraction of the cases in which the nearest hit *does not* belong to the track is $\sim$ 5% (shaded histogram). For those cases the difference between the nearest hit and the correct hit is shown on the right. About a third of the time, the nearest hit and the correct hit are within 220 μm of each other. Since the readout pitch is 110 μm, hits this close together would in fact be merged into a single wide hit. It is only the remaining 3% of tracks which will lead to hit assignment ambiguity. Performing a fit which includes the outer layers will reduce the effects of multiple scattering, the combinatorics, and the effects of residual hit ambiguities from the sixth layer.ISL hit matching improves the track purity. For example, even a crude procedure such as requiring that the nearest hit be within 2.5 mm of the SVX II projection (i.e. full scale in Figure 7.6) improves the purity to S:N = 12:1, with high efficiency.

7.5.2 r-z Tracking

We will show in section 7.6.2 that completing the stereo in the central region with the coverage of the full tracking system is straightforward. For tracking in the plug region without COT, the stereo must be completed using SVX II and ISL alone.

Requiring three out of the four small angle stereo layers in SVX II+ISL, will yield high efficiency and

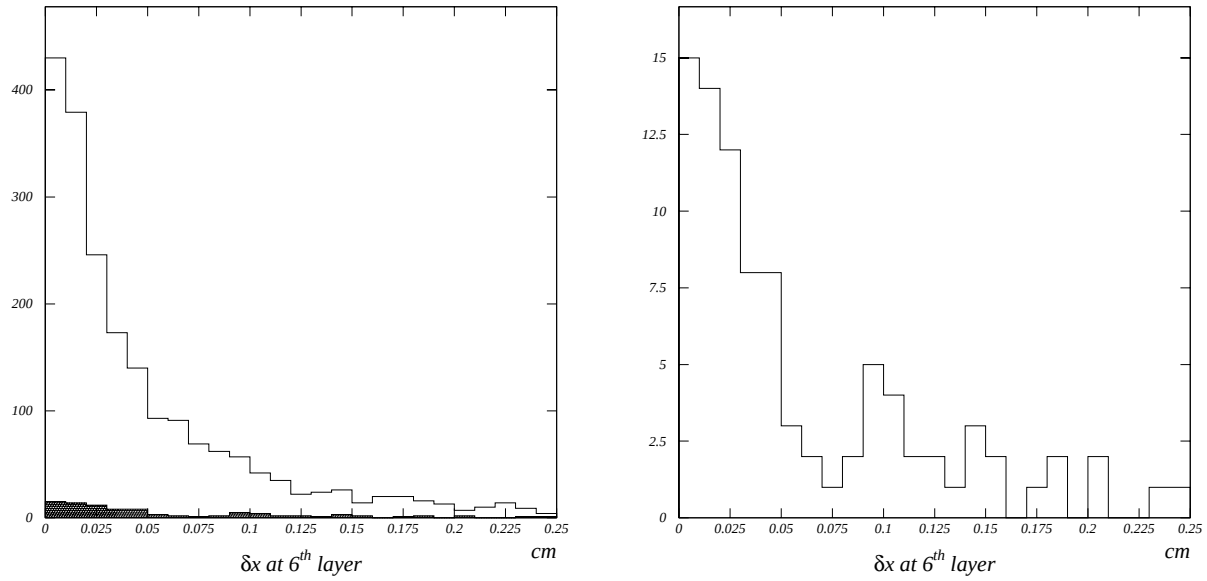

Figure 7.6: Left:The distance between the SVX II projection and the nearest ISL hit at $r = 20$ cm. The open histogram is for all hit combinations. The shaded histogram shows the cases where the nearest hit is not the correct hit.Right: The distance between the ISL hit which is nearest the SVX II projection and the correct hit is plotted for cases in which the nearest hit is *not* the correct hit

still provide z_0 resolution similar to that obtained with the CTC in Run I. It suffices to associate the track with its primary vertex, since all primary vertices will already have been found with high precision using SVX II's 90° stereo layers. Using the precise Z_{vertex} information, with the SVX II+ISL small angle stereo, one can attach the 90° hits in SVX II, and improve the final $\cot\theta$ and z_0 resolutions enough to allow for 3D vertexing.

7.5.3 Resolution of SVX II+ISL System

Once the tracks have been found, the precision space points and long lever arm provided by SVX II and ISL will yield excellent resolution on the helix parameters since the p_T resolution depends on the square of the lever arm. We have studied this with a parameterization of the detector resolutions. As shown in Figures. 7.7 and 7.8, we obtain the following asymptotic resolutions for the forward barrel (two ISL layers at $r = 20$ and 28 cm):

- $\delta p_T/p_T^2 \sim 0.4\%$
- $\delta d_0 = 15$ μm
- $\delta\phi_0 = 0.3$ mrad

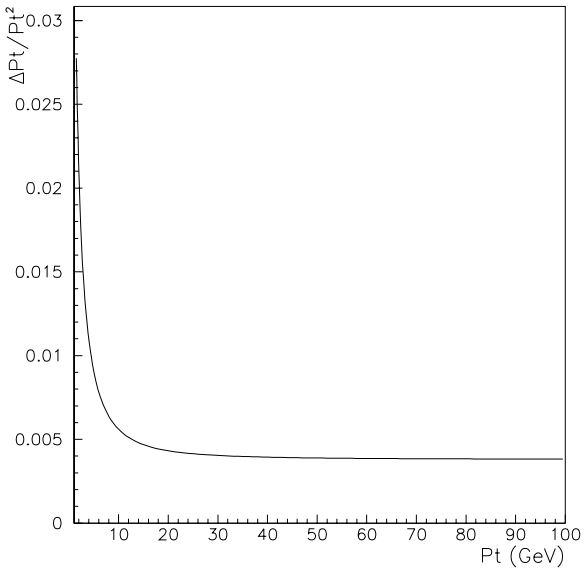

Figure 7.7: The p_T resolution obtained from a parametrization of the ISL resolution is plotted as a function of p_T.

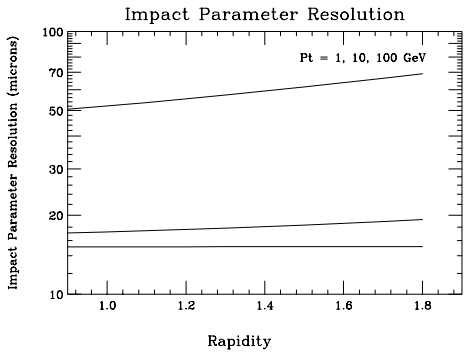

Figure 7.8: The impact parameter resolution obtained from a parameterization of the ISL resolution is plotted as a function of $|\eta|$.

Detector Configuration	Single tag eff.(%)	Double tag eff.(%)
SVX′+CTC	37.6 ± 1.0	6.9 ± 0.5
SVX II+COT	46.7 ± 1.1	8.7 ± 0.6
SVX II+ISL+COT	60.1 ± 1.0	15.1 ± 0.8

Table 7.1: Efficiency for single and double b-tagging in $t\bar{t}$ Monte Carlo for different detector configurations. The results are from a parametric study.

The p_T resolution is within a factor of two of that obtained with the full CTC in Run I and is sufficient for track matching and E/p cuts for electron and photon identification in the plug calorimeter. It will also enable *in situ* calibration of the plug calorimeter energy scale.

The impact parameter resolution is about what was obtained with the CTC+SVX in Run I. It will extend our b-tagging capabilities into the plug region, $|\eta| < 2.0$.

7.5.4 b-tagging for $|\eta| > 1$

We have carried out a parametric study of the b-tagging efficiency with SVX II+ISL. Beginning with generator level 4-vectors, we apply detector acceptance cuts and tracking efficiencies for SVX II, ISL, and COT. Helix parameter smearing is done based on the expected resolutions and the resulting tracks are fed to a vertex fitter to perform two dimensional secondary vertex tagging. The results are shown in Table 7.1. Of most significance is the factor of two increase in double tag efficiency over the Run I configuration. This results from the extension of precision tracking to $|\eta| \sim 2$. This will have a significant impact on the top mass measurement since some of the systematic uncertainties are reduced in double tagged events. It should also allow studies of single top production for which the b quarks tend to be more forward.

7.5.5 Pointing into COT

The SVX II+ISL combination can find tracks efficiently, with high purity, and with good resolution. An added benefit of the integrated silicon tracker is the possibility of using these tracks as an integral part of the overall track reconstruction with the COT. This is especially important in the region $|\eta| > 1$ in which the COT coverage is incomplete. Even if the number of COT super-layer segments is too small to efficiently find full COT tracks with high efficiency, the SVX II+ISL tracks have sufficient pointing resolution to match to the COT segments in the inner super-layers. This can improve the momentum resolution and help in the stereo reconstruction.

The pointing uncertainties at various radii are shown in Table 7.2 for tracks of various momenta (multiple scattering is included assuming normal incidence). Note that for $p_T \geq 3$ GeV, the pointing resolution of the SVX II and just the single ISL layer at r = 22 cm is smaller than the COT cell size (7.6 mm) even at the radius of the outer super-layer. If a hit from the outer ISL layer is included (Table 7.2C), the pointing resolution at the inner COT super-layers (r = 60 cm) is comparable to the COT hit resolution, and the combination of the COT information with the SVX II+ISL track will improve the resolution considerably. This allows a completely different approach to integrating the inner and outer tracking chambers as discussed below.

7.6 Integrated Tracking Performance (SVX II+ISL+COT)

The procedure used during Run I to link SVX′ hits with CTC tracks worked as follows: For a given CTC track, we extrapolated the helix to the outermost layer of the SVX′ and performed a tree search within a road defined by the CTC track. SVX′ hits were attached to the CTC track based on the combined χ^2. Naturally, this method cannot add efficiency; it may

A: SVX II

Radius	p_T = 1 GeV	3 GeV	10 GeV
20 cm	0.24 mm	0.16 mm	0.15 mm
30 cm	0.84 mm	0.53 mm	0.48 mm
80 cm	9.5 mm	5.5 mm	5.0 mm
130 cm	27.5 mm	16.0 mm	14.0 mm

B: SVX II+ISL (r = 22 cm)

Radius	p_T = 1 GeV	3 GeV	10 GeV
30 cm	0.15 mm	0.06 mm	0.04 mm
80 cm	3.4 mm	1.3 mm	0.73 mm
130 cm	11.0 mm	4.0 mm	2.3 mm

C: SVX II+ISL (r=28 cm)

Radius	p_T = 1 GeV	3 GeV	10 GeV
60 cm	0.9 mm	0.3 mm	0.2 mm
80 cm	2.0 mm	0.7 mm	0.4 mm
130 cm	6.7 mm	2.5 mm	1.3 mm

Table 7.2: Pointing resolutions at various radii are shown for tracks of various momenta. The upper table (A) is for SVX II alone. The middle table (B) is for SVX II plus the central ISL layer at r = 22 cm. The lower table (C) is for SVX II plus both of the forward ISL layers (r = 20 cm and r = 28 cm).

only improve the resolution of already found CTC tracks.

This approach represents a minimal baseline algorithm which we understand very well. However, the additional layers of ISL when combined with SVX II, allow implementation of stand-alone silicon based track finding algorithms. These algorithms will substantially improve tracking performance in Run II.

7.6.1 Linking COT with SVX II+ISL: r-ϕ

The algorithm described below uses line segments from the SVX II+ISL+COT system. These line segments are obtained from five axial "super-layers" (four in the COT and one from the SVX+ISL system). The line segments in the various super-layers are then linked to form tracks using the position and direction of the lines.

To evaluate the performance of this algorithm we define line segments as follows:

- **COT**
  In each axial super-layer the position and direction of a Monte Carlo generated particle is smeared by the single hit resolution using the number of un-obscured hits present in the detector.
- **SVX II+ISL**
  We use the reconstructed tracks found in the SVX II+ISL system (see Section 7.5).

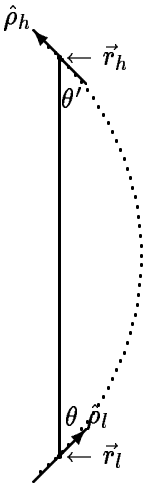

Figure 7.9: Geometry used for line-to-line linking.

For line-to-line linking we parameterize the lines by their position and direction at the super-layer center, $\vec{r}_{l,h}$ and $\hat{\rho}_{l,h}$ where the index l and h refer to the inner and outer line. Matching is by angle as shown in Figure 7.9: angles θ and θ' should match. A cut is put at

$$|\sin\Delta\theta| < 0.025 \qquad (7.1)$$

If more than one outer line matches an inner line (or vice-versa) using the cut above, the links with the lowest $|\sin\Delta\theta|$ are kept and links are stored in both directions, outer to inner and inner to outer. Figure 7.10 shows the result of linking super-layers 7 and 5 within the COT, as well as super-layer 7 and the SVX II+ISL. From this figure we conclude that even in a complicated b-jet from top decay, the line segments can be matched correctly with low fake rates.

We studied the efficiency of this procedure and found the individual line segment linking efficiency to be high. For example: linking super-layers 7 and 5 is $\sim$ 99% efficient whilst super-layer 7 and the SVX II+ISL is $\sim$ 92% efficient. As a result the overall track reconstructing efficiency using all available combinations is expected to be very high.

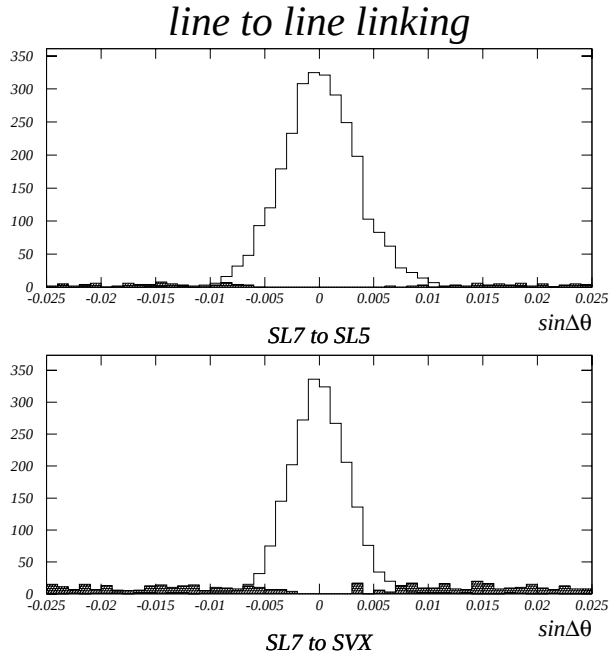

Figure 7.10: $\sin\Delta\theta$ distribution for the correct match and for spurious matches (hashed) is shown for top: super-layers 7 and 5 within COT, and bottom: super-layer 7 in COT and SVX II+ISL

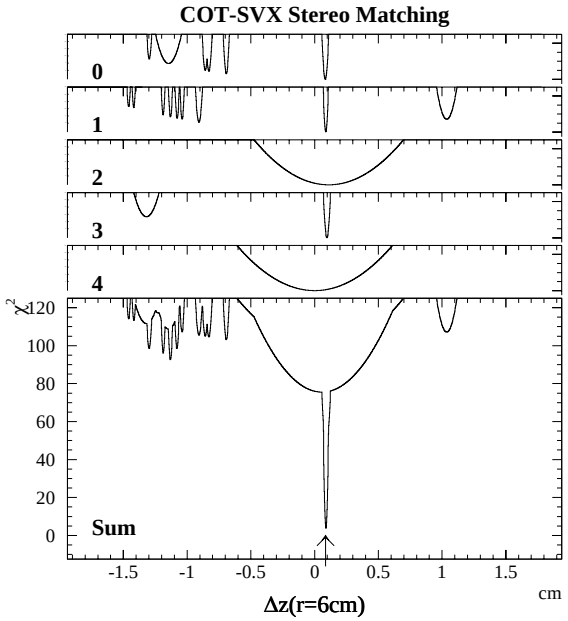

Figure 7.11: Hits in each of SVX II five layers within the 2 cm window, plotted is $\delta(z)$ weighted by the χ^2, and their sum.

It is also instructive to note that the quality of the links between COT super-layer 7 and SVX II+ISL, is better even than that to the nearby COT super-layer 5. This implies that even for large η, this procedure will allow matching of SVX II+ISL tracks to the available information in the COT. The COT measurements would substantially extend the lever arm and correspondingly improve the momentum resolution for such tracks.

7.6.2 Linking COT with SVX II+ISL: r-z

Since both SVX II and ISL are 3-D devices, requiring SVX II-COT track matching in the r-z view is a new possibility. To demonstrate this new capability, we need to show that the r-z track match can be made reliably despite the following potential problems:

- Ambiguities
  Both COT and SVX II are primarily r-ϕ devices Hence, the stereo relies on the r-ϕ result, in both.
  There is an additional ambiguity in the SVX II 90° stereo due to the ganging in the readout.

- The COT resolutions in r-z and r-ϕ are very different:

  $\sim$ 0.5000 cm COT extrapolation in r-z
  $\sim$ 0.0500 cm COT extrapolation in r-ϕ
  $\sim$ 0.0050 cm SVX II resolution in either view
  As a result, the mis-match between the two detectors is much worse in the stereo view.

For these reasons stereo linking of COT to SVX II is more challenging, and was investigated in detail.

The outline of the algorithm used is as follows:

- Assume a 3D COT track has been found, as described in Sec. 7.4.3.

- Assume that correct SVX II axial hits have been identified, as in previous section.

- For each silicon layer, combine z-strip or small angle stereo clusters with COT helix (1C fit), obtain z, χ^2.

- Each silicon hit defines a histogram of χ^2 vs z.

- Combine all hits in a layer as

$$\chi^2_{\rm layer}(z) = \max_{\rm hits} \chi^2_{\rm hit}(z)$$

  (see the upper 5 histograms in Figure 7.11).

- Combine layers as

$$\chi^2_{\rm total}(z) = \sum_{\rm layers} \chi^2_{\rm layer}(z)$$

  (see Figure 7.11 the bottom histogram).

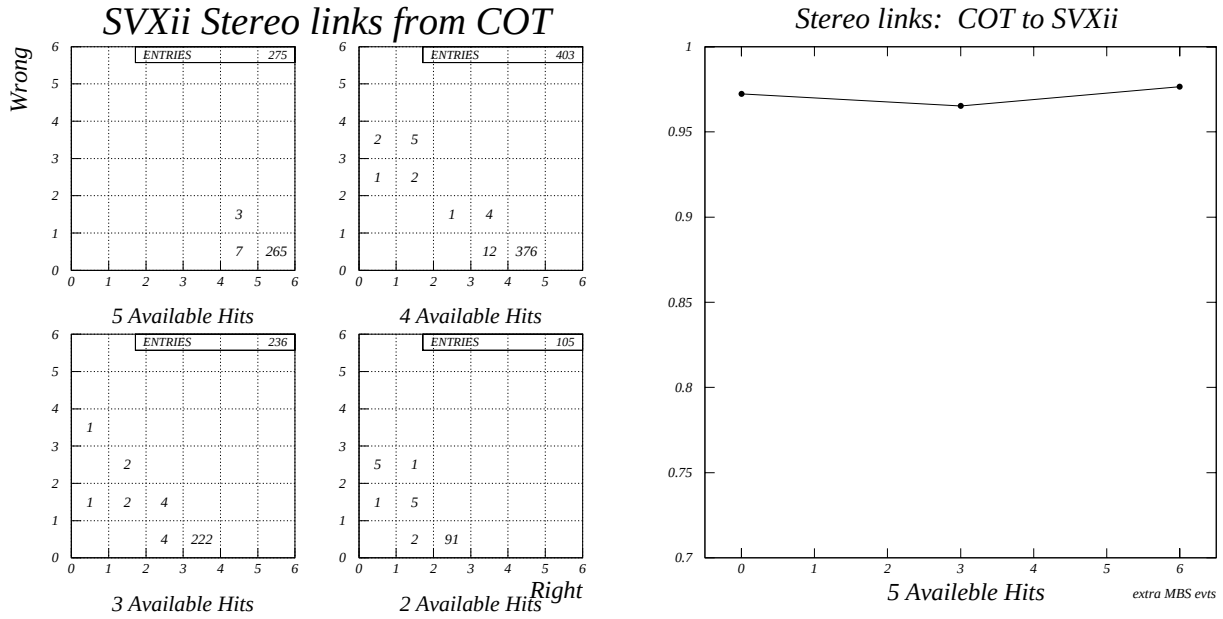

Figure 7.12: Left: Wrong hits linked to COT track vs. right hits, for four cases: 5,4,3, and 2 available hits found in SVX II. Right: Efficiency of linking stereo SVX II hits to COT tracks as a function of luminosity

- Find z with smallest $\chi^2_{\rm total}$

Figure 7.11 ilustrates this procedure for one track. The histograms labeled 0 to 4 correspond to the five SVX II layers. Layer 0 is the inner most. Layers 2, and 4 are the small angle stereo - with worse resolution. The histogram labeled sum, combines all the hits in all five layers. The correct hits will have the same z solution and a low χ^2, and hence have a minimum in this histogram. This approach is fast, because re-fitting is not required for every hit within the road.

For each COT track used, we know from the simulation what the correct hit assignment is. We counted the number of times a wrong hit (i.e. a hit generated by another track, or a noise hit) was linked to the seed COT track. The results are shown on the left in Figure 7.12). The performance of the algorithm on a sample of top events at various luminosities is shown on the right of Figure 7.12. The stereo linking efficiency between COT and SVX II is high, and, within the statistics of this study, shows no degradation up to N = 6 overlapping minimum bias events.

7.6.3 COT+SVX II+ISL Resolution

In order to study the resolution of the integrated COT+SVX II tracking system, we assumed that the hits in the SVX II+ISL have been found. Tracks in the SVX II+ISL were formed by smearing of the ideal helix parameters, using the SVX II+ISL covariance calculated with a single hit resolution of 20μm. We combined this with the COT helix and covariance to perform a global fit.

The left plot in Figure 7.13 shows the helix paramter resolution for the combined COT+SVX II+ISL fit. The combined system results in $\sim 30\mu$m resolutions for both d_0 and z_0. The right plot shows that there is only weak dependence of the resolution of the reconstructed helix on instantaneous luminosity.

In Figure 7.14 the curvature resolution is translated into $\delta p_T/p_T^2$ as a function of p_T for three luminosities.

7.6.4 Conclusions

We have studied the expected performance of the CDF II tracking upgrades using simulation tools tuned to the similar systems used in CDF during Run I. We find

- The COT reconstruction is highly efficient and gives helix paramter resolutions comparable to what we would expect for the CTC, up to the full Run II design luminosity of $2\times10^{32}{\rm cm}^{-2}{\rm s}^{-1}$.

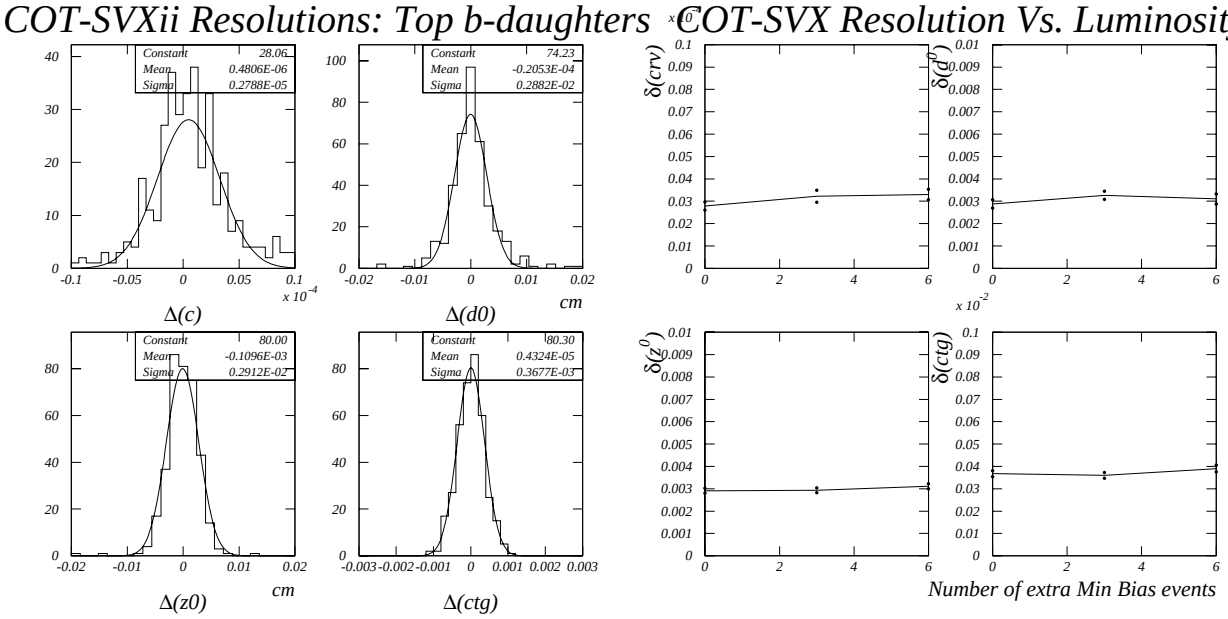

Figure 7.13: Left: Helix parameter resolution for COT+SVX II at low luminosity (the scale of the abscissa is expanded with respect to that used in Figure 7.1). Right: Helix parameter resolutions vs. luminosity

- Track finding in the SVX II+ISL inner tracking system will be efficient, and yield stand-alone silicon track segments with good signal to noise ratio over the full region $|\eta| \leq 2.0$. For tracks with $1.0 \leq |\eta| \leq 2.0$, the seven silicon layers will provide helix parameter resolution adequate to extend electron and muon identification to the plug and IMU, and to allow efficient stand-alone b-tagging.

- The stand-alone SVX II+ISL track segments can be linked to the COT with high efficiency, and the full tracks have excellent helix parameter resolution, comparable to that of the CTC + SVX in Run I. The efficiency and resolution are maintained up to a luminosity of $2 \times 10^{32}\text{cm}^{-2}\text{s}^{-1}$.

- The ability to find stand-alone silicon segments over the region $|\eta| \leq 2.0$ allows the use of a fully integrated tracking strategy, according to the plan and specification of Chapter 3. The excellent performance of the system outlined above is, in part, due to the power of this strategy. We expect that as we gain experience with this system we will learn to raise the efficiency and precision of tracking analyses in Run II far beyond the level achieved in Run I.

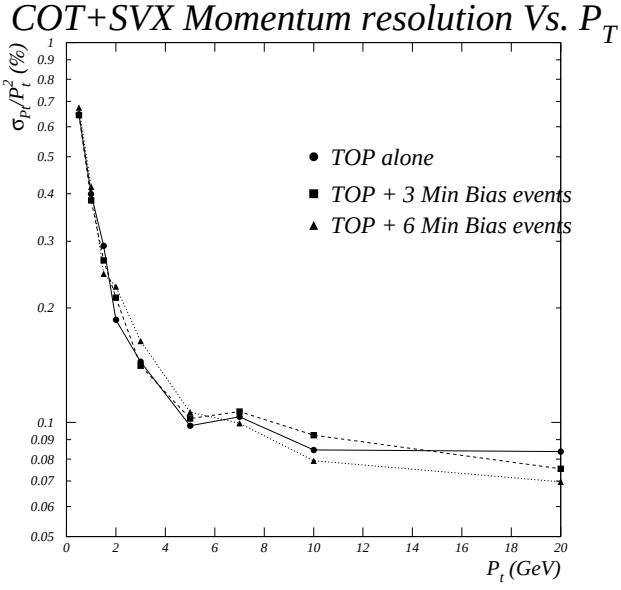

Figure 7.14: Momentum Resolution for COT+SVX II+ISL vs. p_T for three luminosities.

Chapter 8

Central Calorimeter

8.1 Introduction

The CDF central calorimeter is retained largely unchanged other than electronics for Run II. It is a scintillator sampling system with tower segmentation; each tower is 15 degrees in azimuth by about 0.11 in pseudorapidity. Each wedge consists of a lead-scintillator E–M section backed by a steel-scintillator central hadron calorimeter. The wedges are assembled into central arches. The endwall hadron calorimeter consists of modules mounted to the solenoid flux return to provide hadronic coverage from 30° to 45° on both sides.

The PMT energy measurements are fast enough to take full advantage of the Run II 132 ns bunch structure. The wire chambers associated with the E–M calorimeter may need to be integrated over several crossings but their fine granularity implies a low enough occupancy that this should not be a significant problem.

In Run Ib we have a sample of data of average instantaneous luminosity about $10^{31} cm^{-2} sec^{-1}$, which for PMTs corresponds to 6×10^{31} and 1.8×10^{32} for 36 and 108 bunches respectively. These correspond to an average of about 0.9 extra overlying minimum bias events. A minimum bias event on average contributes roughly 15 MeV to a $15° \delta\phi \times 0.11 \delta\eta$ calorimeter tower. For jets, by making the underlying cone correction appropriately luminosity dependent we largely retain the quality of the jet measurements. Inclusive electrons at about 10 GeV E_T see an effective luminosity dependent pedestal shift of up to a few tenths of a per cent for the usual three tower electron energy definition; there should be no significant impact on physics measurements.

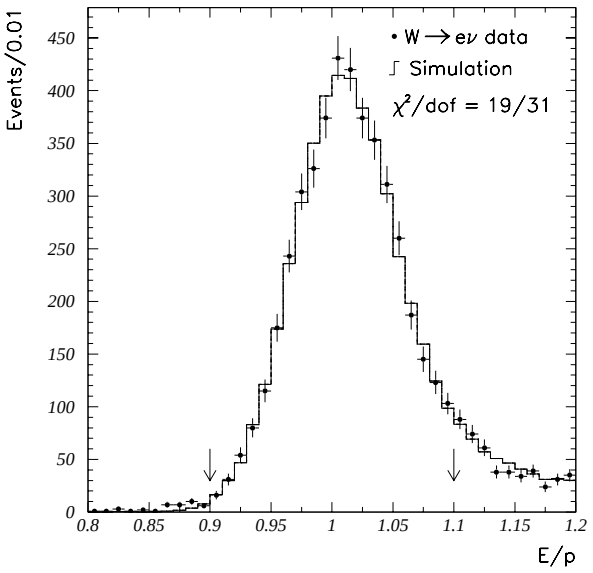

Figure 8.1: Energy over momentum for electrons in the Ia W mass sample. The peak fit region is marked.

8.2 Central E–M Calorimeter

Each 15° wedge has alternating lead and scintillator with an imbedded two dimensional readout strip chamber at shower maximum.[1] Wavelength shifters at the ϕ surfaces direct the light to (Hamamatsu R580) PMTs.[2] Energy resolution in the central electromagnetic calorimeter should be dominated by sampling. The thickness of the lead used in its construction corresponds to $11.6\%/\sqrt{E_T}$. The design specification of more than 100 pe/GeV/tube resulted in a test beam resolution of $13.5\%/\sqrt{E_T}$ which we use as the nominal stochastic resolution. Source calibrations are used to retain testbeam calibration from initial settings[3]; these continue to allow startup with individual tower gains accurate to $\sim \pm 3\%$ and within 2% for overall absolute scale. The source system

is complemented by xenon and LED light flashers, which are useful in diagnosis of problems.

The EM calorimeter, along with tracking and hadron calorimeter, has provided effective identification of electrons[4] and photons[5]. Imperfect corrections for the small variations across the face of a calorimeter cell[6] as well as the statistical error and time drifts in setting individual tower gain calibration result in a constant term in the energy resolution. Calibration of the calorimeter *in situ* has used tracking information in inclusive electrons to determine relative gains and tracking for W electrons to set the absolute energy scale. We measure the tracking material using the E/p tail or conversions and use a radiative Monte Carlo to match the E/p peak as shown in Fig. 8.1. The effective constant term in resolution has been $\pm 2\%$ or less and the absolute energy scale for the W mass measurement is known to $\pm 0.15\%$ for Ia.[7]

The scintillator used is SCSN-38 and the wavelength shifter used is Y7 PMMA; neither should be a radiation damage problem for any luminosity scenario. We have tracked the response since the modules have been assembled, and whether there is beam or not, there is a light yield loss of about 1% per year. About 60% of the loss is directly explained by the gradual shortening of the effective attenuation length of the scintillator as seen in Fig. 8.2. This trend has continued through Ia and Ib.

There is a tendency during data taking for gain to fall more rapidly than the nominal during running with some recovery at shutdowns. This is illustrated for Run Ib in Fig. 8.3. These trends are correlated to calorimeter arches which are thermal masses and share common high voltage supply. The gains are monitored using E/p for inclusive electrons. Run number is a reasonably constant clock and the span is 18 months. The dip in the SE arch was an excursion in high voltage. If there is 20% less light yield than design in 2005, the stochastic resolution would only degrade from 13.5 to $14\%/\sqrt{E_T}$. The effect on the response map is readily monitored and accounted.

The shower maximum chambers have contributed quite effectively to identification of electrons and photons, using the position measurement to match with tracks, the transverse shower profile to separate photons from π^0s, and pulse height to help identify electromagnetic showers. Similar functionality has been proposed for most calorimeters considered since CDF demonstrated the efficacy of a 2 dimensional fine

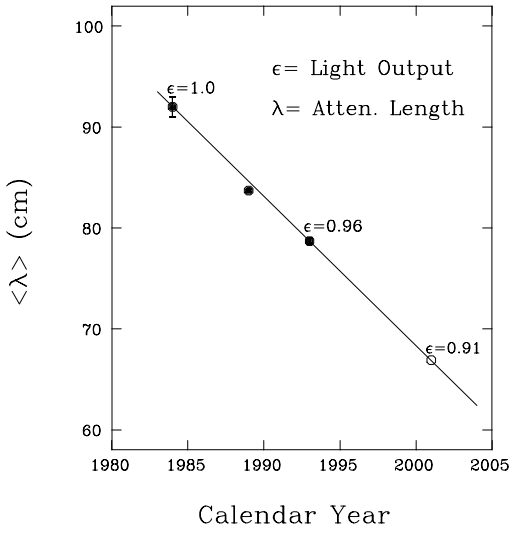

Figure 8.2: Scintillator attenuation length versus year. The observed trend corresponds to 0.6% light loss per year due to transmission loss in the scintillator.

shower maximum detector.

In order to increase available trigger bandwidth some of the shower maximum functionality has recently been implemented into the level 2 trigger.[8] This gave a factor of 2 reduction in electron candidate bandwidth with little loss of signal. This functionality will be expanded in the Run II trigger.

Each gap between adjacent wedge modules is covered by a 12 X_0 tungsten bar backed by a wire chamber. The tungsten serves to recover some of the response for particles, particularly photons, which might otherwise escape completely. The chamber resolution and noise has been too poor to include in energy measurements but the information has been valuable in studying the occasional odd event.

Since the beginning of Run Ia the photon and soft electron identification has been greatly enhanced by preshower wire chambers mounted on the front of the wedges, using the coil and tracking material as a radiator. For example, in the top quark analysis,[9] the soft electron b tagging algorithm uses the CPR to gain a factor of 2 rejection of electron backgrounds after all other identification cuts are applied, while maintaining high efficiency for true electrons. This is illustrated in Fig. 8.4, where the CPR response for a) random tracks that are predominantly pions,

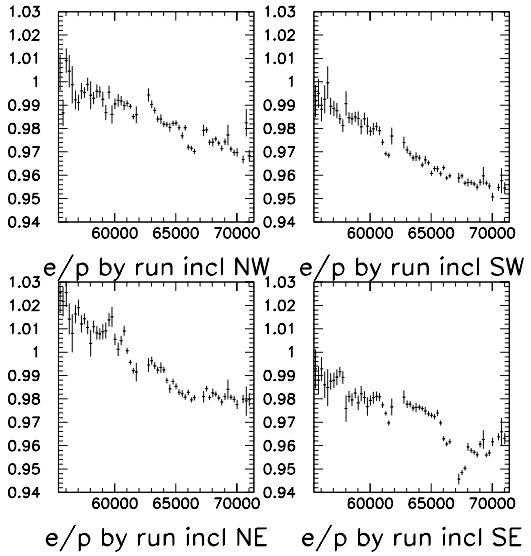

Figure 8.3: Central electromagnetic calorimeter gains by arch (quadrant in the horizontal plane) versus run for Ib (18 months) for inclusive electrons.

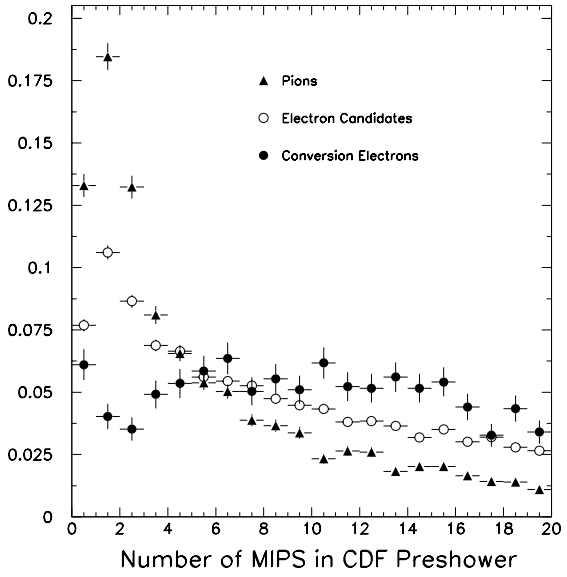

Figure 8.4: The response of the preshower detector to pions, electrons, and electron candidates.

b) pure electrons from conversions, and c) electron candidates that pass all other identification cuts is shown.

In addition, the CPR has been responsible for reducing the systematic uncertainties for direct photon measurements by a factor of 3, giving CDF the most precise measurement of direct photons, as well as extending the measurement in E_T beyond the capability of shower profile measurements.[10] The crucial 1% calibration of the material in front of CPR was performed with reconstructed π^0, η, ρ mesons shown in Fig. 8.5.

The wire chamber readout will be concurrent with digital traffic in the Run II DAQ system so steps are being taken to minimize noise sensitivity. One hopes that the Run II noise levels will not be significantly worse and tests using noise sources have been encouraging.

There is no sign of aging in either shower max or preshower wire chambers. Extrapolation can be made from the current which is drawn during running; one expects about 0.1 mC/cm/fb^{-1} for shower max and 9 mC/cm/fb^{-1} for preshower chambers. Bench tests show little gain loss to 0.4 C/cm.

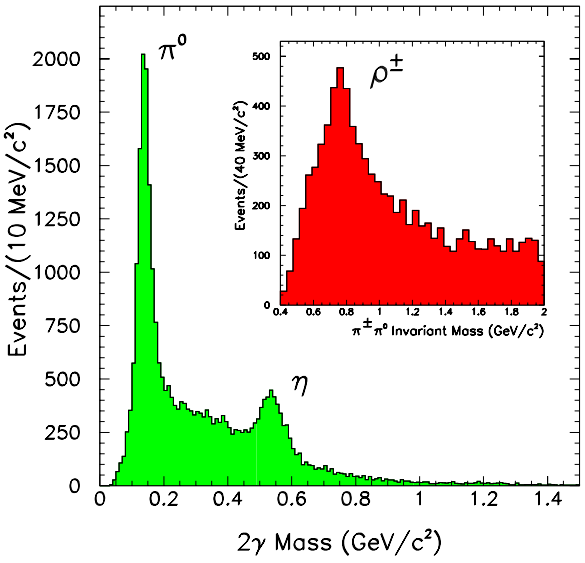

Figure 8.5: The calibration of preshower material was performed with the reconstructed meson peaks as shown.

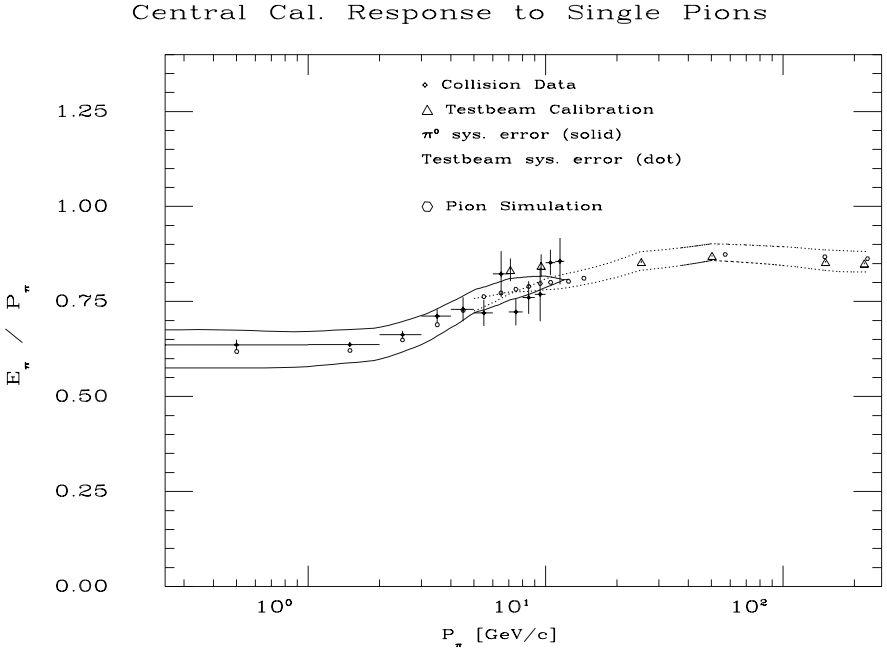

Figure 8.6: Central calorimeter response to pions from test beam measurements and *in situ* isolated particle measurements. The overall level is an artifact of the convention of calibrating the hadron towers in the testbeam using 50 GeV/c pions which were minimum ionizing in the E–M section. The nonlinearity is a characteristic of the lack of compensation in the combined lead and iron calorimeters.

8.3 Central and Endwall Hadron Calorimeters

The central and endwall hadron calorimeters are composed of alternating layers of iron and scintillator. Fingers of wavelength shifter are configured much as fibers are in more recent scintillator calorimeters.[11] Similar to the E–M, the basic calibration is extrapolated from the testbeam using source response. The central hadron calorimeter shares the source drive systems with the E–M. The endwall hadron calorimeter uses a seperate set of sources drives, one per endwall. Operational monitoring is done using a laser flasher system. The test beam calibration is complemented by *in situ* studies using isolated tracks, as shown in Fig. 8.6. Detector systematics are folded in with other systematics in measuring jet energies.[12] These systematics are important for measuring the central jet E_T spectrum[13]. Dijet balance is used to transfer the central calibration to the overall calorimeter. The tracking and EM scales are compared to the jet measurement using photon jet as Z^0 jet balance, shown in Fig 8.7. This confirms the jet energy scale overall

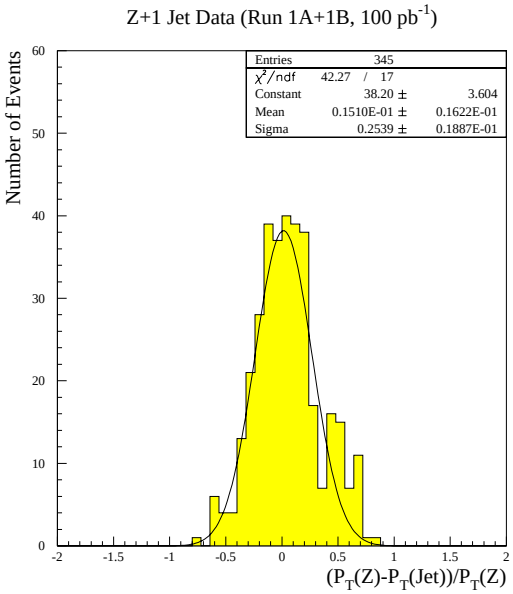

Figure 8.7: Discrepancy between the lepton measurement and the CDF calorimeter in Z plus two jet events.

which is important for measuring the top mass.[9]

The hadron calorimeters use PMMA naphthalene scintillator which should not be sensitive to radiation damage directly from luminosity. Removal of the main ring and attention to shielding from beam halo and other external sources of radiation will be necessary for the survival of this scintillator through Run II. The PMTs, Thorn-EMI 9954 central and Thorn-EMI 9902 endwall, are currently stabilized by running LEDs between bunches; perhaps some scheme for running the LEDs during the abort gaps may be effective or perhaps the PMTs need to be replaced.

Bibliography

[1] L. Balka *et al.*, NIMPR **A267** (1988) 272, L. Nodulman *et al.*, NIM **204** (1983) 351, T. Kamon *et al.*, NIM **213** (1983) 61.

[2] T. Devlin *et al.*, NIMPR **A268** (1988) 209.

[3] S. Hahn *et al.*, NIMPR **A267** (1988) 351.

[4] F. Abe *et al.*, Phys. Rev. **D44** (1991) 91.

[5] F. Abe *et al.*, Phys. Rev. **D48** (1993) 2998.

[6] K. Yasuoka *et al.*, NIMPR **A267** (1988) 315.

[7] F. Abe *et al.*, Phys. Rev. **D43** (1991) 2070, F. Abe *et al.*, Phys. Rev. **D52** (1995) 4784.

[8] K. Byrum *et al.*, NIMPR **A364** (1995) 144.

[9] F. Abe *et al.*, Phys. Rev. **D50** (1994) 2296.

[10] F. Abe *et al.*, Phys. Rev. Lett. **73** (1994) 2662.

[11] S. Bertolucci *et al.*, NIMPR **A267** (1988) 301.

[12] F. Abe *et al.*, Phys. Rev. **D45** (1992) 1448, F. Abe *et al.*, Phys. Rev. Lett. **65** (1990) 968.

[13] F. Abe *et al.*, Phys. Rev. Lett. **62** (1989) 613, F. Abe *et al.*, Phys. Rev. Lett. **68** (1992) 1104, F. Abe *et al.*, Phys. Rev. Lett. **77** (1996) 438.

Chapter 9

Plug Upgrade Calorimeter

9.1 Overview

The Plug Upgrade Calorimeter is a major component of the overall CDF upgrade program. This new calorimeter covers the polar angle region from 37° to 3°, ($1.1 < |\eta| < 3.6$) replacing the existing gas calorimeters, whose time response would have poorly matched the operational conditions of Run II (where the time interval between bunch crossings may be as low as 132 nsec). The top half of one plug is shown in cross section in Fig. 9.1. There is an electromagnetic (EM) section with shower position detection, followed by a hadronic section. In both sections the active elements are scintillator tiles read out by wavelength shifting (WLS) fibers embedded in the scintillator. The WLS fibers are spliced to clear fibers, which carry the light out to photomultipliers tubes (PMT) located on the back plane of each endplug.

The transverse segmentation of the Plug Upgrade Calorimeter is given in Table 9.1 and shown in Fig. 9.2. The segmentation of the EM and hadron towers are the same. This particular segmentation optimizes $e^{\pm}$ identification in $b/\bar{b}$ jets: $b \rightarrow e + X$, the details are discussed in Section 9.2.

The EM calorimeter is a lead/scintillator sampling type, with unit layers composed of 4.5 mm lead and 4 mm scintillator. There are 23 layers in depth for a total thickness of about 21 X_0 (radiation lengths) at normal incidence. The detecting elements are arranged in a tower geometry pointing back towards the interaction region. The η and ϕ segmentation of the central calorimeter is maintained as far as possible. The energy resolution of the EM section is approximately $16\%/\sqrt{E}$ with a 1% constant term.

The scintillator tiles of the first layer of the EM section are made out of 10 mm thick scintillator and are read out by Multi-Anode Photo-multiplier tubes (MAPMT). They will act as a preshower detector. A position detector is located at the depth of the EM shower maximum (approximately 6 X_0). This shower maximum detector is made of scintillator strips read out by WLS fibers; clear fibers carry the light to MAPMTs.

Tower	Tile ID	$\Delta\eta$	$\Delta\theta$	$\Delta\phi$
10	EM Only	1.10-1.20	33-37°	7.5°
11	17,18	1.20-1.32	30-33°	7.5°
12	15,16	1.32-1.41	27-30°	7.5°
13	13,14	1.41-1.52	25-27°	7.5°
14	11,12	1.52-1.64	22-25°	7.5°
15	9,10	1.64-1.78	19-22°	7.5°
16	7,8	1.78-1.93	16-19°	7.5°
17	5,6	1.93-2.11	14-16°	7.5°
18	4	2.11-2.33	11-14°	15°
19	3	2.33-2.61	8-11°	15°
20	2	2.61-3.00	6-8°	15°
21	1	3.00-3.64	3-6°	15°

Table 9.1: The nominal transverse tower segmentation of the upgraded end plug calorimeter. The tower numbering is an extension of the CHA/WHA scheme.

The hadron calorimeter is a 23 layer iron and scintillator sampling device with unit layers composed of 2 inch iron and 6 mm scintillator. The existing iron of the CDF endplugs is used in the new hadron calorimeter. Stainless steel disks are attached to the inner 10° cone to extend the coverage to 3°. Two additional stainless steel disks are added behind the electromagnetic section to increase the thickness of the hadron calorimeter. In this way the magnetic field in the tracking volume and the magnetic forces on the end plugs are unchanged.

The optical systems for the EM, hadron and shower

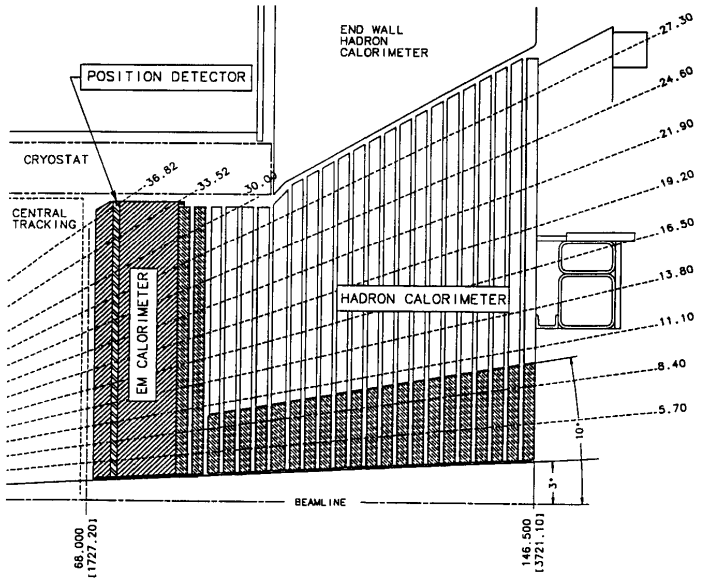

Figure 9.1: Cross section of upper part of new end plug calorimeter.

maximum detectors are very similar. The scintillator elements (tiles or strips) are cut from a large sheet of scintillator, and are assembled in triangularly shaped units called *megatiles*. The megatiles are installed into *pizza pans* that provide top and bottom optical covers and also protect the optical assembly. The pizza pans are installed into the EM (either scintillator tile layers for the calorimeters or scintillator strips for the shower maximum detector) and into the hadron calorimeters. Clear optical fiber cables connected to mass connectors on the outer edges of the pizza pans carry light to the rear face of the plugs. There the optical cables plug into *decoder boxes*,which change the grouping of fibers from pan-oriented to tower-oriented. The fiber groups coming from each tower are read out by PMTs connected to the decoder boxes.

	EM	HAD
Segmentation	$\sim 8 \times 8cm^2$	$\sim 24 \times 24cm^2$
Total Channels	960	864
Thickness	21 X_0, 1 λ_0	7 λ_0
Density	$0.36\rho_{Pb}$	$0.75\rho_{Fe}$
Samples	22 + Preshower	23
Active	4 mm Scint	6 mm Scint
Passive	4.5 mm Pb	2 inch Fe
Light Yield (pe/MIP/tile)	$\geq$3.5	$\geq$2
Resolution	$16\%/\sqrt{E} \oplus 1\%$	$80\%/\sqrt{E} \oplus 5\%$

Table 9.2: Overview of the Plug Upgrade Calorimeter. The EM (hadron) resolution is for a single electron (pion).

A system of movable radioactive sources allows each tile (or strip) of the entire apparatus to be exposed to radiation during the construction phase, permitting us to measure the response of the device as we build it, and assuring us that we are maintaining quality control.

More general information on the Plug Upgrade project can be found in [1]. Table 9.2 summarizes the general characteristics of the Plug Upgrade Calorimeter.

Mechanical modifications to the existing plug iron and supports are discussed in section 9.3.2 of this document,where the EM mechanical structure is also addressed. Section 9.10 describes early R&D studies on the engineering prototype. A detailed discussion of the complete optical system (excluding PMTs) is given in section 9.6. Sections 9.3,9.5 and 9.4 describe design, manufacture, assembly, calibration, and quality control of the EM, hadron and shower maximum detectors respectively. Section 9.6.2 describes the PMT system, and the calibration and stability monitor systems are described in section 9.7 and 9.8. Finally, section 9.9 describes the Test Beam and Cosmic

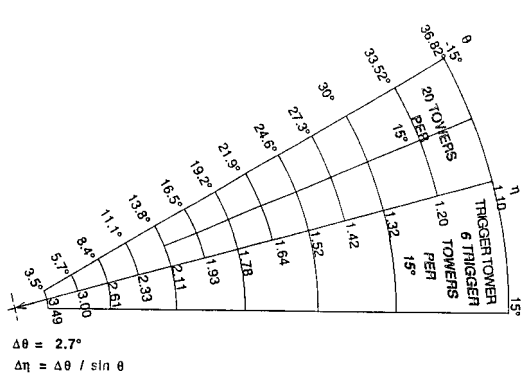

Figure 9.2: Transverse segmentation, showing physical and trigger towers in a 30° section.

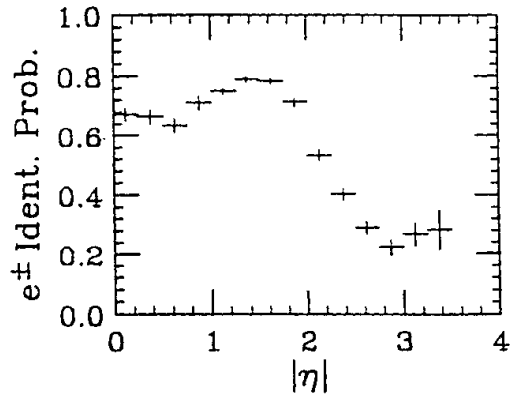

Figure 9.3: Simulation result on the identification probability for electrons from $b \rightarrow e + X$ ($p_t^b > 5$ GeV).

Ray testing that will be performed on the assembled detector as part of the calibration program.

9.2 Specification of Transverse Segmentation

The transverse segmentation of the Plug Upgrade Calorimeter is given in Table 9.1 and shown in Fig. 9.2. It is the same for the EM and hadron compartments, and is the result of a Monte Carlo study on $e^{\pm}$ identification in $b/\bar{b}$ jets: $b \rightarrow e + X$. This is a good topology to use to tune the segmentation because the electron shower is in close proximity to a hadron jet. The Monte Carlo used ISAJET[2] to generate the $b/\bar{b}$ jets and CLEOMC2[3] to decay the resulting $b/\bar{b}$ hadrons. In this study, the $b/\bar{b}$ hadrons were forced to decay into electrons. One electron was required to be in the central region and the other in the plug. The electron tracks were marked and kept for later correlations with EM shower clusters.

A simplified detector simulation was used. It included the solenoidal magnetic field, the transverse EM and hadron shower shapes for transverse energy sharing among towers, and longitudinal energy sharing between the EM and hadron towers. Resolution smearing and detector cracks and transitions were not included. A cluster finder was used to find showers in the EM section. Electron identification cuts were applied to the EM cluster nearest to the electron track. The cuts required that the cluster energy (E_{em}) be consistent with the electron momentum (P_e) and that the energy in the hadron towers (E_{had}) directly behind the towers in the EM cluster be consistent with that for an electromagnetic shower: $E_{em}/P_e > 0.8$ and $E_{had}/E_{em} < 0.1$. Note that charged particle tracking capability down to the highest η is assumed. For the segmentation of Table 9.1, the probability that a $b \rightarrow e + X$ electron is isolated enough to be identified by tracking and calorimetry is shown in Fig. 9.3.

9.3 EM Calorimeter

9.3.1 Design Specification

The energy resolution of the EM calorimeter is given by:

$$(\frac{\sigma}{E})^2 = (\frac{\sigma_1}{\sqrt{E}})^2 + (\sigma_2)^2, \qquad (9.1)$$

where the first term $\sigma_1/\sqrt{E}$ comes from sampling fluctuations and the photostatistics of PMTs, and the second term σ_2 comes from the nonuniform response of the calorimeter. The sampling fluctuations from a 4.5 mm thick lead plate sandwiched between 0.5 mm thick stainless steel plates were estimated to be $14\%/\sqrt{E}$ using an EM shower simulation.

Our first design goal is that the energy resolution due to sampling should be less than $16\%/\sqrt{E}$. To achieve this, the light yield from a tile/fiber per MIP must be larger than 3 pe. The constant term contribution to the energy resolution is required to be less than 1%. To satisfy this requirement, the EM shower simulation showed that the transverse response within a tile/fiber assembly should have an r.m.s. less than 2.5%. The non–linearity of the calorimeter in the energy range between 10 GeV and 400 GeV should be less than 1%. To satisfy this re-

quirement, the variation of responses of tiles within a tower must be less than 10%.

The first layer of the EM calorimeter may be read out separately from the rest of the tiles in the same tower and can be used as a preshower detector, enhancing the physics capabilities of the EM calorimeter, particularly γ physics in the high η region. A careful analysis [13] has shown that to distinguish between γ and π^0 with good efficiency the light yield from the preshower layer at the PMT level must be at least 5 pe/MIP. This light yield will be achieved by increasing the thickness of the first layer tiles to 1 cm, and by using brighter BC-408 scintillator. The readout of the preshower detector will take place through MAPMT.

The design of the EM calorimeter is reviewed in Section 9.3.2 below. A full description of the design and construction of the EM calorimeter can be found in [14].

9.3.2 Mechanical Design

The mechanical structure of the EM calorimeter consists of 23 layers of lead absorber plates. The absorber plates, each 5.5 mm thick and approximately 2.77 m in diameter, are made of a calcium-tin-lead sheet (4.5 mm thick) sandwiched between 0.5 mm stainless steel sheets (Fig. 9.5) . Each lead layer is made of two 180° halves, while the steel sheets are laser cut into 45° sectors. Components are rotated such that edges do not overlap. The steel is epoxied to the lead over the whole surface area with a room temperature cure, while under vacuum.

At the inner diameter, 16 intermediate radial locations, and at 24 locations around the outer perimeter, stainless steel inserts are used in place of the lead and are spot welded to the steel sheets. These create *hard point* locations, which can be used to transfer the load of each sheet to the calorimeter support structure.

In 21 of the 23 layers, the absorber plates are held 8.8 mm apart by stainless steel spacers, allowing for the insertion of the standard EM section pizza pans. The structure thus allows for easy insertion and removal of the scintillator assemblies, and the scintillator assemblies are not loaded by the mechanical structure. This nominal dimension allows for the insertion of the 7 mm thick pans under all conditions, assuming a linear build-up of tolerances and deflections even when the calorimeter is stored horizontally, as in the Cosmic Ray test (see Sec. 9.9.2)

In the two slots corresponding to layers 1 and 5 the spacing is increased to 21 mm and 29.8 mm, respectively, to accommodate the preshower and shower maximum detectors. Layer 1 holds the preshower scintillator assemblies, while both the shower maximum detector and a standard EM pizza pan are placed in layer 5.

The 0.5 inch thick steel front plate of the calorimeter functions as an absorber layer (in terms of radiation lengths) while providing a good mechanical support. The entire structure, weighing about 13 tons (including the first iron layer, called -6 plate, to which the EM calorimeter is attached) is supported at the inside radius of the plates by a cone which transmits the load to the -6 plate, and from there to the hadron supports. In the installed position, the cone acts as a cantilever beam supporting the EM calorimeter, with the intermediate and outer spacers providing stability to the absorber plates as they are sandwiched between the 0.5 inch thick front plate and the 2 inch thick -6 plate. In the horizontal position, the cone and spacers allow for pan insertion and removal by limiting the deflections of each absorber sheet.

The EM calorimeter has the same diameter as the current PEM but is approximately 175 mm thinner. The resulting free space is used to re-establish a 25 mm stay clear zone between the front of the EM calorimeter and the Central Tracking region, and to add 2 more hadron layers behind the EM calorimeter.

9.3.3 Detector Description

The scintillator used for the calorimeter is Kuraray SCSN38 [15]. The WLS fiber and clear fiber are Kuraray multi-clad fibers with polystyrene for the core, polymethylmethacrylate (PMMA) for the inner cladding and fluorinated PMMA for the outer cladding. The 0.83 mm diameter Y11 WLS fibers are thermally spliced to clear fibers of the same diameter. The unspliced ends of the WLS fiber are mirrored by aluminum sputtering and coated with a cover of MgF_2.

The EM scintillator tiles are individually cut and arranged into 15° megatiles. Production starts with a scintillator plate roughly cut into a pair of 15° units. Fiber grooving and fine cutting are then performed. Next, the four edges of an individual tile are painted with a TiO_2 loaded O-de Coat (Nippon Paint). Extensive studies showed that it was best to place the tiles between two layers of white PET film (E65) to

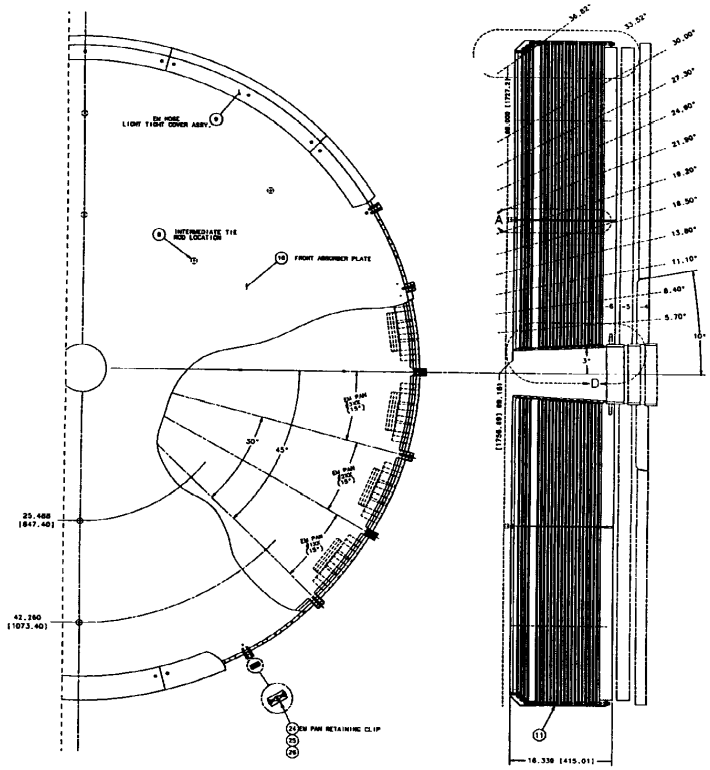

Figure 9.4: EM calorimeter mechanical structure.

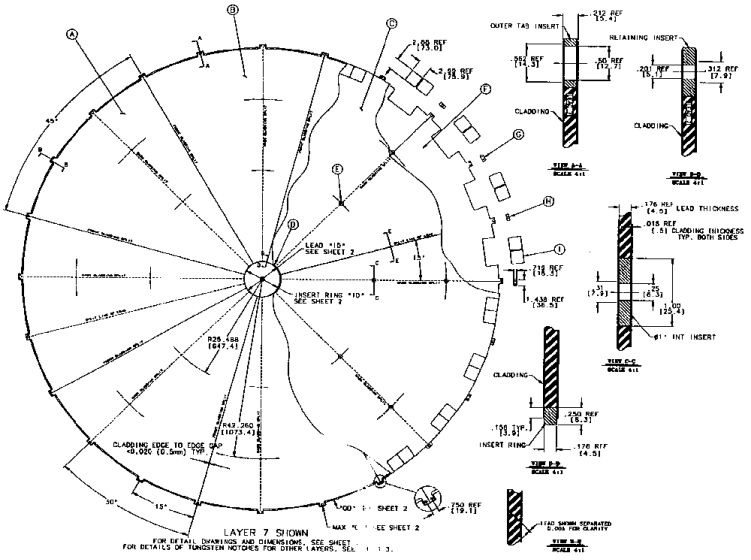

Figure 9.5: Individual EM absorber plate.

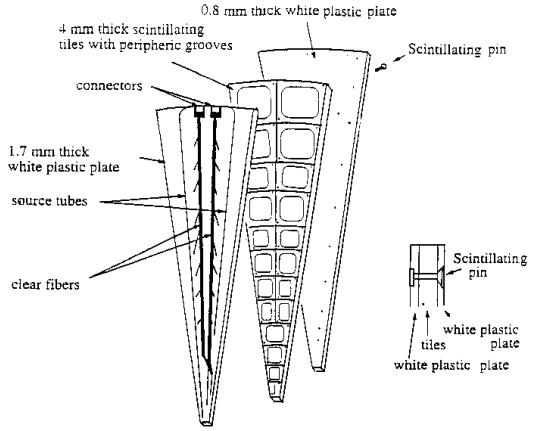

Figure 9.6: Assembly scheme for an EM pizza pan.

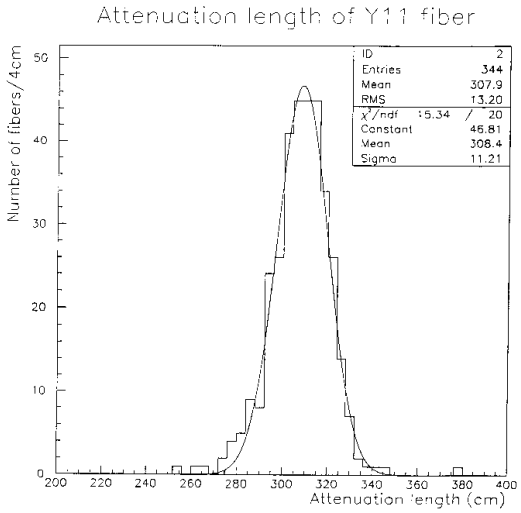

Figure 9.7: Attenuation length distribution for 3 meter long WLS fibers.

provide good reflectivity on the tile surface and transverse uniformity of tile response. The assembly is therefore sandwiched between two layers of 1.7 mm and 0.8 mm thick white plastic sheets.

The tiles are accurately positioned with sets of scintillator pins (Fig. 9.6). The pins are 6.5 mm long and 3 mm in diameter. The scintillator pins were developed to minimize the non-uniformity of the response associated with the pins. Pin positions are staggered in subsequent layers. The scintillator pins were found to recover up to 75% of the light yield lost with conventional plastic pins.

9.3.4 EM Fiber Assembly Quality Control

Diameters of the fibers were checked. For the 0.9 mm clear fibers, the r.m.s. variation in diameter is 3.8 μm and the average diameters are close to 900 μm. No significant variation in average diameter between different production batches has been observed. These results satisfy our requirements of 900$\pm$20 μm. The WLS fibers were required to have diameters of 830$\pm$20 μm; fibers with diameters outside the specifications were rejected.

The WLS fibers were sampled and monitored for light yield and attenuation length. A 4 m long fiber piece was sampled out of every 50 m of WLS fiber. The 4 m fiber was divided into one 1 m long fiber and one 3 m long fiber, used for the light yield and attenuation length measurements respectively. The light intensity was measured by reading the current of a PMT (Hamamatsu H1161) while exciting the fiber from the side with an LED lamp at 5 cm length intervals. The attenuation length λ was obtained by fitting a plot of the light intensity vs. position to an exponential function.

The results of these measurements are shown in Figs. 9.7 and 9.8. The average attenuation length of WLS fibers is 308 cm, and the minimum attenuation length is 250 cm. The r.m.s. variation in attenuation length is 3.6%. The WLS fiber attenuation length was specified to be larger than 1.5 m with an r.m.s. variation from batch to batch below 15%.

For clear fibers, we sampled a pair of 15 m long fibers at the beginning and the end of each batch. The light from a halogen lamp was injected into one end of the clear fiber and the light intensity was measured at the other end by means of a spectrum analyzer at wavelengths of 500 and 670 nm. The fibers were then shortened by 3 m, the fiber ends were polished, and the transmission was measured again. Assuming exponential light attenuation, the attenuation length λ was obtained by the formula:

$$\lambda = -\frac{12\ m}{\ln(I_1/I_2)} \tag{9.2}$$

where I_1 and I_2 are the light intensity of the two measurements.

The average attenuation length of clear fibers at a wavelength of 500 nm is 9.3 m, and its r.m.s. variation is 11%. The average attenuation length of clear fibers at a wavelength of 670 nm is 21.4 m, and its r.m.s. variation is 21% . By an interpolation of the results at 500 nm and 670 nm, the attenuation length

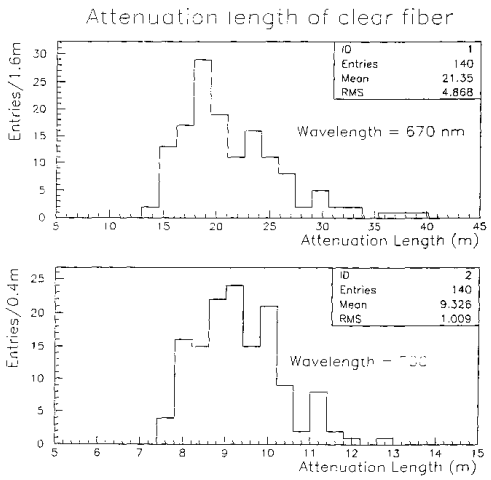

Figure 9.8: Attenuation length for clear fiber at two different wavelengths.

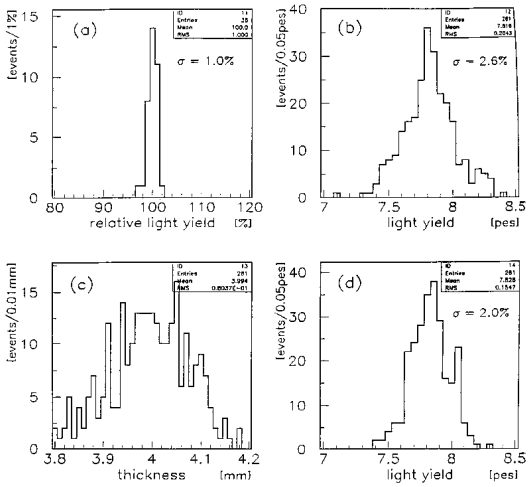

Figure 9.9: Light yield measurements on samples of Kuraray scintillator extracted from the production scintillator plates: (a) reproducibility of the measurement, (b) sample light yield, (c) sample thickness (d) sample light yield after thickness correction.

at 550 nm is estimated to be 12.9 m with an r.m.s. variation of 13.9%. For the clear fibers, the attenuation length was specified to be larger than 10 m and its r.m.s. variation less than 15% at a wavelength of 550 nm.

A full description of the quality control of the EM fiber assemblies can be found in [39].

9.3.5 EM Tile/Fiber Assembly Quality Control

The light yield of scintillator tiles mainly depends on plate thickness and dopant concentration. To ensure uniform response over a tile/fiber system, these two characteristics should be uniform. For samples of scintillator sheets produced by Kuraray, sheet thickness and light yield were measured. The average thickness is 4.0 mm and the r.m.s. thickness variation is 1.6%. The systematic uncertainty of the measurement of thickness variation is less than 0.01%.

The light yield of a block of scintillator sampled from a scintillator plate was required to be more than 130 pe/MIP, and its r.m.s. variation after correction for block thickness to be less than 2%. The light intensity of the sample block was reduced to 5% with a neutral density filter and air gaps in front of the PMT (Hamamatsu H1161). An EM shutter and a quartz glass in front of the PMT were used to keep the PMT high voltage on for the duration of the measurements and hence keep the gain of the PMT stable during the measurement. The light yields of all blocks were more than 140 pe. The results are shown in Fig. 9.9. The r.m.s. variation of the thickness-corrected light yields was 1.7% after subtracting 1% systematic error. These results satisfy the requirements.

To investigate the final response of the tile, about 2% of tiles were sampled and their light yields for MIPs were measured using several standard fibers. The final requirement for the light yield is that the light yield must be at least 3 pe/MIP/tile. In previous studies, it was found that about 20% of the light was lost at the splice, about 10% of the remaining light was lost at the fiber connector, and about 40% of the light was lost in a 5 m clear fiber (the attenuation length of clear fibers is approximately 10 m). In total, approximately 60% of the light from a tile is lost before reaching the PMT.

In measurements of tile/fiber light yield after the tile fabrication, scintillator tiles and standard WLS fibers were used. The WLS fiber length was typically 60 cm, and the light from the WLS fiber was directly measured without clear fiber or fiber connectors. We required that the light yield be more than 12 pe/MIP in this measurement. The light yields from sample tiles were corrected using the light yields from reference tiles. We monitored the light yield of the reference tile before and after all the measurements. The r.m.s. variation of the light yield after subtracting the variations in WLS light yield and sample tile thickness was required to be less than 2%.

After the final assembly, a cosmic-ray test of all the 15° units (1144 units) as a final quality control procedure was done. 15 pans at a time were exposed to cosmic rays for a period of 24 hours. The reproducibility of the light yield measurement is approximately 3%. The quality requirements are

- light yield of the tile per MIP larger than 3.5 photo-electrons,
- light yield within ±30% with respect to the tower average,
- light leakage to adjacent tiles less than 3.5%.

The light yield r.m.s. for tiles of the same size measured by the cosmic ray setup for 880 units was 5.4%. The r.m.s. for tiles belonging to the same tower was measured to be 9.5%. A full description of the quality control of the EM Tile/Fiber Assemblies can be found in [39].

9.4 Shower Maximum Detector

9.4.1 Design Specification

The Plug Upgrade Calorimeter shower maximum detector (SMD) is a position sensitive detector placed at a depth of approximately 6 radiation lengths inside the EM calorimeter. It will cover a circular area 2.6 m in diameter at 1.8 m from the nominal interaction point at B0. Its purpose is twofold:

- measure the position of $e^{\pm}$ and γ showers
- help separate $e^{\pm}$ and γs from π^0.

The design of the SMD is constrained by the overall design of the plug calorimeter. For example, since the EM calorimeter is based on 15° azimuthal sectors, it is prudent to choose the SMD sector angle to be an integer multiple of 15°. Various position detector scenarios have been investigated in the past [20]. The technical solution finally chosen for the SMD consists of scintillator strips read out by WLS fibers. Test beam studies and Monte Carlo simulations [21] have shown that an output of 1 pe/MIP should be sufficient for the measurement of the position of high energy electrons with resolution of approximately 1 mm in a detector made of 5 mm wide strips.

Requirements imposed by physics issues have also been addressed. The segmentation scheme has been finalized after careful studies of π^0/γ separation, occupancy and resolution of ambiguities caused by multiple showers. Although not a design requirement, sensitivity to muons would be useful. Ability to detect minimum ionizing particles efficiently requires about 4 pe/MIP. Test beam studies and Monte Carlo simulations show that an r.m.s. response variation of 10% between detector channels does not significantly degrade position resolution or π^0/γ discrimination.

Since the detector will be read out by a MAPMT and presently available devices generally have channel to channel gain variations greater than 10%, we consider careful channel to channel calibration of this detector a crucial factor in its successful commissioning. Moreover, because of scintillator aging and potential radiation damage, it will be necessary to monitor the calibration during the course of operation. The calibration system employs a 5 mm ^{137}Cs wire source running almost perpendicular to the strips in the SMD plane. The current read out from each channel of the MAPMT provides the strip to strip calibration.

9.4.2 Detector Description

The active elements of the SMD are scintillator strips read out with WLS fibers. The WLS fibers are connected through optical connectors to clear fibers, which carry the light to the MAPMTs located at the rear of the plug.

The SMD is divided into eight 45° sectors, each covering the region from the beam pipe at 11 cm to an outer radius of 130 cm. Each sector contains two layers (called U and V) of 5 mm pitch scintillator strips. The U and V layers are held together by two 1/8" thick lexan covers, and inserted into the fifth sampling slot (behind ≈6 radiation lengths of material) within the EM calorimeter

The placement of the U and V strips in a 45° sector are shown in Fig. 9.10. The two scintillator layers U and V are aligned at +22.5° and −22.5° with respect to the radial dimension, to provide two-dimensional position measurement. Monte Carlo studies show that π^0 rejection increases with increasing U-V crossing angle, and that U-V angles greater than 30° are necessary for good rejection efficiency. This design employs a 45° crossing angle as the most reasonable choice, since larger angles would be difficult to implement mechanically.

Each U or V layer will be assembled with 400 scin-

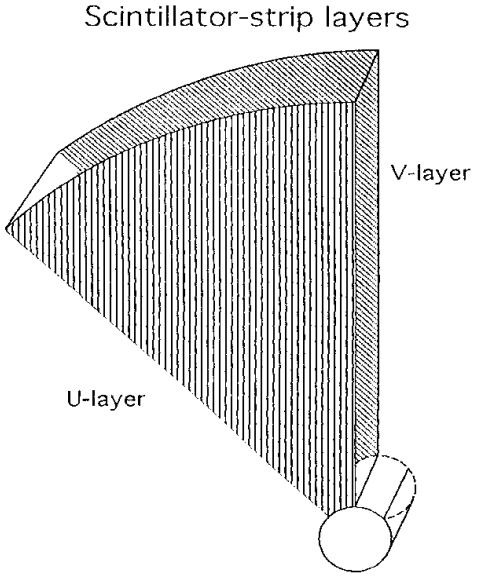

Figure 9.10: Geometry of the SMD in a 45° sector

tillating strips aligned parallel to one edge or the other of the 45° sector. The scintillating strips are 5 mm wide by 6 mm thick and have variable length between 5 and 100 cm. A "ball groove" in each strip (0.89 mm in diameter) accepts a WLS fiber (0.83 mm in diameter) which guides the light to optical connectors mounted near the outer perimeter of the sector. The strips are wrapped like a tennis racket grip with reflective aluminum tape. Groups of 10 strips are taped together and subsequently treated as one unit, which we call a "megastrip". The megastrips are placed in the pizza pans using separators that keep the megastrips parallel to one side of the 45° sector.

The U and V scintillator strip layers are segmented into upper and lower parts, corresponding to η regions 1.13-2.60 and 2.60-3.50 respectively. The upper and lower strips are separated at a line that intersects the side of the panel at a radius of 28.2 cm, matching the EM calorimeter inter tile boundary. The main purpose of η segmentation is to reduce the occupancy of the strips expected from the underlying event. Although the occupancy expected in the lower η segment is approximately two to four times larger than that of the upper segment, further segmentation is impractical. In tests performed, we found that the light yield decreases as the strips become shorter. For efficient light collection, the strip length should not be smaller than 5 cm. For this reason, and also for the practical reason of avoiding very short strips, the short strip corner of the lower sector is serviced by strips from the upper sector, while the short strips of the upper sector are eliminated.

Three megastrips will service the high-η region. The WLS fibers in these megastrips will be spliced to clear fibers routed underneath the scintillator strips of the low-η region, using the grooves milled in the lexan covers.

9.4.3 SMD Fiber Assembly Quality Control

The WLS fibers were prepared prior to the pizza pan assembly in a manner very similar to that described below for the hadron calorimeter. One end of each WLS fiber was polished, mirrored by aluminization, and protected by a thin coating of epoxy glue. The other end was cut to a specified length and inserted into a 10-fiber optical connector. The fiber ends were then glued in place in the connectors and polished. The WLS fibers from the scintillator strips from the lower part were first spliced to clear fibers.

The r.m.s. variation in transmission through the fibers and connector assemblies was around 2%. This value is in agreement with the observation made during the production of the hadron calorimeter (section 9.5) and the difference in quadrature between the two observed r.m.s. values is in good agreement with the values reported in Ref.[7] for the variation in the light transmission through a splice. We accepted all fiber/connector assemblies where the light yield was within 10% ($\pm 4\sigma$) of the average light yield for unspliced fibers and within 15% ($\pm 4\sigma$) of the average light yield for spliced fibers.

9.4.4 SMD Scintillator Strips and Megastrips Quality Control

Before turning to the production of the scintillator strips and megastrips, we measured the individual light yield of all the BC408 scintillator plates received from the vendor (Bicron). We used a ^{207}Bi source to determine the response of samples of scintillator to ~ 1 MeV electrons depositing all their energy in the scintillator All the plates for which the response was more than 10% away from the average response were rejected and sent back to the vendor for replacement.

All assembled pizza pans were scanned sending a wire with a 4 mCi ^{137}Cs source mounted on the tip through the source calibration tubes mounted on each pizza pan, and by scanning all the individual

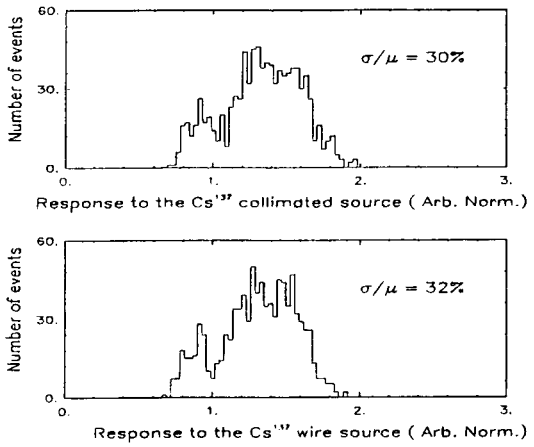

Figure 9.11: Response of the SMD fiber/strip assemblies to the collimated and wire-mounted ^{137}Cs sources.

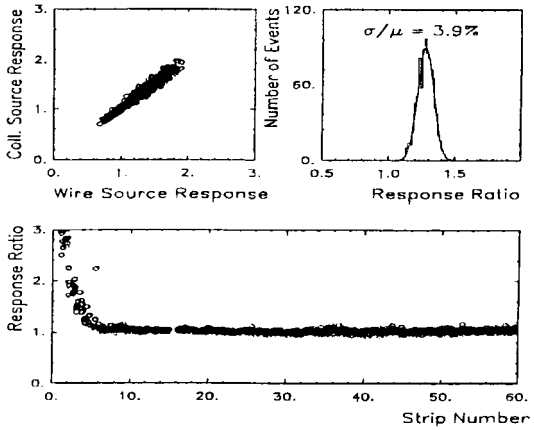

Figure 9.12: Correlation (top) and ratio (bottom) between the responses to the collimated and wire-mounted sources.

strips with a collimated ^{137}Cs source. The strips were read out through a 64 channel MAPMT, the DC anode current of which was measured by a picoammeter. The individual channel read out test was repeated for all the strips in all the pans. The motivation for this test was to determine whether the calibration system (source tubes running on the outside of pizza pan and crossing the strips at an angle of 67.5°) would have ensured a strip to strip calibration uncertainty of 10% (or less).

Figure 9.11 shows the responses of the individual strips to the collimated and wire-mounted sources for a subset of strips where the crossing angle between the source tubes and the strips is constant. The variation in strip response is mainly due to the channel to channel response variation of the MAPMT which are exactly what we want to calibrate out with the wire source. Figure 9.12 (top) shows the correlation between the responses to the collimated and the wire sources. The correlation is outstanding, and the r.m.s. variation in the correlation is about 4% which is more than two times better than required.

Figure 9.12 (bottom) shows the ratio between the responses to the collimated and wire sources as a function of the strip number for the first 60 strips of the full set of shower maximum pizza pans. The higher response in the low numbered channels is due to the fact that the source tube crosses closer to the long axes of these fingers, and the source activity is about 5 mm long. We are presently working to understand all these marginal effects of the wire source system.

9.5 Hadron Calorimeter

9.5.1 Design Specification

The hadron calorimeter has been designed to attain the following performance: first, its $\eta - \phi$ segmentation should allow the topics such as b-physics, W, Z, and γ physics, and jet physics, to be investigated in an efficient and productive fashion. Second, it should have an energy resolution of $\sigma/E \sim (80 - 90)\%/\sqrt{E} \oplus 5\%$. This is dominated by the sampling fluctuations from 2" steel absorber plates rather than by PMT photostatistics and response variation. For such sampling, the sensitivity of the calorimeter to hadron showers is 0.1 GeV/MIP/tile and the intrinsic resolution is $\sim 80\%/\sqrt{E}$. Finally, the calorimeter should be able to identify muons via their dE/dx energy loss.

The engineering prototype and subsequent R&D indicate that the hadron calorimeter will attain the target energy resolution of $(80 - 90)\%/\sqrt{E} \oplus 5\%$. In terms of component performance, the 5% constant term requires that the r.m.s. variation of tile to tile light yield be better than 10% and that the r.m.s. of intra-tile transverse nonuniformity be less than 4% (assuming the nonuniformity is the same for all tiles in a projective tower). An overall tile to tile light output variation of 10% contributes only 3% to the constant term because the hadron shower is typically spread out over more than 10 layers longitudinally.

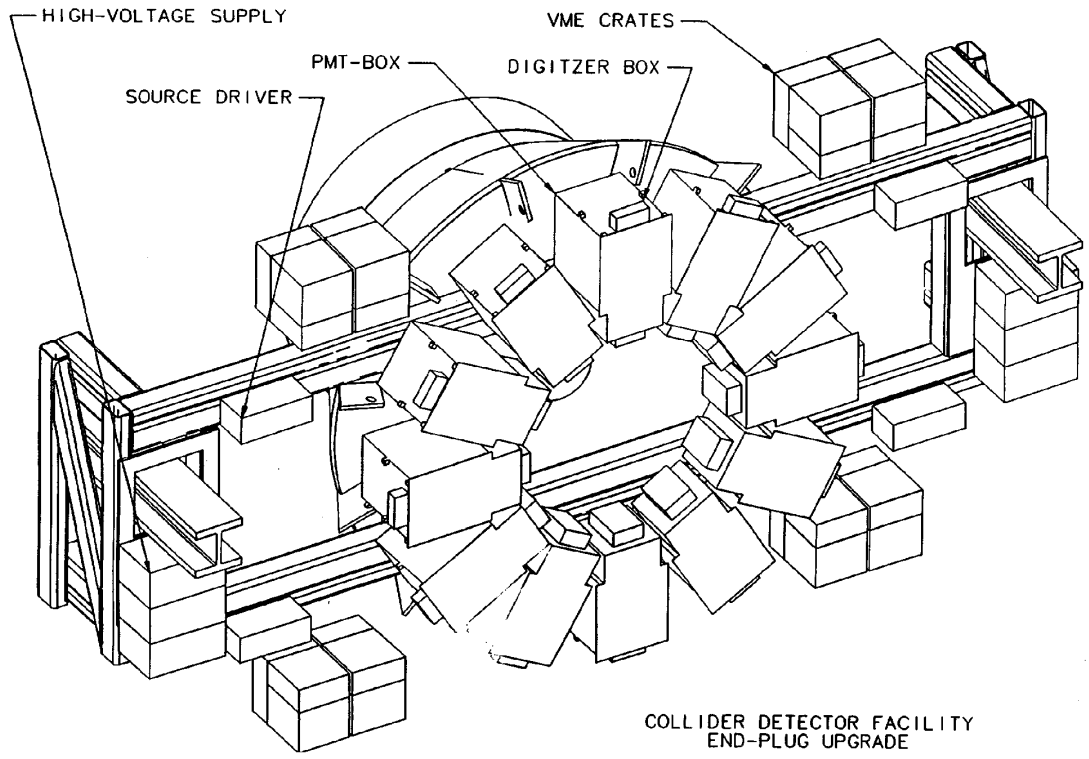

Figure 9.13: End plug calorimeter support structure.

9.5.2 Mechanical Design

9.5.2.1 Hadron Module

The steel structure of the existing hadron calorimeter will be reused, after two modifications: first, the addition of two two-inch thick stainless steel plates to the front of the calorimeter and the replacement of the existing -4 plate; second, the addition of stainless steel disks to each of the existing iron absorber to close the region around the beam line from 10° to 3° (Fig. 9.1).

The additional plates in front of the hadron detector will be supported in the same manner as the plates located in the cylindrical region of the existing hadron calorimeter, namely by cantilever beams which extend forward from the 0 plate every 30° around the perimeter of the device. Each of these additional plates will be attached to the calorimeter in the assembly hall, with the -6 plate arriving as the backplate of the EM calorimeter. The -4 plates will be replaced by spares from the original plugs. The carbon steel portion of the -4 plate will remain 1.75 inch thick, as in the current structure, to minimize change in the magnetic field.

After being stripped of the old calorimeter gas chambers, the existing plug steel will be rotated nose down, and the 10° to 3° stainless steel disks will then be welded to each of the existing hadron plates sequentially, front to back, in the calorimeter. The inner tie ribs which currently support the plates in the 10° region will be taken out; their function is served by rings joining the stainless steel inserts at their inner diameter. These rings will also serve to make the structure light tight in this region.

The additional steel adds about 7 tons to the weight of each end plug, and the center of gravity of each plug moves towards the interaction point. The design for the modifications to the hadron structure have passed the safety review.

9.5.2.2 Design and Analysis of the End Plug Support Structure

The EM and hadron modifications increase the weight of each end plug by approximately 13 tons, to 102 tons total, and move the center of gravity of

each plug towards the interaction point by 175 mm. However, the plugs will continue to be supported by the existing box beam structure after reinforcement in a few critical areas. The removal of several vertical plates on the rear of each plug will create additional area for PMT mounting and electronics, as shown in Fig. 9.13.

The original analysis of the support structure treated the detector in terms of two separate components: the calorimeter and the support structure. However, during assembly the rear plate of the hadron calorimeter was welded to the box beam supports, making the vertical plates redundant. Two of the original four plates have been removed from each plug, and with this upgrade we will remove the remaining two plates, as their function is served by the 2 inch thick hadron steel plate to which the beams are attached. Several 1 inch thick plates will be added to the box beams to increase the overall stiffness of the structure, limiting both the stresses and deflections.

An ANSYS model of the end plug structure has identified these areas of concern, and the new plates can be seen in Fig. 9.13. These plates will be added when the structure is rotated nose down for the addition of the hadron steel disk inserts. The I-beams on the central calorimeter which support the plug as it is rolled into place have also been included in the ANSYS analysis, and some reinforcement of these beams, or limitation of the total travel of the plugs, will have to be implemented.

9.5.3 Hadron Pizza Pan Assembly

In contrast to the EM sector, all 32 tiles within a 30^0 section are cut from a single piece of scintillator. A cross section of the pizza pan unit is shown in Fig. 9.14. The unit begins with a 0.063" thick aluminum bottom cover. Then comes the 6 mm thick SCSN38 scintillator megatile covered on both sides with 0.006" thick white reflective Tyvek [16] paper. The surfaces of the scintillator tiles are grooved to hold the WLS fibers.

Above the megatile is a 0.150" thick white plastic fiber routing sheet. The fibers rise out of the scintillator through a 0.125" $\times$ 1" slot in the white plastic into grooves on the top side of the white plastic. The grooves, 0.063" wide and 0.063" deep, route the fibers to an optical connector at the outside edge of the pan. Source calibration tubes, 0.050" O.D., are placed on the bottom of the white plastic. There are four calibration tubes per megatile and each tile is crossed by one tube. Sheets of black opaque Tedlar are used to make the combined scintillator and white plastic sheets light-tight. Finally, a second 0.090" aluminum cover is located on top to provide a complete protective package.

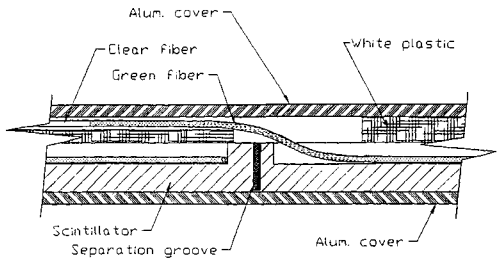

Figure 9.14: Hadron pizza pan cross section.

The megatile unit is held and compressed together by a set of 0.188" diameter rivets spaced 18" or less apart. These rivets keep the inter-component gaps to $\sim$0.015" or less so that fibers can't pop out of grooves and so that the reflective Tyvek paper is held right against the scintillator to minimize both the tile transverse response non-uniformity and tile to tile light cross-talk.

The SCSN38 scintillator megatile is constructed as follows: separation grooves between the tiles are cut into a 6 mm thick plate by a computer controlled machine, leaving $\approx$ 0.25 mm of uncut scintillator at the bottom of the grooves. The grooves are then filled with a white paint/epoxy mixture [17] to glue the individual tiles together. The epoxy is used for both the structural support and as a reflective surface at the edges of the tiles. A black marker is used to paint a line on the surface of the scintillator between the tiles to minimize the light cross-talk. Figure 9.15 shows the light cross-talk between neighboring tiles is less than 2% per edge of the tile.

After the glueing procedure is completed, the megatile is put back on the milling machine and the fiber grooves are cut out. In the next step, the scintillator sheet is wrapped using white reflective Tyvek. Then, a layer of plastic with grooves to route clear fibers is placed on top of the scintillator sheet. At the final assembly stage, the fibers are inserted into all tiles and the megatile is covered with black Tedlar for light-tightness and placed in aluminium pans for the mechanical protection. A full description of the assembly technique and quality control can be found

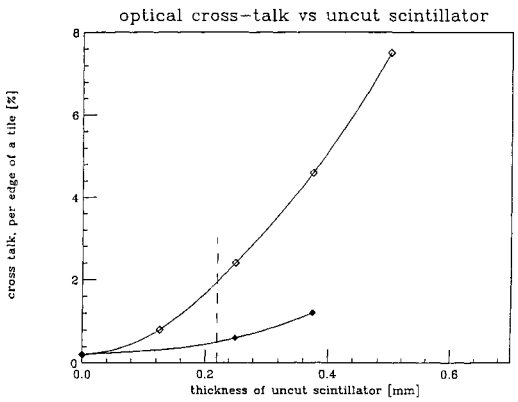

Figure 9.15: R&D studies on the optical cross-talk as a function of the thickness of uncut scintillator. The scintillator thickness was 6 mm. Open diamonds indicate the cross-talk when no black line mark is applied below the separation groove. Black symbols indicate the optical cross-talk for the tiles with a black line under the separation groove.

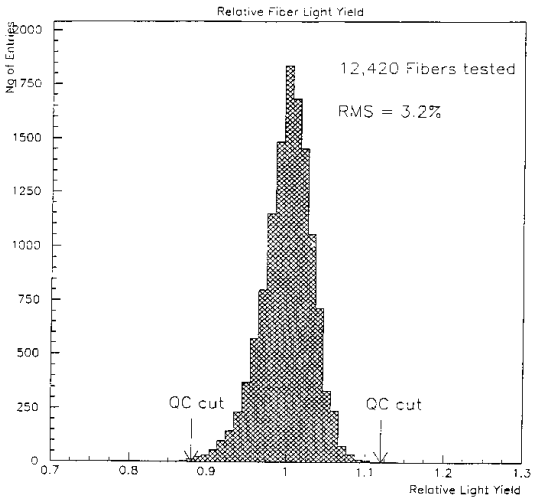

Figure 9.16: Distribution for the relative light yield of hadron calorimeter fibers assembled in the optical connectors.

in [18].

9.5.4 Hadron Fiber Assembly Quality Control

Approximately 2600 fiber/connector assemblies (see section 9.6) are needed for the the hadron calorimeter. After mirroring, splicing and assembly into mass-terminated connectors, the fibers were tested by exciting them from the side with an UV lamp and measuring the light output at the unmirrored end using a photodiode. The lamp was moved in small steps along the length of the fibers and the response of the photodiode was recorded at each position. The peak wavelength of the UV lamp used in this setup was 405 nm: however a blue filter was used to remove the UV light of wavelength less than 385 nm.

By measuring the light yield of individual fibers, we checked the quality of the polishing, the reflectivity of the mirrored surface, the light transmission across the splice between WLS and clear fibers, and the quality of the connector surface. Figure 9.16 shows the distribution of the relative light yield of fibers as measured by the UV setup. The r.m.s. of this distribution is 3.2%. Fiber light yield was normalized to the average light yield of the set of fibers with the same length. Fibers with relative light yield more than 12% below the average were rejected. In those few cases, the particular WLS fiber was replaced and the entire connector was tested again. In some cases the low light yield of a fiber was related to a problem with clear fibers or connector parts. In these cases, the entire fiber/connector assembly was discarded and replaced by a new one.

In a sub-sample of 1600 fiber/connector assemblies, containing over 12,500 fibers in total, 85 fibers ($\approx$ 0.7%) were re-spliced and 40 fiber/connectors assemblies ($\approx$ 2.5%) were rejected. The average and r.m.s. mirror reflectivity, excluding fibers mirrored during a period of sputtering machine problems, were equal to 90% and 5.4% respectively. However, due to the attenuation of light in the WLS fibers, the typical increase of light yield for fibers with mirrored ends was between 30 and 40%. Thus, the contribution to the variation of the fiber light yield originating from the variation in the mirror reflectivity was $\approx$ 1.5-2%.

9.5.5 Hadron Tile/Fiber Assembly Quality Control

Prior to the shipment of scintillator material to Fermilab, the thickness of each scintillator plate was measured by the manufacturer, Kuraray International Corporation. The distribution of the average thickness of scintillator plates is shown in Fig. 9.17. The nominal thickness of the SCSN38 scintillator was 6 mm. Scintillator plates with average thickness below 5.8 mm were rejected by the manufacturer. The distribution of average scintillator plate thickness had an r.m.s. of 1.2%.

To measure the variation in the absolute light yield

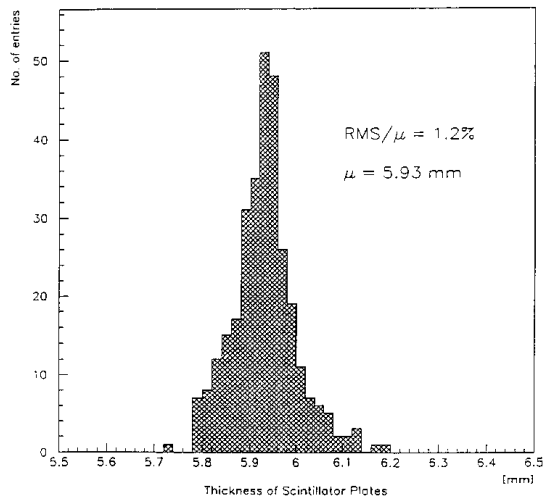

Figure 9.17: Distribution of average scintillator thickness used in the hadron pizza pan production.

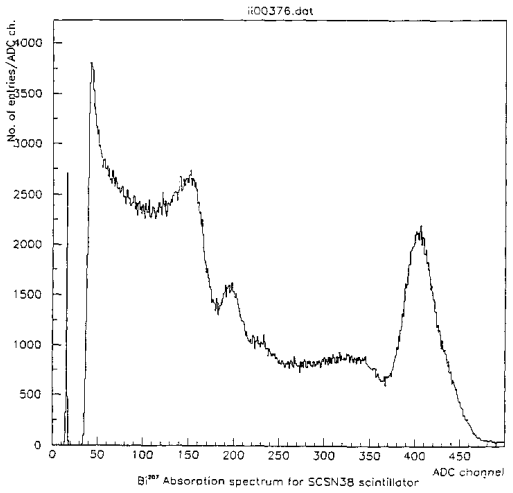

Figure 9.18: Absorption spectrum of the ^{207}Bi source used to check the light yield of the hadron scintillator plates before production. The position of the highest peak was used to determine the relative light yield of each sample.

of the scintillator material, we studied the scintillator absorption spectra using a ^{207}Bi source. Small 2 cm $\times$ 2 cm pieces of scintillator were placed on the face of the PMT and were excited with the β source. Figure 9.18 shows the ADC distribution of the PMT signal corresponding to the absorption spectrum of one scintillator sample. The light yield of each sample, relative to the reference sample, was measured by determining the position (in ADC counts) of the absorption peak corresponding to the largest deposit of energy. From this plot we infer that the distribution of the absolute light yield of scintillator plates had an r.m.s. of 1.6%.

After passing the UV light yield Quality Control (QC) test, the fiber/connector assemblies were inserted into the megatiles. Next, the megatiles underwent QC tests using a collimated ^{137}Cs γ source. We used a PC-controlled motor drive and data acquisition system to record the response of individual tiles to the radioactive source. The megatiles were placed inside a light-tight "scanner box" and positioned against three alignment pins. The relative light yields of the tiles were measured by recording the DC current response of a set of PMTs [1]. Data were taken in sequence by positioning the source over the geometrical center of each of the tiles in a megatile. The gains for the PMTs were measured before and after each megatile test using a control tile.

[1] Hamamatsu R580-17, 10-stage green-extended PMTs, operated at 1350 V, corresponding to a gain of approximately 10^6.

The r.m.s. of the relative gain of each tube measured during the period of QC tests described here (December 1993 through August 1994) was $\approx$ 0.7%-1.0%.

Figure 9.19 shows the distribution of the relative light yield for individual tiles from the first 14 layers. The r.m.s. of the distribution is 6.1%. The few tile/fibers assemblies with relative light yield less than 78% of the mean were repaired. In such cases, we either re-spliced the WLS fiber or replaced the entire fiber/connector assembly. During the production period, during which 378 megatiles were produced, with 1512 connectors and 12,420 fibers, 36 fibers ($\approx$ 0.3%) had to be re-spliced and 26 connectors ($\approx$ 1.7%) had to be replaced.

Therefore as a result of the two QC tests (UV fiber light yield and collimated γ source megatile light yield), 1% of the fibers were re-spliced and 4% of the fiber/connector assemblies were rejected and replaced.

A discussion of the possible sources of the tile/fiber assembly light yield variation is given in [19]. We can define the total variation of the relative light yield distribution, σ_{tot}, as:

$$\sigma_{tot}^2 = \sigma_{fib}^2 + \sigma_{meg}^2 + \sigma_{other}^2 \qquad (9.3)$$

where σ_{fib} is the relative fiber light yield variation (3.2%) and σ_{meg} is the variation of the average megatile light yield. We define the average megatile light yield as the average relative light yield of the

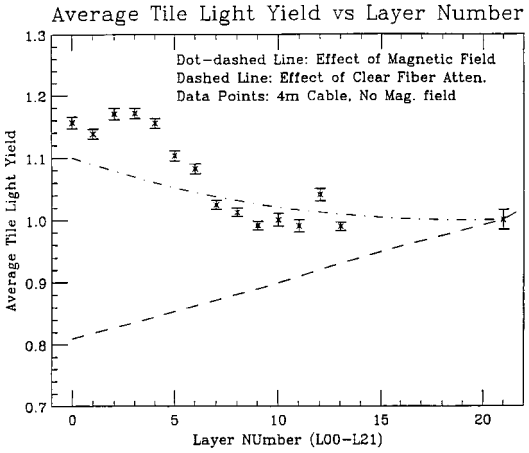

Figure 9.19: Hadron light yield for the first 14 hadron layers.

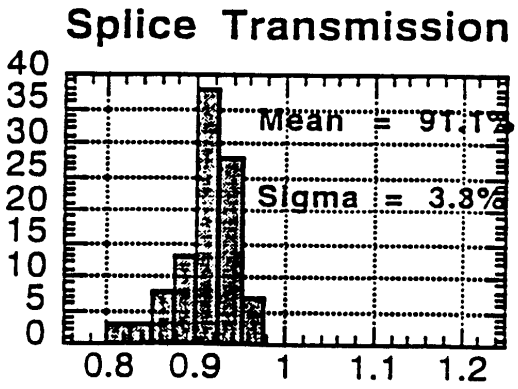

Figure 9.20: Transmission across fiber splices.

32 tiles belonging to a megatile. The term σ_{meg} describes an additional contribution to the tile light yield variation due to systematic factors common to all tiles cut from the same scintillator plate. The term σ_{other} corresponds to the light yield variation due to other factors. These factors include the quality of optical coupling of fibers inside the megatile and local variations in the scintillator material thickness. Using the measured values of $\sigma_{tot} = 6.1\%$, $\sigma_{fib} = 3.2\%$, and $\sigma_{meg} = 3.6\%$, we calculated $\sigma_{other} = 3.7\%$.

9.6 Optical System

9.6.1 Optical Fibers

9.6.1.1 Preparation of Optical Fibers

The optical system needed to route light from the scintillator tiles to the PMTs is a critical part of the Plug Upgrade Calorimeter. One of the most important components of this optical path is the splicing of each WLS fiber to a clear fiber of the same diameter for purpose of better light transmission. The splicing technique was developed to meet the following requirements:

- Transmission across the splice larger than 90%.
- Transmission variation less than 3%.
- Capability of splicing fibers of arbitrary length with no fiber damage.
- Operator-independent or nearly independent splicing machine.

Thermal fusion of plastic optical fibers had been shown to be an adequate technology during the construction of the engineering prototype [6] . For the full production of the hadronic fibers, a semi-automated splicing machine was developed. The central section of the machine includes a 250 W projector lamp to heat and fuse the fibers and two "half tubes" to constrain the fibers during heating. The use of half tubes makes it possible to splice any length of fiber without having to pull one fiber through a whole tube to remove it, a process that would be less efficient and more likely to damage the fiber. The half tubes are attached to bars, which are equipped with chucks to hold the fibers in position. To obtain consistent splices, fiber ends were polished to obtain a very uniform flat surface.

To determine the light transmission across a splice, a large number of Y-11 WLS fibers were cut and spliced approximately at their midpoints. The fibers were then excited transversely by a UV lamp and read out at one end by a photodiode. The difference in light yields for excitation on either side of the splice was used to determine the transmission. Figure 9.20 shows the results on a test sample of 100 fibers. The average transmission is 91%.

A sample of fibers were sent to University of Tsukuba for radiation testing. The splices exhibit no dependence on radiation doses up to 2 Mrad (see table 9.3).

Although the splice transmission is independent of fiber diameter, two characteristics do affect transmission through the splice [9]. The first is the type of cladding, which can be either single-clad or multi-clad. Any damage to the cladding during preparation of the fibers for splicing causes an increase in

the variation in light transmission. Single-clad fibers are more sensitive to cladding damage during polishing than multi-clad fibers.

The other characteristic affecting transmission is a property of the fiber core. The fiber supplier, Kuraray International, produces two versions of each fiber, distinguished as S-TYPE and NON S-TYPE, based on the orientation of the polystyrene chains. In the S-TYPE fibers, the chains are well oriented and the fibers are more flexible. The refractive index, however, is not completely uniform. In NON S-TYPE fibers the chains are fairly randomized and the refractive index is more uniform. The fibers are brittle, however, and easier to break if bent below a minimum radius. The NON S-TYPE fiber used for the hadronic calorimeter has a splice transmission approximately 10% higher than the S-TYPE fiber. A full description of the splicing machine can be found in [7].

Rad Dose (Mrad)	Trans.	Tensile Strength (Kg)	Bending Radius (cm)
Control	90%	3	11.5
0.3	92%	2.4	9.5
0.5	90%	3.2	11.5
1	87%	2	9
2	89%	2.5	8.5

Table 9.3: Results of radiation tests on fiber splices.

A similar splicing device has been developed for the EM calorimeter in Tsukuba. The fiber splicer heats the ends of the fibers inserted in a PEEK tube, which can help align the fiber axes and protects the fused joint mechanically. Since the tube itself is stiff, no structure to hold the fibers is necessary when the fibers are being pressed together during splicing. Various parameters such as the pressure, heating time, distance to the heater, were optimized and controlled by a PC. The transmission across the splice was found to be 95.8% with a r.m.s. spread of 1.3%, which was evaluated as the ratio between the light yield at the end of a piece of 1 m long clear fiber before and after a splice was performed on the middle point. A full description of the EM splicing machine can be found in [37].

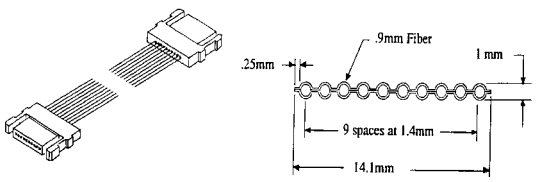

Figure 9.21: Schematic view of a 10-fiber optical cable assembly.

9.6.1.2 Optical Fiber Cables

As with ordinary electrical wires, a large number of optical fibers must be properly grouped to prevent confusion in connections and to provide mechanical protection. Protection of the fibers is important, since the fibers are routed over the end plug structure. We have developed optical fiber cables in which ten 0.9 mm diameter plastic fibers are assembled into a flat ribbon cable. The fiber spacing is 1.4 mm and there is a 50 μm thick protecting jacket made of black Tedlar [10]. The thickness of the jacket ensures enough flexibility in the fiber cable. Loss in light transmission has been tested as a function of the radius of curvature. The study also included an aging test performed using heat cycles. The results, similar to those observed with single fibers, showed no deterioration for radii of 1.5 cm or larger. Figure 9.21 shows a schematic view of a 10-fiber optical cable.

9.6.1.3 Optical Mass Connectors

To provide a convenient way of connecting and disconnecting the optical elements of the calorimeter, it was natural to terminate the optical fiber cables with connectors at both ends. The fibers from the tiles on a megatile are also terminated by connectors mounted on the outside edge of the pizza pan so that a pan is a single mechanical unit.

The most important feature of a connector is its reproducibility rather than its absolute light transmission. It was therefore decided to leave an air gap in the junction without optical grease.

There are two types of connectors: those used inside the EM pans are 3.2 mm thick $\times$ 28 mm wide $\times$ 26 mm long. They are closed by using specially machined shoulder screws which provide sufficient clamping force and precise location. The connectors are attached to the top external surface of the EM

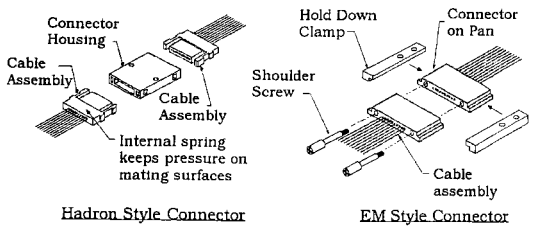

Figure 9.22: Schematic drawings of hadron (left) and EM (right) optical connectors.

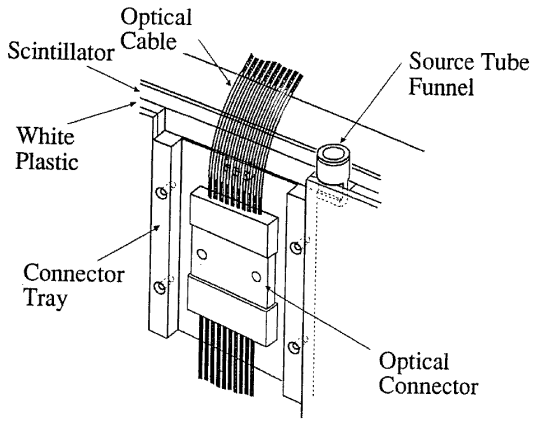

Figure 9.23: Mounting scheme of hadron optical connector on the outer edge of a pizza pan.

pans by clamping. A small L shaped "hold down clamp" screwed to the pan holds down the connector. The connector is set into the pan at a depth that allows the fiber bending radius to be sufficiently large while still remaining within the confines of the light-tight cover.

The 8.8 mm (.346 in.) longitudinal space allotted for the EM pans is not large enough to include both pans and connectors. The lead plates must therefore be cut away locally to create the necessary space for the connectors. Small pieces of tungsten replace the lead in these areas. These tungsten pieces, although thinner than the lead, are thick enough to provide approximately the same total interaction and radiation lengths as the lead they replace.

The shower maximum pans will use connectors identical to those used in the EM pans. These connectors are placed near the perimeter of the pans, some facing radially and some facing at 45° angles to the plug surface.

The hadron connector includes a spring clip assembly making connection and disconnection more convenient. The main features of the optical connectors are shown in Fig. 9.22. Both connectors have been developed at DDK in Japan in conjunction with Tsukuba University and Fermilab, and have been tested both at DDK and Fermilab [38]. Additional space in the hadron section makes it possible to use a connector thicker than the one used for the EM and shower maximum pans. Connectors are fastened to hadron pans as shown in Fig. 9.23. An injection-molded "connector tray" is attached to the pan by sandwiching it between the scintillator and white plastic. The connector housing fits into the connector tray and is positioned by two holes. A cover (not shown) is screwed onto the tray, enclosing the connector housing. Cable assemblies then fit into the housing.

Extensive R&D studies have proven that the optical transmission of the connectors is adequate for our purposes. Approximately 10% of the light is lost due to the inevitable Fresnel reflection which is 5% at the boundaries between the fiber material (n=1.59) and the air gap. The average total light loss is 17%. The r.m.s. of the reproducibility is approximately 2-3%. It should be noted that the variation in light transmission of the individual light paths from the scintillator tiles in a tower is added in quadrature to the intrinsic tile response variation in the same tower. The variation of the light transmission of each light path in the cable connector assembly also affects the tower to tower uniformity.

9.6.1.4 Optical Fiber Routing

The flat fiber ribbon cables described previously route the light signals along the outside surface of the plug to connectors on the optical decoder boxes on the rear face of the plug. The fiber routing scheme is shown in Fig. 9.24. The pattern shown repeats every 15° of azimuth. Fibers from each portion of the detector maintain individual paths. EM fibers in the center are surrounded by hadron fibers, then shower maximum fibers, with the source tubes for all detectors on the edges of each 15° section. A 5 cm wide stay clear region every 15° allows for structural brackets. There is space for 10 rows of EM cables each 5 layers deep in the center.

Since there are only 46 EM cables, 4 empty slots in the EM section can be filled with cables from a proposed preshower detector. Hadron cables are stacked either 4 or 5 deep while shower maximum cables can be from 2 to 4 deep depending on their

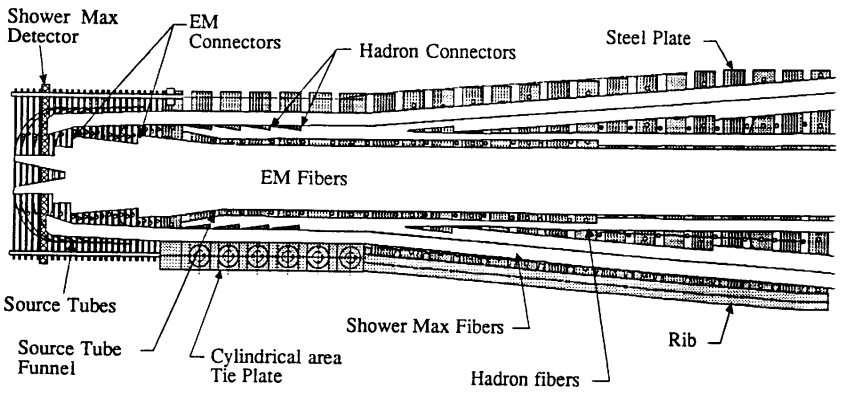

Figure 9.24: Fiber routing scheme on the outer perimeter of the plug. A 30° section is shown.

position. Stacks higher than 5 cables would result in fiber bending radii smaller than the 25 mm specified for the design. The cables must be held in place as they leave the pans and extend along the surface of the plug. Preformed pieces of foam rubber support the cables from above and below as they exit the pans. Brackets to hold down the fibers are attached to studs tack-welded to the surface of the plug. The studs are internally threaded so that light-tight covers can be attached to them.

The entire plug surface must be covered to physically protect the fibers and source tubes and to provide a light-tight enclosure. Covers will be made of .8 mm stainless steel sheet and will each cover 30° in azimuth.

9.6.1.5 PMT Placement

Approximately 1200 PMTs with their mechanical and electrical assemblies (base, light mixer, magnetic and electrostatic shields) and the associated optical decoder boxes for an end plug are grouped into 12 identical PMT boxes (Fig. 9.25) on the rear face of the plug.

The PMT boxes fit into a framework on the back of each Plug; each box can be mounted or dismounted separately of the others. Each PMT box allows space for the MAPMTs needed for the shower maximum detector. Internal to each box are additional subassemblies for the decoder boxes and the PMT mounting plates. The assembly was designed for manufacturability and ease of testing and replacement.

Each PMT box enclosure will be held at a temperature of 25°C and for this reason will be equipped with a thermal control system [11]. At present, the plan is to use solid state thermoelectric devices for cooling and resistive heaters for warming if necessary. A plan for placement of the electronics and power supplies has been established and awaits final design decisions. The PMT box design has been finalized and the boxes are currently being produced.

Cables from the PMT assemblies will be routed inside the enclosure to mass connector blocks mounted on a patch panel. The panel has 10 signal connector blocks (10 channels each), and 12 high voltage connector blocks (8 channels each) associated with the R4125 PMTs. The signal and high voltage cable bundles will use RG-174 cable and crimp coaxial and pin connectors and block connectors similar to those used on the anode, dynode, and high voltage cables from the base packages.

9.6.1.6 PMT Mechanical Assembly

The PMT mechanical assembly and mounting arrangement were designed by Fermilab Technical Support Section physicists and engineers, in cooperation with the Michigan State University physicists and engineers who designed the decoder boxes onto which the PMT assemblies must mount.

Each PMT assembly will slide into an iron pipe screwed into the front plate of a decoder box. The PMT assembly is held in place by an aluminum cap, which presses against a plastic ring and a rubber O-ring. The O-ring makes the package light-tight at the cap end. At the light mixer end of the PMT assembly, the assembly engages with two holes in the "cookie" holding the light fibers bringing light from the calorimeter to the PMT. The assembly consists of

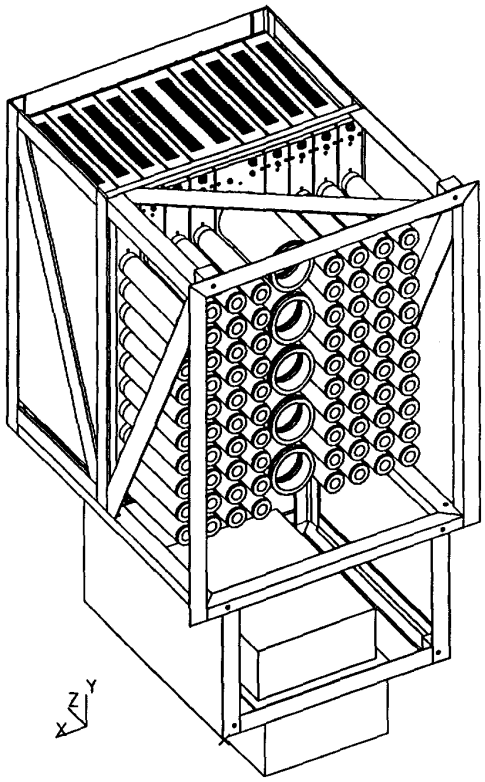

Figure 9.25: Drawing of a fully loaded PMT box. 12 PMT boxes house all the PMTs for an endplug and are mounted on the back face of the plug.

a mu-metal shield, a lucite light mixer, a base package, and several parts which allow the light mixer to be positioned precisely with respect to the cookie surface, leaving a small air gap (2 mm).

As soon as a PMT/base combination has passed all tests, the PMT and base network are built into a complete assembly.

9.6.2 Photomultipliers

9.6.2.1 Single-Channel PMT

The original specifications of the single-cathode PMT to be used for the EM and hadron calorimeter portions are listed here.

- The diameter of the PMT must be less than 40 mm.
- The photocathode should be a green extended bi-alkali with a quantum efficiency of at least 12% at a wavelength of 520 nm.
- The gain times quantum efficiency should be 3.75×10^5 for EM tubes for an operating voltage less than 95% of the maximum rated value.
- The gain times quantum efficiency should be 3.75×10^6 for hadron tubes for an operating voltage less than 95% of the maximum rated value.
- The gain times quantum efficiency should meet previous specifications for an operating voltage less than 2000 V, and all PMTs must have operating voltages within 20% of the mean operating voltage for their respective types.
- The gain times quantum efficiency should be constant to within 2% for anode charges of 750 pC/pulse (corresponding to a peak current of 30 mA for a triangular pulse with a 50 ns base).
- The gain times quantum efficiency should be stable within 1% over any 24-hour period for a constant anode current between 100 and 500 nA at constant temperature after an initial burn-in period of 40 hours.
- The gain times quantum efficiency should have a temperature dependence of less than 0.4%/ °C.
- The gain times quantum efficiency should not change by more than $\pm$ 1% after the voltage has been ramped from its nominal operating value to 300 V and back to the operating voltage.

- The gain times quantum efficiency should not change by more than $\pm$ 1% for pulses as little as 130 ns apart.
- For an instantaneous light flash the duration of the output pulse (FWHM) should be less than 20 ns for a load of 50 Ω.
- The dark current should be less than 1.5 nA when the PMT is at operating voltage.
- The minimum lifetime of the tubes should be greater than 3 years at an average anode current of 25μA.

Small groups (about 10 each) of several commercially available candidate PMT types were evaluated by Technical Support personnel at Fermilab during 1992 and 1993 [22]. Tests of gain versus voltage, dark current, relative quantum efficiency, pulse height resolution, stability, linearity, temperature dependence, and photocathode uniformity were performed at Lab 2. The PMT ultimately chosen for the EM and hadron portions of the calorimeter was the Hamamatsu R4125, a 18.6 mm diameter 10-stage PMT with a green-extended bi-alkali photocathode and K-Cs-Sb dynodes [23].

In the section on PMT testing below, a subset of the PMT performance specifications will be discussed. The complete performance specifications for the Hamamatsu R4125, which were the result of discussions between Plug Upgrade personnel and Hamamatsu Corporation representatives, can be found elsewhere [24]. Delivery of the initial order of 2100 PMTs began during December 1993 and was completed in April 1995.

9.6.2.2 Single Channel Phototubes (PMT) Bases

The base for the R4125 was designed at Fermilab and built by Thorne EMI Corporation; the socket connectors, however, were purchased from Hamamatsu Corporation (part number E678-12H). Design considerations and the details of the circuit have been documented previously [25]. The base network circuit is a conventional resistive chain with ballast capacitors. The circuit has both final dynode and anode outputs. Only the anode outputs will be used in Run II.

The base does not include a "protection network" to limit the build-up of charge on the anode if the PMT is turned on while the anode is not terminated.

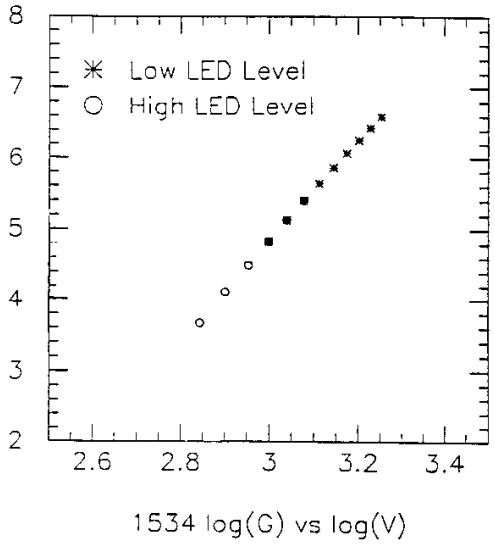

Figure 9.26: Typical R4125 single-anode PMT gain measurement as a function of the operating voltage (1534 is the tube ID).

Instead, this will be done at the anode cable termination at the front end electronics crates.

To keep the base package physically small, surface mount resistors and capacitors were used in the fabrication. To further reduce bulk, RG-174 coaxial cable was chosen for the anode, dynode, and high voltage cables coming out of the base package. Connectors were added to the anode, dynode, and high voltage cable ends by Technical Support personnel. Crimp coaxial connectors (AMP part 226537-1) were attached to the anode and dynode cables. Crimp pin connectors (AMP part 66103-4 for signal, and 66099-4 for ground) were attached to the ground and signal conductors of the high voltage cables. Delivery of 2100 bases was completed in early 1995. All bases were tested by Technical Support personnel during 1995. Only one base had to be returned to the manufacturer for replacement.

9.6.2.3 Single Channel PMT Testing

The 2100 PMTs purchased for the EM and hadron calorimeter are being tested at Fermilab and in Bologna, Italy. Testing is performed in two phases, called "pretest" and "full test". For the "pretest", each PMT/base combination has its gain versus voltage behavior measured. The PMT is then "conditioned" for 48 hours by exposure to steady-state LED light sufficient to produce 2 μA of anode current at

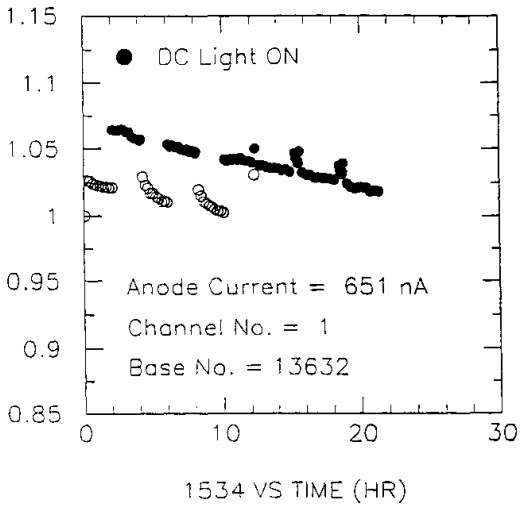

Figure 9.27: A typical R4125 PMT response to the "pulse-DC" and "high voltage ramp" tests. The response of the PMT to pulsed light as the DC background light is cycled is seen in the first 12 hours. At approximately 14 and 18 hours the response change due to cycling the PMT supply voltage is shown.

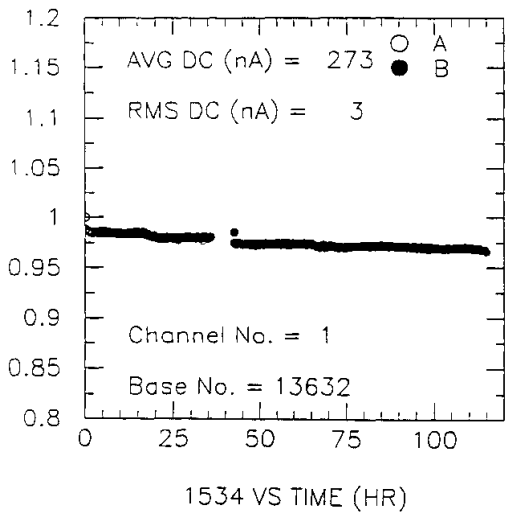

Figure 9.28: Typical R4125 single-anode PMT stability test over a period of 115 hours.

a gain of approximately 5×10^4 (the nominal EM calorimeter gain.) The entire initial order of PMTs was pretested at Fermilab during 1993 and 1994. For the "full test," a number of tests are performed on each PMT/base combination:

Gain versus Voltage: The gain is measured using the "statistical method" [26] at a value of the high voltage that gives a gain close to 10^6. This value of the high voltage is referred to as the "anchor point." Gains at a range of voltage values between 1800 V and 700 V are measured by comparing the average output for 10,000 flashes of the LED system at each voltage with the average output at the anchor point. The dark current of each PMT/base combination is measured at voltages between 700 V and 1800 V. Figure 9.26 shows the gain versus voltage behavior of a typical PMT.

Stability: Three kinds of stability test are performed, all at a gain of 5×10^4. The "pulse-DC" test is a measure of how much the response of a PMT shifts with changes in average anode current. The "high voltage ramp" test measures how long it takes for a PMT to return to within 2% of its nominal response after its high voltage has been reduced to 100 V for 1/2 hour. Figure 9.27 shows the behavior of a PMT in the "pulse-DC" and "high voltage ramp" tests. The PMT response shifts by 4.3% when the DC light is turned on (the specification calls for a shift of no more than 5%). The deviation from nominal response after high voltage restoration is also visible in the figure, but the PMT returns to within 2% of its nominal response within 2 minutes of high voltage restoration (the specification calls for no more than 10 minutes waiting time).

The "long stability" test measures the variations in PMT response to pulsed light over a 72-hour period. Figure 9.28 shows the behavior of a PMT during the long stability test. The vertical axis shows the response of the PMT normalized to its initial value (the gap in the data indicates a period during which data were not recorded due to a computer error). The response of the PMT varies by at most 1.6% over any 48-hour period in the test.

Linearity: early tests on the R4125 showed them to have excellent linearity behavior [27]. After the "long stability" test, the gain versus voltage behavior is remeasured, and linearity is measured at four values of the gain, namely $1\times10^4, 5\times10^4, 1\times10^5$ and 5×10^4, The figure of merit for the linearity measurement is the peak anode current at which a PMT departs from linear output (output proportional to the input light level, as independently measured by a PIN diode) by 2%. Figure 9.29 shows the behavior of a PMT at gain 5×10^5. The PMT output falls 2% below its linear output at a peak anode current of 88 mA, a value which lies above the specification of 70 mA at this gain (the apparent non-linearity at very low peak

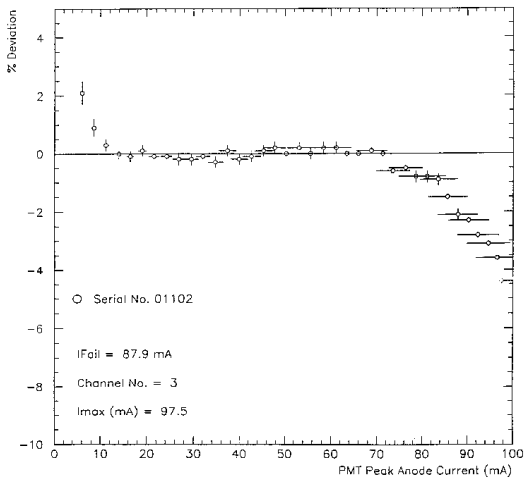

Figure 9.29: Percentage deviation from linearity for a typical R4125 single-anode PMT.

Gain	10^6
Quantum Efficiency	10%
Pixel to Pixel Cross Talk	$\leq 5\%$
Dynamic Range	500
Photocathode Uniformity	33%
Rate Capability	10^6Hz
% Dead Channels	0
DC output	yes

Table 9.4: MAPMT Requirements

anode current is due to the PIN diode, and not the PMT).

Relative Quantum Efficiency: At Fermilab, a subset (about 8%) of the PMTs have their relative quantum efficiency measured. This test is done with a tile/fiber system. The measure of relative quantum efficiency is the number of photoelectrons (N_{pe}) produced by the standard tile/fiber combination. N_{pe} is measured for the three PMTs having lowest cathode blue sensitivity (a parameter measured by the manufacturer) from each "batch" of PMTs tested. In this manner, we measure the "worst case" relative quantum efficiency subsample from each batch. So far, no PMTs have been found with unacceptably poor relative quantum efficiency.

9.6.2.4 Multi-Anode PMTs (MAPMT)

The SMD and the preshower detector are read out using WLS fibers which are 0.83 mm in diameter at the detector level and 1 mm in diameter when they reach the read-out region. In total there are 6400 strips and approximately 1000 preshower tiles to be read out, with limited space available for the photon read-out. The Multi-Anode PMTs responsible for the photon readout of the 6400 SMD scintillator strips must meet the requirements summarized in Table 9.4.

The possibility of using MAPMTs for the photon readout of SMD is one we have been investigating for several years[5]. The first generation of MAPMTs, such as the Hamamatsu 4135A, were plagued by high channel to channel cross-talk and limited dynamic range [28]. The second generation of tubes, such as the Hamamatsu 4140 and Philips XP1702 [29], are significantly improved in these areas, but still have low quantum efficiencies and large channel to channel gain variations.

A third generation of MAPMTs from Hamamatsu has recently become available for testing. We evaluated two of the newest types of MAPMTs: the R6246, an 80 channel tube, and the R5900-M16, a 16 channel tube. Both types use a metal channel plate dynode structure, and have greatly improved performance compared to the previous generations of MAPMTs. The cost per channel and the superior channel to channel gain uniformity drove the selection of the R5900-M16 tube for the photon readout of the SMD.

9.6.2.5 Description of the MAPMT and Test Results

The 16 channels of the R5900-M16 are arranged in a 4×4 grid, which is contained within a 28×28 mm^2 square package 31.5 mm deep, including the vacuum nipple. The tube is of the head-on type, with a metal envelope held at the cathode potential. The dynode structure is the metal channel plate type developed by Hamamatsu, and the window is made of borosilicate glass, with a bi-alkali photocathode. The tube can be operated with negative high voltage for DC-coupled anode output, with gain as high as 1.5×10^7 at the maximum operating voltage of 1000V. The 16 pixels are arranged in a square grid, with uniform pixel to pixel spacing of 4.5 mm. The manufacturer's specification sheets show that the spectral response is strongest between 300 and 650 nm, and that the peak cathode luminous sensitivity is typically 70μA/lm.

The 16 pixels share a common 12-stage dynode structure. We tested tubes with both linear and tapered (1.5:1.5:1.5:1:1:...:2:3.6) base resistor chains.

The total resistance of the linear and tapered bases were 2.6 MΩ and 4.0 MΩ, respectively, implying maximum base currents of 380 and 250 μA at 1000V. The signal output pins are connected to ground through the 50Ω termination provided by the ADCs used in the readout.

The single photoelectron distributions were measured at Fermilab. The first series of tests mapped the response of individual pixels and relative gains of the tapered base tube at operating voltages of 650 and 750 V. According to the manufacturers test sheets, these voltages correspond to overall gains of approximately 10^5 and 5×10^5. During the mapping of individual pixels, all 16 pixels were read out, and the tube face was scanned in 0.25 mm steps. An LED was flashed 60 times at each fiber position with intensity corresponding to approximately 2×10^3 pe output from the photocathode, while the ADCs digitized the anode outputs from each flash. At the end of each step in fiber position, the mean and r.m.s. responses of all 16 channels were recorded.

The spatial response of a typical single pixel is shown in Fig. 9.30. The typical areas for response greater than 90% of maximum are 1.5×2.0 mm^2. The relative responses of all the pixels are plotted in Fig. 9.31, using the point of maximum response, rather than the response measured at a fixed pixel pitch. The inset shows the relative responses measured for each pixel's local maximum relative to the pixel with the highest response. The uniformity was quite good compared to earlier generations of MAPMTs, and did not significantly change between the two operating voltages. The minimum pixel response was 56% of the maximum pixel response.

The relative gains were also measured for this MAPMT using the response at the geometric centers of the pixels. That distribution was less uniform, with the response of the lowest gain pixel 42% of that of the maximum response pixel; still within the 3:1 limit of our specification, however.

The linearity of the R5900-M16 was measured at a gain of 10^5 for output charges between 5 pC and 200 pC. The output for the tube with the linear divider dropped by about 10% for outputs of 100 pC, at a gain of 10^5, which is marginal performance for our application. With a tapered voltage divider in the base, however, the R5900-M16 showed typical deviations of less than 5% for output charges as high as 200 pC.

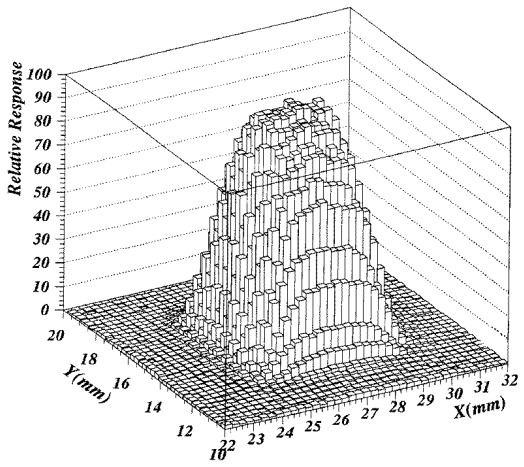

Figure 9.30: MAPMT single pixel response to an illuminating fiber scanned over the pixel surface in steps of 250 μm.

Pixel to pixel cross-talk values were measured by positioning the fiber over the maximal response point of each pixel and reading out all 16 channels. Signals in adjacent channels were gain-corrected and normalized to the illuminated pixel. The cross-talk values are shown in Fig. 9.32. The nearest-neighbor pixels' mean cross-talk was 0.7% and the median was 0.4%. In the diagonal neighbor pixels the cross-talk values averaged less than 0.2%, with a median of 0.09%.

Data taken at the geometric center of the pixels showed no nearest neighbor cross-talk greater than 2%, and the high cross-talk entries in Fig. 9.32 are the result of the variation in the position of the maximal pixel response.

The MAPMTs will be used in an environment that has changing background light levels, and which may require cycling of the operating voltage. For these reasons, the gain stability of the MAPMTs was tested under several conditions. The operating voltage may need to be turned off to prevent damage from large signals at the beginning of a Run II store. The response of a MAPMT should be stable within 10 to 20 minutes after having been turned back on so that no data are lost at the beginning of data taking. The MAPMT response returned to within 1% of the response before the voltage was turned off within 10 minutes of the voltage being turned back on, which is adequate for our purposes.

In our application the MAPMT pixels will see

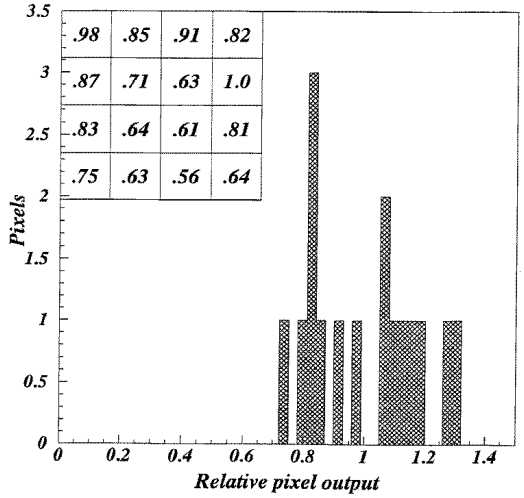

Figure 9.31: Relative responses of the 16 pixels of a MAPMT (Hamamatsu R5900-M16).

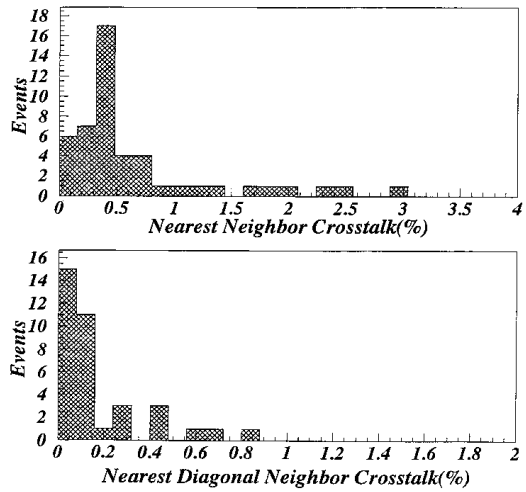

Figure 9.32: Percentage of optical cross-talk between a pixel and its neighbors (Hamamatsu R5900-M16).

quasi-DC light levels sufficient to produce currents from 1 to 100 nA per pixel. Within this range, the average current of a pixel will depend on the position of the corresponding scintillator strip in the SMD; the current will also change during the course of the store and the course of RunII. It is therefore important that the response to large pulses not depend strongly on the background current.

Two tests were performed, each over a period of about 48 hours, using average LED-induced background currents of 10 nA and 1 μA per pixel. The background LED was switched on and off at two hour intervals. For the higher background current, the shift in response to pulses when the LED was switched on and off was still less than 3%. At the lower level, the effect of switching the LED on and off was not observable, although there was a gradual downward drift of about 2% over the 48-hour period of the test.

Our final test compared the R5900-M16 response to a very low light level with that of a reference PMT (Phillips 2081B) having quantum efficiency of about 20% at a wavelength of 500 nm. A plot of the response is shown in Fig. 9.33. Single and double pe peaks are clearly visible, indicating small gain dispersion in the electron multiplication process. The operating voltage was 1000V, corresponding to a gain of approximately 10^7. The ratio of the quantum efficiencies of the MAPMT and reference PMT was derived from the fractions of events in the pedestal bins, which should be exp(-μ), where μ is the mean number of pe produced. In the case of Fig. 9.33, the R5900-M16 plot corresponds to a mean response of 1.06 pe, while the 2081B reference tube gave 2.03 pe for the same illumination. Since the quantum efficiency of the 2081B for 500 nm light is approximately 20%, we infer that the R5900-M16 quantum efficiency is approximately 10%. Both the gain dispersion and the quantum efficiency of the R5900-M16 are considerably improved over those of fine mesh type and other previous generation MAPMTs.

For the preshower detector, at gains of 1×10^5 and luminosity of $\simeq 1 \times 10^{32}$ cm^{-2}s^{-1}, the anode current for the highest η region tiles can reach approximately 0.7 μA due to the overlap of particles from different minimum bias events [40]. The signals of the 16 preshower counters at the smaller η region in a 15° pan are fed to a single MAPMT. The rest of 4 signals in the higher η region are read out by another MAPMT, together with those from three other 15°

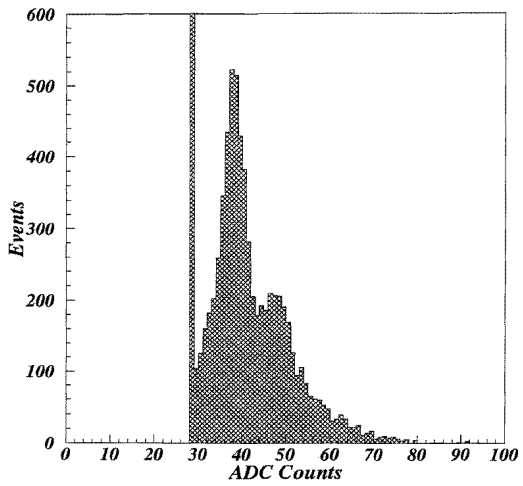

Figure 9.33: Single and double photoelectron peak response for the Hamamatsu R5900-M16.

pans. The anode current of the MAPMT used for the higher η tiles will be $\simeq 8\mu$A at the conditions described above. Tests performed at the University of Tsukuba showed that a linear base for the preshower MAPMT will perform adequately.

9.6.2.6 High Voltage System

The high voltage power supply that will be utilized in the Plug Upgrade is a system recently made available on the market by CAEN [41]. It is a highly modular system, called SY527,consisting of a Crate (Mainframe) that lodges HV generator "plug in" cards of many different kinds. A single Mainframe can lodge up to a maximum of 10 cards of the same kind. The configuration that optimizes costs and performaces still fulfilling the needs, for both the Plug Calorimeter and the Preshower and Shower Max. detectors, was found to be the one based on the an active distributor card called A932 N. The A932 N card fans out the input high voltage to as many as 24 output channels, allowing at the same time a certain amout of high voltage regulation on each output channel; in fact each channel can be independently regulated and monitored within a range of 1000 volts, starting from the input voltage down. Moreover this kind of card encompasses one HV active generator besides the 24 distributed channels thus avoiding the need for an external power supply. The resolution is 0.2 volts . The maximum current is 0.5 μa at 2.5 kV. The active channel can reach 2.5 kV with a maximum of 13 mA.

To optimize the system for the HV need of the plug PMTs and MAPMTs, we need 2880 HV channels, corresponding to 12 Mainframes and 120 cards. At the present time 5 Mainframes and 65 cards are procured. The total hardware procurement will be completed by the midde of 1997.

Long term stability as well as linearity and (absence of) ripples are checked on each individual mainframe and card at the University of Bologna.

9.7 Stability Monitor

The calorimeter response will need to be stable over long periods of time to avoid repeated calibrations. Since the calorimeter response can be compromised by any one of many elements in a long chain, it is necessary to monitor the stability of response continuously, starting at different points in the chain to distinguish between different effects. One needs to distinguish between degradation of the scintillator or the optical transmission elements, such as may be produced by ageing or by radiation damage, and changes in the electronic amplification and digitization system.

Since the EM and hadron calorimeters have been designed to have resolution of $16\%/\sqrt{E}$ and $80\%/\sqrt{E}$ respectively with a constant term below 1% in the EM detector, the stability must be monitored to better than 0.5%. The stability in the amplification/digitization system will be monitored using a system based on the fiber-optic distribution of laser-generated light to all single-anode and multi-anode PMTs.

9.7.1 Design Criteria

The system must be capable of monitoring the stability of $\simeq$ 2100 phototubes to better than 0.5% over a period of years. It should mimic the calorimeter signal as closely as possible, with a rise time of several ns and a fall time of 20 to 50 ns, and it must have a high degree of redundancy.

The system is based on the distribution of light pulses from a single light source to all the PMTs. The use of a single source is advantageous in that it leads to channel-to-channel correlations (both in time and amplitude) which can be exploited during setup and diagnosis. The power requirements can be quantified in terms of the number of photoelectrons produced at the photocathode by a typical signal (e. g. a signal corresponding to 50 GeV deposited in a calorimeter

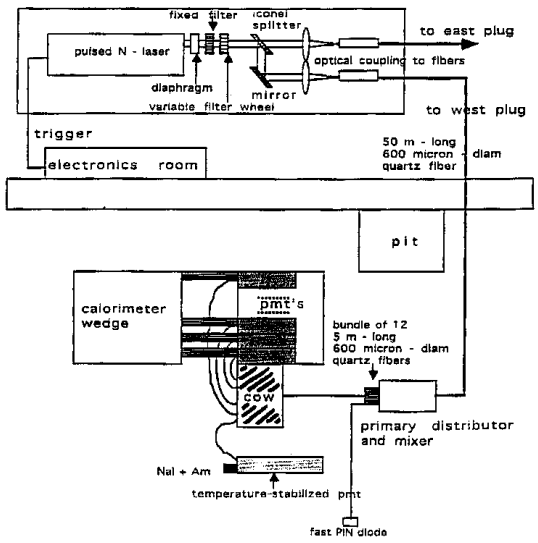

Figure 9.34: Schematic drawing of the laser stability monitoring system.

tower). Given the response expected from the EM and hadron calorimeters (approximately 350 pe/GeV and 19 pe/GeV, respectively), 50 GeV corresponds to about 2×10^4 pe in the EM calorimeter and about 1×10^3 pe in the hadron calorimeter. It is useful to note that, if the resolution σ is determined by Poisson statistics, i.e. if $\sigma = \sqrt{1/n_{pe}}$, then the power requirements corresponding to a convenient (50 GeV) pulse amplitude also correspond to statistics which are sufficient to monitor stability on a pulse by pulse basis.

Pulsed lasers emitting in the UV range satisfy these requirements as well as the need to mimic the calorimeter pulse shape; the wavelength (337.1 nm for the laser chosen) is short enough to excite a piece of scintillator similar to the one used in the calorimeter, and the pulses are narrow enough (generally < 5 ns) that the pulse shape will be determined by the WLS used for light distribution as described below. On the other hand, the 3% pulse to pulse fluctuations typical of such lasers need to be factored out: this is an essential aspect of the system.

9.7.2 Description of the Laser Light Distribution System

Light generation, transmission, and distribution for the stability monitor system are illustrated schematically in Fig. 9.34 and may be summarized as follows:

- the laser beam is split into two beams at the source
- the two beams are coupled into 600 μm-diameter quartz fibers; one for each plug
- each beam is transported 50 m to the primary distribution point
- at the primary distribution point a beam is "mixed" and distributed to each of 12 secondary distribution points ("cows")
- in each cow, the UV light excites a scintillator and the light emitted by the scintillator is distributed to each of 100 WLS fibers;
- the WLS fibers emission peak is at 520 nm and a part of this emission is captured by the fiber and transmitted to a single PMT. In this way, all PMTs are excited by each flash of the laser.

The plastic scintillator inside each cow (Fig. 9.35) emits light at an average wavelength of 420 nm, with a quantum efficiency of 90%. Approximately 25% of the scintillation light is emitted into a cylindrical reflective cavity and reaches the edge, along which are distributed 120 0.83 mm diameter WLS fibers, at intervals of 5 mm. The WLS fibers are of the same kind as those embedded in the tiles of the Plug Upgrade Calorimeter. Of the light reaching the edges of the cavity, 17% (0.83 mm/5 mm) is incident on the 120 WLS fibers and each fiber receives approximately 1% of this light which it converts to 520 nm light within the WLS fiber with an efficiency of 70%. The light is emitted isotropically so that only $\sim$ 8% is captured in the fiber and 50% of this light travels towards the PMT.

This light is transmitted to a 0.9 mm diameter clear plastic fiber by means of the optical connector (section 9.10) and transported 1.5 m to a second optical connector at the interface of one of the decoder boxes. There the 0.9 mm-diameter clear fiber connects to a 1 mm diameter clear fiber. Inside the decoder box each 1 mm diameter clear fiber is incorporated into a bundle of fibers corresponding to a calorimeter tower and optically connected to a PMT. The attenuation introduced by the clear plastic fiber and the two optical connections is estimated to be 50%.

The intensity of the 520 nm light which eventually reaches the PMT cathode is therefore estimated to be $0.9 \times 0.25 \times 0.17 \times 0.01 \times 0.7 \times 0.08 \times 0.5 \times 0.5$ that of the UV light reaching the cow, which corresponds to an attenuation factor A_{cow} of $\sim 5 \times 10^{-6}$. Using this

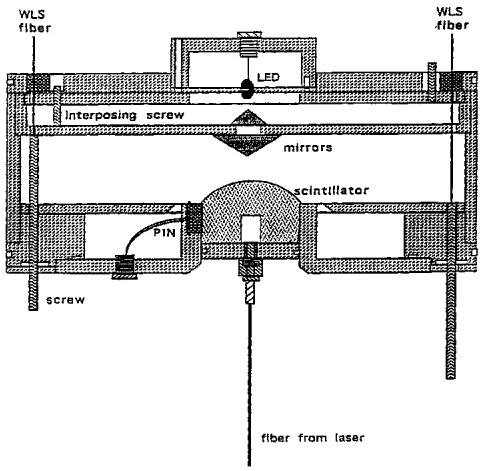

Figure 9.35: Cross-section view of a stability monitoring system secondary light distribution module (COW).

estimate for the attenuation introduced by the cow, and adding in the measured attenuation of the system from the laser to the cow, the overall attenuation A in the distribution system will be: $A = 1.3 \times 10^{-8}$. Given an intensity $L = 4.7 \times 10^{14}$ photons per pulse at source (corresponding to a Photonics LN300 nitrogen laser), the number of photons per pulse reaching the photocathode should be $n_{ph} = 6.2 \times 10^6$ and assuming a photocathode quantum efficiency of 20%, one should obtain a *maximum* of $n_{pe} = 1.2 \times 10^6$ photoelectrons per pulse. Assuming the calorimeter response values quoted in section 9.7.1, this corresponds to a single tower energy of about 3 TeV in the EM section.

The laser intensity fluctuates with a standard deviation σ_L of about 3% from pulse to pulse. This fluctuation is transmitted to the scintillator emission in each cow and, assuming that the scintillator emits isotropically, to each detector viewing this emission. In order to factor out these pulse to pulse laser fluctuations, one must include, amongst the detectors viewing the scintillator emission, at least one stable reference detector. The ratio R between the integrated charge Q_{PM} in the PMT corresponding to a calorimeter channel i and the reference detector charge integral Q_D should then be insensitive to the laser fluctuations. However, statistical requirements must be modified to take the reference detector into account; the fractional variation in pulse to pulse fluctuations of this ratio,

$$\frac{\sigma_R}{R} = \sqrt{\left(\frac{\sigma_{Q_{PM}}}{Q_P}\right)^2 + \left(\frac{\sigma_{Q_D}}{Q_D}\right)^2} \qquad (9.4)$$

must be smaller than 1%.

We have already established that power requirements corresponding to a 50 GeV calorimeter signal are compatible with pulse by pulse stability monitoring. If we want to preserve this capability, we must ensure equal or better statistics in our reference monitor, i.e. $\sigma_R/R <\sim 1\%$. Two such reference monitors have been designed into the system for redundancy. The first is the set of two PIN photodiodes indicated in Fig. 9.35. Though the PIN photodiodes [31] are expected to be very stable with respect to temperature change (0.003% /^{o}C), a temperature monitor was included in each cow. This will also allow eventual effects of temperature-dependent mechanical stress on the light distribution to be monitored. The second reference monitor is a temperature-stabilized PMT which simultaneously views one of the fibers from the cow and an ^{241}Am-loaded NaI scintillator. The stability of the PMT response is monitored with reference to the 5.4 MeV ^{241}Am α -peak in the signal from the NaI scintillator. Residual temperature-related instabilities arise from the temperature dependence of the NaI response ($\sim 0.2\%/^oC$) [32]. The temperature of the PMT must be stabilized to better than 2^{o}C.

9.8 Calibration Scheme

9.8.1 Calorimeter Calibration

Measurements performed on individual tile responses and PMT gains described previously will allow us to know the absolute response of a given tower to approximately 30-40%. In the hadron calorimeter we plan to reach a calibration level of the order of 3-5% with a combination of muon calibration and wire-mounted source calibration. For the EM calorimeter we will use the same methods for a preliminary calibration, but during the course of data taking we will be able to shift to a calibration based on physics signals such as $Z \rightarrow ee$. We could also use $J/\psi \rightarrow ee$ decays provided CDF can track at large η and we can trigger on them.

We have investigated in the past a calibration scheme for low energy electrons based on the reconstruction of $\pi^0 \rightarrow \gamma\gamma$. By measuring the photon energies in different towers and using the shower max-

imum detector to measure the opening angle we obtained some promising results. An extensive study of calibration methods based on the exploitation of physics signals awaits the integration of the Plug Upgrade Calorimeter into a full CDF detector simulation. Here we discuss the calibration scheme based on muons and the wire-mounted source.

9.8.2 Moving Radioactive Sources

The wire-mounted source system is an important part of the calibration system for the CDF Plug Upgrade Calorimeter. The ^{137}Cs source of about 4 mCi is mounted inside the tip of a long flexible stainless steel wire. The source is "parked" inside a lead brass shield on the wire source driver when not in use. The wire is curled several turns on a reel with radius 5 in. The driver uses two motors to direct the wire source into the calorimeter. One motor controls the source tube selection and the other actually drives the wire source along the tube.

The wire source system will be used in the cosmic ray and test beam tests . Data from these tests along with those obtained during megatile production will be used to determine the initial gains of the towers of the fully installed detector at B0. All the layers in the final calorimeter can be source tested when the plugs are pulled out. The following layers can be source tested at any time: the preshower and shower maximum layers; four layers (2, 4, 6, 16) of the EM calorimeter; four layers (0, 6, 12, 19) of hadron calorimeter.

To sample and calibrate these layers when the detector is installed at B0, four drivers will be mounted on the back of each plug, each serving one quadrant. To provide a secured path for the source from the driver to the megatiles, two kinds of tubes will be used. One is stainless steel tube, routed on the outer perimeter of the plug along with the optical fiber cables. One end of each tube is coupled to the tube embedded in the megatile; the other end extends out of the edge of the plug. A flexible nylon tube provides a bridge between the end of the steel tube and the indexing disk of the source driver.

It will take about 30 minutes to scan the frontmost layer (preshower); less time will be required for the back layers. During plug assembly a PC-based stand-alone data acquisition system will be used to test the tiles with the wire source. This system controls the source driver and reads out the position of the wire-mounted source as well as the tile response to the source through ADCs. The ADCs can be read by the PC either through CAMAC or through expansion cards inside the PC. After the detector is commissioned, the PC will still be used to control the source driver mechanism, but the ADC readings will be done by the CDF main DAQ system. The PC will also provide the wire source position to the main DAQ.

In principle, the source calibration could substitute for test beam exposure since:

- every tile has a measured ratio of collimated source to wire source
- the collimated source response should correlate well with either MIP response or hadron response
- every tile can be wire sourced after the final optical cabling and phototubes are installed.

The source calibration can be used to transfer the calibration from the Test Beam tests to B0. However, with the magnetic field on (plugs closed), only a few layers can be scanned with the wire-mounted source. These few layers can be used to determine the effect of the magnetic field on the scintillator.

The primary calibration will be in terms of a minimum ionizing muon signal. That is, all towers will be calibrated relative to one another using the most probable energy deposition, summed over all 22 layers, of a minimum ionizing muon (defined to be a MIP) and shower energies will be expressed in terms of MIPs.

This μ calibration will be obtained for all the EM towers in the full calorimeter using cosmic rays, and for a 60^0 mockup section (see section 9.9) of the hadron calorimeter in the beam test. Since the muons in the test beam will have higher energy than those at B0, the energy dependence of the muon response will be checked by measuring the response of the EM test beam section to both cosmic rays and test beam muons. Data from CCFR [33] and Hanging File experiments [34] indicate the most probable energy deposition of muons in a calorimeter increases by 7% for every 100 GeV of muon energy.

In our design, a muon signal has the same light yield independent of the size of the tile. Consequently, if tower to tower PMT gain variations are normalized to the MIP signal for a tower, the calorimeter's response to localized energy deposition

anywhere (transversely and longitudinally) within it will be uniform. Because of this uniformity and relative energy calibration in terms of MIPs, all 30° pizza pan sectors can be considered to be *identical* calorimeters, *i.e.* to have identical MIP to GeV calibrations.

9.9 Test Stands

9.9.1 Test Beam Module

A mockup consisting of a 45° EM sector (three pizza pans) and a 60° hadron sector will be constructed in a manner identical to the actual device and placed permanently in the CDF test beam facility. No other test beam test will be performed on the full calorimeter. This test beam module (TBM) will be used to obtain the absolute calibration from MIPs to GeV and from wire-source response to GeV. It will also be used to study details of the performance of the full Plug Upgrade Calorimeter.

The TBM will sit on a movable stand that will allow every tower to be illuminated by a momentum-selected beam. Most of the steel absorber for the hadron calorimeter portion of the TBM is from the old 60° mockup of the gas PHA, with modification described in section 9.5.2.1 to simulate the configuration of the plug steel for Run II. The relative MIP calibration of the towers will be done with test beam muons of fixed momentum, as was done in the 1991 test beam run. The absolute calibration of the shower energy in units of MIPs to GeV will be done using momentum-analyzed electron and hadron beams of various energies. The wire-mounted source will also be used on all tiles of the TBM to verify and quantify the source technique for predicting MIP and hadron shower responses. It is expected that the source technique will permit equalizing the tower responses to within a few percent.

The relative calibration in MIP units must also be done on the actual calorimeter at B0. However, because the light yields from ionizing radiation in most scintillators increase in magnetic fields [35], the calibration at B0 must be done with the solenoidal magnetic field turned on. In principle, any increase in light yields due to magnetic field effects will produce an increased MIP response that should compensate the corresponding increase in the hadronic shower response. Thus to first order, if the absolute calibration from MIPs to GeV is obtained from the test beam where there is no magnetic field, this absolute calibration can be transferred to B0 as long as the MIP calibration at B0 is done with the solenoid magnet on.

The magnetic field can have an additional effect: the hadron response of the CDHS iron calorimeter [36] (which is composed of magnetized steel disks in a toroidal geometry) exhibits a change of a few percent when the steel is magnetized. This is presumably due to the increased path length of curling low energy electrons in the magnetized steel. However, in the CDHS toroidal geometry only the steel was magnetized, and the scintillator was in a much lower field. In the CDF plug geometry, the magnetic field in the steel and in the scintillator is similar. The effect is therefore expected to cancel, since the fractional increased path length in the iron and scintillator will be similar.

The change in scintillator response can be monitored with the radioactive source calibration by comparing the "field on" to the "field off" response. The effect is hoped to be the same for calibrations from the source, MIPs, and hadrons. It is conceivable that the small "soft" component of the ^{137}Cs excitation of the scintillator (approximately 5% in the geometry of the hadron megatiles) contains an electronic component which could be steered away from the scintillator by the magnetic field. However, benchtop measurements with and without a few mm of plastic filter between the source tube and a tile (sufficient to remove almost all of the soft component) show no difference in the magnetic brightening curve, within an accuracy of approximately 1% or better. Consequently, it is believed that source excitation will accurately track the brightening of the calorimeter for MIPs and hadrons.

9.9.2 Cosmic Ray Test Stand

The purpose of the cosmic ray test for the complete EM calorimeter is that of obtaining a preliminary calibration to μ since the full EM calorimeter will not be tested on the test beam. The cosmic ray test stand will consist of two tracking chambers, one above and one below the calorimeter under test, and two 9.5 inch thick steel plates which will serve as a support table for the calorimeter and as an absorber for low energy cosmic rays. Figure 9.36 provides a plan view of the cosmic ray test stand.

For purposes of the cosmic ray test, the calorimeter

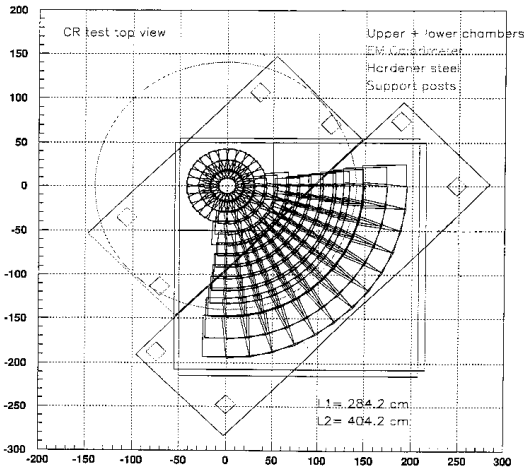

Figure 9.36: Schematic view of the projective region covered by the tracking chambers in the cosmic ray setup.

will be positioned with its axis of symmetry vertical and will rest directly on the hardener steel, which will in turn be supported approximately two feet above the floor by means of steel box-beam supports. The upper tracking chamber will be supported over the calorimeter on two parallel beams, while the lower tracking chamber will be positioned under the hardener steel. Both tracking chambers will use non-flammable gas.

The upper tracking chamber, which measures approximately 1 $m^2 \times$ 0.2 m, will be mounted on the axis of the calorimeter, 1.6 m above the front face of the calorimeter and will provide projective coverage for the entire calorimeter.

Plastic scintillator paddles above and below the upper tracking chamber will provide trigger and timing information.

The lower tracking chamber, which measures approximately 2.5 $m^2 \times$ 0.3 m, will be offset from the axis of the calorimeter as shown in Fig. 9.36 and positioned under the 9.5 in thick hardener steel on which the calorimeter rests. This chamber will provide projective coverage for one quadrant of the calorimeter.

To collect data from successive quadrants of the calorimeter, the calorimeter will be lifted by a crane and rotated by 90°. The calorimeter lifting fixture will straddle the upper tracking chamber, and will support the calorimeter by means of four cables attached to the lower calorimeter plate. The optical cables leading from the calorimeter will be disconnected prior to the rotation.

Two enclosures containing the calorimeter PMTs

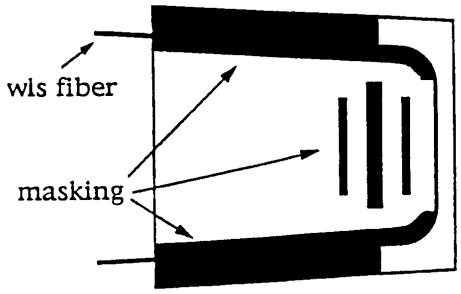

Figure 9.37: Schematic of an engineering prototype tile-fiber assembly.

will be mounted near the calorimeter, on top of the hardener steel. The optical cables leading from the calorimeter to the PMT boxes will be routed under a protective housing covering the area between the two enclosures and the calorimeter.

The DAQ for the cosmic ray test will be essentially the same as for CDF Run 1, interfaced to the DART software from the Computing Division.

9.10 Engineering Prototype Tests

9.10.1 The Engineering Prototype

A full scale engineering prototype detector was built and tested in 1991 at the Fermilab test beam facilities to investigate a number of unknown aspects of the novel technique of tile-WLS fiber calorimetry. The device consisted of EM and hadron calorimeters, and included a fine-grained shower maximum position detector using scintillating fibers.

The EM section of the prototype was composed of 48 projective towers. There were 23 sampling layers, each layer consisting of a 4.8 mm lead plate and 4 mm Bicron BC-408 scintillator tiles. The detector covered 22.5° in ϕ, and a polar angle range of $22° \leq \theta \leq 37.5°$. The 48 tiles of each layer were cut out on a Thermwood CNC milling machine at Fermilab; a U-shaped groove for the WLS fiber was made in each tile on the same machine. The tile and groove geometry is shown in Fig. 9.37. A 1 mm diameter Bicron BCF-91A WLS fiber was inserted into the groove.

Each fiber end was thermally spliced to a 1 mm diameter clear fiber. The 46 clear fibers of each projective tower were then guided along the outside of the detector to an RCA 8575 PMT.

A major goal of the construction and testing was to

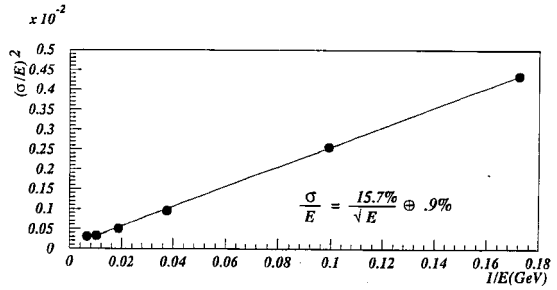

Figure 9.38: Engineering Prototype EM energy resolution obtained from test beam electrons.

achieve uniform light response both within single tiles and from tile to tile. For single tiles the light yield varies with the position of the light generation, the highest light yield typically coming when the light is generated close to the edge of the tile. The approach taken to flatten the response was twofold; first, the position of the WLS fiber within the tile was optimized; second, the response of the high light yield areas was reduced by "masking" those areas with dark paper.

Studies of the effectiveness of both approaches were performed using a radioactive source and a scanning table. Optimal positioning of the fiber resulted in an r.m.s. variation in the light yield across EM tiles of approximately 3%. Masking reduced the r.m.s. variation to less than 2%.

To ensure that the light yield from tile to tile was as constant as possible, a large quality control effort was made in the fiber splicing and tile production processes. Source testing of the tiles showed an r.m.s. variation from tile to tile of approximately 8%. To reduce this variation further within individual projective towers, a program of longitudinal masking was developed. A radioactive source mounted on the tip of a moveable wire was passed over the surface of every tile in the calorimeter, and the peak current for every tile was recorded; this information was then used to calculate the relative light yield of each scintillator tile. Once the relative light yields of all tiles in a projective tower had been calculated, a photographic mask was produced and inserted between the optical fibers and the PMT face. The pattern on the photographic mask was generated so that the light from each tile was reduced to be equal to the light produced by the lowest light yield tile in that tower. In this way r.m.s tile to tile variations were reduced to 2-3%.

A shower maximum position detector was placed in front of the sixth layer of the EM calorimeter at a depth of 5.3 X_0. The shower maximum detector covered 15° in ϕ and a polar angle range of $22° \leq \theta \leq 37.5°$. It consisted of two layers of 2 mm diameter Kuraray SCSF38 scintillating fibers; a 15° crossing angle between the fibers of the two layers made it possible to measure particle positions. The fibers in each layer had 1 mm pitch, and there were 320 fibers per layer. The scintillating fibers were optically coupled to 1 mm diameter clear fibers through a 700 μm thick layer of Dow Corning Silgard 184. The clear fibers were routed along the outside of the EM and hadronic sections to the back of the detector, where they were read out by 8 Hamamatsu R4135A multianode PMTs [30]. These MAPMTs have been described in detail elsewhere [4]; but briefly, they have a crossed wire anode so that up to 228 fibers can be read out using only 36 electronic channels.

The hadronic section of the prototype was similar in design to the EM section, with the following differences: it was composed of 24 projective towers and there were 23 sampling layers, each layer consisting of a 5.0 cm steel plate and 6 mm Kuraray SCSN81 scintillator tiles. The detector covered 45° in ϕ, and a polar angle range of $14° \leq \theta \leq 37.5°$. Because of the larger tile size in the hadron section, two U-shaped grooves were cut in each tile for the WLS fibers. As in the EM section, 1 mm diameter Bicron BCF-91A WLS fibers were used, and the WLS fibers were thermally spliced to 1 mm diameter clear fibers. There were four fibers exiting from each tile, and the 92 fibers from each projective tower were routed to an RCA 8575 PMT mounted on the back of the detector.

9.10.2 Test Beam Studies

The prototype was exposed to electron, hadron, and muon beams in the CDF test beam area at MT. The response of the EM section of the calorimeter was studied to determine its energy resolution, linearity, and uniformity. The PMT gains were set to 10^5. The light yield was measured using a calibrated PMT and was found to be 400 photoelectrons (pe)/GeV, or 4.3 pe/MIP/tile. The relative tower to tower calibration was established using 100 GeV electrons. The electron beam was centered on each tower, and the energies deposited in that tower and its nearest neighbors were used to construct a 3×3 towers energy sum. A calibration constant was determined for each tower by iterating until the responses of all 3×3 tower

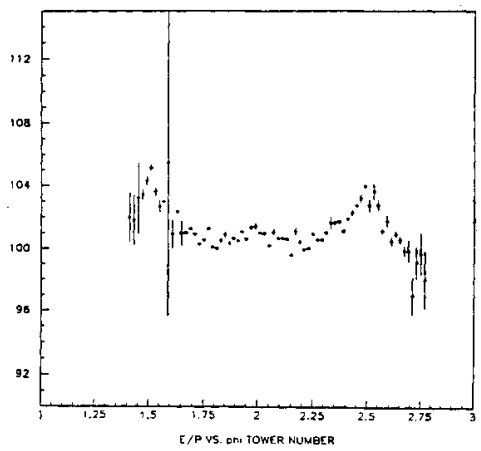

Figure 9.39: Transverse uniformity of response in an EM tower of the engineering prototype.

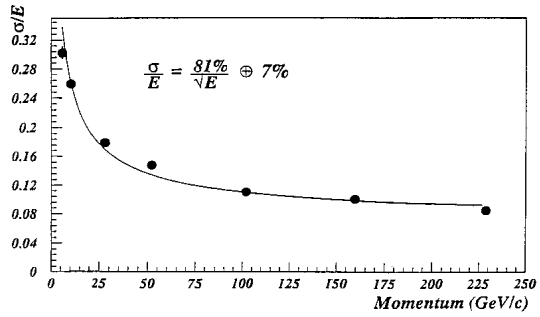

Figure 9.40: Engineering prototype hadron energy resolution obtained from test beam pions.

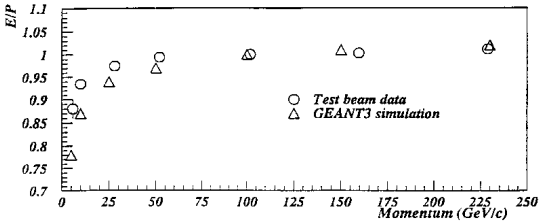

Figure 9.41: Predicted and observed response to hadrons in the engineering prototype.

sums were equal.

The device was also calibrated with high energy muons. The mean of the ratio of the electron to muon response for all towers was 1.0, with an r.m.s. variation of 4%.

The EM section energy resolution for the available electron energies is shown in Fig. 9.38 for a typical tower. Due to limitations in beam time, the energy resolution and linearity were measured for only six towers in total. The non-linearity, defined as the percent difference between the normalized response at 10 GeV and 150 GeV, corrected for leakage out the back of the EM section was typically 1%, although one tower had a non-linearity of 4%.

The transverse uniformity of the towers was also measured: using beam drift chambers to accurately determine the position of the particles, fine scans across tower faces were done with 100 GeV electrons. The results for a typical tower are shown in Fig. 9.39. The r.m.s. variation across the tower was 1.4%, consistent with the variation for single tiles measured using a radioactive source.

The energy resolution, linearity and transverse uniformity of the hadronic section were also studied. In addition, the relative response of this device to electrons and pions was studied. The hadron PMT gains were set to 5×10^5. The light yield was measured to be 39 pe/GeV, or 1.8 pe/MIP/tile. The tower to tower calibration was established by measuring the response of each tower to muons and fitting to the peaks of the resulting Landau distributions.

The energy was measured using a 3×3 tower sum, after correcting for different relative responses. The energy resolution was measured over a range of pion energies from 5 to 230 GeV. The total energy deposited by a particle was assumed to be a linear combination of the energy in the EM and hadronic sections. A fit to the results shown in Fig. 9.40 gives an hadronic energy resolution of $81\%/\sqrt{E} \oplus 7\%$. The response of the detector, divided by the measured momentum, as a function of pion momentum, is shown in Fig. 9.41, along with the GEANT prediction. The data and GEANT prediction are normalized to the same value at a pion momentum of 100 GeV. For low energies the measured E/p is higher than the prediction.

The electron to pion response ratio (e/π) was determined by measuring the response to electrons for a hadron tower at the edge of the calorimeter that was not covered by the EM section, and comparing that response to the response to pions in a central tower. The use of different towers was dictated by the need to have lateral containment of the hadronic showers. The response for 100 GeV electrons and pions is shown in Fig. 9.42. From this data e/π at 100 GeV was measured to be $1.28 \pm 6\%$, where the large uncertainty comes from the calibration uncertainty between the two towers. A more complete de-

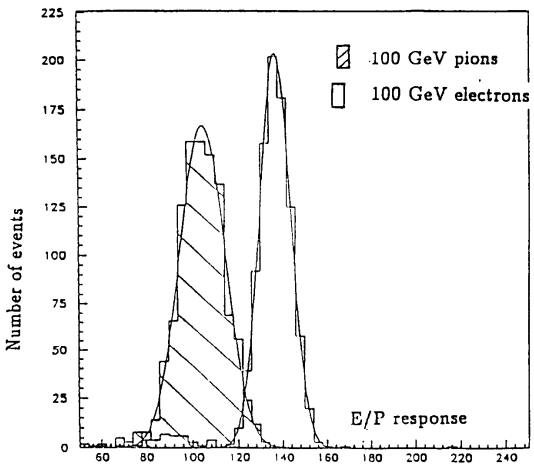

Figure 12: Response to 100 GeV electrons and hadrons.

Figure 9.42: Response to 100 GeV electrons and pions in the engineering prototype.

scription of the test beam results on the engineering prototype can be found in [8].

The shower maximum detector was designed to measure the position of electron and photon showers, and to distinguish isolated electrons and photons from π^0's. This detector and the results obtained with it in the test beam have been described elsewhere in detail [5].

9.10.3 Engineering Prototype Lessons

The device performed to expectations, but several lessons learned during the process required significant additional research and development before construction of a final calorimeter could begin. The largest problem discovered was that of routing the fiber optic readout cables to the PMTs. The readout fibers in the prototype exceeded the space limitations that exist in the real detector, and so considerable work was done to reduce the amount of fibers and to route them in a more compact manner.

In the EM and hadronic sections, the number of fibers was reduced to one per tile and the EM tile size was increased, reducing the number of towers. The scintillator fibers of the shower maximum detector were replaced by 5 mm wide scintillator strips, giving lower, but still adequate position resolution, and greatly reducing the channel count.

In addition, considerable work was done to use flat ribbon fiber cables for readout, considerably improving the packing fraction. The light output decreased when the number of readout fibers per tile was reduced to one, and so considerable work was done to boost the light output by mirroring the fiber end and optimizing the position of the WLS fiber in the tile.

In the end, the results from using a σ fiber pattern in the tile were uniform enough that the masking was no longer necessary. Additionally, the light output using one fiber was actually greater than had been achieved with two at the test beam. The σ pattern, with only one fiber exiting from the tile, was chosen for both the EM and the hadron detectors.

Finally, the packaging and positioning of the tiles were improved. The megatiles used in the hadron section and the scintillator rivets in the EM section were also developed in response to lessons learned in building the engineering prototype.

Bibliography

[1] The CDF Collaboration: *Proposal for an Upgraded CDF Detector* Oct 9,1990 CDF Internal Note 1172.
G.Apollinari,P.de Barbaro and M.Mishina: *CDF Calorimeter Upgrade Project*, Proc. of the 4^{th} Int. Conf. on Calorimetry in High Energy Physics, World Scientific (1994) 200-225.

[2] F.Paige and S.D.Protopopescu, BNL Report No. 38034, 1986 (unpublished).

[3] P. Avery, K. Read, G. Trahern, Cornell Internal Note CSN-212, March 25, 1985.

[4] K.Arisaka *et al.*,*Position Sensitive Photomultiplier with Venetian Blind Dynodes*, UCLA internal note (1990)

[5] J. Hauser *et al.*, Nucl. Instr. and Meth. **A321**, 497-503 (1992)
Arisaka *et al.*, UCLA-HEP-90-007.

[6] G.Apollinari *et al.*, Nucl. Instr. and Meth. **A311**, 520-528 (1992).

[7] J.P.Mansour *et al.*, in Proceedings of the 1993 Scintillating Fiber Workshop, Notre Dame, IN, Nov 5-12,1993

[8] M.A. Lindgren, *The CDF Plug Calorimeter Upgrade*, in Proceedings of the Third International Conference on Calorimetry in High Energy Physics,Corpus Christi, TX, 29 Sep–2 Oct 92, eds. P.Hale and J.Siegrist, World Scientific, (1993).
J. Freeman et al., *The CDF Upgrade Calorimeter*, in Proceedings of the Second International Conference on Calorimetry in High Energy Physics, ed. A.Ereditato, World Scientific (1992), p. 189.

[9] The CDF Collaboration, "Proposal for Run II Tracking System Upgrades for CDF", CDF Internal Note 3079, March, 1995.

[10] Du Pont Tedlar-TCC15BL3, PVF film.

[11] The current candidate air conditioner is the AHP-1801HC made by Thermo Electric Cooling America Corporation (TECA).

[12] S.Kim and K.Kondo, CDF Internal Note 1788, (1991).

[13] J.Strait, CDF Internal Note 2097, (1993).

[14] T. Asakawa *et al.*, Nucl. Instrum. Methods A340(1994) 458-465.
S. Aota *et al.*, Nucl. Instrum. Methods A352(1995) 557-568.

[15] Kuraray International Corp., 200 Park Ave., New York, NY 10166.

[16] Du Pont Tyvek-1055B, spunbonded Olefin film. Mean thickness of 0.006" with 0.0025" r.m.s. spread.

[17] M.Olsson *et al.* CDF Internal Note 2582 (1994)

[18] P.deBarbaro *et al.* "CDF End Plug Hadron Calorimeter Upgrade: Design, Production and Quality Control", submitted to IEEE, Trans. Nucl.Sci. (1995)

[19] P.deBarbaro*et al.* CDF Internal Mote 2778.

[20] G.Apollinari, IEEE Trans.Nucl.Sci. Vol.40, (1993)

[21] P.Melese, "Shower Maximum Detectors Using Scintillator Strips and WLS Fibers",in Proceedings of the 1993 Scintillating Fiber Workshop, Notre Dame, IN, Nov 5-12,1993

[22] W. Koska *et al.*, "Evaluation of Candidate Photomultiplier Tubes for the CDF Plug Upgrade Calorimeter" TS-DET 95-013.

[23] W. Koska *et al.*, "Justification for Purchasing Hamamatsu R4125 Photomultiplier Tubes for the End Plug Calorimeter Upgrade Project," TS-DET 93-052.

[24] The request for quotes (JPM1270) and various addenda such as amendments to the original specifications, as well as the final purchase order, are included in TS-DET 94-034.

[25] W. Koska and S. Delchamps, "CDF Plug Calorimeter Base Design Considerations," TS-DET 93-058.

[26] I. Fiori *et al.*, "Gain and Dark Current versus Voltage Measurements on Hamamatsu and Philips Photomultiplier Tubes" TS-DET 92-001. W. Koska and I. Fiori, "Gain vs. Voltage and Pulse Height Resolution Measurements for the First Twenty Production PMT's" TS-DET 93-072.

[27] Q. Shen, "Linearity of the 19 mm Hamamatsu R4125 Photomultiplier Tubes," TS-DET 93-016.

[28] G. Comby and R. Meunier, Nucl. Instr. and Meth. **A269**, 246 (1988); F. Takasaki *et al.*, Nucl. Instr. and Meth. **A260**, 447 (1987); M. Salomon and S.S.A. Williams, Nucl. Instr. and Meth. **A241**, 210 (1985); and J. Ditta *et al.*, Nucl. Instr. and Meth. **220**, 343 (1984).

[29] P. Cushman and S. Hou, Nucl. Instr. and Meth. **A339**, 456 (1994)
J. Bahr *et al.*, Nucl. Instr. and Meth. **A330**, 103 (1993)
G. Apollinari *et al.*, Nucl. Instr. and Meth. **A324**, 475 (1993).

[30] Hamamatsu Photonics K.K., Electron Tube Center 314-5, Shimokanzo, Toyooka Village, Iwata-gun, Shizuoka-ken, Japan.

[31] S1722-02- type PIN by Hamamatsu Corp., Bridgewater, NJ.

[32] R.L. Heath *et al.*, Nucl. Instr. and Methods, 162 (1979) 431-476.

[33] P. Auchincloss et al., Nucl. Inst. & Methods **A343**, 463 (1994)

[34] A. Beretras et al., Nucl. Inst. & Methods **A329**, 50, (1993)

[35] J.Mainusch et al., Nucl. Instr. and Methods, **A312** (1992) 451
D.Blömker et al., Nucl. Instr. and Methods, **A311** (1992) 505.

[36] H.Abramowicz et al. (CDHS) Nucl. Instr. and Methods, **180** (1981) 429.

[37] K. Hara *et al.*, Nucl. Instrum. and Methods A348 (1994) 139-146.

[38] S. Aota *et al.*, Nucl. Instrum. and Methods A357 (1995) 71-77.

[39] S. Aota *et al.*, CDF Internal Note 3141 (1995)

[40] K. Hara, CDF Internal Note 2958 (1995)

[41] CAEN SpA , e-mail INFO@CAEN.IT, URL: http://www.caen.it, Via Vetraia, 11 I-50049 Viareggio,(Italy)

Chapter 10

Muon Detectors

CDF has traditionally emphasized charged particle tracking and lepton identification. Triggering and reconstructing muons is at the core of several broad physics programs. Top quarks are identified in via muons from decays of their W and b daughters. W bosons are identified in part and their mass measured via their muon decay mode. Systematic effects in the W mass measurement are studied with the large sample of $J/\psi \to \mu^+\mu^-$ decays, a sample that is also central to the CDF B physics program. The asymmetry in W decays constrains parton distribution functions, and many signatures of new physics involve one or more leptons.

In Run I and before, there was a logical distinction between central muons and forward muons. Central muons were identified by their penetrating ability, and detected by chambers located outside substantial material. The momentum of these muons was measured by measuring their bend in the solenoidal field using the central trackers. Forward muons were identified and their momentum measured simultaneously in toroidal magnets in the forward region.

With the improved tracking system of CDF II, especially the inner silicon, momentum resolution in the forward region for high p_T tracks is similar for the solenoid and the toroids. The distinction between "central" and "forward" muons is now purely historic; *all* muons will be identified by their passage through material and have their momentum measured using the solenoid.

The existing central muon systems have performed well in the present run. We are planning a program of incremental improvements rather than major replacements of the detectors. Our goals are to preserve and improve the existing detector performance under the new operating conditions in the Main Injector era.

The existing forward muon system (FMU) is built around two pairs of toroids, one pair at positive rapidity, the other at negative. There are electrodeless drift chambers installed between the toroids and on the outer and inner faces of the toroids, and two planes of scintillation counters. Details of the design and construction of the FMU can be found in [1]. The FMU has fewer channels per unit rapidity, and therefore higher occupancy, than the central detectors. At luminosities of 1.0×10^{32} cm^{-2}/s, the detectors could be made to function with substantial effort, but above that, and certainly by 2.0×10^{32} cm^{-2}/s, muon reconstruction would have been severely degraded. Extrapolations from Run I data estimate reconstruction efficiencies of 70% and below at high luminosities.

For the $|\eta| > 1$ region in Run II, CDF has elected to cover a smaller and lower rapidity interval ($\eta = 1.0 - 1.5$) with sufficient granularity to survive high luminosity, by a) pushing the toroids as close to the central detector as possible, and b) building a cylindrical "barrel" of chambers (with chambers as staves of this barrel) similar to the existing central chambers around the outside radii of the toroids and c) installing scintillation counters for triggering and identifying which beam crossing generated the muon of interest. The design closely parallels that of the central detectors. The 1.0-1.5 region was chosen because:

- It covers more solid angle than the region covered by the original FMU, even in the pushed-up position. For high mass objects such as $t\bar{t}$ pairs and energetic lepton pairs used to constrain quark substructure, solid angle is the figure of merit, not rapidity.
- The W asymmetry is largest in this region.
- The region is contiguous with the existing central detectors.

Between $\eta = 1.5$ and $\eta = 2.0$ there is also muon identification, with granularity (and therefore occupancy) insufficient for triggering, but adequate for identifying high p_T tracks in this region as muons.

There will be four detectors for muon identification in Run II. We summarize design parameters of detectors in Table 10.1. In Sections 10.1, 10.2, and 10.3,

we describe them as they are now. In Sections 10.4 and 10.5, we identify the changes in the detector and read-out planned for Run II. Section 10.6 describes the changes and new detector construction in the $\eta > 1.0$ region. Finally, Section 10.7 contains a discussion of performance issues related to higher luminosities and different bunch structures.

10.1 Central Muon Detector

The CMU, the original set of muon chambers, consists of 144 modules with 16 rectangular cells per module, located behind $\sim 5.5\lambda$ of absorber (the Central Hadron Calorimeter). Each cell is 6.35 x 2.68 x 226 cm in size and has a 50 μm stainless steel wire in the center. The 16 cells in a module are stacked four deep in the radial direction, with a small ϕ offset between the first and third and second and fourth layers. The first and third (and second and fourth) ϕ cells have their wires ganged together in the readout, and each wire pair is instrumented with a TDC to measure the muon's location in ϕ, and an ADC on each end to measure the muon's location in z via charge division.

Table 10.1 lists some design parameters of the CMU.

Further information about the CMU detector can be found in Ref. [2].

10.2 Central Muon Upgrade

The Central Muon Upgrade (CMP) consists of a second set of muon chambers behind an additional 60 cm of steel in the region $55^\circ \leq \theta \leq 90^\circ$. The chambers are of fixed length in z and form a box around the central detector. The pseudo-rapidity coverage thus varies with azimuth as shown in Figure 10.1. The return yoke of the CDF solenoid provides the necessary steel above and below the central detector. Steel has been added on the two sides in the form of two non-magnetized retractable walls. Table 10.1 lists some design parameters of the CMP.

The central upgrade chambers are rectangular, single-wire drift tubes configured in four layers with alternate half-cell staggering. For easy field shaping, the drift cell design cross-section has a 3:1 aspect ratio (2.5 cm $\times$ 15 cm). The chambers are run in proportional mode with a maximum drift time of approximately 1.4 μs.

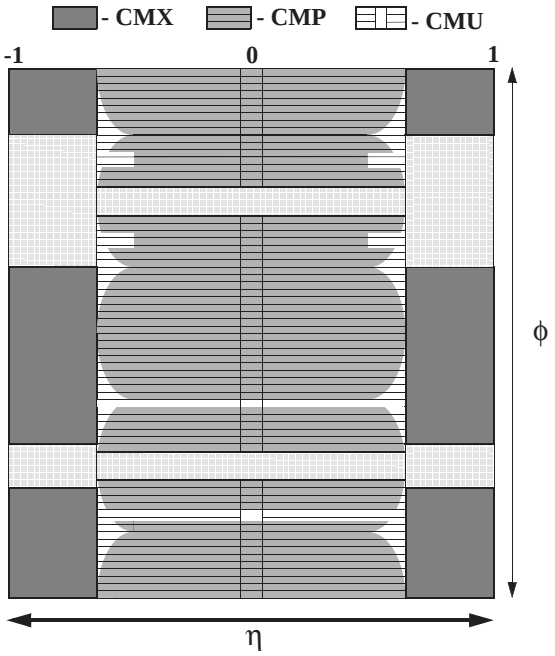

Figure 10.1: Location of the Run I muon upgrade components in azimuth ϕ and pseudorapidity η. The gray cross-hatched region indicates the currently uninstrumented regions of CMP and CMX.

The tubes are made of aluminum extrusions with 0.26 cm walls, having a single wire in the center and field shaping cathode strips on the top and bottom. They are typically 640 cm long, with some shorter sections on the bottom of the detector to avoid obstructions. The extrusions are glued into four-tube stacks with a half-cell staggering of the second and fourth layers relative to the first and third. Preamplifiers are mounted on one end of the stacks. Signals are read out by a single TDC per wire, and trigger hits are formed from coincidences of nearby wires that are used in association with trigger information from the CMU chambers.

A layer of scintillation counters (the CSP) is installed on outside surface [1] of the wall drift chambers. The counters are rectangular in shape: 2.5 cm x 15 cm x 320 cm. Each counter covers two upgrade chambers in width and half the chamber length. The total number of scintillation counters is 216. The counters are read out by single phototubes which are located at the center of the array. The east and west

[1] with respect to the interaction point

	CMU	CMP/CSP	CMX/CSX	IMU
Pseudo-rapidity coverage	$\|\eta\| \leq\sim 0.6$	$\|\eta\| \leq\sim 0.6$	$\sim 0.6 \leq \|\eta\| \leq\sim 1.0$	$\sim 1.0 \leq \|\eta\| \leq\sim 1.5$
Drift tube cross-section	2.68 x 6.35 cm	2.5 x 15 cm	2.5 x 15 cm	2.5 x 8.4 cm
Drift tube length	226 cm	640 cm	180 cm	363 cm
Max drift time	800 ns	1.4 μs	1.4 μs	800 ns
Total drift tubes (present)	2304	864	1536	none
Total drift tubes (Run II)	2304	1076	2208	1728
Scintillation counter thickness		2.5 cm	1.5 cm	2.5 cm
Scintillation counter width		30 cm	30-40 cm	17 cm
Scintillation counter length		320 cm	180 cm	180 cm
Total counters (present)		128	256	none
Total counters (Run II)		269	324	864
Pion interaction lengths	5.5	7.8	6.2	6.2-20
Minimum detectable muon p_T	1.4 GeV/c	2.2 GeV/c	1.4 GeV/c	1.4-2.0 GeV/c
Multiple scattering resolution	12 cm/p (GeV/p)	15 cm/p	13 cm/p	13-25 cm/p

Table 10.1: Design Parameters of the CDF II Muon Detectors. Pion interaction lengths and multiple scattering are computed at a reference angle of $\theta = 90°$ in CMU and CMP/CSP, at an angle of $\theta = 55°$ in CMX/CSX, and show the range of values for the IMU.

counters are offset in x to allow the inter-leaving of phototubes at the middle, minimizing the space occupied by the light-guide/PMT assembly.

Further information about the CMP detector can be found in Ref. [5].

10.3 Central Muon Extension

The central extension consists of conical sections of drift tubes (CMX) and scintillation counters (CSX) located at each end of the central detector and extending in polar angle from 42° to 55°. At 55° the CMX/CSX system slightly overlaps the coverage provided by the central muon system and extends its pseudorapidity coverage from 0.65 to 1.0. No additional steel was added for this detector; however, as seen in Figure 10.2, the large angle through the hadron calorimeter, magnet yoke, and steel of the detector end support structure yields considerably more absorber material on average than in the original central muon system. Table 10.1 lists some design parameters of the CMX and CSX detectors.

The azimuthal coverage of CMX/CSX has a 30° gap at the top of the detector for the Tevatron Main Ring and the solenoid refrigerator. There is also a 90° azimuthal gap at the bottom of the detector where the conical sections are interrupted by the floor of the collision hall. However, there is a narrow vertical gap between this section of floor and the bottom of the magnet yoke (see Fig. 10.6), and we plan to install a fan-shaped 90° CMX/CSX section in this gap completing the coverage at the bottom.

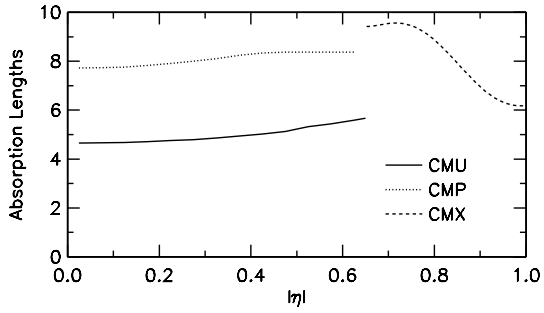

Figure 10.2: Number of absorption lengths as a function of pseudorapidity averaged over azimuthal acceptance of the CMU, CMP and CMX systems.

The CMX drift tubes are arrayed as a logical extension of the central system. There are four logical layers of twelve tubes for each 15° ϕ sector, and successive layers are half-cell offset to eliminate ambiguities. Each logical layer consists of two physical layers of drift tubes which partially overlap each other. The

overlap is greater at the inner edge of the detector as a result of forming a conical surface with rectangular cells. This overlap not only provides redundancy - the average muon intersects six cells - but the resulting stereo angle of 3.6 mrad between adjacent cells permits the measurement of the polar angle of the track.

The drift tubes for the CMX conical sections differ from those of the CMP only in length. They are 180 cm long. The total number of tubes installed in the conical sections of the central extension is 1536. The lower fan-shaped section will require 576 somewhat longer tubes when it is installed.

A layer of four CSX scintillation counters is installed on both the inside and the outside surfaces of each 15° CMX sector. The counters are trapezoidal in shape with the same length (180 cm) as the drift tubes and with a width of 30 cm at the smaller end and 40 cm at the larger end. The counters on the inside and outside layers are half-cell staggered with respect to each other thereby doubling the effective granularity of the system. The total number of scintillation counters in the conical sections is 256.

The counters are read out by single phototubes which are located on opposite ends for the inside and outside layers. The mean time of the signals from a particle traversing both layers is independent of the location of the track along the length of the counters, and the distribution of hit arrival time for real tracks is smeared only by the track path length difference due to the distribution of interaction z vertex. The mean time is calculated in the trigger, and the excellent timing resolution of the counters is used to reject large CMX backgrounds from out-of-time interactions in the beam pipe and the face of the forward calorimeter.

Further information about the CMX and CSX detectors can be found in Ref. [5].

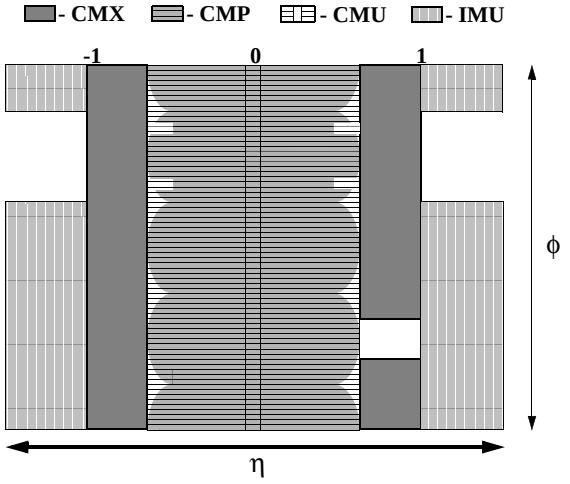

Figure 10.3: Location of the central muon upgrade components in azimuth ϕ and pseudorapidity η for Run II.

10.4 Muon Detector Upgrades for Run II

For Run II, we plan to complete the coverage of the original muon upgrade projects as described in the 1990 CDF upgrade conceptual design[3] and to make other improvements as necessary to handle the shorter bunch-crossing time. We will add chambers to the Central Muon Upgrade and Central Muon Extension detectors to fill existing gaps. The final coverage, shown in Fig. 10.4 (compare to Fig. 10.1) and listed in Table 10.4, will improve the acceptance of the CMP and CMX systems by 17% and 45% respectively. We will also add scintillation counters near the Central Muon Upgrade chambers to identify the beam crossing that produced the muon. These additions are described in Sections 10.4.1 and 10.4.2.

The gas gain of the Central Muon Detector will be reduced in Run II. This will require us to upgrade the the detector front-end electronics to handle the smaller signal. This is described in Sec. 10.5.1. The CMP/CSP and CMX/CSX front ends will not change, but we do plan to change the pre-amplifier motherboard system for the Central Muon Upgrade detector to improve operational efficiency and data quality (Sec. 10.5.2). This involves a change in the high voltage distribution and grounding scheme, not the pre-amplifier. Finally, a new TDC is necessary to accommodate the pipelined DAQ structure and to implement the trigger buffering scheme; this is described in Secs. 11.3-11.4.

10.4.1 Completion of the Central Muon Upgrade and Upgrade Scintillator

Completion of the Central Muon Upgrade (CMP) requires the following additional chambers and corresponding scintillator:

- Chambers to instrument the gap between the chambers on top of the north wall and those on

	CMU	CMP	CMX	CMUP	CM$\overline{U}$P	CMU$\overline{P}$	all
Run I	0.396	0.363	0.196	0.278	0.084	0.118	0.676
Run II	0.396	0.425	0.283	0.328	0.097	0.068	0.776
ratio	1.000	1.172	1.449	1.180	1.142	0.575	1.148

Table 10.2: Comparison of central muon detector acceptances in Runs I and II. Acceptance is computed for a 30 GeV/c muon with a uniform distribution in azimuth and pseudorapidity, $|\eta|$ <1.2, and no z vertex smearing. The changes due to a Gaussian z vertex distribution with σ = 30 cm are negligible (< 0.001) The CMUP region is the overlap between the CMU and CMP detectors; CM$\overline{U}$P is the region covered by CMP but not CMU, and CMU$\overline{P}$ is the region covered by CMU but not CMP.

the north yoke

- Chambers to instrument the gap between the return yokes on the top
- Additional chambers to extend the coverage at the south end of the south yoke to cover the gap between the south yoke and the chambers on the top of the south wall
- Chambers to instrument the gap between the return yokes on the bottom

These additions will increase the CMP coverage by approximately 17%.

Additional steel is required in front of these chambers. The steel will be extended on the north side of the top north yoke and the south side of the top south yoke. Steel will be installed between the return yokes on the top and the bottom. (See Fig. 10.4). For this baseline design the number of additional chamber stacks required is 36 total.

There are mechanical complications with this design. On the north end, at the natural location for the chambers (i.e. the level of the yoke) there is an interference with the pivot for the large overhead cable tray. Furthermore, placing steel in the yoke gap precludes access to instrumentation for the central calorimeter in the two (notch) wedges. This problem already exists at the bottom, and is ameliorated by locating the readout electronics outside the notch, but occasional access to the PMTs on the wedges is still essential. On the bottom, necessary access is accomplished by pulling an arch, but this will not work at the top because the solenoid blocks lift access to the photomultiplier tubes.

We are now considering a different construction which would suspend the steel and chambers for this region from the ceiling, The primary issue with this

1 – Baseline design	
Distance from beam-line	186 in.
Width of steel absorber	75.3 in
Volume of steel absorber	263 ft^3
Equivalent length of MR shielding	241 in
Load replacement factor	N/A
2 – Installation above cable tray	
Distance from beam-line	228 in.
Width of steel absorber	92.4 in.
Volume of steel absorber	323 ft^3
Equivalent length of MR shielding	295 in.
Load replacement factor	1.2
3 – Installation at ceiling height	
Distance from beam-line	254 in.
Width of steel absorber	102.9 in.
Volume of steel absorber	360 ft^3
Equivalent length of MR shielding	329 in.
Load replacement factor	1.3

Table 10.3: Comparison of the absorber parameters for 3 different positions of the top CMP fill-in.

plan is the load on the collision hall ceiling. Engineering studies are in progress. Until the full calculation is available, we argue that the load on the ceiling will be acceptable, because we would be trading the weight of main ring shield for a much shorter length of muon steel.

The steel shielding for the main ring currently runs the length of the hall and is suspended directly from the ceiling at a position slightly off of the detector centerline. (See Fig. 10.4). The load of a two foot thick slab of steel is approximately the same as the equivalent length of shielding. Thus we would be trading the load of the main ring shield for the load

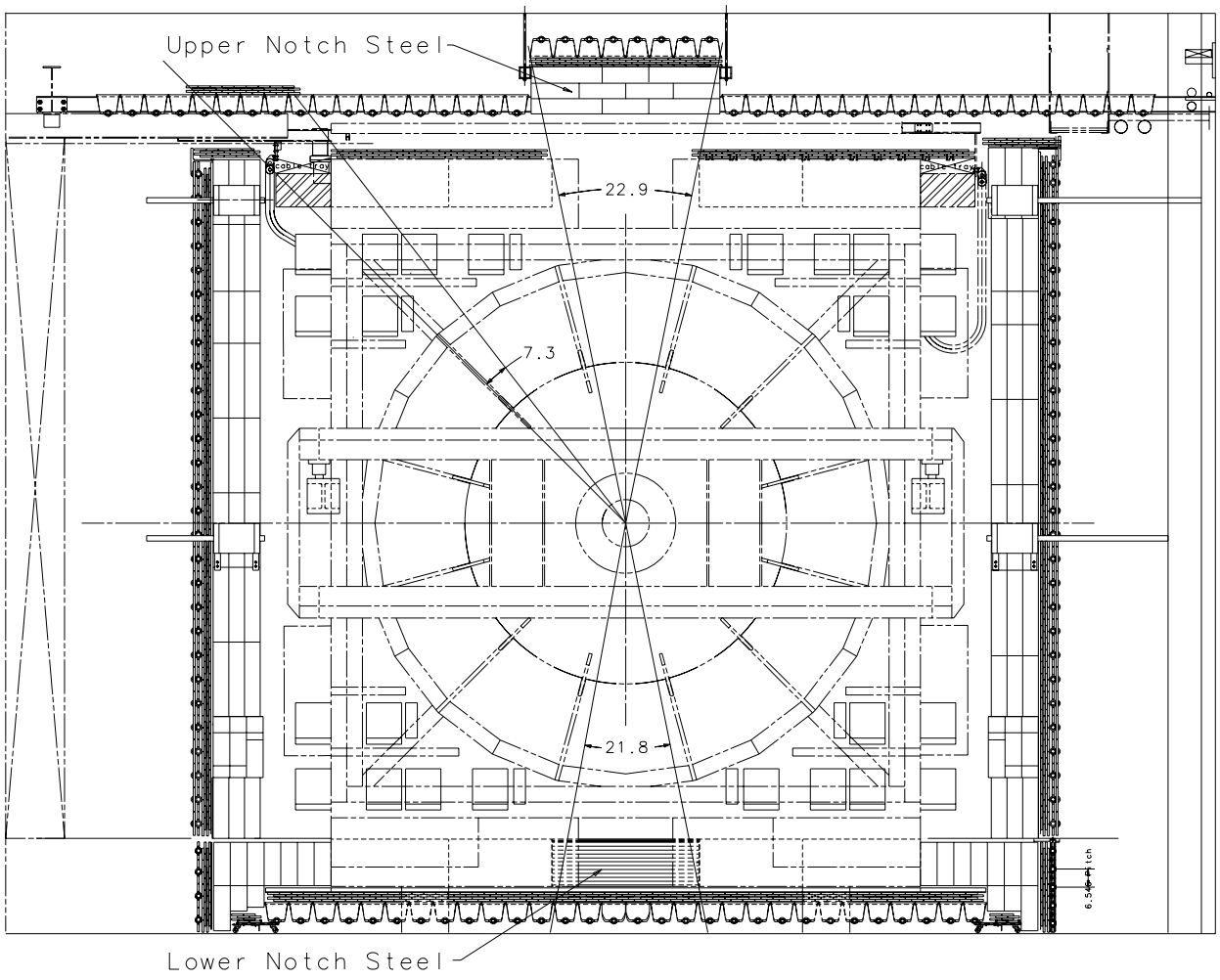

Figure 10.4: Configuration of the Central Muon Upgrade detector (CMP), Upgrade Scintillator (CSP) and steel absorber in Run II. On the walls the circles are the ends of PMTs. On the top and bottom the trapezoids are the lightguides viewed end-on.

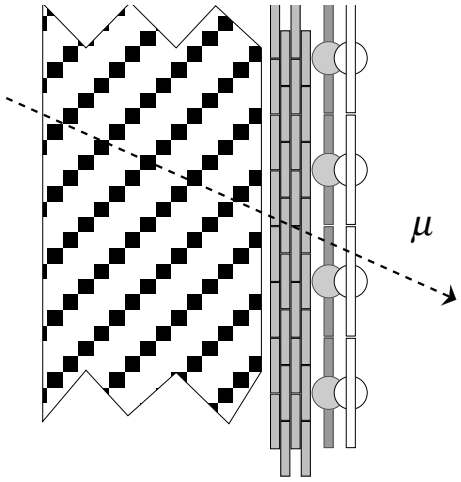

Figure 10.5: Detail showing the configuration of steel, chambers and counters for the Central Muon Upgrade walls. A muon track is drawn to establish the interaction point. Counter readout is located at z=0. Counters layers are offset from the chambers and from each other in x to allow overlapping light guides and PMTs, minimizing the space required.

of the steel absorber, but over a much shorter length, and moving the loading point slightly to the center of the detector, reducing the overall load on the ceiling.

Table 10.3 gives a summary of the relevant parameters for three CMP mounting alternatives at the top of the detector. For installation at ceiling height, we would increased the current load by a factor of 1.3 for a length of 21 feet over the central detector, but everywhere else, the load is gone. The impact on the detectors is shown in Table 10.4. The number of additional stacks is 4-5 and the decrease in acceptance due to the increased radius is very small.

As with the additions on the top, placing steel in the bottom yoke gap precludes access to the PMTs for the central calorimeter in bottom notch wedges. In addition, the procedure for closing the central arches uses an "observer" in this notch to guide the closing. We nevertheless propose to finish CMP in this region as proposed in the baseline plan. We will permanently install steel in the notch and chambers beneath. The chambers in the notch will be installed in the same manner as on the north and south return yokes. On the bottom, we solve the difficulties noted above as follows:

- We will eliminate the need for an observer in the notch by upgrading the guide and control system for moving the arches.
- Access to the PMTs for the lower notch wedges will be provided from above rather than below. For access to the PMTs (a rare occasion) an arch will be pulled; personnel will go through the hole exposed at the center of the arch and drop down to the PMT from above.

Because adding carbon steel in either of the regions between yoke gaps has the potential to change the return flux, and because any change in the return flux will change the forces on the plug and could conceivably change the magnetic field in the central tracker, we choose to use stainless steel for these regions. We believe that the field changes with carbon steel would probably be small, but our knowledge of the magnetic field has been hard won and the cost of regenerating it with a different magnetic configuration would be much larger than the cost of using non-magnetic (stainless) steel in the bottom notch.

On the top, since the additions are above the return yoke, carbon steel is acceptable. We currently have the analog of the top yoke extensions at the bottom. This steel is magnetic and is separated from the central detector by a thin layer of G10 for electrical isolation. We propose to construct the top yoke extensions in the same way.

Completing the Upgrade scintillator is substantially less difficult. These counters are necessary to identify the beam crossing of the muon track. As shown in Figures 10.4 and 10.5, scintillator was installed on the two steel walls before Run Ib. The top and bottom regions must still be instrumented. The counters will be installed as close to the chambers as possible to minimize the difficulties in matching. Note that there are design problems with the counters that are not faced with the chambers. For full efficiency the counters must be as long as the chambers, but the counter light guide extends beyond the end of the counter.

10.4.2 Completion of the Central Muon Extension and Extension Scintillator

Completion of the Central Muon Extension (CMX) and Scintillator (CSX) requires:

	Increase in CMP coverage	Fraction of CMU with CMP coverage	number of stacks needed	Volume of steel (ft^3)
1	1.186	0.830	12	263
2	1.171	0.839	16	323
3	1.164	0.824	17	360

Table 10.4: Comparison of the 3 alternatives for filling the top yoke gap. The first column is the ratio of the Run II CMP coverage to the Ib coverage. The second column is the fraction of CMU covered by CMP. For Run Ib this is 0.703. The third and fourth column give the number of stacks (4-chamber unit) needed to instrument the gap and the volume of steel needed to provide 2 feet of absorber respectively.

- Chambers to instrument the top 30 degrees (2 wedges) in phi on the west side of the detector
- Chambers to instrument the bottom 90 degrees (6 wedges) of phi

These bottom detectors, commonly called the "mini-skirt", are shown in Fig. 10.7. The chambers penetrate the nominal floor of the collision hall and require a different geometrical configuration than that of the upper 270 degrees. (See Fig. 10.6.) The conical geometry will not work.

The design of the mechanical support structure for the upper two wedges was completed before the beginning of Run Ia in 1992. The parts were also fabricated. The wedges were not installed due to mechanical interference between the upper surface of the mechanical support structure and the main ring shielding. Installation of the detectors in Run II requires the removal of one wedge on the north-west CMX stand and its subsequent reinstallation. The height of the stands requires that this take place in the collision hall.

The top wedges on the east side interfere with the cryogenics system for the CDF solenoid. Installation of additional detectors here would require a different configuration for the cryogenics or for the chambers. We do not plan to instrument this region for Run II.

The design, parts, and fabrication for the mini-skirt are complete at the time of this report. The chamber cross section is identical to that of the already installed chambers. The counters cover a smaller part of azimuth (6 per 15° wedge, as opposed to 4 in the rest of the detector). The geometrical arrangement of the detector is also slightly different. Instead of lying on a truncated cone, the chambers form a flat pin-wheel structure with the wire lying along the spokes of the pin-wheel. There is only one layer of counters on the inner surface; the counters have a PMT on each end to allow the computation of a mean-time. The chamber wire and counter mid-planes are at a constant phi as in the rest of the detector.

The chambers and counters at the middle of the detector are shorter than the nominal length due to interferences with the detector sub-floor. This slightly reduces the coverage of the detector. The chambers and counters are glued into "wedgelets" consisting of 8 layers of chambers and 1 layer of counter. The wedgelets slide into place on a frame that rests partly on the nominal collision hall floor and partly on the sub-floor (Fig. 10.7 and 10.6).

10.5 Front-End Electronics

The front-end electronics for the Central Muon Detector will be upgraded for Run II. To survive the higher luminosity and event rates, the CMU gain will be reduced and the chambers will operate in proportional rather than limited-streamer mode. New pre-amplifiers and ASDs are being developed to match the dynamic range of the CMU chamber. Additionally, the wire ganging scheme will be changed to provide finer granularity in the position information at the trigger level, allowing tighter matching between muon "stubs" [2] and central tracks, which will improve purity. The ganging is performed on the CMU end electronics. When the front-end upgrades for

[2] We will call the short tracks reconstructed in the muon chambers "stubs' to distinguish them from tracks reconstructed in the central tracker.

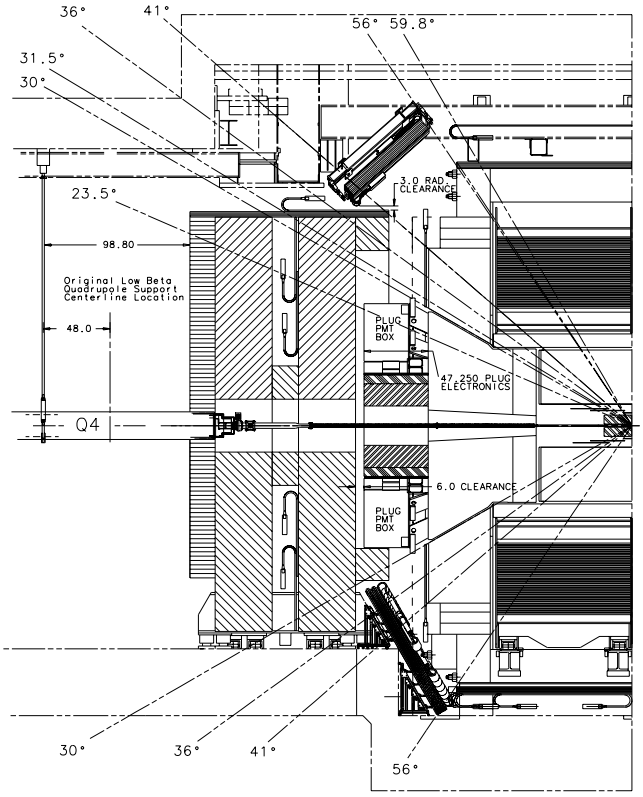

Figure 10.6: Side view showing the placement of chambers to complete the CMX coverage. Note the lower CMX detectors are supported on the floor and sub-floor. The IMU barrel chambers and scintillation counters, the toroid counters and the endwall counters are also shown.

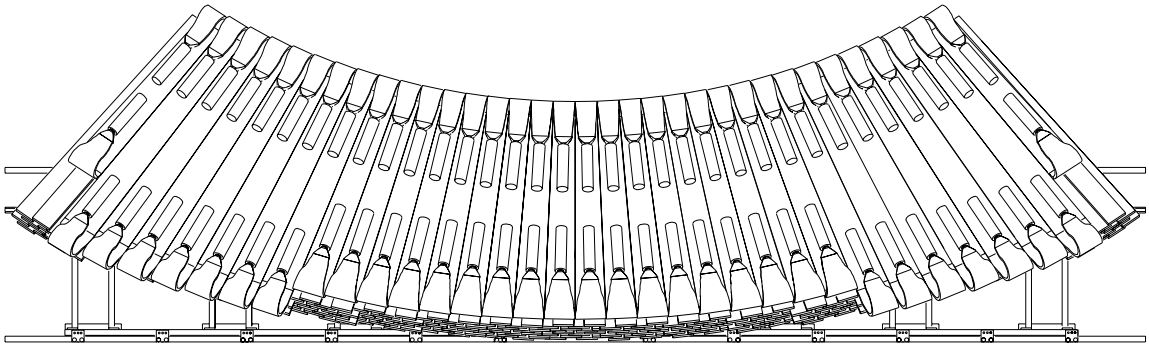

Figure 10.7: Lower chambers for the Central Muon Extension and Scintillators.

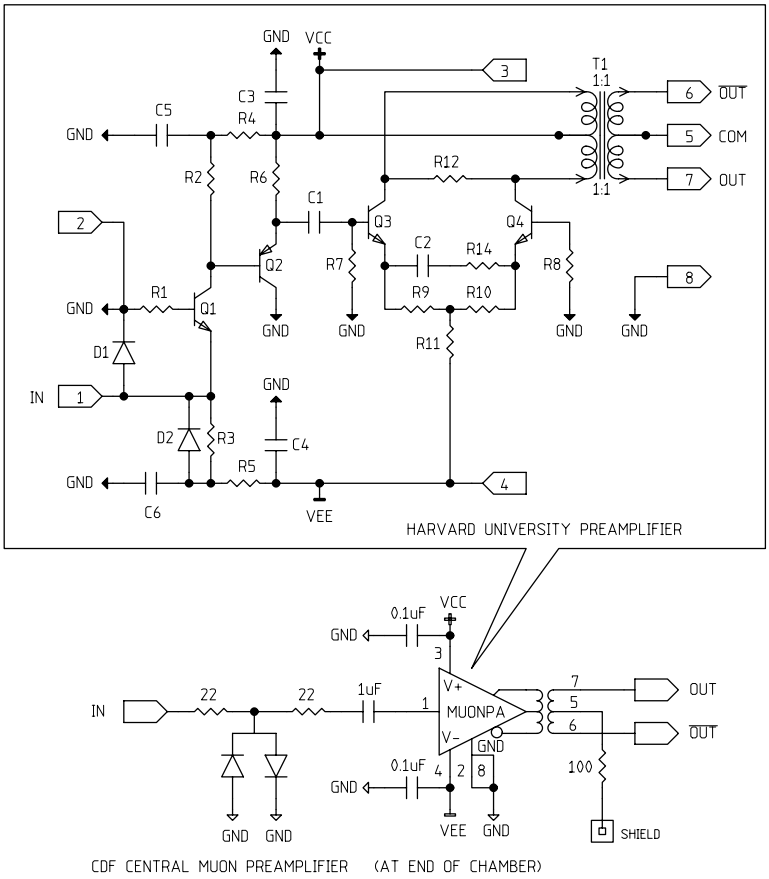

Figure 10.8: Hybrid pre-amp circuit for the Run II Central Muon detector readout

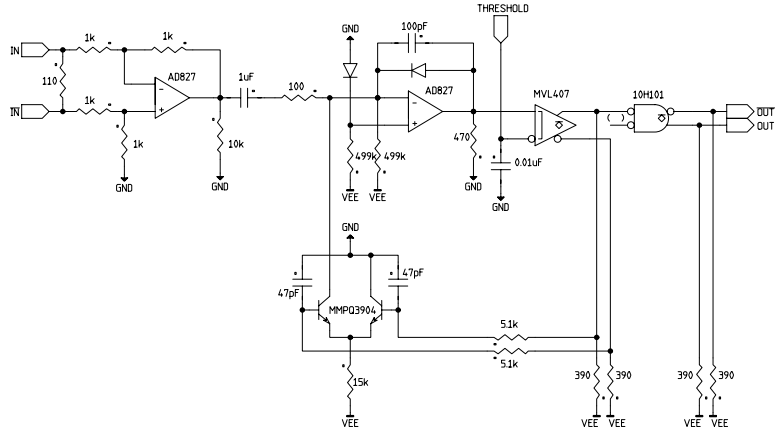

Figure 10.9: ASD/ToT circuit for the Run II Central Muon detector readout

Run II are complete, the readout for the three muon drift-tubes systems will be identical in concept and nearly the same in implementation. The two counter readout systems will similarly be identical conceptually and very similar in implementation.

The detector readout for CMP and CMX consists of a chamber-mounted pre-amplifier, an **a**mplifier-**s**haper-**d**iscriminator card in the collision hall converting the analog signal to a logic-level signal. The signal is digitized by TDC cards in the counting room. The chamber, pre-amplifier, and ASD for the CMP and CMX are identical with the exception of chamber length. The only change planned in the read-out is to change the pre-amplifier mother-board system (not the pre-amplifier) for the Central Muon Upgrade detector.

The read-out of the counters consists of a photomultiplier feeding a discriminator in the counting room. The discriminated hit signals for the CSP go directly to a TDC. The discriminated hit signals for the overlapping extension scintillator counters are input to a board for computing the mean time of the coincidence signal. This signal is then sent to a TDC.

Chambers and counters use the same TDC unit. In order to accommodate the pipelined DAQ structure and trigger buffering scheme, a new TDC is being developed to replace the current LeCroy 1879 module. The TDC is described in Secs. 11.3-11.4.

10.5.1 Changes in the Central Muon Upgrade Front-End Electronics

The Central Muon System (CMU) has proven to be a reliable and efficient detection device throughout Run I. In Run I the CMU drift chambers were operated in the limited streamer mode. In past runs we have experienced some minor difficulty in keeping the chambers running due to glow mode current runaway induced by high particle fluxes. Additionally, the chambers are aging. For these reasons we have decided to reduce the gain of the system and operate in the proportional regime, for the high luminosity running of Run II. In order to implement this we need to recoup the gain by installing pre-amplifiers on the chambers. The outputs of the pre-amps will drive amplifier-shaper-discriminator(ASD) cards, followed by TDC's.

The transverse coordinate is measured using the usual distance-to-drift-time relation; there is no change from the Run I scheme, and the resolution is unchanged. The z-coordinate is measured using charge division as before, but in the new scheme the charge is determined by time-over-threshold (TOT) instead of charge-to-voltage conversion. The z-resolution is degraded with respect to Run I due to the significantly lower chamber gain. Cosmic ray test stand measurements show a resolution of 10 cm, which is adequate to pin down the muon to one trigger tower, and is comparable to our most stringent physics analysis cuts applied to high p_T muons. For $J/\psi \to \mu^+\mu^-$ decays, the multiple scattering for the muon is typically around 8 cm, so the worsened z resolution will have a slight impact: the background level may rise by a few percent.

10.5.1.1 Pre-amplifier

The pre-amplifiers reside on mother boards attached to the end of the CMU chambers. The mother board is a redesign of the original CMU end board with provisions for pre-amp power and additional calibration pulse inputs.The pre-amp has a low-impedance grounded-base input followed by amplification and an output stage providing differential signals to a 100Ω impedance transmission line. The differential output reduces common mode noise, an advantage in the relatively noisy CDF environment. A schematic diagram of the pre-amplifier is shown in Fig. 10.8.

10.5.1.2 ASD/TOT

The amplifier-shaper-discriminator and time-over-threshold circuit (ASD/TOT) accepts signals from the CMU pre-amplifiers via a 5 meter 100Ω flat ribbon cable. The ASD cards reside in a VME crate at the back of each 15 degree wedge. The signals are differentially received and amplified. The current is integrated on a capacitor and then discharged with a constant current source. The output of the following discriminator is then linearly related to the total charge. The transverse coordinate of the muon track is given by the leading edge of the discriminator whereas the z-coordinate is related to the ratio of the TOT's of adjacent channels.The outputs of the discriminators are sent via differential ECL signals to TDCs residing in the first floor counting room. A schematic diagram of the ASD/TOT circuit is shown in Fig. 10.9.

10.5.1.3 Bunch Crossing Ambiguity

Since the maximum drift time of the CMU chambers is on the order of 700 ns and the bunch crossing separation is 132 ns, one does not know which of six bunches the muon belongs to. In order to resolve this ambiguity a muon track will be associated with six bunches and, as such, can contribute to a Level 1 trigger with any of these. The correct bunch within the six must be determined by associating the muon stub with an XFT track and appropriate calorimeter hit: TDC's on the Central Hadron Calorimeter are capable of resolving a single bunch crossing. Additionally, triggers requiring CMP confirmation (e.g. high p_T muons from W decay) will have their crossing identified by the CSP scintillators.

10.5.2 Changes in the Central Muon Upgrade Front-End Electronics

We have had intermittent problems with oscillations since the chambers were installed. It is now clear that these problems were due to design flaws in the preamplifier circuit boards. We reduced the severity of the problem in Run Ib by installing relays in the pre-amplifier power distribution so that we can shut off individual channels from the counting room. This allows us to stop the oscillations without making an access, and has reduced the amount of bad data due to CMP oscillations from about 4% in Run Ia to well under 1% in Run Ib. Nevertheless, lost data is lost data: 1% of the Run II goal of 2fb^{-1} is equivalent to the entire Run Ia dataset.

For Run II, we wish to solve this problem at its root. We have completed a new design for these pre-amplifier boards. Ten prototype boards were installed and tested at the end of Run Ib. They performed well during the limited data-taking. No oscillations were found during the 4 month running period. We plan to replace all the pre-amplifier boards with ones using the improved design for Run II.

10.6 Intermediate Muon Detection

10.6.1 Overview

The importance of lepton identification does not stop at $\eta = 1$, and to that end CDF has designed a system that builds on the successes of CDF's central muon identification and on a major strength of CDF II, charged particle tracking at mid-rapidity. The IMU is designed to trigger on muons with $|\eta| \leq 1.5$ and to identify off-line muons with $|\eta| \leq 2.0$. The heart of the detector is a barrel of CMP-like chambers and CSP-like scintillation counters mounted on the outer radius of the FMU toroids. Additionally, there are pinwheels of counters on the endwall and between the toroids for triggering. A muon is identified by a stub in the chambers, with a time-stamp provided by the barrel counters in coincidence with the pinwheel counter projective with the vertex. Note that in all cases, there is a substantial volume of steel between the barrel and pinwheel counters.

Unfortunately, we cannot extrapolate Run II IMU performance from Run I IMU performance, but we can compare the IMU to the existing detectors. The IMU is behind 6.2-20 interaction lengths of steel, on average more shielding than CMP. Figure 10.10 shows the amount of absorber between the detector and interaction vertex as a function of η. The IMU has smaller chambers, which reduces the mean occupancy for two reasons. First is the geometric factor - each counter covers less solid angle. Second is that the maximum drift time is shorter, so the number of effective interactions the IMU sees is smaller than the number the CMU sees. Additionally, having a set of scintillation counters projective with the IMU barrel provide additional redundancy. Monte Carlo studies are underway. Preliminary results indicate that occupancies even at 2×10^{32} are well below acceptable limits.

10.6.2 Toroid Modifications

Three modifications to the existing toroidal magnets will be made. First, the toroids will be pushed from their present position 5.5 m closer to the interaction. This will involve construction of a toroid movement system similar to that for the present CMP. This increases the solid angle subtended by the IMU. Next, a ring of steel $\sim$ 60 cm square in cross-section will be welded onto the inner face of the toroids. This ring will provide shielding for the IMU barrel chambers, and will additionally shield the CMX from tertiary particles. Monte Carlo studies indicate that this modification reduces the trigger rate by a factor of 6. Finally, the toroids will not be energized. Momentum will be measured using the solenoidal magnetic field. The silicon (SVX and ISL) gives superior momentum resolution if either of the following conditions is true:

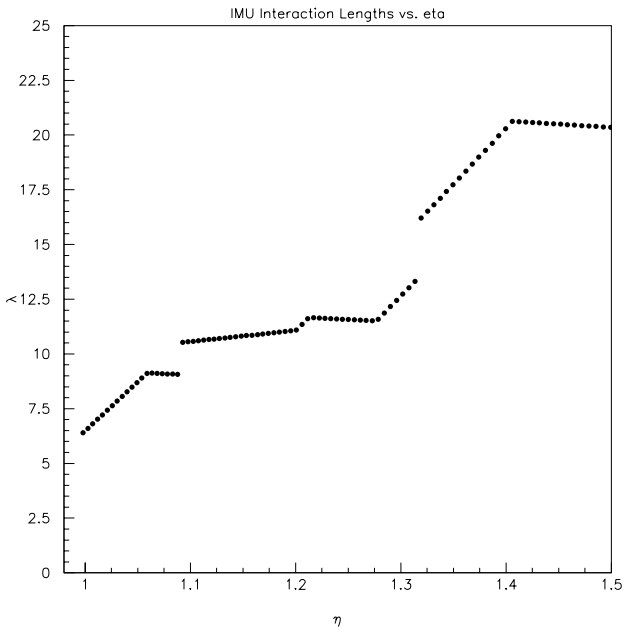

Figure 10.10: The amount of steel absorber (measured in interaction lengths) between the IMU Barrel and the interaction point, as a function of pseudo-rapidity.

$p_T(\mu) \leq 50$ GeV or $|\eta(\mu)| \leq 1.5$.

10.6.3 IMU Barrel Chambers and Counters

Surrounding the toroids in a barrel geometry will be 1728 chambers, 864 on the east side of the detector, and 864 on the west. The chambers are 11.9' long, 1" deep, and 3.3" wide, with each chamber covering 1.25° of azimuth. The chambers are assembled in stacks 4 deep (in radius), with the second and fourth layers staggered relative to the first and third to resolve hit assignment ambiguities. Apart from size, these chambers are identical to the CMP chambers described above, single wires through aluminum extrusions, with cathode strips for field shaping. The preamplifier will be similar to the that used in the CMP, and the system will use the same ASD's and TDC's as the CMP and CMX. The intent is to minimize the development and engineering necessary for this system and to take advantage of the excellent performance of the existing CMP detector and readout chain.

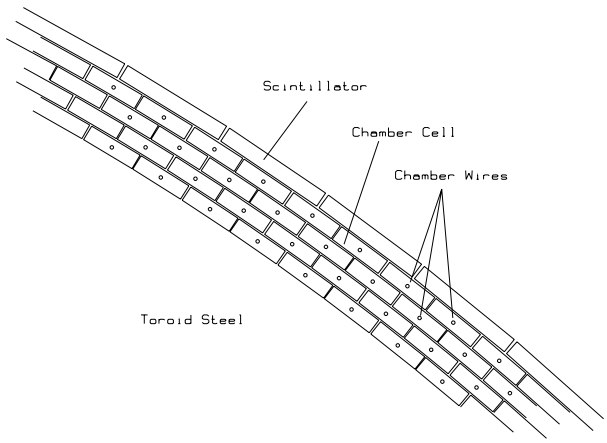

Figure 10.11: A detailed section of the IMU Barrel, showing several chamber cells and corresponding scintillator.

These chambers cover the top 270 degrees of the toroids; the floor interferes with installation of the bottom quarter. The 3.8 m of steel in the toroids provides substantial shielding from spray off the beamline.

The 3.3" width of these chambers implies a maximum drift time of about 1 microsecond, longer than the beam crossing times of 396 ns or 132 ns. To identify which beam crossing produced the muon, an array of rectangular scintillator counters is installed just outside of the barrel IMU detector. As with the CSP, each counter covers two chambers in ϕ and half a chamber in η: one set of counters covers between η=1.0 and 1.25 and the other set of counters covers between η=1.25 and 1.5. Note that this design provides some η information at the trigger level. There are 432 counters on the barrel (216 on each side), read out by phototubes mounted at the outside ends. Readout will be identical to the CSP.

Figures 10.11, 10.6 and 10.12 show the IMU Barrel in various views.

10.6.4 IMU Toroid Counters

In the CMX/CSX, there are two scintillation counters per chamber stack, one on the inner and one on the outer radius of the stack. The IMU also has two layers of scintillator everywhere, but rather than mounting the second set within inches of the first, the second set in the IMU is separated by substantial

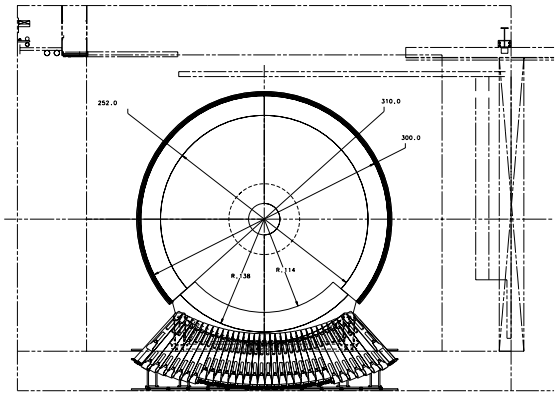

Figure 10.12: Elevation view of the IMU Barrel, viewed along the beam axis. The IMU chambers and scintillators are represented by the outer circle around the toroids. Toroid coils (not shown) may interfere with IMU installation at $\pm 45^\circ$ and $\pm 135^\circ$. The CMX lower 90° section is also shown.

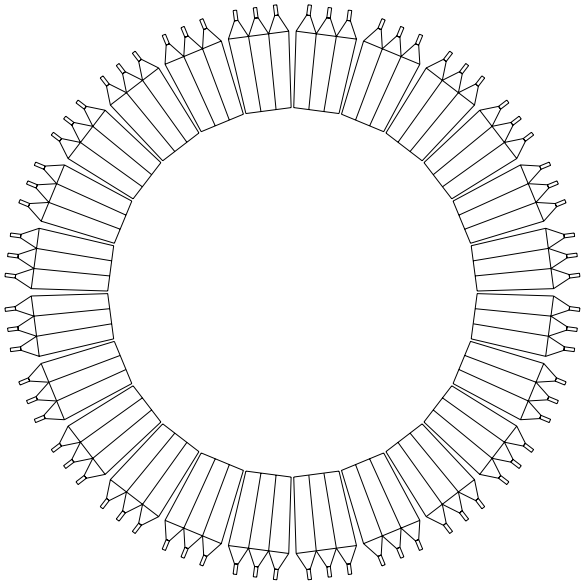

Figure 10.13: The geometry of the endwall muon counters. The small gaps every 15° correspond to the wedge boundaries on the endwall. The toroid counters are similar, except that the gaps are absent.

distance and steel from the first set. This adds the requirement that the coincidence between two counters have a projective geometry, and that any single particle that causes the coincidence be able to penetrate a large volume of steel; background triggers caused by soft tertiary hadrons, a problem early on in the CMX, are strongly suppressed in this design.

One pinwheel of 144 counters is mounted between the inner and outer toroids, with a granularity of 5° in ϕ and covering $\eta = 1.3 - 1.5$. A second set is mounted at lower radius, covering $\eta = 1.5 - 2.0$, also with 5° ϕ segmentation. The inner set is used for identifying high p_T isolated tracks as muons. Presently, CDF considers isolated high p_T tracks with minimum ionizing energy deposition in the calorimeter as possible muon candidates. The purity of this sample can be substantially improved by requiring that the candidate penetrate an additional meter of steel and be detected by the $\eta = 1.5 - 2.0$ counters. The 288 toroid counters use the phototubes and bases of the existing FMU scintillator counters, although the aging original scintillator (now over a decade old) will be replaced with new plastic.

10.6.5 IMU Endwall Counters

The toroid counters cannot cover $\eta \leq 1.3$, so we will install another pinwheel of 144 counters on the endwall calorimeter. These counters are 5° wide and cover $\eta = 1.0 - 1.3$. Space on the endwall is tight, but there is room for 1" thick scintillator. Additional space for the photomultiplier tubes is available just outside the endwall calorimeter (in radius). Test counters were installed on the endwall and operated during the last four months of Run I. Data from these counters indicates that the singles rates are not too high in this region of the detector, even for counters in close proximity to the endwall ^{137}Cs source.

10.6.6 Triggering on $\eta \geq 1$ Muons

The ϕ granularity of the IMU is designed to match the granularity of the trigger. The XFT reports tracks in 1.25° bins, so the chambers cover 1.25° in phi. The barrel scintillation counters each cover two XFT ϕ bins, (2.5°) and the endwall and toroid planar counters each cover 4. (5°) There are four elements in coincidence that are necessary to form a trigger:

- A "stub" of at least 3 hits in the IMU chambers. The slope $d\phi/dr$ can be measured by the drift time differences between the hits in a manner sim-

ilar to the present CMU. While in the CMU, the slope is a function of the p_T of the muons, in the IMU, muons have traversed a significant fraction of the magnet's return field so all muons from the interaction point are close to radial. Background stubs from the typical sources (spray from the beampipe, albedo, etc.) are not necessarily radial, so the stub slope extracted from timing information allows us to reject background.

- A scintillator hit in the barrel scintillator. This identifies which interaction produced the muons.
- A scintillator hit in the appropriate pinwheel counter. This rejects against accidental coincidences between real particles at the IMU barrel, and real high p_T tracks that were unassociated with the particles detected in the IMU.
- A track found in the appropriate ϕ bin in the XFT. At the present time, the XFT reports tracks with $|\eta| \leq 1.2$, so the trigger is limited to this region. (As more forward tracks become available at the trigger level, however, the IMU's triggering capability will be likewise extended.) Unlike the other muon systems, a crude z matching requirement can be imposed between the track and the muon stub at the trigger level. Since the XFT only finds tracks with $|\eta| < 1.2$, we can require that the $\eta = 1.0 - 1.25$ barrel scintillator (as opposed to the scintillator covering $\eta = 1.25 - 1.5$) be hit. Because tracks with $\eta = 1.0 - 12$ will traverse only the innermost three axial superlayers in the COT, we can require that the outermost COT superlayer be *missed.*

10.6.7 Summary

To summarize, the IMU is a system designed for excellent identification of muons in the range $\eta = 1.0 - 2.0$, with emphasis on the low rapidity region. It has several features designed to reject background both offline and at the trigger level: a large volume of steel shielding, the ability to require a coincidence between counters separated by shielding and distance, and the ability to measure stub angles and thus to reject stubs that were not produced by muons from the interaction point. The system is extremely similar to the existing muon systems, both in mechanical and electrical design, using the best features of each of the central muon systems, and saving both cost and effort in detector development. Initially, the IMU can be used to trigger on muons with $|\eta| \leq 1.2$, with the ability to expand to 1.5 as soon as tracks at these rapidities become available at the trigger level. Although we do not propose this as part of this Report, the possibility of an upgrade involving energized toroids and additional detector elements to track muons through the toroids is not precluded by this design. Such a system could tag muons beyond $\eta = 2.0$ and trigger beyond $\eta = 1.5$.

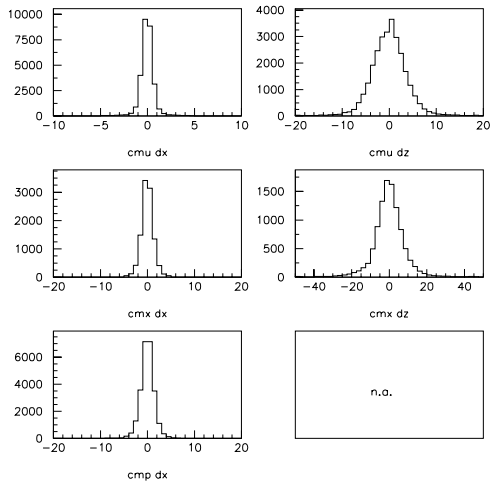

Figure 10.14: Resolution for matching between muon stubs and extrapolated tracks measured with high p_T muons from W and Z decays.

10.7 Performance: Extrapolation From Run I

The existing muon detectors have performed admirably during Run I. Figure 10.14 shows the x and z residuals for muons from W and Z decay in the CMU, CMX and CMP. Figure 10.15 shows the J/ψ mass from muons with both legs in the CMU, at least one with CMP confirmation and at least one in the CMX. In all three of these examples, the background to the J/ψ peak is quite low, and although the background is lowest when upgrade confirmation is required, it is quite possible to do excellent physics with the signal-to-noise ratio in any of these cases.

We would obviously like to maintain this performance in the Run II era, and we believe that the proposed system will do this. We briefly review here the expected effects of Run II luminosities and beam conditions on detector aging, occupancy, and offline reconstruction. We do not discuss the performance

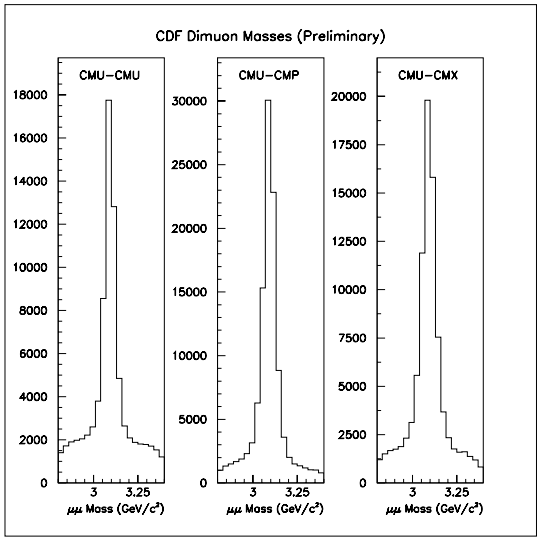

Figure 10.15: Reconstructed J/ψ mass for various detector decay topologies.

of the trigger, other than to comment that 2/3 of the CMU trigger rate comes from the 1/3 of the detector without CMP confirmation. Completing the CMP coverage will therefore provide substantial purity improvement at the trigger level. The trigger is discussed in Sec. 12.

Most ($\geq$ 95%) of the ionization detected in the CDF muon system is not from Tevatron produced particles, either from $p\overline{p}$ collisions or beam halo, but rather comes from the Main Ring. We have monitored the total ionization in the chambers, and the dominant time structure is the Main Ring cycle, with the currents highest at injection, transition, and extraction. We have compared single hit chamber occupancies from (otherwise identical) runs with the main ring on and off, and they differ by between one and two orders of magnitude.[3] Clearly the Main Ring is what these detectors see, and the Tevatron is a perturbation on top of that.

We have examined the CMP and CMX for signs of main ring induced aging by comparing chambers near the main ring (highest integrated flux) to chambers near or under the floor, (lowest integrated flux) and to chambers never exposed to the beam. We see no difference in pulse characteristics and conclude that there is no significant radiation induced aging in these

occupancy	CMU	CMP	CSP	CMX	CSX
Run I	0.01	0.9	0.2	0.5	0.02
Run II	0.007	0.04	0.01	0.2	0.01

Table 10.5: Channel occupancy (%/channel/event) in minimum bias events. These are computed from Ib data, corrected to 1 minimum bias event per crossing. The reduction in rate expected when the main ring is removed is also included. This is computed from the top-bottom asymmetry in the azimuthal hit occupancy distribution.

systems.

A similar comparison for the CMU shows a decrease in the single hit efficiency of a few percent. This is not large enough to be visible in the muon finding efficiency (where we require 3 of 4 hits) with the Run I data. Reducing the CMU gain by a factor of 30 or so will slow this aging by the same factor, and removing the main ring will slow it an additional factor of 100 or more. Even going to very high luminosities is quite safe. More than 90% of the charge that will ever be collected from the CMU has already been deposited.

In Run II, with the Main Ring gone and the beam pipe shielded (see Sec. 14.4), the environment of the central muon detectors will be much less harsh. The raw detector occupancy measured online in Run Ib minimum-bias events [6] is given in the first row of Table 10.7, and the occupancy of stubs in minimum-bias events is given in Table 10.7. We expect substantially reduced occupancy (Tables 10.7 and 10.7) in Run II. In CMU and CMP the expected reduction is estimated from measurements of the top-bottom asymmetry in the azimuthal occupancy distribution. In CMX the expected reduction factor is estimated from the ratio of in-time to out-of-time stubs. This removes both the main ring component and some fraction of the particles from interactions in the beam pipe. [4] The expected Run II occupancies are shown in the bottom lines of Tables 10.7 and 10.7, and represent significant improvements over the Run I situation.

Shielding will have an even larger effect since the timing cut does not perfectly separate signal and noise. A preliminary shielding plan for CDF II is

[3]The largest variation is between in-time occupancies and between total currents. This is not unexpected; one requires coincidence with the beam crossing, and the other does not.

[4]The timing cut implemented corresponds to that used in the trigger and is corrected for the corresponding loss in efficiency (15%).

occupancy	CMU	CMP	CMX
Run I	0.034	0.14	0.35
Run II	0.023	0.0084	0.026

Table 10.6: Mean stub occupancy (stubs/event) in minimum bias events. These are computed from Ib data, corrected to 1 minimum bias event per crossing. The potential improvement when the main ring is removed and shielding can be installed around the beam pipe is also given. The occupancy is not Poisson distributed: the fraction of events with no stubs is much larger than $e^{-<n>}$.

bunch	$\bar{N}$	CMU	CMP	CMX
132 ns	2	2.2%	0.39%	0.71%
396 ns	5	1.8%	0.33%	0.59%

Table 10.7: Probability of a stub from an underlying minimum bias event overlapping with a stub of interest in a physics event at a luminosity of $2 \times 10^{32} cm^{-2} s^{-1}$.

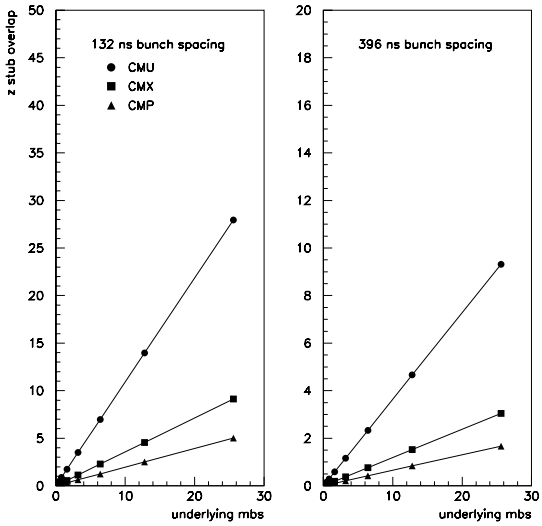

Figure 10.16: Probability of a stub from an underlying minimum bias event overlapping with a stub of interest in a physics event.

discussed in Sec. 14.4. We estimate that the installation of shielding around the beam pipe will reduce rates by a factor between 50 and 100. Additionally, the additional steel welded onto the toroids for the IMU will substantially reduce the background stubs in the CMX.

There is also a concern that offline reconstruction will be difficult because the muon chambers integrate over several crossings. However, the CMX and the CMP have scintillators that will time stamp the crossing with the muons (i.e. will identify which beam crossing is associated with the muon of interest). The CMU can be correlated with times from TDC's attached to the central hadron calorimeter readout, and the fast drift times in the tracking chambers will allow unambiguous association of a matching track with a given beam crossing. As a figure of merit we calculate the probability that a muon track of interest is obscured by another in an underlying event. We consider the muon track to be "obscured" when two particles overlap within the maximum drift time of the chamber in a unit of azimuth defined by the scintillator used to identify the beam crossing.[5] This probability is plotted as a function of the number of underlying minimum bias events in Figure 10.16 and listed for the Run II crossing rates at $2 \times 10^{32}\mathrm{cm}^{-2}\mathrm{s}^{-1}$ in Table 10.7. The probability of a pure stub overlap is a few %. In these situations with overlap we will be able to resolve the two tracks with a slightly more complicated reconstruction algorithm which will be slower for this rare category of events. We conclude that this kind of overlap is not a problem.

To summarize, we expect that the improvements to the CDF II muon systems outlined here will substantially enhance Run II performance over Run I:

- The Main Ring will be removed, decreasing occupancy.
- The CMX will be shielded by the IMU, further decreasing occupancy.
- The ϕ coverage of the CMP will be increased. Scintillator will identify each muon's bunch crossing.
- The ϕ coverage of the CMX will be increased.
- The new IMU will allow muons to be identified out to $\eta = 2.0$, and triggered on out to $\eta = 1.5$. ($\eta = 1.2$ at the beginning of Run II)

[5] This figure of merit arises naturally from the simplest extension of the current stub finding algorithms to Run II conditions.

Bibliography

[1] K. Byrum, et. al., "The CDF Forward Muon System", NIM A268 (1988) pp. 46-49.

[2] G. Ascoli, et. al., "The CDF Central Muon Detector", NIM A268 (1988) pp. 33-40.

[3] The CDF Collaboration, "Proposal for an Upgraded CDF Detector", CDF Internal Note 1332 (PinkBook), December, 1990.

[4] Brandenburg, et. al., "A Proposal to Upgrade the CDF Muon System", CDF Internal Note 773, October, 1988.

[5] Fermilab, Harvard, Illinois, Pisa, Osaka, Tsukuba, Pisa, Frascati, etc., "The 1992 CDF Muon System Upgrade", CDF Internal Note 2858, October, 1994

[6] L. Nodulman, "Detector Counting Rates in the 94-96 Run", CDF Internal Note 3643, April, 1996.

[7] S. Abachi, et. al., "The D0 Upgrade: Forward Preshower, Muon System and Level 2 Trigger", Fermilab Technical Note FERMILAB-FN641, April, 1996.

Chapter 11

Front-End Electronics and DAQ

11.1 Overview

The CDF electronics systems must be substantially altered to handle run-II accelerator conditions. The increased instantaneous luminosity requires a similar increase in data transfer rates. However it is the reduced separation between accelerator bunches that has the greatest impact, necessitating a new architecture for the readout system.

Figure 11.1 shows the functional block diagram of the readout electronics. To accommodate a 132 nsec bunch-crossing time and a 5.5 μsec decision time for the first trigger level, all front-end electronics are fully pipelined, with on-board buffering for 42 beam crossings. Data from the calorimeters, the central tracking chamber, and the muon detectors are sent to the Level-1 trigger system, which determines whether a $\bar{p}p$ collision is sufficiently interesting to hold the data for the Level-2 trigger hardware. The Level-1 trigger is a synchronous system with a decision reaching each front-end card at the end of the 42-crossing pipeline. Upon a Level-1 trigger accept, the data on each front-end card are transferred to one of four local Level-2 buffers. The second trigger level is an asynchronous system with an average decision time of 20 μsec.

A Level-2 trigger accept flags an event for readout. Data are collected in DAQ buffers and then transferred via a network switch to a Level-3 CPU node, where the complete event is assembled, analyzed, and, if accepted, written out to permanent storage. These events can also be viewed by online monitoring programs running on other workstations.

With the new system architecture, both the Level-1 and Level-2 accept rates will be an order of magnitude larger than in run I. For example, with a 40 KHz accept rate from Level 1 and a 300 Hz rate out of Level 2, the system deadtime will be $< 10\%$. The expected rate of events written to mass storage is 30-50 Hz.

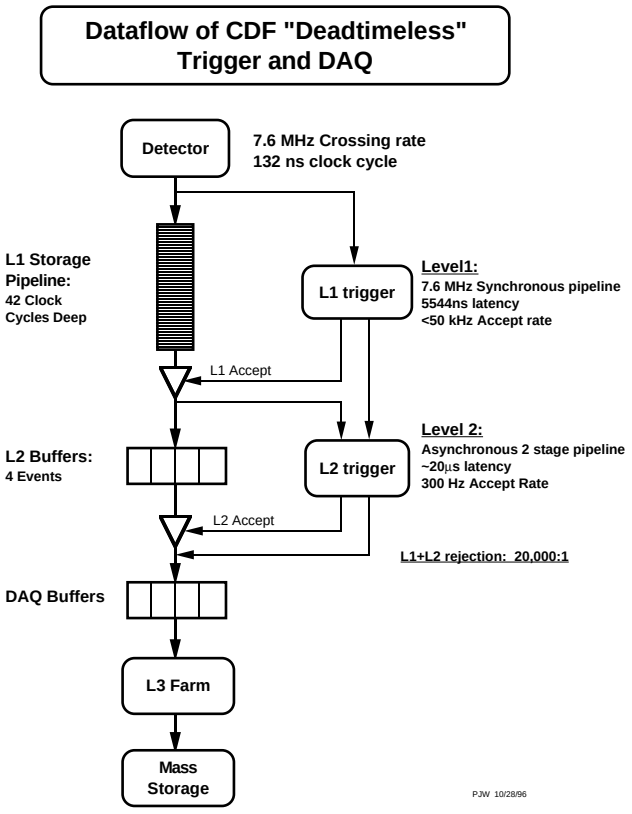

Figure 11.1: The run-II readout functional block diagram.

In this chapter, we begin with a detailed description with the front end electronics for the calorimeter, central outer tracker, and muon systems. We then describe the data acquisition system and the online computing. The readout of the silicon systems is detailed in Chapter 5 and the trigger is described in further detail in Chapter 12.

11.2 Calorimeter Front-End

The installation of new scintillator-based calorimeters in the plug region allows a common design to be used for much of the front-end electronics for the central and plug calorimeters and their associated preradiators and shower-maximum detectors. The calorimeter ADC readout is based on the QIE (Charge Integrating and Encoding) chip, a custom multi-ranging circuit developed at Fermilab for the KTEV experiment. A VME based front-end board carries the QIE, a commercial ADC, and FPGA based circuits to perform pipeling, buffering, and the creation of tranverse-energy sums for the trigger. A simplified version of the QIE design is used for all shower maximum and preshower detectors.

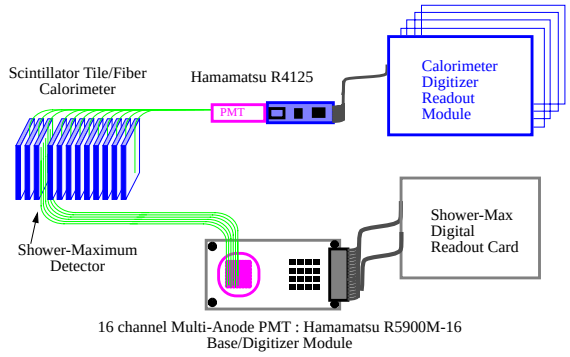

Figure 11.2: Plug-calorimeter readout.

11.2.1 Calorimeter ADC: The QIE

The readout of the calorimeters is done by integrating the charge coming from the individual calorimeter photomultiplier tubes (Fig. 11.2). The anticipated maximum signals from the PMT's will be greater than the present electronics were designed for. Estimates of the maximum signals for a collider energy of 2 TeV and an integrated luminosity of 2 fb^{-1} have been made for all of the calorimeters[1]. The conclusion is that the maximum signal expected is approximately a factor of two larger than that seen in the data up to now. The increase in maximum signal size requires one bit of dynamic range more than the present 16 bits. In addition, of course, the minimum time between bunch crossings will be reduced from 3.5 μsec to 132 nsec. We felt a multi-range solution was needed to solve the inherent difficulties of fast digitization of signals with large dynamic range. Because the signals from the PMTs can be as long as 80 nsec, there is not time to integrate, read out, and reset the integrating capacitor before the next bunch crossing, so the system also must be pipelined. These requirements fit reasonably well with an ASIC that was originally conceived for the SDC experiment at the SSC, and later adapted for use with the KTEV CsI calorimeter. The QIE (Charge Integrating and Encoding) custom integrated circuit[2] is used with a commercial ADC. The QIE and ADC are both mounted on a small front-end module, which is mounted in turn on an adc/memory (ADMEM) VME board. Each ADMEM board holds 20 of the front-end modules, provides the Level-1 trigger with transverse-energy sums, and also provides level-2 storage.

The QIE is the heart of the front-end module (Fig. 11.3). It has five major sections: a current splitter, a gated integrator/switch, a comparator, an encoder, and an analog multiplexer. The processing of signals within the chip is done in a four-stage pipeline. In the first step, the current splitter divides the incoming PMT current into 8 binary-weighted current outputs. The outputs are applied through a current switch to eight identical 2.6 pf integrating capacitors for a period of 132 nsec. The voltage integrated on the capacitor that receives half the charge (I/2 range) is the largest, with the voltage decreasing on the other capacitors down to a minimum at the last capacitor (I/256 range). At the end of the first step, the current switches to the next set of eight integrating capacitors. The capacitor voltages are then applied to a set of comparators to determine which capacitor voltage should be sent to the ADC for digitization. The selected range is encoded as a three-bit number, which is sent to the output for use as the exponent of a floating point number(the ADC value forms the mantissa). In the third step, the comparator outputs are used to control a multiplexer that selects one of the capacitor voltages to be digitized by the ADC. Following this, the capacitors are reset.

Tests were initially done using a version of the QIE that was the final preproduction version of the KTEV chip, fabricated using the Orbit 2.0μ process, along with an 8-bit Analog Devices AD9002 FADC. That chip has a full-scale charge input of 500 pC, and was not optimised for our power supply levels or clock speeds. The design was then modified to CDF specifications, which include the following: full-scale in-

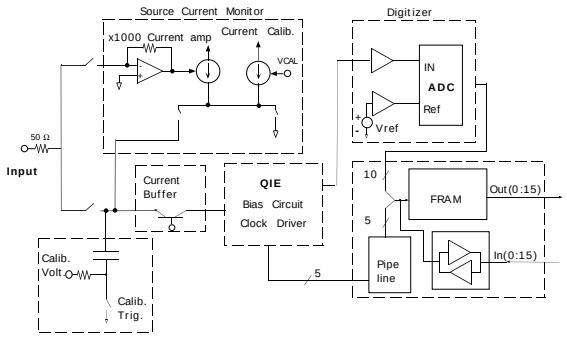

Figure 11.4: Simplified schematic of the front-end module.

Figure 11.3: Simplified schematic of the QIE ASIC

put charge of 1300 pC, maximum instantaneous current of 50 mA, linearity better than .2% or 10 fC, whichever is larger, and temperature stability greater than .2% (or 10 fC, whichever is larger) per degree Celsius.

A schematic of the front-end module is shown in Fig. 11.4. It includes a current buffer, a charge-injection circuit for calibration, a radioactive-source current-calibration circuit, the QIE, a 10-bit ADC to digitize the voltage presented by the QIE, and digital memory for converting the floating-point QIE+ADC output to a dual-range linear 16-bit number. The input impedance of the QIE is not a constant 50Ω, which is not a problem in its original application where it was located very close to the PMT base. However in our application, the QIE will be some tens of nanoseconds from the PMT base, so the input impedance needs to be well controlled to minimize reflections back down the cable and subsequent mismeasurement of the signal. The design of the QIE is such that it is intrinsically difficult to control the input impedance to the level required, so an external, low power-consumption circuit has been designed for use between the PMT base and QIE. The performance of prototype circuits in conjunction with the QIE has been excellent, maintaining the required linearity, with a power consumption no greater than 50 mW.

The QIE has 32 integrating capacitors, 8 ranges for each of 4 pipeline depths. One possible source of error in the charge measurement is miscalibration of those capacitors. Several circuits have been designed and tested to inject a known charge into the QIE for calibration. The basis of the current design is capacitive discharge using a precision voltage source. The circuit must be quite linear and capable of injecting near full-scale charge inputs($\approx$ 1000 pC) in less than 132 ns. Initial tests were capable of measuring the middle ranges to the required accuracy, but large QIE input impedances for small inputs, and nonlinearities for large pulses made testing the circuit challenging for the low and high ranges(Fig. 11.5). The final circuit development will be done after the prototype CDF QIE is in hand.

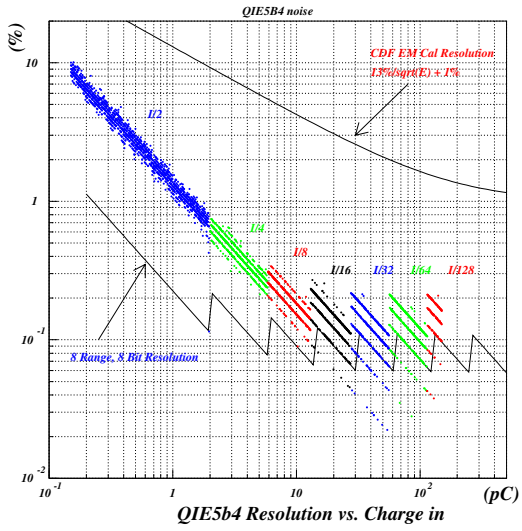

Figure 11.5: Noise performance of the prototype QIE5b4 ASIC compared with the calorimeter resolution and the ideal curve for an 8-range, 8-bit ADC system.

The other calibration circuit is needed to measure the DC current from the PMTs when a radioactive

source is passed in front of the calorimeter scintillator. Both the plug and central calorimeters adjust tube gains based on this information, and both plan to use this information to carry calibrations from the test beam to the collision hall. The source strength is such that the typical current from a PMT is about 100 nA. A 1% measurement of the current is desired. The circuit uses a high-gain current amplifier and the QIE to read out the source current. A 100 nA current integrates only 13 fC of charge in 132 ns, and only half of that goes to the I/2 range. Using a 10-bit ADC gives 5.2 fC per count in the I/2 range, so a gain of several hundred will be needed to achieve the required accuracy.

There is also digital memory on the front-end module. The output of the QIE contains a 2-bit integrating-capacitor ID and a 3-bit range ID. With the 10-bit ADC output, that makes 15 bits per channel per bunch crossing. These bits will be converted to a linearized 15-bit number, plus a 1-bit range, in a 1-Mbyte Flash RAM. The calibration constants for doing the conversion will be determined using the charge-injection circuit described above.

The 16-bit output of the flash RAM is sent off the front-end module to a Xilinx field-programmable gate array (FPGA), which is also mounted on the ADMEM Boards. The Xilinx sums the digitized data into trigger towers and passes that data to another flash RAM which converts E into E_T and delivers a 10-bit number to the Level-1 trigger. The digitized data are also stored in the Xilinx for a period of 42 bunch crossings(about 5.5 μsec). That is the time required for the Level-1 trigger decision to reach the front-end crates. A Level-1 accept causes the data to be written into one of four Level-2 buffers, and a Level-1 reject causes the data at the end of the pipeline to be discarded. A Level-2 accept will cause the VMEbus Readout Controller(VRC) to do a block read of the data in each ADMEM card.

11.2.2 Shower-max detectors and preradiators

The shower-maximum and preshower detectors will also use the QIE technology. A simplified ASIC has been developed and tested that has lower resolution, an integral 5-bit flash ADC, and Level-1 and Level-2 storage on chip. The circuit has 8 ranges and sufficient matching of the integrating capacitors that channel-by-channel calibration constants will not be needed (Fig. 11.6). The chip uses the Orbit 1.2μ double-poly, double-metal process. The power dissipation per channel is about 100 mW. Rather than mounting the chip on a VME board, we will construct readout boards containing 32 to 80 channels that are connected to a VME shower-max readout board via flat cables, as shown in Fig. 11.7. The plug-detector outputs can go directly to the shower max QIE, but the gas-based central shower-max detector outputs must first go to a preamplifier circuit, described in the next section.

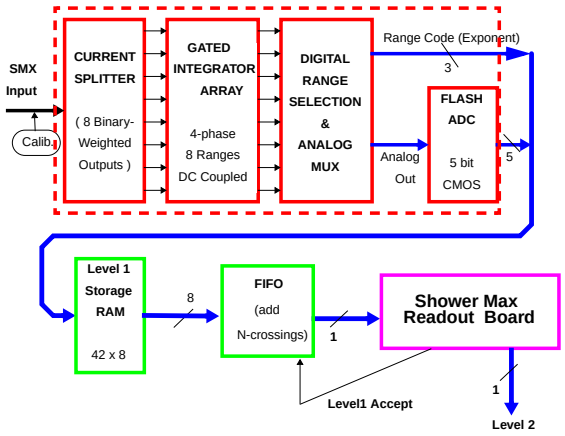

Figure 11.6: Schematic showing the general layout of the shower-max digitizer boards.

11.2.2.1 Central shower-max preamplifiers

The central-calorimeter shower-maximum proportional chambers measure the charge deposition on orthogonal strips and wires. In the run-I configuration, the Rabbit electronics matched the gain of the strip and wire signals, giving the same dynamic range to both. In the upgraded run-II configuration, we plan to use a preamplifier circuit to match the gains in the two views. As described in the previous section, separately-housed front-end cards will contain both the preamplifier circuit and the shower-max QIE. The digitized output from these cards will be multiplexed and sent to the DAQ electronics and to the trigger as shown in Fig. 11.7. We plan to mount the front-end card at the rear of the detector wedge as close as possible to where the cables emerge.

One of the key criteria for the selection of a preamplifier is the intrinsic noise of the circuit. Since the strip signal is sensitive to digital traffic, we want

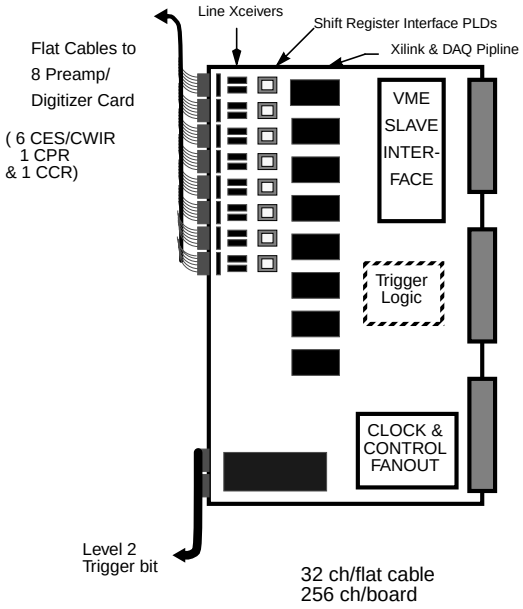

Figure 11.7: Schematic showing the general layout of the shower-max VME readout-boards.

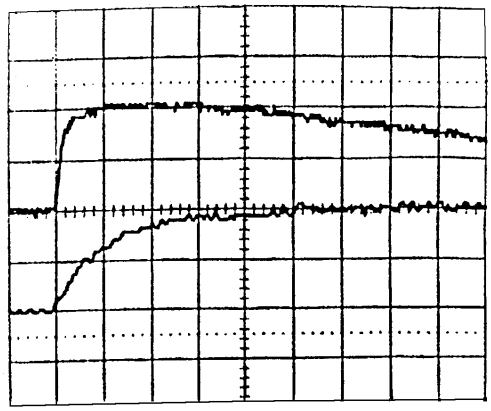

Figure 11.8: Time dependence of the amplified central-strip-chamber wire signal as observed. The top trace is 1μs per division, the bottom trace 200 ns per division.

our preamplifier circuit to introduce minimal additional noise. Recently, noise studies performed on the shower-max detector in the B0 collision hall showed that digital-traffic noise could be reduced by a factor 2-5 by using a different detector grounding scheme. This could impact where we mount the front-end cards, giving us more flexibility.

Another feature of the central strip and wire signals is the long signal rise time ($\tau_{\rm rise}$(wires)=530 ns).(Fig. 11.8) We plan to digitize the signals every 132 ns, but sum the signals from several consecutive windows on the VME readout board.

11.2.2.2 Central preradiator (CPR) and crack preamplifiers (CCR)

The central preradiator detector and central-crack chambers will also use the front-end cards containing both a preamplifier circuit and the shower-max QIE. Although the preradiator cabling is shielded twisted pair, the crack chambers have unshielded cable which will need to be replaced. We may add gain before the cable run (at the front of the wedges) for both the CPR and CCR; the preamp for the run-I VTX tracking chamber is a possible candidate.

11.2.3 Calorimeter TDC's

CDF has historically utilized timing on the hadronic calorimeter, and the need for this information continues into Run-II [3]. Timing requirements on hadronic energy deposition are important for the removal of cosmic-ray background. The cosmic-ray background for Run II will be comparable to that of Run I given the ADC and TDC gate widths and the luminosity. In addition to suppressing background, hadron-TDC information can be used to search for energy deposition from exotic heavy stable charged particles.

The baseline conceptual design of the CDF Run II Hadron-TDC upgrade is to pick off and discriminate the phototube dynode signals for the central, wall, and plug hadron calorimeters, and send the discriminated outputs to 96-channel pipelined TDC boards of the same kind used in the muon and tracking systems. The TDC design is described in the next section.

Although CDF has not used or considered timing on the EM channels in the past, we are now beginning to appreciate the importance of cosmic ray backgrounds to low rate signals from exotic processes involving photons. SUSY signatures in $ee\gamma\gamma\not\!\!E_T$, and $b\gamma\not\!\!E_T$, discussed in Sec. 2.4 are timely examples. The cost and schedule issues associated with TDC's on the EM calorimeter channels are under consideration, but will not be discussed further here.

	COT	Muon	Had	JMC96
Multi Hit Capability	yes	yes	yes	yes
Number of channels	30,240	8,773	1,200	40,213 total
Leading and trailing edge	yes	yes	yes	yes
Timing resolution	1 nsec	2 nsec	1 nsec	1 nsec
Max. drift time	100 nsec	2000 nsec	-	2048 nsec

Table 11.1: TDC requirements and specification

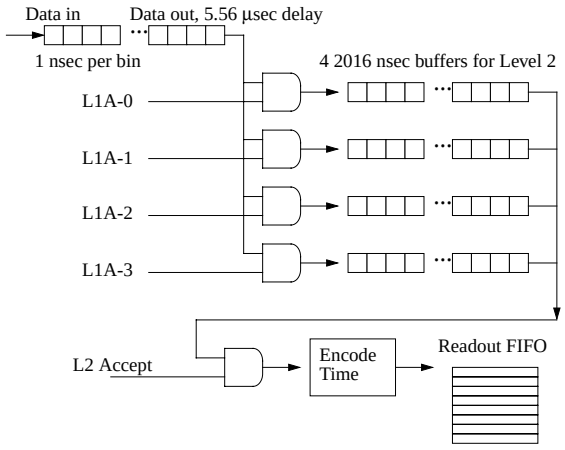

Figure 11.9: Schematic diagram of JMC96 chip.

11.3 Pipelined TDCs

The hadron calorimeters, scintillators, muon chambers, and the central drift chamber all require TDC's for recording signal times. The requirements for these systems, and the specification for the TDC are listed in Table 11.1. While there is some difference in the requirements for the three systems, there is enough commonality that a single solution is viable. In addition the TDC must obey the DAQ protocol of a 5.3 microsecond Level 1 buffer followed by four Level 2 buffers. The combination of these requirements were not available in any commercial module, and a custom circuit has been designed at the University of Michigan. The design includes the custom integrated circuit, 96 channel VME boards, and a calibration system.

The TDC chips, the JMC96, incorporate all of the features of the TDC required for the capture of the signals, the Level 1 and Level 2 buffering, and encoding data for readout. A functional diagram for the chip is shown in Fig. 11.9. The signal to be digitized is brought into the chip and is transmitted down a 48 stage delay cell line. Each delay cell has 4 transistors, and the delay per stage is controlled by a voltage. The overall delay as determined from this voltage is derived from a phase locked loop which is in turn driven by an external crystal controlled oscillator. Thus the absolute timing accuracy is determined by the accuracy of the crystal, which can easily be made to 100 parts per million. Once every 48 nanoseconds the content of the delay line is copied to a 48 bit register. This register then contains the history of the input signal for the last 48 nanoseconds. The register is then written to a static on-chip memory which is operated in a FIFO mode. The FIFO is large enough to hold 5.2 microseconds of data.

When a Level 1 accept is generated the data coming out of the FIFO is stored in one of four Level 2 buffers. Which buffer to use is specified in the Level 1 accept message. There are four level 2 buffers in the JMC96. Each buffer has forty-two 48 bit words, so that the level 2 buffers store up to 2 microseconds of data. The DAQ protocol specifies that Level 1 accepts may be generated on consecutive crossings. If this happens, then the output of the Level 1 TDC buffer will be written to multiple Level 2 buffers with a 132 nanosecond time offset. The minimum time between Level 1 accepts for the TDC chip is 96 nanoseconds. The Level 1 accept signal is recorded in a second 48 stage delay cell line, and the content of this line is written to one of four registers.

When a Level 2 accept is generated the data stored in the Level 2 buffers is digitized. The content of the Level 1 accept buffer is first read in order to calculate a t0. The Level 2 buffer is then scanned and the time of each transition from 0 to 1 or 1 to 0 is calculated. The time of the level 1 accept is then subtracted, resulting in a 12 bit word - 11 bits indicate the time within the 2 microsecond window, and the 12'th bit

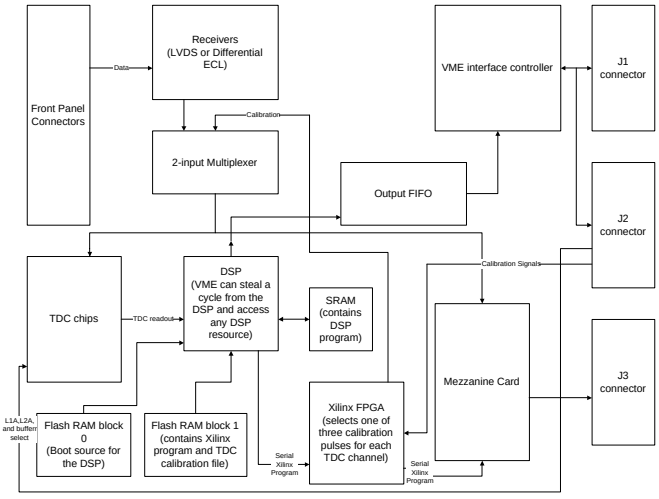

Figure 11.10: Block diagram of the 96 channel TDC boards

indicates a leading or trailing edge. The 12 bit word is then written into an on-chip 16 word FIFO.

The TDC board contains 96 JMC96 chips and the associated circuitry needed to receive and process the data. A block diagram of the board is shown in Fig. 11.10. The receiver is either ECL or LVDS. The board is manufactured with sockets for both ECL and LVDS receiver chips. It is most likely that the muon and scintillator systems will use ECL and the COT will use LVDS. This allows the boards to be manufactured in the same way and the final determination of the input voltage level is determined by which chips are plugged in. After the signals are received they are input to a 2-input multiplexor. The second input of the multiplexer comes from the onboard calibration circuit which can be programmed to produce up to three different calibration pulses and distribute them to any combination of the 96 channels. This calibration system will allow testing of not only the TDC board but also of muon or XFT trigger systems that get input from the TDC board.

A DSP on the TDC board is used for reading data out of the TDC chips and storing it in a memory. After a level 2 accept all 96 TDC chips encode the data in the level 2 buffer and store the hit times in a on-chip FIFO. The DSP queries the status of each TDC chip, and if it has data, reads it out. The DSP will then try to match leading and trailing edges of a pulse and convert the two edges into a single word that has the pulse width, the time of the leading edge, and the channel number. Several cuts can be made on the hits by the DSP. The pulses can be required to have a minimum pulse width before they will be readout. This can be used to reduce the number of noise hits and reduce the size of the event record. A limit on the maximum drift time can be set. The TDC records 2 microseconds of data, which is much longer than the 100 nanoseconds drift time of the COT. A cut on the maximum time removes hits from previous crossing. A cut can be placed on the maximum number of hits per channel in order to suppress noisy channels, and a channel can be marked a bad or dead and excluded from the readout entirely. When all channels for an event have been readout the header word, a word count, and the timing data are written to a FIFO on the TDC's. The data is read out of the other end of the FIFO through VME.

The COT TDC's will be mounted on the detector. Fifteen VME crates are needed to house the 315 TDC cards. The signals from the COT are transmitted from the chamber-mounted ASD's over small coax. There may have to be a transition card to a lower loss cable before the signals are sent to the TDC.

The TDC board has connectors to support a mezzanine card. The mezzanine card will be used for processing or transmitting the timing signals to trigger circuits. Different systems will have different mezzanine cards. The COT mezzanine card has circuits to identify the prompt and delayed hits for each cell and multiplex the hits to connectors on the backplane. The signals will then be transmitted by the existing Ansley cable to the trigger room for use by the XFT track processor.

11.4 Muon-Detector TDCs

The muon system share the TDC design with the COT, as described above. The muon TDC's reside on the first floor counting room. Signals are transmitted from the detector via the existing Ansley cable. The TDC receives the signals and records the hit times. A mezzanine card mounts on the TDC board which generates a copy of the muon signals to be transmitted to the muon trigger. A total of about 91 TDC modules are required for the muon systems.

11.5 Silicon Front-End Electronics

The design of the front-end and DAQ electronics for SVX II is intimately connected with the detector's mechanical design because of the need to minimize

the amount of material between the beamline and the COT. Consequently, the SVXII and ISL electronics is described along with the SVXII detector in Chapter 5.

11.6 Data Acquisition System

11.6.1 Overview

The Data Acquisition System is responsible for collecting data fragments from front-end electronics systems for events satisfying the Level-2 trigger and sending them to the Level-3 trigger subsystem. There complete events are built and more sophisticated algorithms classify events and determine whether they should be saved. Events passing the Level-3 trigger criteria are sent to mass storage. The Online Computing System, described below, provides processes that control and monitor the functioning of the detector and data acquisition system.

A block diagram of the system is shown in Fig. 11.11. The basic architecture is very similar to that used successfully in Run Ib [7]. Front-end and trigger electronics are housed in VME crates replacing the FASTBUS and RABBIT crates used in the original detector. Timing signals associated with the beam crossing are distributed to each crate by the Master-Clock subsystem. Trigger decision information is distributed by the Trigger-System-Interface subsystem. Commercial processors read data from modules in their local crate and deliver it to the Event-Building subsystem. This system concentrates the data and delivers it to the Level-3 trigger subsystem through a commercial network switch. The Level-3 trigger is a "farm" of parallel processors, each fully analyzing a single event. The Data-Logging subsystem delivers events to mass storage and also to online monitoring processes to verify that the detector, trigger, and data acquisition system are functioning correctly. While the architecture is similar to the run-Ib system, many individual components will be upgraded or replaced. This is necessary to deal with the new VME-based front-end electronics, and to provide increased throughput required for the higher luminosity now expected in run II. And in some cases commercial products in the run-Ib system are no longer supported by the manufacturer and must be replaced.

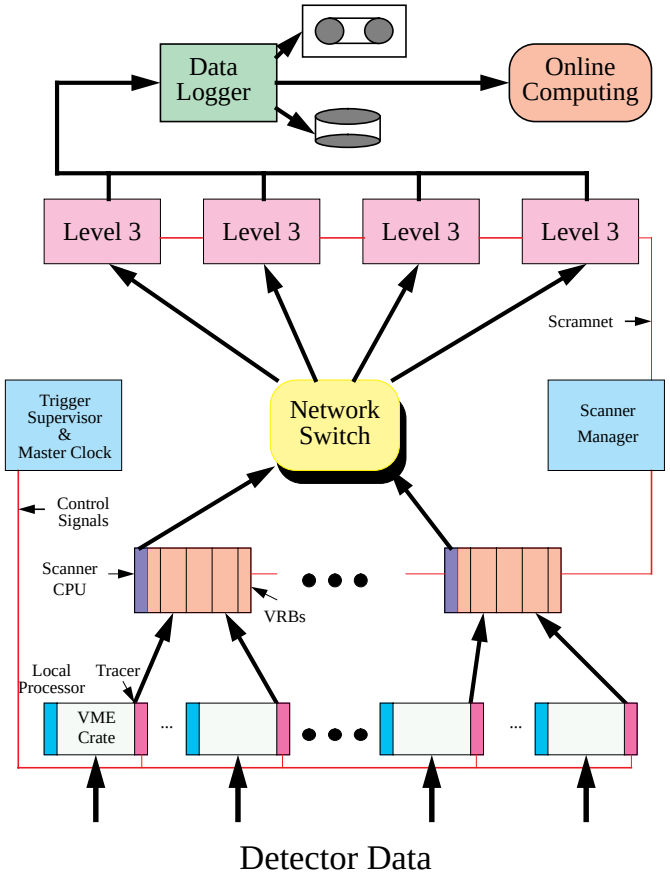

Figure 11.11: A schematic of the CDF Data Acquisition system, showing data flow from the front-end and trigger VME crates to the Online Computing system.

11.6.2 Front-End Crates and Controllers

All front-end and trigger electronics are packaged as VME modules and housed in standard 21-slot commercial VME crates. These modules process detector signals and make the data available to the data acquisition system via the VME bus. In addition to the front-end modules, each front-end and trigger crate will contain a commercial VME-based processor for event readout, and a "TRigger And Clock + Event Readout" (Tracer) module. The Tracer receives serial fast control messages such as Level-1 and Level-2 Accept from the Trigger Supervisor and fans them out on dedicated lines on the backplane. It also provides the interface to the serial data link to the Event-Builder subsystem.

11.6.2.1 VME Crates and Modules

Modules and crates will conform to VME standards including the VME64 extensions (ANSI/IEEE 1014-1987 and ANSI/VITA 1-1994, VITA 1.1-199x) [8]. Among these extensions are 64-bit transfers, additional ground and user-defined backplane pins, better EMI protection, geographical addressing, and board keying. They will also conform to the proposed VME International Physics Association (VIPA) standard (VME-P) [9] that defines additional specifications for high-energy-physics applications. These include crate and card mechanics for 9U x 400 mm systems, including rear transition cards as well as additional power required for analog or other custom applications.

Of the approximately 120 crates in the system, half each are located on the detector and in the counting room. User-defined pins on the standard J2 backplane will be used to distribute fast control signals such as Level-1 Accept, Level-2 Accept, and the crossing clock to all modules in a crate. Most systems will employ a custom J3 backplane. In some cases this will be used to receive signals from the detector via a 9U x 120mm rear transition card. Another use of J3 will be communication of trigger information to adjacent boards where required. The newly defined J0 connector will be implemented and used primarily to provide additional power.

In addition to following the VSO standards, front-end cards are required to present a common interface to the data-acquisition system. They receive fast timing and control signals via specific backplane pins. On receipt of a Level-1 accept, they must store the data for the appropriate crossing into the specified one of the four Level-2 buffers. Then on receipt of a Level-2 accept, this data must be readable over VME by a single D32 block transfer. Data from each module will include a header word containing a module ID and event number for use in data integrity checks higher up in the system.

All crates are specified to have 300 amp +5V power supplies. Additional power is system dependent. Some systems require separate supplies for sensitive analog circuits, others additional voltages for ECL or 3.3V applications.

Crates both on the detector and in the counting rooms will be individually cooled by fans and air-water heat exchangers. These will be configured to provide cooling to rear transition cards as well as the main crate. The cooling system will be designed to support a maximum power dissipation of 2 KW per crate. Most crates will be well under this limit. Racks in the counting rooms will contain 2 VME crates each. Protection circuits in each rack will automatically shut off power in case of fan failure, overtemperature, or detection of smoke or water.

11.6.2.2 Local Processor

Each crate will contain a local VME-based processor. On receipt of a Level-2 accept, this processor will read data from the front-end modules and send it via the Tracer module to the Event-Building network. Also, the processor provides the interface between the host control programs and the front-end modules for initialization and diagnostics.

The event data readout may be accomplished in one of two ways. In the direct mode, the front-end data are transmitted to the Tracer as they are read from the modules as described in more detail below. In the second mode, this Tracer "spy" mode is disabled, and data are first read into the processor. The processor then applies calibration corrections and removes channels where there are no hits. The compressed data are then written back to the Tracer data link. For the calorimeter crates, a significant reduction in data size may be accomplished by removing the empty channels. Benchmarks have shown this compression can be accomplished within the allotted time.

The processor will also provide the only external path into the crate for downloading and monitoring operations; there will be no other intercrate network. Commands and data are sent from the host to the local processor via ethernet. The required VME operations are done, and the results communicated back to the host. Commands may be single VME operations, or more complex operations such as an entire begin-run initialization sequence.

Currently the processor is specified to be a Motorola MVME-162 This is the choice due to both its excellent performance as a VME master and its modest cost. The processors will run the VxWorks operating system [10]. VxWorks provides a multitasking operating system with priority-based scheduling and fast interrupt response. It also provides excellent networking including BSD sockets, remote file access via nfs, and remote logins. Code is developed and compiled on a host unix system, then downloaded to the

processor. Since the processor form factor is 6U x 160mm, a 6U-9U adapter card will be used to install the modules in the crates.

11.6.2.3 Tracer Module

The Tracer module provides the interface between the front-end modules and the Trigger Supervisor and Master Clock for fast control signals. It also provides the data interface between the front-end modules and the Event Building Network.

Serial control messages from the Trigger Supervisor (Level-1 Accept, Level-2 Accept and Reject, Control) are received and decoded by the Tracer. In addition, timing signals from the Master Clock (Beam Crossing, Bunch 0, Abort Gap, and Clock) are also received by the Tracer. All these signals are distributed via the J2 backplane to all modules in the crate.

To provide maximum efficiency for event readout, the Tracer contains a "spy" function that enables it to clock event data from the backplane as the VME Readout Controller reads it. The Tracer stores the event data in a local FIFO. A sequencer on the Tracer will then read the FIFO, serialize it, and then transmit the data to the Event Building Network. Should the higher level not be able to accept data (due to its internal buffers being full) a BUSY signal will be transmitted and inhibit data transfer until the condition clears.

Finally, the Tracer provides a means by which to issue a crate reset. The VMEbus signal SYSRESET* will be pulsed low on the backplane if a reset pulse is detected from the CDF Reset Crate. The Reset Crate contains a set of IndustryPak output registers that drive RS-422 signals to a front-panel connection on each Tracer. A signal is sent from the Reset Crate to a Tracer if a reset is desired. This capability is required in case a local processor board hangs.

11.6.3 Trigger System Interface

The Trigger-Interface subsystem provides the interface between the hardware trigger (Levels 1 and 2) and the data-acquisition system. Trigger decisions are received by this subsystem and forwarded to the front-end electronics. Then, when a Level-2 trigger has been successfully processed, the Event Building Network is informed and manages readout of the event into the Level-3 trigger. Components of this subsystem include a set of Trigger-Supervisor modules, one per partition, and a set of crosspoint modules that link signals from the Trigger Supervisors to the front-end crates in the appropriate partition.

11.6.3.1 Protocol

The global-trigger-decision subsystem will send results of the Level-1 trigger to the Trigger Supervisor each beam crossing. In addition, when a Level-2 decision is available, this is also sent to the Trigger Supervisor. The information is forwarded to the front-end crates in the form of serial messages.

Each beam crossing, two frames of 9 bits each are transmitted to each Tracer card, which decodes the messages and drives the appropriate lines on the backplane. The first frame contains the results of the Level-1 decision for the crossing that is emerging from the front-end pipeline. If the decision is positive, the data is stored in one of four Level-2 buffers as indicated by another field in the frame. Otherwise data from the crossing is discarded.

The second 9-bit frame may be either a Level-2 decision, a Calibration enable, or Control message. The Level-2 decision word indicates which is the pertinent buffer of the four, as well as a reject or accept indication. If the event is accepted, the data is moved from the Level-2 buffer to a buffer awaiting readout by the DAQ system. The Calibration Enable message causes generation of a calibration event by previously enabled pulsers in the crate. The Control message is used to halt, reset, and start the Level-1 pipeline so that all crates are synchronized. It also includes an encoded field that may be used to alter the default readout, for example in the case of calibration events.

Information is returned from the Tracer to the Trigger Supervisor via four (nonserial) cables. These include Done, which is deasserted on receipt of Level-2 Accept and reasserted when the front end is ready to accept further triggers. Error is asserted if some fatal error is encountered. In response, the Trigger Supervisor will halt and reset the Level-1 pipeline. Should there be no place to store data from a Level-2 accept due to a backup from higher levels in the data-acquisition system, then the Wait signal is asserted. Level 1 Done is issued following a Level-2 reject to indicate the specified buffer is ready for another Level-1 accept. This is required only in the SVX system where there can be a delay of many beam crossings before a capacitor cell may be reused following a Level-1 accept.

The system will be clocked every 132 ns even when

there are only bunches present every 396 ns, as expected during the first part of Run II. Level-1 rejects will be issued on empty crossings. When the situation arises that there are no free Level-2 buffers, Level-1 rejects are issued, thus incurring dead time. This can occur due to the time required for Level-2 trigger processing and data-acquisition system processing of Level-2 accepts. The Trigger Supervisor will keep track of the live fraction and provide a Live Gate to external scaler modules to enable proper computation of the live integrated luminosity.

11.6.3.2 Trigger Supervisor

The Trigger Supervisor will be a custom 9U x 400 mm VME module. A series of state machines will manage the Level-1, Level-2, and readout sequences. These will be implemented using Xilinx gate arrays. A custom J3 backplane will connect the Trigger Supervisors to the Crosspoint modules. Should an error condition be encountered such as failure to receive an expected message from the trigger or front end, status information will be stored in the module. A task in the local crate processor will note the condition and inform the Run-Control program.

11.6.3.3 Crosspoints

Two different types of crosspoint modules route signals between the Trigger Supervisors and front-end crates. For the serial data, custom VME modules based on the Triquint TQ8016 chip are used. There are 16 channels per board. Each output is attached to a single front-end crate, and may be individually programmed to select data from any Trigger Supervisor as input. The output messages are transmitted via fiber-optic cables. In addition, each channel has a programmable delay to account for differences in propagation time to different detector components. For the signals returning from the front-end crates (Done, Busy, Error, Level-1 Done), the use of commercial latches is under consideration.

11.6.4 Master Clock

The Master Clock subsystem is responsible for distributing timing signals to the front-end electronics and trigger. Four signals are distributed to all systems: Beam Crossing, Bunch 0, Abort Gap signifying the current crossing is in the accelerator abort gap and so there is no collision, and Clock (every 132 nsec). The Beam-Crossing signal is used to gate front-end ADCs and TDCs and should be stable with respect to the beam crossing to better than 1 ns. The Bunch-0 signal is used for synchronizing the front-end pipelines following a reset operation. As it indicates there is no beam collision, the Abort Gap signal is used by the SVX system to reset the front-end amplifiers to baseline. This information is also used to occasionally trigger pulsers to generate calibration triggers during a data-taking run. In addition, the SVX will use a 53 MHz clock derived from the Tevatron RF system to clock serial data links.

A variation on the Master Clock system developed for the D0 experiment [11] will be used. This consists of three module types. The first, the Phase Coherent Clock (PCC) module phase locks a 53 MHz oscillator to an RF signal from the Tevatron. This, together with a marker signal, is input to the Master Sequencer module. The sequencer module drives a number of output signals whose state at each of the 1113 RF buckets is determined by a lookup memory. Groups of four of these outputs will be configured as the base set of timing signals for each detector system. These signals are fed to Selector/Fanout modules where they are distributed to the various crates within a subsystem. These modules can add a delay in nanosecond increments for each channel to fine tune the timing for each channel.

Past experience has shown medium-term drifts in the Tevatron input signals relative to the beam crossing time of several ns. This drift was measured using precisely-timed information from the detector beam counters, and manual adjustments made to compensate for the drifts. For the Run-II system, a more automated feedback mechanism will be developed.

11.6.5 Event Building Network

The Event Building Network takes data from the front-end crates and delivers it to the Level-3 trigger where the fragments are assembled into complete events. First the data are received by VME Readout Boards (VRBs) distributed among 11 VME crates. A processor in the VRB crates ("Scanner CPU") reads data from the VRBs in that crate and sends it via a data switch to the Level-3 subsystem. Data flow is controlled by a Scanner-Manager task running in a separate processor. It communicates with the Level-3 processors and Scanner CPUs over a separate control network so as to not interfere with the event data

traffic.

11.6.5.1 VME Readout Boards (VRB)

Rather than going directly into the data switch, the serial data from the front-end crates are received by custom VME Readout Boards (VRBs). The amount of data per event ranges from a few hundred bytes to a few kilobytes over the different crates in the system. This extra VRB layer combines data from different front-end crates so as to approximately equalize the data size on each switch link. It also reduces the number of switch ports required by over a factor of 10. This greatly reduces the cost and complexity of the switch as well as improves switch utilization.

The VRB module contains a number of serial data inputs together with a set of dual ported memory buffers for each. An event fragment received via the data link is placed in one of the buffers. It is held in the buffer, available for later asynchronous readout via the VME slave interface. Buffers are managed in a FIFO manner, input of one buffer and VME readout of another may occur simultaneously. If a channel cannot accept more data, a BUSY signal is transmitted back to to the Tracer module to halt flow of data. This will also be transmitted to the Trigger Supervisor. Data from all channels for a given event may be read by a single VME64 block-read operation to minimize the overhead.

For all systems except the SVX, slower 256 Mbps TAXI links will be used rather than the 1 Gbps GLinks used by the SVX. This is because data are only transmitted on every Level-2 accept rather than every Level-1 accept. Also, the slower links allow additional multiplexing to give 10 rather than 5 data links per board. The data links are implemented on rear transition cards, allowing the core part of the module to be the same for all systems.

11.6.5.2 Scanner CPU

The Scanner CPU is a commercial VME-based processor that reads all fragments for an event from all VRBs in its local crate and sends it to the Level-3 trigger via the Network Switch. In addition to a high bandwidth VME64 interface, these processors must also support an interface to the network switch. The MVME 162s used in the front-end crates only have a VME interface. In this application the switch interfaces would also have to be VME slaves, meaning the data would have to travel over the limited bandwidth VME bus twice. To avoid this situation, current R&D has focused on Power-PC-based processors with Peripheral Component Interconnect (PCI) buses [12]. PCI is a synchronous 32-bit 33-MHz bus with a total bandwidth of 132 MB/sec. The network interface connects directly to the PCI bus, hence the system throughput is not limited by the VME bus. Evaluation of these and other modules will continue. The Scanner CPUs will also run the VxWorks operating system.

11.6.6 Network Switch

Data collected by the Scanner CPUs is sent to the Level-3 system through the Network Switch. Data flow is managed such that event fragments are flowing in parallel from all Scanner CPUs to all Level-3 systems simultaneously. The proposed configuration in Table 11.2 shows that each link must sustain an average of about 5 MB/sec for 300 Hz operation. This is the throughput that must be sustained including all software-driver and data-flow-control overheads and hardware-link inefficiencies. This is usually less than the peak data rate on the physical link. About 45 MB/sec is the required aggregate bandwidth for 300 Hz operation.

The Ultranet system used in Run Ib is no longer supported by the manufacturer. It also does not have sufficient performance to deal with the luminosities now expected in Run II; hence it must be replaced. A number of other commercial options developed for telecommunications or computer-networking applications exist and are under study. These include Asynchronous Transfer Mode (ATM) [13], FiberChannel (FCS) [14] and HIPPI [15] among others.

Currently a detailed evaluation of ATM technology for this application is in progress at Fermilab. In ATM, data blocks are broken into cells of 48 bytes plus a 5-byte header for transmission. A test system with an 8-port ATM switch from Fore Systems [16] has been constructed. Data links are 155 Mbps. Eight Power-PC processors with PCI-based ATM interfaces are used as data sources and sinks. When faster 622 Mbps links are available, they will be evaluated as well. Evaluation of other technologies at other labs [17] will be monitored and serve as input to the final technology choice.

System	Crates	Total Bytes	Switch Links
Calorimeter Total	44	30544 (6800)	2(1)
Central Calorimeter	24	16704(2600)	
Endwall Calorimeter	4	2128 (500)	
Endplug Calorimeter	16	11712(3700)	
Central Tracking	18	27000	2
Muon System Total	9	2000	1
SVX II	3	40000	3
ISL	2	16000	1
Trigger	42	30000	2
Total	120	148204(122800)	11(10)

Table 11.2: Summary of the data acquisition configuration. For the estimated data size, a luminosity of $2 \times 10^{32}/cm^2/sec$ is assumed. Quantities in parentheses are following data compression by the front-end processors.

11.6.6.1 Event Data Flow Control

Data flow between the Scanner CPUs and Level-3 system is controlled by the Scanner Manager. This is a task running on an independent VME-based processor. Communication with the Scanner CPUs and Level-3 processors is over an independent reflective-memory network.

After the front-end processors have completed readout of an event, the Trigger Supervisor passes the Level-2 accept message to the Scanner Manager. Level-3 processors, when they become active, make their presence known to the Scanner Manager. The Scanner Manager then directs the Scanner CPUs to read the events from the VRBs and send the fragments to a specific processor in the Level-3 system. This is done in such a manner so that multiple Scanner CPUs are not sending to the same Level-3 port at the same time so as to improve switch utilization. For ATM, this can be accomplished by making use of the rate division capabilities built into the hardware. For other switch types, messages between the scanner manager and scanner CPUs can be used. While this centralized strategy results in more message traffic, it allows better control of the traffic distribution among the switch ports and Level-3 systems. In the Level-3 system, events are built by dedicated tasks then queued to the algorithm task.

The Scramnet reflective-memory network [18] used in Run Ib will continue to be used for message transmission. This network provides a very low overhead communication path that does not interfere with data traffic. Each Scanner CPU and Level-3 system in the Event-Building network contains a Scramnet module. Short control messages are written to the memory by the local processors, and automatically transmitted ("reflected") to the analogous memory modules in all other crates. This transfer incurs no overhead beyond that of a simple VME single-word write, plus approximately 1 microsecond per network node.

11.6.7 Level 3 Trigger

The Level-3 trigger subsystem receives event fragments from the Scanner CPUs and builds complete events into the appropriate data structures for analysis. The events are then passed to a trigger algorithm that categorizes the event and makes the decision as to whether it is written to mass storage. Events destined for mass storage and also other event categories requested by online monitor programs are passed on to the Data-Logger subsystem. During the event building process, the event integrity is checked and complaints are issued about mismatched fragments or other problems. The same algorithm is run on all processors. This method does not require careful tuning of the event distribution to maximize processor utilization. Also events satisfying multiple Level-2 triggers require no special handling as would be the case if events were allocated to processors based on trigger type.

The Level-3 algorithms take advantage of the full detector information and improved resolution not available to the lower trigger levels. This includes full

3-dimensional track reconstruction and tight matching of tracks to calorimeter and muon-system information. Results from the lower levels are used to drive the algorithms. For example, if the Level-2 trigger indicates only the presence of an electron candidate, only those portions relevant to verifying it are invoked. In previous runs the overall rejection factor has been approximately 80%. For Run II, use of SVX information and targeting triggers at more specific physics analyses will be used to increase the rejection.

The overall algorithm structure is based on the offline analysis package. This is a modular system consisting of a number of general reconstruction modules and separate filter modules for specific triggers. Algorithms are provided by various detector and physics groups and integrated into a final package by the Level-3 group. As the offline system is expected to evolve for Run II, this evolution will be carried over into the Level-3 algorithm structure. This includes evolution in both the general framework and the programming languages supported.

The system operated in Run I contains four Silicon Graphics Challenge XL systems each with 8 processors and 4 VME bus interfaces. The baseline plan is to replace the existing processors with the fastest available at the time they must be purchased. This takes advantage of the large investment in the Challenge-system classes. In addition to raw processing capacity, the input I/O capability is very important. Assuming a 50% increase in processing per event compared to Run Ib, approximately 45,000 MIPS will be required to meet the 300 Hz input rate goal. It is expected that the price/performance of these processors will improve such that this upgrade can be supported within the current budget. Of course as reconstruction programs are written for new detectors and trigger algorithms developed this estimate must be continually evaluated.

Due to the extended time scale for Run II, support for the Challenge platform by Silicon Graphics could be an issue, as they will likely be superceded by new systems in the next few years. The marketplace will be continually monitored during this time. If a more cost-effective solution than upgrading the Challenges is found, that could be adopted instead. Note that in addition to the raw processing speed requirements, any alternate solution must be configurable with of order 16 high-bandwidth interfaces to the data switch as well as links to the Scramnet network. Any alternate platform must also be supported by the CDF offline system in order to develop trigger algorithms.

11.6.8 Data Logging

Events passing the Level-3 trigger are delivered to mass storage by the Data-Logging subsystem. Also a sample of events are sent to monitoring processes in the online computing system. The default strategy is to send all events to a dedicated data-logging/monitoring machine. The expected event rate is around 30-50 Hz corresponding to 7.5 - 12.5 MB/sec. This corresponds to a trigger cross section as high as 250 nb at 2×10^{32} luminosity. An alternative would be to log events directly from the Level-3 processor systems. However this method makes calculation of the integrated luminosity for a run more difficult in case of a crash or other failure in a part of the Level-3 system. This is because events may not be evenly distributed across all systems; hence the fraction of luminosity seen by a particular part is not easily determined.

In Run Ib, the same Ultranet network used for event building was also used for transmission of accepted events to the data logger. Although the output data volume from Level 3 is much smaller than the input, it still disrupts the traffic in the switch, making it more difficult to minimize contention. Hence a separate network for accepted events will be implemented. Since the required aggregate bandwidth is much less than for the Event-Building network, a less costly loop topology rather than a switch topology should be sufficient. Several commercial possibilities exist. A dedicated FDDI ring may barely have sufficient bandwidth. Another possibility is FibreChannel Arbitrated Loop [19] This logically is similar to FDDI but supports much greater data rates. Other possibilities includes Serial Storage Architecture (SSA) [20] and FireWire [21]. The commercial marketplace will be tracked and a technology choice made closer to the start of the run. A FibreChannel test-bed is begin constructed at Fermilab to evaluate its use for data logging.

Also no decision has been made on the mass storage medium. For reliability reasons it is very desirable to migrate from the 8mm tape used in the past to a different technology. New technologies that would meet the requirements include Digital Linear Tape (DLT) [22], and the RedWood tape [23]. For operational convenience, the possibility of sending raw

data directly to the computing center will be considered. Depending on the future cost of disk storage, it may be feasible to leave the data on disk until the offline production analysis has run. Then the production output and raw data may be written together to mass storage.

11.6.9 Partitioning

A key element of the system is the concept of partitioning. This is the ability to operate different parts of the data-acquisition system in parallel to facilitate debugging. No recabling is ever required to accomplish this. The system is designed to support a maximum of eight partitions. Software in the host control programs controls allocation of resources, ensuring that multiple partitions do not access the same front-end crates.

The lowest-level granularity is a single front-end VME crate. This makes it possible to repair a faulty crate within a detector system while continuing operation of the remainder of that detector. An exception is the main physics trigger, which may not be divided among multiple partitions. However simple triggers appropriate for calibrations may be routed by a multiplexor to any partition.

A Trigger Supervisor is assigned to each partition. Crosspoint modules route the control messages from the partition's Trigger Supervisor to the selected set of front-end crates. Software in the Event Building Network and Level-3 trigger supports multiple partitions. A specific portion of the Level-3 system is allocated to each partition. This method is chosen rather than sending events from any partition to any Level-3 processor and routing the output based on partition. Different Level-3 algorithms may thus be used in different partitions; also throughput is not affected by a different partition generating a very high trigger rate.

11.7 Online Computing System

The Online Computing System is responsible for configuration, calibration, monitoring, and diagnostics for the data-acquisition system and front-end and trigger electronics. It also provides monitoring of a sample of the data stream to insure that the detector is functioning correctly. And finally it provides for control and monitoring of the detector systems such as high voltages and VME crate power. Each of these subsystems provides an operator interface, as well as automated error detection and reporting.

Data-acquisition control and monitoring is provided by unix workstations connected via a local-area network to all embedded processors in the system. Event monitoring programs also run on unix workstations, receiving data either directly from the data logger or via the local network. Slow control and monitoring of the detector systems is provided by the ALARMS subsystem. This is tightly integrated with the accelerator control system (ACNET). It is distinct from the data-acquisition control system in both hardware and software, though interfaces are provided to transfer information between the two.

A diagram of the logical architecture is shown in Fig. 11.12. Shown are the Run Control, Event Monitoring, and ALARMS subsystems and their relationships to the Data Acquisition and Offline systems.

11.7.1 Run Control

The Run-Control subsystem provides the following functions:

- Primary user interface to the data-acquisition system. This includes starting and stopping runs, viewing the system status, etc.
- Initialization of all front-end and trigger hardware.
- Configuration of the data-acquisition system.
- Automatic startup of event monitor tasks.
- Any additional procedures required to perform calibrations.
- Monitoring of system performance parameters.
- Reporting of any errors in any part of the system and taking action to recover if appropriate.

Each partition runs a separate copy of the Run-Control program. A partition manager allows the user to select parts of the detector while preventing multiple partitions from accessing the same pieces. For initialization, configuration information such as the correspondence between physical modules and logical detector components, hardware trigger tables, calibration constants etc. is retrieved from various databases. A finite-state-machine model is applied to the components of the system and the system as a

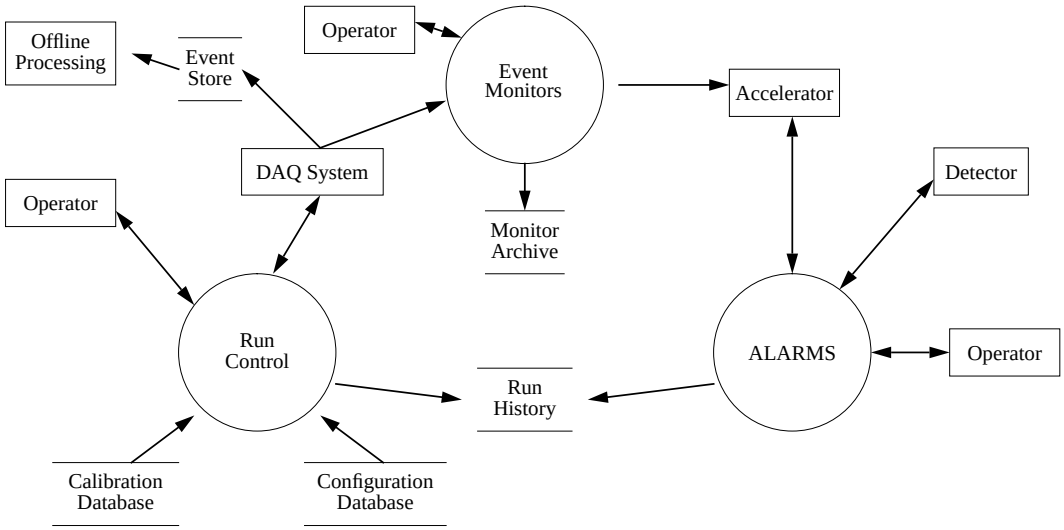

Figure 11.12: Logical model of the Online Computing system.

whole. A state manager communicates transition requests to all components and collates the replies into an overall system state transition. Error messages from all components are received by a centralized message server and displayed. Should data taking be stopped due to some error, the operator is notified and a recovery procedure may be attempted.

The command-line-driven VMS-based program used in the past will be replaced by a unix version with an X-window-based graphical user interface. It will be location independent (with appropriate security) to allow for remote diagnosis of system problems. The overall design will follow an object-oriented model; this maps well to components of the data-acquisition system. A modular design will be followed to allow easy integration of various detector components.

Higher level code will be written in an object-oriented language. Although C++ is perhaps the most obvious candidate, scripting languages including object-oriented extensions to tcl/tk [24] such as itcl [25] should give adequate performance for most high-level functions while being more straightforward to program. In addition the tk toolkit provides an easier way of generating graphical user interfaces than Motif or related C++ toolkits. Also under evaluation is the Java[26] language recently developed by Sun Microsystems. This is an object-oriented language that lacks many of the difficulties and pitfalls associated with C++. It includes class libraries for GUI generation and several networking protocols. Although currently not very mature, it is rapidly developing and shows some promise for this application. Lower-level code including all code residing in VME-based processors will be written in C. Fortran will not be used within the Run-Control system.

The calibration database developed for the offline system will also be used for storage of online calibration data. Other databases are required for various types of configuration information, and run summary information. No decision has yet been made on the implementation of any of these. Commercial relational and object-oriented databases will be evaluated. The dart information server (dis) [27] developed at Fermilab will be considered for configuration information. For some configuration information, flat files may be adequate.

Communication with the large number of front-end processors is an issue. For random access (diagnostics, monitoring), TCP/IP will be used. However state transitions such as begin-run initialization must be performed in parallel to minimize the time required. Hence some multicast protocol will be necessary. One existing package that may meet these requirements is the dart multicast services (dms) [27]. Other possibilities that will be evaluated are SNMP, CORBA event services, and the Network Data Delivery Service (NDDS) [28].

All source code will be maintained in a code management system such as the Concurrent Version System (CVS). As the requirements for code distribution are more relaxed than for the offline system, and the number of developers is much fewer, packages other than CVS that provide more functionality

will be considered. Versioning will be done for all component packages and the Run-Control package as a whole. An Integrated Developer Environment (IDE) will be used for development of at least the core portion of the system. These generally include a graphical debugger, editor, interface to the code management system, class browser, and automatic documentation extraction in an integrated package. CASE tools which aid in development of the overall system object model are also under evaluation.

11.7.2 Event Monitoring

A sample of events, which may or may not be destined for mass storage, is sent to monitoring processes from the data-logging system. The trigger type can be used by a monitor task to select a specific class of events, such as minimum-bias triggers. These processes look at per channel occupancies, energy flow, trigger rates, the trigger decision, etc. to assess whether the detector is functioning properly. Comparisons may be made to a set of template information. If discrepancies are found, then an alarm is signaled to the operator.

Also some events are used to provide course calibration constants for several systems such as drift velocities for the central tracking chamber. As these constants are determined, they are fed back for use by the Level-3 trigger algorithms. One such monitor task will reconstruct vertices using the SVX and relay information on the beam position to the accelerator control system.

The VMS based programs used for Run Ib will be converted to unix as well as be modified for the upgraded trigger and detector components. Those tasks requiring the largest rates will run on the same (multiprocessor) system as the data logger. Other monitors receive events via the local area network (FDDI, ethernet).

The general structure of the monitors follows that of offline analysis programs. This allows them to run either online, receiving data from Level 3, or offline, receiving data from disk or tape, without any changes to the code. Other offline standards regarding programming languages, histogramming packages, database access etc. will also be followed by these programs.

Most monitor programs will consist of an analysis portion that runs in a background mode storing histograms and other information in shared memory. Operators will then use a display program based on PAW, Histoscope or a successor to view this information. Summary information from each run may be archived. Programs that analyze data for calibration runs will be structured in a similar manner.

11.7.3 Hardware Configuration

A block diagram of the proposed hardware configuration is shown in Fig. 11.13. A series of unix workstations will be used for Run Control and Event Monitor functions. Workstations may be used interchangeably for either. Additional workstations will be used for program development. X-window terminals will be used for auxiliary displays as well as for program development. A central file server provides storage for code, databases, monitor archive, and program development facilities for remote users. A local area network consisting of ethernet and FDDI interconnects the file server, workstations, and processors in the Data-Acquisition system. There will be a high speed connection to the offline computing systems at the Feynmann Computer Center. Routers to isolate portions of the network from external traffic and switches to improve performance will be used as needed.

The computing system will be configured for reliability so as to be able to operate in case of the failure of single components. Workstations and displays are interchangeable so the failure of one does not affect operation. Disk files critical to operation will be stored in RAID arrays. These will be attachable to multiple CPUs so the files should always be accessible. Operation will be possible without a general network link outside of the experimental area. Internal networking will be configured to minimize the single points of failure.

All code will be as platform independent as practical. However there will be some limitations. Workstations used for Event Monitor tasks must be supported by the offline system. Third-party support particularly in the area of VxWorks host software also restricts the range of allowable platforms. Currently supported platforms for Run-Control related functions include Silicon Graphics (IRIX) and Sun (Solaris). It is expected that these choices will evolve. The progress of Windows-NT will be followed and this platform may be supported if deemed appropriate.

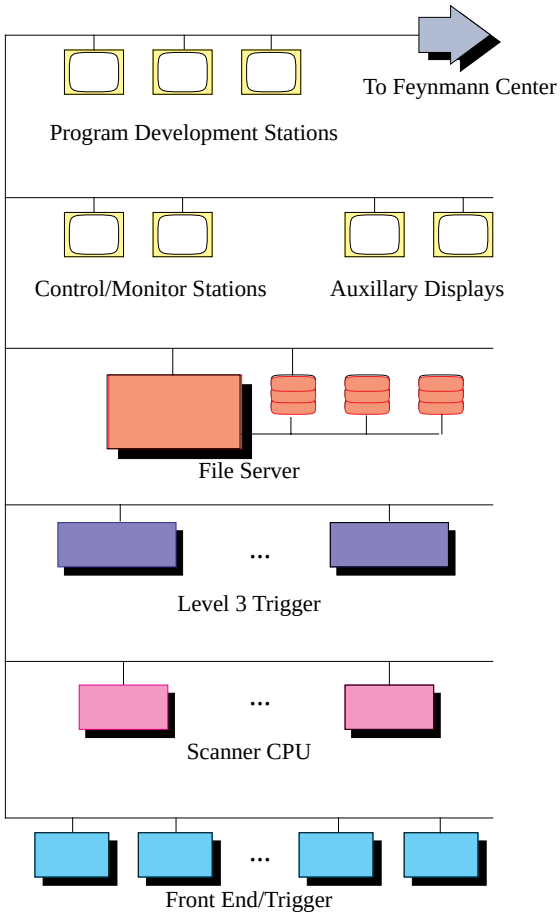

Figure 11.13: A schematic of the Online Computing system. In the actual implementation, the local-area network will be segmented using routers and switches that are not shown.

11.7.4 CDF ALARMS

CDF contains about 20 different detector systems. The Alarms, Limits and Remote Monitoring System (ALARMS), provides the interface between the on-shift personnel and control and monitoring of the detector systems. CDF ALARMS is a fully integrated node on the accelerator-wide network, ACNET, and allows the monitoring of the accelerator status at the beginning and during beam stores as well. ALARMS data is not part of the normal event data stream. There are three primary functions of the CDF ALARMS system: high-voltage control, online monitoring, and data logging. A brief comment on each is given below:

- CDF ALARMS is the primary mode of High Voltage Control and online status display for detector systems. The High Voltage Control function can be used to set individual detector channels, segments of a certain detector system, or an entire detector system.

- CDF ALARMS provides online monitoring and display of the HV status (on, off, or standby), the status of low-voltage power, temperatures, and the detector systems.

- Data-logging and time plots for luminosity and various detector functions are also plotted on the CDF ALARMS consoles.

The CDF control room contains three ACNET Consoles (Fig 11.14) and two dedicated monitors for displaying detector status. The Consoles are presently VAX workstations running the VAX/VMS operating system. Any X-station can run the ALARMS program and display the various plots pertaining to detector status. The heart of the monitoring system are two "i386" Front-End processors that continuously monitor the detector from the first floor of the B0 assembly building. The ACNET consoles communicate with the Front-End processors via ethernet, and the Front-End processors communicate with the Central Database and Operations VAX via ethernet as well. They also communicate with a series of IBM-compatible PCs that control high voltage for all wire-chamber systems.

CDF displays three types of Alarms: normal, ignored, and severe. Severe alarms require immediate action and are triggered if crucial channels are out of tolerance. Data taking is stopped and cannot resume until the problem is fixed; severe alarms are announced by DECTALK as they appear. Normal alarms indicate a channel that may have drifted out of tolerance, but data taking can continue. However if a large number of normal alarms appear, then a severe alarm is set, and data taking is inhibited. Ignored alarms allow the shift personnel to be reminded that a number of problems do exist but that these can be fixed later. Normal alarms can be ignored by clicking on the alarm. Severe alarms cannot be ignored.

Information may be exchanged between the ALARMS and data-acquisition control systems in several ways. At begin run, the ALARMS system accesses the daq-system configuration database to

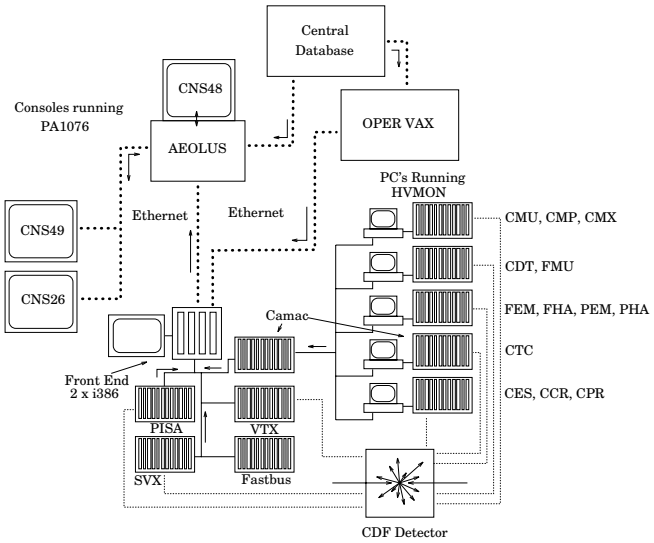

Figure 11.14: A schematic of the CDF ALARMS system as configured for Run Ib showing the consoles, Front End, and control of the detector systems.

record high-voltage settings and other detector information. Alarms encountered during the run are similarly recorded. In a few cases some ALARMS hardware is duplicated in the daq system allowing information such as the solenoid magnetic field to appear in the data stream for each event. Should a high-voltage trip condition be encountered, a signal is provided to the trigger system to inhibit the generation of Level-1 accepts. And finally, a software interface is available from the Computing Division to allow a DAQ process to exchange information with ACNET. This will be used, for example, to send to ACNET the beam position as measured by SVX tracks reconstructed online.

The CDF ALARMS system has been running successfully now for several years. No major upgrades are planned for ALARMS. Substantial work will be required to install the new detector systems into ALARMS for Run-II. The collaboration will continue to use the system through Run II.

Bibliography

[1] P. Chang, V. Papadimitriou, "Specifications for Calorimeter Front-end Electronics", CDF note CDF/DOC/CALORIMETRY/CDFR/3646.

[2] R.J.Yarema et. al., *A Fast, Wide Range Charge Integrator and Encoder ASIC for Photomultiplier Tubes*, IEEE Trans. on Nuclear Science, **Vol 4** (August 1993), pp. 750-752.

R.J.Yarema et. al., *A High Speed, Wide Dynamic Range Digitizer Circuit for Photomultiplier Tubes*, Presented at the 6'th Pisa Meeting on Advanced Detectors, (22-28 May, 1994) La Biodola, Isola d'Elba, Italy.

[3] V. Papadimitriou, "Calorimeter TDCs for Run II and Beyond", CDF note 2209.

[4] Many operational details are given in the description of the earlier SVX2 chip: "A Beginner's Guide to the SVX2," Ray Yarema, *et. al.,* FERMILAB-TM-1892, 1994.

[5] The current SVX3 specifications are contained in "Device Specifications for the SVX3 Chip Set," Raimund Strohmer and Walter Knopf, http://www-ese.fnal.gov/eseproj/svx/svx3/svx3spec.html.

[6] S. R. Amendolia et al., "IFT Upgrade Project: Readout System Overview"

[7] J. Patrick *et. al.*, "The CDF Ultranet Based Data Acquisition System", Proc. Conf. Comp. High Energy Phys. (1994).

[8] VME International Standards Organization, Scottsdale, AZ

[9] VME-P Committee, VITA 1.X-199X.

[10] Wind River Systems, Alameda, CA.

[11] C. Rotolo *et. al.* Proc. IEEE Nucl. Sci. Symp. (1991).

[12] PCI standard v2.1, PCI Special Interest Group and PCI Mezzanine Card (PCM) standard, IEEE 1386.

[13] ATM Standard, Internation Telegraph and Telephone Consultive Committee.

[14] ANSI Standard X3T9.3/91-071, Fibre Channel Association, Austin TX.

[15] HIPPI, ANSI Standard X3T9.3/91-005 and Serial HIPPI, Rev 2.2, Serial HIPPI Implementors Group.

[16] Fore Systems Inc., Pittsburgh PA.

[17] Proc. First Int. Data Acquisition Conf., Fermilab (1994).

[18] Systran Inc., Dayton OH.

[19] FC-AL, ANSI X3T11, Fibre Channel Association, Austin TX.

[20] International Business Machines, Kingston, NY.

[21] Apple Computer, Cupertino, CA.

[22] Quantum Corp., Milpitas CA.

[23] StorageTek, Boulder CO.

[24] J. Ousterhout, "Tcl and the Tk Toolkit", Addison Wesley.

[25] M. McLennan, "The New itcl", Proc. 1995 Tcl/Tk Workshop.

[26] Sun Microsystems Inc., Sunnyvale, CA.

[27] G. Oleyik *et. al.*, "Fermilab DART Run Control", Proc. IEEE Real Time Conference (1995).

[28] Real-time Innovations, Sunnyvale, CA.

Chapter 12

Trigger

12.1 Overview

The trigger plays an important role in hadron collider experiments because the collision rate is much higher than the rate at which data can be stored on tape. In run II the collision rate will be effectively equal to the crossing rate of 7.6 MHz while the tape writing speed will be less than 50Hz. The role of the trigger is to efficiently extract the most interesting physics events from the large number of minimum bias events. For example, the total $t\bar{t}$ cross section is approximately nine orders of magnitude smaller than the minimum bias cross section.

Due to changes in the detector and the accelerator the entire trigger system used in run 1 must be replaced for run II. The primary reason for replacing the trigger electronics along with all CDF front-end electronics, is the reduction in the accelerator bunch spacing from 3.5μsec to $132 - 396$nsec. In the past, trigger signals from the calorimeters were sent to the control room, where they were processed, with the trigger decision sent back to the detector before the next beam crossing. As a result, the data from only one crossing needed to be stored on the detector. In run II there will not be enough time to send detector signals to the control room between bunch crossings, let alone make a trigger decision and distribute it back to the detector. In addition most of the old trigger is incompatible with new or upgraded detector elements.

In run 1b, the trigger had to reduce the raw collision rate by a factor of 10^5 to reach the tape writing speed of < 10 Hz. In run II, the conditions will be more challenging as the luminosity will increase by an order of magnitude, but the rate of data written to tape will only increase by a factor of 3 to 5. This will require the trigger to have a larger rejection factor while maintaining high efficiency for the broad range of physics topics we study.

The CDF trigger system has a three level architecture with each level providing a rate reduction sufficient to allow for processing in the next level with minimal deadtime. Level-1 uses custom designed hardware to find physics objects based on a subset of the detector information and makes a decision based on simple counting of these objects (e.g. one 12 GeV electron or two 1.5 GeV muons). The Level-2 trigger uses custom hardware to do a limited event reconstruction which can be processed in programmable processors. The Level-3 trigger uses the full detector resolutions to fully reconstruct events in a processor farm.

Figure 11.1 is a functional block diagram of the three level pipelined and buffered trigger system. To allow time for transmission and processing of the trigger signals to make the trigger decision, we have selected a 5.5 μsec Level-1 latency. This requires each detector element to have local data buffering for the 42 beam crossings (at 132 nsec separation) that occur during the latency period.

If an event is accepted by the Level-1 trigger, the front-end electronics move the data to one of four onboard Level-2 buffers. This is sufficient to average out the rate fluctuations and allow a 40 kHz Level-1 accept rate with $\leq 10\%$ deadtime for the anticipated 20 μsec Level-2 processing time. The data acquisition system will allow the Level-2 trigger to accept as many as 300 events per second. These are transferred to the Level-3 trigger processor farm where the events are reconstructed and filtered using the complete event data, with ≤ 50 Hz written to permanent storage. The custom Level-1 and Level-2 trigger hardware is described in this chapter while the Level-3 trigger is described in Chapter 11.

Both the Level-1 and Level-2 trigger systems will be provided with detector information not available

in the respective run 1 systems. These enhanced capabilities are required to provide the rejection power needed for run II while significantly expanding the triggers physics potential. The most significant change for Level 1 is the addition of track finding. Previously available only at Level 2, tracks in the outer tracking chamber will be reconstructed within 2.7 μsec after a $\bar{p}p$ collision. This allows a track to be matched to an electromagnetic-calorimeter cluster for improved electron identification, a track to be matched to a stub in the muon system for better muon identification and momentum resolution, and tracks to be used alone for triggers such as $B^0 \to \pi^+\pi^-$.

The most significant addition to the Level-2 trigger is the Silicon Vertex Tracker (SVT) which will more fully exploit the physics potential of the high precision silicon vertex detector. A major effort has been made to build this system that, for the first time in a hadron-collider experiment, can trigger on secondary vertices. This will make accessible a large number of important processes involving hadronic decay of b-quarks outlined in section 2.6. In addition, the SVT provides improved momentum resolution for tracks and finer angular matching between muon stubs and central tracks.

The block diagram for the run-II trigger system is presented in Fig. 12.1. The input to the Level-1 hardware comes from the calorimeters, tracking chamber, and muon detectors. The decision to retain an event for further processing is based on the number and energies of electron, muon, and jet candidates, as well as the $\not\!\!E_T$ in the event. A Level-1 accept can also be generated based on the kinematic properties of observed track pairs.

Events accepted by the Level-1 system are processed by the Level-2 hardware. All of the information used in the Level-1 decision is available to the Level-2 system, but with higher precision. In addition, data from the central calorimeter shower-max detector allows improved identification of electrons and photons. Jet reconstruction is provided by the Level-2 cluster finder; secondary-vertex information is produced by the SVT. A Level-2 accept initiates full detector readout for the event. An extension of the Level-2 system to include tracking in the $1 < |\eta| < 2$ region using the Intermediate Silicon Layers is under consideration.

The Trigger System Interface (TSI) and Clock systems which synchronize the trigger and DAQ systems are described in sections 11.6.3 and 11.6.4. All subsystems of the Level-1 and Level-2 triggers use the VME hardware and protocols described in section 11.6.

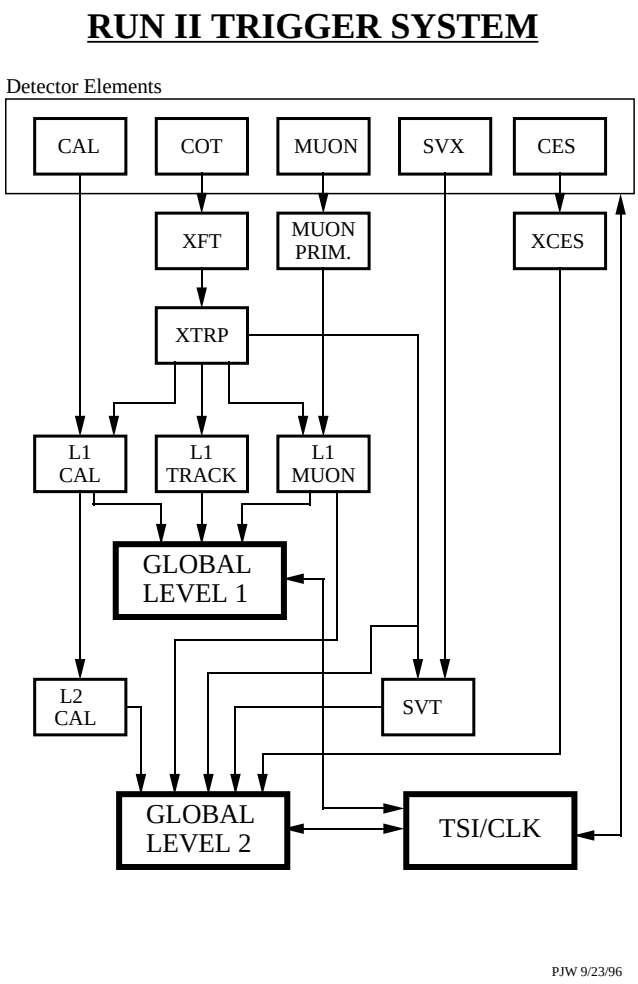

Figure 12.1: The run-II trigger-system block diagram.

12.2 Level 1 Trigger hardware

The Level-1 hardware consists of three parallel synchronous processing streams which feed inputs of the single Global Level-1 decision unit. One stream finds calorimeter based objects (L1CAL), another finds muons (MUOM PRIM-L1MUON) while the third finds tracks in the central tracking chamber (XFT-XTRP-L1 TRACK). Since the muon and electron triggers require the presence of a track pointing at the corresponding outer detector element, the tracks must be sent to the calorimeter and muon streams as well as the track only stream. Up to 64 different

triggers can be formed using simple ANDs and ORs of objects from these streams.

All elements of the Level-1 trigger are synchronized to the same 132nsec clock with a decision made every 132nsec by Global Level-1. During abort gaps events are automatically rejected. When the accelerator is operating in 36 bunch mode (396nsec), the trigger will be clocked every 132nsec with the two intermediate clock cycles rejected automatically.

12.2.1 Level 1 calorimeter hardware (L1CAL)

The goal of the Level-1 (L1) calorimeter trigger is to trigger on electrons, photons, jets, total event transverse energy (ΣE_T) and missing transverse energy ($\not\!\!E_T$). The calorimeter triggers are divided into two types: object triggers (electrons, photons and jets) and global triggers ($\sum E_T$ and $\not\!\!E_T$). The object triggers are formed by applying thresholds to individual calorimeter trigger towers, while thresholds for the global triggers are applied after summing energies from all towers. In turn, the object triggers are of two types: single object triggers (e.g. electrons from $W \rightarrow e\nu$) where finding one in the event is sufficient to generate a L1 accept, and di-object triggers where the rate is too high to trigger on only one (e.g. electrons from $J/\psi \rightarrow ee$).

Through each board of the trigger, there are two parallel paths: one for the object triggers and one for the global triggers. In the object trigger path, thresholds are applied to the individual tower energies, then the number of towers passing each threshold is counted. For the single-object triggers, this is a 1-bit sum (0, $\geq$ 1 towers) and for the di-object triggers it is a 2-bit sum (0, 1, 2, $\geq$ 3 towers). Electron and photon triggers are formed by applying energy thresholds to the electromagnetic (EM) energy in a tower, while jet triggers are formed using the total (EM + HAD) energy in a tower. To reduce the low-E_T electron trigger rate, tracks from the Level-1 track processor (XFT) are available for matching to the tower, and towers with significant HAD energy can be rejected. The global path sums the total energy (HAD+EM) in all the towers (with appropriate weighting for the $\not\!\!E_T$ calculation) and applies thresholds to these sums.

A total of 16 object-trigger bits are available for use by all single and di-object triggers. The default system configuration parses the 16 bits into 10 single-object triggers and 3 di-object triggers. There is a limited capability to reconfigure the bit usage to allow for more or fewer di-object triggers. There is also flexibility in how many can be electron/photon and how many jet, with a limitation of no more than 8 of either kind. A total of 4 thresholds are available for the global triggers: 2 for $\sum E_T$ triggers and 2 for $\not\!\!E_T$ triggers. The result is a 20-bit word presented to the final Level-1 decision card to summarize the calorimeter triggers.

12.2.1.1 Data Flow

The data flow in the calorimeter trigger is shown in Fig. 12.2. The digitized calorimeter data are summed into trigger-tower energies and weighted by $\sin\theta$ on the front-end (ADMEM) cards to produce E_T. Studies of Level-1 trigger rates for Run II[1, 2] indicate that the tower segmentation of the original CDF trigger provides acceptable rates. The existing segmentation[3] of the central and wall calorimeters, with towers of approximately $\Delta\eta = 0.2 \times \Delta\phi = 15^\circ$, is carried into the new plug calorimeter, resulting in a 24×24 map in $\eta - \phi$ space. The tower at highest η on either side of the detector covers $2.6 < |\eta| < 3.6$. The same segmentation is used for the hadronic and electromagnetic calorimeters.

The data are transmitted upstairs to the trigger as 10-bit parallel words, with a least count of 125 MeV and a full scale E_T of 128 GeV[4], on SCSI-type cable consisting of 10 twisted pairs.

The data are processed in 6 L1CAL crates with final global sums and trigger summaries made in the Global L1 crate. The data are forwarded from the L1CAL system to the Level-2 cluster finder (L2CAL) for use after a L1 accept.

A more detailed view of the L1CAL pipelines is presented in Fig. 12.3. The whole L1 system is pipelined with each stage taking less than 132 ns and processing a new event every 132 ns. The bulk of the L1 processing takes place on 16 Digital Information Receive And Compare(DIRAC) boards in each of 6 L1CAL VME crates. The DIRAC boards are arranged in sets of four, handling the data from a full-rapidity, $\Delta\phi = 15^\circ$ wedge of the calorimeter: West Plug, West Central, East Plug and East Central. Each DIRAC card has 12 channels covering 6 EM towers and the 6 corresponding HAD towers. The central cards each cover 5 towers in the central and the first tower in the plug, reaching $\eta = \pm 1.3$. Each

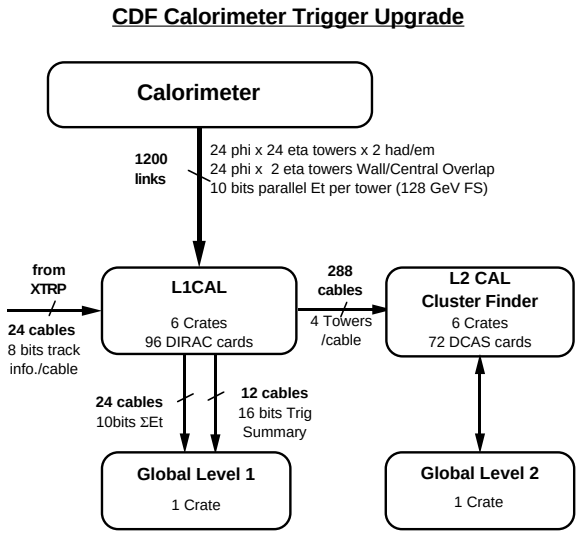

Figure 12.2: Overview of the calorimeter-trigger data flow.

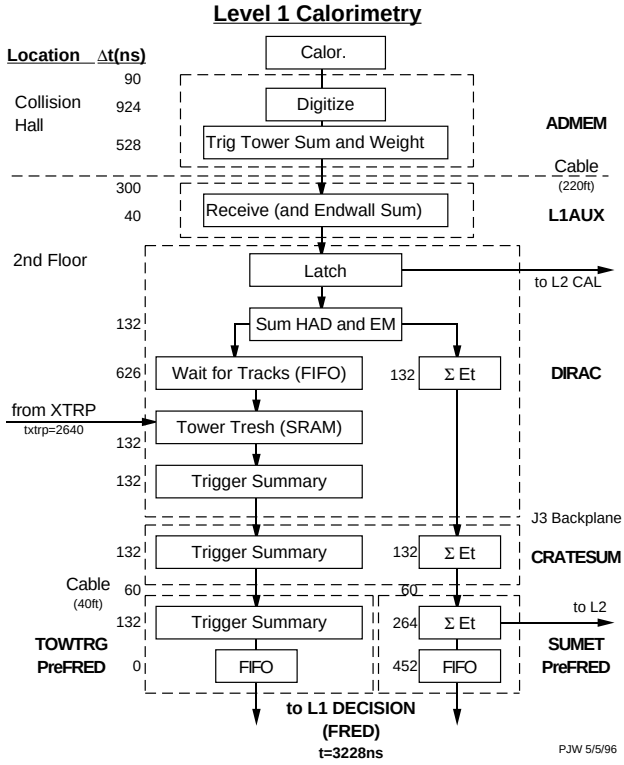

Figure 12.3: Block diagram of the Level-1 calorimeter trigger. The dashed outlines indicate different cards in the L1 CAL system. An estimate of the elapsed time for each block is also shown.

DIRAC card is mated through the P3 connector with a 9U X 120mm VME auxiliary (L1AUX) board which receives the input signals for that DIRAC card. Since there is an overlap of one hadron tower between the Central and Wall calorimeters (trigger tower 3), the central L1AUX cards have 13 input towers and sum together the overlapping towers.

Combining the information from the 96 DIRAC boards is a two-step process involving a pair of CRATESUM boards in each L1CAL crate and 3 PreFRED modules in the GLOBAL L1 crate. The CRATESUM boards summarize results from 8 DIRAC boards (2 wedges).

12.2.1.2 DIRAC Card

The DIRAC board truncates the calorimeter tower energy to 8 bits, time aligns it with track information coming from the XFT, and makes triggers by requiring the tower energy to pass programmable thresholds and optionally matching a track to the tower. A summary of how many towers passed each threshold is then made. Simultaneously the E_T sum for all towers on the board is calculated.

At the beginning of the first stage of DIRAC, data from each of the 12 channels are latched. At this point any of the towers can be masked off to block bad channels from both L1 and L2. There are 4 outputs of the first processing stage:

1. 8 bits of EM tower energy (250 MeV LSB, 64 GeV FS),
2. 8 bits of total (EM + HAD) tower energy (250 MeV LSB, 64 GeV FS),
3. the 3 least significant bits of HAD energy (for HAD/EM in electron/photon triggers),
4. 10 bits of HAD and 10 bits of EM (after masking) to L2 cluster finder.

The first three items are fed into an alignment FIFO to wait for data from the track processor. As shown in Fig. 12.3, in normal operation calorimeter data will spend approximately 4-5 crossings in this FIFO. The total energy is also sent directly into a set of summers to form ΣE_T for the board.

The two central DIRAC cards receive an 8-bit word from the Extrapolation (XTRP) boards describing the highest P_T XFT track pointing at the wedge. This input is also provided on the plug cards in case high η tracks can be provided in the future. The eight bits are envisaged to include 6 bits of P_T, 1 bit for

track isolation, and 1 bit to flag $|\eta| > 1$. Track P_T thresholds are applied, and 3 bits are fanned-out to the 6 trigger towers.

The tower threshold cuts and track P_T cuts are performed in two 32k-byte SRAMs per tower, one for jet triggers and one for electromagnetic triggers. The inputs to the jet-trigger SRAM are 8 bits of Total energy and 3 bits of track information. The SRAM for electrons and photons receives 8 bits of EM energy and 3 bits of track data and the 3 least significant bits of HAD energy for HAD/EM. Each of these SRAMs has an 8-bit output corresponding to the 8 possible triggers (combination of threshold(s) and track condition). For example, a low-E_T electron trigger might consist of a tower over 3 GeV of energy, a track with P_T greater than 3.0 GeV/c, and no more than 250 MeV of HAD energy. Note that the cuts for a particular trigger could be different for different regions of η since each tower has its own SRAM.

The next DIRAC stage summarizes how many towers passed each of the thresholds on the board. The single-object triggers are ORed together and the di-object triggers are summed. The 16 bit summary is transmitted to the CRATESUM card using 16 dedicated lines on the J3 backplane. The allocation of these bits among EM and Jet is programmable, as is the number of di-object triggers.

In parallel with the tower trigger logic, there is a series of adders which calculates the total ΣE_T for the board. The input to these adders is the 8-bit sum of HAD+EM energy for each of the 6 towers. A tower is only included in the sum if its energy is above a programmable threshold, to reduce sensitivity to multiple interactions. The output is an 8-bit word that is transmitted on the J3 backplane to the CRATESUM card.

The tower-trigger and ΣE_T outputs are not time aligned; the data for the ΣE_T path leaves DIRAC several crossings before the triggered tower data. The data is treated this way since the processing of the ΣE_T data requires more pipeline stages in the CRATESUM and PreFRED cards. As shown in Fig. 12.2 mismatches in timing between paths are corrected using FIFOs at the end of processing on the PreFRED modules. In fact all PreFRED modules have FIFOs to ensure that the data presented to FRED is correctly aligned.

12.2.1.3 Crate Summary Card

The Level-1 Crate Summary card (CRATESUM) receives the 16 bits of trigger data and 8 bits of ΣE_T data from each of 8 DIRAC cards. The trigger data are summarized into one 16-bit word in the same fashion as on DIRAC. This summary from each CRATESUM is transmitted differentially over twisted pair cable to the TOWTRG PreFRED module in the GLOBAL Level-1 Crate. This PreFRED card combines trigger bits from all 12 CRATESUM cards into the final 16-bit summary of the tower triggers which is put into a FIFO to align it with the bits from other parts of the trigger system. These 16 bits are sent via the J3 backplane to the L1 Decision card (FRED).

In an independent pipeline, CRATESUM forms the ΣE_T for each of the 2 wedges covered by its 8 DIRAC cards. The 10 bit summary for each wedge is transmitted over twisted-pair cable to the SUMET PreFRED module in the GLOBAL Level-1 Crate. The SUMET PreFRED receives the ΣE_T word from all 24 wedges (12 CRATESUMS) and calculates the total ΣE_T and $\not\!\!E_T$. For the $\not\!\!E_T$ calculation, each of the $\sum E_T$ words received from the CRATESUMs is weighted by $\cos\phi$ and $\sin\phi$ for the corresponding wedge to form ΣE_{Tx} and ΣE_{Ty} from which $\not\!\!E_T{}^2$ is calculated. Thresholds are then applied, two for ΣE_T and two for $\not\!\!E_T$. The four $\Sigma E_T/\not\!\!E_T$ bits are aligned using a FIFO and sent via the J3 backplane to FRED. The calculated ΣE_T and $\not\!\!E_T$ are stored in L1 FIFOs and are transmitted to the L2 processors after a L1 accept for use in the L2 decision.

The DIRAC, CRATESUM and PreFRED cards are all 9U x 400mm VME cards [5]. These cards are addressable through VME to download thresholds and to read out trigger information [5] into the event data stream. There are also registers that can be loaded or read back through VME for diagnostic purposes.

12.3 The eXtremely Fast Tracker (XFT)

During Run I, CDF used an online track processor (the CFT) to identify high-momentum charged tracks in the Central Tracking Chamber (CTC). The tracks found were linked with clusters in the EM calorimeter and muon stubs in the muon chambers to identify electron and muon candidates. These were then used

in the Level-2 trigger decision.

Since the CTC will be replaced by the COT for Run II, the CFT will also need to be replaced. In addition, the change in bunch timing for Run II (396 or 132 nsec) implies that this replacement must be pipelined. This new device, the XFT (eXtremely Fast Tracker), will be highly parallel and will process the data from each bunch crossing. The tracking results from the XFT will be available in time to be used in the Level-1 trigger decision.

The minimum design specifications for the XFT are set by the requirement that it perform at least as well as the CFT. The design specifications are:

- The track-finding efficiency will be greater than 96% when the single-hit efficiency of the central tracker is greater than 92%.
- The momentum resolution reported to the trigger will be $\Delta P_T/P_T^2 < 2\%$.
- The resolution on ϕ_0 will be better than 6 mrad.
- The fake-track rejection will be at least twice as good as the CFT.
- The minimum track P_T will be 1.5 GeV/c.

The goal of high track efficiency is set by the desire to be efficient for high-P_T physics. Good momentum resolution is a requirement for the high-P_T muon triggers where the primary handle on rate, after matching with muon chamber stubs, is the track momentum in the central tracker. The improved fake-track rejection is also needed to reduce the high-P_T muon trigger rate at high luminosity. The lower P_T cutoff is set by the desire to maximize the acceptance for B decays that can be used, for example, to measure CP violation. The resolution on ϕ_0 is set by the requirement that XFT tracks will be used as the seed for the SVT at Level 2.

12.3.1 Algorithm Description

A block diagram of the XFT is shown in Fig. 12.4. The processor works off of hit data from the 4 axial layers of the COT. There are a total of 16,128 axial wires, and the data on each wire is classified as prompt and/or delayed, for a total of 32,356 bits of information. The definition of prompt or delayed will depend upon the maximum drift in the COT. Assuming that this maximum is $\sim$ 100 nsec, a prompt hit occurs whenever there is a hit in the time window

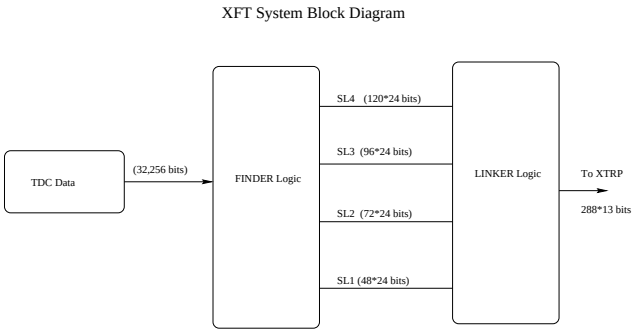

Figure 12.4: Block diagram of the XFT trigger.

0-33 nsec, and a delayed hit is defined as a hit falling in the window 33-100 nsec.

Track identification is accomplished in two processes, the Finder and the Linker. The Finder searches for high-P_T track segments in each of the outer-four axial superlayers of the Central Tracker. Each found segment is characterized by a mean-ϕ position in the axial superlayer. The Linker searches for a four-out-of-four match among segments in the 4 layers, consistent with a prompt high-P_T track. An example of a track traversing the COT is shown in Fig. 12.5.

A block diagram of the Finder logic is shown in Fig. 12.6. TDC information is brought from the detector to the XFT on Ansley cables. These cables can carry up to 24 signal pairs. The TDC data is multiplexed 4:1, such that prompt and delayed hit information for 4 neighboring COT cells comes in on a single cable. The Finder is designed to look for valid track segments in each of these 4 cells. A track segment is then defined by the cell it traverses for each of the 12 wire planes in a superlayer, and whether it generated a prompt or delayed hit. A collection of the cell numbers and hit types for the 12 wires in an axial superlayer is called a mask. The mask will change depending on the ϕ of the track, and its angle through the cell (or P_T). The finder works by storing

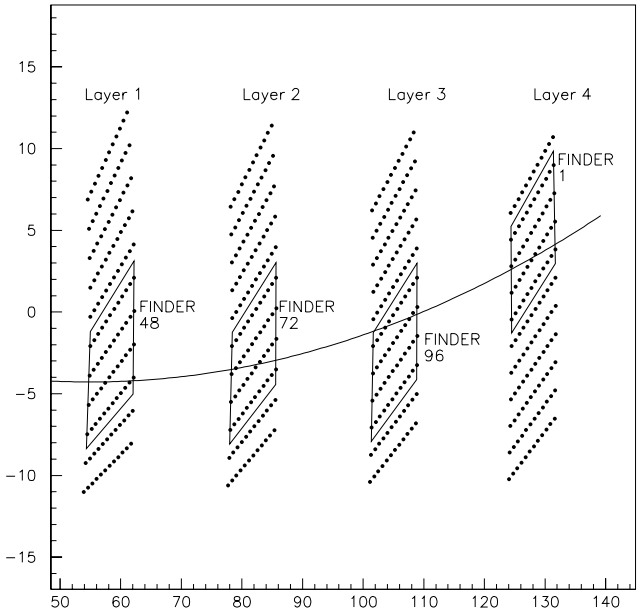

Figure 12.5: A close up view of a track in the COT. All cells in all four axial layers are shown. The relevant Finder in each layer is highlighted.

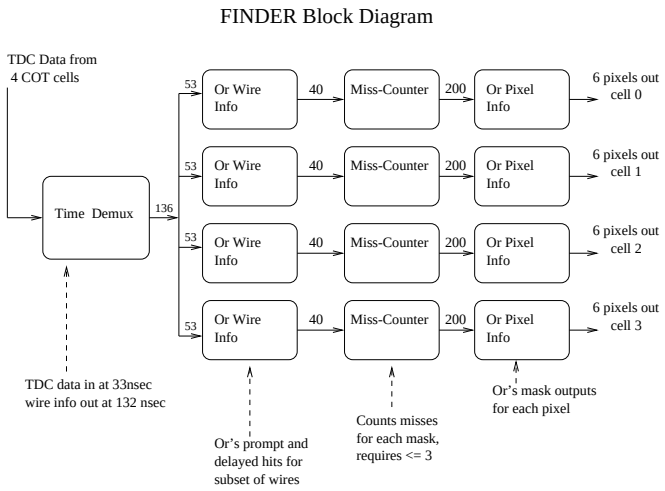

Figure 12.6: Logic flow for the Finder part of the XFT trigger.

all possible masks for tracks with $P_T \geq 1.5$ GeV/c in a database (or equivalently, hard wired on a chip). To keep the total number of masks relatively low, the prompt and delayed bits are "or"ed together on a subset of the wires. The finder compares incoming TDC information with all masks for the given axial superlayer, allowing a programmable (up to 3) number of missed wire planes. Every 132nsec, the finder outputs 24 bits per cell (6 pixels for each of the 4 possible cells) to the linker.

Since all of the cells in a given layer are identical, only one set of masks is needed for each layer. At present it is planned to perform the finding for 4 adjacent cells in one Finder. There will be only one set of masks stored, and the inputs from the 4 separate cells will be multiplexed one at a time. The masks required for each of the superlayers is slightly different, so there will be a separate Finder design for each superlayer.

A block diagram of the Linker logic is shown in Fig. 12.7. Each Linker is given all of the pixel information from the Finders needed to find the tracks in a $\Delta\phi = 1.25°$ phi-slice of the tracking chamber. The Linker begins by searching (in parallel) a list of about 1300 roads, where a road is a group of 4 pixels, one from each axial superlayer, corresponding to a valid track with $P_T \geq 1.5$ GeV/c. The roads are defined by their P_T and the pixel position in layer 3. The roads are then "or"ed down to 128 P_T bins and 8 pixel locations. Found tracks are passed through a priority encoder to find the highest-P_T track in each ϕ bin. Finally, all ϕ bins in a Linker are combined and the highest-P_T track in the 1.25° region covered by the Linker is identified.

12.3.2 Algorithm Simulation

A software simulation of the XFT algorithm has been developed using FORTRAN. This simulation models the COT geometry, the expected pulse width ($\sim$ 40nsec) of hits in the COT, and the occupancy expected under Run II conditions. We assume 132 nsec bunch spacing. The simulation was run on a data sample from Run I. This data sample was collected requiring a muon stub as defined at the trigger level. To simulate the performance under Run II conditions, additional hit data from minimum bias events from Monte Carlo are added, so that the effective luminosity of this sample can be dialed from 2×10^{32} cm^{-2}sec^{-1} to 10×10^{32} cm^{-2}sec^{-1} (at 132nsec bunch spacing). The number of Finder masks used for the simulation is approximately 200 per super-

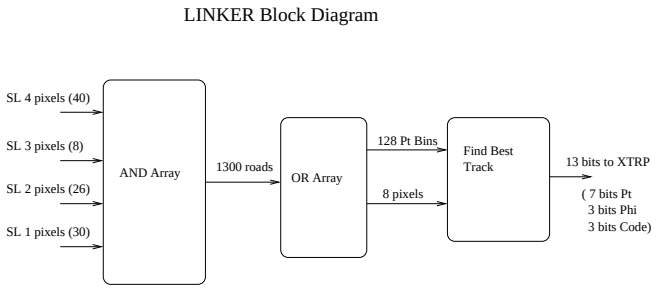

Figure 12.7: Logic flow for the Linker part of the XFT trigger.

layer, and both the Finder masks and the Linker roads are specified using a database.

To assess the expected performance of the XFT, we study the following benchmarks:

- Track finding efficiency,
- Momentum resolution,
- ϕ_0 resolution,
- Muon trigger rate vs P_T,
- Fake track rate vs P_T.

These are studied at a luminosity of 2×10^{32} cm^{-2}sec^{-1} at 132nsec bunch spacing. The performance is dependent upon the wire efficiency of the COT. The lower the true chamber efficiency, the more misses the Finder needs to allow to attain high segment finding efficiency. Unfortunately, the performance degrades the more misses are allowed. We study the performance at a wire efficiency of 92% and 99%. For these two cases, the number of misses allowed is 3 and 1 respectively.

We begin by studying the track finding efficiency. First we determine which of the muon triggers are associate with a real track with $P_T^{offline} \geq 1.5\ GeV/c$, as determined by our standard offline algorithm. Of this sample, the percentage found by the XFT is (96.5 ± 0.7)%.

The momentum resolution is defined as $(P_T^{Offline} - P_T^{XFT})/(P_T^{Offline})^2$ where $P_T^{Offline}$ is the momentum using our offline tracking algorithm and P_T^{XFT} is the momentum returned by the XFT. To calculate the ϕ_0 resolution, we use the P_T and pixel position at the third layer, and extrapolate the track to the origin (assuming a beam constraint). This gives an estimate of the ϕ_0 of the track and can be compared with ϕ_0^{true} of the track. In Fig. 12.8 we show the momentum and ϕ_0 resolution obtained in the simulation, for the two different wire efficiencies. We observe a momentum resolution of 1.0-1.2%$/GeV/c$ and a ϕ_0 resolution of 2.5-3.5mRadians, which are well within our specifications.

We next examine muon trigger rates. A muon trigger at Level 1 (for Run II) is defined as a muon stub match with an XFT track. A muon stub is defined as a pattern of hits in the muon chambers consistent with the passage of a charged particle. Matching is done by extrapolating XFT tracks to the muon chambers and looking for the presence of a muon stub within 5°. This will overestimate the true rate since in run II the matching requirement will be 2.5°. To calculate the muon trigger rates, we assume a muon stub cross section of 10 μb (measured in from run 1 data). We use the simulation to determine what fraction of XFT tracks match with muon triggers. We then increase expected rate by a factor of 1.3 for increased coverage expected for the muon chambers for Run II. In Fig. 12.9 we show the muon trigger rate vs the XFT P_T threshold imposed. This is the rate expected at a luminosity of 2×10^{32} cm^{-2}sec^{-1}, 132nsec bunch spacing. For a P_T threshold of 10 GeV/c the rate is approximately 30 Hz. This is clearly well within the Level 1 budget of 50 Khz, but more importantly is also well under the Level 2 budget of 300 Hz. Recall that there is very little to reduce the muon rate at Level 2 besides increasing the threshold.

Finally, each XFT track is classified as either fake or real, by comparing with the list of tracks found by our standard offline algorithm. The XFT track is required to match an offline track to within 1 pixel at 3 of the 4 layers to be considered as a real track, otherwise it is classified as fake. In the bottom plot of Fig. 12.9 we show the fraction of muon triggers which are caused by fake XFT tracks. This is is quite low, and there is little evidence of any growth vs P_T threshold. A comparison of XFT specifications vs a full simulation of the conceptual design is shown in Table 12.1.

	Specification	Simulation
Track finding efficiency	$\geq 96\%$	96%
Momentum resolution	$\leq 2.0\%/GeV/c$	$1.1\%/GeV/c$
ϕ_0 resolution	$\leq$ 8mR	3.0mR
μ Trigger rate (@10 GeV/c)	$\leq$ 50 Hz	30 Hz
Fake Fraction (@10 GeV/c)	$\leq 50\%$	$\leq 10\%$

Table 12.1: Comparison of XFT specifications vs results obtained from simulation. The luminosity used in the simulation is 2×10^{32} cm^{-2}sec^{-1} at 132nsec bunch spacing.

12.3.3 Algorithm Implementation

As mentioned above, we plan to use the existing cable plant to drive trigger information from the TDC's mounted on the endwall of the detector to the XFT located in the first floor counting room. Since the Ansley cables can carry 24 signal wires, and we plan on 4:1 multiplexing in 132nsec, each Ansley covers 4 adjacent COT cells.

The Finders will also cover 4 adjacent COT cells. This reduces the total chip count for the Finders, but is dependent on how fast we can run the Finder chips, and how many masks can be stored on a single chip. This setup matches the inputs of one Finder to one Ansley cable, However, since the COT cells are tilted with respect to the radial, each Finder will also need neighbor wires, from either side of the set of 4 cells.

We are pursuing implementation of the Finder using field programmable gate arrays (FPGAs). The great advantage of these devices is the ability to reprogram them in-situ. The EPF10K50 series from Altera Corp meets our needs in terms of the available logic gates, I/O pins, and speed. We have implemented about 90% of the design shown in Fig. 12.6 using Altera design software. This preliminary work indicates that we can fit about 250 masks, running 4 cells serially in a single Finder, in 132 nsec. This indicates that we will need to "or" some subset of wires in the two outer axial layers to fit them in the 10K50 chips. Another possibility is increasing the total number of Finders used for the outer two layers. This approach is under consideration. Note that the performance of the system using a maximum of 200 masks per layer is excellent. The total number of Finders needed is 336.

We also plan to implement the Linker using Altera FPGAs. As mentioned above, the Linker contains approximately 1300 roads. The automatic place and route software indicates that this design will fit into a much smaller device than the Finder. The number of Linkers required for the full system is 288. The track information output by the Linker is in the following format:

- 7 bits of P_T (includes sign),
- 3 bits of ϕ,
- 1 bit indicating if the track did *not* go through axial layer 4 (i.e. a possible high-eta track),
- 1 bit indicating that the track is isolated,
- 1 bit undefined, reserved for future use.

We plan to place Finder and Linkers on separate boards. The Finders will be arranged on boards in phi slices of 7.5°. Each board would contain 2, 3, 4, and 5 Finders from layers 1, 2, 3, and 4, respectively. We plan on arranging Linker boards such that 6 or 12 Linkers are on a board, so that the information can be brought off of the board in 7.5° increments. The reason for this is that the rest of the detector is segmented into 15° slices. Each board sends its list of tracks to the extrapolation unit (XTRP). For each of these tracks, the above 13 bits of information are sent to XTRP. The XTRP is responsible for mapping the XFT tracks onto muon and electron primitives found by other Level 1 trigger processors, and will be described in the following section.

One problem not highlighted earlier is that very often neighboring Linkers finder the same physical track. If both tracks are kept, this could present a problem for the trigger. On a single board, we can eliminate this problem by only keeping one track. This algorithm will be implemented by passing track information from neighboring LINKERs into another FPGA. However, this procedure is difficult to implement when we reach Linkers on separate boards.

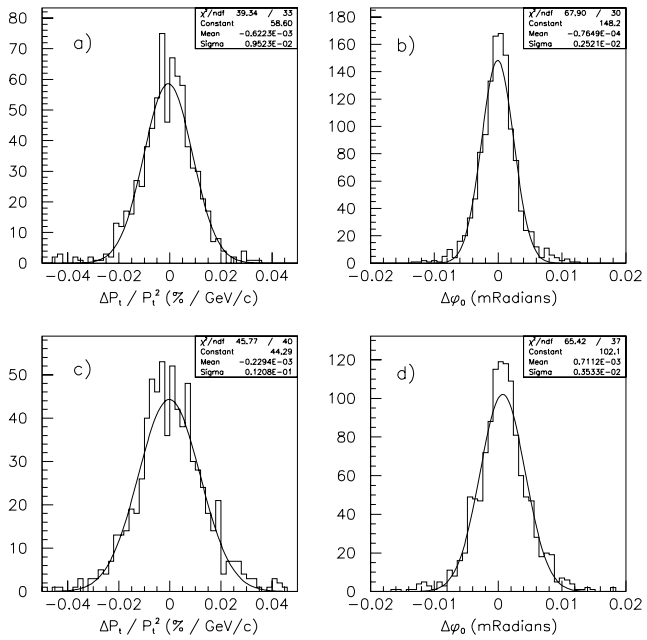

Figure 12.8: Expected performance of the XFT. Figures a) and b) shows the momentum resolution and ϕ_0 resolution expected when the chamber wire efficiency is 99%. Figures c) and d) shows the momentum resolution and ϕ_0 resolution expected when the chamber wire efficiency is 92%.

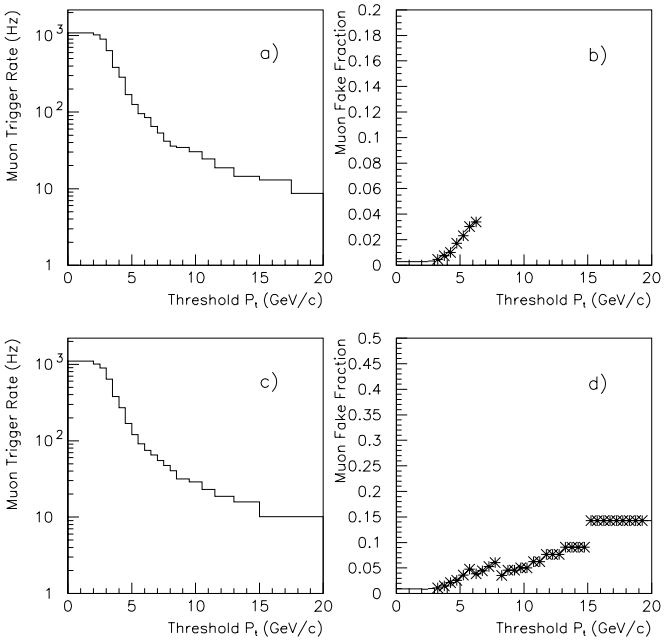

Figure 12.9: Expected muon stub plus XFT track rate. The top plot shows the total rate (in Hz) vs minimum P_T threshold. The bottom plot is the same, except for the subset of XFT tracks determined to be fakes.

These will instead be handled by the XTRP, using the same algorithm.

12.3.4 The Extrapolation Unit (XTRP)

The purpose of the XTRP is to receive tracks from the XFT and distribute the tracks or information derived from the tracks to the Level 1 and Level 2 trigger subsystems. After receiving the tracks from the XFT, signals are sent to the Level-1 muon system (L1MUON), the Level 1 Calorimeter trigger (L1CAL), and the Level 1 Track Trigger (L1TRACK) as shown in Fig. 12.1. The tracks are also put into a pipeline and upon receiving a Level 1 accept are stored in Level 2 buffers. The tracks then sent to the Level 2 processor and the silicon vertex trigger (SVT).

To remind the reader, the XFT logically divides the COT into 288 segments, each covering 1.25 degrees. One track is allowed per segment. Each track has 6 P_T bits, a sign bit, 3 mini-phi bits, an isolation bit, a superlayer 6/8 bit, and one spare bit. Every 132 ns, data from all 288 segments are sent from the XFT to the XTRP even if no track is found. See section 12.3 for more details.

The following information is sent to the Level 1 trigger subsystems:

- **CMU and CMX muon systems (L1 MUON).** Each XFT track is extrapolated to the radii of the CMU and CMX chambers by means of look-up tables. One or more bits, corresponding to 2.5 degree segmentation, are set according to P_T, ϕ, and amount of multiple scattering. These bits are sent to the Level 1 Muon Trigger system. Three separate P_T thresholds are available.

- **Central Calorimetry (L1 CAL).** A set of eight bits for each 15 degree wedge segment is sent to the Central Calorimetry Level 1 trigger. These bits correspond to eight separate momentum thresholds. Track extrapolation is done using look-up tables so that tracks crossing wedge boundaries are handled correctly.

- **Level 1 Track Trigger (L1 TRACK).** The Level 1 Track Trigger is an adjunct to the XTRP. It resides in the same VME crate and provides Level 1 triggers based on XFT track information only. The XTRP modules select tracks above a given P_T threshold and passes them on a bus to the Track Trigger. The total number of tracks is counted. If 5 or more tracks are found an automatic Level 1 accept is generated. If there are 2, 3, or 4 tracks, the P_T and ϕ information is used to interrogate look-up tables to generate various Level 1 triggers.

After sending out the Level 1 trigger information all tracks are put into a pipeline and stored pending the Level-1 trigger decision. If a Level 1 accept is received the tracks are latched into Level 2 buffers. All non-trivial tracks are then extracted and put into two separate FIFO's for delivery to the Level 2 processor and to the SVT respectively.

12.3.5 Level-1 Muon Trigger (L1 MUON)

The purpose of the Level-1 muon trigger is to provide single and dimuon objects for the Level-1 trigger decision. The run II Level-1 muon trigger includes three major upgrades over the run 1 hardware. First, it is designed to provide deadtimeless Level-1 operation for 132 nsec bunch separation. Second, it uses central-tracking information in the pipelined Level-1 decision to reduce the Level-1 trigger rate. Third, to reduce accidental triggers, it takes advantage of the full detector granularity in matching muon stubs to tracks.

The muon system is composed of wire chambers and scintillators stacked radially from the interaction point. For the purposes of muon identification, the list of detectors traversed by a muon in traveling from the interaction region defines the components of the muon system. The central region is represented in the $\eta - \phi$ map of Fig. 12.10. In the central-most region, $|\eta| < 0.6$, a muon from the interaction region encounters the central tracker, the hadron calorimeter, the

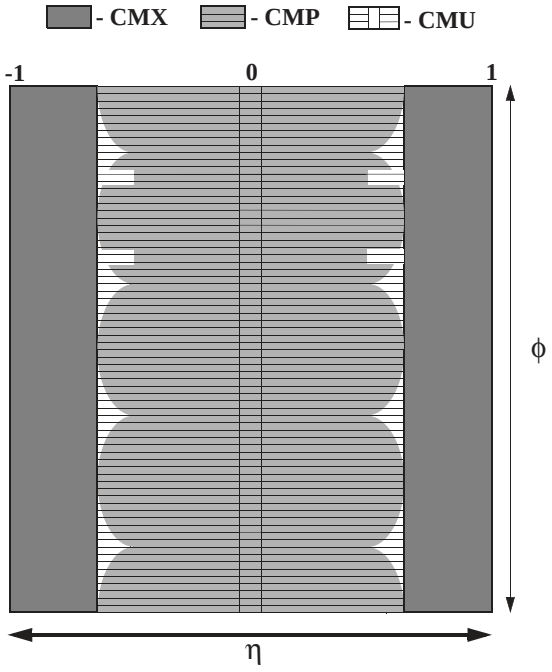

Figure 12.10: CDF $\eta - \phi$ map for central muons.

projective wires of the CMU, the half-cell-staggered chambers of the CMP, and the CSP scintillators. Beyond the central-most region in η, a muon traverses the central tracker, the hadron calorimeter, and the wire chambers and scintillators of the central muon extension, CMX/CSX.

In contrast to Run I where muon-track matching was performed in 5° ϕ segments, the Run-II muon trigger makes use of the finest granularity available from the detector elements for Level-2 processing. For speed and simplicity, this data is combined into fixed 2.5° azimuthal intervals and four η intervals for Level-1 processing. The utility of the fine match has been demonstrated in CDFNOTE-3416. For Level 2, the match is 1.25° in azimuth for CMU and CMX, and for the CMP with its rectangular geometry, the segment is a one-tube stack. The angular interval subtended by a tube stack varies from $\sim$ 1.25° for the nearest chambers to about half that at the corners of the rectangle.

12.3.5.1 Muon Trigger Primitives

The signal flow begins with the generation of candidate track "primitives" separately in each detector element. These primitives are developed in each 132 nsec crossing and are synchronously pipelined by the

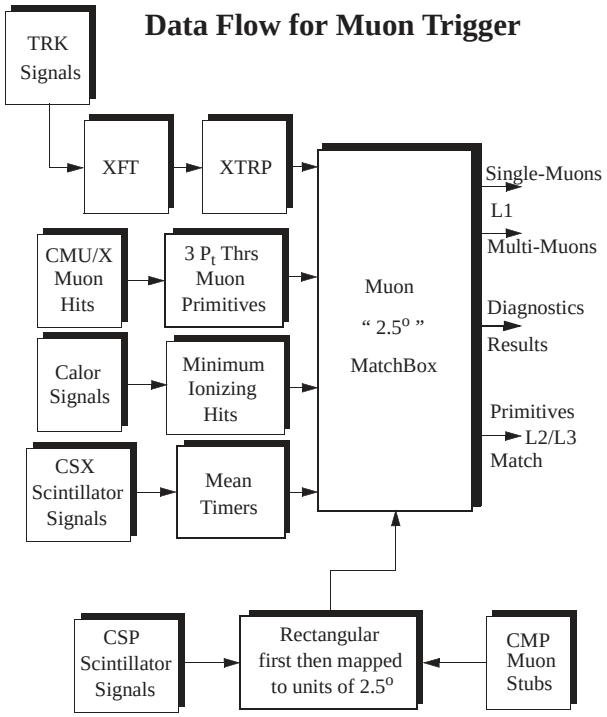

Figure 12.11: Data flow for the muon trigger.

beam-crossing clock. The primitives are derived from single hits or coincidences of hits for the scintillators of the muon system. For the wire chambers the primitives are derived from patterns of hits or from pairs of hits on projective wires with the requirement that the difference in the arrival times of signals be less than a preset threshold. This maximum allowed time difference imposes a minimum P_T requirement for hits from a single track. The wire chamber primitives are also refered to as muon "stubs". CMU and CMX primitives represent a pair of hits on projective wires with a time difference less than some downloaded value. The value is set to select tracks above a P_T threshold. CMP primitives represent the presence of a pattern of hits in a tube stack consistent with the passage of a track of interest. The information flow is shown in Fig. 12.11 which illustrates the primitive sources and the interconnection of units that process the data into trigger signals.

Trigger primitives are generated from the various muon detector elements according to Table 12.2. The name of the trigger card originating the data flow is given in the table.

12.3.5.2 Muon and Track Match

The Level-1 trigger match has a 2.5° granularity. Since the geometry of the CMP and CSP is rectangular, data from these detectors are combined in rectangular format, saved for Level 2, and then converted to the nearest 2.5° cylindrical bin for correlation with other detector data at Level 1. The detectors that have 1.25° segmentation are also saved for Level 2 in this finer unit and merged in pairs to 2.5° for matching in the Level-1 ϕ-correlation unit. The cards that perform the rectangular match for the CMP/CSP are the Pre-Match cards. The cards that form the 2.5° Level-1 correlation, the Match cards, are designed to handle 30° each, or twelve 2.5° segments. The Match cards form the Level-1 and Level-2 trigger signals. There are many outputs from each 30 degree Match card representing the presence of high, medium, and low P_T muons. These signals are combined in a Muon summary card and presented to FRED as 8 independent bits. The summary card is programable for flexibility. For example, one might program individual bits for $\geq$ 1 high-P_T muons found, $\geq$ 1 medium-P_T muons found, $\geq$ 1 low-P_T muons seen, $\geq$ 2 medium-P_T muons seen, $\geq$ 2 low-P_T muons seen, and have 3 spare bits for expansion. The 3 P_T bins are derived from the XTRP unit which has higher precision than that available from the differential timing of the CMU/CMX projective wires. The P_T thresholds are separately programble for the various regions, CMU and CMX, both in the XTRP and muon primitives cards. To avoid double counting when computing $\geq$ 2 low or medium P_T muons, an intervening empty 2.5° segment is required for separate muons. These signals are transmitted to FRED as Level-1 trigger imperatives. If a Level-1 accept is received by the 30° card, it transfers the pipelined data (both input to and output from the 30° card) to one of four Level-2 buffers. The information in the buffer is also output to the Level-2 trigger. The Pre-Match cards provide similar data for Level 2.

12.3.6 Global Level-1

The Level-1 Decision card or "FRED" module is located in the Global Level-1 crate and is responsible for issuing the Level-1 trigger decision. Single-bit trigger signals from the various calorimeter, muon, and tracking PreFRED modules, which are also located in the Global L1 crate, are combined by FRED to form the final Level-1 triggers. The Run-II FRED

Detector	Basic Unit	Unit	CARD	Algorithm Description	# Outputs
CMU	Wire pair	1.25°	MU1T	Hi, low P_t, plus a "lefover to 384ns" determined from differential timing.	288 x 2 x 2 ϕ x η x P_t
CMP	4 tube stack	0.6° 1.2°	MP1T	2 or 3 out of 4 hits for patterns from radial tracks	336 ϕ
CMX	Wire pair	1.25°	MX1T	Hi, low P_t, plus a "lefover to 384ns" determined from differential timing	288 x 2 x 2 ϕ x η x P_t
CSX	Coincidence	15°/8	MS1X	Gated Mean Time from1/2 overlapped scintillators	192 x 2 ϕ x η
CSP	Scintillator	1.2° 2.4°	MS1P	Gated Scintillator hit	168 x 2 ϕ x η
HAD	Calorimeter	15°	MH1T	Signal in calorimeter PMT for η intervals 0/4, 4/5 and 6/9	24 x 6 ϕ x η

Table 12.2: The muon primitives produced for each of the central muon detectors.

module (Level-1 Decision card) has the following features:

- receives up to 64 Level-1 inputs from a possible 8 PreFRED modules
- generates up to 64 Level-1 triggers, each based on a subset of 8 of the 64 Level-1 inputs
- has the ability to prescale or rate limit each of the 64 Level-1 triggers separately
- provides the Level-1 trigger decision to the Trigger Supervisor (TS) running the physics partition
- provides the 64 Level-1 trigger bits to the 7 Level-2 processors
- provides signals to scalers to count the Level-1 input rates, the raw Level-1 trigger rates, and the prescaled/rate-limited Level-1 trigger rates
- contains 4 Level-2 buffers that can be read out over VME

12.3.6.1 The Global Level-1 Crate

The Global L1 crate is a VME crate with 9U $\times$ 400 mm slots. A schematic diagram of the crate is shown in Fig. 12.12. The 64 separate Level-1 inputs to the FRED module arrive from the various calorimeter, muon, and tracking PreFRED modules over a custom J3 backplane. Each PreFRED module receives information via cables from the appropriate section of the trigger and summarizes it for presentation to FRED. Before being transmitted on the J3 backplane, the output bits pass through a FIFO which phases all 64 FRED inputs to ensure that they come from the same event. The TOWTRG and SUMET PreFRED modules, which summarize the calorimeter trigger, were described in section 12.2.1.3. Since the Muon and Track bits need no further processing in the PreFRED module, these PreFREDs contain only differential receivers and the time-alignment FIFO.

Event data is read out from the FRED and PreFRED modules using the standard VRC and TRACER modules discussed in section 11.6 in reference [6]. The VRC is also used to configure FRED at the start of a run. Custom-built scalers, which are also located in the Global Level-1 crate, keep track of the "raw" input signal rates and the final L1 trigger rates.

12.3.6.2 The Global Decision (FRED) Module

Since the FRED module is part of the run-II pipelined architecture, trigger decisions are made on a cyclic basis, with a cycle time of 132 nsec to accommodate the maximum crossing rate expected for run

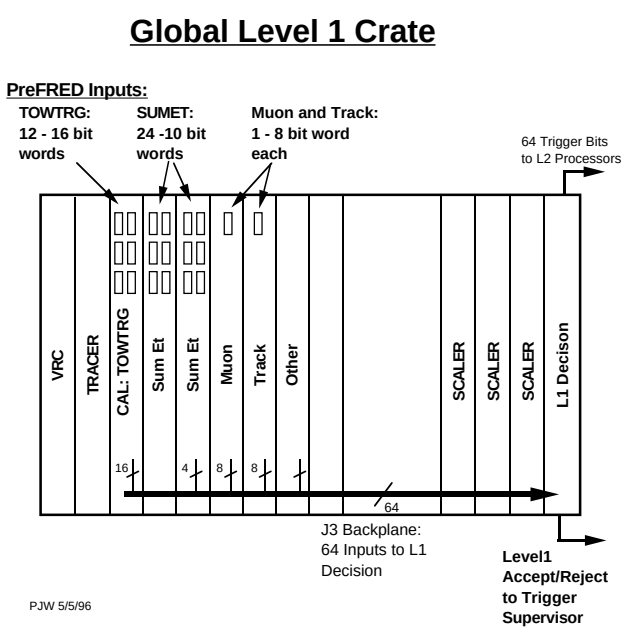

Figure 12.12: The Global L1 Crate.

II.

The FRED module expects the Level-1 inputs from the PreFRED modules to be valid at the rising edge of the 132 nsec system clock. The 64 inputs arrive in parallel, pass through buffers, and are latched. They are then multiplexed down to subsets of 8 inputs using AMCC S2024 "Crossbow" chips. The subset of inputs to be used is part of the information downloaded at the beginning of a run via the VME interface. Each subset of 8 inputs addresses a static RAM to determine if this pattern of 8 inputs constitutes a valid trigger. The contents of the SRAM are also downloaded at the beginning of the run. Each SRAM has 8 outputs. Thus a single "L1 trigger block" allows for 8 separate L1 triggers using a selection of 8 inputs (or some subset of these 8 inputs). The current design uses 8 such L1 trigger blocks. Thus for any given run there would be a total of 64 separate L1 triggers.

Each output line from the SRAMs is latched after a fixed delay in order to allow the SRAM outputs to become valid and stabilize. The rate-limiting and prescaling logic is then enabled. The presence of any trigger bits after this stage causes a Level-1 accept signal to be sent to the Trigger Supervisor.

The FRED module has the ability to independently prescale each Level-1 trigger. The prescale logic is implemented with a divide-by-N counter implemented in Xilinx FPGAs. The values for the prescaling are downloaded at the beginning of the run.

The Level-1 Accept/Reject signal is sent to the Trigger Supervisor over a dedicated cable on the front of the VME card. All other communication between the FRED module and the Trigger Supervisor, such as the transmission of the final Level-1 decision back to FRED, is done via the TRACER module and the VME backplane.

The event data to be read from the FRED module include the latched Level-1 inputs and the Level-1 RAM outputs. The event data are stored in the standard L1 pipeline and L2 buffer system described in chapter 11. Upon receipt of a Level-1 accept from the Trigger Supervisor, the 64 Level-1 trigger bits will also be sent to the Level-2 processors through a dedicated cable to aid in the L2 trigger decision .

12.4 Level 2 Trigger Hardware

The Level-2 trigger consists of several asynchronous subsystems which provide input data to programmable Level 2 Processors in the Global Level-2 crate which evaluate if any of the Level-2 triggers are satisfied. In run II, we expect about 100 different Level-2 triggers to check compared 64 different triggers in run 1.

Processing for a Level-2 trigger decision starts after the event is written into one of the four Level-2 buffers on all front-end and trigger modules by a Level-1 accept. While Level-2 is analyzing the event that buffer cannot be used for additional Level-1 accepts. If all four Level-2 buffers are full then the experiment starts to incur deadtime. The time required for a Level-2 decision needs to be less than about 80% of the average time between Level 1 accepts in order to keep the deadtime at an acceptable level. For a 50 kHz Level-1 rate, this would mean that the average decision time needs to be 16μsec or less. The best estimate of the Level-2 processing time is 20μsec. The Level 1 rate would be limited to 40 kHz to keep the deadtime below 20%.

In order to keep the Level-1 rate at 50 kHz, we have decided to pipeline Level-2 in two stages each taking approximately 10μsec. Although the latency remains 20μsec, the time between Level-2 decisions will be 10μsec resulting in minimal deadtime even with a Level-1 accept rate of 50 kHz.

The first stage of the Level-2 pipeline is an event

building stage: data is collected from the Level-2 buffers of the Level-1 trigger systems (XFT and L1 MUON) and from the calorimeter shower maximum detector (XCES). Simultaneously a hardware cluster finder (L2CAL) processes the calorimeter data and a track processor finds tracks in the silicon vertex detector (SVT) . All the Level-2 event data is collected into the memory of the Level 2 processors. We estimate that this stage will take 10 microseconds. After all of the data is stored in the processors the event is examined to find out if the criteria for any of the Level 2 triggers is satisfied. Analysis of an event in the L2 processors can occur at the same time as the data for the next event is loaded into memory.

12.4.1 Level-2 Cluster Finder (L2CAL)

Since jets are not fully contained by trigger towers in the Level-1 trigger, the Level-1 thresholds must be set much lower than the jet energy to provide an efficient trigger. This results in rates that are too high for readout into Level-3. To provide a reduction in the jet trigger rates at Level-2 these triggers use the E_T from clusters of trigger towers. The Level 2 cluster finding algorithm is essentially the same as was used in run 1. In this algorithm, contiguous regions of calorimeter towers with non-trivial energy are combined to form clusters. Each cluster starts with a tower above a "seed" threshold (typically a few GeV) and all towers above a second somewhat lower "shoulder" threshold that form a contiguous region with the seed tower are added to the cluster. The cluster finder design effort has focused on implementing the algorithm in the multi-buffered deadtimeless architecture, with emphasis on improving performance with a parallel implementation of high speed Xilinx FPGA's.

The data from the calorimeter system is collected and processed by the Level-1 trigger as described in section 12.2.1 and shown in Fig. 12.2. The towers are summed on the detector into trigger towers of 0.2 by 15°, resulting in a 24×24 array for a total of 1152 towers (576 EM and 576 HAD). The tower energies are weighted by $\sin\theta$ and are gain and offset corrected. The data from each crossing is output from the DIRAC boards, received by the Digital Cluster And Sum (DCAS) boards and stored in FIFOs. Upon a Level-1 accept the data is latched into one of four Level-2 buffers in the DCAS board.

The cluster finding process starts as soon the DCAS boards are given the address of the next Level 2 buffer to process. The cluster finder algorithm is explained in Fig. 12.13. The size of each cluster expands until no towers adjacent to the cluster have energy over the shoulder threshold. After the complete cluster is found the tower energies are sent to an adder tree and the next seed tower is selected. The seed finding, clustering and summing processes are pipeplined such that while the summing is carried out for one cluster the seed finding and clustering can start for the next cluster. For each cluster found the total EM and Had energies are calculated and recorded along with the number of towers, and the η and ϕ coordinates of the seed tower. The energy weighted η and ϕ positions which were available in run 1 are not calculated since they were found to be unneccasry.

Each DCAS card performs the local clustering and summing for 16 trigger towers (8 EM + 8 HAD). For each 15° calorimeter wedge there are 3 DCAS boards which receive data from 4 DIRAC boards. The 12 DCAS cards are contained in each of 6 VME crates mounted directly above each of the L1CAL crates. A single local controller (LOCOS) provides control over clustering in each crate and forms crate-wide sums. The local controllors are in turn controlled by a single Cluster Queen (CLIQUE) in the L2 Processor crate. The CLIQUE forms the final cluster sum and forwards it to the L2 Processors.

After cluster finding on the event in buffer N is finished, cluster finding on another buffer can start. This allows the data collection and data analysis phases of Level 2 to be pipelined.

A "hook" for expansion is built into the cluster finder. The η and ϕ address of each cluster is sent to a slot which can contain a Neural-Net Processor (NN). This board can read the individual energies from the seed tower and the surrounding towers. There are separate data paths for cluster finding and NN reading. This will allow the implementation of the NN photon trigger and NN tau trigger used in Run I.

12.4.2 Level-2 Shower Maximum Data Used in the Trigger

The shower maximum detectors of the EM caloritmeters can be used to reduce trigger rates for electron and photon triggers. For both electrons and photons, requiring a cluster above threshold in the shower maximum detector eliminates the background

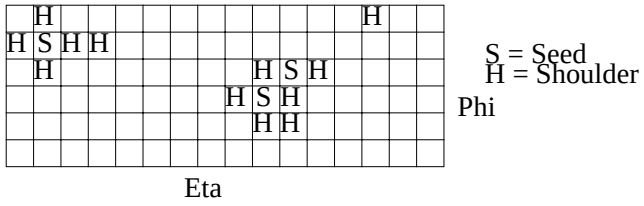

1. The inputs from DIRAC are checked to see if they are over the seed or shoulder threshold.

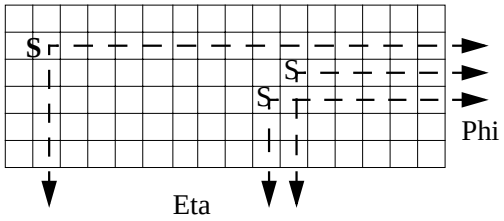

2. The Cluster Control board tells the DCAS's to enable their Phi and Eta address lines for all seeds. The Control board then selects the seed with the lowest Eta address, and then within that Eta, the lowest Phi address to begin cluster finding.

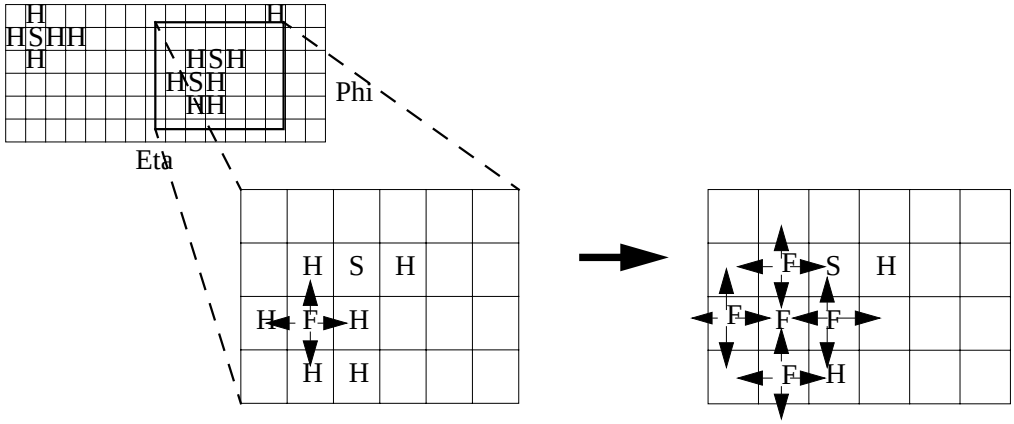

3. Cluster finding then begins with the selected seed sending a "found" bit to its four orthogonal neighbors. If the neighbors are over the shoulder threshold and receive a "found" bit, they in turn send out the signal to their four orthogonal neighbors, and so on, and so on.

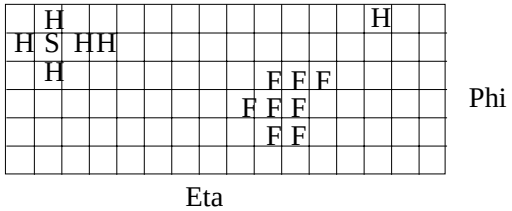

4. When a tower is "found" it is disabled from being found in another cluster. i.e. if the tower is a seed and is found in a cluster initiated by another seed, it will not enable its address lines when the control board prompts for seed addresses. After one cluster is found, the tower energy values are enabled into an adder tree. Steps two through four are repeated until all clusters are found.

Figure 12.13: Calorimeter trigger cluster finding

from single-phototube discharge. Since the spatial resolution is much smaller than a calorimeter wedge, matching tracks from the central tracker to the shower maximum provides a signicant reduction in combinatoric background for electron triggers.

CDF upgraded the electron and photon trigger hardware for run 1b to make use of shower maximum information from the central shower maximum detector (CES) in the Level-2 trigger decision[8]. For electrons, this upgrade resulted in a 50% reduction in backgrounds, while retaining approximately 90% of the signal. Topics in b physics such as the search for rare processes demand a low trigger threshold. By using the XCES, we were able to lower the inclusive electron threshold to 8 GeV, which is 1 GeV lower than the threshold for run 1a, while maintaining the same bandwidth of events accepted by the CDF hardware Level-2 trigger.

12.4.2.1 Central Shower Maximum (XCES)

While the frontend electronics are completely different, the basic scheme for the XCES trigger is the same for run II as for run 1b. The signals from four adjacent CES wires are summed together and compared to a threshold to form an XCES bit with $\sim 2^\circ$ azimuthal segmentation. This bit can then be matched in azimuth and momentum to a XFT track to generate a Level-2 trigger. There are 16 XCES bits per detector wedge (8 bits times 2 thresholds) yeilding a total of 768 XCES bits.

The QIE for shower max digitizes each crossing, and stores the data in a level 1 pipeline, awaiting a Level-1 trigger decision. The data is compressed into a floating point format, consisting of 3 bits representing the measurement range, and 5 bits of ADC data, for a total of 8 bits. Once a Level-1 accept has been issued, 4 time slices for each wire of digitized data are received by the VME readout boards. The CES VME readout board will have an extra trigger circuit to produce the trigger output bits (XCES) to be used in the Level-2 decision. This circuit converts the floating point output to a linear format and sums the 4 time slices for each wire. The signals from four adjacent wires at a time are summed and compared to a threshold to define an XCES bit. Two ADC thresholds will be implemented in the trigger. One, on the order of a few GeV, will be used for the $J/\psi \rightarrow ee$ trigger. The other, on the order of 8 GeV, will be used for the inclusive electron trigger. The XCES bits are received by the Level-2 Processor within 10 microseconds of a Level-1 accept where the matching of the XCES cluster in momentum and azimuth to a XFT track is performed to generate a Level-2 trigger.

12.4.2.2 Plug Shower Maximum (XPES)

Because this is a new detector, with a substantially different geometry from the CES, the options for using information from it in the level 2 trigger are numerous. The plug shower maximum interface is planned to match the signals of the strips with a signal over some threshold to a listing of the plug calorimeter towers that should also have a signal. There are two alternatives being investigated at present. The first sums the signals from 4 adjacent strips and compares the result to a threshold value, much as is done for the XCES. The 50 resulting bits per 45 degree phi sector are then used to match calorimeter towers to the strips. The other possibility is to use the last dynode output from each multianode PMT, which is equivalent to summing the signals from 16 adjacent strips. In either case some logic will have to be performed to correlate the strips over threshold in each view to the appropriate calorimeter tower using a series of ands and ors. The performance and possible implementation of each scheme is still being investigated at this point, and we plan to have the design finalized in the late fall of 1996.

12.4.3 Silicon Vertex Tracker (SVT)

The ability to use impact-parameter information in the trigger to detect secondary vertices can substantially increase the physics reach of a hadron-collider experiment. For example, the resolution and mass-scale systematics for the top-quark mass determination could be measured and controlled if there were a large-statistics dijet mass peak from W or Z decay. Unfortunately the large QCD jet cross section makes the signal-to-background ratio poor and the trigger rate prohibitively high. Impact-parameter triggering, however, can provide a $Z \rightarrow b\bar{b}$ signal, for which the continuum background is substantially reduced. With the Silicon Vertex Tracker (SVT), we expect a large sample of $Z \rightarrow b\bar{b}$ events sitting well above the continuum background.

Studies of B decay will also be greatly enhanced by the SVT. Some of the decay channels that are important in the study of CP violation will be virtually undetectable at the Tevatron without an impact

parameter trigger (*e.g.* $B^0 \to \pi^+\pi^-$) [9]. Other interesting decay modes (*e.g.* $B^0 \to J/\Psi K_s$), although accessible by requiring one or two leptons in the final state, will benefit from an impact parameter trigger in terms of better rejection against background and higher statistics on tape.

Some physics processes not involving b quarks will also be aided by the SVT. The high-P_T inclusive-muon trigger, needed for the W-mass measurement, has a high Level-2 rate. The SVT can both reduce the accidental rate by demanding an SVX track pointing at the primary vertex and remove lower-P_T muon background by using the improved momentum resolution to tighten the P_T threshold.

In order to obtain impact-parameter information in the Level-2 trigger, the SVX II is read out after each Level-1 trigger. The SVT combines this data with the Level-1 tracking information from the central tracking chamber and computes track parameters (ϕ, P_T, and impact parameter d) with resolution and efficiency comparable to full offline analysis. Figure 12.14 displays the resolution of the impact parameter in Monte Carlo for a full SVT simulation, including detector misalignments within tolerances, and for the offline reconstruction.

We give a brief summary of the SVT below. A full description of the device can be found in Ref.[10].

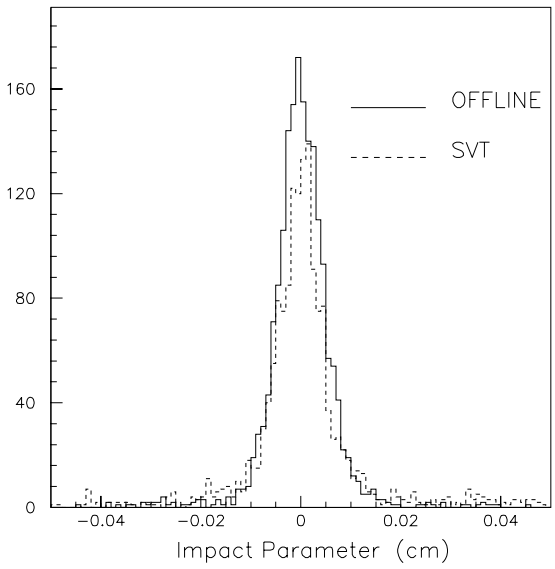

Figure 12.14: Comparison of the impact-parameter distribution of SVX tracks from the SVT trigger simulation and offline procedures.

12.4.3.1 Implementation

The strategy we follow combines the use of the Associative Memory (AM) technique with a processor farm. The overall architecture of SVT is shown in Fig. 12.15.

SVX-II data digitization and sparsification occur in the front end. From each of the SVX-II readout chips, there is an 8-bit data stream consisting of the chip ID and status words and a series of word pairs containing a channel number and the digitized pulse-height in that channel. The data is transmitted over fiber optic lines to a splitter where one output goes to the SVX-II readout and the other output goes to the SVT. There are 12 fibers for each of the 12 SVX-II ϕ sectors. These are fed into G-link Fiber-Receiver transition cards where the data is demultiplexed and transmitted through the backplane to the Hit Finder boards, three for each ϕ sector. The Hit Finder performs pedestal subtraction and bad channel suppression. It then scans the data stream for clusters of hit strips. When acceptable clusters are found, the Hit Finder computes and outputs the centroid of each cluster, the most probable track intersection point at that SVX layer.

The output from the three Hit Finders for each ϕ sector are merged into one stream with a Merger board. Communication between SVT boards is standardized. The transmission is over 50-conductor flat-ribbon twisted-pair cable. The data is pushed by the transmitting board at 30 MHz into a FIFO on the receiving board.

While the Hit Finders process SVX data, the list of tracks found in the outer tracking chambers during Level-1 processing is transmitted from the XTRP to the Associative Memory Sequencer (AMS). As soon as the clusters from the Hit Finder are available from the output of the Merger, they are also transmitted to the Associative Memory Sequencer. The AMS uses a lookup table to convert the 14-bit cluster centroid into a coarser Superstrip in preparation for the pattern-recognition stage. The size of the Superstrip is programmable. It is a compromise between a small size that would provide more precise pattern recognition and produce fewer fake-track candidates but require a larger memory, and a large size which would output more fakes but require a small memory. (The fakes would be rejected at the next stage, but they

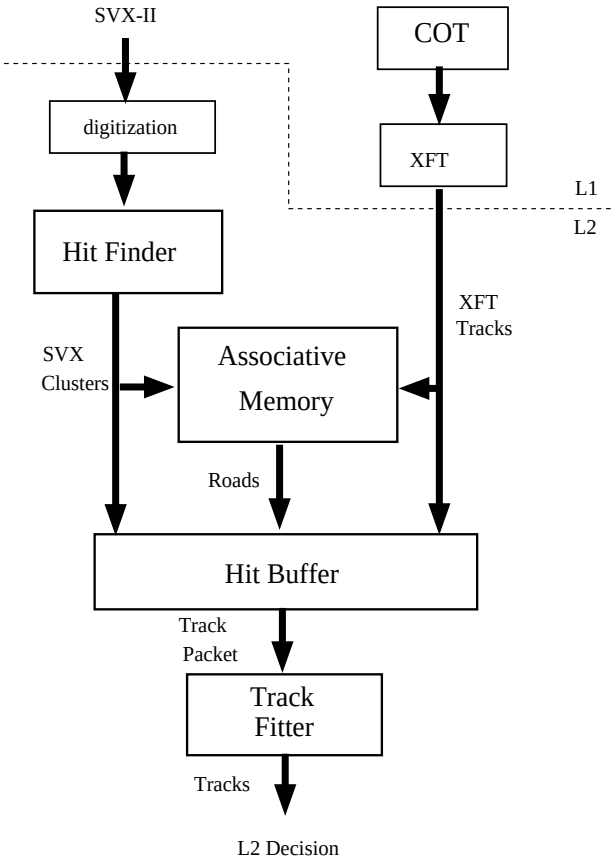

Figure 12.15: Architecture of the SVT trigger.

waste time.) A study of the compromise results in the choice of a 250 μm Superstrip.

Each AMS broadcasts the outer tracks and coarse SVX clusters on the backplane where they are received by two Associative Memory (AM) boards. Each AM board fans this data stream out to 128 AM chips mounted on the board. The AM chip is a custom CMOS device that contains 128 roads. It is implemented in 7μ technology and runs at 30 MHz. Each chip stores 128 combinations of outer tracks and coarse SVX hits. Each combination represents a legitimate particle trajectory and is called a *road*. As the outer tracks and clusters are received, each chip checks to see if all of the components of one of its roads (outer track and four SVX hits) are present in the data stream. If so, the chip records the track candidate's road number. The roads are downloaded, so they can be modified, for example to correct for geometric misallignment or to select which layers to use.

At the same time the clusters and outer tracks are sent to the AMS, they are also sent to the Hit Buffer where they are stored by Superstrip number. Once the AM is done, the road numbers of candidates are also sent to the Hit Buffer. The hit buffer uses another lookup table to find the Superstrips which correspond to each road. It then goes to those Superstrip bins and retrieves the full outer-track and SVX-cluster information.

This set of one outer-track and four SVX hits is called a track packet. The Hit Buffers sends these packets to the Track Fitters. The collection of Track Fitters, the Track-Fitter Farm, is designed so that tracks are distributed equally to all Fitters, and enough Fitters are included so that each one fits on average one track per event. Studies indicate that ten Fitters will meet these requirements. The fit is a linear approximation, consisting of a set of scalar products. It takes 70 cycles on a currently available commercial CPU, approximately 3.5μs. Other methods currently under study may be significantly faster, even though the processing time with the current technology is not a concern.

12.4.3.2 Expected Performance

The resolution of the fit is nearly as good as offline reconstruction. The expected resolution is $\sigma_d = 35$ μm (at $P_T = 2$ GeV), $\sigma_\phi = 1$ mrad and $\sigma_{P_T} = .3\%P_T^2$ (where P_T is in GeV). The track parameters are available for the Level-2 trigger decision.

To see the power of the SVT, consider $B^0 \to \pi^+\pi^-$. This is one of our most difficult trigger problems because the rate for two low-P_T tracks is so high. At Level 1, only the outer-track information is available. We will require one track with P_T >2 GeV, and a second, oppositely-charged track with P_T >3 GeV and $30^\circ < \Delta\phi < 135^\circ$. The rate for this at $\mathcal{L} = 10^{32}$ is 16 kHz, well within the Level 1 design limit of 50 kHz. At Level 2, the SVT provides impact parameter information. Applying full SVT simulation to SVX′ data taken during run Ib, we find that a cut of $|d| > 100$ μm provides three orders of magnitude in rejection; such a cut is 50% efficient for the signal. The resulting Level-2 rate is < 10 Hz, much smaller than the design limit of 300 Hz.

There are two potential problems that must be controlled. The first is the precise mechanical positioning of the SVX II. Since the SVT does not have z information for tracks, an angular misalignment between the SVX and the beam would produce incorrect impact-parameter results. Therefore SVX-II detectors must be aligned collinear to the beam to within 100 μrad. The ladders themselves must be aligned to each other within this specification during

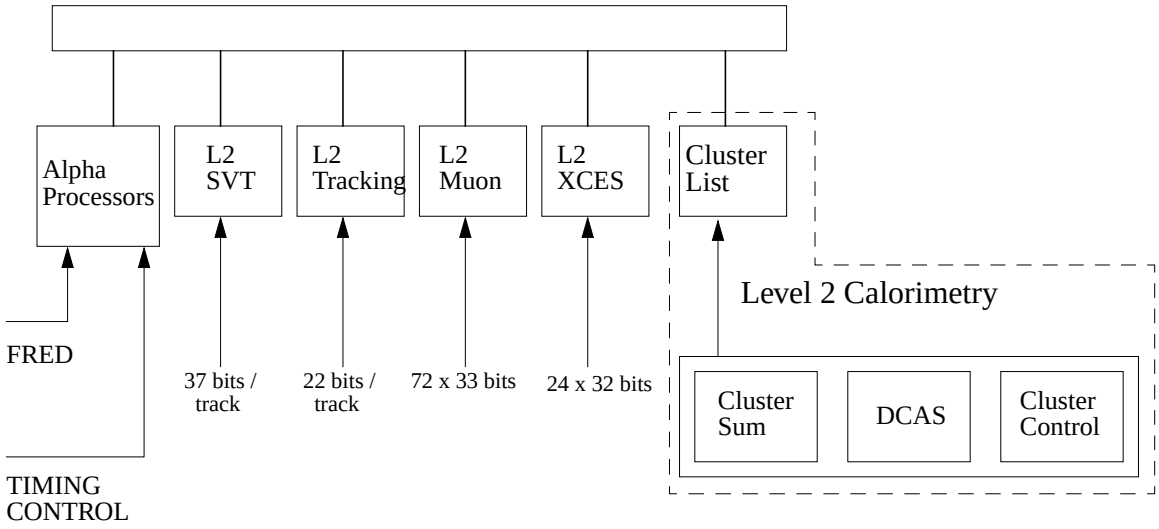

Figure 12.16: The Level-2 decision crate.

construction. It will also be necessary to align the beam to the detector during the first few minutes of each run. Studies have been performed showing that the SVT itself can provide the needed feedback to the accelerator control room.

The other potential problem is the occupancy of the SVX II (Section 5.8.1), which directly impacts the ability of the SVT to complete its calculation in time for the Level-2 trigger decision. To study this, a Monte Carlo simulation was tuned until it could accurately reproduce the occupancy of the current SVX detector over a wide range of luminosities. The occupancy is observed to be proportional to the luminosity, as expected. The tuned Monte Carlo was run with an SVX-II simulation and run-II luminosity to produce a data sample for SVT timing simulations. The result shows that the SVT will complete its calculations well before the end of its allotted 17μs.

12.4.4 Level-2 Decision Hardware (Global Level 2)

The final Level-2 decision is made in a set of four Level-2 Processors in the Level 2 crate. There are five major sources of data for the Level 2 trigger. The data from each source is collected into a single board in the Level 2 crate as shown in Fig. 12.16. The data is stored in a device dependent format in FIFO's. The data from the output of the FIFO is formatted into a 128 bit word and transmitted to the Level 2 processors. The processors store the data directly into memory locations (common blocks in Fortran parlance). The storing of data in all processors occurs simultaneously. Each data source maps the type of data (tracks, calorimeter clusters, SVT, muon, XCES) and the Level 2 buffer number into the distinction address. This allows data for one buffer to be assembled while the processors are examining an event in a different buffer.

The cluster list board collects information about each calorimeter cluster. The η and σ address, number of towers, and EM and hadronic energy for each cluster is encoded into a 64 bit word. A 2 bit field indicating which one of the four sets of seed and shoulder thresholds was used is stored in each cluster list element. The L2 buffer address is also sent for diagnostic purposes. The cluster list card takes two clusters and transmits them in a 128 bit transfer to the Level 2 processors.

The trigger data from the cetral strip chambers (XCES) consist of 32 bits per wedge, for a total of 24 $\times$ 32 bits. This data is packed into six 128 bit words and transmitted to the Level 2 processors. The XCES information is used to require hits in the central strip chambers for low energy electrons and photons.

The tracking data comes from two sources, the XFT tracks from the XFT via the XTRP, and the tracks from the SVX processed by the SVT to give impact parameter. The tracks from XTRP are trans-

mitted immediately after a Level 1 accept. They are received by the L2 tracking module, packed 4 tracks per 128 bits and transmitted to the Level 2 processors.

The data from the SVT arrives later than the data from the other four systems. The data from the SVX must first be transmitted from the detector, then processed in the SVT and combined with XFT tracks. This will take a minimum of 7μsec and most likely 10μsec. Since this is the total time allocated to collect Level 2 data, the processors will start analyzing the event before the SVT data is complete. Only if the impact parameter required to make the Level 2 decision will the SVT data be used. If all triggers which require SVT impact parameters are rejected by other cuts (e.g. kinematics), then the impact parameter cut won't be tested.

The data from the muon match board is zero suppressed and then transmitted to the Level 2 system. The muon information is packed into 72 bits representation each 2.5° wedge for each muon system, and then transmitted to Level 2 processors.

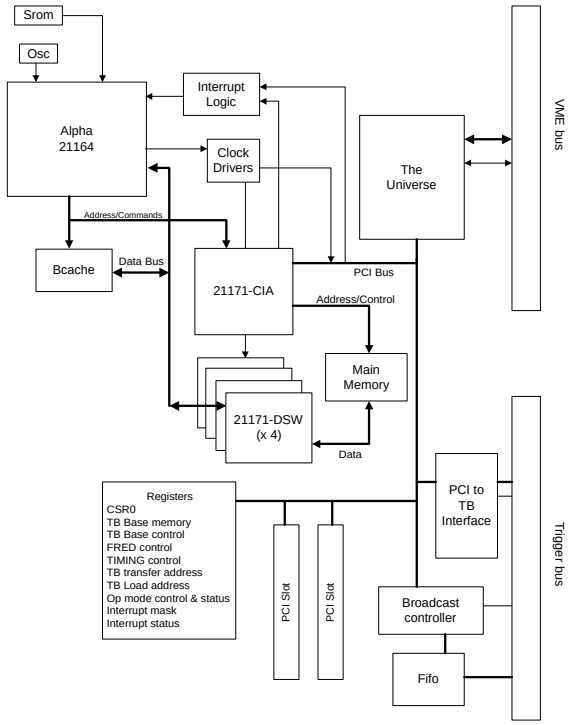

Figure 12.17: Block diagram of the Level-2 processor board.

12.4.4.1 Level-2 Processors

The Level 2 processors are custom VME modules based on the Dec 21164 Alpha chip. Figure 12.17 shows a block diagram of the processor board design which is an extension of the processors used in run 1b. The new processors have a 433 MHz clock instead of a 150 MHz clock. The data path into the board is 128 bits wide instead of 64 bits. The memory and I/O interface use the 21172 chip set instead of discrete logic. The boards use VME format and reaout instead of Fastbus used in run 1b.

The data from the data collection boards is transmitted over a 128 bit wide bus ("Magic Bus") using a custom J3 backplane. The address is used as a 'DMA channel' and determines which of the 4 L2 buffers are being processed and which of the 5 data sources are sending the data. There will be four Level 2 processors in the system.

All four Level 2 processors latch the data from all the data collection boards. The data is initially stored in a FIFO and then transmitted to the main memory. Care will be taken that successive Level 2 buffers do not map to the same cache lines. This will allow the processor to analyze one event out of the third level cache while data from another Level 2 buffer is being written to main memory and invalidating the cache lines holding the event the previously came in on this buffer. The second level cache is on chip and is 3-way set associative.

Each of the four Level 2 processors will be assigned a set of triggers to examine. The triggers will be distributed across the processors by hand. All muon triggers will be in one processor and all electron triggers will be in another. The processor forming the electron plus muon trigger will have to find the low P_T electrons and muons in parallel with the electron processor and the muon processor. This allows the triggers to be ordered such that most triggers will not have to be evaluated. For example, if the 6 GeV central muon trigger fails, then any trigger requiring a 6 GeV or greater muon need not be tested. This kind of optimization was used successfully in run 1. Each of the four processors will independently forward a Level-2 accept or reject for the set of triggers it is examining to the Trigger Supervisor.

Negotiations are underway with the Michigan State DØ group to use the same processor in DØ.

12.5 Trigger Rates

The CDF trigger system is very flexible. It can pick event topologies that are simple, like a single high-P_T lepton, or complex, like two charged particles in a narrow mass window coming from a secondary vertex, or a multiple-jet system with large $\not\!\!E_T$. In run I, we normally took data with over 50 separate trigger paths. This will also be the case in run II. However, as in the past, the trigger rate, and thus potential deadtime problems, will be dominated by a few triggers. Here we focus on the three highest-rate triggers; the single-electron and single-muon triggers give the largest Level-2 rates, and the two-track trigger has the highest Level-1 rate.

The high-P_T inclusive-electron trigger is used for the W and top-quark studies as well as many exotic-particle searches. In the central rapidity region, current trigger rates can be reliably extrapolated to run II. For a calorimeter tower with EM $E_T > 16$ GeV matched to a track with $P_T > 12$ GeV, the Level-2 trigger rate will be 20 Hz for 2×10^{32} luminosity and 132 nsec bunch separation. Since both calorimeter and tracking information are available to the Level-1 system, that rate won't be much higher. In the plug rapidity region, studies of the trigger rate with IFT/SVT tracks are in progress. We do however have an upper limit based on use of calorimeter information only. The Level-2 rate is < 100 Hz. A track requirement should reduce this by at least a factor of two.

A lower-threshold central-electron trigger is important for B physics and calibration samples for the W mass. The Level-2 trigger rate for $E_T > 8$ GeV will be 85 Hz. For calibration samples, prescaling is an acceptable way to reduce the rate. For B physics, a large impact-parameter requirement in the SVT reduces the rate by more than an order of magnitude.

For the single-muon trigger, again there are two rapidity regions to be considered. In the central region covered by the CMUP detector, the Level-1 trigger rate for $P_T > 12$ GeV is 45 Hz, again for 2×10^{32} luminosity and 132 nsec bunch separation. At Level 2 with its tighter match between the track and muon stub, the rate drops to 15 Hz. For $0.6 < |\eta| < 1.0$, the region covered by the CMX system, the Level-2 rate will also be 15 Hz for $P_T > 12$ GeV. This rate increases to 25 Hz for $P_T > 6$ GeV, so lower thresholds for B physics can be accommodated.

The greatest challenge for the Level-1 system is the $B^0 \to \pi^+\pi^-$ trigger. As presented in the SVT section, the Level-1 rate is 16 kHz at 10^{32} luminosity when one track is required with $P_T > 3$ GeV and a second track is found with $P_T > 2$ GeV and $30° < \Delta\phi < 135°$ relative to the first track. At Level 2, with an impact parameter > 100 μm required, the rate drops to < 10 Hz. This will provide 6000 $B^0 \to \pi^+\pi^-$ events on tape per fb^{-1} for a branching ratio of 1×10^{-5}.

The trigger system will allow us to collect data for our broad range of physics topics even at the highest planned luminosity.

Bibliography

[1] C.Campagnari, M.Miller, M.Shochet, and G.Sullivan, *Estimates of trigger rates and efficiencies for the 1993 CDF calorimeter level 0 trigger.*, CDF/DOC/TRIGGER/CDFR/1180 (1990).

[2] F.Ukegawa, *Low Momentum Electron Trigger Rates*, CDF/ANAL/BOTTOM/CDFR/2480 (1994).

[3] H. Frisch and P. Wilson, *Trigger Tower organization and summing in $\eta - \phi$ space for Run II and beyond*, CDF/DOC/TRIGGER/CDFR/-2045 (1993).

[4] C. Campagnari *et al.*, *Specifications for the Calorimeter Front End Electronics*, CDF/PIG/-DOC/2060, (1994).

[5] T. Shaw and G.Sullivan, *A CDF standard VME readout crate for the Upgrade*, CDF/DOC/TRIGGER/CDFR/2388, (1993).

[6] T. Shaw and G. Sullivan, "A Standard Front-End and Trigger VME Readout Crate for the CDF Upgrade," CDF note #2388; T. Shaw and W. Stuermer, "Designer's Guide for Modules to go into the CDF Custom Backplane."

[7] "Trigger Supervisor Protocols for Run II", CDF Group/Yale University, October 10, 1995.

[8] K. Byrum *et al.*, NIM in Physics Research A364 (1995) 144-149.

[9] S.Donati and G.Punzi, "$B^0 \to \pi\pi$ Trigger Studies with Run 1a Data", CDF Note #3167, 1995.

[10] S.Belforte *et al.*, "Silicon Vertex Tracker Technical Design Report", CDF Note #3108, 1994.

Chapter 13

Computing and Software

There are a large number of computing challenges that CDF must face in Run II. The data rates will be much higher than those we have dealt with in the past. Consequently we will have much larger datasets which must be stored and made accessible in a timely fashion to many physicists at many collaborating institutions. In addition we would like to evolve our software environment to use more modern programming techniques and languages such as Object Oriented programming and C++.

In the next section we review the present Run I system followed by a section describing the expected data volume in Run II. The remaining sections describe the computing model, the software environment, the event reconstruction, the calibration database, and finally the simulation requirements.

13.1 The Run I System

In Run I CDF recorded 64 million events in the main data stream (Stream B) which were processed in real-time and made available to the physicists within about 2 weeks of the data being taken. In addition, 3.7 million events out of the total were also recorded in a separate "express line" stream (Stream A) and processed within hours. This stream contained the high-transverse momentum leptons necessary for the top quark search. It was also used to monitor data quality during the run. An additional 28 million events were recorded for processing after the data taking ended (referred to as Stream C). These events were mainly low-transverse momentum leptons intended for studies of b-quarks.

The analysis computing needs for Run I were provided by a mix of central and desktop systems. These systems were a combination of VAX/ALPHA machines running VMS plus Silicon Graphics and IBM machines running UNIX. The central VMS system consisted of about 1200 MIPS of CPU (FNALD) and the central UNIX system (an SGI Challenge XL with 28 processors - CDFSGA) consisted of 2400 MIPS. In addition, the desktop systems add 3000 MIPS of VMS computing and 1600 MIPS of UNIX computing.

The production computing needs were met by the centrally supported UNIX farms. CDF had an allocation of 3000 MIPS of farm computing in the form of 63 SGI 4D/35 nodes and 32 IBM 320H nodes. The data were processed on the farm nodes and then split up into physics datasets on the farm I/O nodes and then staged to 8mm tape.

The data sizes and volumes are summarized in Table 13.1. There were 27 DST datasets and 39 PAD (PAD - Physics Analysis DST) datasets. The DSTs from the main data stream are not heavily used in analysis. The total data volume for Run I was 41 Terabytes, of which 16 Terabytes was due to inclusion of raw data on the inclusive and split DSTs. The information about where a file is located is stored in an experiment specific database which uses FORTRAN indexed files and is kept on FNALD.

The primary means of data storage for Run I was 8mm tape (double density tapes with 5 Gbytes of storage and a maximum I/O rate of 450 Kbytes/second). Selected datasets were further reduced and stored in an STK tape robot which had an initial capacity of 1 Terabyte and has recently been upgraded to 3 Terabytes. This system is accessed via the FATMEN catalog system (a CERN product) and an automatic staging system - users do not need to know which tape the data is stored on, only the filename. The central UNIX and VMS systems also have about 500 Gbytes of disk devoted to physics datasets. There is over 200 Gbytes of disk in the staging pool for the STK robot. There are also significant disk resources (about 600 Gbytes) attached to desktop systems.

Data Type	Size (Kbytes)	Total Volume (Terabytes)	Comments
RAW	130	8.3	
Inclusive DST	190	12	The DST includes the RAW data
Split DST	190	16	There is a 30% overlap of events on the split DST
Inclusive PAD	32	2	
Split PAD	32	2.7	There is a 30% overlap of events on the split PAD

Table 13.1: Summary of the Run Ib data volume.

Copies of selected datasets were made for distribution to remote institutions. In Run Ib about 17000 8mm tape copies were made. About 3600 of these were kept on site at Fermilab for use by physicists in the CDF Portakamp complex and the rest were sent offsite.

The software environment uses FORTRAN as the primary programming language with limited use of C in system level applications. A mix of experiment developed applications, Fermilab Computing Division products and CERN products are used in the software development and analysis. The code is presently supported on VAX/ALPHA VMS, SGI UNIX and IBM AIX platforms.

13.2 Expected Data Volume and processing requirements

The upgraded DAQ system is expected to be able to handle a Level 3 input rate of about 300 Hz with an peak output rate of 30-40 Hz assuming a 90% rejection factor. We expect the raw event size to be about 250 Kbytes per event, hence the Level 3 output rate is expected to be 7.5-10 Mbytes/second to mass storage. Past experience has shown us that the 40 Hz peak translates to a 20 Hz average rate while there is beam in the accelerator and the experiment is recording data. This implies that we will record about 300 million events per year, yielding 80 Terabytes of raw data. This is about 10 times the total Run I volume. In a two year run which is assumed to be about 2 fb^{-1} the dataset will be 600 million events and 160 Terabytes in size. This corresponds to the main dataset, we have not included any low priority stream such as the Run I Stream C data.

In order to estimate the sizes for the reconstructed data we have assumed that the reconstructed data size remains at about 50% of the raw data size and that the size of a PAD event will be about 15% of the raw data size. We also assume that there will be an "express-line" stream which will be about 10% of the total dataset, and that these events will be written out separately so they can be processed immediately. As noted above, we have duplicated the raw data on both the inclusive DSTs and the split DSTs. We will assume that this is no longer practical due to the larger data volumes expected and so the DST format will no longer include the raw data. We will also assume that for most data streams there will not be a split DST. Under these assumptions the DST+PAD information will add 75 Terabytes of information. For ease of access we will probably need to store the split PAD events separately which will add another 24 Terabytes of data. The "express-line" raw data will be 16 Terabytes and the DST+PAD information will add 8 Terabytes. The split "express-line" PADs will be another 2 Terabytes. So the total volume will be about 300 Terabytes for a 2 fb^{-1} run (allowing for a 30streams). Note that if the DAQ system delivers more Level 3 output rate then these numbers will increase. We take 300 Terabytes for 2 fb^{-1} as our baseline.

At present we do not have an estimate of the CPU time per event for reconstruction in Run II. Much of the code will be new and does not yet exist. We

can make an estimate of the production requirements based on the execution time per event in Run I. In Run Ia the execution time was 400 MIPS seconds/event for an average instantaneous luminosity of 3×10^{30} cm^{-2} s^{-1}. In Run Ib the execution time was 700 MIPS seconds/event at an average luminosity of 9×10^{30} cm^{-2} s^{-1}. This increase was due to the extra interactions per crossing at the higher luminosity. Although the luminosity will increase further in Run II, the number of bunches in the accelerator is increasing so we estimate only an additional 20% increase in processing time from this source. Allowing for some increase in processing time we will use 1200 MIPS second/event for our baseline execution time for Run II. We need to process 300 million events per calender year, i.e. 6 million events per week. The input rate required would be 2-3 Mbytes/second and the CPU requirements for processing would be between 15,000 MIPS to 25,000 MIPS depending on the processing efficiency.

13.3 Computing Model

In this section we describe the proposed computing model for Run II and its various components. We will first describe the Run I computing model. The Run II model will be similar but with some important changes to provide faster and more transparent access to large datasets.

13.3.1 Run I Computing Model

In Run I we have followed a model where the data and the CPU are tightly coupled. We have not provided high-bandwidth access from desktop systems to the central data stores. In addition, we have no dedicated batch systems, all the central systems are used for both batch and interactive computing.

The current CDF data persistency package is YBOS[1]. The data is stored in YBOS banks. The raw data is stored on 8mm tape. The event reconstruction is then performed on farms of UNIX workstations. A subset of the YBOS banks containing physics information from the reconstruction are also compressed to create PAD events. The events are also split into production datasets. These datasets are taken by the physics groups and futher split or compressed. This can be a lengthy step and difficult to recreate if a problem is discovered later. This is an I/O intensive job and is usually performed on the central systems (usually by a small number of people) where there is efficient access to large production datasets on 8mm tape. The resulting datasets are stored on disk or if they are too large for disk they are placed in the STK tape robot. Up to this point in the process, the data is still in the form of YBOS banks and access to the events is file-based.

The users doing physics analyses perform further selections of these datasets, normally on the central systems. The result of these event selections is typically an ntuple[2] which stores the data in ZEBRA RZ[3] format. These ntuples are usually small enough to be transferred to the desktop system for further analysis. Most physics analyses start from the PAD data. However a small number of analyses such as the W-mass measurement require the DST data. All analyses may require the full DST for a small number of events. The amount of data used from the 32 Kbyte PAD event ranges from 1 Kybte for exotic searches to about 10 Kbyte for a typical b-quark analysis.

13.3.2 The Run II Computing Model

The primary operating system in Run II will be UNIX. The VMS operating system will not longer be a supported operating system at Fermilab and will not be part of the Run II computing environment. We do not yet know what role personal computers (PCs) might play. The goal is to design a system that is as operating system independent as possible to allow us to respond to future trends in computing with minimal upheaval.

Production UNIX farms are a cost effective way to obtain the necessary CPU cycles to perform the event reconstruction and we expect that this will be the primary method of doing bulk event reconstruction in Run II. However, we do not ignore the possibility that farms of PCs running LINUX, for example, could play a role.

The production farm I/O servers will read raw data directly from the tape robot and write the processed data back to the same robot. The processed information for an event will not be stored in the same file or tape as the raw information. As stated above, the DST format will no longer include the RAW data as this will significantly increase the storage requirements. The data will also be split into physics streams at this stage. In most cases the splitting

will be done at the PAD level. Only for a few selected datasets would split DSTs be produced. The information about dataset location and which events belong to a particular dataset would be recorded in a central database.

Mass Storage and Data Access The baseline data volume expected in Run II is 250 Terabytes. It is not practical to imagine storing this quantity of data on 8mm tape. We plan to write the data to staging disk at the experiment and transmit it directly to staging disk attached to a robotic tape store in Feynman Computing Center (FCC). Tape robots already exist that can handle the data volume we will have in Run II with the required data transfer speeds to and from the magnetic media. Clearly the exact choice of technology will be made closer to the start of Run II. In addition to the robot, one requires Heirarchical Storage Management (HSM) software to control the robot.

It may be desireable to store all the information about a particular type of physics object in one location in the robot to improve the access time for event selections, which typically look at a small amount of information.

A database will be necessary to record the information about which events belong to a dataset and on which physical tape they reside. The database must interface to the HSM software to allow the information to be retrieved from the tape. Retrieval of data ahould be transparent to the user, i.e., the user need only know the name of the dataset they are interested in, not the list of files that make up that dataset. Also the user should not need to know the physical organization of the dataset. Users would submit event selection requests to the central database by specifying which dataset they want to access and providing a set of selection criteria. The physics datasets could be created from the production dataset in the same way. If these datasets were large it would probably not be practical to physically duplicate the events. Instead the list of events that make up the dataset would be recorded in the central database.

The robot will be attached to the central analysis facility which will consist of some number of multiprocessor UNIX machines coupled together by a high-speed network. These machines will support both batch and interactive use. Users could also submit event selection requests to the central database from their desktop workstation and have the selected data returned to the workstation. The event selection will run on the central system, thus ensuring efficient access to the central data store, and only the selected data will be returned, thus minimizing the network traffic. A goal would be to read a 2 Terabyte dataset in a few days, this requires tape speeds of the order of 10-20 Mbytes/second. If we are able to read pieces of events then this time could be reduced even further. With this kind of access time, remaking a dataset would not incur a severe time penalty.

Clearly, there will still be a need to export datasets to remote institutions. The wholesale duplication of some of the larger production datasets may not be practical. It may be more useful to provide copies of the physics datasets which will be smaller. Given the goals stated above for reading datasets, it will also be possible for users to create specialized datasets on the central system and copy them to tape for export.

Most frequently accessed datasets would be kept on disk. It might be necessary, in order to maximize the use of the disk space, to keep only the most frequently accessed components of the events on disk, .e.g. for a QCD dataset we may decide that it is not necessary to keep the tracking data on disk. If a component of an event is requested and the component is not on disk then a staging operation would be performed to retrieve the necessary information. This would be transparent to the user.

Another idea that is being investigated is the concept of "data mining". A subset of the data is stored on disk in a format which allows for fast event selection queries to be run over large amounts of data. The selected data can be output in a user-selected format, e.g. ntuples. The event selection only uses the disk resident scannable data but can then trigger retrieval of additional data from tape for any given event. This approach is under investigation in the High Performance and Parallel Computing group in the Fermilab Computing Division.

Some of these goals imply changes to the CDF persistency package YBOS. This package treats events as a sequential list of banks which is too restrictive for Run II. We are presently evaluating alternative persistency mechanisms. One option is to rewrite the YBOS package in C++ to include the necessary features. Some work has already been done on this option and it looks feasible. Another interesting option is the use of an Object Oriented database to store the data. This approach is being seriously studied by the RD45 project at CERN [4]. The potential cost of

such an approach is an issue as is the maturity of the technology. Even if this is not a viable option for the beginning of Run II, we should not design a system that prevents the use of such approaches later on.

Networking We are at present planning an upgrade to the networking infrastructure at CDF which will bring fiber to each desktop, thus opening up the possibility of FDDI, ATM etc. to the user's workstation. This upgrade should be sufficient to meet the desktop networking needs for Run II.

In the central systems we may require higher bandwith connections. We will have to connect together multiple multiprocessor UNIX machines and provide each with a high-bandwidth connection to the robot. Possible candidates include Fiber Channel or HIPPI.

A dedicated 10-20 Mbyte/second connection between B0 and FCC may also be necessary for the transfer of the raw data from the staging disks in B0 to the robot in FCC.

Analysis Computing The analysis computing will be provided by a mix of central systems plus desktop workstations. As stated above, the machines will be running the UNIX operating system. The role of PCs in the system has not been considered at present.

We can make a rough estimate of the CPU needs by scaling from Run I. This suggests that we will require roughly 30,000-40,000 MIPS of computing to meet the Run II analysis needs. This can be spread between central systems and desktops.

13.4 Software environment

In this section we describe the various components of the software environment. This is the part of the computing environment that most directly impacts the user and includes such things as the choice of programming languages and the framework used for analysis.

13.4.1 Software Methodology and Languages

The computing problem faced by a large experiment in high-energy physics involves the manipulation of large volumes of complex, structured data which describe the observed physical interactions, components of the detector, and the intellectual framework used to interpret the data. Low-level data structures are combined to form lists which are utilized by algorithms to generate structures at a higher level of abstraction. A typical example of this process is the assembling of hit data from a tracking chamber into found track segments, which are then assembled into track helix parameters.

There is a natural relationship of this process to the concepts of the object-oriented programming methodology. Indeed, the current CDF software may be described as an object-oriented data design operating within a Fortran framework. To accomplish this goal, very significant extensions of the native Fortran environment have been provided in the past, using customized products with a very large overhead in maintenance and low portabililty.

Mapping of software objects into code may be naturally accomplished by an object-oriented programming language such as C++, in which object description is provided at a low, native level in the compiler. In addition, other potentially useful features of the OO model, such as inheritance and overloading, are provided in such a language.

The use of the C++ programming language will be a feature of the software development environment for the CDF Run II upgrade. We expect to devote a large effort to providing the necessary design tools and support required by this initiative. The choice of C++ is mandated by its wide use in scientific and technical fields, including most new projects in high energy physics (BaBar, CLEO III, and LHC experiments).

Because of the extensive existing software base of the CDF experiment, we expect to need to continue support for the Fortran 77 programming language. The exact level at which the two languages must interact is still under discussion. One possible model is to allow the use of relatively large scale software units ("modules") in either Fortran or C++, but to require language consistency within a single module.

13.4.2 Code Mangement and Distribution

For a software project of the scope of the CDF upgrade, it is necessary to provide an adequate structure to manage and track the development of the system. Developers must be able to easily access the code they are working on and transparently benefit from the work of others. In some instances, a reservation mechanism can prevent conflicting changes in

programs; at the least a mechanism for detecting such changes is essential. It is also desirable to provide access control to protect the software and avoid unauthorized modifications.

The primary code repository for the CDF Run II upgrade software will be the central UNIX computing facility located at Fermilab. CDF is currently carrying on active discussions on implementation of this repository in the context of the Configuration Management Working Group, a joint working group of CDF, D0 and the Fermilab Computing Division. It is very likely that the recommendations of this group will focus on the Concurrent Versioning System (CVS) utility, which is widespread on UNIX systems and in the high energy physics community. A system based on CVS allows any part of a directory tree to be accessed, modified, and tracked as a unit, from individual files to the entire repository.

We expect to provide a mechanism for accessing code in the CVS repository using a client-server model. This technique, for which there is a working large system to serve as a prototype (the Sloan Digital Sky Survey), will allow developers to work on local UNIX systems with the code they require, then merge it back into the primary code repository. It also provides the possibility of integration of user-defined procedures for such functions as detailed access control and required testing at check-in time. CVS permits concurrent changes by multiple developers and blocks assembly of conflicting changes. If reservations are deemed necessary, a user-defined procedure can be used to provide this feature.

The software package must be distributed to collaborating institutions and other supported computing installations (e.g. the distributed desktop systems used by CDF physicists). We expect to use the functionality provided by the code management system described above to allow on-demand updates of the code while it is under development (this is an ongoing process). Tagged releases of packages will be distributed via batch updates in compressed format, as we have successfully used in Collider Run I.

13.4.3 Reconstruction and Analysis Framework

A framework for experimental application programs should provide adequate flexibility to address the diverse computing needs of the CDF collaboration. These include Monte Carlo Simulation, bulk production of analysed datasets, user analysis, and the Level 3 trigger system of software filtering. The framework should support both interactive and batch operation, and transparently address all supported media.

CDF has a framework which has been used with great success in Run I and previously. It enables the user to define a set of software modules which are then incorporated at run time into sets which correspond to particular analysis pathways. Standard modules provide, for example, data i/o and reporting of data contents. The intrinsic modularity of the structure encourages a great deal of software reuse. Application building tools have been provided to assist the user.

The current CDF framework is heavily dependent on custom utilities to handle internal communications and generate the user interface. We plan to reduce reliance on these products as they become increasingly unmaintainable. This will require modifications to the framework software to maintain compatibility. The design and implementation of these changes, including possible new products, will benefit heavily from our extensive experience in this area. Other experiments are also active in this area, and we will examine the possibility of joint solutions.

The user interface for the Run II framework will take advantage of developments in third-party graphical user interfaces (GUI). One possible candidate for such an interface is the TCL/TK scripting language and toolset. The BaBar experiment has a prototype framework based on this product, which we are testing. Other public domain and commercial products will also be evaluated where appropriate.

13.5 Event Reconstruction

In Run II we will have many new detector subsystems for which we must write new event reconstruction code. As stated above, we expect use of the C++ programming language to feature in the Run II reconstruction package. A number of detector groups in CDF (SVXII, IFT) are experimenting with the use of C++ in their reconstruction code. The results look promising.

The event reconstruction package is constructed of a number of independent "modules" that each perform a specific task. Each module communicates its data to another by use of a well defined interface (presently this interface is YBOS data banks). Modules execute sequentially and in a given order, i.e., the

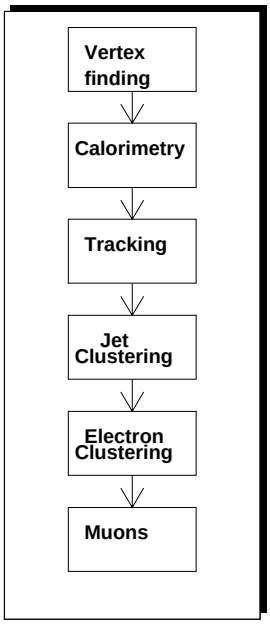

Figure 13.1: The logical flow of CDF event reconstruction in Run I

tracking module must run before the electron finding module because electron identification requires tracks. This will be true even in an object-oriented model. Parameters can be set at run-time that govern the behaviour of a particular module. In Fig. 13.1 we show the logical flow of the existing CDF event reconstruction.

As described previously, the event reconstruction is carried out on farms of UNIX workstations (worker nodes) connected to a central I/O server. Each event is read from tape or disk and sent to a worker node for processing. when processing is complete the event is sent back to the I/O server for output. The CPS (Cooperative Process Software) product devloped by the Fermilab Computing Division has been used to carry out the event distribution. We anticipate continuing to use a similar product for Run II.

13.6 Calibration Database

In order to maintain an adequate record of detector performance, detailed information on calibrations, detector status, and beam conditions is recorded during checkout and running. Since a great deal of calibration is performed locally, the calibration information can be divided into data required by offline processing (which must be served to the processing clients) and strictly local information, which is maintained at the experiment for diagnostic purposes. In addition, the information may be generated either by hardware calibrations in advance of datataking, or by monitoring software during datataking. (Examples of the latter are dead channel counts and information on beam conditions.)

In previous runs, calibration data has been maintained everywhere in a custom database using YBOS as its primary keying mechanism and data retention mechanism. A run-number based index provided efficient access to the data. Changes in YBOS will have implications for calibration data.

Design decisions for the calibration database will be based on an analysis of the amount of calibration information to be generated by the experiment and where it will be needed during reconstruction. The results of this analysis will likely constrain our choices of implementation. An example is the use of commercial databases, which may only be useful in limited locations due to licensing costs.

In light of past experience, and considering the large amount of new hardware being commisioned for Run II, we expect to need to be able to modify the detailed implementation of our calibration storage. A well-designed interface to the calibration data will make this evolution possible. We plan to test such an interface during FNAL testbeam running, even if the final low-level implementation is still changing.

13.7 Simulation

The CDF simulation will require major modifications before the next Tevatron run. These modifications are necessary both because the detector itself is changing (new tracking detectors, new calorimetry in region $\eta > 1.0$ and a change in the z position of the forward muon toroid) and because the CDF software environment is changing. In particular, if CDF decides to move towards the use of the C++ programming language, the simulation will move in

that direction as well.

For Run I, CDF has two independent simulation packages, a fast simulation (QFL) that produces as its output high-level reconstruction banks and a slow simulation (CDFSIM) that produces raw data banks. Both simulations rely completely on CDF-specific code (i.e. neither one uses the GEANT simulation package). Both run within the CDF analysis framework and use the CDF persistency mechanism (YBOS).

The purpose of the CDF fast simulation (QFL) is to provide an appropriate tool for generating large statistics Monte Carlo samples to determine the overall acceptance for various physics analyses and to study the dependence of this acceptance on systematic variations in either the detector response or the physics model. The philosophy of the package has been to make the highest level data structures possible rather than simulate raw data and to use parameterized responses rather than a first principle approach. Significant effort has been put into parameterizing the response of the calorimeter (including calibration, non-linearities, cracks and variations in gain across the face of the detector), the muon system (including non-uniform magnetic field effects and multiple scattering), the pre-radiator and the strip detectors at shower max. Because the performance of the silicon vertex detector plays such an important role in the top analysis, this detector has received special attention. In this case, raw hits are simulated (including the effects of multiple scattering and Landau fluctuations) and the CDF pattern recognition and fitting code is used to associate these hits with tracks. In the case of the central tracking chamber, however, the simulation does not produce raw hits. Instead the tracking resolution is parameterized by generating a 5x5 covariance matrix for each track and then using this covariance matrix to create the smeared track parameters. Thus, the fast simulation does NOT allow detailed studies of pattern recognition efficiencies. Instead, pattern recognition studies are performed using the slow Monte Carlo (CDFSIM). An alternative technique which is commonly used in CDF is to measure track reconstruction efficiencies is to imbed single Monte Carlo tracks in real data events.

The current version of QFL can simulate a $t\bar{t}$ event in approximately 0.7 MIP-sec. By comparison, full reconstruction of such events from raw data takes about 700 Mip-sec. The speed of the package results from the fact that the number of volumes in the simulation is small ($\sim$ 30) and the step size is large, from the fact that hadronic and electromagnetic showers are parameterized and from the fact that pattern recognition in the central tracker is not performed. In QFL, the step size is set by the path length to the volume boundary unless a discrete process (bremsstrahlung, pair production, decay-in-flight) occurs within the volume, in which case the particle is stepped to the point where that process occurs. The trajectory is corrected for continuous processes (energy loss and multiple scattering) at the exit point of the volume. At each step, the track trajectory (momentum and position) is stored in a data structure. Genealogical information relating generated tracks and vertices to the simulated tracks is stored, including information necessary to trace a generated particle's fate through discrete processes such as decays. Structures that store the genealogical relationship between generated tracks and hits in the detector are available as an option. All such structures can be output as part of the standard CDF event record.

Our goal for Run II is to maintain the speed and functionality of the current fast simulation, while improving its flexibility. In particular, we plan to incorporate current CDFSIM functionality (the creation of raw hits in the tracking data) as an option within the fast simulation framework.

We are currently exploring options for restructuring the simulation. One possibility would be to use a GEANT4 framework. In this case, GEANT4 routines would be used to trace particles through the detector. To maintain the speed of the simulation, we would continue to use CDF specific parameterizations of calorimeter showers and we would keep the geometry description extremely simple. A second option for Run II would be to use as a framework the MCFAST simulation package currently being developed by the Fermilab Computing division. The third option would be to continue the current practice of using CDF-specific code. Prototyping efforts on all 3 approaches are currently underway. A final decision on the framework will be made in Spring 1997, several months after the first beta-test release of GEANT4.

Bibliography

[1] YBOS is an extension of the BOS package from DESY. It is written in FORTRAN and combines the functions of data persistency and memory management.

[2] An ntuple is like a table where each event is a row of the table and each variable in the event is a column. It is part of the CERN HBOOK package and is widely used in HEP experiments.
HBOOK, CERN Program Library Long Writeup Y250, Version 4.2, Application Software Group, Computing and Networks Division, CERN, 1993.

[3] ZEBRA is a CERN package that performs the same functions as YBOS. It is written in Fortran and combines the functions of data persistency and memory management.
ZEBRA, CERN Program Library Long Write-ups Q100/Q101, Application Software Group, Computing and Networks Division, CERN, 1993.

[4] RD45 is a CERN project to study persistent object managers for HEP. Their latest status report can be found at http://wwwcn.cern.ch/pl/cernlib/rd45.

Chapter 14

Experimental Facilities

The proceeding chapters have focussed on the detector, and have not addressed a number of important issues related to the interface with the Tevatron, the experimental infrastructure and hall. We discuss below pertinent aspects of the the solenoid and cryogenics, the beam pipe design, Tevatron monitors, Tevatron shielding, the detector gas supply systems, and the heating, ventilation, and air conditioning (HVAC) systems.

14.1 Solenoid and Cryogenics

The CDF detector employs a large magnetic field volume instrumented with tracking devices to determine the trajectories, sign of electric charge, and momenta of charged particles. The magnetic field is provided by a superconducting solenoid. The solenoid provides an axial magnetic field of 1.5 Tesla over a useful volume 2.8 m in diameter and 3.5 m long. The solenoid was designed by a collaboration of physicists and engineers from Fermilab and Tsukuba University in Japan. The coil was built in Japanese industry. The power supply, controls, and refrigeration system were built by Fermilab. The solenoid provides a 1.5 Tesla uniform axial field by creating a cylindrical current sheet with a uniform current density of 1200 A/m. The magnet is indirectly cooled (no direct contact between LHe and the superconductor) and employs a high purity Aluminum stabilized NbTi conductor with a maximum operating current of 5000 Amps. For most of the magnet's life an operating current of 4650 Amps has been used corresponding to a central field of 1.41 Tesla. The high purity aluminum conductor is "soft" and is supported against the large electromagnetic loads produced via an external support cylinder of 5083 Aluminum. Turn-to-turn insulation is Kapton with b-staged epoxy. Ground plane insulation is G-10 and polyester resin. The refrigeration is provided by a STAR version Tevatron satellite refrigerator located in B0 with 600 W capacity. The magnet was first operated in 1985 and has run regularly for high energy physics and cosmic ray data taking with a field availability of $> 99\%$.

14.1.1 Lifetime

The initial design of the coil specified a "10 year lifetime". However, the entire coil structure was designed to operate well within the elastic limits of the materials chosen and therefore it is expected to have a lifetime not limited by fatigue considerations. Similar design rules were used for the support structures which are subjected to cyclic stresses each time the magnet is powered. The entire coil structure is subject to cooldown stresses each time the magnet is cooled to its LHe temperature operating point. The magnet cooldown procedures followed are intended to limit stresses on the coil materials such that stresses are limited and fatigue failures are not a problem. The materials chosen for the coil construction were all chosen to be radiation tolerant at the several mega-Rad level. This is well beyond the expected radiation dose the coil will receive during a Run-II exposure of 2 fb^{-1} ($<$ few kRad at the radius of the coil) The coil package was deliberately designed using welded construction with a minimal number of O-rings. Where O-rings were employed the design used "double" O-rings with a vacuum pumpout between for reliability. The 24 radial support adjustments each have two "double" O-rings as does the main cryostat vacuum relief port. We believe that whatever age related failures might occur in these devices will be soft failures that would not interrupt the run in progress.

14.1.2 Necessary Repairs

A small vacuum leak has been present in the CDF magnet's "Control Dewar" since it was commisioned. The Control Dewar contains the 5000 AMP He gas cooled current leads that make the transition from the cold LHe temperature superconductor to the warm 5000 Amp copper bus. Since the coil is indirectly cooled, the superconductor resides in the insulating vacuum space. Inside the Control Dewar, the superconductor makes a transition from the vacuum space into a "pot" of LHe via 5000 Amp ceramic insulators (the pot serves to thermally anchor the bottom of the gas cooled leads). Since failure of the ceramic insulators would represent a single point failure mode for the magnet if they were to leak LHe into the insulating vacuum space, a secondary vaccuum space and a second backup set of insulators were provided. This turned out to be useful in that a very small leak of the primary insulators was observed shortly after the magnet was commissioned. The decision was made to "live" with the leak rather than repair it since the net effect of this leak was that the small secondary vaccuum space had to be pumped out periodically (approximately once per 2 weeks). This insured that the vacuum remained good enough to provide adequate electrical insulation during a fast discharge of the coil. The leak rate into this space was essentially unchanged over many years of operation and over several cooldown cycles.

During a refrigerator interruption and subsequent rapid recooling of the magnet during Run Ib we observed an increase in this leak rate by a factor of about four. Although still a small leak manageable by pumping, this change suggests that we should consider repairing this problem before Run II. Changing the insulator is possible but would require substantial effort in disassembly and reassembly of this complicated component. It is our intention to study less drastic repairs using a bore-scope first. Provided adequate engineering manpower is provided in a timely fashion to study and address this problem, this repair should not be difficult. Even assuming the worst (i.e. replacing the entire control dewar), the schedule for Run II should not be affected. The cost of the repair will vary depending on the technique chosen.

14.1.3 Controls upgrade

The cryogenic controls system used to operate the Satellite refrigerator and CDF solenoid was designed in 1983 and first became operational in 1984. The system uses many components, display devices, and software "borrowed" from the accelerator controls system (ACNET). CDF received support from the Accelerator Division to maintain and operate this system. For Run II much of the Accelerator controls system that operates the satellite refrigerators will be upgraded by the Accelerator Division. The old system components and software will no longer be supported. Therefore CDF must upgrade its cryogenic controls system.

The Research Division plans to replace the CDF refrigerator control system with a modern commercial control system using a Moore APACS controller with Intellution's FIX-DMACS man machine interface software. This same package has been installed for other helium refrigerators operated by the Research Division. As part of the control system replacement, we also plan to simplify and upgrade the solenoid interlock system.

14.2 Beam Pipe

The CDF beam pipe will consist of three pieces which span the B0 interaction region between the B0 low beta quadrapoles. A schematic diagram of the B0 beam pipe system is shown in Fig. 14.1.

The center section, which is inside the CDF tracking volume, will be a 1.0625" inside diameter, 0.020" wall beryllium pipe. The maximum outside diameter of the beryllium beam pipe will be 1.438", occurring at the low profile end connections of the pipe. For reference the Be pipe in Run I had an inside diameter of 1.335" and an outside diameter of 1.5". In the current design, the beryllium portion consists of three roll-formed and brazed sections joined by two machined beryllium couplings. The total length of the beryllium is 131". Two inch long stainless steel end pieces will be brazed to the ends of the beryllium to provide a surface for the knife edges of the low profile vacuum flange connections. The resulting Run II beam pipe will have an overall length of 135". A 1.0625" inside diameter pipe of this length is an acceptable aperture in the Tevatron at B0 [1], including anticipated deformations (sag, out of roundness).

Spanning the gap between the beryllium pipe and the low beta quadrapole magnets on each side of the collision hall will be a low mass stainless steel bellows pipe. The exact dimensions of this section are not completely defined, however, the design will be

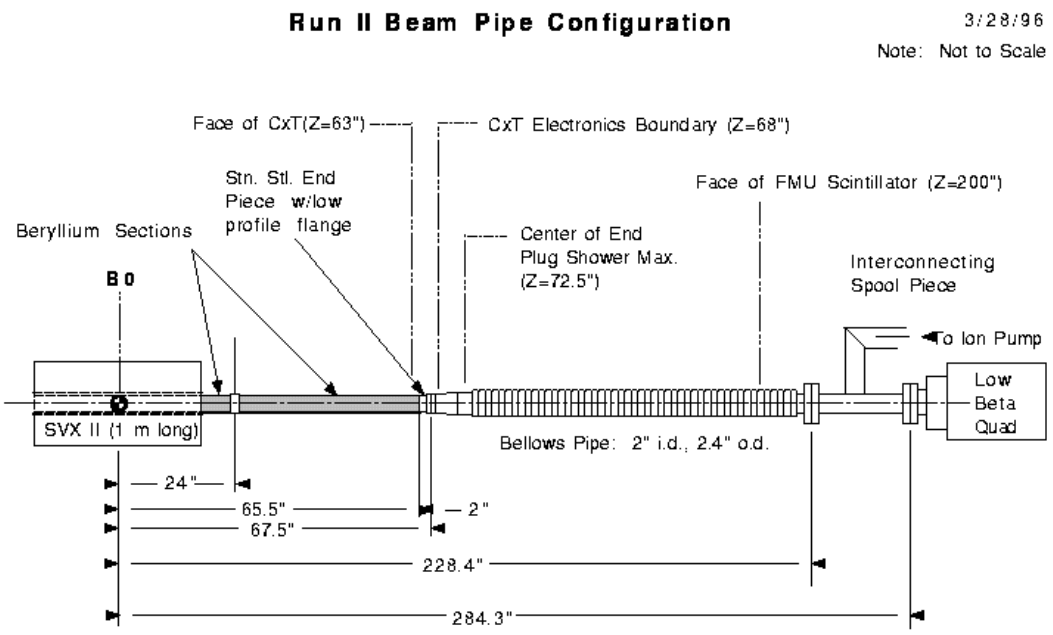

Figure 14.1: CDF beam pipe design for Run II.

quite similar to the Run Ib bellows-pipe. That pipe consisted of a 130" long stainless steel bellows section with end transition pieces and flanges for an overall length of a 133". The ID was 2" and the OD was 2.4". The pitch between each convolution was 0.144", and the wall thickness was 0.006". For Run II the bellows-pipe section would have the same ID and OD, with an overall length of roughly 161".

A low mass flange has been designed for the connection between the Be pipe and the bellows pipe. This flange is smaller in every dimension than the Run Ib flange and is constructed primarily of aluminum rather than stainless steel. For comparison, the Run I flange system consisted of approximately 1.5 pounds of stainless steel, where the Run II low mass flange will be approximately 0.22 pounds of Aluminum. This design, with its smaller cross section, and mass should result in significantly reduced background rates, even compared with the acceptable Run Ib flange. However, before deciding on the final lengths of the Be section, the low mass flange and the bellows-pipe design, we intend to perform a detailed simulation to study possible backgrounds.

Historically, the connecting spool piece from the bellows-pipe to the low beta quads was designed and constructed by the accelerator division. The Run Ib spool piece will not work because the location of the vacuum pipes will be different in Run II, due to the relocation of the forward calorimeter and the forward muon toroids. We will work with the Accelerator Division to ensure that this piece (which could also cause backgrounds in our detector) is low profile and low mass, and is included in our beam-background simulations.

14.3 Tevatron Monitor

The Tevatron Monitor in Run II for CDF consists of two fundamental parts: the luminosity/loss monitor and the beam-position/profile monitor.

Although the luminosity monitor is essential to CDF for Run II, its design is relatively simple and its implementation can be quickly accomplished. In addition, it will use technology that is well understood and similar to the Run I luminosity monitor, with which we have a great deal of experience. Although the instantaneous luminosity will increase from $2.0 \times 10^{31} cm^{-2} sec^{-1}$ in Run I to $2.0 \times 10^{32} cm^{-2} sec^{-1}$ in Run II (chiefly by increasing the number of bunches from 6 to 36), the average luminosity per bunch will not increase dramatically. Therefore the plan for the Run II monitor is similar to that of Run I, and uses

arrays of scintillators on both sides of the interaction region. Coincidence timing defines luminosity as particles moving in both directions away from the interaction region, while a separate coincidence defines Tevatron losses as particles moving through the interaction region in the proton or pbar directions.

In Run I, CDF determined the transverse beam position by analyzing the CTC and SVX tracks coming from the vertex. The track data were obtained from the CDF DAQ and analyzed on-line by a dedicated VAX Alpha work-station. Running on this computer, the software of the beam-position monitor was able to provide an ± 5 micron estimate of the beam position in about 5 minutes, sending the information to the Tevatron via ACNET immediately, and saving it in the CDF database for use in the offline data analysis. The same data was analyzed to give estimates of the beam slopes, transverse beam profiles, and interaction region betastars with a slower update frequency (about 2 hours). In Run II, we plan to enhance the monitoring software to accommodate the increase in the number of bunches, and substitute a faster computer if one is available at a reasonable cost. At this time, we forsee no further design changes, but leave open the possibility for further enhancements. One possible enhancement is use of the SVT trigger processor (see section 13.9) to calculate the beam parameters at CDF with a 1 Hz update frequency.

Radiation monitoring for Run II will be very similar to the Run I system for CDF [2] with only minor technical modifications. The system uses PIN diodes and Tevatron Beam Loss Monitors to detect fast losses and set alarms. During Run I the system was used to abort the Tevatron beam cleanly under well defined conditions, avoiding large radiation doses on the SVX detectors.

14.4 Tevatron Shielding

Backgrounds appear in the detector from real collisions at the interaction point and from the single beams (protons or antiprotons) as they pass through the focusing quads. The muon systems are most sensitive to these backgrounds and require shielding in Run II.

14.4.1 Shielding from real collisions

As discussed in Section 10.6, the CMX muon detectors are sensitive to losses from the Tevatron. The mechanism is production of particles at the interaction point followed by secondary interactions of these particles in the far forward parts of the beampipe. Since the the CMX trigger is based on pattern recognition of radial tracks, low energy secondary particles produced in the beampipe can fake a muon track stub. Building on similar work done for Run I [3], we are beginning to model this Run II loss pattern using CDFSIM and GEANT.

Preliminary Monte Carlo work indicates that a shield around the beampipe will be essential in Run II and a conceptual shield attached to the back of the Plug Calorimeter is illustrated in Fig. 14.2. The shield will be mostly made of steel, but additional layers of polyethylene and lead are also being studied. Such a shield has mass near the beampipe and can produce even more radial backgrounds via the interplay between multiple scattering and the CMX radial pointing resolution. Evaluation of thinner shields having larger inside diameters (the outside diameter is constrained by the Plug Calorimeter PMT boxes) will be done before choosing the final design.

From measurements in Run I, we also know that most of the background rate in CMX occurs in the 1/3 of the chambers at highest rapidity. This area will be effectively shielded by the additional 60 centimeters of steel to be added to the toroids for the Intermediate Muon Upgrade (see Sec 10.6. Our Monte Carlo work indicates that this "IMU snout" will be crucial in the control of Run II background rates in the CMX.

14.4.2 Shielding from Proton and Antiproton Beams

The Tevatron also produces substantial losses from the individual proton and antiproton beams as they enter the collision hall from the Tevatron tunnel. In order to understand these losses, a special "proton only" test run was made during Run Ic. At the end of a normal store the $\overline{p}$'s were shifted in time by 1.75μsec, and the detector was triggered on the crossing clock, so the occupancy was due entirely to the circulating current of 1×10^{12} p's moving from west to east through the detector. We explicitly studied the E-775 Forward Muon system (FMU) of chambers located on the front, middle, and rear of the toroids. The results are shown in Figure 14.3, compared to a normal high luminosity 1.8 TeV collider run. The FMU occupancy is the total number of wire hits in all

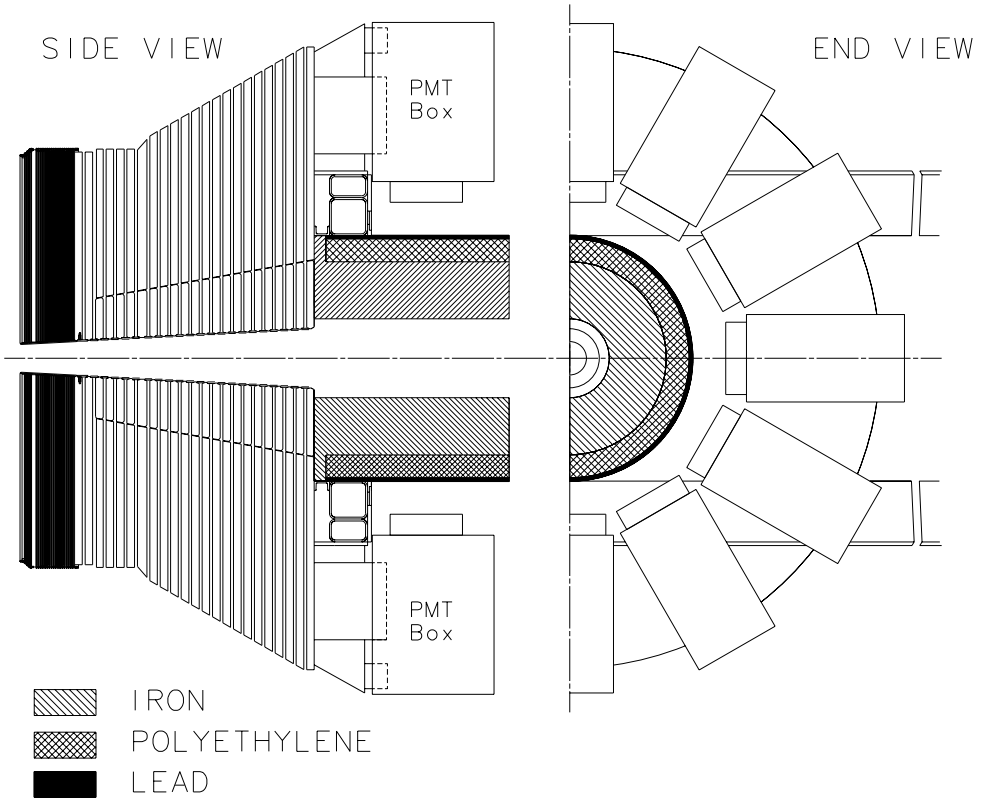

Figure 14.2: Conceptual design of a Tevatron Beampipe Shield for CMX

24 chambers of a given plane per CDF trigger. Note that for the proton only store there were almost no hits anywhere except in the west rear planes, where the occupancy was comparable to that observed under normal colliding beam conditions. This radiation was attenuated by more than a factor of 15 by the 1 meter thick toroid steel between the rear and mid planes. This special run also produced data on the radial and azimuthal pattern of the losses.

Calculations of Tevatron losses using the MARS code have been done[4] for the CDF specific case, begining with the special Run Ic proton only conditions discussed above. By comparing the observed Run I total rate, azimuthal rate, and radial rate to the MARS Monte Carlo, we have gained confidence in the Monte Carlo and can use the Monte Carlo to understand the loss source(s) and optimum shielding arrangements for Run II. As of this writing, MARS models the rear FMU plane very well in both radial and azumuthal distributions, but seems to work less well (off a factor of three and generally too low) for the middle FMU plane.

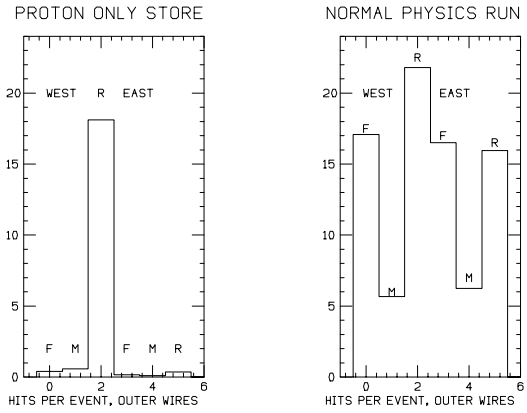

Figure 14.3: FMU Occupancies per CDF trigger

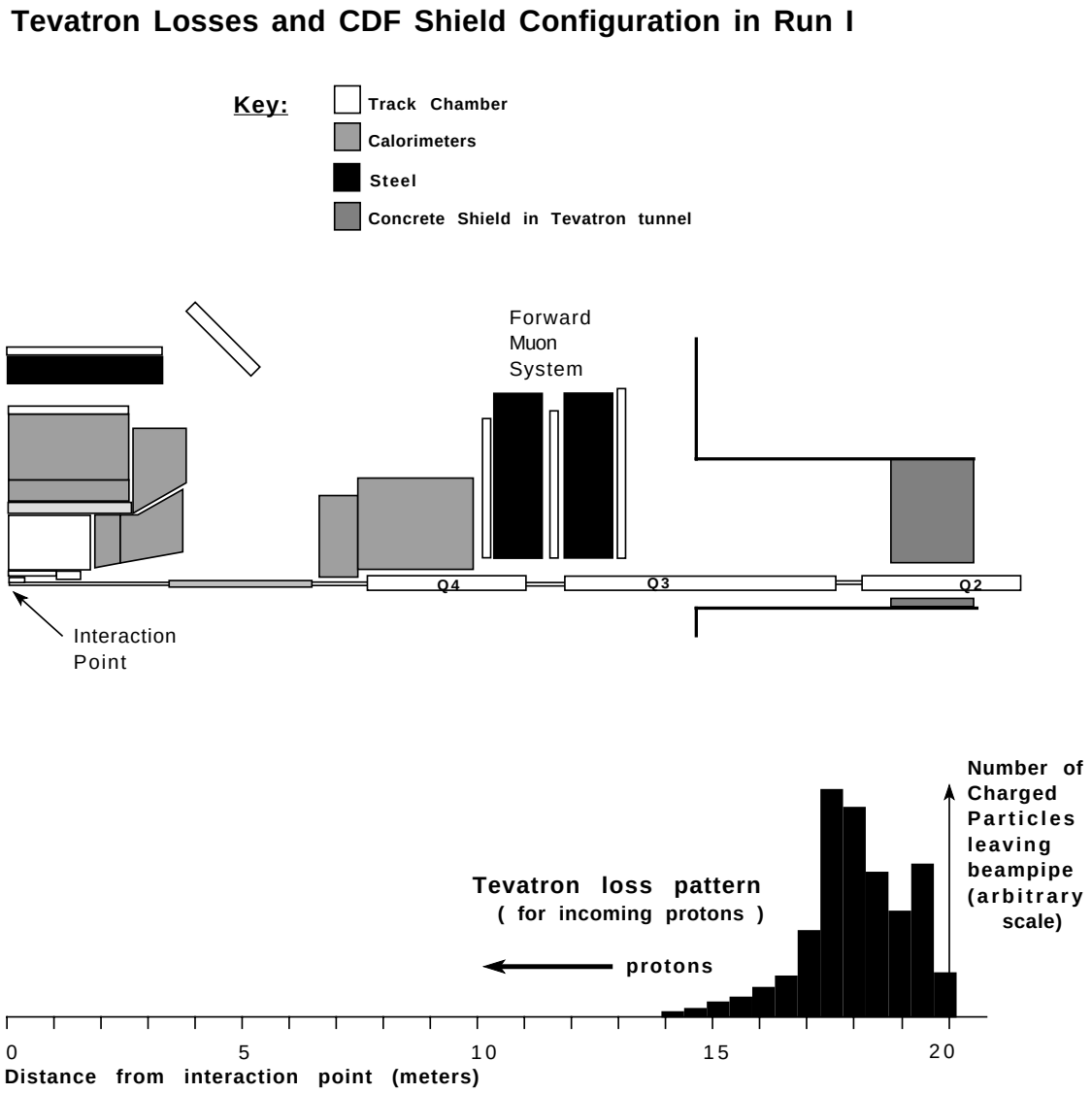

Figure 14.4: Tevatron Beamline losses superposed on the Run I geometry

CDF Shielding Design for Run II

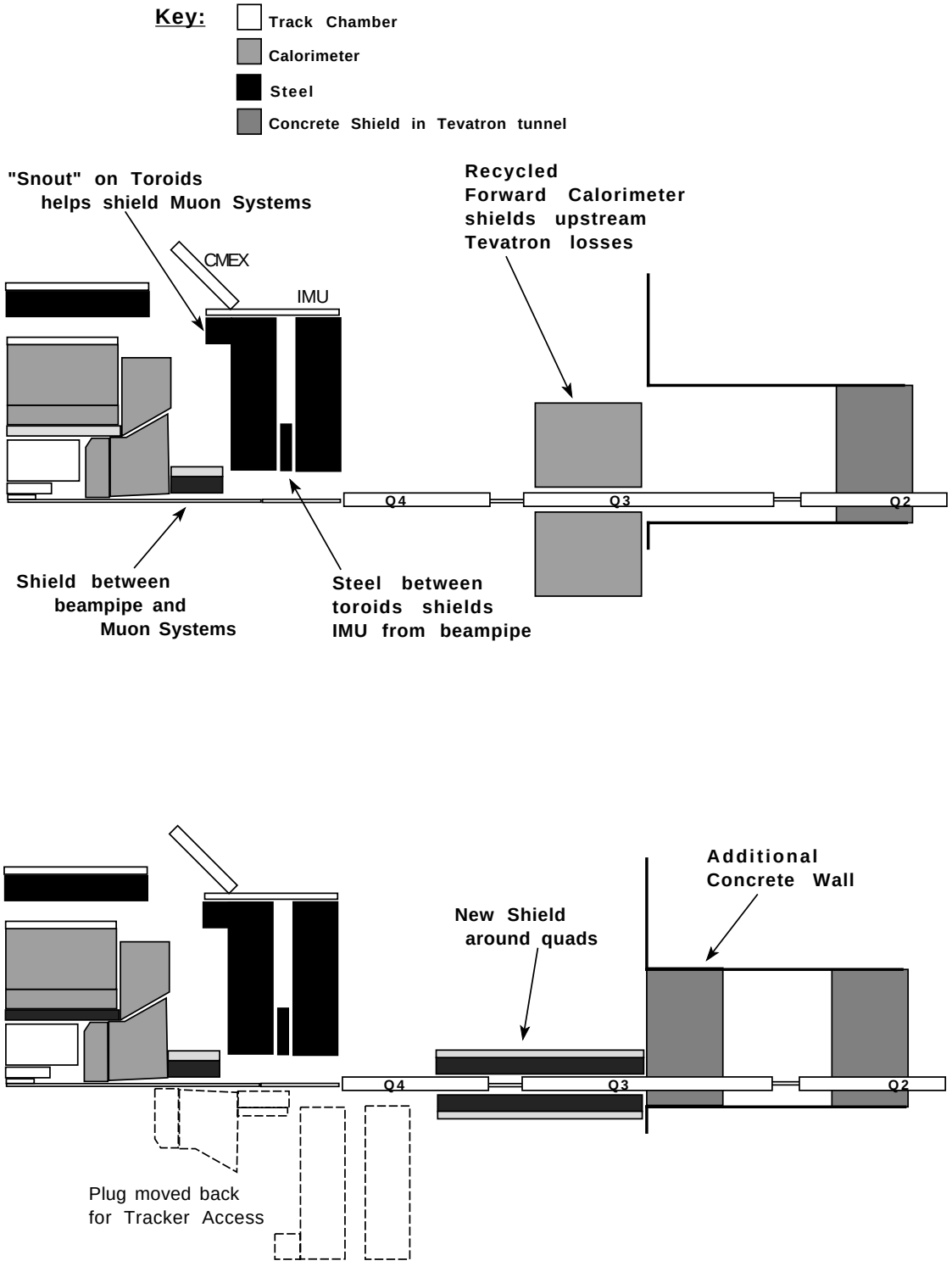

Figure 14.5: Tevatron Beamline shielding scenarios for Run II

Fig. 14.4 shows the CDF configuration during Run I with the MARS calculated loss density in the low beta quadrupoles superimposed. The calculated main loss point is the upstream end of the Q3 quad, but additional losses equal to that shown in the figure come from as far as 35 meters from the interaction point. These far upstream losses are partially shielded by a 6 foot thick concrete wall, but particles still enter the hall through an 18 inch radius hole in the concrete wall around the quads. In Run I this hole was stuffed with bags of polyethylene beads and the MARS code shows that bags of sand with 10% polyethylene would give a clear improvement.

Two possible shielding scenarios for Run II are shown in Fig. 14.5. The upper diagram shows the E-775 Forward Hadron Calorimeter[6] steel repositioned behind the toroids and interleaved with polyethylene in the slots originally occupied by the Forward Hadron proportional chambers. This shield would have a total of 1.37 m of steel and 0.69 cm of polyethylene in 27 layers with a 4 m x 4 m cross section centered on the Tevatron. Thirty layers of 0.5 cm thick lead with a 3 m x 3 m cross section are also available via recycling the E-775 Forward Electromagnetic Calorimeter and could be used in place of some polyethylene.

The lower diagram in Fig. 14.5 shows a shield like that proposed for Dzero[5] with a box around the Q4 / Q3 quads composed of 40 cm of steel, 10 cm of polyethylene, and 4 cm of lead. The lower diagram also shows an additional 6 foot thick concrete wall at the mouth of the tunnel. So far, studies with MARS indicate that the shield box scheme is better (by a factor of 15) than the recycled calorimeter, but these studies have been restricted to the losses seen at the rear of the toroids.

Given the measured Run I attenuation from the 1 meter thick toroid alone, it is possible that no additional shielding will be required for the IMU muon system beyond upgrading to sandbags around the quads. After additional MARS studies of losses in the mid toroid plane and at the outside radius of the toriods where the IMU chambers and scintillators are positioned, we will choose a final shield design based on need, effectiveness, and cost.

14.5 Mixing Facility for Detector Gases

The CDF complex includes a gas mixing system for Argon + Ethane built for Run I. The Argon source is boil-off from a liquid storage tank, while the Ethane source is tube trailers of purchased gas with a tight specification on allowed contaminants. This system allows a mixture of 50% Argon + 50% Ethane with an error on each component below 0.1 % via comparison to gravametric standard gases. The 0.1 % specification was set by the gain stability required for the Run I gas calorimeters. The system has a storage capacity of 17,880 standard cubic feet (SCF) to service a total detector chamber volume of 3,200 SCF. The total operational flow in Run I was 128 Standard Cubic Feet per Hour (SCFH), but the system had a flush rate capacity of 200 SCFH. Each subsystem using this gas added individual amounts of Ethanol or Isopropyl Alcohol, and none of the gas was recycled. As discussed in section 5.5.1, chamber aging effects seen in Run I lead to an extensive examination and cleaning of this gas system and even more cleaning may be required. Specifically we are considering replacing a fraction of the stainless steel piping and cleaning four large storage tanks.

For Run II the gas calorimeters and several drift chambers have been removed, reducing the total chamber volume to 2,300 SCF. The total required flow is reduced to 85 SCFH with most of this flow (60 SCFH) used by the muon systems. This reduced flow will simplify operations by increasing the mean time between mixes by 50%.

The new COT tracker will require 25 SCFH but must have CF_4 added at the 5-15% level (see section 5.5.2). The plan is to use the mixed 50% Argon + 50% Ethane as input to a separate new mixing system for the COT as shown in Fig. 14.6, then adding CF_4 and Argon to effectively replace a percentage of the Ethane. The COT system may include recirculation of the gas due to the cost of CF_4. The muon systems do not require CF_4, and they cannot tolerate gas recirculation due to outgassing materials used in their construction.

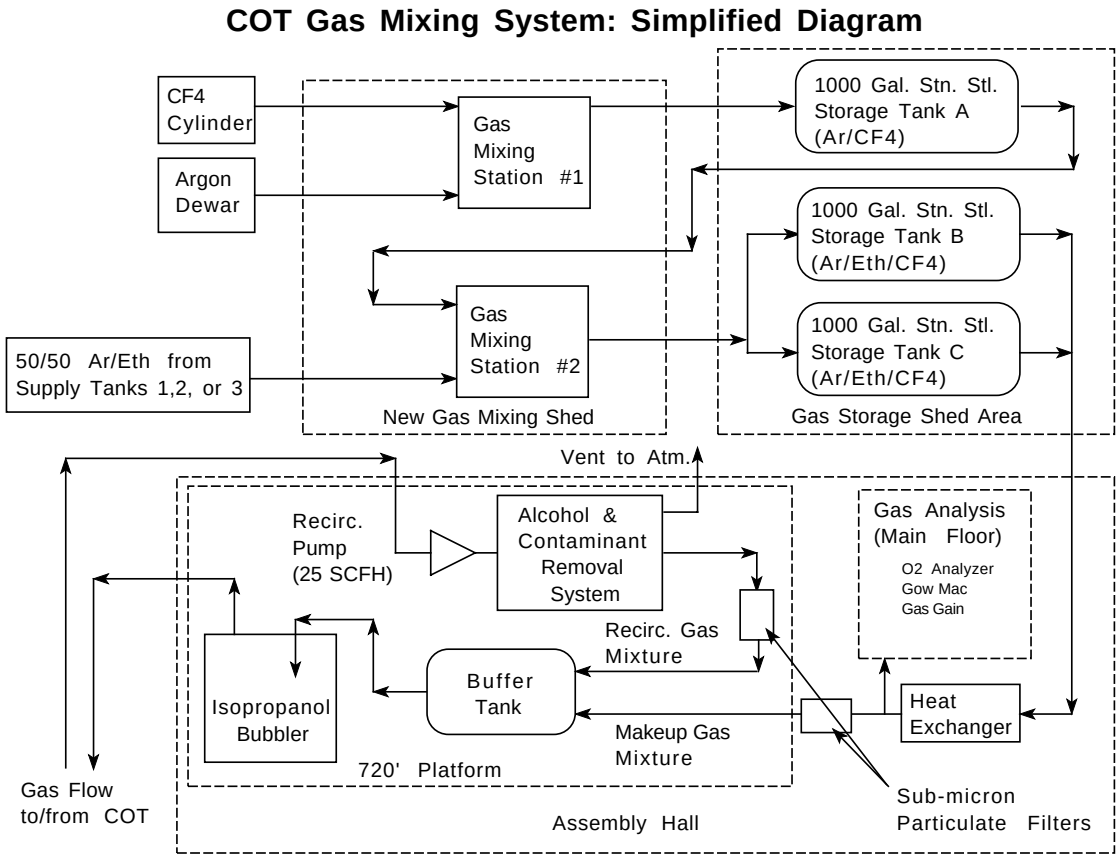

Figure 14.6: CF4 Gas Mixing System for Run II.

14.6 Heating, Ventilation, and Air Conditioning

14.6.1 Overview

The CDF upgrade for Run II forces changes to the Heating, Ventilation, and Air Conditioning (HVAC) plant in the CDF Assembly Hall and the B0 Collision Hall. The heat loads in the Collision Hall change because of additional electronics for new detector components and because of repositioned electronics systems for existing detectors. The loads are generally more difficult to reach with air cooling because they are boxed inside the muon upgrades. The heat loads in the Assembly Hall counting rooms will also change. A large portion of the air cooled load in the first floor counting room will not exist in Run II, and experience in Run I shows that other counting room loads are less difficult to cool than envisioned in the 1981 design.

Additional changes to the HVAC system are driven by operational and maintenance concerns for Run II. Some of the existing equipment is very old and at the end of its useful life. Other equipment has proven difficult to maintain and new options are now available. For completeness the entire HVAC plan is described here, even though some parts fall more naturally in the equipment budget (e.g. new air-water heat exchangers for new upgrade electronics crates), while other parts will be covered within the operating budget (e.g. replacement of the existing unmaintainable humidifiers).

With input from CDF on environmental specifications and estimates of the electronics heat loads in Run II, The Fermilab Facility Engineering Services Section has completed a Criteria Review Set[7] This is a design at the 30% level, equivalent to Title I and with project contingencies understood at the 25% level. The elements of this design are described in the next three sections.

14.6.2 Collision Hall Specification and Design

The environmental specifications for the Collision Hall during Run II are detailed in Table 14.1 and compared to the observed conditions in Run I. Table 14.2 shows the expected heat loads and Criteria Review Set design cooling sources for the Collision Hall. Three separate balance sheets are shown for the airborne heat load, the chilled water heat load, and the low conductivity water (LCW) heat load. Actual numbers are shown for Run I during steady state operations and for Run I during repair access periods. Estimates are shown for Run II.

During Run I, the heat load in the Collision Hall was distributed among four main sources: the electronics crates, a standard building load of 3.5 kW per 200 sq. ft., the power load for four large fan coil cooling units in the hall, and the forward muon toroid coils. Cooling in Run I was supplied by two outside air handlers (AC-2 and AC-3), the four fan coil units, and LCW to the toroid coils. The cooling capacity was adequate during collider operations but insufficient during repair periods, causing degraded data quality following repair periods.

For Run II we have done a bottoms up calculation of the electronics heat loads and find that all the new VME crates should generate less than 0.6 kW each. For the HVAC design, we have used 1.0 kW per crate to insure adequate headroom. The real difficulty in Run II is caused by the toroids, which are moved closer to the interaction point and will block airflow to the crates. Similar airflow restrictions already existed in Run I due to the Central Muon Upgrade walls and the Central Muon Extension stands. The Run II toroid position just provides the final cork to the bottle.

The plan is to split detector cooling in the Collision Hall between air cooling and direct chilled water cooling via air-water heat exchangers associated with every electronics crate. The new use of direct cooling accommodates the severe space constraints, increases cooling efficiency, and improves temperature control in local areas. The direct cooling chilled water system will run in a copper pipe header with festoons to moveable sections of the detector. A similar alternate header in the Assembly Hall will supply chilled water to the detector during commissioning.

In addition, the existing fan-coil units in the Collision Hall will be removed, eliminating 25% of the Run I heat load. Air cooling in Run II will be entirely supplied by upgraded replacements of the existing outdoor air handlers, AC-2 and AC-3. Small local fans inside the Collision Hall will assist in maintaining stable temperature stratification patterns. The toroid LCW system will also be upgraded by switching from pond water cooling (which operates with 16 - 41°C water depending on the season) to a constant temperature chilled system maintained at 18°C. This follows the scheme employed successfully at Dzero, will further remove airborne heat load from the collision hall, and will contribute to improved temperature stability. Air temperature within the collision hall will be lowered by 2°C from the present conditions. Beam-off repair accesses into the collision hall will not require adjustment of the cooling system, resulting in temperature stability during all data taking periods.

14.6.3 First Floor Counting Room Specification and Design

The specification for the Counting Rooms is identical to the Collision Hall except the pressure requirement is dropped and we expect only modest stratification between the floor and the ceiling. Table 14.3 shows the expected heat loads and Criteria Review Set design cooling sources for the First Floor Counting Room. Actual values seen in Run I are also shown for comparison.

The heat load in the first floor counting room will be reduced by about 25% in Run II. Twenty racks of air cooled electronics will be removed and the existing water cooled Fastbus crates will be converted to water cooled VME crates. A bottoms up estimate of the heat loads in each VME crate does not yet exist, so an estimate has been done with an administrative limit of 2.5 kW per crate imposed on the electronics design. We expect to meet this administrative limit with ease on most crates, allowing flexibility for some crates to push beyond the limit to the "CDF specific VME crate" power limit of 6 kW.

Air cooling for this counting room will continue to be supplied by two Liebert AC units in the room and by cooling from the building AC unit, AC-1. AC-1's capacity will be beefed up by eliminating a kitchen area and two restrooms from its zone, thus devoting AC-1 to the single purpose of electronics cooling with most of the additional cooling diverted to the second floor.

Variable	Run I observation	Run II specification	Notes (below)
Temperature Stability (°C)	± 3	± 1	(1)
Temperature range, top to bottom of hall (°C)	18-29	16-27	(2)
Relative humidity	40-60%	40-60%	(3)
Delta pressure relative to outside (inches of water)	0.014	0.050	(4)

1. During Run I, the temperature stability in a given location reached this level after the hall had been closed for a week following an access. Even larger temperature swings occurred during an access because part of the cooling had to be turned off for hearing protection. The Run II specification is set by the (0.4 ± 0.6)% gain per degree Centigrade seen in the central EM calorimeter phototubes. This temperature variation has a direct impact on precision measurements with electrons, e.g. the W mass.
2. This is the same range but with a reduced maximum intended to increase electronics component lifetime.
3. The range observed in Run I is that during stable operation. However, the system was notoriously unstable and swings from 20% to 80% relative humidity were observed during frequent equipment failures. This has a direct influence on some trigger rates due to increased sporadic electrical breakdown around phototube photocathodes in the central calorimeters.
4. In Run I this specification was set by the need to keep fragile windows on gas calorimeters from popping their seals. With the replacement of the gas calorimetry by scintillator, the specification can be relaxed to the more modest needs of the central tracker output bubblers.

Table 14.1: Environmental Specification for the Collision Hall

14.6.4 Second Floor Trigger & Control Room Design

Table 14.4 shows the expected heat loads and Criteria Review Set design cooling sources for the Second Floor Trigger and Control Rooms. Actual values seen in Run I are also shown for comparison.

Tests of the cooling system for the second floor rooms following Run I indicated that nearly all the Run I heat load was removed by the Fastbus chilled water system. These Fastbus crates were different from those in the first floor counting room because the power supplies were also water cooled. While the first floor Fastbus crates were operated with loads at the 2.5 kW limit, on the second floor the heat loads were much smaller. Most of the crates generated less than 1.0 kW, and five crates had essentially zero heat load. Meanwhile the Fastbus chilled water system supplied water to an air/ water heat exchanger for each crate capable of cooling 2.5 kW per crate. Since the racks were open to the room, the second floor Fastbus crates acted as a net cooling source.

In Run II the Fastbus crates will be converted to VME crates and these crates will be isolated from the room air. A bottoms up estimate of the heat loads in each crate has been done and we expect 0.86 kW per crate. For the HVAC design we have used 1.5 kW per crate as the water cooled load, insuring adequate headroom and using the same air/water heat exchangers planned for the first floor crates. The two Liebert AC units on the second floor will be removed to increase floor space by 50 square feet in a cramped area. Air from AC-1 will easily handle the remaining load on the second floor.

14.6.5 Other General HVAC Issues

To accommodate the changes described above another air cooled chiller will be installed outdoors and connected to the main chilled water supply loop. This will increase the total cooling capacity to 2800 kW, with 2 chillers @ 665 kW and 3 other chillers @ 490 kW each. Total chiller capacity is sized to allow any one unit out of service for repairs without downtime to the experiment.

The entire chilled water system plant will be converted to 40% propylene glycol to permit year round chiller operations outdoors, eliminate persistent coil freezing problems, and allow improved heat transfer to AC-2 and AC-3 through elimination of the present glycol heat exchanger and pump arrangement. Continuous operation will eliminate the seasonal turn-on and turn-off cycles which plagued the chilled water system during Run I, causing downtime due to cool-

Collision Hall Air	**Run I (kW) Operations**	**Run I (kW) in Access**	**Run II (kW) Ops=Access**
Heat to Air Load			
Air cooled electronics crates	98	98	7
Power supplies for air cooled crates	17	17	1
Crate muffin fans	24	24	1
Detector electronics outside crates	1	1	23
Plug PMTs (24 @ 100W in heating mode)	did not exist	did not exist	3
Silicon Detector chiller	1	1	4
Three Air loads from Water Cooled devices (assumes 10% inefficiency)			
Water cooled VME Crates	did not exist	did not exist	8
Power Supplies for crates	did not exist	did not exist	2
Air recirculation blowers in crates	did not exist	did not exist	1
400 Hz transformers	3	3	3
Building Load	87	87	87
Controls for Pressure, Relative Hum.	35	35	35
4 Fan Coil Units	90	off	removed
Toroid coils (LCW cooled)	24	off	off
Toroid jumper cables	5	off	off
Solenoid leads (LCW cooled)	7	7	0
Heat to air total:	392	273	175
Air Cooling			
4 Fan coil units	560	0	removed
Building Air Handler, AC-2	128	128	190
Building Air Handler, AC-3	128	128	190
Total air capacity:	816	256	380

Collision Hall Chilled Water	**Run I (kW) Operations**	**Run I (kW) in Access**	**Run II (kW) Ops=Access**
Heat to chilled water load (assume 90% efficiency)			
76 VME crates @ 1 kW each	did not exist	did not exist	68
Power Supplies (10% of 2 kW/crate)	did not exist	did not exist	14
Recirculation Blowers (10% of 430 W/crate)	did not exist	did not exist	3
Plug PMTs (24 @ 100 W in cooling mode)	did not exist	did not exist	3
Chilled water total:	0	0	88
Chilled Water Cooling Capacity	0	0	146

Collision Hall LCW	**Run I (kW) Operations**	**Run I (kW) in Access**	**Run II (kW) Ops=Access**
Heat to LCW load (80% efficiency in Run I, 100% in Run II)			
Toroid coils (@ 200 v, 600 amps)	96	off	off
Solenoid leads (@ 8 v, 4650 amps)	30	30	37
LCW total:	126	30	37
LCW Cooling Capacity	500	500	236

Table 14.2: Collision Hall Heat Loads and Cooling Capacities

First Floor Counting Room Air	Run I (kW)	Run II (kW)
Heat to Air Load		
Air cooled custom "MX" racks	41	removed
NIM and CAMAC crates @ 0.7 kW each	42	53
Gas Calorimeter High Voltage Crates	8	0
Calorimeter PMT High Voltage Supplies	4	8
Other High Voltage Supplies	19	19
5 Air loads from Water Cooled devices:		
Fastbus water cooled crates and PS	33	removed
(30% water cooling inefficiency in Run II)		
Water cooled VME Crates (10U version)	did not exist	9
VME Power Supplies (10U version)	did not exist	1
VME crates (6U version)	did not exist	1
VME Power Supplies (6U version)	did not exist	0
(10% water cooling inefficiency in Run II)		
Fans and miscellaneous equipment	3	3
Transformers	11	11
1st Floor Kitchen and Restroom load	11	removed
Building Load	16	16
Heat to Air total:	188	121
Air Cooling		
2 Liebert AC units in the room	182	182
Part of Building AC unit, AC-1	28	10
Total air capacity:	210	192

First Floor Counting Room Chilled Water	Run I (kW)	Run II (kW)
Heat to Chilled Water Load		
39 Fastbus crates and PS @ 2.5 kW each	65	removed
(Run I system was 70% efficient)		
42 (10U) VME crates @ 2.2 kW each	did not exist	83
42 VME Power Supplies @ 0.3 kW	did not exist	11
9 (6U) VME crates @ 1.1 kW each	did not exist	9
9 VME power supplies @ 0.1 kW each	did not exist	1
(Run II system aims at 90% efficiency)		
Chilled Water Total:	65	104
Chilled Water Cooling Capacity	98	173

Table 14.3: First Floor Counting Room Heat Loads and Cooling Capacities

Second Floor Trigger and Control Room Air	**Run I (kW)**	**Run II (kW)**
Heat to Air Load		
NIM and CAMAC crates @ 0.7 kW each	13	6
Trigger Room workstations @ 1.2 kW	1	1
Trigger Room monitors @ 0.25 kW	1	1
Control Room workstations @ 1.2 kW	6	6
Control Room monitors @ 0.25 kW	3	3
Miscellaneous PCs @ 0.6 kW	6	6
Four Air loads from Water Cooled devices:		
Fastbus water cooled crates	-26	removed
5 "empty" Fastbus water cooled crates	-10	removed
(Fastbus crates provided cooling in Run I)		
VME Crates (10U version)	did not exist	0
VME Power Supplies	did not exist	0
400 Hz transformer	1	1
Building Load	16	16
Heat to Air total:	11	40
Air Cooling Capacity		
Trigger Room Liebert AC unit	61	removed
Control Room Liebert AC unit	61	removed
Part of Building AC unit (AC-1)	14	60
Total air capacity:	136	60

Second Floor Trigger and Control Room Chilled Water	**Run I (kW)**	**Run II (kW)**
Heat to Chilled Water Load		
26 Fastbus water cooled crates @ 2.5 kW	65	removed
5 "empty" Fastbus water cooled crates	13	removed
(Includes Water cooled power supplies)		
42 (10U) VME crates @ 1.5 kW each	did not exist	63
42 VME Power Supplies @ 0.3 kW each	did not exist	13
Chilled Water Total:	78	76
Chilled Water Cooling Capacity	98	126

Table 14.4: Second Floor Trigger and Control Room Heat Loads and Cooling Capacities

ing trips in electronics racks.

The existing Fastbus cooling water pump system located in the first floor counting room will be replaced with a larger VME cooling water pump and heat exhanger system housed in the Assembly Hall (west mezzanine at the 725' level). The VME cooling water system will be a clean distilled water system, separated from the general chilled water system by a plate and frame water-water heat exchanger, and connected to both the collision hall and the counting rooms. The new VME system will run in new copper pipes since the existing Fastbus system in black iron pipes is fouled and has reduced flow. The water-water heat exchanger separation will allow the VME cooling water to be maintained without glycol for electronics protection and permit the outside air cooled chiller change to propylene glycol.

In Run I AC-2 and AC-3 each had "preheat" coils upstream of individual humidifiers in turn located upstream of the mixing point for the Collision Hall input air duct. One consequence was a ± 2 microradian low beta quad motion observed in Run Ib during periods when the two component AC system became untuned and developed $\pm 3^{\circ}$C temperature swings with a 20 minute cycle time. For Run II the "preheat" coils will be replaced by a single "reheat" coil in the duct following mixing of air from the two AC units. A single Collision Hall humidifier steam dispersion panel will be downstream of the "reheat" coil with steam supplied by upgraded electric units insensitive to water conductivity changes. This mixing change should produce better humidity and temperature control. Additional HVAC monitoring will be installed to give information on temperatures at sensitive electronics crate locations and to provide some redundant monitoring for the controls system.

Bibliography

[1] J. Marriner, email to B. Flaugher, March 22, 1996.

[2] D.Amidei et al., NIM A350, 73 (1994).

[3] S.Belforte et al., Monte Carlo Beampipe Studies, CDF Note 1816, 1992.

[4] N. Mokhov and O. Krivosheev, private communication.

[5] N. Mokhov, talk presented at the TeV33 Workshop, Physics at a High Luminosity Tevatron Collider, May 10-11, 1996. See also S. Abachi et al., Fermilab-FN-641, April, 1996.

[6] S. Cihangir et al., NIM A267, 249 (1988).

[7] S. Krstulovich et al., CDF HVAC Upgrade Criteria Review Set, June 1996.

Chapter 15

Publications

1. "Transverse-momentum Distributions of Charged Particles Produced in $\bar{p}p$ Interactions at $\sqrt{s}$ = 630 and 1800 GeV," F. Abe et al., The CDF Collaboration, Phys. Rev. Lett. 61, 1819 (1988).

2. "The CDF Detector: An Overview," F. Abe et al., The CDF Collaboration, Nucl. Instrum. Methods A271, 487 (1988).

3. "Measurement of the Inclusive Jet Cross Section in $\bar{p}p$ Collisions at $\sqrt{s}$ = 1.8 TeV," F. Abe et al., The CDF Collaboration, Phys. Rev. Lett. 62, 613 (1989).

4. "Measurement of W Boson Production in 1.8 TeV $\bar{p}p$ Collisions," F. Abe et al., The CDF Collaboration, Phys. Rev. Lett. 62, 1005 (1989).

5. "Limits on the Masses of Supersymmetric Particles from 1.8 TeV $\bar{p}p$ Collisions at CDF," F. Abe et al., The CDF Collaboration, Phys. Rev. Lett. 62, 1825 (1989).

6. "Dijet Angular Distributions from $\bar{p}p$ Collisions at $\sqrt{s}$ = 1.8 TeV," F. Abe et al., The CDF Collaboration, Phys. Rev. Lett. 62, 3020 (1989).

7. "Measurement of the Mass and Width of the Z° Boson at the Fermilab Tevatron," F. Abe et al., The CDF Collaboration, Phys. Rev. Lett. 63, 720 (1989).

8. "Search for Heavy Stable Particles in 1.8 TeV $\bar{p}p$ Collisions at the Fermilab Collider," F. Abe et al., The CDF Collaboration, Phys. Rev. Lett. 63, 1447 (1989).

9. "K_s^0 Production in $\bar{p}p$ Interactions at $\sqrt{s}$ = 630 and 1800 GeV," F. Abe et al., The CDF Collaboration, Phys. Rev. D40, 3791 (1989).

10. "Search for the Top Quark in the Reaction $\bar{p}p \rightarrow$ Electron + Jets at $\sqrt{s}$ = 1.8 TeV," F. Abe et al., The CDF Collaboration, Phys. Rev. Lett. 64, 142 (1990).

11. "Search for New Heavy Quarks in Electron-Muon Events at the Fermilab Tevatron Collider," F. Abe et al., The CDF Collaboration, Phys. Rev. Lett. 64, 147 (1990).

12. "Measurement of the Ratio $\sigma(W \rightarrow e\nu)/\sigma(Z \rightarrow ee)$ in $\bar{p}p$ Collisions at $\sqrt{s}$ = 1.8 TeV," F. Abe et al., The CDF Collaboration, Phys. Rev. Lett. 64, 152 (1990).

13. "Two-Jet Differential Cross Section in $\bar{p}p$ Collisions at $\sqrt{s}$ = 1.8 TeV," F. Abe et al., The CDF Collaboration, Phys. Rev. Lett. 64, 157 (1990).

14. "Measurement of D^* Production in Jets from $\bar{p}p$ Collisions at $\sqrt{s}$ = 1.8 TeV," F. Abe et al., The CDF Collaboration, Phys. Rev. Lett. 64, 348 (1990).

15. "Jet-Fragmentation Properties in $\bar{p}p$ Collisions at $\sqrt{s}$ = 1.8 TeV," Phys. Rev. Lett. **65**, 968 (1990).

16. "Measurement of the W-Boson Mass," F. Abe et al., The CDF Collaboration, Phys. Rev. Lett., 65, 2243 (1990).

17. "Search for a Light Higgs Boson at the Fermilab Tevatron Proton-Antiproton Collider," F. Abe et al., The CDF Collaboration, Phys. Rev. D41, 1717 (1990).

18. "Two-Jet Invariant Distribution at $\sqrt{s}$ = 1.8 TeV," F. Abe et al., The CDF Collaboration, Phys. Rev. D41, 1722 (1990).

19. "Pseudorapidity Distributions of Charged Particles in $\bar{p}p$ Interactions at $\sqrt{s}$ = 630 and 1800 GeV," F. Abe et al., The CDF Collaboration, Phys. Rev. D41, 2330 (1990).

20. "Top-Quark Search in the Electron + Jets Channel in Proton-Antiproton Collisions at $\sqrt{s}$ = 1.8 TeV," F. Abe et al., The CDF Collaboration, Phys. Rev. D43, 664 (1991).

21. "Measurement of the W-Boson Mass in 1.8 TeV $\bar{p}p$ Collisions," F. Abe et al., The CDF Collaboration, Phys. Rev. D43, 2070 (1991).

22. "Measurement of the W-Boson p_T Distribution in $\bar{p}p$ Collisions at $\sqrt{s}$ = 1.8 TeV," F. Abe et al., The CDF Collaboration, Phys. Rev. Lett. 66, 2951 (1991).

23. "Measurement of $\sigma B(W \rightarrow e\nu)$ and $\sigma B(Z^0 \rightarrow e^+e^-)$ in $\bar{p}p$ Collisions at $\sqrt{s}$ = 1800 GeV," F. Abe et al., The CDF Collaboration, Phys. Rev. D44, 29 (1991).

24. "Measurement of QCD Jet Broadening in $\bar{p}p$ Collisions at $\sqrt{s}$ = 1.8 TeV," F. Abe et al., The CDF Collaboration, Phys. Rev. D44, 601 (1991).

25. "A Determination of $\sin^2\theta_W$ from the Forward-Backward Asymmetry in $\bar{p}p \rightarrow Z^0X \rightarrow e^+e^-X$ Interactions at $\sqrt{s}$ = 1.8 TeV," F. Abe et al., The CDF Collaboration, Phys. Rev. Lett. 67, 1502 (1991).

26. "Measurement of the e^+e^- Invariant-Mass Distribution in $\bar{p}p$ Collisions at $\sqrt{s}$ = 1.8 TeV," F. Abe et al., The CDF Collaboration, Phys. Rev. Lett. 67, 2418 (1991).

27. "Search for $W' \rightarrow e\nu$ and $W' \rightarrow \mu\nu$ in $\bar{p}p$ Collisions at $\sqrt{s}$ = 1.8 TeV," F. Abe et al., The CDF Collaboration, Phys. Rev. Lett. 67, 2609 (1991).

28. "Measurement of the $Z\,p_T$ Distribution in $\bar{p}p$ Collisions at $\sqrt{s}$ = 1.8 TeV," F. Abe et al., The CDF Collaboration, Phys. Rev. Lett. 67, 2937 (1991).

29. "Measurement of $B^0\bar{B}^0$ Mixing at the Fermilab Tevatron Collider," F. Abe, The CDF Collaboration, Phys. Rev. Lett. 67, 3351 (1991).

30. "A Lower Limit on the Top Quark Mass from Events with Two Leptons in $\bar{p}p$ Collisions at $\sqrt{s}$ = 1.8 TeV," F. Abe et al., The CDF Collaboration, Phys. Rev. Lett. 68, 447 (1992).

31. "Inclusive Jet Cross Section in $\bar{p}p$ Collisions at $\sqrt{s}$ = 1.8 TeV," F. Abe et al., The CDF Collaboration, Phys. Rev. Lett. 68, 1104 (1992).

32. "Lepton Asymmetry in W Decays from $\bar{p}p$ Collisions at $\sqrt{s}$ = 1.8 Tev," F. Abe et al., The CDF Collaboration, Phys. Rev. Lett. 68, 1458 (1992).

33. "A Search for New Gauge Bosons in $\bar{p}p$ Collisions at $\sqrt{s}$ = 1.8 TeV," F. Abe et al., The CDF Collaboration, Phys. Rev. Lett. 68, 1463 (1992).

34. "Topology of Three Jet Events in $\bar{p}p$ Collisions at $\sqrt{s}$ = 1.8 TeV," F. Abe et al., The CDF Collaboration, Phys. Rev. D45, 1448 (1992).

35. "Properties of Events with Large Total Transverse Energy Produced in Proton-Antiproton Collisions at $\sqrt{s}$ = 1.8 TeV," F. Abe et al., The CDF Collaboration, Phys. Rev. D45, 2249 (1992).

36. "A Limit on the Top Quark Mass from Proton-Antiproton Collisions at $\sqrt{s}$ = 1800 GeV," F. Abe et al., The CDF Collaboration, Phys. Rev. D45, 3921 (1992).

37. "Measurement of the Isolated Prompt Photon Cross Section Measurement in $p\bar{p}$ Collisions at $\sqrt{s}$ = 1.8 TeV," F. Abe et al., The CDF Collaboration, Phys. Rev. Lett. 68, 2734 (1992).

38. "Measurement of the Ratio $\sigma \cdot B(W \rightarrow \tau\nu)/\sigma \cdot B(W \rightarrow e\nu)$ in $p\bar{p}$ Collisions at $\sqrt{s}$ = 1.8 TeV," F. Abe et al., The CDF Collaboration, Phys. Rev. Lett. 68, 3398 (1992).

39. "A Measurement of the B Meson and b Quark Cross Section at $\sqrt{s}$ = 1.8 TeV Using the Exclusive Decay $B^{\pm} \rightarrow J/\psi K^{\pm}$," F. Abe et al., The CDF Collaboration, Phys. Rev. Lett. 68, 3403 (1992).

40. "A Measurement of the Production and Muonic Decay Rate of W and Z Bosons in $p\bar{p}$ Collisions at $\sqrt{s}$ = 1.8 TeV," F. Abe et al., The CDF Collaboration, Phys. Rev. Lett. 69, 28 (1992).

41. "Limit on the Rare Decay $W^{\pm} \rightarrow \gamma + \pi^{\pm}$ in $\bar{p}p$ Collisions at $\sqrt{s}$ = 1.8 TeV," F. Abe et al., The CDF Collaboration, Phys. Rev. Lett. 69, 2160 (1992).

42. "The Dijet Angular Distribution at $\sqrt{s}$ = 1.8 TeV," F. Abe et al., The CDF Collaboration, Phys. Rev. Lett. 69, 2897 (1992).

43. "Search for Squarks and Gluinos from $p\bar{p}$ Collisions at $\sqrt{s}$ = 1.8 TeV," F. Abe et al., The CDF Collaboration, Phys. Rev. Lett. 69, 3439 (1992).

44. "Inclusive J/ψ, ψ' and b-Quark Production in $\bar{p}p$ Collisions at $\sqrt{s}$ = 1.8 TeV," F. Abe et al., The CDF Collaboration, Phys. Rev. Lett. 69, 3704 (1992).

45. "Limits on the Production of Massive Stable Charged Particles," F. Abe et al., The CDF Collaboration, Phys. Rev. D, Rapid Communications, 46, R1889 (1992).

46. "A Measurement of Jet Shapes in $\bar{p}p$ Collisions at $\sqrt{s}$ = 1.8 TeV," F. Abe et al., The CDF Collaboration, Phys. Rev. Lett. 70, 713 (1993).

47. "A Measurement of the Bottom Quark Production Cross Section using Semileptonic Decay Electrons in $\bar{p}p$ at $\sqrt{s}$ = 1.8 TeV," F. Abe et al., The CDF Collaboration, Phys. Rev. Lett. 71, 500 (1993).

48. "Search for $\Lambda_b \rightarrow J/\psi\,\Lambda^0$ in $p\bar{p}$ Collisions at $\sqrt{s}$ = 1.8 TeV," F. Abe et al., The CDF Collaboration, Phys. Rev. D, Rapid Communications, 47, R2639 (1993).

49. "Study of Four-jet Events and Evidence for Double Parton Interactions in $p\bar{p}$ Collisions at $\sqrt{s}$ = 1.8 TeV," F. Abe et al., The CDF Collaboration, Phys. Rev. D47, 4857 (1993).

50. "Measurement of the Cross Section for Production of Two Isolated Prompt Photons in $p\bar{p}$ Collisions at $\sqrt{s}$ = 1.8 TeV," F. Abe et al., The CDF Collaboration, Phys. Rev. Lett. 70, 2232 (1993).

51. "Measurement of the Dijet Mass Distribution in $p\bar{p}$ Collisions at $\sqrt{s}$ = 1.8 TeV," F. Abe et al., The CDF Collaboration, Phys. Rev. D48, 998 (1993).

52. "A Prompt Photon Cross Section Measurement in $\bar{p}p$ Collisions at $\sqrt{s}$ = 1.8 TeV," F. Abe et al., The CDF Collaboration, Phys. Rev. D48, 2998 (1993).

53. "Comparison of Jet Production in $\bar{p}p$ Collisions at $\sqrt{s}$ = 546 and 1800 GeV," F. Abe et al., The CDF Collaboration, Phys. Rev. Lett. 70, 1376 (1993).

54. "A Measurement of Jet Multiplicity in W Events Produced in $\bar{p}p$ Collisions at $\sqrt{s}$ = 1.8 Gev," F. Abe et al., The CDF Collaboration, Phys. Rev. Lett. 70, 4042 (1993).

55. "The Center-of-Mass Angular Distribution from Prompt Photons Produced in $p\bar{p}$ Collisions at $\sqrt{s}$ = 1.8 TeV," F. Abe et al., The CDF Collaboration, Phys. Rev. Lett. 71, 679 (1993).

56. "A Measurement of the Bottom Quark Production Cross Section in 1.8 TeV $p\bar{p}$ Collisions Using Muons from b-Quark Decays," F. Abe et al., The CDF Collaboration, Phys. Rev. Lett. 71 2396 (1993).

57. "Inclusive χ_c and b-Quark Production in $\bar{p}p$ Collisions at $\sqrt{s}$ = 1.8 TeV," F. Abe et al., The CDF Collaboration, Phys. Rev. Lett. 71, 2537 (1993).

58. "A Search for First-Generation Leptoquarks in $\bar{p}p$ Collisions at $\sqrt{s}$ = 1.8 TeV at CDF," F. Abe et al., The CDF Collaboration. Phys. Rev. D, Rapid Communications, 48, R3939 (1993).

59. "Observation of the Decay $B_s^0 \rightarrow J/\psi\,\phi$ in $\bar{p}p$ Collisions at $\sqrt{s}$ = 1.8 TeV," F. Abe et al., The CDF Collaboration, Phys. Rev. Lett. 71, 1685 (1993).

60. "Search for Quark Compositeness, Axigluons and Heavy Particles using the Dijet Invariant Mass Spectrum Observed in $p\bar{p}$ Collisions," F. Abe et al., The CDF Collaboration, Phys Rev. Lett. 71, 2542 (1993).

61. "Measurement of the Average Lifetime of B-Hadrons Produced in $p\bar{p}$ Collisions at $\sqrt{s}$ = 1.8 TeV," F. Abe et al., Phys. Rev. Lett. 71, 3421 (1993).

62. "Measurement of Drell-Yan Electron and Muon Pair Differential Cross-Sections in $\bar{p}p$ Collisions

at $\sqrt{s}$ = 1.8 TeV," F. Abe et al., The CDF Collaboration, Phys. Rev. D, Rapid Communications, 49, R1 (1994).

63. "Search for the Top Quark Decaying to a Charged Higgs in $p\bar{p}$ Collisions at $\sqrt{s}$ = 1.8 TeV," F. Abe et al., The CDF Collaboration, Phys. Rev. Lett. 72, 1977 (1994).

64. "Search for Excited Quarks in $p\bar{p}$ Collisions at $\sqrt{s}$ = 1.8 TeV," F. Abe et al., The CDF Collaboration, Phys. Rev. Lett. 72, 3004 (1994).

65. "Measurement of the B^+ and B^0 Meson Lifetimes," F. Abe et al., The CDF Collaboration, Phys. Rev. Lett. 72, 3456 (1994).

66. "Measurement of the Ratio $\sigma B(W \rightarrow e\nu)/\sigma B(Z \rightarrow e^+e^-)$ in $\bar{p}p$ Collisions at $\sqrt{s}$ = 1.8 TeV," F. Abe et al., The CDF Collaboration, Phys. Rev. Lett. 73, 220 (1994).

67. "Evidence for Top Quark Production in $\bar{p}p$ Collisions at $\sqrt{s}$ = 1.8 TeV," F. Abe et al., The CDF Collaboration, Phys. Rev. D 50, 2966 (1994).

68. "Evidence for Top Quark Production in $\bar{p}p$ Collisions at $\sqrt{s}$ = 1.8 TeV," F. Abe et al., The CDF Collaboration, Phys. Rev. Lett. 73, 225 (1994).

69. "A Measurement of the B Meson and b Quark Cross Sections at $\sqrt{s}$ = 1.8 TeV using the Exclusive Decay $B^0 \rightarrow J/\psi\, K^*(892)^0$, F. Abe et al., The CDF Collaboration, Phys. Rev. D 50, 4252 (1994).

70. "Measurement of the Small Angle Antiproton-Proton Elastic Scattering at $\sqrt{s}$ = 546 and 1800 GeV," F. Abe et al., The CDF Collaboration, Phys. Rev. D 50, 5518 (1994).

71. "Measurement of the $\bar{p}p$ Single Diffraction Dissociation at $\sqrt{s}$ = 546 and 1800 GeV," F. Abe et al., The CDF Collaboration, Phys. Rev. D 50, 5535 (1994).

72. "Measurement of the Antiproton-Proton Total Section at $\sqrt{s}$ = 546 and 1800 GeV," F. Abe et al., The CDF Collaboration, Phys. Rev. D 50, 5550 (1994).

73. "Evidence for Color Coherence in $p\bar{p}$ Collisions at $\sqrt{s}$ = 1.8 TeV," F. Abe et al., The CDF Collaboration, Phys. Rev. D. 50, 5562 (1994).

74. "W Boson + Jet Angular Distribution in $p\bar{p}$ Collisions at $\sqrt{s}$ = 1.8 TeV," F. Abe et al., The CDF Collaboration, Phys. Rev. Lett. 73, 2296 (1994).

75. "A Precision Measurement of the Prompt Photon Cross Section in $p\bar{p}$ Collisions at $\sqrt{s}$ = 1.8 TeV," F. Abe et al., The CDF Collaboration, Phys. Rev. Lett. 73, 2662 (1994).

76. "Search for Top Quark Decaying to a Charged Higgs Boson in $\bar{p}p$ Collisions at $\sqrt{s}$ = 1.8 TeV," F. Abe et al., The CDF Collaboration, Phys. Rev. Lett. 73, 2667 (1994).

77. "Direct Measurement of the W Boson Width," F. Abe et al., The CDF Collaboration, Phys. Rev. Lett. 74, 341 (1995).

78. "The Charge Asymmetry in W-Boson Decays Produced in $p\bar{p}$ Collisions at $\sqrt{s}$ = 1.8 TeV," F. Abe et al., The CDF Collaboration, Phys. Rev. Lett. 74, 850 (1995).

79. "Observation of Rapidity Gaps in $\bar{p}p$ Collisions at 1.8 TeV," F. Abe et al., The CDF Collaboration, Phys. Rev. Lett. 74, 855 (1995).

80. "Measurement of W-Photon Couplings with CDF in $p\bar{p}$ Collisions at $\sqrt{s}$ = 1.8 TeV," F. Abe et al., The CDF Collaboration, Phys. Rev. Lett. 74, 1936 (1995).

81. "Limits on Z-Photon Couplings from $p\bar{p}$ Interactions at $\sqrt{s}$ = 1.8 TeV," F. Abe et al., The CDF Collaboration, Phys. Rev. Lett. 74, 1941 (1995).

82. "Search for New Gauge Bosons Decaying into Dielectrons in $\bar{p}p$ Collisions at $\sqrt{s}$ = 1.8 TeV," F. Abe et al., The CDF Collaboration, Phys. Rev. D, Rapid Communications, 51, 949 (1995).

83. "Observation of Top Quark Production in $\bar{p}p$ Collisions with CDF Detector at Fermilab," F. Abe et al., The CDF Collaboration, Phys. Rev. Lett. 74, 2626 (1995).

84. "Search for Charged Bosons Heavier than the W in $p\bar{p}$ Collisions at $\sqrt{s}$ = 1800 GeV," F. Abe et al., The CDF Collaboration, Phys. Rev. Lett. 74, 2900 (1995).

85. "Kinematical Evidence for Top Pair Production in W + Multijet Events in $p\bar{p}$ Collisions at $\sqrt{s}$ = 1.8 TeV," F. Abe et al., The CDF Collaboration, Phys. Rev. D 51, 4623 (1995).

86. "Search for New Particles Decaying to Dijets in $p\bar{p}$ Collisions at $\sqrt{s}$ = 1.8 TeV," F. Abe et al., The CDF Collaboration, Phys. Rev. Lett. 74, 3538 (1995).

87. "Measurement of the B_s Meson Lifetime," F. Abe et al., The CDF Collaboration, Phys. Rev. Lett. 74, 4988 (1995).

88. "A Measurement of the Ratio $\sigma \cdot B(p\bar{p} \rightarrow W \rightarrow e\nu)/\sigma \cdot B(p\bar{p} \rightarrow Z^0 \rightarrow ee)$ in $p\bar{p}$ Collisions at $\sqrt{s}$ = 1800 GeV," F. Abe et al., The CDF Collaboration, Phys. Rev. D 52, 2624 (1995).

89. "Measurement of the W Boson Mass," F. Abe et al., The CDF Collaboration, Phys. Rev. Lett. 75, 11 (1995).

90. "Search for Squarks and Gluinos via Radiative Decays of Neutralinos in Proton-Antiproton Collisions at $\sqrt{s}$ = 1.8 TeV," F. Abe et al., The CDF Collaboration, Phys. Rev. Lett. 75, 613 (1995).

91. "Properties of High-Mass Multijet Events at the Fermilab Proton-Antiproton Collider," F. Abe et al., The CDF Collaboration, Phys. Rev. Lett. 75, 608 (1995).

92. "A Search for Second Generation Leptoquarks in $p\bar{p}$ Collisions at $\sqrt{s}$ = 1.8 TeV," F. Abe et al., The CDF Collaboration, Phys. Rev. Lett. 75, 1012 (1995).

93. "Limits on WWZ and WWγ Couplings from WW and WZ Production in $p\bar{p}$ Collisions at $\sqrt{s}$ = 1.8 TeV," F. Abe et al., The CDF Collaboration, Phys. Rev. Lett. 75, 1017 (1995).

94. "Measurement of the B Meson Differential Cross-Section, $d\sigma/d_{pT}$, in $p\bar{p}$ Collisions at $\sqrt{s}$ = 1.8 TeV," F. Abe et al., The CDF Collaboration, Phys. Rev. Lett. 75, 1451 (1995).

95. "Identification of Top Quarks using Kinematic Variables," F. Abe et al., The CDF Collaboration, Phys. Rev. D, Rapid Communications, 52, 2605 (1995).

96. "Measurement of the Polarization in the Decays $B_d \rightarrow J/\psi K^{*0}$ and $B_s \rightarrow J/\psi\phi$," F. Abe et al., The CDF Collaboration, Phys. Rev. Lett. 75, 3068 (1995).

97. "Measurement of the W Boson Mass," F. Abe et al., The CDF Collaboration, Phys. Rev. D 52, 4784 (1995).

98. "Study of $t\bar{t}$ Production in $p\bar{p}$ Collisions Using Total Transverse Energy," F. Abe et al., The CDF Collaboration, Phys. Rev. Lett. 75, 3997 (1995).

99. "Υ Production in $p\bar{p}$ Collisions at $\sqrt{s}$ = 1.8 TeV," F. Abe et al., The CDF Collaboration, Phys. Rev. Lett. 75, 4358 (1995).

100. "Measurement of Correlated μ-$\bar{b}$ Jet Cross Sections in $p\bar{p}$ Collisions at $\sqrt{s}$ = 1.8 TeV," F. Abe et al., The CDF Collaboration, Phys. Rev. D53, 1051 (1996).

101. "Reconstruction of $B^0 \rightarrow J/\psi K^0_S$ Ratios of Branching Ratios Involving $B \rightarrow J/\psi K^{(*)}$," F. Abe et al., The CDF Collaboration, Phys. Rev. Lett. 76, 2015 (1996).

102. "Search for the Rare Decay $W^{\pm} \rightarrow \pi^{\pm} + \gamma$," F. Abe et al., The CDF Collaboration, Phys. Rev. Lett. 76, 2852 (1996).

103. "Measurement of $\sigma B(W \rightarrow e\nu)$ and $\sigma B(Z^0 \rightarrow e^+e^-)$ in $p\bar{p}$ Collisions at $\sqrt{s}$ = 1.8 TeV," F. Abe et al., The CDF Collaboration, Phys. Rev. Lett. 76, 3070 (1996).

104. "Measurement of the Mass of the B^0_s Meson," F. Abe et al., The CDF Collaboration, Phys. Rev. D53, 3496 (1996).

105. "Search for Gluino and Squark Cascade Decays at the Fermilab Tevatron Collider," F. Abe et al., The CDF Collaboration, Phys. Rev. Lett. 76, 2006 (1996).

106. "Search for Charged Higgs Decays of the Top Quark Using Hadronic Tau Decays," F. Abe et al., The CDF Collaboration, submitted to Phys. Rev. D January 5, 1996. FERMILAB-PUB-96/004-E.

107. "Search for Chargino-Neutralino Production in $p\bar{p}$ Collisions at $\sqrt{s}$ = 1.8 TeV," F. Abe et al.,

The CDF Collaboration, Phys. Rev. Lett. 76, 4307 (1996)

108. "Measurement of the B^- and $\bar{B}^0$ Meson Lifetimes Using Semileptonic Decays," F. Abe et al., The CDF Collaboration, Phys. Rev. Lett. 76, 4462 (1996)

109. "Search for Flavor-Changing Neutral Current B Meson Decays in $p\bar{p}$ Collisions at $\sqrt{s} = 1.8$ TeV," F. Abe et al., The CDF Collaboration, Phys. Rev. Lett. 76, 4675 (1996)

110. "Inclusive Jet Cross Section in $\bar{p}p$ Collisions at $\sqrt{s} = 1.8$ TeV," F. Abe et al., The CDF Collaboration, Phys. Rev. Lett. 77, 438 (1996).

111. "Properties of Jets in Z Boson Events from 1.9 TeV $\bar{p}p$ Collisions," F. Abe et al., The CDF Collaboration, Phys. Rev. Lett. 77, 448 (1996)

112. "Measurement of Λ_b^0 Lifetime Using $\Lambda_b^0 \to \Lambda_c^+ \ell^- \bar{\nu}$," F. Abe et al., The CDF Collaboration, Phys. Rev. Lett. 77, 1439 (1996).

113. "Measurement of the Lifetime of the B_s^0 Meson Using the Exclusive Decay Mode $B_s^0 \to J/\psi\phi$," F Abe et al., The CDF Collaboration, Phys. Rev. Lett. 77, 1945 (1996).

114. "Forward-Backward Charge Asymmetry of Electron Pairs Above the Z^0 Pole," F. Abe et al., The CDF Collaboration, Phys. Rev. Lett. 77, 2616 (1996).

115. "Further Properties of High-Mass Multijet Events at the Fermilab Proton-Antiproton Collider," F. Abe et al., The CDF Collaboration, Phys. Rev. D54, 4221 (1996)

116. "Ratios of Bottom Meson Branching Fractions Involving J/ψ Mesons and Determination of b Quark Fragmentation Fractions," F. Abe et al., The CDF Collaboration, submitted to Phys. Rev. D June 3, 1996. FERMILAB-PUB-96/119-E.

117. "Measurement of the $\gamma + D^{*\pm}$ Cross Section in $\bar{p}p$ Collisions at $\sqrt{s} = 1.8$ TeV," F. Abe et al., The CDF Collaboration, submitted to Phys. Rev. Lett. June 25, 1996. FERMILAB-PUB-96/152-E.

118. "Measurement of $b\bar{b}$ Production Correlations, $B^0\bar{B}^0$ Mixing, and a Limit on ϵ_B in $p\bar{p}$ Collisions at $\sqrt{s} = 1.8$ TeV," F. Abe et al., The CDF Collaboration, submitted to Phys. Rev. D August 8, 1996. FERMILAB-PUB-96/216-E.

119. "Observation of $\Lambda_b^0 \to J/\psi\Lambda$ at the Fermilab Proton-Antiproton Collider," F. Abe et al., The CDF Collaboration, submitted to Phys. Rev. D August 28, 1996. FERMILAB-PUB-96/270-E.

120. "Measurement of the Branching Fraction $B(B_u^+ \to J/\psi\pi^+)$ and Search for $B_c^+ \to J/\psi\pi^+$," F. Abe et al., The CDF Collaboration, submitted to Phys. Rev. Lett. September 9, 1996. FERMILAB-PUB-96/300-E.

121. "Observation of W^+W^- Production in $\bar{p}p$ Collisions at $\sqrt{s} = 1.8$ TeV," F. Abe et al., The CDF Collaboration submitted to Phys. Rev. Lett. September 12, 1996. FERMILAB-PUB-96/311-E.